Probing the Impact of Solvent on Lewis Acid Catalysis via Fluorescent Lewis Adducts

Amy Elizabeth Laturski

A thesis submitted to the Faculty of Graduate Studies in partial fulfillment of the requirements for the degree of Master of Science

Graduate Program in Chemistry

York University
Toronto, Ontario

July 2021

Abstract

Over the years, various multiparameter methods have been developed to measure the strength of a Lewis acid. However, a major challenge for these measurements lies in the complexity that arises from variables, such as solvent and other fundamental interactions, as well as perturbations of Lewis acids as their reaction environment changes. Herein, we evaluate the impact of solvent effects on the Fluorescent Lewis Adduct (FLA) method using a series of representative Lewis acids. The solution-state nature of the FLA method offers the ability to correlate Lewis Acid Units (LAUs) obtained from the FLA measurement with reactivity. The binding of a Lewis acid in various solvents quantitatively reveals a dichotomy between both polarity and donicity of the solvent. While not strictly separable, as solvent polarity increases observed LAU values increase; however, as solvent donicity increases observed LAU values decrease. This dichotomy was confirmed by titration data and catalytic Diels-Alder cycloaddition and hydrosilylation reactions, illustrating that solvation effects can be appropriately gauged by a LAU value determined from the FLA method.

Acknowledgments

I would like to thank my supervisors, Professor Thomas Baumgartner, and Professor Christopher Caputo for all their support and guidance. I am truly grateful in having the opportunity to be co-supervised by two amazing scientists, who have taught me so much through their courses, seminars, and meetings (in person and on zoom). Their encouragement and mentorship, along with the friendly and inclusive work environment have helped me grow and become a better scientist. I would like to thank my committee member, Professor Jennifer Chen, for her invaluable feedback and positive insight on my research project, as well as taking the time to write a letter of recommendation for my Ph.D. applications. I would also like to acknowledge my external examiner, Professor Paul O'Brien, for taking the time to be part of my M.Sc. defence.

I would also like to thank all the Baumgartner and Caputo group members, past and present for all their advice, support, and friendships throughout my time here. I would like to thank Dr. Joshua Gaffen and Jordan Bentley for mentoring me when I first joined the lab and providing support throughout my research, in particular, the time taken to edit my thesis and first published paper.

Thank you to the fantastic support staff in the department. A special thanks to Dr. Howard Hunter for his extensive knowledge, counselling, and technical support with NMR. Finally, I would like to thank my parents, my sisters, and my boyfriend, for their love, support, and encouragement throughout my academic endeavors.

Table of Contents

List of Tables

List of Figures

List of Schemes

List of Abbreviations and Symbols

Å	angstroms, 10^{-10} meters
δ	chemical shift
Δ	heat or change in
ΔH	enthalpy
ν	frequency
λ	wavelength
λ_{abs}	wavelength maximum absorption
λ_{emis}	wavelength maximum emission
μ	chemical potential
η	chemical hardness
ω	global electrophilicity index
μL	microliters, 10^{-6} mol/liter
μM	micromolar, 10^{-6} liters
bpy	benzylpyridyl
$CDCl_3$	deuterated chloroform
CIE	commission international de l'eclairage
CRANAD	named after first author C. Ran and linked to Alzheimer's disease
d	doublet
D	deuterium
DCM	dichloromethane
dd	doublet of doublets
dept	first derivative of the product
DFT	density functional theory
EC50	half maximal effective concentration
eq.	equivalent
ESP	electrostatic potential
Et	ethyl
Et_2O	diethyl ether
$E_T(30)$	Reichardt's empirical polarity parameter
FIA	fluoride ion affinity
FLA	fluorescent Lewis adduct

FLP	frustrated Lewis pair
FMO	frontier molecular orbital
GB	Guttman Beckett
GEI	global electrophilicity index
HOMO	highest occupied molecular orbital
Hz	Hertz, s^{-1}
I	intensity
k	rate constant
K	binding constant
kcal	kilocalories, 10^3 calories
LA	Lewis acid
LAU	Lewis acid unit
LUMO	lowest unoccupied molecular orbital
m	multiplet
Me	methyl
MeCN	acetonitrile
Mes	mesityl
mM	millimolar, 10^{-3} mol/litre
mmol	millimoles, 10^{-3} moles
NA	not applicable
nm	nanometers, 10^{-9} meters
NMR	nuclear magnetic resonance
OLED	organic light emitting diodes
OTf	trifluoromethanesulfonate
p	para
PCM	polarized continuum model
Ph	phenyl
PhCl	chlorobenzene
pK_a	acid strength, negative log of the acid dissociation constant
ppm	parts-per-million, 10^{-6}
ppy	phenylpyridyl
q	8-hydroxyquinolate or quartet

R	substituent
RT	room temperature
rDA	retro Diels-Alder
s	singlet
t	triplet
Tol	toluene

Chapter 1 Introduction

1.1. History of Lewis Acid-Base Chemistry

Several definitions of what constitutes an acid and a base have been developed over the years. The three most prevalent definitions of an acid and base are the Arrhenius, Brønsted-Lowry, and Lewis theories. The Arrhenius theory, proposed in 1884, defines an acid as a substance that dissociates in water to form hydrogen ions and a base as a substance that dissociates in water to form hydroxide ions.[1] Unfortunately, the Arrhenius theory only describes acid-base chemistry in an aqueous solution. This led to the development of the Brønsted-Lowry and Lewis theories. In 1923, Johannes Brønsted and Thomas Lowry introduced a more general definition of acids and bases, defining an acid as a proton donor and a base as a proton acceptor.[1] This theory overcomes the restrictions of the Arrhenius theory, unfortunately, it cannot account for all acids and bases.

In 1916, Gilbert Lewis introduced the concept of Lewis acidity and basicity, published in his work titled *The Atom and the Molecule*. In it, he classifies molecules as either electron pair acceptors or electron pair donors when undergoing certain types of reactions, later defined in 1923 as Lewis acids and bases, respectively (**Scheme 1-1**).[2,3] Lewis' theory provides a more general scope, encompassing a wide range of chemistry, as it is based on structure and bonding. The classical reactivity model of Lewis acids and bases predicts the interaction of the electrons in the highest occupied molecular orbital (HOMO) of the Lewis base with the lowest unoccupied molecular orbital (LUMO) of the Lewis acid to form a dative bond. A prototypical example is ammonia-borane; the lone pair of the nitrogen is the electron pair donor, making the amine the Lewis base, and the vacant p-orbital of the borane is the electron pair acceptor, making it the Lewis acid. By donating electron density from the HOMO of the Lewis base to the LUMO of the Lewis acid, the donor-acceptor adduct affords a lower HOMO than the Lewis base and a lower LUMO than the Lewis acid, resulting in a favorable interaction, while not formally generating a bonding interaction. The concept of Lewis acids and bases play a vital role in our understanding of modern transition metal and main group chemistry.[4–6]

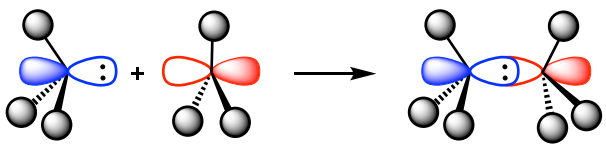

Scheme 1-1. The formation of the classical Lewis acid-base adduct.

1.2. Applications of Lewis Acid Chemistry

1.2.1. Traditional Lewis Acid Catalysis

Lewis acids have found numerous applications in organocatalysis[4,7] and transition metal chemistry.[8,9] Various type of Lewis-acid-catalyzed reactions have been developed over the years and have become classical reactions in forming new carbon-carbon bonds or carbon-heteroatom bonds. Some examples include, the Friedel-Crafts reaction, the Aldol reaction, the Sakurai reaction, cationic olefin polymerization, various pericyclic processes, such as the Diels-Alder reaction, and the hydrosilylation reaction.[10] These classical Lewis-acid-catalyzed reactions have significantly impacted the field of organic and main-group chemistry.

In 1877, Charles Friedel and James Crafts develop the Friedel-Crafts reactions: Friedel-Crafts alkylation (**Scheme 1-2a**) and Friedel-Crafts acylation (**Scheme 1-2b**).[11,12] In the presence of a strong Lewis acid, such as aluminum chloride ($AlCl_3$) or ferric chloride ($FeCl_3$), both reactions proceed by an electrophilic aromatic substitution mechanism to form a new carbon-carbon bond. These reactions have become a staple in synthetic chemistry, allowing chemist to introduce functional groups directly onto the aromatic ring. In addition, modification to the Lewis acid catalysts and substrates has improved reaction efficiency and selectivity for the Friedel-Crafts reactions of arene alkylation and acylation making these reactions prominent in various chemical industries.[13,14]

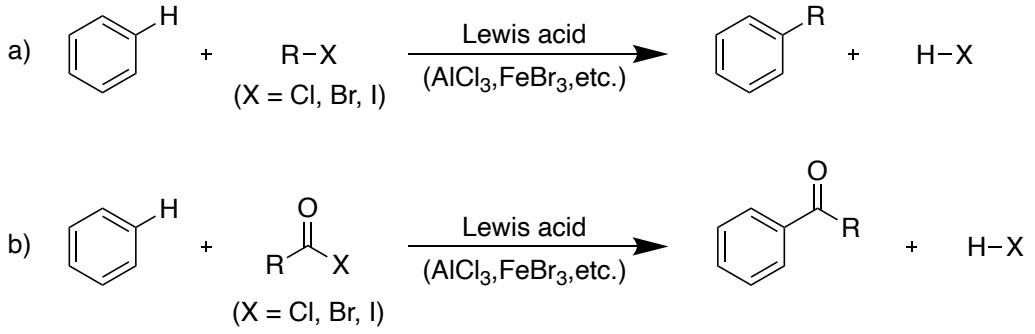

Scheme 1-2. Friedel-Crafts reactions of arenes; a) alkylation, b) acylation.

Within the 20th century, another well-established Lewis acid catalyzed reaction that has been recognized as a vital tool for chemists in synthesizing new carbon-carbon bonds is the Diels-Alder cycloaddition. The Diels-Alder reaction introduced in 1928 by Otto Diels and Kurt Alder has become a staple reaction for synthetic chemists due to its proficiency in synthetizing complex molecules from relatively simple starting materials in a predictable manner.[15] This chemical reaction involves a conjugated diene and a substituted

alkene, commonly known as a dienophile, to form a six membered ring (**Scheme 1-3**). At standard temperature (25 °C), the Diels-Alder cycloaddition proceeds slowly, however, this reaction can be greatly accelerated by Lewis acids via complexation to the dienophile.[16] Over the years, expressed through mechanistic studies and frontier molecular orbital (FMO) theory, the donor–acceptor interaction between the dienophile and the Lewis acid catalyst results in the LUMO of the dienophile being significantly stabilized, leading to a smaller $HOMO_{diene}$–$LUMO_{dienophile}$ energy gap, which lowers the activation barrier and enhances the rate of the Diels-Alder cycloaddition.[16]

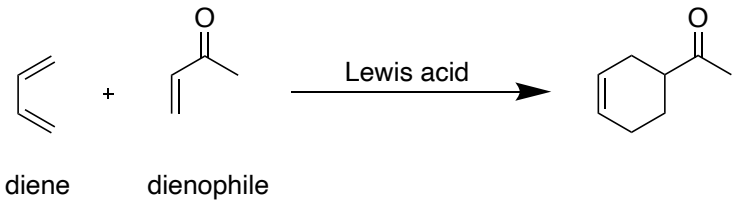

Scheme 1-3. Diels-Alder reaction via [4+2]-cycloaddition of a conjugated diene and a substituted alkene.

The use of Lewis acids in the Diels-Alder cycloaddition offers good control over regio- and stereochemical outcomes, which has led to various synthetic applications, for instance, being used in the agrochemical and pharmaceutical industries.[17] Since the discovery of this classical reaction, it has become a prototypical example of a pericyclic reaction with a concerted mechanism. Over the years, various kinds of pericyclic reactions have been developed, such as electrocyclization, ene reactions, sigmatropic rearrangements, chelotropic reactions, and group-transfer reactions.[10] In particular, Lewis acids can be employed in many of these reactions, for instance, the Nazarov reaction is a type of electrocyclization, that uses Lewis acids as a promoter for the synthesis of cyclopentenones.[18]

In addition to main-group Lewis acids, transition metals can also act as Lewis acids by accepting electron pairs from donor Lewis bases to form complex ions. Transition metal catalyzed reactions are also key to synthesizing new carbon-carbon as well as carbon-heteroatom bonds. A prime example is the hydrosilylation reaction, it has become one of the most useful Lewis-acid catalyzed reactions in forming organosilanes and organosilicones.[19] Hydrosilylation occurs via addition of and H-Si species to an unsaturated bond, utilizing a main-group or transition metal Lewis acid catalyst (**Scheme 1-4**). Over the years, main-group Lewis acids have become the primary catalyst for hydrosilylation reactions. Although the utility of platinum catalysts has been widely recognized in this field, these precious metals unfortunately are not ideal, thus chemists have moved towards developing main group Lewis acids catalysts that are more efficient, selective and cheaper.[20] In the search for novel Lewis acids for catalysis

new and old, these well studied Lewis-acid catalyzed reactions; Friedel-Crafts reactions, Diels-Alder reaction, and hydrosilylation, have become the standards by which to test the potential of new Lewis acid catalysis processes.

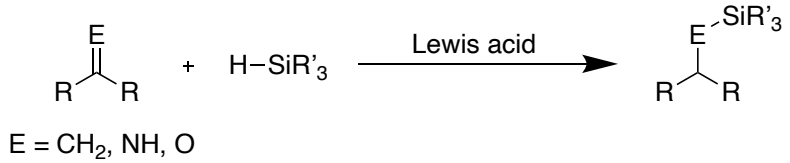

Scheme 1-4. Hydrosilylation via addition of H-Si across unsaturated bond.

1.2.2. Frustrated Lewis Pairs and Metal-Free Catalysis

As the field of Lewis acid-base chemistry developed, and new catalytic applications for Lewis acids were introduced, exceptions to Lewis' concept were discovered. In the subsequent years, numerous reports illustrated deviations from the formation of the classical Lewis acid-base adduct. The first exception, reported was in 1942 by H.C. Brown, which discussed the impact of steric strain on the Lewis acid-base adduct.[21] He observed no adduct formation in the presence of BMe_3 and 2,6-lutidine (**Scheme 1-5a**); whereas the expected donor-acceptor adduct was generated with BF_3 and 2,6-lutidine, due to the less sterically encumbered system. In the following years, Witting and Rückert in 1950 demonstrated the ring-opening reaction of THF consisting of a bulky trityl anion and BPh_3 as the Lewis pair (**Scheme 1-5b**).[22] A few years later, Wittig reported another non-classical adduct, the addition of PPh_3 and BPh_3 across benzyne to form the ortho-disposed phosphonium borate zwitterion (**Scheme 1-5c**).[23] In similar work, Tochtermann reported in 1966, the 1,2-addition of trityl anion and BPh_3 to 1,3-butadiene, rather than the anticipated olefin polymerization (**Scheme 1-5d**).[24] Finally, Erker reported in the 1990's, a phosphorus ylide undergoing a *para*-attack on the pentafluorophenyl group of $B(C_6F_5)_3$, forming a linked phosphonium fluoroborate zwitterion rather than the classic Lewis adduct (**Scheme 1-5e**).[25,26]

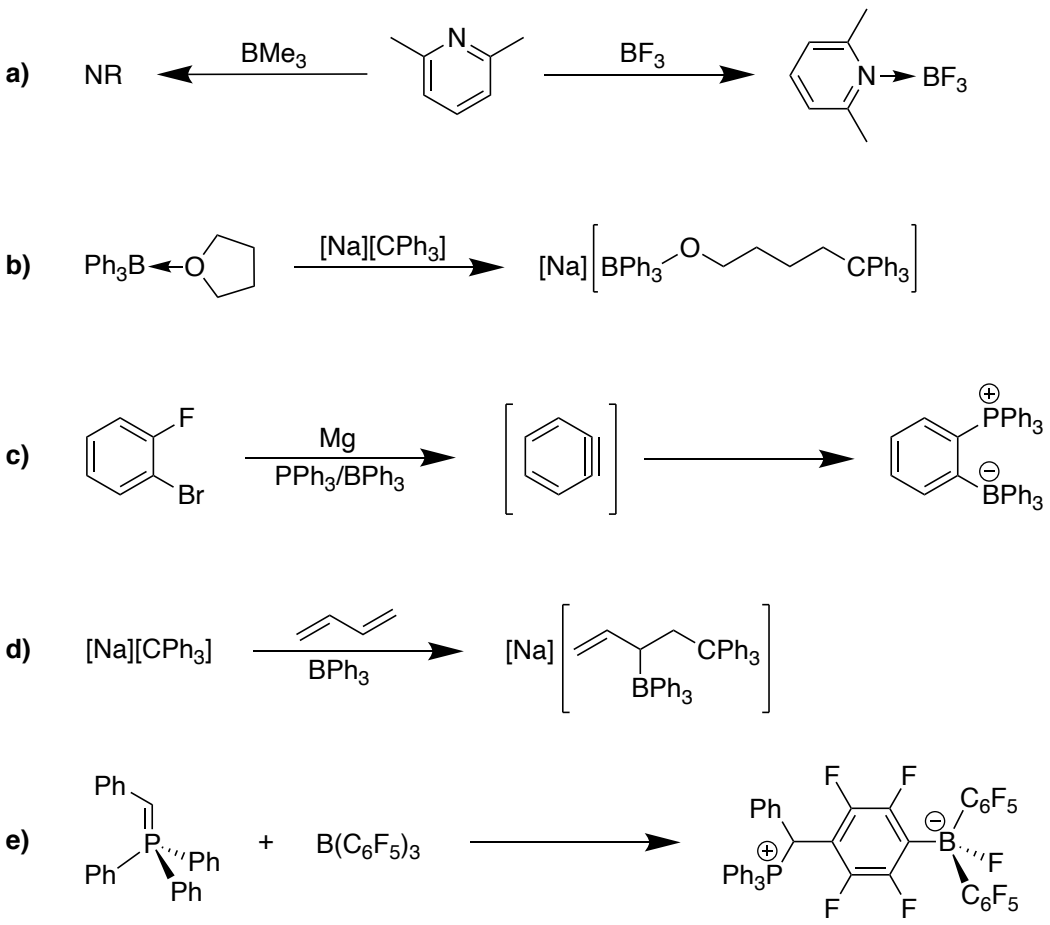

Scheme 1-5. Exceptions to the classical Lewis acid-base adduct.

These deviations opened the doors to a new concept called Frustrated Lewis pair (FLP) chemistry, which was coined by Stephan and coworkers to described sterically encumbered Lewis acids and bases that are unable to form the classical Lewis acid-base adduct (**Scheme 1-6**).[27] The Lewis acids and bases in FLPs contain bulky substituents that prevent adduct formation, resulting in coordination of the acid and base without stabilizing the HOMO and LUMO by generating an adduct. FLPs can exploit the unquenched reactivity between the Lewis pair and induce further reactivity with other molecules, facilitating novel reactions, in particular small-molecule binding and activation.[28]

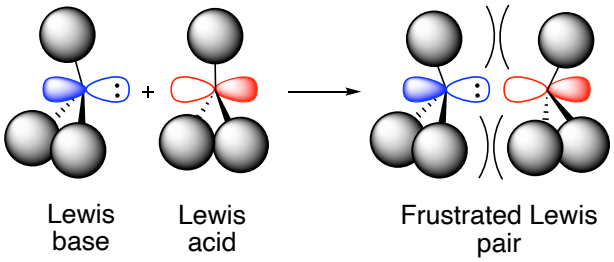

Scheme 1-6. The formation of frustrated Lewis pairs.

For instance, dihydrogen activation before FLP chemistry had been almost exclusively conducted using transition metals by utilizing the d-orbitals to interact with both dihydrogen σ and σ^* orbitals, something not accessible to lighter and non-transition metal elements.[29] However, this perspective changed in 2006, when Stephan and co-workers reported the first example of metal-free reversible H_2 activation (**Scheme 1-7**).[30] They developed a sterically encumbered phosphino-borane system, $Mes_2P(C_6F_4)B(C_6F_5)_2$ that could heterolytically cleave dihydrogen to form the zwitterionic salt, $Mes_2PH(C_6F_4)BH(C_6F_5)_2$. This zwitterionic salt when heated to elevated temperatures, 150°C, could release hydrogen gas and regenerate the linked phosphine-borane species. This remarkable reaction has opened the field to other organomain-group catalyst-driven reactions, that would have normally been attributed to transition metal chemistry, with the donor and acceptor orbitals acting in a similar fashion to the lobes of the d-orbitals in transition metals.[31–34] As such, a wide range of electron donors and acceptors, in which steric demands precluded dative bond formation, have been explored.[26]

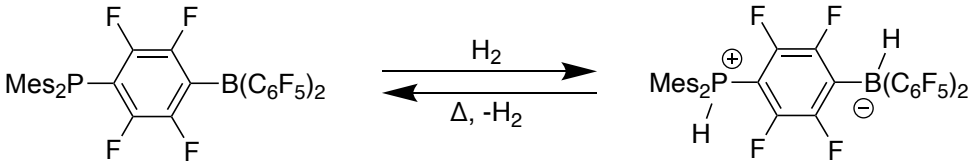

Scheme 1-7. First example of metal-free reversible H_2 activation.

In the ensuing years, various examples of both intramolecular and intermolecular FLPs have emerged, demonstrating the capability of activating hydrogen or reacting with a variety of other substrates, such as N_2O,[35] CO_2,[36] alkenes,[37] and alkynes. In addition, FLP chemistry has also expanded to include a wider range of Lewis acids and bases in the efforts to make more air- and moisture-stable FLPs and chiral FLPs that can achieve specific reactivity.[38] These developments have uncovered new reactivity of main group systems and led to advances in metal-free catalysis.[39] In addition, the concept of FLP chemistry has found applications in several other areas in the chemical sciences beyond main group chemistry. For instance,

with applications in organic, polymer and radical synthesis as well as in the diverse area of materials chemistry.[28] Since the discovery of FLP chemistry, the field of Lewis acids has broadened dramatically, bringing forth a new interest in Lewis acid-base development.

1.2.3. Functional Main-Group Materials

Lewis-acid chemistry has recently been used in the advancement of materials chemistry; the unique structural and bonding environments of main-group elements offer promising avenues towards new functional materials.[40] In particular, the versatile chemistry of boron has grown beyond its conventional use in organic chemistry (i.e., as reagents and catalysts) and has impacted various facets of material sciences.[40]

In 1972, Williams and coworkers reported the first functional material using boron.[41] They incorporated bulky mesityl substituents around the boron center to afford a sufficiently stabilized π-electron system, that when combined with π-electron-donating groups such as borylaniline systems (**Scheme 1-8a**), they provided unique photophysical properties owing to the intramolecular charge-transfer transitions. Nearly a decade later, Kaim reported the electrochemical properties for this borylaniline system.[42] In the following years, various π-conjugated systems consisting of the Mes_2B-functionality as the electron-accepting group began being applied to numerous functional materials. For instance, unique photophysical properties can be demonstrated by introducing the π-system consisting of the Mes_2B- group with dimethylamine substituents as the electron-donating group (**Scheme 1-8b**), offering applications as a non-linear optical and two-photon-absorbing material.[43,44] Another avenue used the incorporation of the Mes_2B- groups to the terminal position of oligothiophenes (**Scheme 1-8c**) to develop hole-transport materials.[45,46] Also, by incorporating the Mes_2B- groups to the lateral positions of the oligothiophene (**Scheme 1-8c**), a strong fluorescence can be activated, making these π-conjugated systems an ideal material for turn-on/off fluorescence sensors in fluoride or cyanide sensing.[47] As a result of these initial compounds, a wider variety of boron-containing π-conjugated systems have been introduced with a broader range of functional groups,[40] followed by an incorporation into polymeric materials that contain other main-group elements.[48]

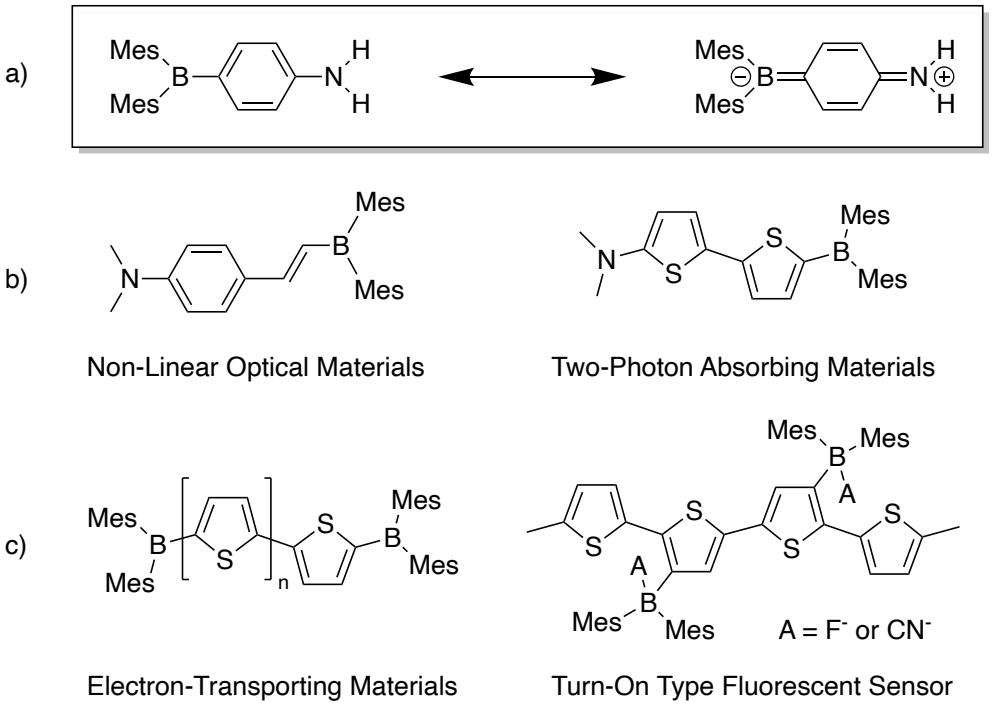

Scheme 1-8. Examples of Mes_2B-substituted functional materials.

The field of functional organo-main group hybrid materials has evolved into several diverse and extensive subfields with applications in optoelectronics, sensing, batteries, as well as in the biomedical fields.[40,48] In 1987, Tang and co-workers reported the first example of an organic light-emitting diode (OLED) composed of a N,O-chelate compound Alq_3 (q = 8-hydroxyquinolate) (**Scheme 1-9**).[49] This compound is a well-known green emitter and an electron-transport layer material in OLEDs that has demonstrated good performance, and an increased lifetime compared to blue emitting OLEDs. More recently, functional main-group materials, specifically tetracoordinated boron materials have expanded into biological imaging.[40] These luminogens offer bright, color-tunable emission that are high selective and efficient in monitoring biological targets. For example, in 2014, Ran and co-workers developed a compound called CRANADs which are a set of two-photon absorbing boron coordinated curcumoids that are used to identify β-amyloid deposits associated with Alzheimer's disease (**Scheme 1-9**).[50] As the field continuous to grow, the next step is developing fully integrated electronic systems composed of various functional main-group material devices. The Bao group at Stanford University has pioneered the research of intrinsically stretchable electronic skin and has fabricated the first skin-like electronic sensor system (**Scheme 1-9**);[51,52] composed of multi-functional sensors to obtain various bio-signals from the human body, integrated circuits to electrically process the signals, light-emitting diodes to display and convey the analyzed data to the user, as well as power supplies. Many of these specific applications that are

incorporated into electronic skins utilize Lewis acid materials, for instance, incorporating BN-heterocycles, such as (ppy)$BMes_2$ or (bpy)$BMes_2$ into OLEDs,[40] or Lewis-acid dopants for organic semiconductors into thin-film transistors.[53] The use of Lewis acids in functional materials has grown tremendously, the continuous development of new Lewis acids and the desire to constantly improve the current properties of functional materials has increased activity in the field of materials chemistry.

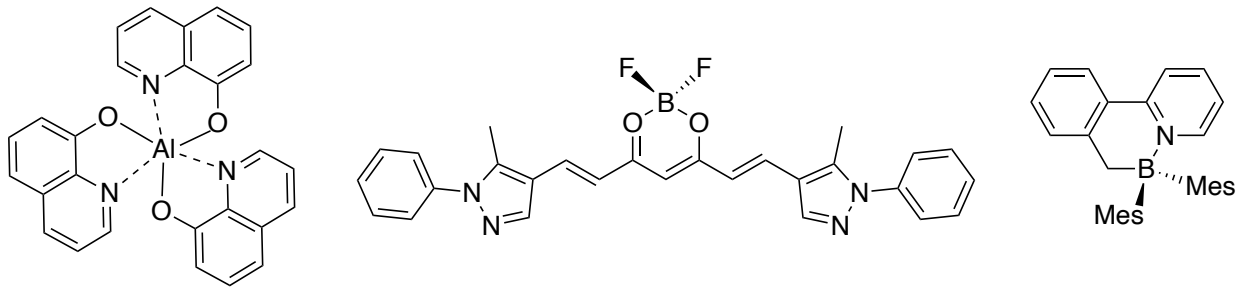

Scheme 1-9. Applications of Lewis acids in functional materials.

1.3. Methods for Measuring Lewis Acidity

As Lewis-acid chemistry begins to permeate other disciplines, the need to correlate the acceptor strength of a Lewis acid to their efficacies in their proposed application becomes vital. However, determining the specific reactivity of Lewis acids remains ambiguous, creating challenges in selecting an appropriate Lewis acid to achieve a desired reaction. Currently, Lewis acidity cannot be described by a single measured property, and several parameters, such as electronics, steric effects, and solvent interactions must be considered jointly in order to select a potent Lewis acid catalyst,[54–56] whereas Brønsted acids can be measured by the pKa scale.[57] The proton transfer is a key integral to the Brønsted acid–base interaction which allows for a meaningful quantitative comparison.[1,2] Therefore, the need to develop a Lewis acidity scale, similar to the pKa scale for Brønsted acidity, is highly desired, yet challenging.

Historically, several different multiparameter models have been developed as a quantitative description of Lewis acidity. One of the most employed measures of Lewis acidity currently used in the literature, is the Gutmann-Beckett (GB) method, owing in part to its experimental ease.[58,59] In this method, the Lewis acid is treated with triethylphosphine oxide, Et_3PO, to form the Lewis acid-base adduct between the Lewis basic oxygen of the phosphoryl and the Lewis acidic center (**Scheme 1-10a**). The back donation of the phosphoryl (oxygen to phosphorus) is weakened due to the donation of electron density from the oxygen to the Lewis acid. The phosphorus center becomes more electron-deficient, resulting in the ^{31}P NMR resonance shifting downfield relative to the free Et_3PO. The change in the chemical shift, $\Delta\delta$, is directly proportional to the strength of the Lewis acid. Other related NMR spectroscopy techniques have also been reported by the Childs,[60] and Hilt groups.[61] The Childs method utilizes an α,β-unsaturated ketone or aldehyde that is treated with a Lewis acid (**Scheme 1-10b**). Upon coordination, the chemical shift in the ^1H NMR resonance for the β-proton on the C=C bond is shifted more downfield relative to the free α,β-unsaturated ketone or aldehyde. The change in the chemical shift, $\Delta\delta$, is consistent with the strength of the Lewis acid. More recently, in 2000, Hilt reported the use of a [D_5]pyridine probe and correlated the change in ^2H NMR to the Lewis acidity (**Scheme 1-10c**). Unfortunately, these experimental methods are strongly dependent on the Lewis base that is used for the measurement. By utilizing a hard donor, such as Et_3PO, it prefers to bind with a hard Lewis acid, whereas a softer Lewis base, like crotonaldehyde, will prefer a softer Lewis acid. For instance, in the GB method, the Lewis acidity order for tris(pentafluorophenyl)borane, $B(C_6F_5)_3$, versus tris(pentafluorophenyl)borate, $B(OC_6F_5)_3$ is the complete opposite for the Childs method.[62] Indicating that hard-soft acid-base effects play a significant role in impacting the Lewis acidity for these spectroscopy methods. In addition, spectroscopic methods rely on

core-shell electrons, which may not be strongly impacted by the dative interaction between the Lewis acid and the Lewis base.

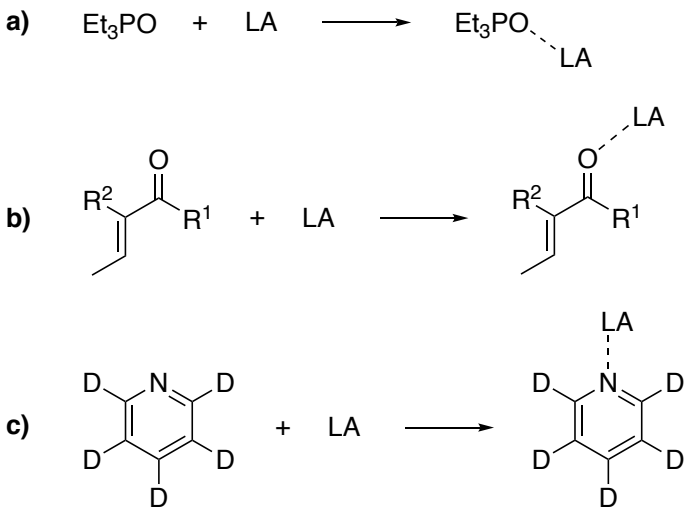

Scheme 1-10. Spectroscopy methods used for measuring Lewis acidity (LA = Lewis acid); a) Gutmann-Beckett method, b) Childs method, c) Hilt method.

Besides experimental methods, computational methods have become a more prominent area of study, offering the advantage to quickly calculate Lewis acidity without requiring the need to synthesize each individual compound and subject them to an experimental method. In particular, fluoride ion affinity (FIA), introduced by Christe et. al., has become a powerful computational tool in evaluating Lewis acidity;[63] due to size and basicity of the ion, it can interact with most Lewis acids. The FIA calculates the binding affinity of the Lewis acid with a fluoride ion (FIA = -ΔH), determined using quantum chemical calculations in isodesmic reactions, **Equations 1-1**, **1-2**, and **1-3**.

$$CF_3O^- + LA \rightarrow CF_2O + LA\text{-}F^- \quad \textbf{(1-1)}$$

$$CF_2O + F^- \rightarrow CF_3O^- \quad \textbf{(1-2)}$$

$$LA + F^- \rightarrow LA\text{-}F^- \quad \textbf{(1-3)}$$

Christe and co-workers reported the FIA of a series of Lewis acids calculated against the enthalpy of formation of the adduct of COF_2 and F^-, which is known experimentally, and used as a standard against FIA calculations.[63] Utilizing this known value, Hess' Law was applied to obtain the calculated absolute FIA of each Lewis acid. For the FIA, the energies of the optimized structures of both the Lewis acid and

its fluoride adduct, as well as those of COF_2 and CF_3O^- are required. Other ion affinity methods have also been explored. In analogy to FIA, Krossing and co-workers have calculated Lewis acidity using hydride ion affinity and methyl ion affinity.[64] Both methods are defined and determined in the same way as FIA, except with different references to the respective ion. Unfortunately, an underlying issue with these methods is that they do not measure general Lewis acidity; rather they are, more accurately, measures of fluoridophilicity and hydrophilicity, respectively.[63,64] In 1999, Parr and co-workers introduced the global electrophilicity index (GEI),[65] built upon previous work from Maynard and co-workers to measure Lewis acid strength in the absence of a Lewis base.[66] The GEI is a base-independent metric of Lewis acidity, the values calculated are derived solely from the energies of the HOMO and LUMO of the optimized Lewis acid in question. Thus, overcoming one of the challenges of the previous methods, by provides a simple quantitative assessment of Lewis acidity that does not rely on a specific base.

The GEI (ω) measures the ability of a molecule to behave as an electrophile, taking up electrons in a vacuum, and is defined by **Equation 1-4**:

$$\omega = \frac{\mu^2}{2\eta} \qquad \textbf{(1-4)}$$

where μ is the chemical potential and η is the chemical hardness, calculated from **Equations 1-5** and **1-6**.[67]

$$\mu = \frac{1}{2}(E_{HOMO} + E_{LUMO}) \qquad \textbf{(1-5)}$$

$$\eta = E_{LUMO} - E_{HOMO} \qquad \textbf{(1-6)}$$

Based on the GEI equation, a more electronegative and softer molecule will demonstrate a more electrophilic behaviour.[67] Recently, Stephan and co-workers have reported the Lewis acidity for a wide range of different main group systems using the GEI.[68] Unfortunately, there are drawbacks associated with the GEI, as seen with the other methods for quantifying Lewis acidity. For instance, the GEI is a better gauge of Lewis acidity for softer Lewis acids than for hard Lewis acids, correlating more closely to the the Childs method.[68] In addition, Lewis acids that are within the same chemical family can only be compared in the GEI, i.e. various boranes GEI values can be compared to each other, however directly comparing the GEI values of boranes to those of carbocations would led to inaccurate comparisions as the computational results only compares the Lewis acidity of a compound in a specific configuration and does not take into account other properties that may be influencing Lewis acidity.[68]

Although these multiparameter methods have generally been adopted by the scientific community, they unfortunately have given inconsistent results throughout the literature. For instance, theoretical methods only model the Lewis acid in one geometrically optimized state,[63,68] despite, for example, something like $AlCl_3$ having various Lewis acidic species in solution.[69] Also, depending on the Lewis base and parameter used, certain multiparameter methods are a better gauge of Lewis acidity for softer Lewis acids than for harder Lewis acids,[68] thus struggling to measure specific types of Lewis acids, such as organometallic systems for the Gutmann-Beckett method,[58] or ionic systems for fluoride ion affinity.[64] In addition, these methods also lack necessary details, such as solvent effects or fundamental interactions and perturbations of Lewis acids, as their reaction environment changes. While these experimental and computational methods are suitable for the estimation of Lewis acidity, determining the specific reactivity of Lewis acids remains ambiguous and difficult to predict. A major drawback lies in the complexity and the inclusive results of these techniques in establishing a quick and accurate Lewis acidity value for a large library of compounds in varying reaction environments. With the field of Lewis acid-base chemistry now bustling with activity due to the developments of FLP and metal-free catalysis,[28] along with the various facets of materials science,[40] establishing a method for measuring Lewis acidity that is simple, direct and less prone to errors, is highly desired.

1.4. A New Method: The Fluorescent Lewis Adduct (FLA)

Fluorescence spectroscopy has proven to be an ideal technique for sensing due to its high sensitivity, (i.e., micro-detection limits), versatility (i.e., inert-atmosphere or in-vivo conditions) and the ability to easily detectable a distinct change in luminescent properties (i.e., Lewis base probe).[70] As a result, fluorescent probes have expanded their applications, finding utility as sensors for anions (i.e., F^- and CN^-),[48,71] small molecules and various biological systems.[40,70] Thus, a fluorescence-based method has the potential to overcome many of the limitations seen with the previous methods used for measuring Lewis acidity.

In 2019, the Baumgartner and Caputo groups introduced a new methodology based on fluorescence spectroscopy to enumerate Lewis acidity, termed Fluorescent Lewis Adducts (FLA).[72,73] This method derives a basis for Lewis acidity by utilizing a series of fluorescent dithieno[3,2-*b*:2',3'-*d*]phosphole oxide probes,[74–76] that when bound to a Lewis acid in solution, undergo a bathochromic shift (**Scheme 1-11a**).[73] The degree of the bathochromic shift is proportional to the Lewis acid strength, as the method is based on the coordination of the Lewis acid altering the polarity of the exocyclic P=O bond by reducing the negative hyperconjugation of the π-bond (**Scheme 1-11b**).[73,77] For example, a strong LA will increase the polarity of the P=O bond, strengthening the σ^*-π^* interaction, which will lower the LUMO, and lead to a larger bathochromic shift (red-shifted emission).

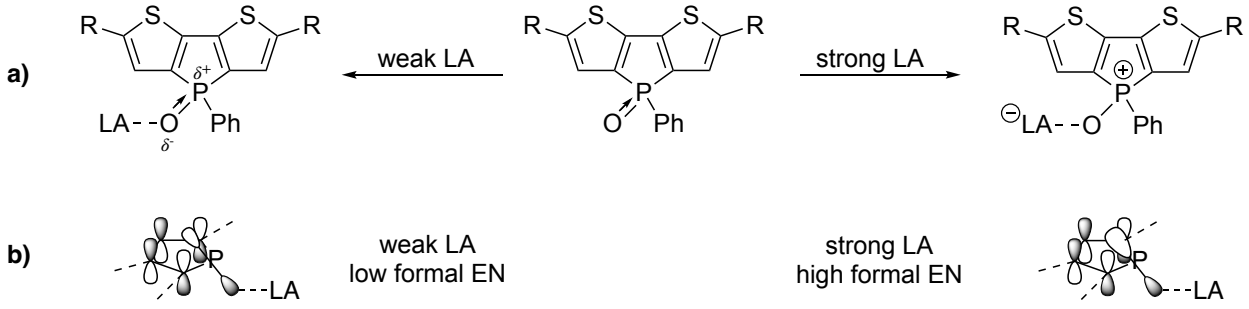

Scheme 1-11. Concept for Fluorescent Lewis adduct method (LA = Lewis acid); a) Lewis-acid strength impacting P=O bond polarization, b) Lewis-acid strength impacting the energy of orbitals for the σ^*-π^* interaction.

The commission international de l'éclairage (CIE) coordinates of the FLAs are the foundation of the method, as chromaticity is determined from the entirety of the emission spectrum of a given compound.[72,73] The CIE space is defined within the visible spectrum (380 nm to 780 nm), where each

color is prescribed by the unitless variables x, y, and z, representing color as a function of hue, saturation, and intensity.[78]

The FLA method differs from typical Lewis-acid measurements in that it leverages the impact of the Lewis acid on several Lewis bases to determine the binding with an "ideal" Lewis base. To eliminate the dependency on a single Lewis base, eight dithienophosphole oxide probes with different emission colors were used (**1-8**) (**Scheme 1-12**).[72]

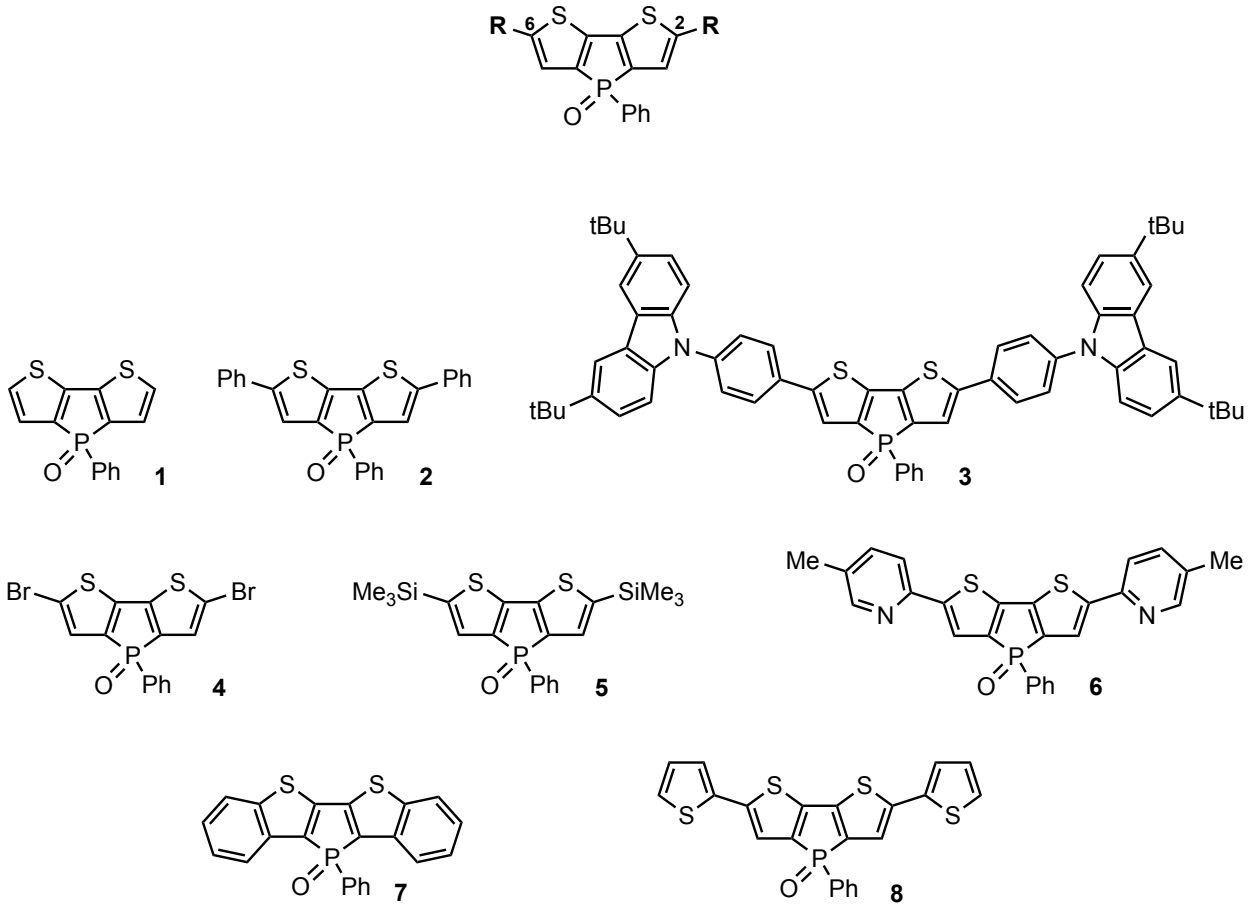

Scheme 1-12. Dithienophosphole probes **1-8** used in the Fluorescent Lewis adduct method as the Lewis base.

These probes are highly stable, and their optical properties can be easily modified to span the chromaticity space by altering the conjugated scaffold via the 2,6-position of the thiophene framework, without compromising the general function of the phosphole oxide unit.[79] The different π-conjugated backbones can translate to different Lewis basicities for the phosphoryl groups,[79] whose CIE coordinates can be fit parabolically (**Figure 1-1**).[72] The parabolic function obtained expresses the CIE coordinates of any given

dithienophosphole oxide probe, which means that any point within the curve, restricted to the boundaries of the CIE diagram, corresponds to a phosphole with a different degree of σ^*-π^* interaction and therefore Lewis base strength. Similarly, to the free probe parabola, the FLA parabola is composed of eight measured adducts, the eight Lewis base probes to a single Lewis acid.[72] The chromaticity of these eight FLAs generated a parabolic trend within the CIE space. Thus, utilizing these two parabolic functions, the free probe parabola, and the FLA parabola, we can conclude that the intercept of the two functions describes an *ideal* FLA binding pair (**Figure 1-2**).[72,73]

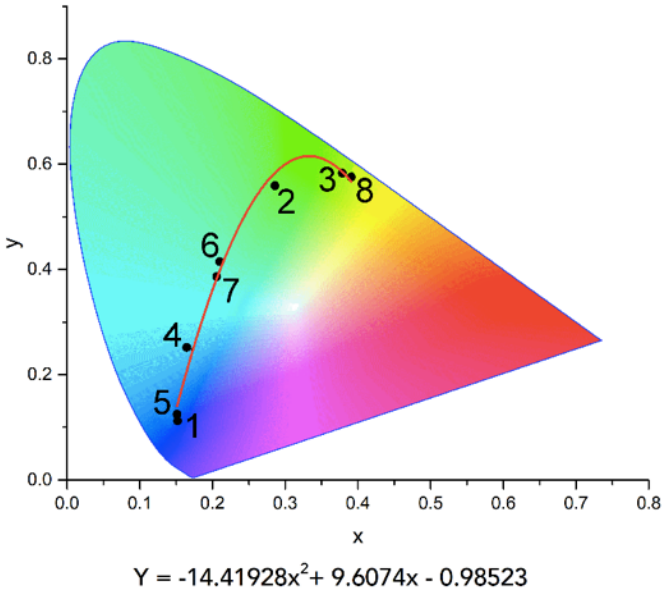

Figure 1-1. CIE diagram overlaid with the parabolic fit in toluene of the eight dithienophosphole probes. Figure is adapted with permission from reference [72] (© 2020, American Chemical Society).

To be more specific in measuring the Lewis acidity, a vector-based approach was used to exploit the full CIE diagram.[72] As previously stated, chromaticity defines color in a three-coordinate space, however, only two coordinates are needed, since all three coordinates will equal to one, i.e., $x + y + z = 1$.[78] Since the coordinates of color are radial, a parabolic fitting approach was used for the resulting FLA chromaticities with each Lewis acid and the dithienophosphole oxide Lewis base probes. We used the x and y coordinates that define the color at the intersection point of the two parabolas to accurately interpolate the relative Lewis acid strength defined in our method as Lewis acid units (LAUs).[72,73] These vectors were at fixed points, at the apex (maximum green) and the root (maximum red) of the dithienophosphole oxide probe parabola, corresponding to the weakest and strongest possible Lewis basic dithienophosphole (**Figure 1-2**).[72] The ratio of the magnitude of the two vectors (i.e., maximum green and maximum red) was then used

to define the Lewis acid strength. We observed that an increase in the x-coordinate corresponded to an increase in the Lewis-acid strength, whereas an increase in the y-coordinate correlated to a decrease in the Lewis-acid strength. This two-dimensional vector-based approach, affords the system high versatility,[72] while the use of fluorescence, and chromaticity specifically, affords a high sensitivity.[70] Consequently, widening the measurable LAU range from zero to theoretically infinity allows for a wide range of Lewis acids, such as classical main-group, cationic, and transition-metal-based Lewis acids to accurately be measured and compared.[72] Similarly, this method can theoretically be performed in any solution, which we refer to as a "solution-state measurement". As long as the Lewis acid is not independently fluorescent, the FLA method provides the opportunity to gain important insight into the characteristics and reactivity of Lewis acids.

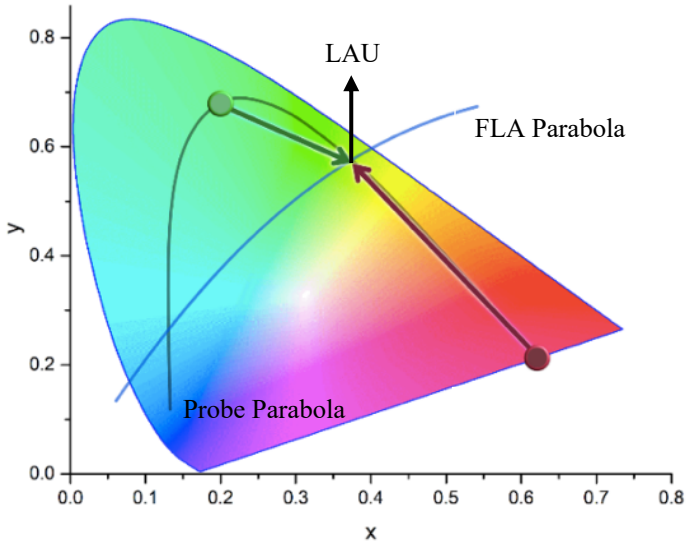

Figure 1-2. Measuring Lewis acidity via the FLA method (LAU = Lewis acid units). Figure is adapted with permission from reference [72] (© 2020, American Chemical Society).

1.5. Scope of Thesis

Thus far, the FLA method has shown itself to be robust, accurate and simple at measuring the nature of Lewis acidity in solution. The use of fluorescence and chromaticity, along with the solution-state nature of this methodology, affords an extreme sensitivity towards small structural and electronic perturbations that allow us to measure the Lewis acidity of a Lewis acid as it may act in real reaction conditions. We herein report that certain aspects that impact the Lewis acidity of solution may be directly inferred via a series of tests using our method, such as the impact of solvent. Thus, the focus of this research was to explore the impact of solvent effects in the FLA method and showcase the variability of Lewis acidity in select species with varying polar solvents. The results obtained from the methodology have provided us with insight into additional aspects of Lewis acid catalyzed reactions and allowed us to correlate the FLA method directly to the efficacy of a Lewis acid in catalysis.

Chapter 2 Results and Discussion

2.1. Impact of Solvent on the Dithienophosphole Oxide Probes

The FLA method utilizes eight dithienophosphole oxide Lewis base probes whose emission chromaticities span the CIE diagram. It was previously shown that only three or four are needed for appropriate accuracy.[72] Thus, we sought to utilize the simplest dithienophosphole oxide probe (**1**) which demonstrated a pronounced blue luminescent nature (λ_{emis} = 446 nm).[74] Next, we utilized a benzo-fused dithienophosphole oxide probe (**7**) with a blue-green emission (λ_{emis} = 483 nm),[75] and a phenyl-extended dithienophosphole oxide probe (**2**) that had an emission (λ_{emis} = 520 nm) in the green region of the optical spectrum.[74] Finally, to maximize the use of the color space we introduced the thienyl-extended dithienophosphole oxide probe (**8**) which had a pronounced green-yellow emission (λ_{emis} = 545 nm).[75] These four probes, (**1**, **2**, **7**, and **8**) appropriately span the CIE diagram and were used to measure their respective emission profiles in varying polar solvents. The selected solvents ranged in polarity from non-polar to polar based on the Dimroth-Reichardt $E_T(30)$ parameter derived from the betaine indicator dye; toluene (Tol, 33.9 kcal/mol), diethyl ether (Et_2O, 34.6 kcal/mol), chlorobenzene (PhCl, 37.5 kcal/mol), dichloromethane (DCM, 41.1 kcal/mol), and acetonitrile (MeCN, 46.0 kcal/mol).[80] Previously, the FLA method had been solely performed in toluene for its benign reactivity and the sufficient solvation of our probes and measured substrates.[72,73] We were interested to see, if we would observe a variance in the emission of the probes based on the solvent used. As reported in the literature, some phosphorus-bridged bithiophene species have shown solvatochromism. For instance, the emission maxima of the following species, compounds **9**, **10**, **11**, and **12** (**Scheme 2-1**), have all demonstrated positive solvatochromism effects (a red-shifted emission with increasing solvent polarity) indicated by the electronic state after excitation being more polar than the ground state.[81–83]

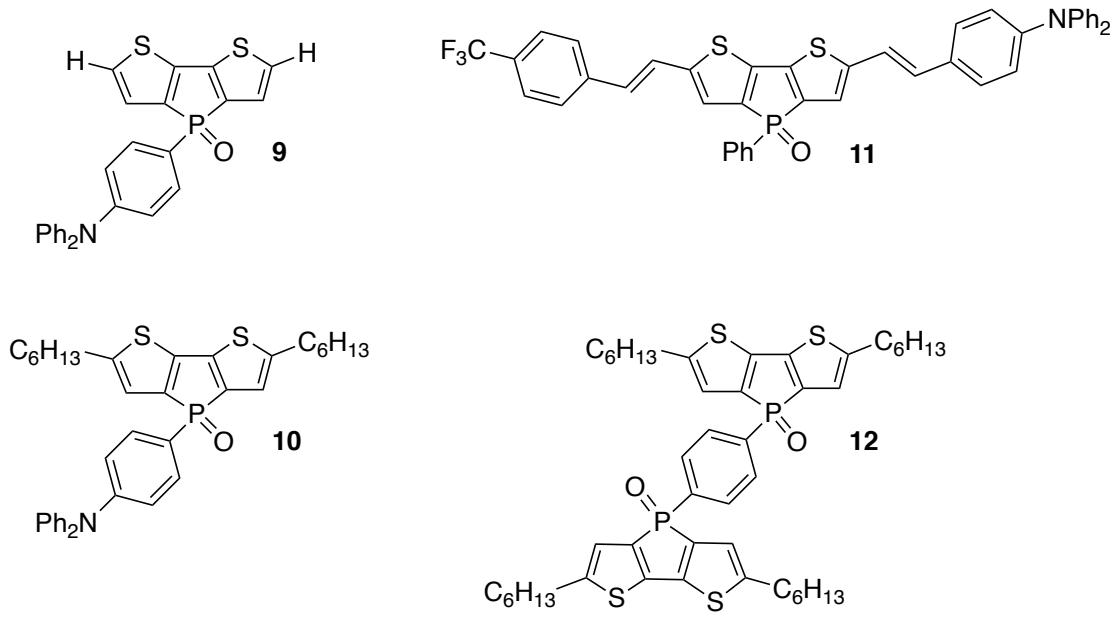

Scheme 2- 1. Phosphorus-bridged bithiophene species that have shown solvatochromism.

Taking this into account, we measured each dithienophosphole probe and generated a corresponding fit function in each solvent. We then, overlaid the probe parabolas in the varying solvents and observed that the polarity of the respective solvents was found to not affect the emissions of the probes (**Figure 2-1**). The lack of any notable solvatochromism with the Lewis base probes in the varying polar solvents enabled us to infer that any observed solvatochromism within the FLA method can be owed to the Lewis adduct formation. Even though solvatochromism was negligible, we utilized the specific solvent probe parabolic function when measuring the Lewis acid unit (LAU) values in the FLA method, to obtain the most accurate measurements for the Lewis acids in that particular solvent.

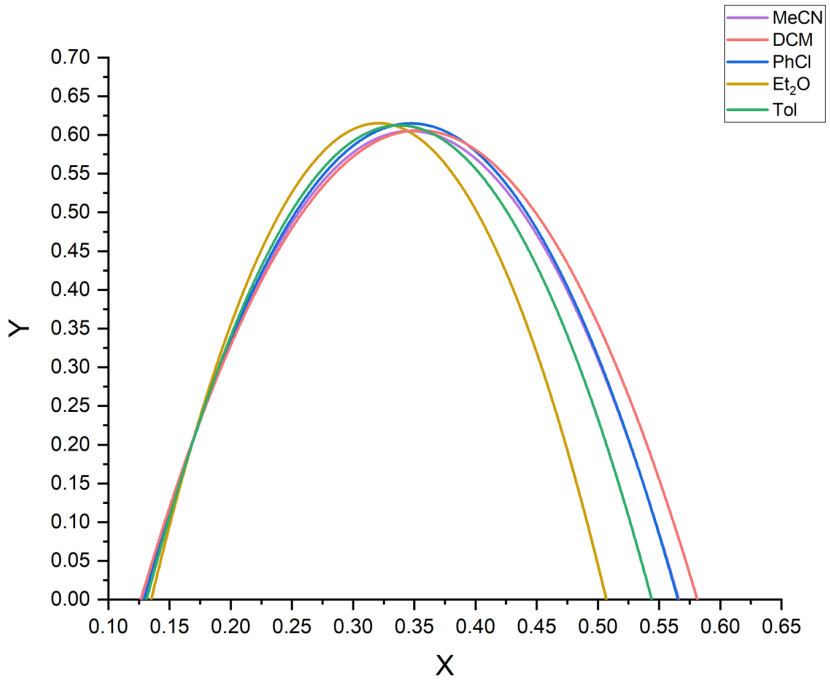

Figure 2-1. Parabolic fits of the chromaticity data of the dithienophosphole probes in varying polar solvents.

2.2. Impact of Solvent on Lewis Acid Binding

The initial proof-of-concept for the FLA method reported in 2019, demonstrated the simplicity and sensitivity,[73] whereas in our groups' most recent report published in 2020, highlighted the robustness and broad application of the FLA method, by expanding our library of measured Lewis acids to over 50, consisting of both common and esoteric species that could not be measured by existing methods (**Figure 2-2**).[72] These initial contributions have provided a considerable step forward in developing the FLA method, allowing us to explore a variety of dissimilar Lewis acids in an otherwise identical chemical environment. So far, the FLA method has only been performed in toluene, in order to provide true utility, the FLA method must also show robustness across varied chemical environments.

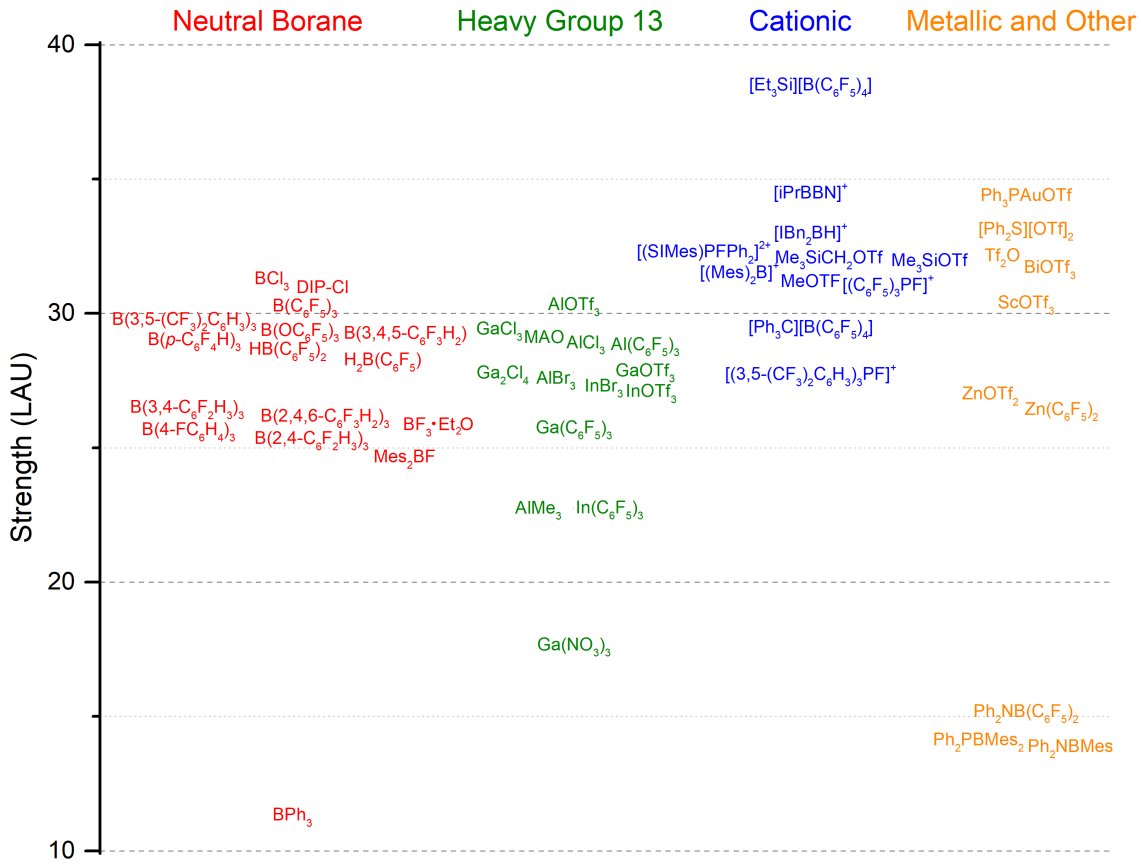

Figure 2-2. Lewis acid unit (LAU) values of 50 Lewis acids measured relative to one another in toluene. Figure is adapted with permission from reference [72] (© 2020, American Chemical Society).

Thus, as part of this thesis, we explored the impact of solvent effects in the FLA method by first selecting $B(C_6F_5)_3$ as our representative Lewis acid due to its notoriety,[84] as well as having generally served as a reference point throughout our groups' previous studies.[72,73] Using the previously reported procedure,[72] the LAU values for $B(C_6F_5)_3$ in the aforementioned solvents were determined. Looking at this data, we

noticed two general trends. We observed an increase in LAU values relative to the polarity of the respective solvent, as shown in **Figure 2-3** and **Table 6-1**. However, we also observed that the donor potential of the solvent can lower the LAU value; utilizing a stronger donating solvent can allow for a more rapid generation of solvates, which limits the formation of the fluorescent Lewis adduct. For example, MeCN precluded formation of the FLA adduct with $B(C_6F_5)_3$ entirely, even with a large excess of Lewis acid, due to the strong Lewis acid-base adduct formed between the solvent and $B(C_6F_5)_3$.[85] To compare the donor potential of the solvents chosen, we refer to the donor number introduced by Gutmann *et al*., defined as the negative reaction enthalpy of the 1:1 adduct formation between a standard Lewis acid, such as $SbCl_5$ and the electron pair donor (EPD) solvent in 1,2-dichloroethane (0 kcal/mol).[86] The donor number measures the ability of a solvent to solvate the standard Lewis acid, the selected solvents used in this report ranged in donor ability from non-coordinating to coordinating; toluene (Tol, 0.1 kcal/mol), dichloromethane (DCM, 1.0 kcal/mol), chlorobenzene (PhCl, 3.0 kcal/mol), acetonitrile (MeCN, 14.1 kcal/mol), and diethyl ether (Et_2O, 19.2 kcal/mol). [86]

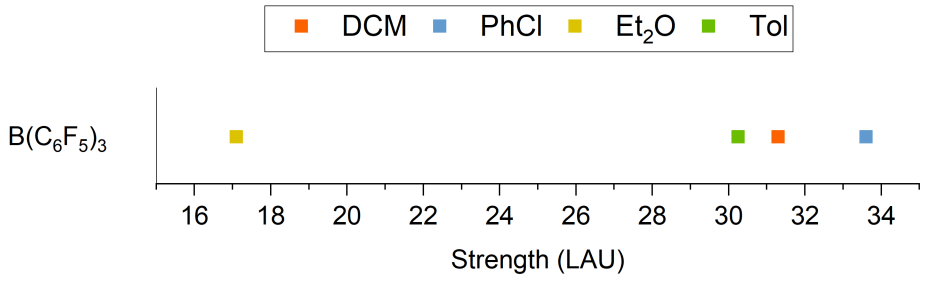

Figure 2-3. Lewis-acidity scale (in Lewis acid units, LAU) for $B(C_6F_5)_3$ in varying polar solvents.

To further elaborate the observed relationship between the FLA adduct and solvent in terms of polarity and donor potential, titration studies of $B(C_6F_5)_3$ against the four chosen probes were conducted in the various solvents. The binding constants were determined from the concentration and the ratio of emission intensities of the adduct and the dithienophosphole oxide at equilibrium on the basis of **Equation 4-4**, and are presented in **Table 6-7**.[70] In toluene, the binding constant of probe **1** with $B(C_6F_5)_3$ was relatively large, $1x10^5$ M^{-1}, suggesting a strong interaction between the phosphoryl group and boron center. Upon introducing weakly coordinating solvents, such as DCM and PhCl, the binding constant lowered by nearly an order of magnitude, ~$3x10^4$ M^{-1}. Employing an even stronger coordinating solvent, such as Et_2O, the binding constant lowered by another order of magnitude, ~$3x10^3$ M^{-1}. In MeCN, however, no fluorescent Lewis adduct was formed and thus a binding constant could not be measured. As anticipated and seen in the LAU scale for $B(C_6F_5)_3$, the results from the titration study demonstrated that the stronger the

coordinating solvent, the weaker the binding constant and LAU value. For example, $B(C_6F_5)_3$ presented an LAU of 33.59 in PhCl, 31.27 in DCM, 30.25 in Tol, 17.14 in Et_2O, and unmeasurable in MeCN. These results imply that the interaction between the Lewis acid and base probe becomes less prevalent in polar coordinating solvents. Polar solvents increase the *effective* Lewis acid strength in solution, while strong donor solvents reduce or even quench the *effective* Lewis acid strength by competing with binding to the Lewis acid. This dichotomy displays the complexity of Lewis acids, and the choice of solvent, an intuitive statement that our method appropriately demonstrates in measurable terms.

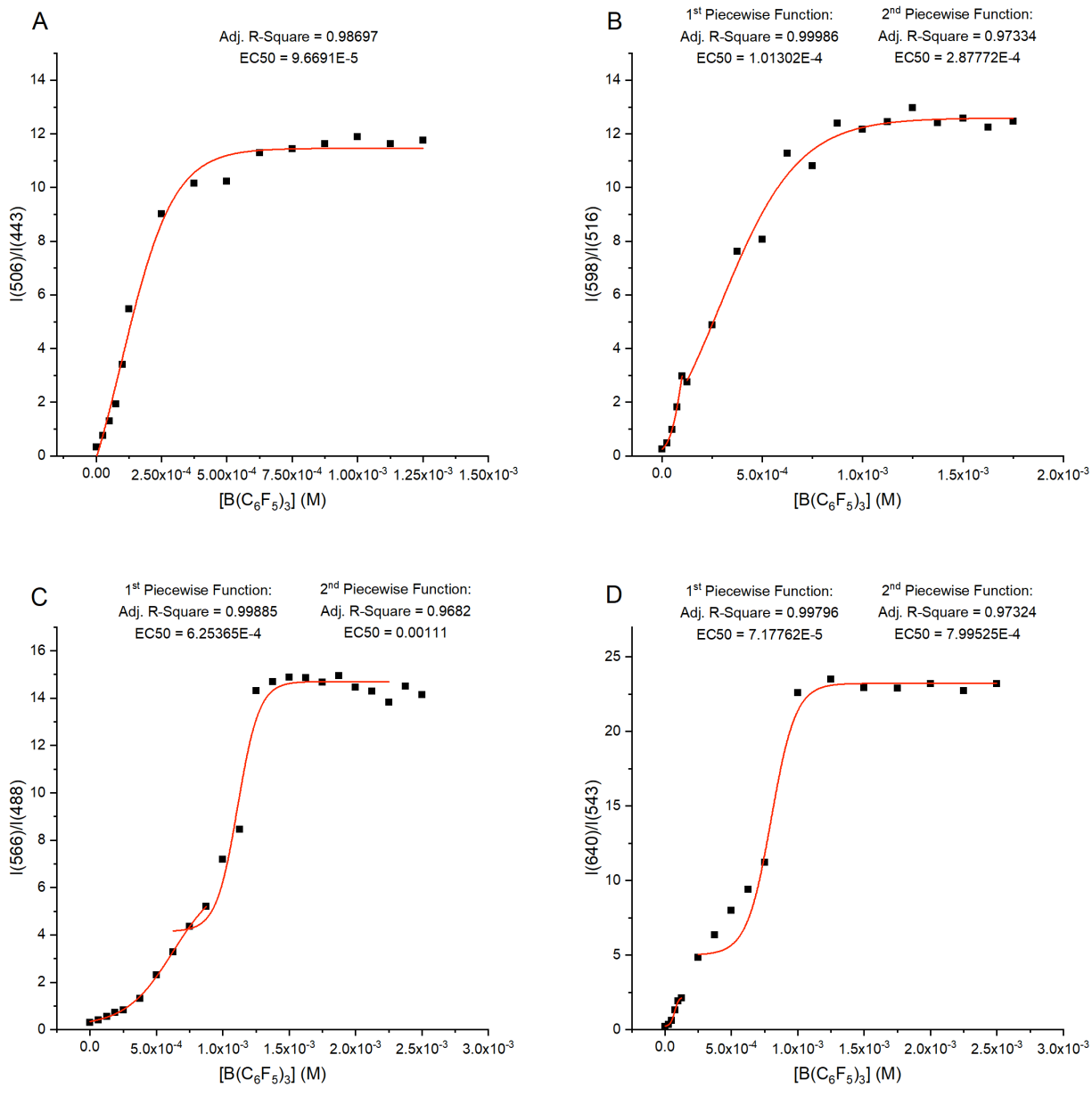

Figure 2-4. Sigmoidal fit of the titration of $B(C_6F_5)_3$ in diethyl ether with probes a) **1**, b) **2**, c) **7**, and **8**.

In addition, the titration experiments conducted in diethyl ether, specifically, afforded an intriguing perspective that arises from this dichotomy. Originally appearing anomalous, in the moderately donating solvent, a clear two-step equilibrium process was observed (**Figure 2-4**). Since, our FLA method consists of three components: a Lewis acid, a Lewis base, and the solvent,[73] it is reasonable to propose that the interaction we observe are the difference in the binding of a free Lewis acid, and a solvated Lewis acid with the Lewis basic probe (**Scheme 2-2**).[87] The two-step equilibrium process was easily observed in the titration curves as two distinctly separate equilibria, specifically when utilizing the weaker Lewis base **8**. Upon increasing the relative donor strength of the dithienophosphole probe (via modification of the conjugated backbone), the rate of (a) increases (**Scheme 2-2**), resulting in an overlap in the measure of the two competing equilibria. Thus, utilizing the relatively strongest Lewis base probe **1**, it becomes unclear as to the distinction between the two equilibria in the titration data (**Figure 2-4**), giving rise to the observation of only one equilibrium. Although the competing reaction is likely occurring in solution, the rates have become so similar that they are nearly impossible to separate experimentally. These competing equilibria likely occur with other Lewis acids and solvent combinations; however, it may not be feasible to separate them.

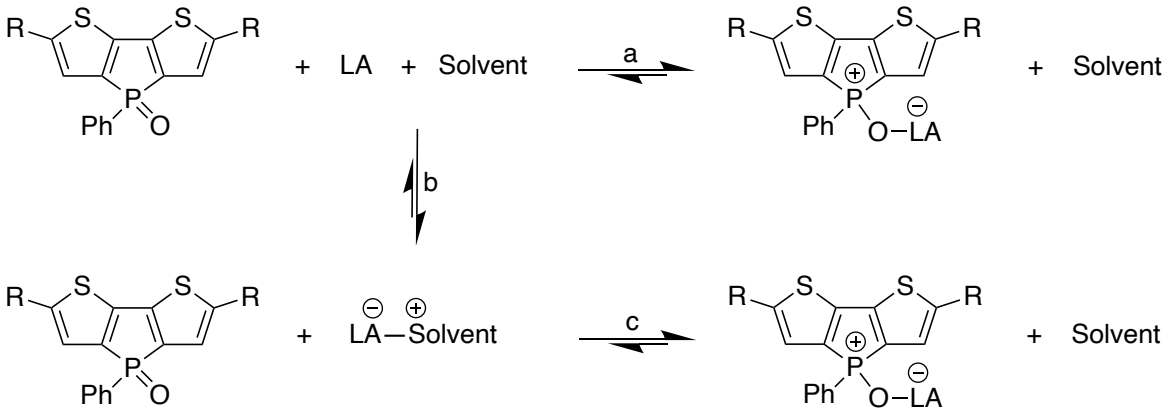

Scheme 2-2. Proposed competing equilibria during the formation of the fluorescent Lewis adduct (FLA). A stronger Lewis base (i.e., P=O) increases the forward rate of (a), while a stronger donor solvent (acetonitrile) increases the forward rate of (b). With a mild Lewis base and a mildly coordinating solvent (ether) (a) and (c) can both be seen and measured independently in part due to the slow rate of (b).

Our titration studies conducted with $B(C_6F_5)_3$ demonstrate the impact of coordinating solvents on the FLA method. Introducing a coordinating solvent resulted in a competing equilibrium between solvation and adduct formation, lowering the *effective* Lewis acid strength of the Lewis acid in solution. This dichotomy could be directly measured using the FLA method, but the observation of the competing equilibria

demonstrates the versatility of the FLA method in providing data for the *effective* Lewis acid strength of the solution. While these equilibria may not typically be separable, they likely occur with many other Lewis acids and solvent combinations. Regardless, the FLA method affords a measure of the linear combination of all possible states of Lewis acid in solution, and therefore incorporates the potential mixture of solvents into the LAU value, to represent the effective strength of the Lewis acid solution in an application.

2.3. Lewis Acidity - Dependence on Solvent

To expand on the observed dichotomy seen in the solvent properties of the FLA method, the following ten representative Lewis acids were chosen based on their utility in catalysis: $AlCl_3$, $B(4\text{-}C_6FH_4)_3$, $B(2,4,6\text{-}C_6F_3H_2)_3$, $B(3,4\text{-}C_6F_2H_3)_3$, $B(p\text{-}C_6F_4H)_3$, $B(OC_6F_5)_3$, $In(OTf)_3$, $Sc(OTf)_3$, $Zn(OTf)_2$, and $[Et_3Si][B(C_6F_5)_4]$.

One of the most commonly used Lewis acids in catalysis is $AlCl_3$, which has been utilized in a variety of selective reactions,[7] specifically in Friedel-Crafts reactions.[12,88] Although highly effective as a catalyst, unfortunately its actual structure is extremely complex due to its equilibrium mixtures; forming dimers, cationic species or tetracoordinate species in solution.[69] The effectiveness of $AlCl_3$ as a catalyst is a result of the aluminum atom having an open valence shell, which can take on various forms depending on the environment, thus altering its geometry and electronic properties in solution. As a result, we selected $AlCl_3$ to provide additional information on the effect various Lewis acid species in solution can have on measuring Lewis acidity in the FLA method with respect to solvent.

In addition to $AlCl_3$, boranes are among the most popular Lewis acids as a result of being easily synthetically accessible and highly tunable through their substituents. For example, $B(C_6F_5)_3$ has become a staple in Lewis-acid catalysis due to its broad utility in reactions,[84] thus being utilized as a representative Lewis acid throughout our studies.[72,73] We also selected a wide variety of arylboranes with varying electron deficiency: $B(4\text{-}C_6FH_4)_3$, $B(2,4,6\text{-}C_6F_3H_2)_3$, $B(3,4\text{-}C_6F_2H_3)_3$, $B(p\text{-}C_6F_4H)_3$, and $B(OC_6F_5)_3$. Reported in the literature, the number and positioning of the fluorine substituents on the arylboranes have been known to have noticeable effects on Lewis acidity.[62] In the FLA method, the LAU values measured in toluene correlated well to the reported literature trends for Lewis acidity; for instance, $B(4\text{-}C_6FH_4)_3$ (25.32 LAU), $B(2,4,6\text{-}C_6F_3H_2)_3$ (25.84 LAU), $B(3,4\text{-}C_6F_2H_3)_3$ (26.41 LAU), $B(p\text{-}C_6F_4H)_3$ (29.23 LAU), $B(OC_6F_5)_3$ (29.35 LAU), and $B(C_6F_5)_3$ (30.25 LAU).[72] Thus, we were interested in exploring Lewis acids with similar electronic and structural properties to further determine the impact of solvent effects on Lewis acidity in the FLA method.

Transition metals have also demonstrated to be intrinsically Lewis acidic as a result of their redox activity and accessible d-orbitals.[89] We selected two distinctly different transition metals as their triflate salts, scandium for its empty d-orbital shell and zinc with a filled d-orbital shell. $Sc(OTf)_3$ and $Zn(OTf)_2$ are different from typical Lewis acids, such as $AlCl_3$, BF_3, or $SnCl_4$; most Lewis acids will decompose or be deactivated in the presence of highly polar solvents, however, $Sc(OTf)_3$ and $Zn(OTf)_2$ are stable and can be used as a Lewis acid catalyst.[90] $Sc(OTf)_3$ can lose a triflate moiety in coordinating solvents, due to the

empty d-orbital shell and act as a stronger Lewis acid.[91] Although possible with $Zn(OTf)_2$, it is less likely to lose a triflate in coordinating solvents due to its stability. These two Lewis acids were selected to further explore their acidity in varying polar solvents.

Finally, we selected a cationic Lewis acid, $[Et_3Si][B(C_6F_5)_4]$, the strength of which has previously been difficult to determine via traditional methods, [92] but was readily measured using the FLA method and had an LAU value of 38.48 in toluene.[72] Cationic Lewis acids are generally much stronger than their neutral counterparts, owing to their positive charge, which results in them being more electrophilic and willing to readily coordinate with a Lewis base. We were interested in determining whether the FLA method would struggle in measuring this Lewis acid in the various polar solvents.

Having already established the correlation between bathochromic shift and Lewis acidity, as well as the relative inertness of our probe emissions to solvent effects, we were then interested in whether we would observe solvatochromic fluorescence behavior, similar to the Reichardt dyes that demonstrated a negative solvatochromic effect.[93,94] The preliminary studies conducted with $B(C_6F_5)_3$ in the varying polar solvents shed light on a dichotomy seen in the solvent properties of the FLA method. To further elaborate on the observed relationship, ten additional Lewis acids varying in chemical composition and reactivity, were selected to provide us with a wider scope on the variation of our methodology in respect to solvent effects.[95]

Original studies on the FLA method reported in our groups previous work,[73] showed no correlation between Lewis acidity and the absorption of the FLA adduct or emission. However, since this study compares the same Lewis acids in several solvents, we again started by attempting to correlate the absorption and emission spectra to the Lewis acidity. We first looked at the absorption data for the adducts of all eleven Lewis acids (**Table 6-3**, **6-4**, **6-5**, and **6-6**). Unfortunately, the UV-vis absorption spectra of the corresponding adduct did not show any correlation to varying the polarity of the solvent for the Lewis acids. Using the absorption data, we then obtained emission spectra for the Lewis acids of the corresponding adducts (**Table 6-3**, **6-4**, **6-5**, and **6-6**). By altering the polarity of the respective solvents, no clear positive or negative solvatochromic effects in the emission spectra were observed.

The emission spectra demonstrate an apparent correlation between Lewis acid strength and magnitude of the observed bathochromic shifts for the FLAs. Strong Lewis acids consistently exhibited the largest Stokes shifts, regardless of solvent. In addition, we also observed an impact of the solvent donor potential on the emission data. This similar effect was seen in our titration studies conducted with $B(C_6F_5)_3$, in that

the interaction between the Lewis acid and Lewis base probe becomes less prevalent in polar coordinating solvents. Across nearly all the Lewis acids tested, we observed that polar solvents can increase the *effective* Lewis acid strength in solution; however, strong donor solvents can inhibit or even quench the *effective* Lewis acid strength by competing with binding to the Lewis acid. For instance, in the emission data for $[Et_3Si][B(C_6F_5)_4]$, the degree of the bathochromic shift ($\Delta\lambda$) decreases with stronger coordinating solvents. Initially seen with the largest bathochromic shift in dichloromethane, chlorobenzene and toluene, the bathochromic shift is seen at par with a weak Lewis acid, such as $Zn(OTf)_2$ in diethyl ether. By employing an even stronger coordinating solvent, such as acetonitrile, no bathochromic shift was observed, once again a similar effect seen with $B(C_6F_5)_3$. As with our previous FLA studies, the emission data afford some details into the Lewis acid properties; however, the full understanding of the impact of solvation on the effective Lewis acid strength cannot be completely determined by Stokes shifts and emission maxima alone.

After analyzing the data, a correlation with donor potential of a solvent and Lewis-acid strength was seen in the magnitude of the observed bathochromic shifts for the FLAs. However, no consistent solvatochromic effects were seen; the change in color is based on various interactions and permutations of the Lewis acid in solution. The chromaticity of the sample is not based solely on the absorption or emission maxima, but rather on the totality of the emission events in solution. The broadness of the peak can be attributed to a complex range of electronic and vibrational states, confirmed in our previous studies conducted.[73] To properly determine the color of a sample, elements such as hue, saturation, and intensity must be considered simultaneously.[78] Utilizing the CIE diagram, the chromaticity information can be obtained, and the Lewis acidity in the FLA method can be measured.

The LAU values of these ten Lewis acids were determined using our previously reported procedure based on chromaticity.[72] We observed the same trends seen with $B(C_6F_5)_3$ for these additional ten Lewis acids in the different solvents. The LAU values were found to proportionally increase relative to the polarity of the respective solvent, as shown in **Figure 2-5**, whereas lower LAU values were observed with stronger donating solvents. As previously stated, stronger donating solvents allow for a more rapid generation of solvates, which limits the formation of the fluorescent Lewis adduct. This was specifically seen with all the arylboranes in acetonitrile, no fluorescent Lewis adduct was formed due to the stronger donating nature of acetonitrile compared to the dithienophosphole probes, which prevented an LAU value from being measured.

In addition to the general trend presented above, we observed that the magnitude of polarity versus donicity is strongly dependent on the Lewis acid strength. In presence of a stronger Lewis acid, the LAU values tend to be more effected by the polarity of the solvent whereas in the presence of a weaker Lewis acid, the LAU values tend to be more effected by the donicity of the solvent. For instance, looking at $B(C_6F_5)_3$ and $AlCl_3$, which are considered strong Lewis acids in both the FLA method as well as the current methods available, we observed higher LAU values in PhCl ($B(C_6F_5)_3$, 33.59 LAU and $AlCl_3$, 32.47 LAU) and in DCM ($B(C_6F_5)_3$, 31.27 LAU and $AlCl_3$, 30.35 LAU) compared to Tol ($B(C_6F_5)_3$, 30.25 LAU and $AlCl_3$, 28.89 LAU). However, when comparing the LAU scale of a weaker Lewis acid, such as $B(3,4\text{-}C_6F_2H_3)_3$ or $Zn(OTf)_2$, we observed lower LAU values in PhCl ($B(3,4\text{-}C_6F_2H_3)_3$ 25.81 LAU and $Zn(OTf)_2$, 23.94 LAU) and in DCM ($B(3,4\text{-}C_6F_2H_3)_3$ 21.64 LAU and $Zn(OTf)_2$, 25.66 LAU) compare to Tol ($B(3,4\text{-}C_6F_2H_3)_3$ 26.41 LAU and $Zn(OTf)_2$, 26.48 LAU). After analyzing the LAU scale, we were able to clearly see that the strength of the Lewis acid can affect the magnitude of the solvent effect, in terms of polarity and donicity.

The solution-state measurements in the FLA method can afford us the potential to measure how Lewis acids may differ under environmental changes, such as potential donors or dipolar species in solution. Across the Lewis acids measured, the general trends seen in the LAU values were consistent with the observed dichotomy from the titration studies with $B(C_6F_5)_3$. However, we observed that the LAU values for $Sc(OTf)_3$ differed, possibly due to the aforementioned generation of cationic species.[91] Thus, summarizing the impact of solvent on the LAU scale, we can observe two key, yet not mutually exclusive factors influencing measured Lewis acidity, the *polarity* and *donicity* of the solvent.

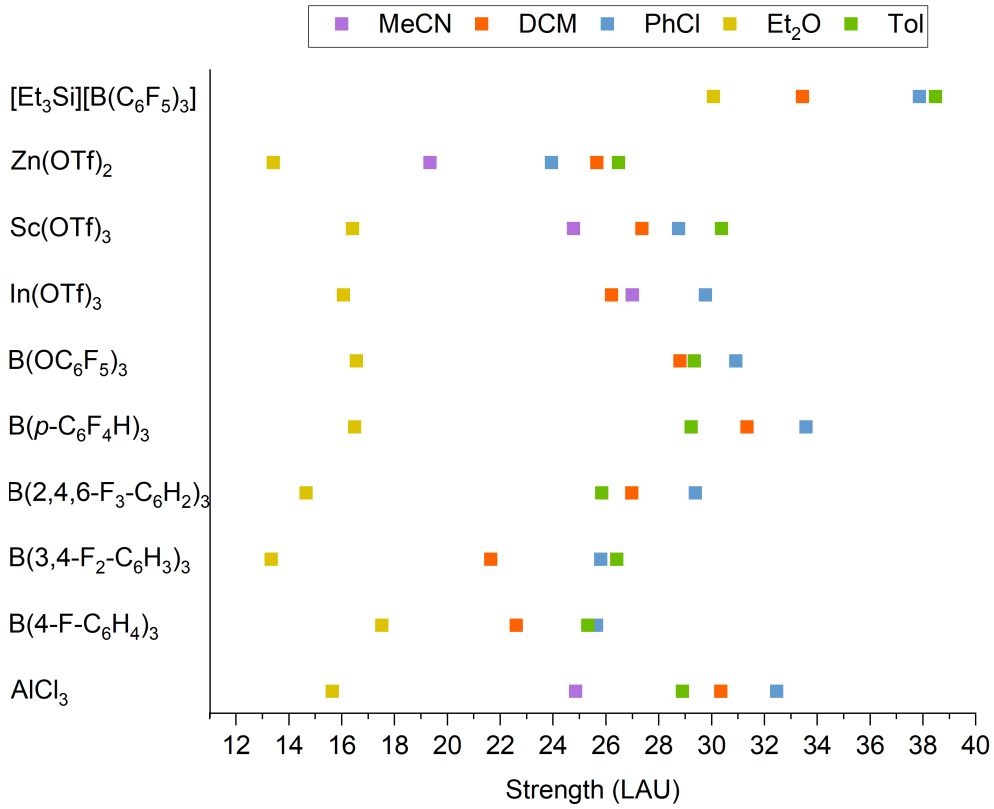

Figure 2-5. Lewis-acidity scale (in Lewis acid units, LAU) for ten different Lewis acids in varying polar solvents.

To further confirm this observation, computational studies were conducted in hopes to better understand the solvent effect on Lewis acidity, specifically the accessibility of the Lewis acidic center of the Lewis acid towards the solvents utilized in the study. The following six neutral boranes were selected for a more uniform comparison of Lewis acids, $B(C_6F_5)_3$, $B(p\text{-}C_6F_4H)_3$, $B(OC_6F_5)_3$, $B(2,4,6\text{-}C_6F_3H_2)_3$, $B(3,4\text{-}C_6F_2H_3)_3$ and $B(4\text{-}C_6FH_4)_3$. Density functional theory (DFT) calculations were performed at the B3LYP/6-31G+(d) level for structure optimization. Electrostatic potential (ESP) maps of these six neutral borane Lewis acids were calculated using an Atoms-in-Molecules (AIM) approach,[96] which are illustrated in **Figure 2-6**.

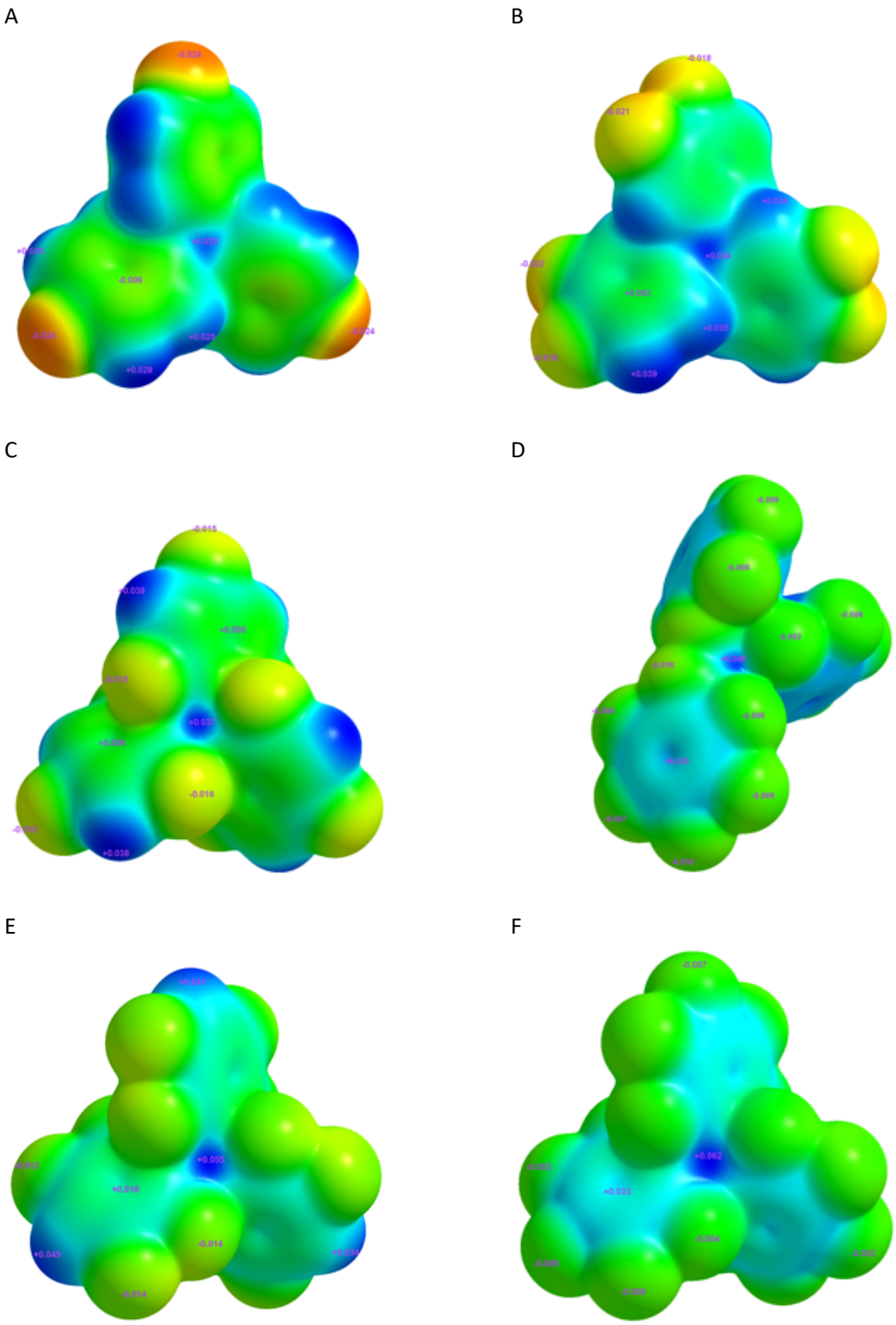

Figure 2-6. Electrostatic potential (ESP) maps of six neutral boranes in the absence of solvent with electron-rich regions coloured in red, and electron-poor regions coloured in blue; a) $B(4\text{-}C_6FH_4)_3$, b) $B(3,4\text{-}C_6F_2H_3)_3$, c) $B(2,4,6\text{-}C_6F_3H_2)_3$, d) $B(OC_6F_5)_3$, e) $B(p\text{-}C_6F_4H)_3$, and f) $B(C_6F_5)_3$.

Based on the ESP maps, we were able to estimate the acceptor potential of the boranes by comparing the electron density on the boron atom. The electron-poor nature of the boron center is akin to GEI,[65,68] effectively measuring the electrophilicity of that boron center by showing the increase and decrease in acceptor strength via strictly the degree of electron poorness. For instance, $B(C_6F_5)_3$ was identified as the strongest Lewis acid, indicated by having the lowest electron density value on the boron center, whereas $B(4\text{-}C_6FH_4)_3$ had the highest electron density on the boron atom, making it the weakest Lewis acid. By incorporating more fluorine atoms on the phenyl rings surrounding the boron center, an induction effect occurs, causing the electron deficiency on the boron atom to increase, thus increasing the Lewis acid acceptor strength.

The electrostatic potential maps for these six neutral boranes matched the trends seen in FLA method as well as in the literature.[62,68,73] As previously stated, the number and positioning of the fluorine substituents on the arylboranes have been known to have noticeable effects on Lewis acidity. According to the ESP maps and the compiled fluorescence emission data used to calculate the LAU values, the Lewis acid strength decreases in the following order: $B(C_6F_5)_3 \approx B(p\text{-}C_6F_4H)_3 > B(OC_6F_5)_3 > B(2,4,6\text{-}C_6F_3H_2)_3 > B(3,4\text{-}C_6F_2H_3)_3 > B(4\text{-}C_6FH_4)_3$.

In addition to the acceptor potential of these Lewis acids, the ESP maps can also provide insight into the accessibility of the Lewis acidic center of the Lewis acid. The term accessibility is in reference to the Lewis acidic borane center being able to interact and coordinate with a Lewis base or solvent molecule. By analyzing the geometry, size and degree of electron density surrounding the Lewis acid center, we were able to estimate the accessibility of the boranes. The slight variation in the number and location of the fluorinated aryl rings on the triarylboranes demonstrated a significant difference on the accessibility of the Lewis acidic center in forming the acid-base adduct, even though an adduct was not specifically modelled. Based on the mapping, $B(C_6F_5)_3$ had the most accessible Lewis acidic center, whereas $B(4\text{-}C_6FH_4)_3$ had the least accessible Lewis acidic center out of all six neutral boranes. By reducing the number of fluorine atoms on the phenyl ring, the electron density surrounding the Lewis acid center becomes more electron rich, making the Lewis acid site less accessible and thus weakening the attraction in forming the Lewis acid-base adduct. With the increasing number of hydrogen atoms on the phenyl rings, more electron-poor regions are introduced, hindering the accessibility of the Lewis acidic center, and thus, allowing the Lewis base to interact with the hydrogen atoms and undergo hydrogen bonding rather than forming the desired Lewis acid-base adduct (**Figure 2-6**).

Taking this into account, we were interested in seeing whether the ESP maps for these Lewis acids would change, if we applied a standard solvation model of an external electrostatic field. We conducted DFT-calculations, using the B3LYP functional and the 6-31G basis set with the polarized continuum model (PCM) in dichloromethane, chlorobenzene, diethyl ether, and toluene. The optimized structures from the DFT-calculations were then used to obtain the ESP maps of the six neutral boranes in the different aforementioned solvents. Unfortunately, we observed no change in the electrostatic potential maps, the charge densities were nearly identical, regardless of the solvents utilized (**Figure 2-7**). These calculations, initially conducted to reinforce the FLA method was found to be insufficient in modeling the level of detail needed to extrapolate a correlation between solvent effects and Lewis acidity. Notwithstanding, the ESP maps provided us with information on Lewis acidity to a degree, however, they were unable to explain or even measure all the permutations and interactions of the Lewis acid, specifically solvent effects, which was similarly seen in the challenges denoted in the GEI.[65,68] As a result, we were unable to compare our LAU values obtained with the different solvents to extrapolate a clear correlation from the ESP maps in respect to the accessibility of the Lewis acidic center of these six neutral boranes towards the varying polar solvents.

However, the titration and solvent experimental studies conducted using the FLA method allowed us to measure the Lewis acidity with respect to solvent effects. Owing to the solution-state nature of this methodology, we were able to measure how Lewis acids may differ under environmental changes and provide a better ability to determine the activity of a Lewis acid in a reaction based on solvent. Just as the chromaticity of our measured adducts is sensitive to minor changes in Lewis acidity, the efficacy of a Lewis acid in as a catalyst relies on measuring the impact of a series of minor permutations and interactions between the Lewis acid and its binding site, precisely the type of precision our method allows us to measure and potentially correlate to chemical reactivity.

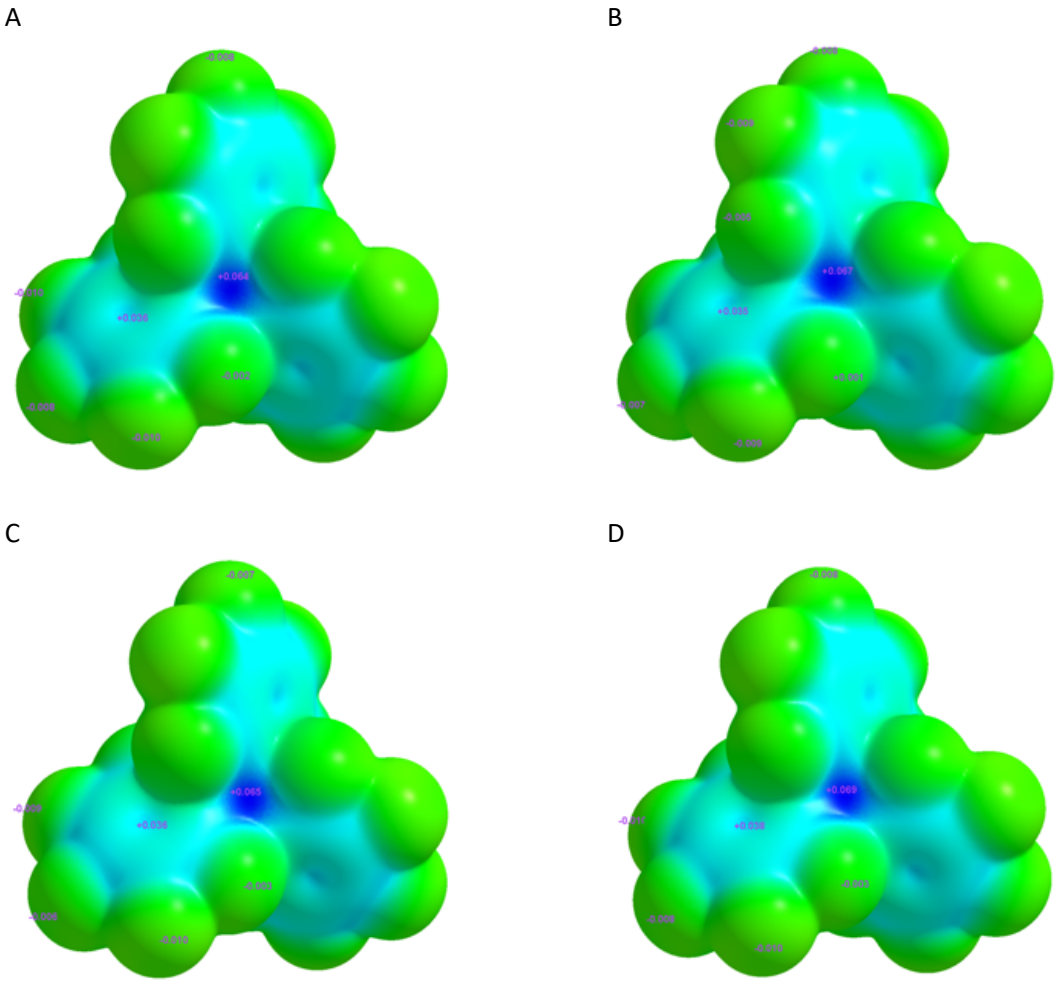

Figure 2-7. Electrostatic potential (ESP) maps of $B(C_6F_5)_3$ in a.) dichloromethane, b.) chlorobenzene, c.) diethyl ether, and d.) toluene.

2.4. LAU Values & Catalysis: Across Varied Lewis Acids

2.4.1. Selecting Chemical Reactions to Explore

The solvent studies illustrated that the FLA method can measure the variance of a Lewis acid's acceptor ability in differing environments, even those in which additional Lewis acid species are present. Due to the solution-state nature of the FLA methodology, we can potentially provide an insight into the effectiveness of these Lewis acids in specific reaction environments and allow us to correlate the FLA measurements directly with catalytic reactions. To determine the value of this observation and the predictive potential of an LAU value, we investigated two representative Lewis acid-catalyzed reactions to interpolate any correlation between catalytic activity and the FLA scale: Diels-Alder cycloaddition of 2,3-dimethyl-1,3-butadiene with methyl acrylate (**Scheme 2-3a**),[97] and hydrosilylation of benzophenone (**Scheme 2-3b**).[98]

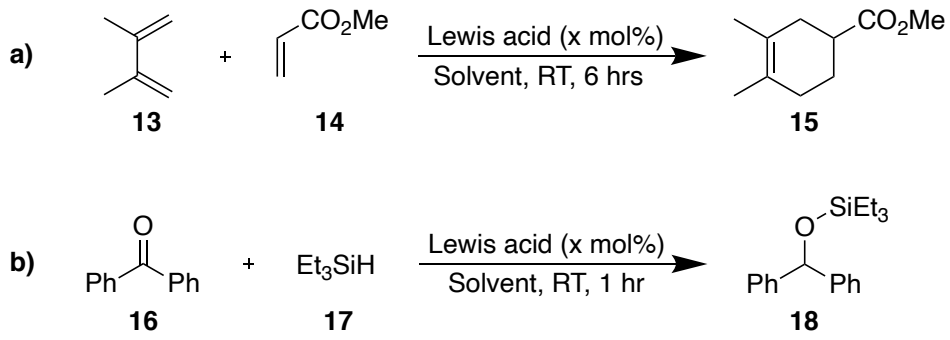

Scheme 2-3. Two representative Lewis-acid catalyzed reactions: a.) Diels-Alder cycloaddition of 2,3-dimethyl-1,3-butadiene with methyl acrylate and b.) hydrosilylation of benzophenone.

The progression of the two representative reactions catalyzed by the same Lewis acids were monitored by ^{1}H NMR spectroscopy in the respective solvents. For the Diels-Alder cycloaddition, the reaction was monitored by the integration of the multiplet -C*H*CO resonance of methyl-3,4-dimethyl-3-cyclohexenecarboxylate, **15** compared to the singlet -CH_2 resonance of cyclohexane, as the internal standard. For the hydrosilylation reaction, the reaction was monitored by the integration of the multiplet -OC*H*Ph$_2$ resonance of triethyl(1,1-diphenylmethoxy)silane, **18**, against the singlet -CH_2 resonance of cyclohexane, the internal standard.

2.4.2. Preliminary Studies with the Diels-Alder Cycloaddition and Hydrosilylation

Our initial efforts focused on the evaluation of a broad range of Lewis acids to interpolate any correlation between catalytic activity and the FLA scale. For our preliminary experiments, we selected the following six Lewis acids out of the eleven previously measured using the FLA method in the aforementioned solvents: $AlCl_3$, $B(2,4,6\text{-}C_6F_3H_2)_3$, $B(C_6F_5)_3$, $In(OTf)_3$, $Sc(OTf)_3$, and $Zn(OTf)_2$. The aim in selecting these six Lewis acids was to provide a more in-depth analysis on the fundamental interactions and perturbations of Lewis acids as their reaction environment changes in respect to catalytic activity and potentially identify any discrepancies.

We first explored the Diels-Alder cycloaddition, using 5 mol% of $AlCl_3$, in the varying solvents (**Table 2-1**). The progress of the reaction was significantly impacted by the polarity and donicity of the varying solvents, exemplified in **Figure 2-8**. In a more polar solvent, we observed the reaction progressing at a faster rate with a higher product conversion over 4 hours, while the coordinating ability of the solvent negatively influenced the progress of the reaction, demonstrated by a slower and lower product conversion over the same time frame. The results obtained from the Diels-Alder cycloaddition with $AlCl_3$ matched well with the trends seen in the titration experiments with $B(C_6F_5)_3$ (*vide supra*), in that the dichotomy of polarity versus donor ability of a solvent can be identified in the catalytic reactions.

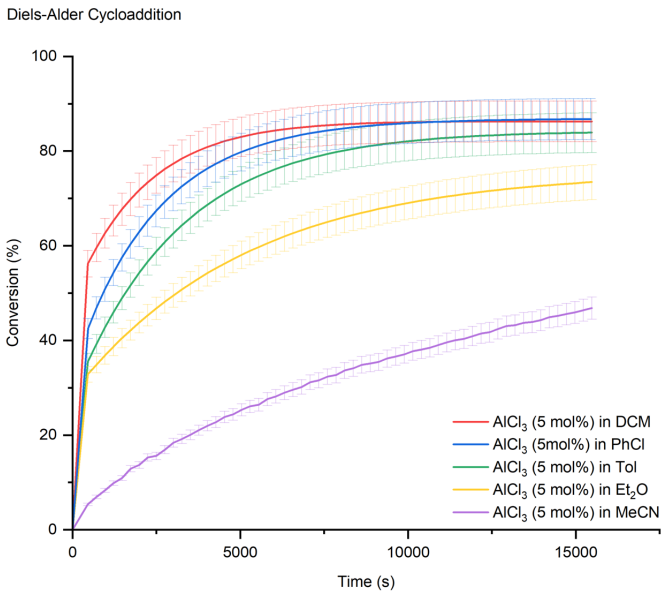

Figure 2-8. Product conversion in percent yield for the Diels-Alder cycloaddition over 4 hours; $AlCl_3$ used as the Lewis acid catalyst in varying polar solvents.

Table 2-1. Results of the Diels-Alder cycloaddition of 2,3-dimethyl-1,3-butadiene and methyl acrylate with various Lewis-acid catalysts in varying polar solvents.

Entry	Lewis acid	Catalyst loading (x mol %)	Solvent	Conversion (%)[a]
1	$AlCl_3$	5	MeCN	48[b]
2	$AlCl_3$	5	Et_2O	75[b]
3	$AlCl_3$	5	Tol	84[b]
4	$AlCl_3$	5	PhCl	85[b]
5	$AlCl_3$	5	DCM	87[b]
6	$B(C_6F_5)_3$	5	MeCN	0
7	$B(C_6F_5)_3$	5	Et_2O	72
8	$B(C_6F_5)_3$	5	Tol	80
9	$B(C_6F_5)_3$	5	PhCl	83
10	$B(C_6F_5)_3$	5	DCM	87
11	$B(2,4,6\text{-}F_3\text{-}C_6H_2)_3$	30	Et_2O	6
12	$B(2,4,6\text{-}F_3\text{-}C_6H_2)_3$	30	Tol	9
13	$B(2,4,6\text{-}F_3\text{-}C_6H_2)_3$	30	PhCl	11
14	$B(2,4,6\text{-}F_3\text{-}C_6H_2)_3$	30	DCM	20
15	$In(OTf)_3$	5	MeCN	4
16	$In(OTf)_3$	5	Et_2O	5
17	$In(OTf)_3$	5	Tol	5
18	$In(OTf)_3$	5	PhCl	7
19	$In(OTf)_3$	5	DCM	4
20	$Sc(OTf)_3$	5	MeCN	41
21	$Sc(OTf)_3$	5	Et_2O	25
22	$Sc(OTf)_3$	5	Tol	16
23	$Sc(OTf)_3$	5	PhCl	21
24	$Sc(OTf)_3$	5	DCM	10
25	$Zn(OTf)_2$	5	NA[c]	0
26	$B(4\text{-}F\text{-}C_6H_4)_3$	30	NA[c]	0
27	$B(3,4\text{-}F_2\text{-}C_6H_3)_3$	30	NA[c]	0
28	$B(OC_6F_5)_3$	5	Et_2O	8
29	$B(OC_6F_5)_3$	5	Tol	16
30	$B(OC_6F_5)_3$	5	PhCl	27
31	$B(OC_6F_5)_3$	5	DCM	28
32	$B(p\text{-}C_6F_4H)_3$	5	Et_2O	45
33	$B(p\text{-}C_6F_4H)_3$	5	Tol	48
34	$B(p\text{-}C_6F_4H)_3$	5	PhCl	56
35	$B(p\text{-}C_6F_4H)_3$	5	DCM	56

[a]NMR conversion, cyclohexane, used as internal standard.

[b]Reaction was monitored for 4 hours.

[c]No product formation regardless of solvent used (MeCN, Et_2O, Tol, PhCl, DCM).

To ensure this was not simply the result of this specific Lewis acid chosen, but instead a direct correlation to the FLA method, we explored the five other Lewis acids as catalysts in the cycloaddition. For $B(C_6F_5)_3$ and $B(2,4,6\text{-}C_6F_3H_2)_3$ the same trend as for $AlCl_3$ was observed (see **Figure 2-9a** and **2-9b**). Both the LAU values and the percent yield of product conversion in the Diels-Alder cycloaddition increased by solvent polarity and were lowered by donor ability; $B(C_6F_5)_3$: DCM (87%, 31.27 LAU), PhCl (83%, 33.59 LAU), Tol (80%, 30.25 LAU), Et_2O (72%, 17.14 LAU) and $B(2,4,6\text{-}C_6F_3H_2)_3$: DCM (20%, 26.98 LAU), PhCl (11%, 29.38 LAU), Tol (9%, 25.84 LAU), Et_2O (6%, 14.65 LAU).

Interestingly, the trend also holds for $In(OTf)_3$, despite undergoing a retro Diels-Alder cycloaddition (rDA) (**Figure 2-9c**); $In(OTf)_3$ is known to be a chemical activator for rDA reactions with certain dienes and dienophiles.[99] For $Sc(OTf)_3$, the reverse general trend was observed (**Figure 2-9d**); *higher product conversion* was seen in stronger coordinating solvent. The results are as followed, $Sc(OTf)_3$: MeCN (41%, 24.77 LAU), Et_2O (25%, 16.41 LAU), PhCl (21%, 28.75 LAU), Tol (16%, 30.37 LAU), and DCM (10%, 27.36 LAU). This is likely due to $Sc(OTf)_3$ losing a triflate moiety in coordinating solvents, en route to a stronger, cationic species that possibly remains coordinated to the product, de facto poisoning the catalyst. Unfortunately, we were unable to make any comparisons with $Zn(OTf)_2$, as no product formation was observed in any of the solvents, likely due to both the insolubility and weak Lewis-acid strength of the zinc species.[73]

A correlation between the LAU values and the product yield for the Diels-Alder cycloaddition was observed with the neutral boranes, $AlCl_3$, and $In(OTf)_3$. By increasing the polarity of the solvent, both the LAU value and percent yield increased, whereas in the presence of a stronger donating solvent, a decrease in LAU value and percent yield was seen. In general, the results obtained from the Diels-Alder reactions supported our initial solvation studies, suggesting that the FLA method can, in fact, provide a "solution-state" measure to accurately correlate LAU values to the solvent impact of catalytic activity.

In order to further support this claim, we then investigated the hydrosilylation reaction (**Table 2-2**). For $B(C_6F_5)_3$ and $B(2,4,6\text{-}C_6F_3H_2)_3$, we observed similar results as seen in the Diels-Alder cycloaddition. The reaction progression varied significantly as a function of polarity and donicity of the solvent (see **Figure 2-10a** and **2-10b**). On the other hand, we were unable to correlate our FLA method to "solution-state" measurements with the other four non-borane Lewis acids: $AlCl_3$, $In(OTf)_3$, $Sc(OTf)_3$, and $Zn(OTf)_2$. In the hydrosilylation with $Sc(OTf)_3$ and $Zn(OTf)_2$ as catalyst, no reaction was observed at room temperature, whereas for $AlCl_3$ and $In(OTf)_3$, additional peaks were seen in the ^1H NMR spectrum, suggesting complex reaction mixtures. The mechanism for the hydrosilylation of ketones has been well explored and shown

to favor specific substrates, such as boranes, which first activate the Si-H bond in the silane then undergo a subsequent attack by the ketone.[98,100] It should be noted that these non-borane Lewis acids can mechanistically act differently in solution and depending on the solvent can undergo alternative reactions.[101–103]

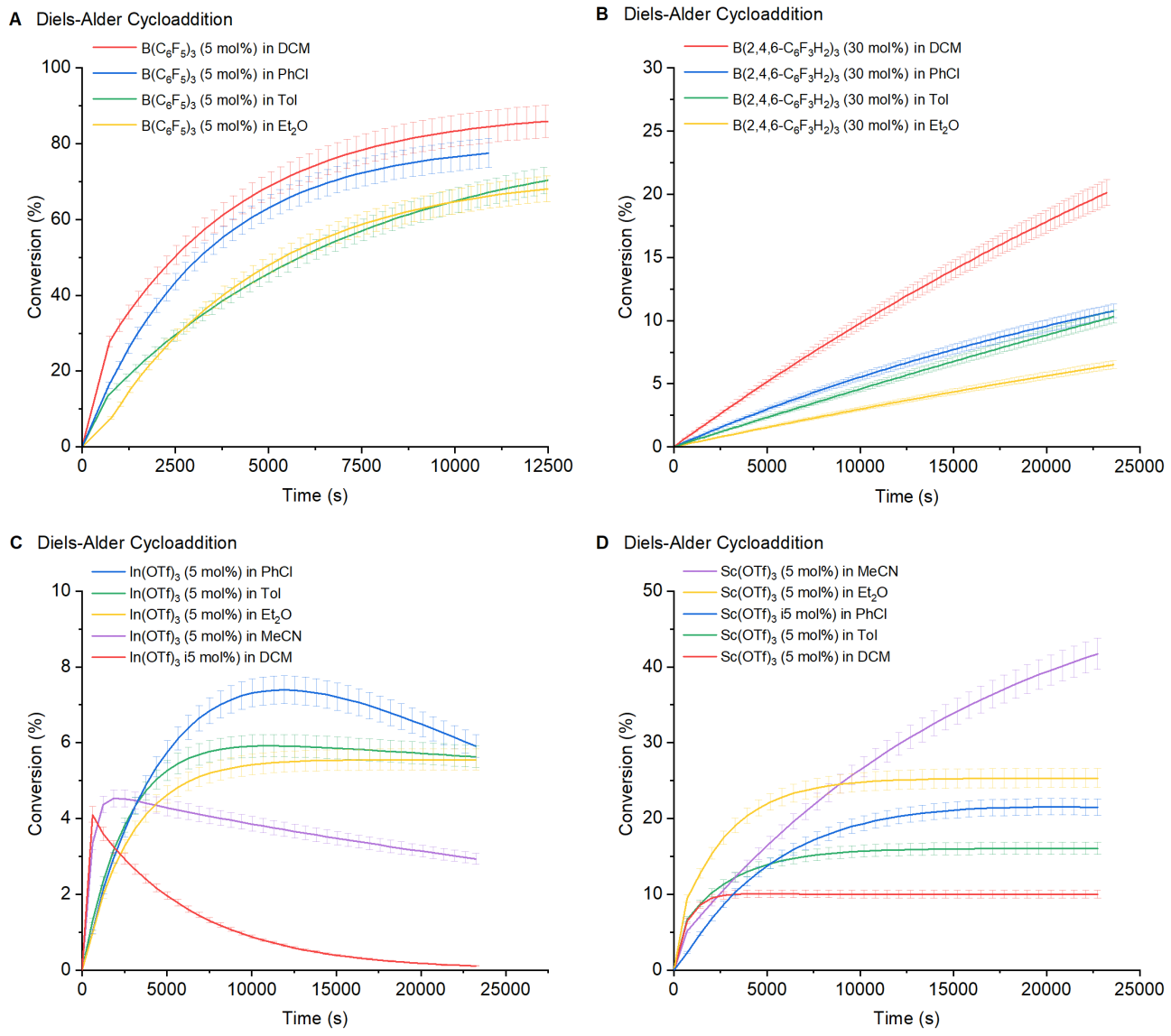

Figure 2-9. Product conversion in percent yield for the Diels-Alder cycloaddition over 6 hours in varying polar solvents utilizing a) $B(C_6F_5)_3$, b) $B(2,4,6\text{-}C_6F_3H_2)_3$, c) $In(OTf)_3$, and d) $Sc(OTf)_3$.

Table 2-2. Results of the hydrosilylation of benzophenone and triethylsilane with various Lewis acid catalysts in varying polar solvents.

Entry	Lewis acid	Catalyst loading (x mol %)	Solvent	Conversion (%)[a]
1	$AlCl_3$	30	NA[b]	0
2	$B(C_6F_5)_3$	0.01	Et_2O	99
3	$B(C_6F_5)_3$	0.01	Tol	99
4	$B(C_6F_5)_3$	0.01	PhCl	99
5	$B(C_6F_5)_3$	0.01	DCM	99
6	$B(2,4,6\text{-}F_3\text{-}C_6H_2)_3$	1	Et_2O	85
7	$B(2,4,6\text{-}F_3\text{-}C_6H_2)_3$	1	Tol	99
8	$B(2,4,6\text{-}F_3\text{-}C_6H_2)_3$	1	PhCl	99
9	$B(2,4,6\text{-}F_3\text{-}C_6H_2)_3$	1	DCM	99
10	$In(OTf)_3$	10	NA[b]	0
11	$Sc(OTf)_3$	10	NA[b]	0[c]
12	$Zn(OTf)_2$	10	NA[b]	0[c]
13	$B(4\text{-}F\text{-}C_6H_4)_3$	30	NA[b]	0
14	$B(3,4\text{-}F_2\text{-}C_6H_3)_3$	5	Et_2O	86
15	$B(3,4\text{-}F_2\text{-}C_6H_3)_3$	5	Tol	99
16	$B(3,4\text{-}F_2\text{-}C_6H_3)_3$	5	PhCl	99
17	$B(3,4\text{-}F_2\text{-}C_6H_3)_3$	5	DCM	99
18	$B(OC_6F_5)_3$	30	Et_2O	25[d]
19	$B(OC_6F_5)_3$	30	Tol	28[d]
20	$B(OC_6F_5)_3$	30	PhCl	31[d]
21	$B(OC_6F_5)_3$	30	DCM	32[d]
22	$B(p\text{-}C_6F_4H)_3$	0.01	Et_2O	99
23	$B(p\text{-}C_6F_4H)_3$	0.01	Tol	99
24	$B(p\text{-}C_6F_4H)_3$	0.01	PhCl	99
25	$B(p\text{-}C_6F_4H)_3$	0.01	DCM	99

[a]NMR conversion, cyclohexane, used as internal standard.

[b]No product formation regardless of solvent used (MeCN, Et_2O, Tol, PhCl, DCM).

[c]Reaction was monitored for 24 hours, no product formation.

[d]Reaction was monitored for 6 hours.

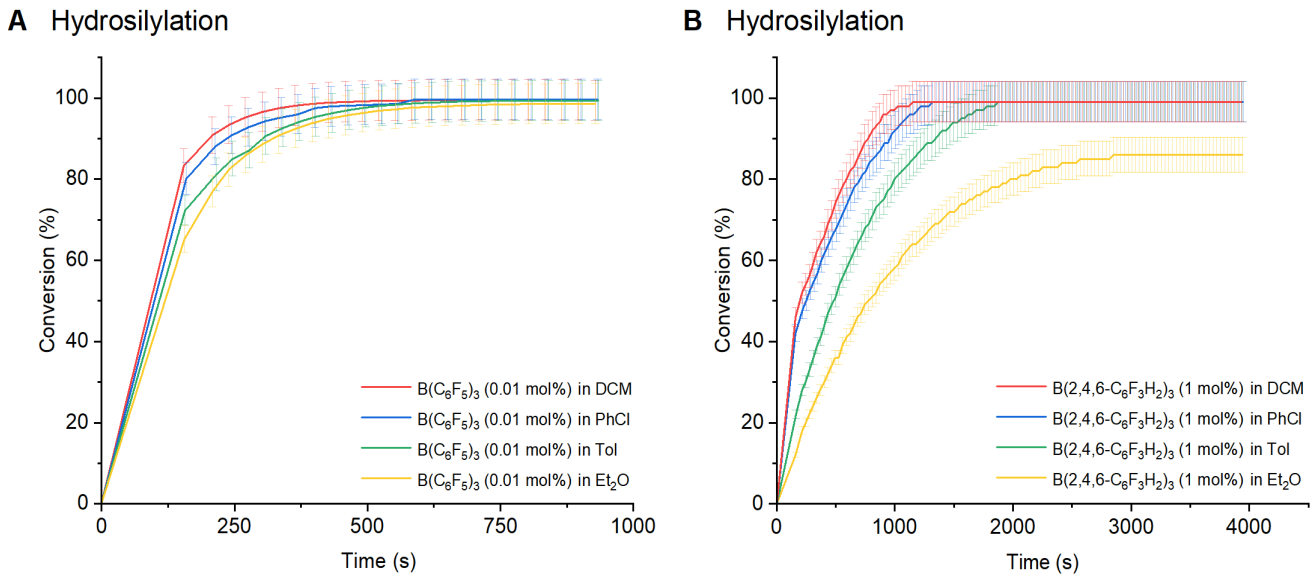

Figure 2-10. Product conversion in percent yield for the hydrosilylation of benzophenone over 1 hour in varying polar solvents utilizing a) $B(C_6F_5)_3$, and b) $B(2,4,6\text{-}C_6F_3H_2)_3$.

Although we were unable to provide additional comparisons with these four non-borane Lewis acids in the hydrosilylation, the results clearly demonstrate that the FLA method can measure the changes in solution. However, we cannot use it to determine the specific nature of all the active Lewis acid species, and therefore cannot predict if or when a Lewis acid may generate a species in solution that is incompatible with the reaction it is catalyzing. Such chemical incompatibilities cannot be directly predicted by the FLA method but should remain under consideration by the performing chemist.

While the solvation studies proved to be consistent over the variety of Lewis acids tested, the catalytic reaction conditions proved much more variable for our measurements, as factors not accounted for in the FLA method can impact the results, for example, the impact of a charged species on the catalyzed transformation and chemical binding to the product. Although the FLA method can appropriately measure known discrepancies, the exact nature of the solution is unknown. Thus, for a better, more solid comparison of Lewis acids, the following neutral boranes were applied for reaction monitoring: $B(p\text{-}C_6F_4H)_3$, $B(OC_6F_5)_3$, $B(3,4\text{-}C_6F_2H_3)_3$ and $B(4\text{-}C_6FH_4)_3$.[72] Again, the LAU values proved to be consistent for the catalytic application of the Lewis acids in the respective solvents. The trend seen previously with $B(C_6F_5)_3$ showcasing the dichotomy of polarity and donor ability of the solvent was observed with the various neutral boranes (**Figure 6-190** and **6-192**), except for $B(4\text{-}C_6FH_4)_3$ due to the formation of additional emissive species present in solution. For instance, we observed slower reactions where a lower LAU value was measured, typically in the presence of a stronger donating solvent, and faster reactions

where higher LAU values were measured, with a weaker donating, but more polar solvent (see **Figures 6-191** and **6-193**). In addition, by increasing the polarity of the solvent in both the Diels-Alder cycloaddition and hydrosilylation reactions, the transition state in both reactions becomes more stabilized, causing the reaction to proceed at a faster rate and thus higher product conversion. Overall, the results obtained from the Diels-Alder cycloaddition and hydrosilylation reactions with the neutral boranes, support our initial solvation studies and demonstrated that the solvent effect on a Lewis acid generally follows the impact measured by the FLA method.

2.4.3. Can the LAU Scale and Chemical Reactivity be Correlated?

Taking the results above into consideration, we sought to determine if an LAU value was universal, or in other words, does an LAU value for one Lewis acid in one solvent result in the same catalytic response as a different Lewis acid in a different solvent with the same LAU value. To probe this correlation, Lewis acids with similar LAU values were then analyzed. We first selected $B(C_6F_5)_3$ in Tol (30.25 LAU) and $Sc(OTf)_3$ in Tol (30.37 LAU). After monitoring the reaction for 6 hours, we observed significantly different yields, 80% for $B(C_6F_5)_3$ and 16% for $Sc(OTf)_3$ (**Figure 2-11a**). However, since the dissociation of $Sc(OTf)_3$ is integral to its acid strength,[91] it may be more complicated to compare. Although these Lewis acids have similar LAU values, they may act differently catalytically than they do in a bulk solution and while the LAU value accounts for all active Lewis acid species in solution, it does not account for mechanistic difference resulting from those different species.

Since the catalytic ability of the neutral boranes readily correlated with the LAU measurements, we decided to compare borane Lewis acids with similar LAU values to each other to again determine, if an LAU value is predictive of solution-state activity. The first comparison was between two strong boranes, selecting $B(C_6F_5)_3$ in DCM (31.27 LAU) and $B(p\text{-}C_6F_4H)_3$ in DCM (31.34 LAU), both of these Lewis acids are functionally close to each other and are equivalent in strength such that there is often debate in literature as to which is the stronger Lewis acid.[104] Based on our previous comparison, we expected similar behavior in reactivity. However, in both the Diels-Alder and hydrosilylation reactions we observe a clear qualitative difference in catalyst activity, shown in **Figure 2-11b (Table 2-1 and Table 2-2)**, even upon removing the variable of solvent. By comparing the rate constants of these reactions, however, the difference in catalytic reactivity becomes clear. Looking closely at the kinetics of $B(C_6F_5)_3$ in the Diels-Alder cycloaddition, partway through the reaction the rate constant changes (**Figure 2-12**). We presume that this non-linearity is related to anomalous binding data we attributed to a competing equilibrium (*vide supra*). As noted from our ESP maps, $B(C_6F_5)_3$ demonstrated to be the more accessible Lewis acidic site out of the six neutral boranes, meaning it may be prone to generate solvates. This complex equilibrium observed can potentially be the result of competing reactions between the free and solvated Lewis acid.[87] Although dichloromethane is a weakly coordinating solvent,[80] we can still observe the impact of the coordinating ability in the reaction rates. We propose that the reaction rate is first set by the free Lewis acid, however, as the reaction progresses the equilibrium is shifted towards the more solvated Lewis acid. This may even impact the rate of dissociation of the Lewis acid catalyst from the product, which the FLA method currently has no means of testing. A series of competing reactions persist between the solvation

of the Lewis acid and the catalytic activity which is strongly dependent on solvent and Lewis acid. In addition, the active Lewis acid species for catalysis may be either solvated Lewis acid, free Lewis acid, or both. While the FLA measures the sum of the active Lewis acid species in solution, it does not address the chemical compatibility of those species with catalytic activity. The potential for the FLA method to determine such measures requires further development and continues to be an active line of research for our group in expanding the methodology.

We then compared $B(OC_6F_5)_3$ in Et_2O (16.55 LAU) and $B(p\text{-}C_6F_4H)_3$ in Et_2O (16.49 LAU) (**Table 2-1**). In the Diels-Alder reaction, we observed significantly different reaction rates (**Figure 2-11c**) despite identical LAU values. The impact of the donor solvent on each species had a noticeable difference on the rate of the reaction. Effectively, the change in strength between the free Lewis acids against their diethyl ether solvate is significant and this difference directly impacts the rate of the Lewis-acid-catalyzed reaction. Likely, again related to competing equilibria of the active Lewis acid species in solution (*vide supra*). To further elucidate our claim, we looked at $B(OC_6F_5)_3$ in Tol (29.35 LAU) and $B(p\text{-}C_6F_4H)_3$ in Tol (29.23 LAU). Demonstrated in **Figure 2-11d**, utilizing a non-coordinating solvent the same effect can be seen. As the rate of the catalytic reaction is dependent on both solvated and free Lewis acid (active Lewis acid species in solution), both the solvated and the free Lewis acid LAU values may need to be taken into consideration to predict the overall efficacy of a Lewis acid for catalytic activity. While we can measure and propose that the competing equilibria exist, we cannot determine if both are accessible for catalytic activity. In that case, the effective Lewis acidity might measure all Lewis acid species in solution, but it does not measure all catalytic species in solution for situations in which all Lewis acids may not act catalytically. The FLA method can measure the LAU value of all active Lewis acids species in solution; however, it cannot infer the chemical compatibility of each species toward the specific catalytic need.

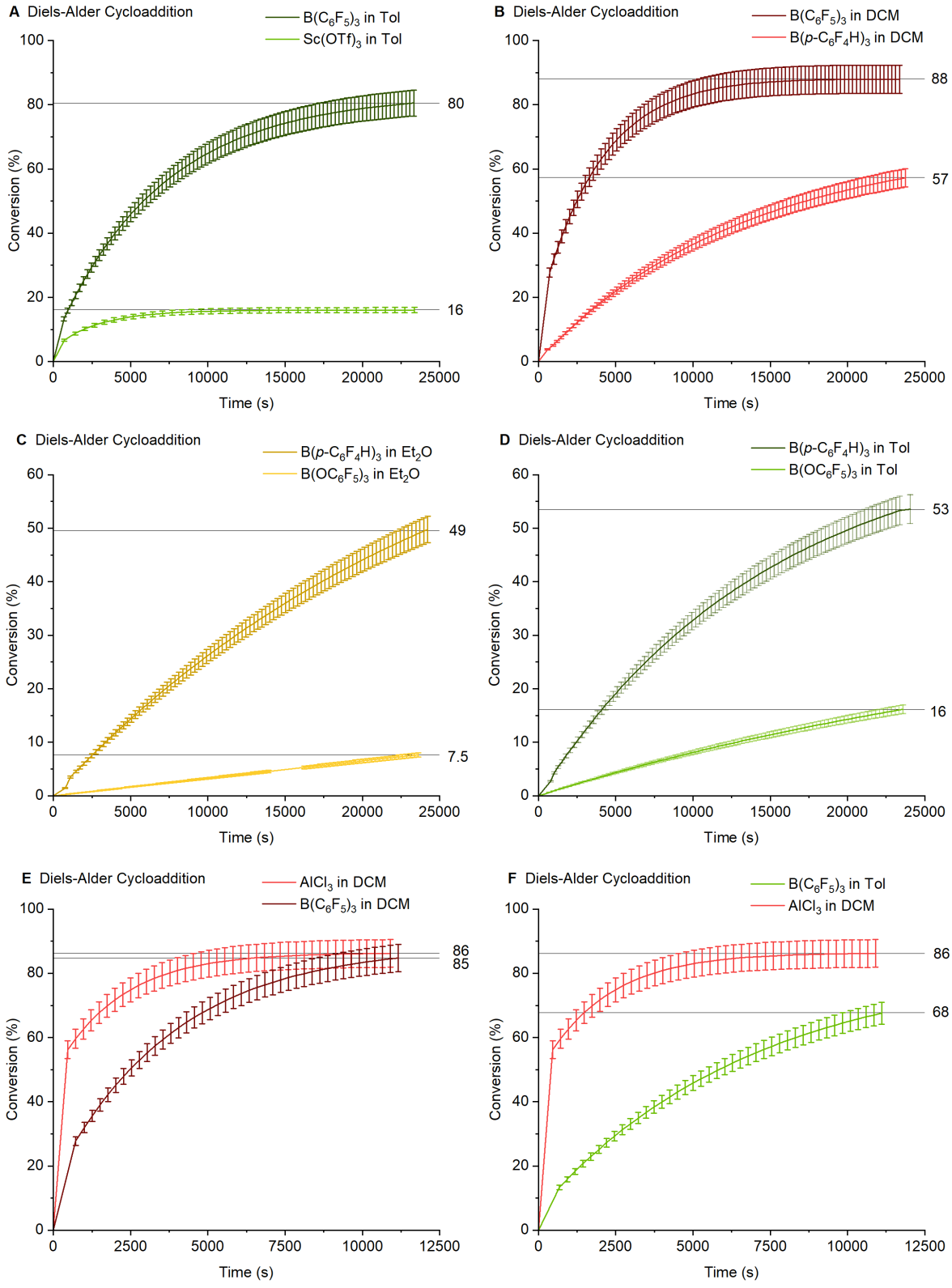

Figure 2-11. Comparable study of Lewis acid activity with reported catalyst and solvents utilized, monitored by product conversion rate in percent yield over time for the various Diels-Alder cycloadditions.

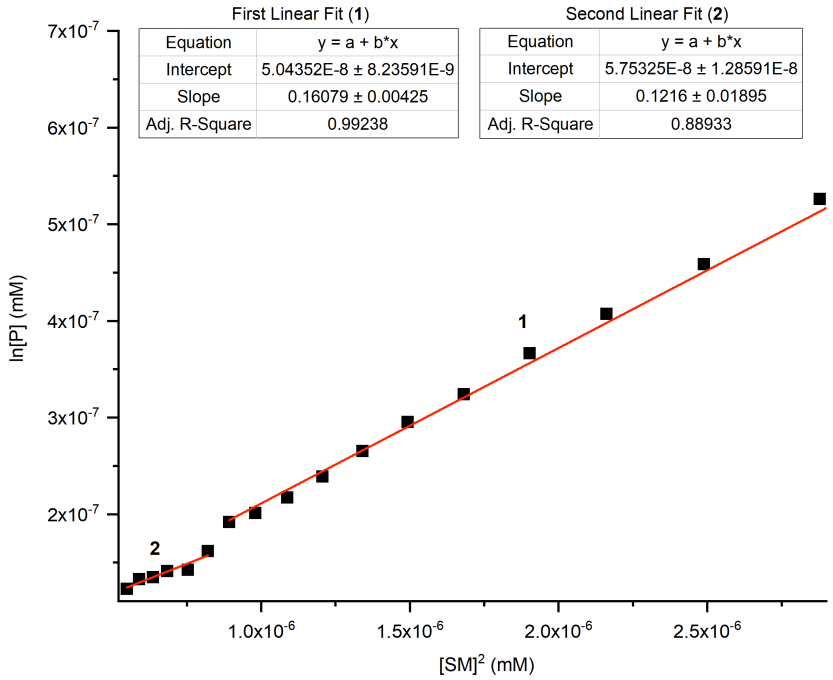

Figure 2-12. Plot of the rate constant (k) for $B(C_6F_5)_3$ in the Diels-Alder cycloaddition determined by the slope (y = mx + b) based on the first derivative of the product concentration (ln[P]) versus the concentration of starting material ($[SM]^2$).

Our final comparison worth noting is between $AlCl_3$ in DCM with an LAU of 30.35 and $B(C_6F_5)_3$ in Tol with an LAU of 30.25. After monitoring the Diels-Alder cycloaddition for 3 hours (**Figure 2-11e)**, we noticed that $B(C_6F_5)_3$ in toluene did not proceed as quickly as $AlCl_3$ in dichloromethane. Since, dichloromethane is a more polar solvent compare to toluene and polar solvents can help stabilize the transition state in the Diels-Alder cycloaddition, allowing the reaction to proceed at a faster rate. Taking this concept into consideration, we then compared $B(C_6F_5)_3$ in DCM to $AlCl_3$ in DCM (**Figure 2-11f)**. Although, $B(C_6F_5)_3$ has a slightly higher LAU value of 31.27, we can still see that under a more polar solvent like dichloromethane, $B(C_6F_5)_3$ does proceed at a faster rate and yields a higher product conversion that is almost identical to $AlCl_3$ in DCM. We are observing that rate of the reaction is being enhanced when carried out in a more polar organic solvent due to the stabilization of the transition state. This comparison demonstrated that Lewis acid strength is not the only parameter to consider and that solvent is just as important in effecting catalysis.

Thus far, the FLA method has shown itself to be robust at measuring the nature of Lewis acidity in solution regardless of the actual properties and nature of the solution itself. Rather allowing us to measure Lewis acidity as it may act in real reaction conditions without specifically knowing the active Lewis acid

species. Our methodology has afforded us the precision and accuracy to measure these discrepancies and provide insight into additional aspects of Lewis acid catalyzed reactions, highlighting some of the fundamental interactions and perturbations of Lewis acids as their reaction environment changes.

Chapter 3 Conclusion and Future Work

In conclusion, we have demonstrated the impact of solvent on the FLA method and provided insight into predicting chemical reactivity. Two significant factors influencing the measured Lewis acidity in the FLA method are the polarity and donating potential of the solvent. In the presence of a more polar non-coordinating solvent, we observed higher LAU values compared to a less polar coordinating solvent. This trend generally holds true across varied Lewis acids and proves to be generally the case when measuring the catalytic ability of these species in varying solvents. Since, the FLA method is based on the binding affinity of a Lewis acid to a specific theoretical Lewis base in a particular solvent, we observed the binding of the free Lewis acid to the Lewis base probe. However, depending on the coordinating ability of the solvent, a complex equilibrium may be observed. This was specifically seen in the titration data with diethyl ether and a strong Lewis acid. Two equilibria are present, and we hypothesize that the first equilibrium involves the free-Lewis acid, and the second equilibrium; the solvated Lewis acid. This likely occurs in any donating solvent but was not always separable in our measurement. In addition, the discrepancy seen in the FLA method can be observed in the chemical reactions conducted. As a result of the solution-state nature of the FLA methodology, we were able to provide insights into the effectiveness of these Lewis acids in specific reaction environments and demonstrate through reaction monitoring a correlation that coordinates the FLA measurement directly to catalytic reactions.

Although, the FLA method and LAU scale performed admirably when discussing catalytic efficiency of Lewis acids, there currently remain limitations to the method for it to be able to be truly predictive. While our method can be used to observe competing equilibria caused by solvation of a Lewis acid, and be used to discuss that effect on catalyst activity, it is limited strictly to binding of the Lewis acid, and not unbinding, which is vital in understanding how different Lewis acids behave differently in a catalytic environment. Additionally, the method cannot account for alternate chemistry, such as the reaction of the borate during hydrosilylation of a benzophenone, seen above, which can only be predicted from understanding the limitations of the reaction being performed. Nonetheless, the results of the binding of a Lewis acid, even as impacted by solvent, both polarity and donor potential, and solvation can be appropriately gauged by the LAU value determined from the FLA method.

To continue advancing the FLA approach into a more robust and practical method that can be used to predict chemical reactivity, we are further investigating approaches to measuring such discrepancies using the FLA method. Our groups are interested in confirming the identity of the two equilibria observed in the

titration studies. Currently, presented in the thesis is a hypothesis of what potentially may be occurring in the titration solutions. However, further experiments, such as low temperature NMR experiments may provide us with the insight needed to confirm the competing reaction. Also, additional titration experiments with other neutral borane Lewis acids can be explored to confirm whether this competing equilibria is applicable with varying Lewis acidity. These additional experiments can provide our groups with a better understanding on the overall discrepancy seen in the catalytic reaction rates.

Another, avenue required in confirming the discrepancies seen in the catalytic reactions conducted is determining the impact that the deuterated solvent had on the rate constants of the reactions. For all catalytic reactions, the same amount of deuterated chloroform and solvent was used, since chloroform is a weakly coordinating solvent, it could potentially interact with the Lewis acid in the chemical reactions and result in a competing equilibrium. To confirm whether the deuterated solvent will promote, hinder, or have no effect on the overall reaction, a blank set of reactions in deuterated chloroform can be conducted and monitored using ^{1}H NMR spectroscopy. The results obtained can be compared to the results measured in this thesis. Overall, the insight so far obtained in this study and the future avenues that will be conducted by our groups will further our understanding in predicting Lewis acid reactivity and advance the design and development of the FLA method for measuring Lewis acidity.

Chapter 4 Experimental

4.1. General Considerations

All reactions and manipulations were performed under nitrogen (N_2) or argon using either a MBraun LABstar Glove Box Workstation or standard Schlenk techniques. All glassware was either oven-dried at 110 °C or flame dried. Commercially available reagents were purchased from either Sigma-Aldrich, TCI Chemicals, or Oakwood Chemicals and employed without further purification, unless otherwise stated. All fluorescent Lewis base probes (**1**-**8**),[73–76] and the following Lewis acids: $B(C_6F_5)_3$, $B(p\text{-}C_6F_4H)_3$, $B(OC_6F_5)_3$, $B(2,4,6\text{-}F_3\text{-}C_6H_2)_3$, $B(3,4\text{-}F_2\text{-}C_6H_3)_3$, $B(4\text{-}F\text{-}C_6H_4)_3$, and $[Et_3Si][B(C_6F_5)_4]$ were synthesized according to literature procedures.[106–112] Solvents were obtained from an MBraun MB-SPS 800 solvent drying system (acetonitrile, diethyl ether, methylene chloride and toluene) or dried over calcium hydride (dichloromethane) and sodium (cyclohexane), then distilled under reduced pressure. All solvents were stored over activated 4 Å molecular sieves in the glovebox. All nuclear magnetic resonance (NMR) experiments utilized chloroform-d, $CDCl_3$. Chloroform-d was transferred to a Strauss flask and dried over activated 4 Å molecular sieves, then degassed by freeze-pump-thaw technique, followed by immediate transfer to the glovebox. All experiments monitored by NMR were conducted in NMR tubes (8" x 5 mm) equipped with J-Young screw caps. Proton (^1H) NMR spectra were recorded on either Bruker DRX 700 MHz or Bruker DRX 600 MHz spectrometers. NMR spectra were analyzed using either TopSpin 4.0.1 or MestReNova 6.0.2-5475 software. Chemical shifts are reported relative to tetramethylsilane ($SiMe_4$) and referenced to the residual solvent signal, ^1H to $CHCl_3$ (δ 7.26). Chemical shifts are reported in ppm and coupling constants as scalar values in Hz. The conventional abbreviations were used as follows: s (singlet), d (doublet), t (triplet), q (quartet), dd (doublet of doublets), dddd (doublet of doublets of doublets of doublets), m (multiplet). All absorption and fluorescence experiments were conducted in quartz cuvettes (1cm x 1cm) equipped with a Teflon seal and sealed with parafilm. Absorption measurements were conducted with a Cary 5000 UV-Vis-NIR Spectrophotometer from Agilent Technologies. The instrument was operating in single beam mode with the recording obtained at 25 °C and referenced to the respective solvent, providing the excitation wavelength for the FLA solution. Emission and excitation measurements were conducted with an Edinburgh Instruments FS5 Spectrofluorometer. Emission spectra were excited at their respective absorption maxima with the recording obtained at 25 °C and referenced to the respective solvent, providing the chromaticity coordinates for the FLA and probe solutions, and confirmed if any additional emissive species were present in solution. All absorption, emission and excitation measurements were graphed and analyzed

using both OriginLab's Origin and Microsoft Excel. In addition, all photophysical and chromaticity data regarding toluene has been previously report in our group's original and recent manuscript.[72,73]

4.2. General Guide to the FLA Method

All samples for optical spectroscopy measurements were prepared in the glovebox and the reactions were conducted in 20 mL scintillation vials. The solvents utilized for the optical spectroscopy measurements were acetonitrile (MeCN), chlorobenzene (PhCl), diethyl ether (Et_2O), dichloromethane (DCM) and toluene (Tol). A solution of the Lewis acid with one of the dithienophosphole oxide probes (**1**, **2**, **7**, **8**) in the respective solvent was generated. A 0.025 mM stock solution of each probe was prepared, and all Lewis acids were assembled to a final concentration of 0.25 mM in the appropriate solvent. The fluorescent Lewis adduct measurements, reported in Lewis acid units (LAU) are based on 90% saturation of the Lewis acid in the Lewis base solution. Typically, 1:1 stoichiometry of Lewis acid to Lewis base is required, however for weak Lewis acids several thousand equivalence are needed to obtain a saturated solution, which was determined from the emission spectra of the fluorescent Lewis acid-base adduct.

To calculate the LAU values, we recorded the chromaticity coordinates from the emission spectrum. The x and y coordinates generated from the 1931 CIE space were used to generate a polynomial fit of a second order (parabola) for the FLA and Lewis base probes. Using a solving software, such as WolframAlpha online, we set the parameters of the fit equation generated for the FLA in question and the parabolic fit of the dithienophosphole oxide probes in the respective solvent equal to each other. The polynomial fit equations for the probes and FLA in the different solvents are shown in **Table 6-1**. The software generated two intercepts; the farthest right (largest positive value) was used for the remaining calculations as it was the value most impacted by the bathochromic shift and was identified as the x-coordinate of the intersection between the two trends. The y coordinate was then calculated by solving the FLA fit function at the x value. The x and y coordinates represent the chromaticity values of the adduct between the Lewis acid being measured and a "theoretical dithienophosphole oxide" of a specific strength, shown in **Table 6-2**. By subbing in the x and y coordinates into **Equation 4-1**, the Lewis acid strength in LAUs was generated. In all cases, to minimize the potential of error, the probe fit function corresponding to the solvent being tested was always used. The measured margin of error for the LAU values was determined to be 0.25 and was reported in our group's most recent manuscript.

$$\text{Strength} = \frac{\sqrt{(\text{x}-\text{green vector x}-\text{coordinate})^2+(\text{y}-\text{green vector y}-\text{coordinate})^2}}{\sqrt{(\text{x}-\text{red vector x}-\text{coordinate})^2+(\text{y}-\text{red vector y}-\text{coordinate})^2}} \quad \textbf{(4-1)}$$

4.3. Experimental Procedures

4.3.1. Preparation for Titration Studies of $B(C_6F_5)_3$

Each of the four dithienophosphole oxide probes (**1**, **2**, **7**, **8**) underwent fluorescence titrations with $B(C_6F_5)_3$ in acetonitrile (MeCN), dichloromethane (DCM), chlorobenzene (PhCl), diethyl ether (Et_2O), and toluene (Tol). The titrations were conducted by generating 3 solutions: a solution of 12.5 mL of $B(C_6F_5)_3$ in the selected solvent (concentration varied from 25 μM to 1 μM), a solution of 12.5 mL containing 12.5 μM of the dithienophosphole oxide probe in the same selected solvent, and a solution containing 12.5 mL of the Lewis acid combined with 12.5 mL of the free Lewis base probe solution in the same solvent. For each system, two fluorescent compounds in solution were present: the free dithienophosphole oxide, and the Lewis base probe-$B(C_6F_5)_3$ adduct, which was seen by the clear isosbestic point, demonstrated by stacking the emission spectra.[73] Since, we have a system containing two fluorescent species in equilibrium, we were able to use the method developed by the Lakowicz group,[70] modeled in **Equation 4-2** to determine the binding constant of the Lewis acid-base adduct.

$$\frac{I_A}{I_F} = \frac{\frac{I_{A0}}{I_{F0}} + \frac{I_{A\infty}}{I_{F\infty}} K[LA]^n}{1 + K[LA]^n} \qquad \textbf{(4-2)}$$

The ratio of the intensity for the emission of the adduct and fluorophore ($\mathbf{I_A/I_F}$) were plotted against the concentration. The data was then fitted to a sigmoidal curve, and the equilibrium concentration was solved by determining the inflection point on the curve. The binding constant was then determined from **Equation 4-2**, and are shown in **Table 6-7**. Further details on the procedure for calculating the equilibrium concentration and the binding constant can be determined precisely as described in the supporting information of our groups' original manuscript.[70]

4.3.2. Catalytic Reaction Procedures

Reactions were monitored using ^{1}H NMR spectroscopy as a means of investigating the correlation between the FLA method and chemical reactivity. Two reactions were explored, the Diels-Alder cycloaddition of 2,3-dimethyl-1,3-butadiene with methyl acrylate,[97] and the hydrosilylation of benzophenone.[98] For both reactions, a wide range of Lewis acids was utilized: $AlCl_3$, $B(4\text{-}F\text{-}C_6H_4)_3$, $B(3,4\text{-}F_2\text{-}C_6H_3)_3$, $B(2,4,6\text{-}F_3\text{-}C_6H_2)_3$, $B(OC_6F_5)_3$, $B(C_6F_5)_3$, $B(p\text{-}C_6F_4H)_3$, $In(OTf)_3$, $Sc(OTf)_3$, and $Zn(OTf)_2$ in a variety of solvents, such as acetonitrile (MeCN), dichloromethane (DCM), chlorobenzene (PhCl), diethyl ether (Et_2O), and toluene (Tol). All experiments were conducted in NMR tubes (8" x 5 mm) equipped with J-Young screw caps.

For the Diels-Alder cycloaddition, the reaction was monitored by the formation of methyl-3,4-dimethyl-3-cyclohexenecarboxylate **15**. An equimolar amount of 2,3-dimethyl-1,3-butadiene **13**, (2.53 mmol, 208 mg) and methyl acrylate **14**, (2.53 mmol, 218 mg) were dissolved in 400 µL of deuterated chloroform and 200 µL of cyclohexane. Unless otherwise stated, the catalyst (mol%) was dissolved in 400 µL of the appropriate solvent being investigated and then added to the reaction mixture. The ^{1}H NMR spectra were recorded on either Bruker DRX 700 MHz or Bruker DRX 600 MHz spectrometers and acquired every 4 minutes for six hours. The product conversion in the Diels-Alder cycloaddition reaction was determined by the relative integrations of the multiplet -C*H*CO resonance of **15**, and the singlet -CH_2 resonance of cyclohexane, the internal standard. The product conversion of compound **15** relative to the internal standard was plotted over time.

For the hydrosilylation of benzophenone, the reaction was monitored by the formation of triethyl(1,1-diphenylmethoxy)silane **18**. An equimolar amount of benzophenone **16**, (1.0 mmol, 182 mg) and triethylsilane **17**, (1.0 mmol, 116 mg) were dissolved in 400 µL of deuterated chloroform and 200 µL of cyclohexane. Unless otherwise stated, the catalyst (mol%) was dissolved in 400 µL of the appropriate solvent being investigated and then added to the reaction mixture. The ^{1}H NMR spectra were recorded on either Bruker DRX 700 MHz or Bruker DRX 600 MHz spectrometers and acquired every 30 seconds for 1 hour. The product conversion of the hydrosilylation was determined by the relative integrations of the multiplet -OC*H*Ph resonance of **18**, and the singlet -CH_2 resonance of cyclohexane, the internal standard. The product conversion of compound **18** relative to the internal standard was plotted over time.

For both reactions, the Lewis acid triflates were specifically added directly into the J-Young NMR tubes, followed by the solvent, due to their insolubility. Specifically, to the hydrosilylation, a stock solution of $B(C_6F_5)_3$ and $B(p\text{-}C_6F_4H)_3$ in cyclohexane was made, due to the low catalyst loading (0.01 mol%) required. In a 20 mL scintillation vial, approximately 2 mg of the Lewis acid was weighed out and dissolved in 8 mL of cyclohexane, 200 μL was then pipetted into the J-Young NMR tube followed by the solvent.

Table 4-1. Details of ^{1}H NMR characterization of Diels-Alder cycloaddition reagents and products.

 **13**	Compound **13** – 2,3-dimethyl-1,4-butadiene ^{1}H NMR (700 MHz, $CDCl_3$): δ = 1.90 (s, 6H), δ = 4.94 (s, 2H), δ = 5.04 (s, 2H).
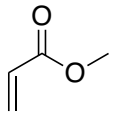 **14**	Compound **14** – methyl acrylate ^{1}H NMR (700 MHz, $CDCl_3$): δ = 3.68 (s, 3H), δ = 5.72 (d, $^3J_{H\text{-}H}$ = 10.4 Hz, 1H), δ = 6.08 (dd, $^3J_{H\text{-}H}$ = 17.6 Hz, $^3J_{H\text{-}H}$ = 10.4 Hz, 1H), δ = 6.36 (d, $^3J_{H\text{-}H}$ = 17.6 Hz, 1H).
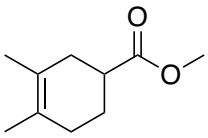 **15**	Compound **15** – methyl-3,4-dimethyl-3-cyclohexenecarboxylate ^{1}H NMR (700 MHz, $CDCl_3$): δ = 1.54-1.67 (m, 7H), δ = 1.90-2.24 (m, 5H), δ = 2.48 (dddd, $J_{H\text{-}H}$ = 11.5 Hz, $J_{H\text{-}H}$ = 10.1 Hz, $J_{H\text{-}H}$ = 5.7 Hz, $J_{H\text{-}H}$ = 2.8 Hz, 1H), δ = 3.60 (s, 3H).

Table 4-2. Details of ^{1}H NMR characterization of hydrosilylation reagents and products.

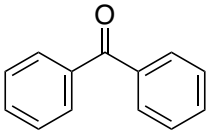 **16**	Compound **16** – benzophenone ^{1}H NMR (700 MHz, $CDCl_3$): δ = 7.44-7.47 (m, 4H), δ = 7.54-7.57 (m, 2H), δ = 7.77-7.79 (m, 4H).
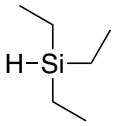 **17**	Compound **17** – triethylsilane ^{1}H NMR (700 MHz, $CDCl_3$): δ = 0.59 (q, $^3J_{H\text{-}H}$ = 7.86 Hz, 6H), δ = 0.99 (t, $^3J_{H\text{-}H}$ = 7.89 Hz, 9H), δ = 3.64 (m, 1H).
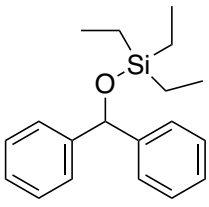 **18**	Compound **18** – triethyl(1,1-diphenylmethoxy)silane ^{1}H NMR (700 MHz, $CDCl_3$): δ = 0.58 (q, $^3J_{H\text{-}H}$ = 8.0 Hz, 6H), δ = 0.89 (t, $^3J_{H\text{-}H}$ = 8.0 Hz, 9H), δ = 5.76 (s, 1H), δ = 7.13-7.16 (m, 2H), δ = 7.22-7.24 (m, 4H), δ = 7.34-7.36 (m, 4H).

4.3.3. Procedures for Determining the Rate Constant

The rate constants were determined only for the neutral boranes in the Diels-Alder reaction. Before determining the rate constants, the rate law of this reaction was identified based on previous literature.[113,114] The rate law for the Diels-Alder reaction is demonstrated in **Equation 4-3**.

$$\text{Rate law} = k[A][B] \quad \textbf{(4-3)}$$

The Diels-Alder reaction was identified as an elementary reaction, shown below in **Equation 4-4**:

$$aA + bB \rightarrow cC \quad \textbf{(4-4)}$$

where both starting materials, 2,3-dimethyl-1,3-butadiene (A) and methyl acrylate (B) are first order, and the overall reaction is second order. In **Equation 4-3**, **[A]** and **[B]** express the concentrations of the starting materials in the reaction, respectively, in units of moles per liter. However, since the concentrations of both starting materials were nearly identical (same concentration), we can assume second order for either starting material, shown in **Equation 4-5**.

$$\text{Rate law} = k[A]^2 \text{ or Rate law} = k[B]^2 \quad \textbf{(4-5)}$$

As previously stated in the general considerations, ^{1}H NMR spectra were recorded on either a Bruker DRX 700 MHz or a Bruker DRX 600 MHz spectrometer. The NMR spectra were then analyzed using MestReNova 6.0.2-5475 software, specifically the reaction monitoring tool to obtain the concentrations for the starting material and product of the Diels-Alder reaction. Each reaction was conducted twice, and the average concentration of the starting material and product were used in calculating the rate constant. All rate constant determinations were plotted and analyzed using OriginLab's Origin. The first derivative of the product was calculated, and the starting material was squared based on **Equation 4-5**. The first derivative of the product (dept) and the starting material squared (**[A]**^{2}) were then plotted against each other to obtain the rate constant (**k)** based on **Equation 4-6**. The linear fit of the data was then determined, and the slope of the near linear fit was identified as the rate constant (**k**) of the reaction.

$$k = \frac{[A]^2}{dept} \quad \textbf{(4-6)}$$

4.3.4. Procedure for Generating Electrostatic Potential Maps

All density functional theory (DFT) calculations were carried out on the Gaussian 09 program. The geometry optimizations and frequency calculations of the arylboranes were performed using the RCAM-B3LYP functional with the 6-31+G(d) basis set, and then further optimized using the same level of theory with a PCM (Polarized Continuum Model) solvation model in toluene, chlorobenzene, dichloromethane, diethyl ether and acetonitrile. The visualization of the electron charge and the electrostatic potential of the molecules were obtained using the AIMSum program, which is a component of the AIMAll package.[96] The AIMQB program was used to convert the formatted checkpoint file obtained in the Gaussian 09 program into a wavefunction file, that could be read by the AIMSum program to generate the electron density map of the molecule. Using the Gaussian output file, we were able to generate the 3D-representation model of the total electrostatic potential map around the arylborane molecules.

Chapter 5 References

(1) Kolb, D. *J. Chem. Educ.* **1978**, *55*, 459–464.

(2) Lewis, G. N. *J. Am. Chem. Soc.* **1916**, *38*, 762–785.

(3) Lewis, G. N. *Valence and the Structure of Atoms and Molecules*; Chemical Catalogue Company: New York, 1923.

(4) Sereda, O.; Tabassum, S.; Wilhelm, R. *Asymmetric Organocatalysis*; Springer, 2009.

(5) Denmark, S. E.; Beutner, G. L. *Angew. Chem. Int. Ed.* **2008**, *47*, 1560–1638.

(6) Stephan, D. W. *Org. Biomol. Chem.* **2008**, *6*, 1535–1539.

(7) Yamamoto, H. *Lewis acids in organic synthesis*; Wiley-VCH Verlag, 2008.

(8) Wang, C.; Xi, Z. *Chem. Soc. Rev.* **2007**, *36*, 1395–1406.

(9) Becica, J.; Dobereiner, G. E. *Org. Biomol. Chem.* **2019**, *17*, 2055–2069.

(10) Wade, L. G. *Organic Chemistry*; Pearson, 2013.

(11) Groves, J. K. *Chem. Soc. Rev.* **1972**, *1*, 73–97.

(12) Crafts, J. M.; Friedel, C. *Compt. Rend.* **1877**, *84*, 1392–1395.

(13) Heravi, M. M.; Zadsirjan, V.; Momeni, T. *RSC Adv.* **2018**, *8*, 40061–40163.

(14) Rueping, M.; Nachtsheim, B. J. *Beilstein J. Org. Chem.* **2010**, *6*.

(15) Diels, O.; Alder, K. *Liebigs Ann. Chem.* **1928**, *460*, 98–122.

(16) Vermeeren, P.; Hamlin, T. A.; Fernández, I.; Bickelhaupt, F. M. *Angew. Chem. Int. Ed.* **2020**, *59*, 6201–6206.

(17) Funel, J. A.; Abele, S. *Angew. Chem. Int. Ed.* **2013**, *52*, 3822–3863.

(18) Frontier, A. J.; Collison, C. *Tetrahedron* **2005**, *61*, 7577–7606.

(19) Marciniec, B. *Hydrosilylation A Comprehensive Review on Recent Advances*; Springer, 2009.

(20) Nakajima, Y.; Shimada, S. *RSC Adv.* **2015**, *5*, 20603–20616.

(21) Brown, H. C.; Schlesinger, H. I.; Cardon, S. Z. *J. Am. Chem. Soc.* **1942**, *64*, 325–329.

(22) Wittig, G.; Rückert, A. *Justus Liebigs Ann. Chem.* **1950**, *566*, 101–113.

(23) Wittig, G.; Benz, E. *Chem. Ber.* **1959**, *92*, 1999–2013.

(24) Tochtermann, W. *Angew. Chem. Int. Ed. Engl.* **1966**, *5*, 351–371.

(25) Döring, S.; Erker, G.; Fröhlich, R.; Meyer, O.; Bergander, K. *Organometallics* **1998**, *17*, 2183–2187.

(26) Welch, G. C.; Cabrera, L.; Chase, P. A.; Hollink, E.; Masuda, J. D.; Wei, P.; Stephan, D. W. *Dalton Trans.* **2006**, *31*, 3407–3414.

(27) Stephan, D. W.; Erker, G. *Angew. Chem. Int. Ed. Engl.* **2015**, *54*, 6400–6441.

(28) Stephan, D. W. *Science (80-.).* **2016**, *354*, aaf7229–aaf7221.

(29) Li, Y.; Liu, J.; Huang, X.; Qu, L. B.; Zhao, C.; Langer, R.; Ke, Z. *Eur. J. Org. Chem.* **2019**, *25*, 13785–13798.

(30) Welch, G. C.; San Juan, R. R.; Masuda, J. D.; Stephan, D. W. *Science (80-.).* **2006**, *314*, 1124–1126.

(31) Lam, J.; Szkop, K. M.; Mosaferi, E.; Stephan, D. W. *Chem. Soc. Rev.* **2019**, *48*, 3592–3612.

(32) Chase, P. A.; Jurca, T.; Stephan, D. W. *Chem. Commun.* **2008**, *14*, 1701–1703.

(33) Chernichenko, K.; Madarász, Á.; Pápai, I.; Nieger, M.; Leskelä, M.; Repo, T. *Nat. Chem.* **2013**, *5*, 718–723.

(34) Scott, D. J.; Fuchter, M. J.; Ashley, A. E. *J. Am. Chem. Soc.* **2014**, *136*, 15813–15816.

(35) Otten, E.; Neu, R. C.; Stephan, D. W. *J. Am. Chem. Soc.* **2009**, *131*, 9918–9919.

(36) Mömming, C. M.; Otten, E.; Kehr, G.; Fröhlich, R.; Grimme, S.; Stephan, D. W.; Erker, G. *Angew. Chem. Int. Ed.* **2009**, *48*, 6643–6646.

(37) McCahill, J. S. J.; Welch, G. C.; Stephan, D. W. *Angew. Chem. Int. Ed.* **2007**, *46*, 4968–4971.

(38) Weicker, S. A.; Stephan, D. W. *Bull. Chem. Soc. Jpn.* **2015**, *88*, 1003–1016.

(39) Fontaine, F. G.; Courtemanche, M. A.; Légaré, M. A.; Rochette, É. *Coord. Chem. Rev.* **2017**, *334*, 124–135.

(40) Baumgartner, T.; Jäkle, F. *Main Group Strategies towards Functional Hybrid Materials*; Wiley, 2017.

(41) Doty, J. C.; Babb, B.; Grisdale, P. J.; Glogowski, M.; Williams, J. L. R. *J. Organomet. Chem.* **1972**, *38*, 229–236.

(42) Kaim, W.; Schulz, A. *Angew. Chem. Int. Ed. Engl.* **1984**, *23*, 615–616.

(43) Yuan, Z.; Collings, J. C.; Taylor, N. J.; Marder, T. B.; Jardin, C.; Halet, J. F. *J. Solid State Chem.* **2000**, *154*, 5–12.

(44) Liu, Z. Q.; Fang, Q.; Cao, D. X.; Wang, D.; Xu, G. B. *Org. Lett.* **2004**, *6*, 2933–2936.

(45) Noda, T.; Shirota, Y. *J. Am. Chem. Soc.* **1998**, *120*, 9714–9715.

(46) Tetsuya Noda; Ogawa, H.; Shirota, Y. *Adv. Mater.* **1999**, *11*, 283–285.

(47) Li, H.; Lalancette, R. A.; Jäkle, F. *Chem. Commun.* **2011**, *47*, 9378–9380.

(48) Jäkle, F. *Chem. Rev.* **2010**, *110*, 3985–4022.

(49) Tang, C. W.; Vanslyke, S. A. *Appl. Phys. Lett.* **1987**, *51*, 913–915.

(50) Zhang, X.; Tian, Y.; Yuan, P.; Li, Y.; Yaseen, M. A.; Grutzendler, J.; Moore, A.; Ran, C. *Chem. Commun.* **2014**, *50*, 11550–11553.

(51) Tee, B. C. K.; Wang, C.; Allen, R.; Bao, Z. *Nat. Nanotechnol.* **2012**, *7*, 825–832.

(52) Son, D.; Kang, J.; Vardoulis, O.; Kim, Y.; Matsuhisa, N.; Oh, J. Y.; To, J. W.; Mun, J.; Katsumata, T.; Liu, Y.; McGuire, A. F.; Krason, M.; Molina-Lopez, F.; Ham, J.; Kraft, U.; Lee, Y.; Yun, Y.; Tok, J. B. H.; Bao, Z. *Nat. Nanotechnol.* **2018**, *13*, 1057–1065.

(53) Bridges, C. R.; Baumgartner, T. *J. Phys. Org. Chem.* **2020**, *33*, e4077.

(54) Carlson, R.; Lundstedt, T.; Nordahl, Å.; Prochazka, M. *Acta Chem. Scand.* **1986**, *40*, 522−533.

(55) Jensen, W. B. *Chem. Rev.* **1978**, *78*, 1–22.

(56) Murray, P. M.; Tyler, S. N. G.; Moseley, J. D. *Org. Process Res. Dev.* **2013**, *17*, 40–46.

(57) Himmel, D.; Radtke, V.; Butschke, B.; Krossing, I. *Angew. Chem. Int. Ed.* **2018**, *57*, 4386–4411.

(58) Beckett, M. A.; Strickland, G. C.; Holland, J. R.; Varma, K. S. *Polymer* **1996**, *37*, 4629–4631.

(59) Mayer, U.; Gutmann, V.; Gerger, W. *Monatsh. Chem.* **1975**, *106*, 1235–1257.

(60) Childs, R. F.; Mulholland, D. L.; Nixon, A. *Can. J. Chem.* **1982**, *60*, 801–808.

(61) Hilt, G.; Nödling, A. *Eur. J. Org. Chem.* **2011**, 7071–7075.

(62) Sivaev, I. B.; Bregadze, V. I. *Coord. Chem. Rev.* **2014**, *270–271*, 75–88.

(63) Christe, K. O.; Dixon, D. A.; McLemore, D.; Wilson, W. W.; Sheehy, J. A.; Boatz, J. A. *J. Fluor. Chem.* **2000**, *101*, 151–153.

(64) Müller, L. O.; Himmel, D.; Stauffer, J.; Steinfeld, G.; Slattery, J.; Santiso-Quiñones, G.; Brecht, V.; Krossing, I. *Angew. Chem. Int. Ed.* **2008**, *47*, 7659–7663.

(65) Parr, R. G.; Szentpály, L. V.; Liu, S. *J. Am. Chem. Soc.* **1999**, *121*, 1922–1924.

(66) Maynard, A. T.; Huang, M.; Rice, W. G.; Covell, D. G. *PNAS* **1998**, *95*, 11578–11583.

(67) Parr, R. G.; Pearson, R. G. *J. Am. Chem. Soc.* **1983**, *105*, 7512–7516.

(68) Jupp, A. R.; Johnstone, T. C.; Stephan, D. W. *Dalton Trans.* **2018**, *47*, 7029–7035.

(69) Hog, M.; Schneider, M.; Studer, G.; Bäuerle, M.; Föhrenbacher, S. A.; Scherer, H.; Krossing, I. *Chem. Eur. J.* **2017**, *23*, 11054–11066.

(70) Lakowicz, J. R. *Principles of Fluorescence Spectroscopy*; Springer, 2006.

(71) Wade, C. R.; Broomsgrove, A. E. J.; Aldridge, S.; Gabbaï, F. P. *Chem. Rev.* **2010**, *110*, 3958–

3984.

(72) Bentley, J. N.; Elgadi, S. A.; Gaffen, J. R.; Demay-Drouhard, P.; Baumgartner, T.; Caputo, C. B. *Organometallics* **2020**, *39*, 3645–3655.

(73) Gaffen, J. R.; Bentley, J. N.; Torres, L. C.; Chu, C.; Baumgartner, T.; Caputo, C. B. *Chem* **2019**, *5*, 1567–1583.

(74) Baumgartner, T.; Neumann, T.; Wirges, B. *Angew. Chem. Int. Ed. Engl.* **2004**, *43*, 6197–6201.

(75) Dienes, Y.; Durben, S.; Kárpáti, T.; Neumann, T.; Englert, U.; Nyulászi, L.; Baumgartner, T. *Chem. Eur. J.* **2007**, *13*, 7487–7500.

(76) Baumgartner, T.; Bergmans, W.; Kárpáti, T.; Neumann, T.; Nieger, M.; Nyulászi, L. *Chem. Eur. J.* **2005**, *11*, 4687–4699.

(77) Baumgartner, T. *Acc. Chem. Res.* **2014**, *47*, 1613–1622.

(78) Broadbent, A. D. *Color Res. Appl.* **2004**, *29*, 267–272.

(79) Romero-Nieto, C.; Baumgartner, T. *Synlett* **2013**, *24*, 920–937.

(80) Reichardt, C. *Angew. Chem. Int. Ed. Engl.* **1979**, *18*, 98–110.

(81) Romero-Nieto, C.; Kamada, K.; Cramb, D. T.; Merino, S.; Rodríguez-López, J.; Baumgartner, T. *Eur. J. Org. Chem.* **2010**, *27*, 5225–5231.

(82) Chua, C. J.; Ren, Y.; Baumgartner, T. *Org. Lett.* **2012**, *14*, 1588–1591.

(83) Ren, Y.; Orthaber, A.; Pietschnig, R.; Baumgartner, T. *Dalton Trans.* **2013**, *42*, 5314–5321.

(84) Lawson, J. R.; Melen, R. L. *Inorg. Chem.* **2017**, *56*, 8627–8643.

(85) Shcherbina, N. A.; Pomogaeva, A. V.; Lisovenko, A. S.; Kazakov, I. V.; Gugin, N. Y.; Khoroshilova, O.V.; Kondrat'ev, Y. V.; Timoshkin, A. Y. *Z. Anorg. Allg. Chem.* **2020**, *646*, 873–881.

(86) Gutmann, V. *Electrochim. Acta* **1976,** 21, 661-670.

(87) Mayer, R. J.; Hampel, N.; Ofial, A. R. *Chem. Eur. J.* **2021**, *27*, 4070–4080.

(88) Groggins, P. H. *Ind. Eng. Chem. Res.* **1931**, *23*, 152–160.

(89) Kuzu, I.; Krummenacher, I.; Meyer, J.; Armbruster, F.; Breher, F. *Dalton Trans.* **2008**, *43*, 5836–5865.

(90) Kobayashi, S. *Eur. J. Org. Chem* **1999**, *1*, 15–27.

(91) Iacobucci, C.; Jouini, N.; Massi, L.; Olivero, S.; De Angelis, F.; Duñach, E.; Gal, J. F. *Chempluschem* **2017**, *82*, 498–506.

(92) Großekappenberg, H.; Reißmann, M.; Schmidtmann, M.; Müller, T. *Organometallics* **2015**, *34*, 4952–4958.

(93) Dimroth, K.; Reichardt, C.; Siepmann, T.; Bohlmann, F. *Justus Liebigs Ann. Chem.* **1963**, *661*, 1–37.

(94) Reichardt, C. *Chem. Rev.* **1994**, *94*, 2319–2358.

(95) Krygowski, T. M.; Fawcett, W. R. *J. Am. Chem. Soc.* **1975**, *97*, 2143–2148.

(96) AIMAII (Version 19.10.12) Keith, T. A. TK Gristmill Software, Overland Park KS, USA, 2019 (aim.tkgristmill.com)

(97) Vermeeren, P.; Tiezza, M. D.; van Dongen, M.; Fernández, I.; Bickelhaupt, F. M.; Hamlin, T. A. *Chem. Eur. J.* **2021**, *27*.

(98) Bach, P.; Albright, A.; Laali, K. K. *Eur. J. Org. Chem.* **2009**, *12*, 1961–1966.

(99) Thakur, A. J. *Synlett* **2003**, *6*, 899–900.

(100) Parks, D. J.; Piers, W. E. *J. Am. Chem. Soc.* **1996**, *118*, 9440–9441.

(101) Nikonov, G. I. *ACS Catal.* **2017**, *7*, 7257–7266.

(102) Whitmore, F. C.; Pietrusza, E. W.; Sommer, L. H. *J. Am. Chem. Soc.* **1947**, *69*, 2108–2110.

(103) Prajapati, A.; Kumar, M.; Thakuria, R.; Basak, A. K. *Tetrahedron Lett.* **2019**, *60*, 150955.

(104) Mummadi, S.; Kenefake, D.; Diaz, R.; Unruh, D. K.; Krempner, C. *Inorg. Chem.* **2017**, *56*, 10748–10759.

(105) Morgan, M. M.; Marwitz, A. J. V.; Piers, W. E.; Parvez, M. *Organometallics* **2013**, *32*, 317–322.

(106) Naumann, D.; Butler, H.; Gnann, R. *Z. Anorg. Allg. Chem* **1992**, *618*, 74–76.

(107) Massey, A. G.; Park, A. J. *J. Organomet. Chem.* **1964**, *2*, 245–250.

(108) Santi, M.; Ould, D. M. C.; Wenz, J.; Soltani, Y.; Melen, R. L.; Wirth, T. *Angew. Chem. Int. Ed.* **2019**, *58*, 7861–7865.

(109) Jia, X.; Zhang, M.; Li, M.; Pan, F.; Ding, K.; Jia, L.; Crandall, L. A.; Engle, J. T.; Ziegler, C. J. *Organometallics* **2017**, *36*, 1122–1132.

(110) Nicasio, J. A.; Steinberg, S.; Inés, B.; Alcarazo, M. *Eur. J. Org. Chem* **2013**, *19*, 11016–11020.

(111) Ullrich, M.; Lough, A. J.; Stephan, D. W. *Organometallics* **2010**, *29*, 3647–3654.

(112) Lambert, J. B.; Zhang, S.; Ciro, S. M. *Organometallics* **1994**, *13*, 2430–2443.

(113) Wright, M. R. *Introduction to Chemical Kinetics*; Wiley, 2005.

(114) Inukai, T.; Kojima, T. *J. Org. Chem.* **1967**, *32*, 872–875.

Chapter 6 Appendix

6.1. Chromaticity Data and LAUs

Table 6-1. Fit data of the parabolic functions generated for the dithienophosphole oxide Lewis base probes in the different solvents, where a, b, and c are the parameters of the parabolic fit ax^2+bx+c and the maximum point located at the apex of the parabolic function represents the green vector (x, y coordinate) and the minimum point located at the root of the parabolic function represents the red vector (x, y coordinate).

Solvent	a	b	c	Green Vector (x)	Green Vector (y)	Red Vector (x)	Red Vector (y)
Acetonitrile	-12.6071	8.74961	-0.91302	0.34701	0.60509	0.53250	0.17133
Chlorobenzene	-12.9249	8.97868	-0.94441	0.34734	0.61492	0.53197	0.17433
Diethyl Ether	-17.7898	11.4187	-1.27140	0.32093	0.56092	0.48220	0.09827
Dichloromethane	-11.7166	8.29264	-0.86135	0.35388	0.60597	0.54619	0.17267

Table 6-2. Fit data of the parabolic functions generated where a, b, and c are the parameters of the parabolic fit ax^2+bx+c and R^2 is the root mean squared error of the fit function.

Lewis Acid	Solvent	Strength (LAU)	a	b	c	R^2
None	Acetonitrile	--	-12.6071	8.74961	-0.91302	0.99696
	Chlorobenzene	--	-12.9249	8.97868	-0.94441	0.99612
	Diethyl Ether	--	-17.7898	11.4187	-1.27140	0.99374
	Dichloromethane	--	-11.7166	8.29264	-0.86135	0.99700
$AlCl_3$	Acetonitrile	24.85	-4.26204	3.44630	-0.15502	0.99266
	Chlorobenzene	32.47	-3.45466	2.76427	-0.02206	0.99140
	Diethyl Ether	15.64	-3.86342	3.12588	-0.09382	0.98840
	Dichloromethane	30.35	-3.48780	2.82073	-0.03901	0.98453
$B(4\text{-}F\text{-}C_6H_4)_3$	Chlorobenzene	25.64	-5.62172	4.53926	-0.36815	0.99628
	Diethyl Ether	17.52	-4.62106	3.78079	0.243360	0.99535
	Dichloromethane	22.60	-7.32699	5.70432	-0.55231	0.97615
$B(3,4\text{-}F_2\text{-}C_6H_3)_3$	Chlorobenzene	25.81	-4.79959	3.94127	-0.26248	0.99243
	Diethyl Ether	13.33	-5.69041	4.58960	-0.37302	0.99902
	Dichloromethane	21.64	-5.41076	4.38279	-0.33380	0.99111
$B(2,4,6\text{-}F_3\text{-}C_6H_2)_3$	Chlorobenzene	29.38	-3.80394	3.07176	-0.08214	0.98827
	Diethyl Ether	14.65	-4.31100	3.48408	-0.15999	0.99392
	Dichloromethane	26.98	-3.96734	3.21123	-0.11013	0.99002
$B(OC_6F_5)_3$	Chlorobenzene	30.92	-3.72986	3.03645	-0.08439	0.98840
	Diethyl Ether	16.55	-3.64015	2.93829	-0.05927	0.99034
	Dichloromethane	28.80	-3.78984	3.08421	-0.09279	0.98926
$B(C_6F_5)_3$	Chlorobenzene	33.59	-2.90763	2.28492	0.08031	0.98687
	Diethyl Ether	17.14	-3.09578	2.45071	0.04521	0.98962
	Dichloromethane	31.27	-3.09970	2.45970	0.04249	0.98598
$B(p\text{-}C_6F_4H)_3$	Chlorobenzene	33.57	-3.02047	2.38807	0.05685	0.98716
	Diethyl Ether	16.49	-3.29629	2.61438	0.01499	0.98928
	Dichloromethane	31.34	-3.19876	2.55002	0.02179	0.98638
$In(OTf)_3$	Acetonitrile	27.00	-3.77502	3.04232	-0.07686	0.98738
	Chlorobenzene	29.77	-3.89516	3.16771	-0.10744	0.98744
	Diethyl Ether	16.07	-3.97717	3.22096	-0.11582	0.99837
	Dichloromethane	26.22	-4.12004	3.33957	-0.13521	0.98748
$Sc(OTf)_3$	Acetonitrile	24.77	-4.20296	3.40136	-0.14635	0.99115
	Chlorobenzene	28.75	-3.99906	3.26053	-0.12551	0.98564
	Diethyl Ether	16.41	-4.09400	3.34218	-0.14699	0.99815
	Dichloromethane	27.36	-3.96230	3.23120	-0.12060	0.98564
$Zn(OTf)_2$	Acetonitrile	19.34	-5.73106	4.56977	-0.35340	0.99728
	Chlorobenzene	23.94	-6.22865	4.92687	-0.41974	0.99957

	Diethyl Ether	13.41	-5.32864	4.26701	-0.30311	0.99996
	Dichloromethane	25.66	-6.12660	4.84339	-0.40977	0.99201
$[Et_3Si][B(C_6F_5)_4]$	Acetonitrile	--	--	--	--	--
	Chlorobenzene	37.87	-2.98427	2.44843	0.01403	0.98635
	Diethyl Ether	30.07	-0.90885	1.15966	0.15997	098078
	Dichloromethane	33.44	-3.10600	2.50016	0.02106	0.98675

Table 6-3. Chromaticity data of all Lewis acids tested. Strength is reported in Lewis acid units; x and y correspond to the chromaticity x-coordinate and y-coordinate respectively at the FLA fit/probe fit intercept; blue vector is the magnitude of the vector from intersection to the weakest FLA measurable; red vector is the magnitude of the vector from the intersection to the strongest FLA measurable.

Lewis Acid	Solvent	Strength (LAU)	x	y	Green Vector	Red Vector
$AlCl_3$	Acetonitrile	24.85	0.41842	0.54080	0.09608	0.38669
	Chlorobenzene	32.47	0.42937	0.52794	0.11956	0.36819
	Diethyl Ether	15.64	0.38710	0.53729	0.07026	0.44920
	Dichloromethane	30.35	0.43550	0.52792	0.11293	0.37210
$B(4\text{-}F\text{-}C_6H_4)_3$	Chlorobenzene	25.64	0.42001	0.54667	0.09969	0.38880
	Diethyl Ether	17.52	0.39077	0.52842	0.07703	0.43976
	Dichloromethane	22.60	0.42335	0.54943	0.08957	0.39628
$B(3,4\text{-}F_2\text{-}C_6H_3)_3$	Chlorobenzene	25.81	0.42026	0.54618	0.10021	0.38826
	Diethyl Ether	13.33	0.38158	0.54974	0.06167	0.46255
	Dichloromethane	21.64	0.42160	0.55224	0.08644	0.39950
$B(2,4,6\text{-}F_3\text{-}C_6H_2)_3$	Chlorobenzene	29.38	0.42537	0.53621	0.11083	0.37750
	Diethyl Ether	14.65	0.38491	0.54237	0.06661	0.45463
	Dichloromethane	26.98	0.43060	0.53702	0.10315	0.38225
$B(OC_6F_5)_3$	Chlorobenzene	30.92	0.42741	0.53205	0.11523	0.37268
	Diethyl Ether	16.55	0.38894	0.53289	0.07356	0.44451
	Dichloromethane	28.80	0.43331	0.53206	0.10849	0.37670
$B(C_6F_5)_3$	Chlorobenzene	33.59	0.43073	0.52505	0.12260	0.36504
	Diethyl Ether	17.14	0.39008	0.53012	0.07570	0.44157
	Dichloromethane	31.27	0.43676	0.52549	0.11552	0.36940
$B(p\text{-}C_6F_4H)_3$	Chlorobenzene	33.57	0.43071	0.52509	0.12256	0.36508
	Diethyl Ether	16.49	0.38882	0.53318	0.07334	0.44482
	Dichloromethane	31.34	0.43685	0.52532	0.11570	0.36921
$In(OTf)_3$	Acetonitrile	27.00	0.42169	0.53477	0.10257	0.37996
	Chlorobenzene	29.77	0.42590	0.53514	0.11197	0.37607
	Diethyl Ether	16.07	0.38799	0.53517	0.07183	0.44694
	Dichloromethane	26.22	0.42941	0.53913	0.10085	0.38462
$Sc(OTf)_3$	Acetonitrile	24.77	0.41829	0.54103	0.09583	0.38694
	Chlorobenzene	28.75	0.42451	0.53795	0.10899	0.37916
	Diethyl Ether	16.41	0.38867	0.53356	0.07305	0.44523
	Dichloromethane	27.36	0.43117	0.53597	0.10427	0.38107
$Zn(OTf)_2$	Acetonitrile	19.34	0.40880	0.55696	0.07832	0.40499
	Chlorobenzene	23.94	0.41734	0.55158	0.09440	0.39428
	Diethyl Ether	13.41	0.38180	0.54927	0.06197	0.46204
	Dichloromethane	25.66	0.42852	0.54070	0.09915	0.38638

$[Et_3Si][B(C_6F_5)_4]$	Acetonitrile	--	--	--	--	--
	Chlorobenzene	37.87	0.43556	0.51431	0.14359	0.35825
	Diethyl Ether	30.07	0.40757	0.48164	0.15268	0.33397
	Dichloromethane	33.44	0.43959	0.51990	0.14271	0.36291

6.2. Photophysical Data

6.2.1. Spectroscopic Properties

Table 6-4. Spectroscopic properties for the FLAs of probe **1** in varying polar solvents.

Lewis Acid	Solvent	λ_{abs} (nm)	λ_{emis} (nm)	Stoke Shift (cm^{-1})	$\Delta\lambda_{emis}$ (nm)
None	Acetonitrile	361	450	5479	--
	Dichloromethane	362	453	5549	--
	Chlorobenzene	361	450	5479	--
	Diethyl Ether	357	443	5438	--
	Toluene	362	446	5203	--
$AlCl_3$	Acetonitrile	379	496	6224	46
	Dichloromethane	385	502	6054	49
	Chlorobenzene	387	502	5919	52
	Diethyl Ether	382	498	6098	55
	Toluene	387	503	5959	57
$B(4\text{-}F\text{-}C_6H_4)_3$	Dichloromethane	362	461	5932	8
	Chlorobenzene	368	479	6297	29
	Diethyl Ether	374	488	6246	45
	Toluene	371	479	6077	33
$B(3,4\text{-}F_2\text{-}C_6H_3)_3$	Dichloromethane	377	480	5692	27
	Chlorobenzene	381	484	5586	34
	Diethyl Ether	374	479	5861	36
	Toluene	384	501	6082	55
$B(2,4,6\text{-}F_3\text{-}C_6H_2)_3$	Dichloromethane	382	497	6057	44
	Chlorobenzene	383	498	6029	48
	Diethyl Ether	379	494	6142	51
	Toluene	384	496	5880	50
$B(OC_6F_5)_3$	Dichloromethane	381	497	6126	44
	Chlorobenzene	383	497	5989	47
	Diethyl Ether	381	502	6326	59
	Toluene	382	500	6178	54
$B(C_6F_5)_3$	Dichloromethane	390	507	5917	54
	Chlorobenzene	388	508	6088	58
	Diethyl Ether	388	507	6049	64
	Toluene	391	509	5929	63
$B(p\text{-}C_6F_4H)_3$	Dichloromethane	401	508	5253	55
	Chlorobenzene	404	509	5106	59
	Diethyl Ether	388	507	6049	64

	Toluene	392	509	5864	63
$In(OTf)_3$	Acetonitrile	380	500	6316	50
	Dichloromethane	379	495	6183	42
	Chlorobenzene	381	496	6085	46
	Diethyl Ether	381	495	6045	52
	Toluene	380	497	6195	51
$Sc(OTf)_3$	Acetonitrile	378	496	6294	46
	Dichloromethane	380	496	6154	43
	Chlorobenzene	380	495	6114	45
	Diethyl Ether	381	494	6004	51
	Toluene	380	497	6195	51
$Zn(OTf)_2$	Acetonitrile	369	481	6310	31
	Dichloromethane	370	477	6063	24
	Chlorobenzene	367	467	5835	17
	Diethyl Ether	373	483	6106	40
	Toluene	370	470	5750	24
$[Et_3Si][B(C_6F_5)_4]$	Dichloromethane	388	510	6165	57
	Chlorobenzene	396	518	5948	68
	Diethyl Ether	381	514	6791	71
	Toluene	388	515	6356	69

Table 6-5. Spectroscopic properties for the FLAs of probe **2** in varying polar solvents.

Lewis Acid	Solvent	λ_{abs} (nm)	λ_{emis} (nm)	Stoke Shift (cm^{-1})	$\Delta\lambda_{emis}$ (nm)
None	Acetonitrile	420	521	4616	--
	Dichloromethane	422	524	4613	--
	Chlorobenzene	422	527	4721	--
	Diethyl Ether	418	516	4544	--
	Toluene	423	521	4447	--
$AlCl_3$	Acetonitrile	439	575	5388	54
	Dichloromethane	440	590	5778	66
	Chlorobenzene	453	592	5183	65
	Diethyl Ether	445	583	5319	67
	Toluene	449	589	5294	68
$B(4\text{-}F\text{-}C_6H_4)_3$	Dichloromethane	429	553	5227	29
	Chlorobenzene	437	565	5184	38
	Diethyl Ether	433	559	5206	43
	Toluene	438	541	4347	20
$B(3,4\text{-}F_2\text{-}C_6H_3)_3$	Dichloromethane	440	564	4997	40
	Chlorobenzene	447	574	4950	47
	Diethyl Ether	437	560	5026	44
	Toluene	448	581	5110	60
$B(2,4,6\text{-}F_3\text{-}C_6H_2)_3$	Dichloromethane	444	582	5340	58
	Chlorobenzene	428	558	5443	31
	Diethyl Ether	441	575	5284	59
	Toluene	446	580	5180	59
$B(OC_6F_5)_3$	Dichloromethane	445	584	5349	60
	Chlorobenzene	448	586	5257	59
	Diethyl Ether	442	585	5530	69
	Toluene	448	586	5257	65
$B(C_6F_5)_3$	Dichloromethane	454	596	5248	72
	Chlorobenzene	450	600	5556	73
	Diethyl Ether	450	594	5387	78
	Toluene	453	597	5325	76
$B(p\text{-}C_6F_4H)_3$	Dichloromethane	450	595	5416	71
	Chlorobenzene	452	597	5374	70
	Diethyl Ether	447	591	5451	75
	Toluene	450	596	5444	75
$In(OTf)_3$	Acetonitrile	441	580	5434	59
	Dichloromethane	445	581	5260	57
	Chlorobenzene	450	586	5127	59

	Diethyl Ether	423	575	6249	59
	Toluene	443	581	5362	60
$Sc(OTf)_3$	Acetonitrile	440	578	5426	57
	Dichloromethane	446	586	5357	62
	Chlorobenzene	447	586	5307	59
	Diethyl Ether	445	576	5111	60
	Toluene	442	582	5442	61
$Zn(OTf)_2$	Acetonitrile	429	554	5260	33
	Dichloromethane	432	557	5195	33
	Chlorobenzene	429	546	4995	19
	Diethyl Ether	435	559	5099	43
	Toluene	433	557	5141	36
$[Et_3Si][B(C_6F_5)_4]$	Dichloromethane	458	596	5056	72
	Chlorobenzene	457	602	5271	75
	Diethyl Ether	439	599	6085	83
	Toluene	453	600	5408	79

Table 6-6. Spectroscopic properties for the FLAs of probe **7** in varying polar solvents.

Lewis Acid	Solvent	λ_{abs} (nm)	λ_{emis} (nm)	Stoke Shift (cm^{-1})	$\Delta\lambda_{emis}$ (nm)
None	Acetonitrile	401	496	4776	--
	Dichloromethane	405	499	4651	--
	Chlorobenzene	403	497	4693	--
	Diethyl Ether	397	488	4697	--
	Toluene	402	494	4633	--
$AlCl_3$	Acetonitrile	421	549	5538	53
	Dichloromethane	431	564	5471	65
	Chlorobenzene	436	571	5423	74
	Diethyl Ether	427	558	5498	70
	Toluene	431	562	5408	68
$B(4\text{-}F\text{-}C_6H_4)_3$	Dichloromethane	402	510	5268	11
	Chlorobenzene	416	532	5241	35
	Diethyl Ether	404	516	5373	28
	Toluene	410	527	5415	33
$B(3,4\text{-}F_2\text{-}C_6H_3)_3$	Dichloromethane	421	536	5096	37
	Chlorobenzene	425	544	5147	47
	Diethyl Ether	417	533	5219	45
	Toluene	431	555	5184	61
$B(2,4,6\text{-}F_3\text{-}C_6H_2)_3$	Dichloromethane	427	555	5401	56
	Chlorobenzene	446	583	5269	86
	Diethyl Ether	423	552	5525	64
	Toluene	431	553	5119	59
$B(OC_6F_5)_3$	Dichloromethane	427	560	5562	61
	Chlorobenzene	428	560	5507	63
	Diethyl Ether	426	562	5681	74
	Toluene	428	562	5571	68
$B(C_6F_5)_3$	Dichloromethane	436	569	5361	70
	Chlorobenzene	433	571	5582	74
	Diethyl Ether	431	566	5534	78
	Toluene	435	570	5445	76
$B(p\text{-}C_6F_4H)_3$	Dichloromethane	432	567	5512	68
	Chlorobenzene	434	570	5498	73
	Diethyl Ether	429	565	5611	77
	Toluene	433	570	5551	76
$In(OTf)_3$	Acetonitrile	422	554	5646	58
	Dichloromethane	426	552	5358	53
	Chlorobenzene	426	556	5489	59

	Diethyl Ether	422	555	5679	67
	Toluene	429	560	5453	66
$Sc(OTf)_3$	Acetonitrile	422	552	5581	56
	Dichloromethane	427	553	5336	54
	Chlorobenzene	427	554	5369	57
	Diethyl Ether	428	559	5475	71
	Toluene	430	559	5367	65
$Zn(OTf)_2$	Acetonitrile	411	530	5463	34
	Dichloromethane	406	511	5061	12
	Chlorobenzene	412	527	5296	30
	Diethyl Ether	414	592	7263	104
	Toluene	411	535	5639	41
$[Et_3Si][B(C_6F_5)_4]$	Dichloromethane	433	571	5582	72
	Chlorobenzene	438	576	5470	79
	Diethyl Ether	403	522	5657	34
	Toluene	402	493	4592	-1

Table 6-7. Spectroscopic properties for the FLAs of probe **8** in varying polar solvents.

Lewis Acid	Solvent	λ_{abs} (nm)	λ_{emis} (nm)	Stoke Shift (cm^{-1})	$\Delta\lambda_{emis}$ (nm)
None	Acetonitrile	439	552	4663	--
	Dichloromethane	445	558	4551	--
	Chlorobenzene	447	554	4321	--
	Diethyl Ether	444	543	4106	--
	Toluene	446	548	4173	--
$AlCl_3$	Acetonitrile	461	616	5458	64
	Dichloromethane	476	632	5186	74
	Chlorobenzene	483	623	4653	69
	Diethyl Ether	470	620	5148	77
	Toluene	482	619	4592	71
$B(4\text{-}F\text{-}C_6H_4)_3$	Dichloromethane	447	584	5248	26
	Chlorobenzene	457	598	5159	44
	Diethyl Ether	455	593	5115	50
	Toluene	455	560	4121	12
$B(3,4\text{-}F_2\text{-}C_6H_3)_3$	Dichloromethane	463	601	4959	43
	Chlorobenzene	474	611	4730	57
	Diethyl Ether	459	595	4980	52
	Toluene	474	611	4730	63
$B(2,4,6\text{-}F_3\text{-}C_6H_2)_3$	Dichloromethane	466	618	5278	60
	Chlorobenzene	471	622	5154	68
	Diethyl Ether	463	612	5258	69
	Toluene	466	610	5066	62
$B(OC_6F_5)_3$	Dichloromethane	469	625	5322	67
	Chlorobenzene	476	625	5008	71
	Diethyl Ether	465	624	5480	81
	Toluene	469	613	5009	65
$B(C_6F_5)_3$	Dichloromethane	486	637	4877	79
	Chlorobenzene	477	642	5388	88
	Diethyl Ether	474	635	5349	92
	Toluene	491	631	4519	83
$B(p\text{-}C_6F_4H)_3$	Dichloromethane	476	635	5260	77
	Chlorobenzene	481	638	5116	84
	Diethyl Ether	470	630	5403	87
	Toluene	482	627	4798	79
$In(OTf)_3$	Acetonitrile	463	621	5495	69
	Dichloromethane	466	619	5304	61
	Chlorobenzene	471	622	5154	68

	Diethyl Ether	464	615	5292	72
	Toluene	467	604	4857	56
$Sc(OTf)_3$	Acetonitrile	462	616	5411	64
	Dichloromethane	466	626	5485	68
	Chlorobenzene	467	623	5362	69
	Diethyl Ether	466	614	5173	71
	Toluene	467	618	5232	70
$Zn(OTf)_2$	Acetonitrile	451	593	5310	41
	Dichloromethane	452	585	5030	27
	Chlorobenzene	455	589	5000	35
	Diethyl Ether	454	532	3229	-11
	Toluene	458	581	4622	33
$[Et_3Si][B(C_6F_5)_4]$	Dichloromethane	489	641	4849	83
	Chlorobenzene	504	671	4938	117
	Diethyl Ether	447	576	5010	33
	Toluene	490	633	4610	85

6.2.2. Absorption Spectra

6.2.2.1. AlCl3

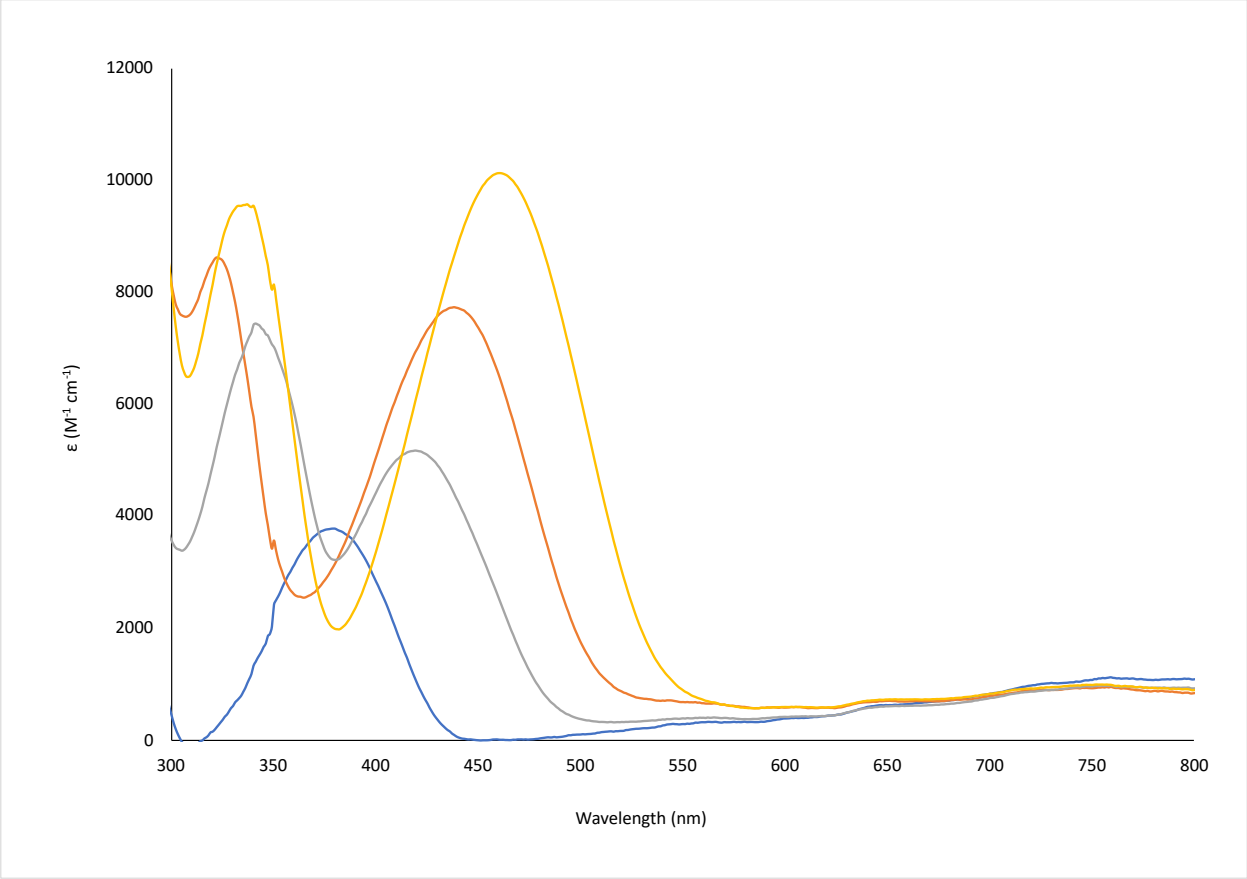

Figure 6-1. Stacked UV-Vis absorption spectra of probe 1 (blue, 100 eq.), 2 (orange, 100 eq.), 7 (grey, 100 eq.), and 8 (yellow, 100 eq.) with $AlCl_3$ in MeCN; 12.5 µM samples.

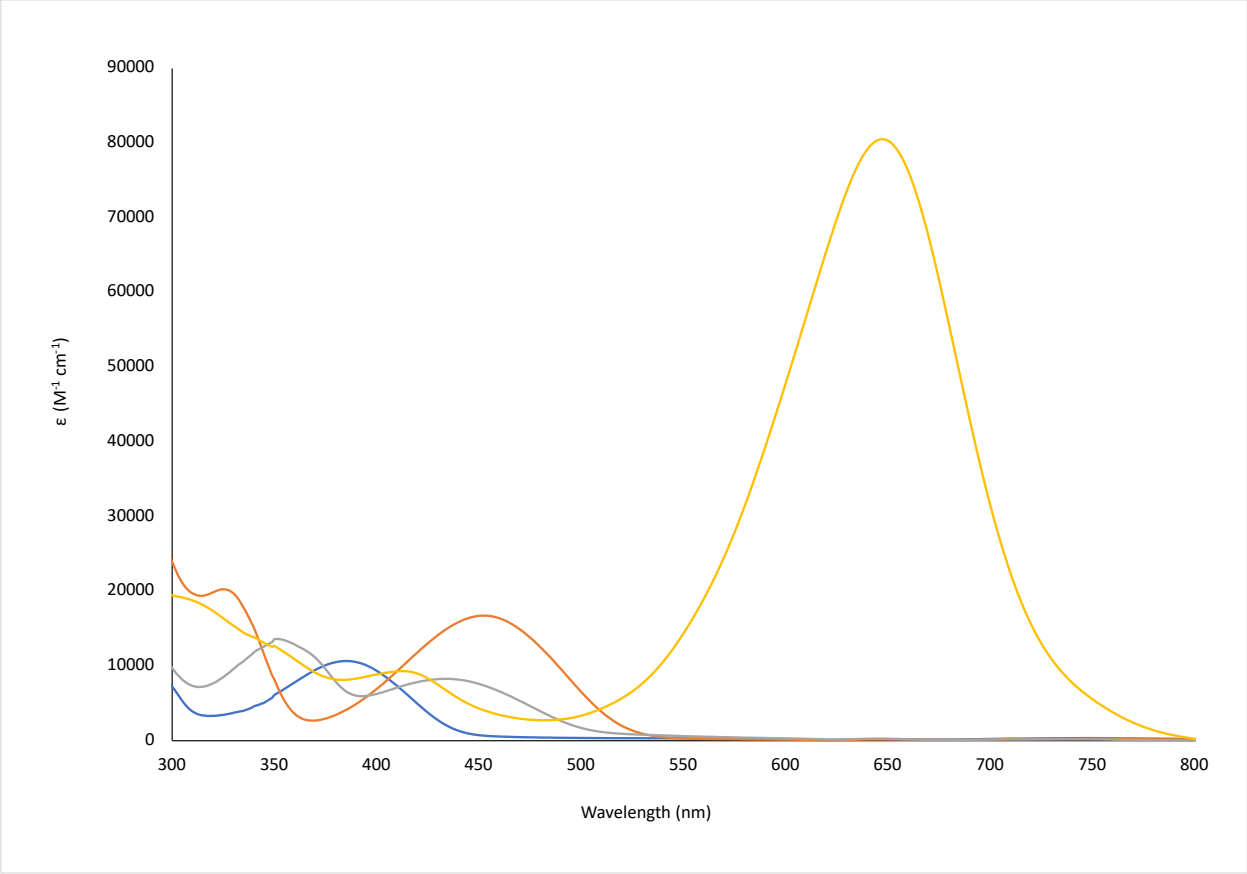

Figure 6-2. Stacked UV-Vis absorption spectra of probe 1 (blue, 10 eq.), 2 (orange, 10 eq.), 7 (grey, 10 eq.), and 8 (yellow, 10 eq.) with $AlCl_3$ in PhCl; 12.5 μM samples.

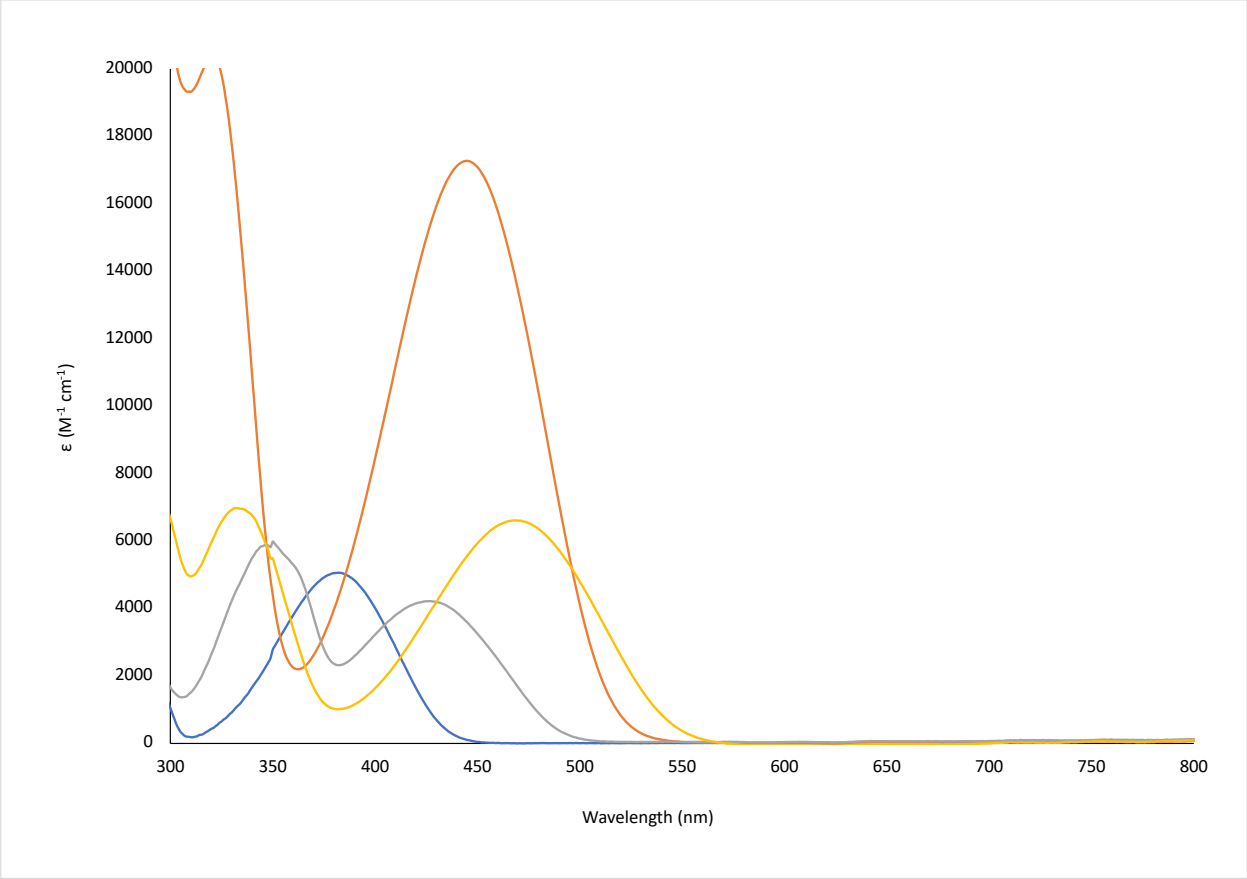

Figure 6-3. Stacked UV-Vis absorption spectra of probe 1 (blue, 50 eq.), 2 (orange, 50 eq.), 7 (grey, 50 eq.), and 8 (yellow, 50 eq.) with $AlCl_3$ in Et_2O; 12.5 μM samples.

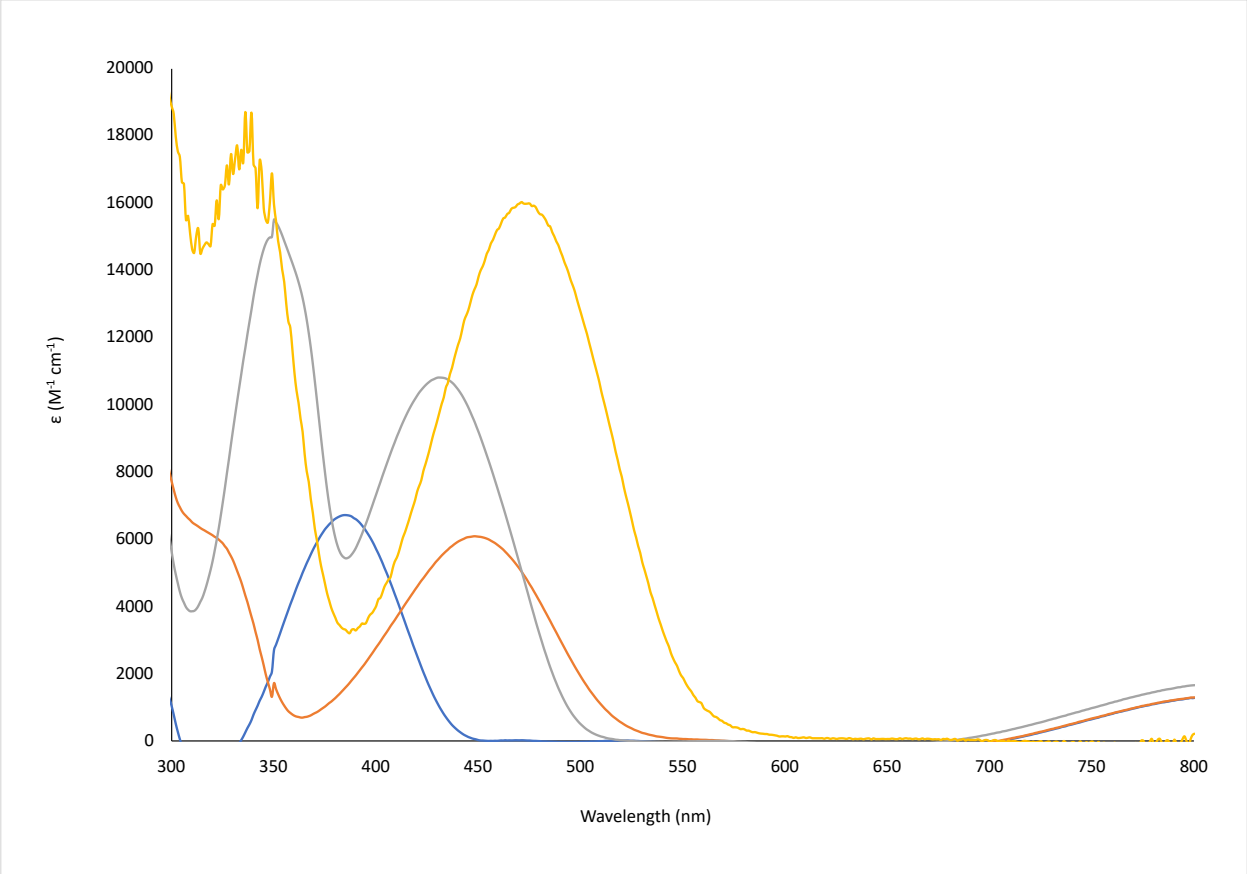

Figure 6-4. Stacked UV-Vis absorption spectra of probe 1 (blue, 10 eq.), 2 (orange, 10 eq.), 7 (grey, 10 eq.), and 8 (yellow, 10 eq.) with $AlCl_3$ in DCM; 12.5 μM samples.

6.2.2.2. $B(4\text{-}F\text{-}C_6H_4)_3$

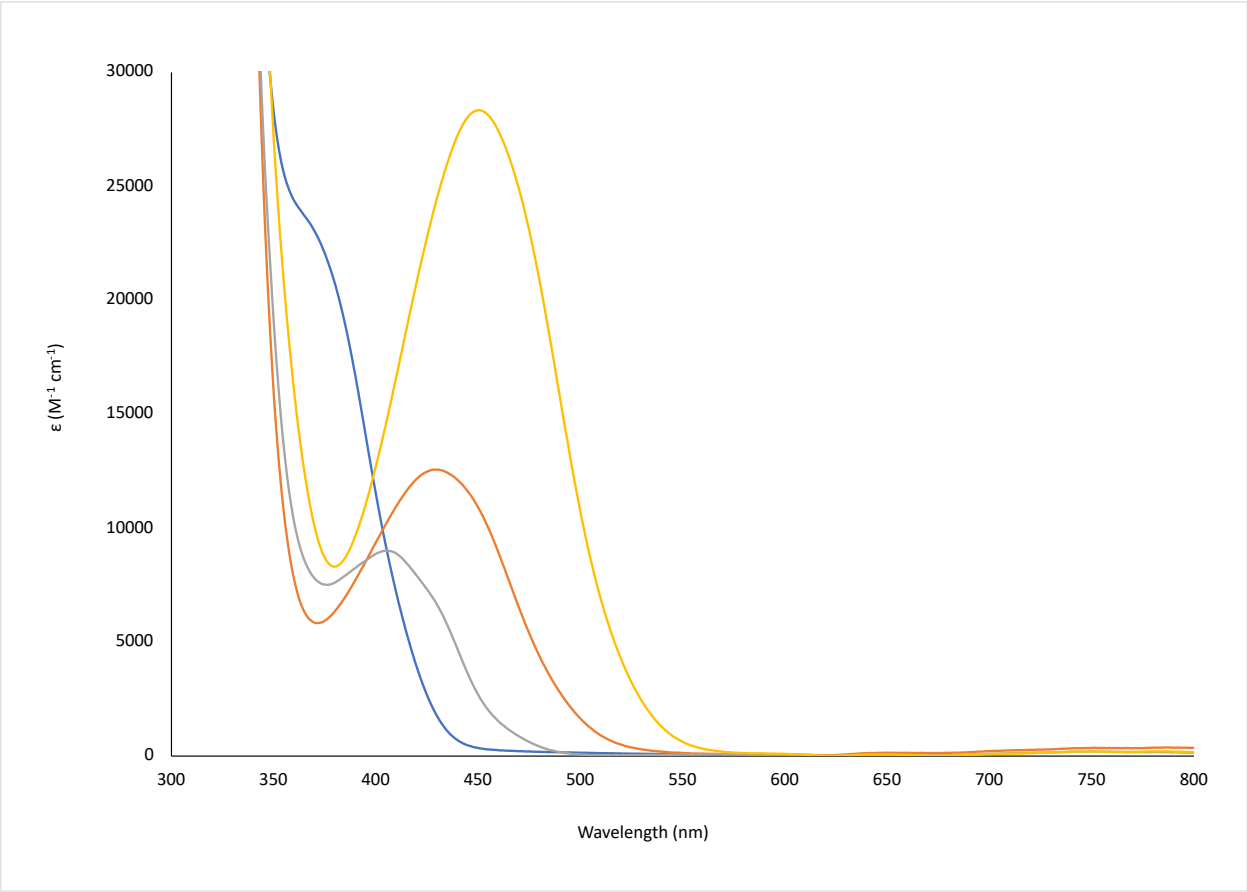

Figure 6-5. Stacked UV-Vis absorption spectra of probe 1 (blue, 1000 eq.), 2 (orange, 1000 eq.), 7 (grey, 1000 eq.), and 8 (yellow, 1000 eq.) with $B(4\text{-}F\text{-}C_6H_4)_3$ in PhCl; 12.5 µM samples.

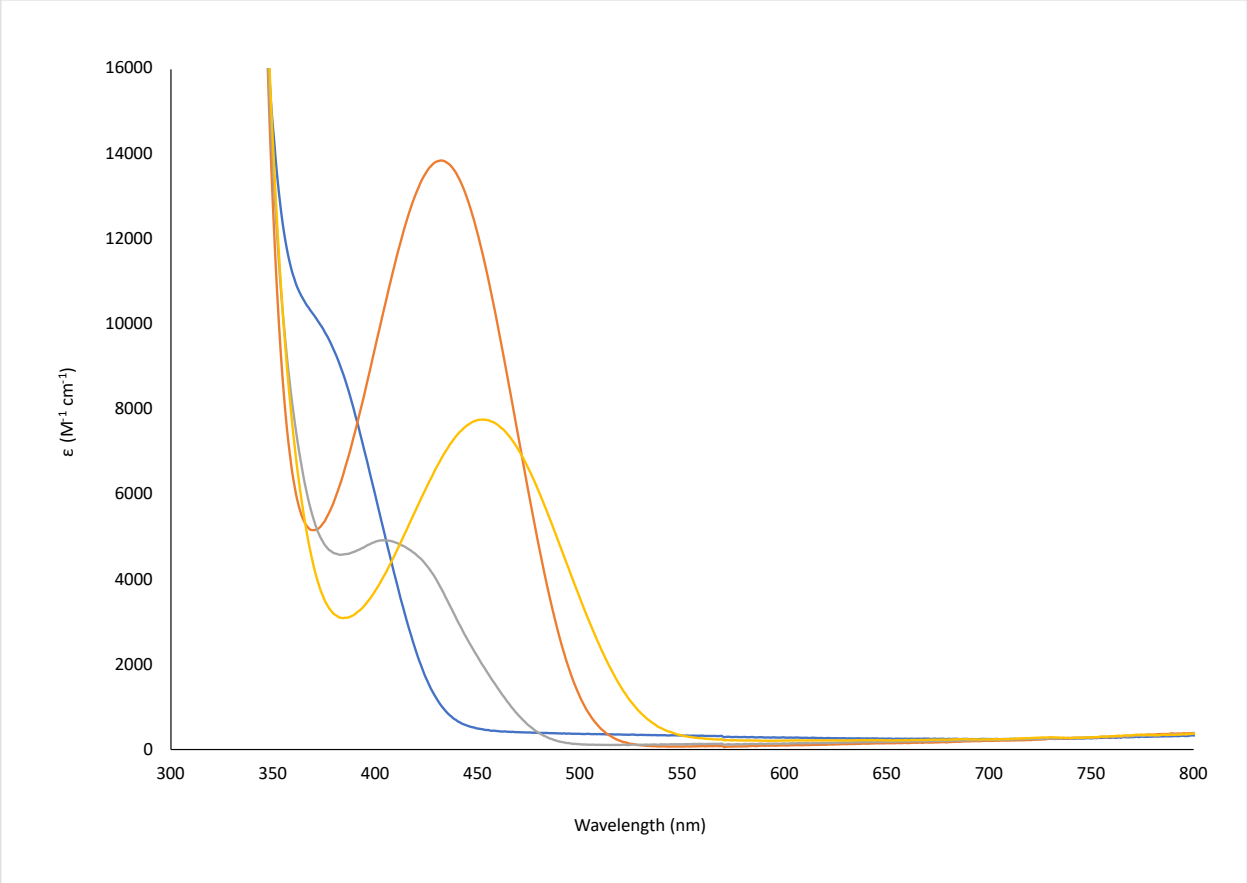

Figure 6-6. Stacked UV-Vis absorption spectra of probe 1 (blue, 1000 eq.), 2 (orange, 1000 eq.), 7 (grey, 1000 eq.), and 8 (yellow, 1000 eq.) with $B(4\text{-}F\text{-}C_6H_4)_3$ in Et_2O; 12.5 μM samples.

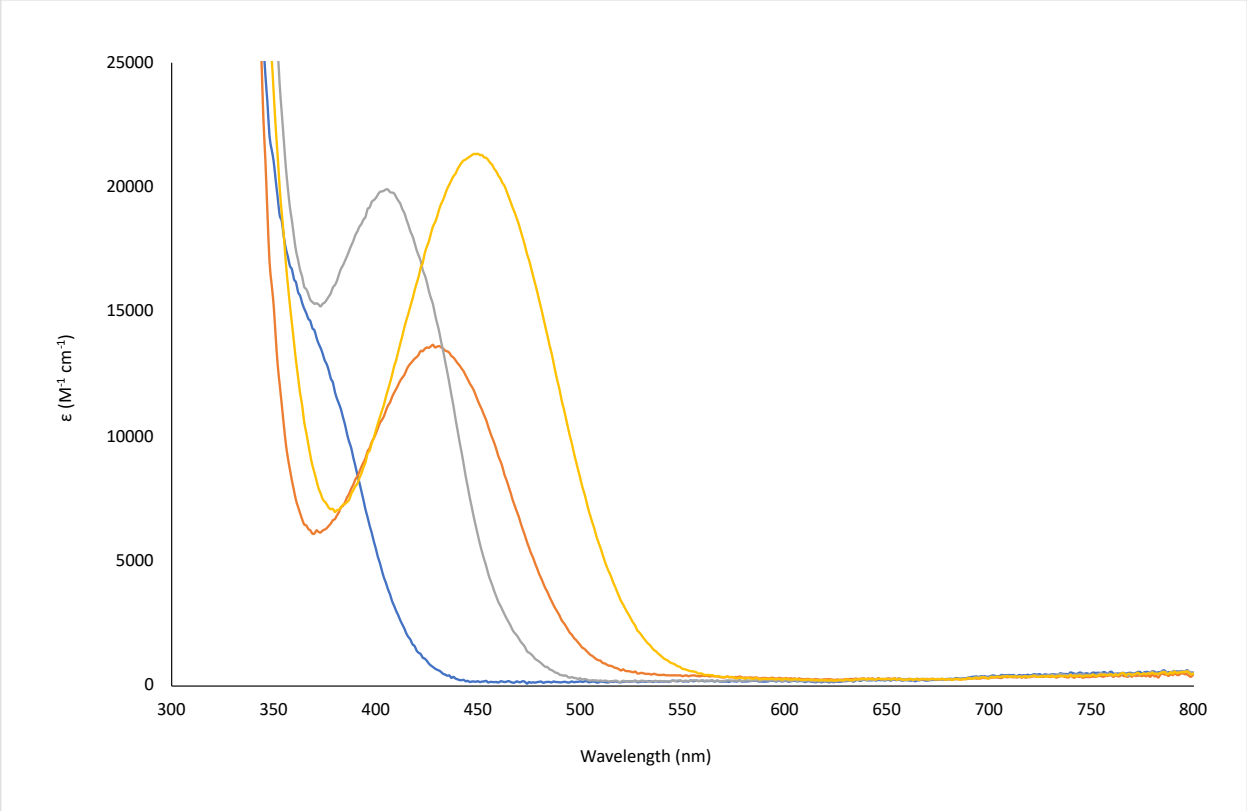

Figure 6-7. Stacked UV-Vis absorption spectra of probe 1 (blue, 1000 eq.), 2 (orange, 1000 eq.), 7 (grey, 1000 eq.), and 8 (yellow, 1000 eq.) with $B(4\text{-}F\text{-}C_6H_4)_3$ in DCM; 12.5 μM samples.

6.2.2.3. $B(3,4\text{-}F_2\text{-}C_6H_3)_3$

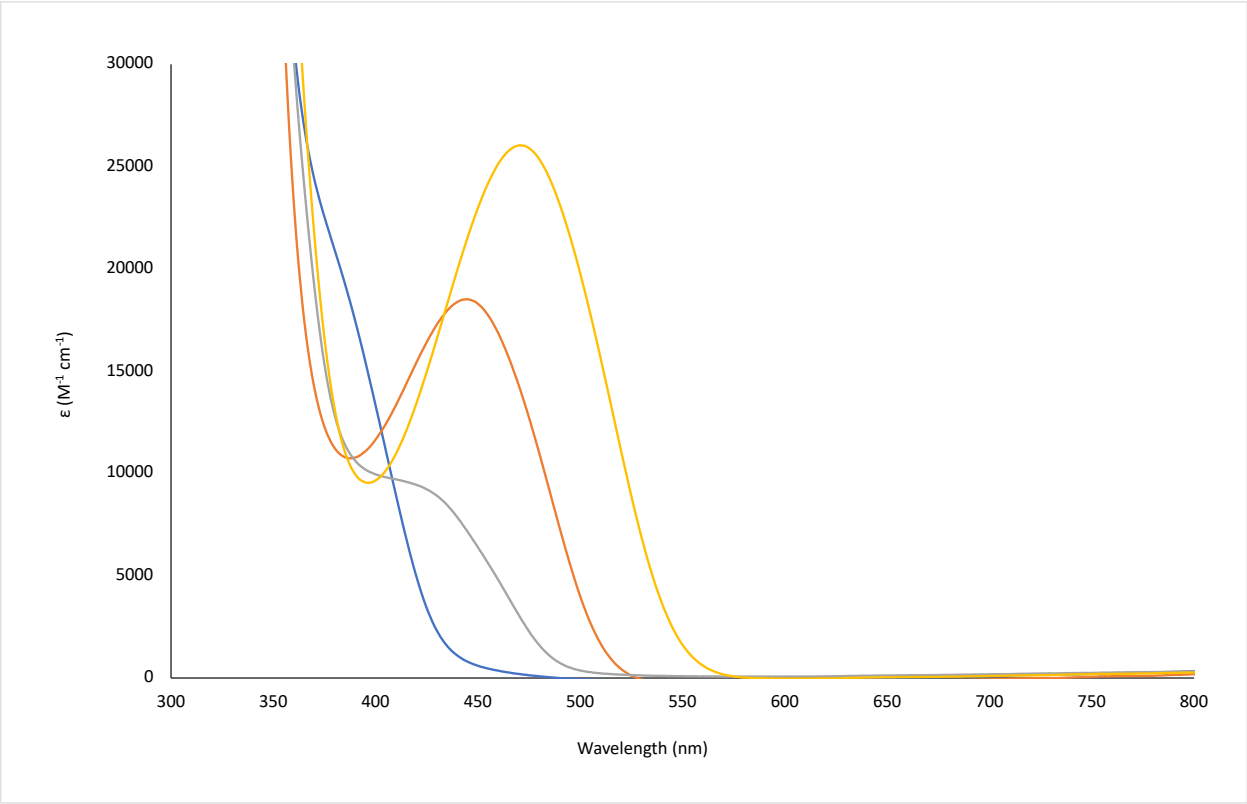

Figure 6-8. Stacked UV-Vis absorption spectra of probe 1 (blue, 750 eq.), 2 (orange, 750 eq.), 7 (grey, 750 eq.), and 8 (yellow, 750 eq.) with $B(3,4\text{-}F_2\text{-}C_6H_3)_3$ in PhCl; 12.5 μM samples.

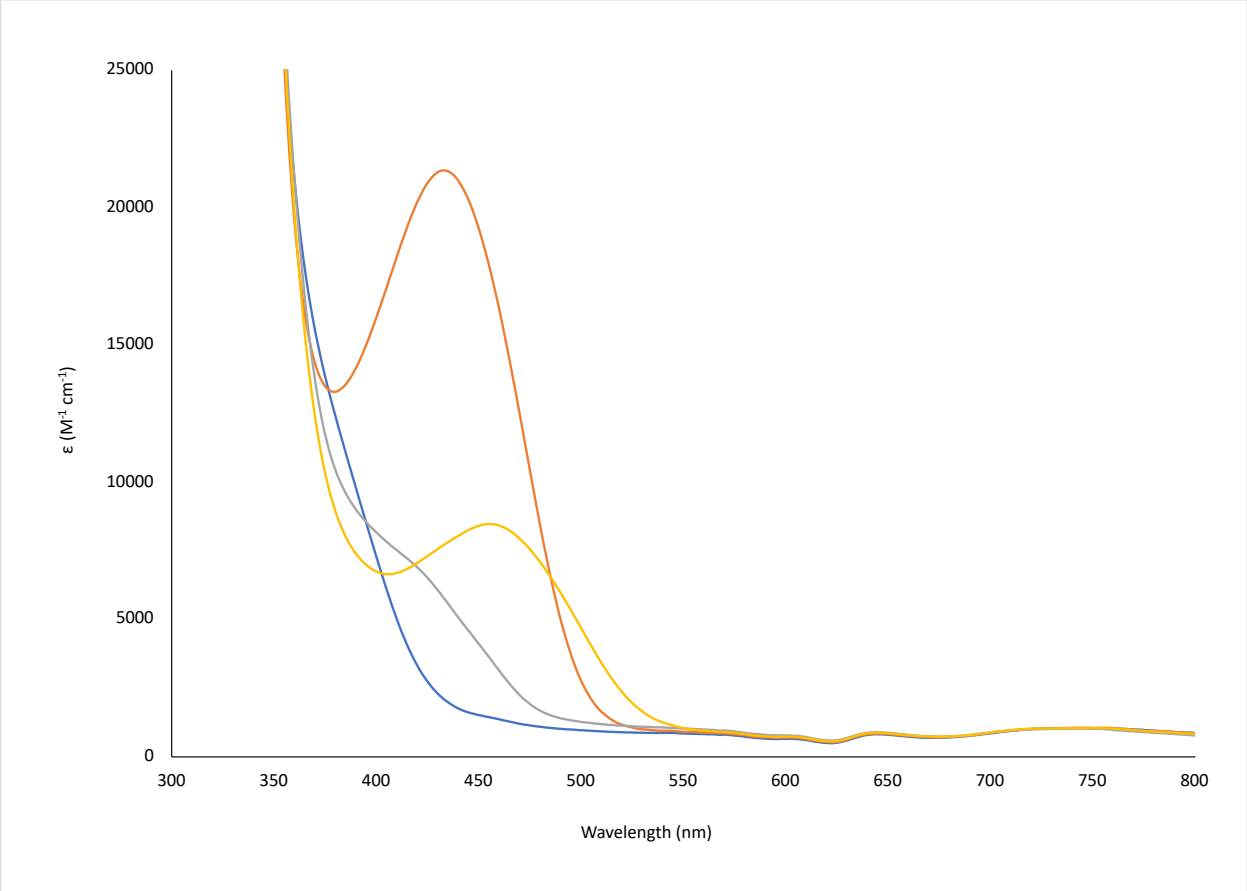

Figure 6-9. Stacked UV-Vis absorption spectra of probe 1 (blue, 1000 eq.), 2 (orange, 1000 eq.), 7 (grey, 1000 eq.), and 8 (yellow, 1000 eq.) with $B(3,4\text{-}F_2\text{-}C_6H_3)_3$ in Et_2O; 12.5 μM samples.

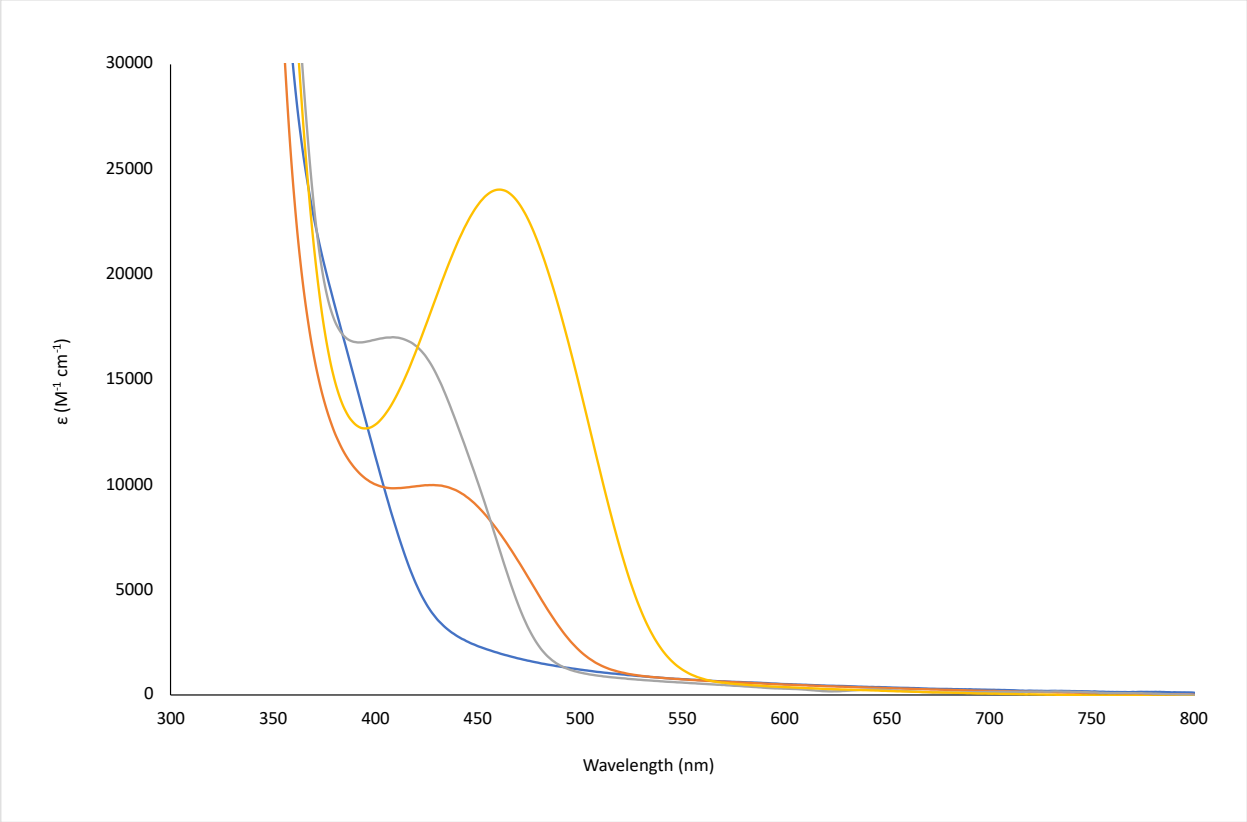

Figure 6-10. Stacked UV-Vis absorption spectra of probe 1 (blue, 750 eq.), 2 (orange, 750 eq.), 7 (grey, 750 eq.), and 8 (yellow, 750 eq.) with $B(3,4\text{-}F_2\text{-}C_6H_3)_3$ in DCM; 12.5 μM samples.

6.2.2.4. $B(2,4,6\text{-}F_3\text{-}C_6H_2)_3$

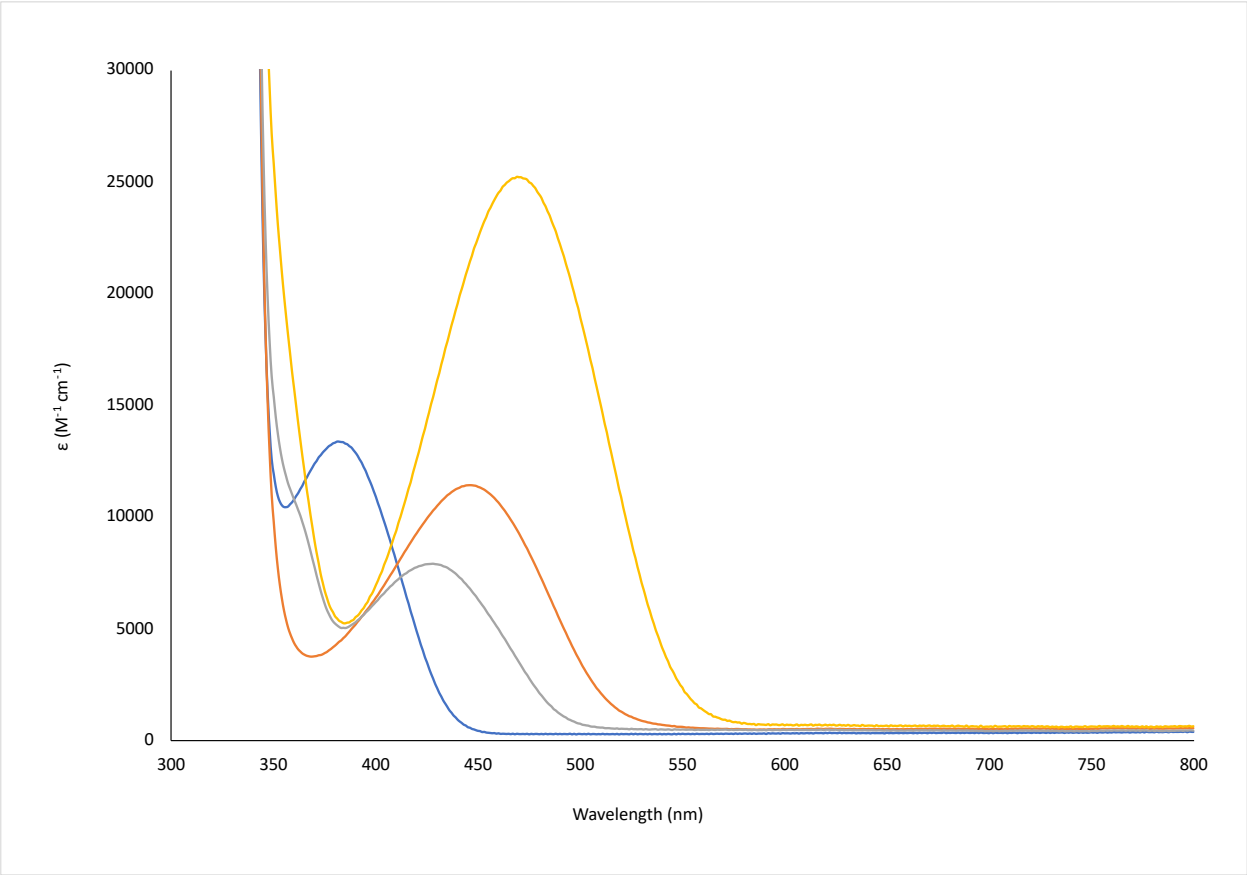

Figure 6-11. Stacked UV-Vis absorption spectra of probe 1 (blue, 750 eq.), 2 (orange, 750 eq.), 7 (grey, 750 eq.), and 8 (yellow, 750 eq.) with $B(2,4,6\text{-}F_3\text{-}C_6H_2)_3$ in PhCl; 12.5 μM samples.

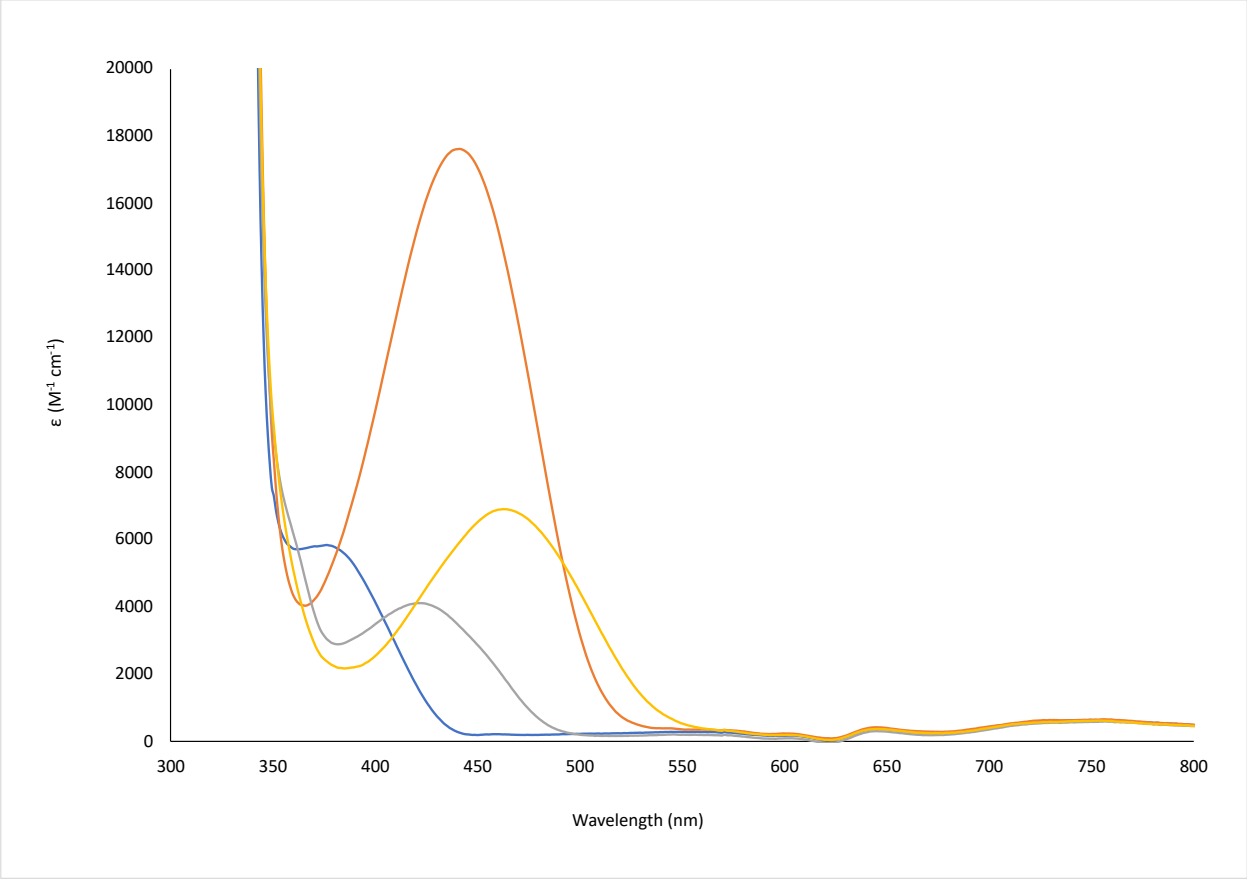

Figure 6-12. Stacked UV-Vis absorption spectra of probe 1 (blue, 1000 eq.), 2 (orange, 1000 eq.), 7 (grey, 1000 eq.), and 8 (yellow, 1000 eq.) with $B(2,4,6\text{-}F_3\text{-}C_6H_2)_3$ in Et_2O; 12.5 μM samples.

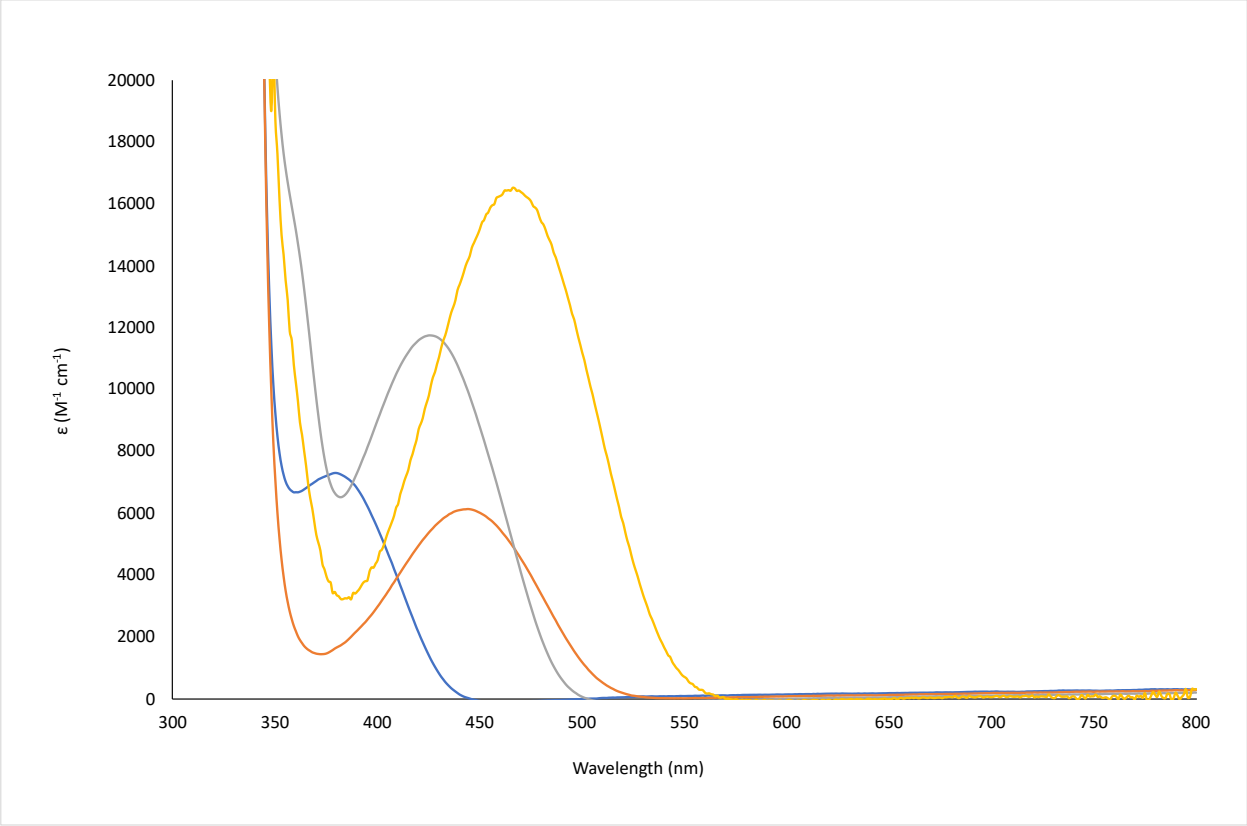

Figure 6-13. Stacked UV-Vis absorption spectra of probe 1 (blue, 750 eq.), 2 (orange, 750 eq.), 7 (grey, 750 eq.), and 8 (yellow, 750 eq.) with $B(2,4,6\text{-}F_3\text{-}C_6H_2)_3$ in DCM; 12.5 μM samples.

6.2.2.5. $B(OC_6F_5)_3$

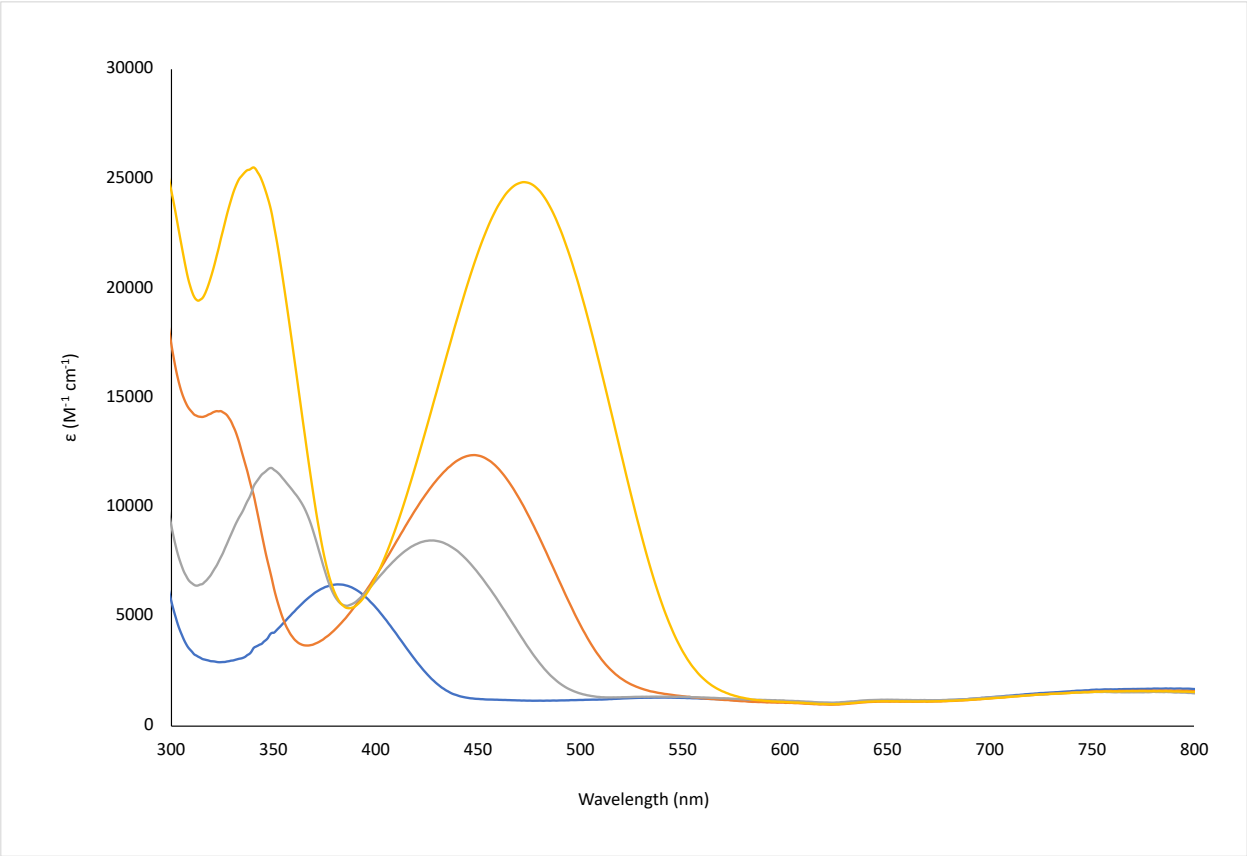

Figure 6-14. Stacked UV-Vis absorption spectra of probe 1 (blue, 750 eq.), 2 (orange, 750 eq.), 7 (grey, 750 eq.), and 8 (yellow, 750 eq.) with $B(OC_6F_5)_3$ in PhCl; 12.5 µM samples.

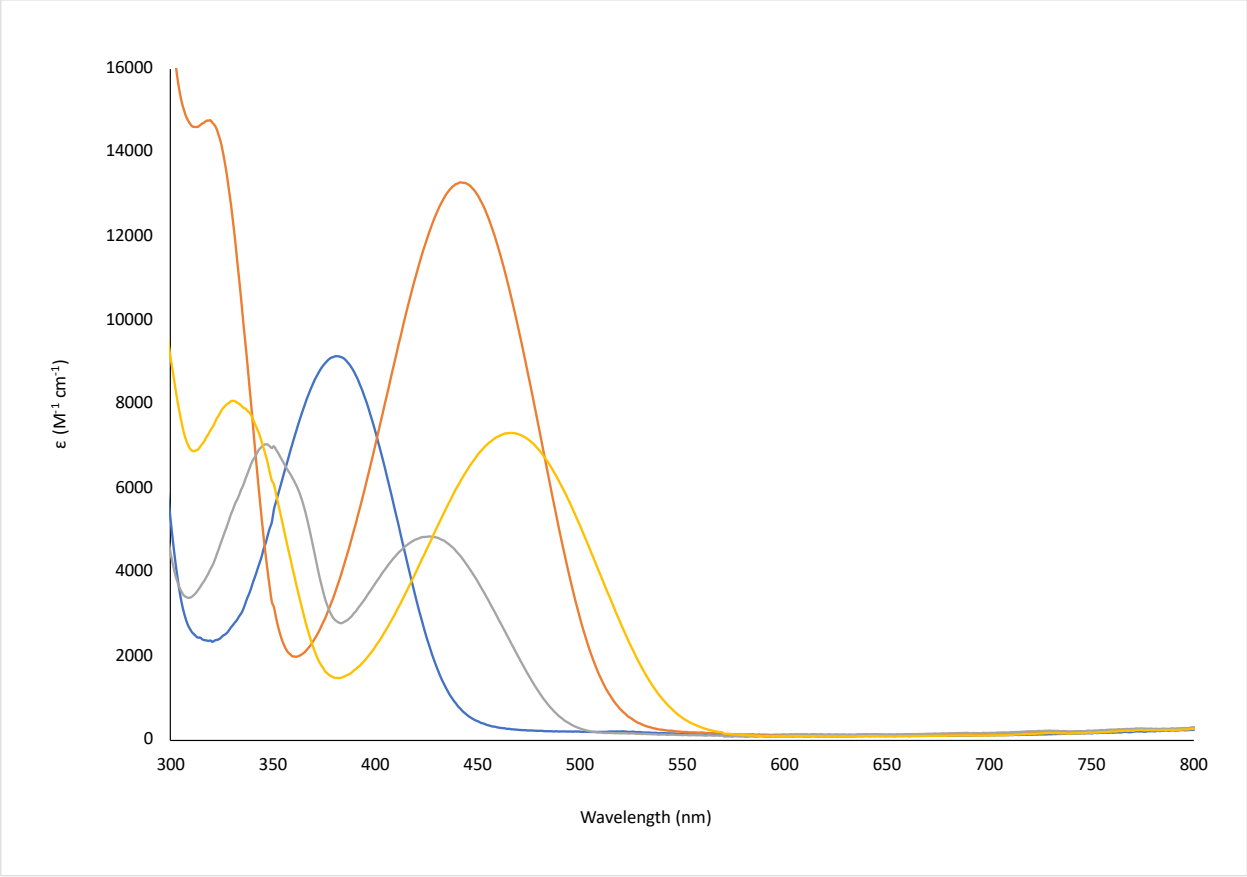

Figure 6-15. Stacked UV-Vis absorption spectra of probe 1 (blue, 1000 eq.), 2 (orange, 1000 eq.), 7 (grey, 1000 eq.), and 8 (yellow, 1000 eq.) with $B(OC6F_5)_3$ in Et_2O; 12.5 μM samples.

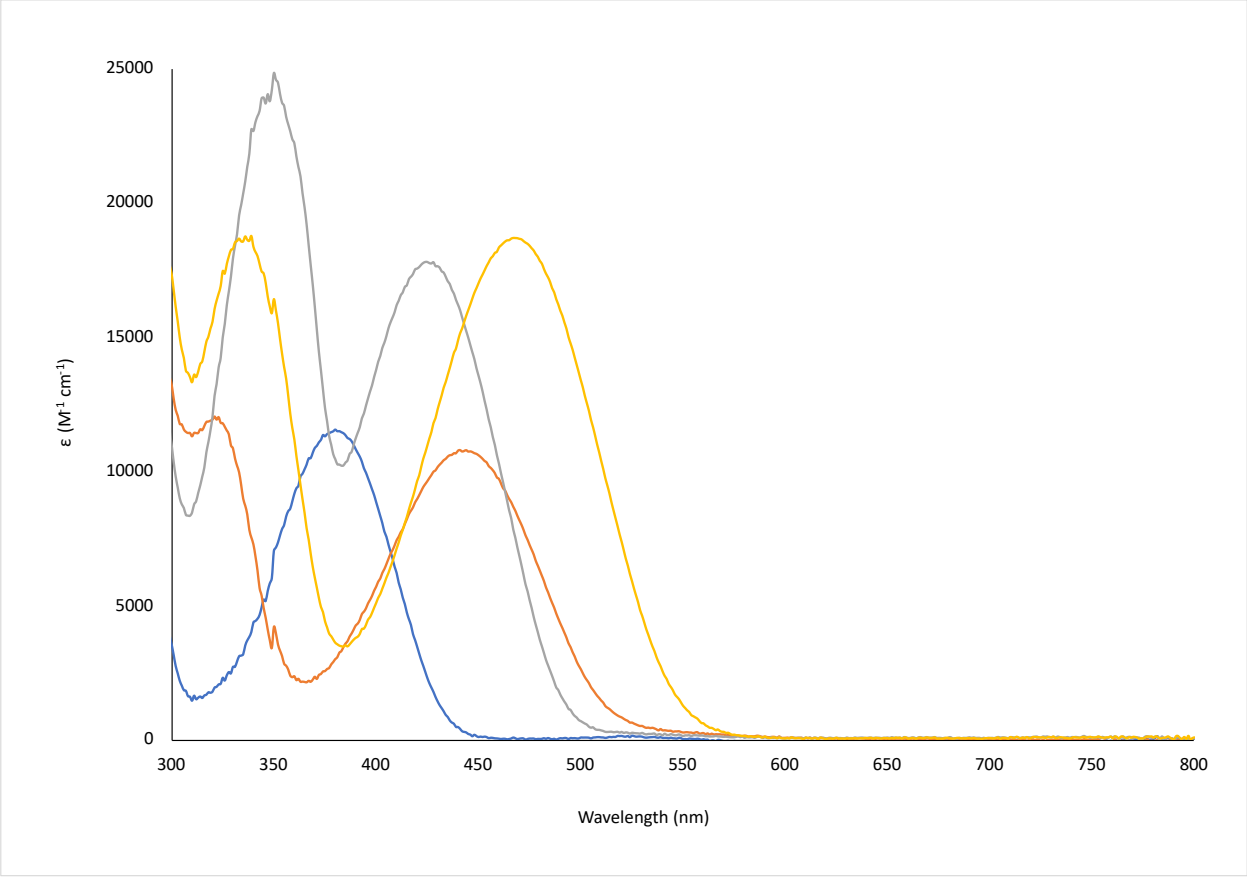

Figure 6-16. Stacked UV-Vis absorption spectra of probe 1 (blue, 750 eq.), 2 (orange, 750 eq.), 7 (grey, 750 eq.), and 8 (yellow, 750 eq.) with $B(OC_6F_5)_3$ in DCM; 12.5 µM samples.

6.2.2.6. $B(C_6F_5)_3$

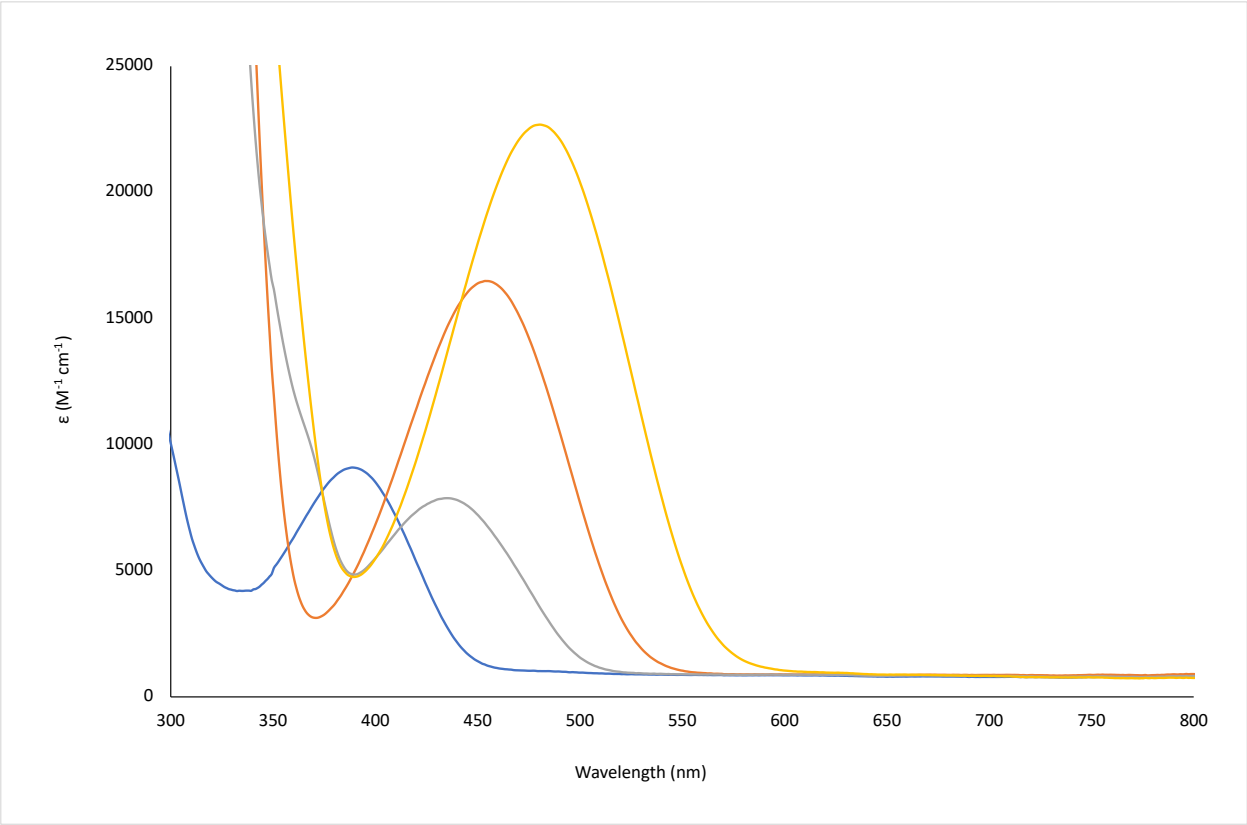

Figure 6-17. Stacked UV-Vis absorption spectra of probe 1 (blue, 10 eq.), 2 (orange, 10 eq.), 7 (grey, 10 eq.), and 8 (yellow, 10 eq.) with $B(C_6F_5)_3$ in PhCl; 12.5 μM samples.

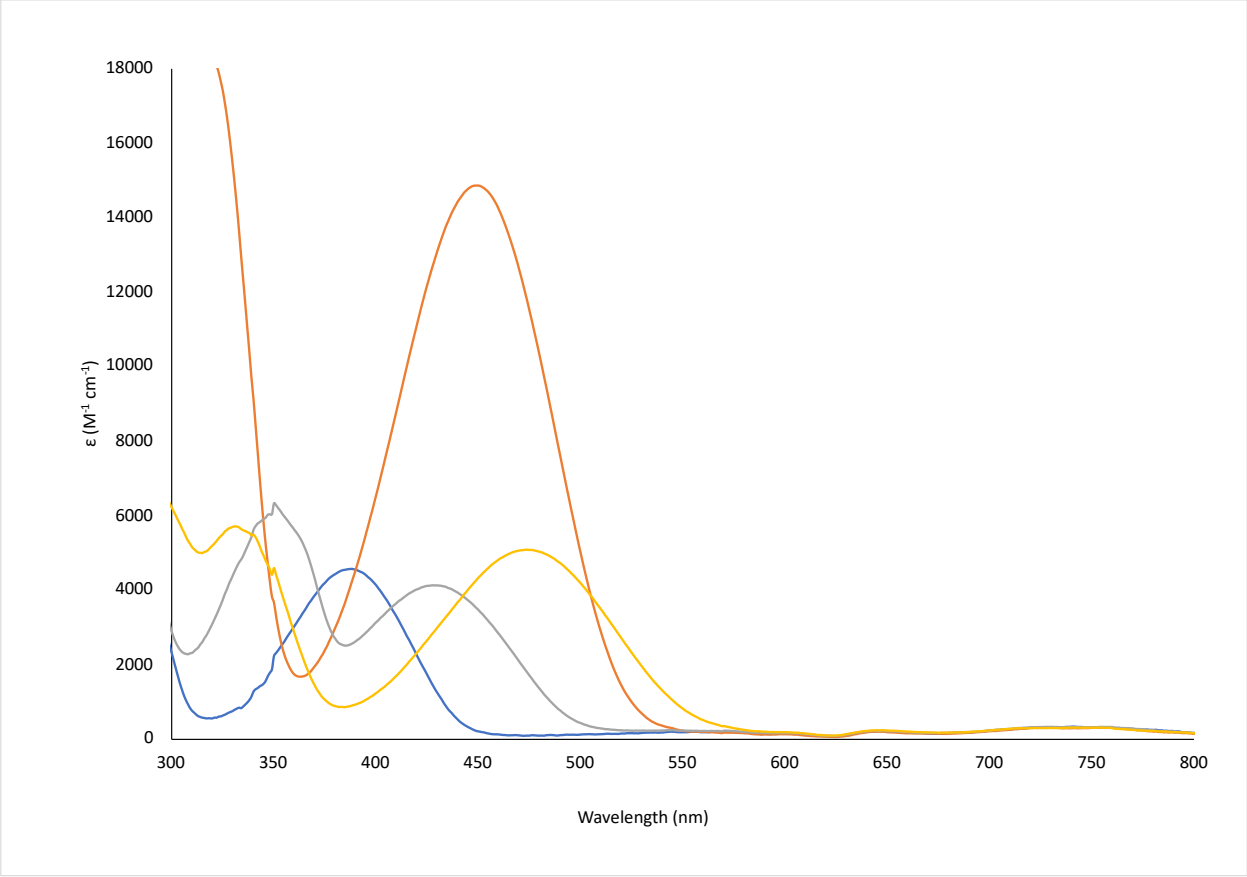

Figure 6-18. Stacked UV-Vis absorption spectra of probe 1 (blue, 50 eq.), 2 (orange, 50 eq.), 7 (grey, 50 eq.), and 8 (yellow, 50 eq.) with $B(C_6F_5)_3$ in Et_2O; 12.5 μM samples.

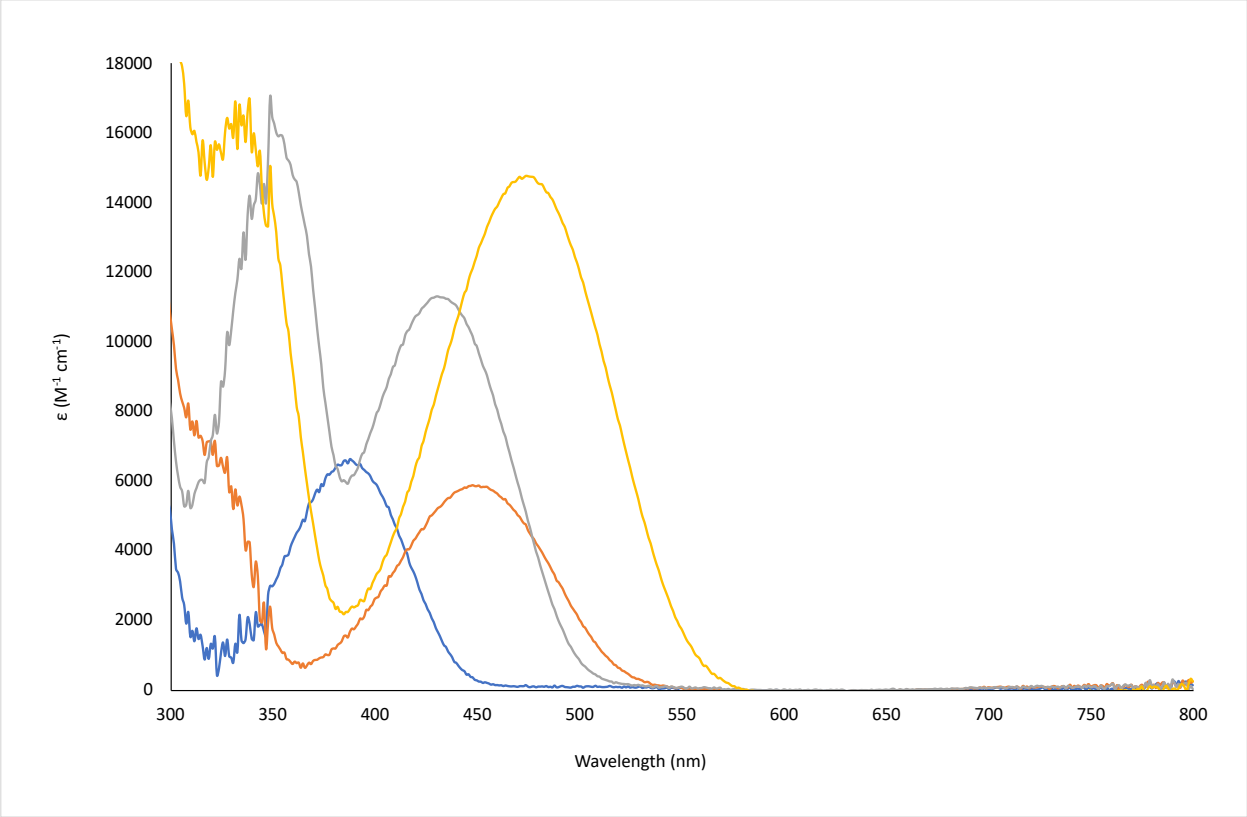

Figure 6-19. Stacked UV-Vis absorption spectra of probe 1 (blue, 10 eq.), 2 (orange, 10 eq.), 7 (grey, 10 eq.), and 8 (yellow, 10 eq.) with $B(C_6F_5)_3$ in DCM; 12.5 μM samples.

6.2.2.7. B(*p*-F_4-$C_6H)_3$

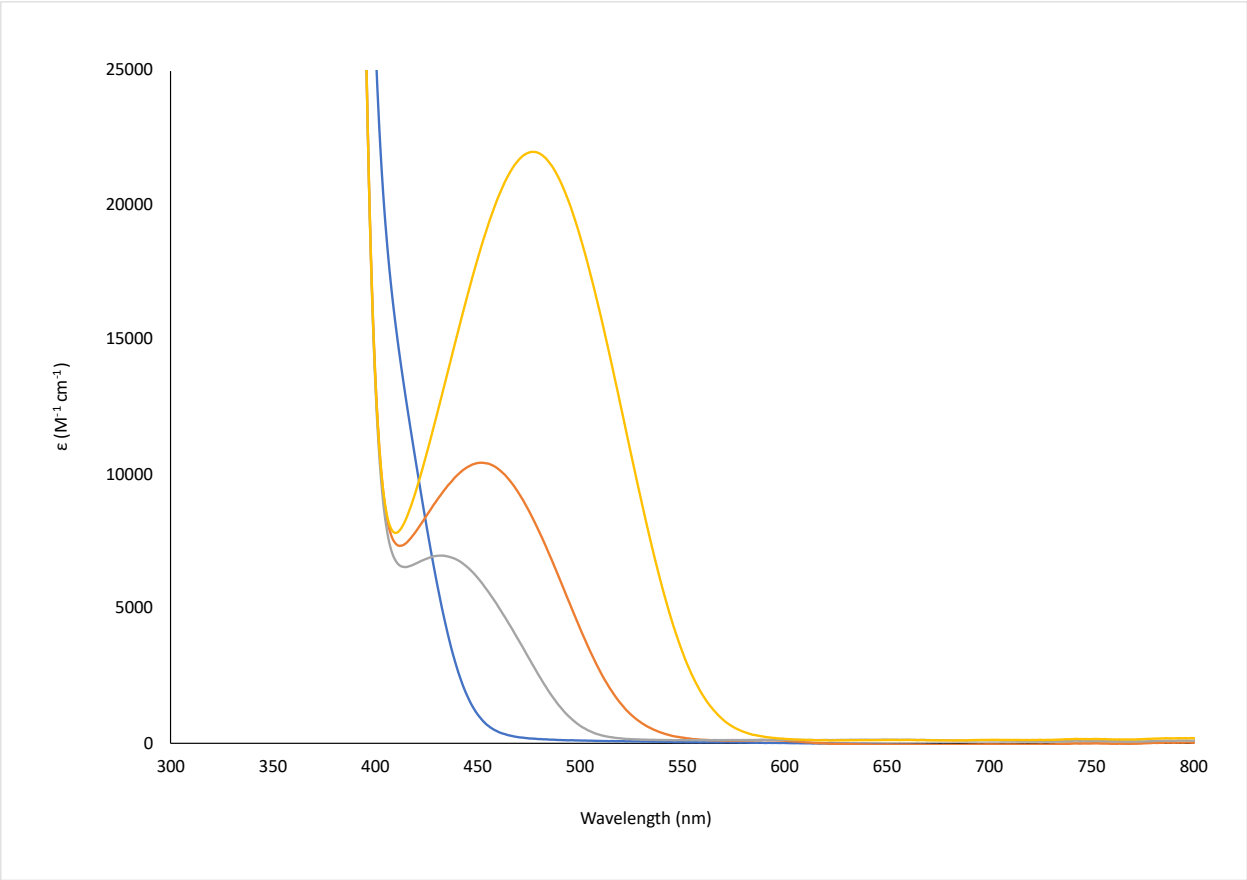

Figure 6-20. Stacked UV-Vis absorption spectra of probe 1 (blue, 10 eq.), 2 (orange, 10 eq.), 7 (grey, 10 eq.), and 8 (yellow, 10 eq.) with B(*p*-F_4-$C_6H)_3$ in PhCl; 12.5 μM samples.

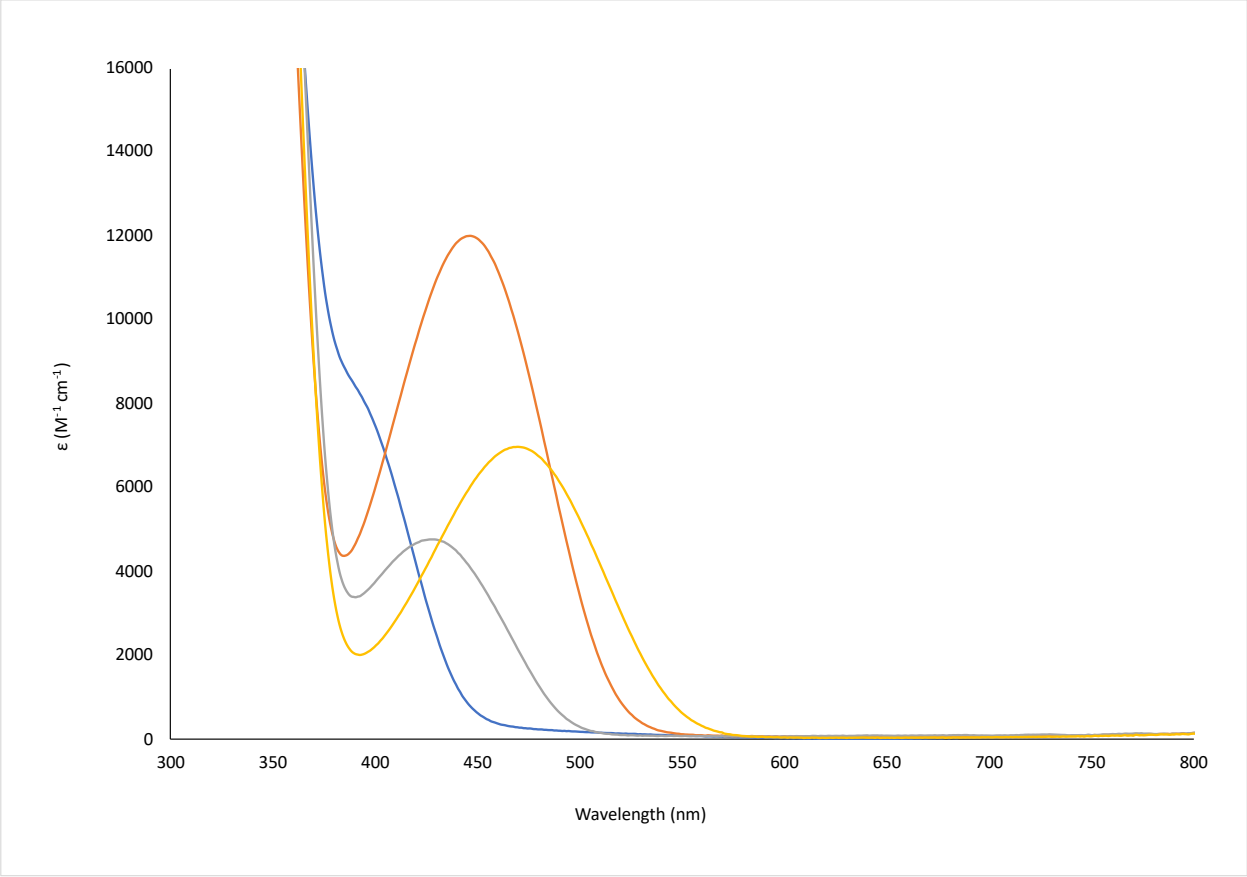

Figure 6-21. Stacked UV-Vis absorption spectra of probe 1 (blue, 50 eq.), 2 (orange, 50 eq.), 7 (grey, 50 eq.), and 8 (yellow, 50 eq.) with B(*p*-F_4-$C_6H)_3$ in Et_2O; 12.5 μM samples.

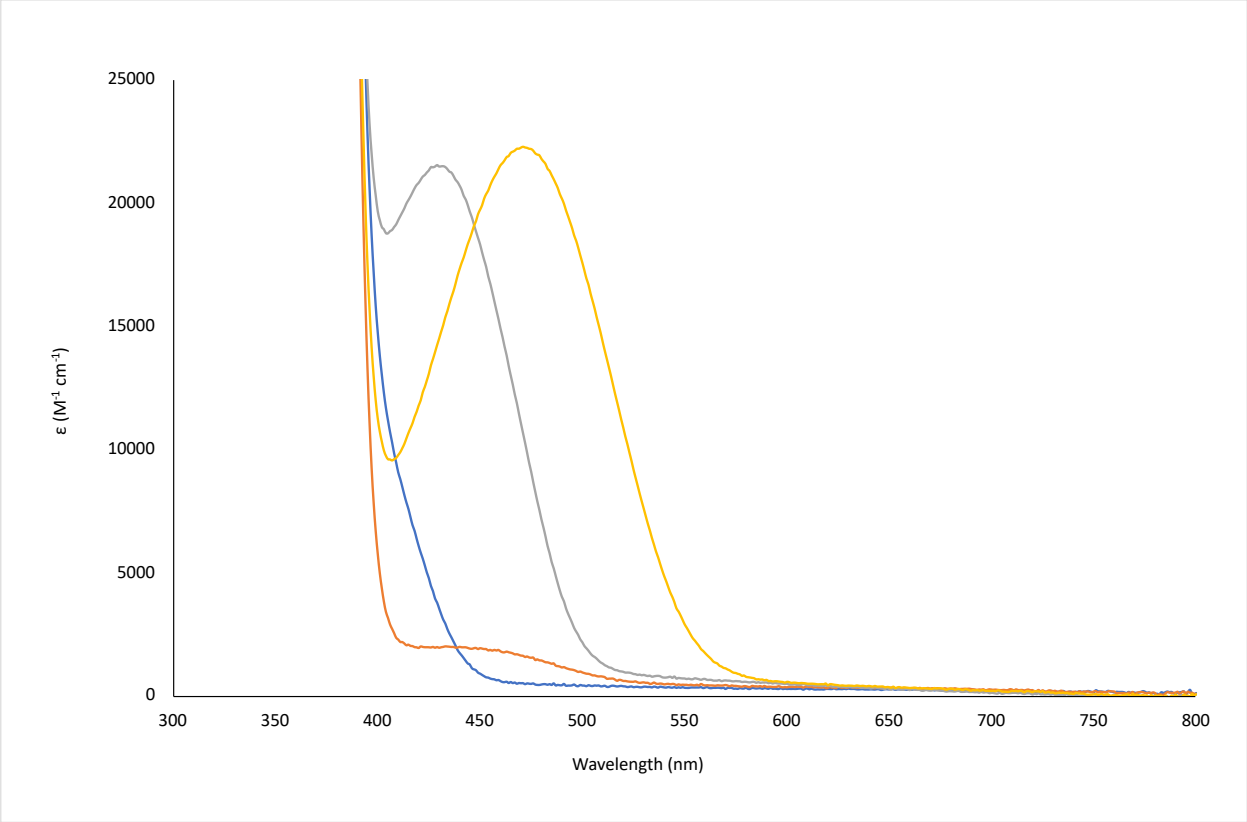

Figure 6-22. Stacked UV-Vis absorption spectra of probe 1 (blue, 10 eq.), 2 (orange, 10 eq.), 7 (grey, 10 eq.), and 8 (yellow, 10 eq.) with B(*p*-F_4-$C_6H)_3$ in DCM; 12.5 µM samples.

6.2.2.8. $In(OTf)_3$

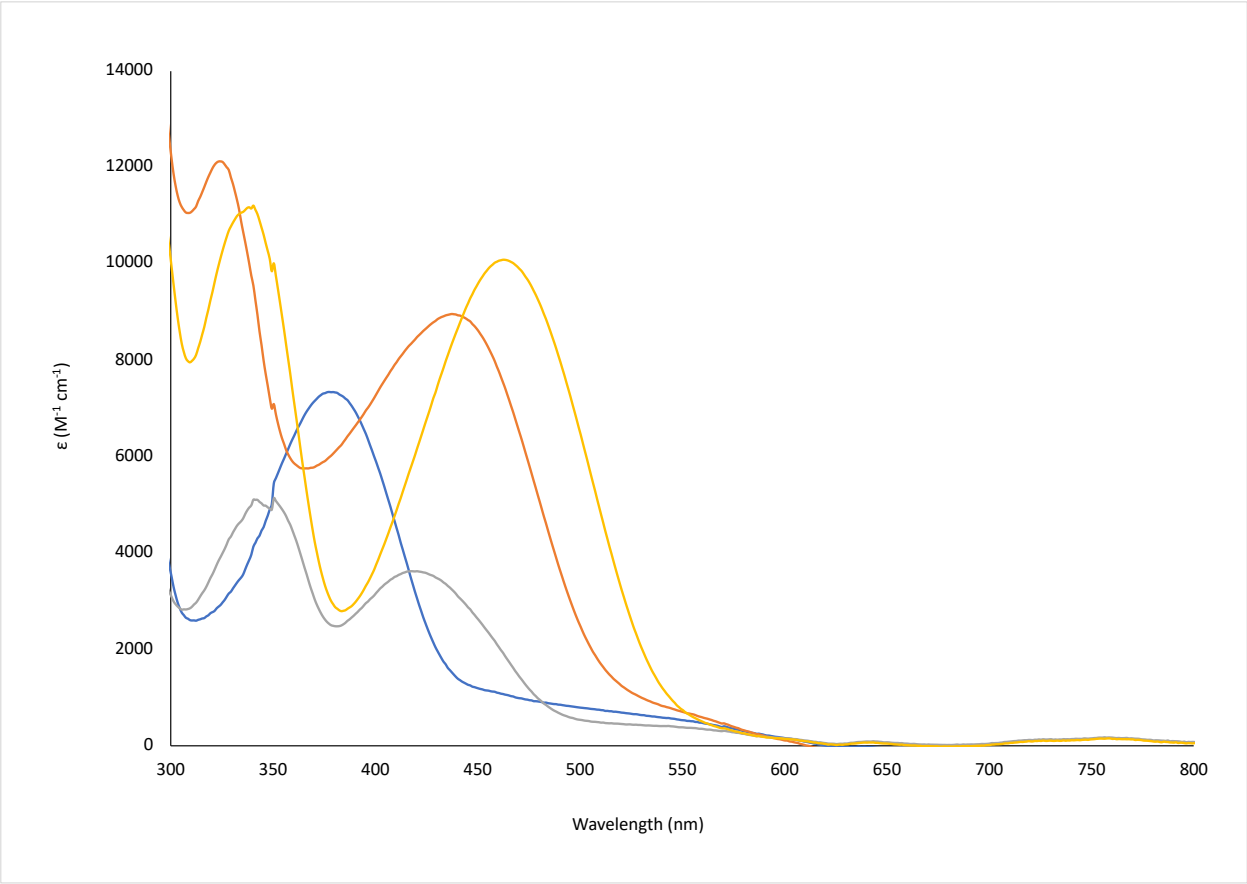

Figure 6-23. Stacked UV-Vis absorption spectra of probe 1 (blue, excess), 2 (orange, excess), 7 (grey, excess), and 8 (yellow, excess) with $In(OTf)_3$ in MeCN; 12.5 μM samples.

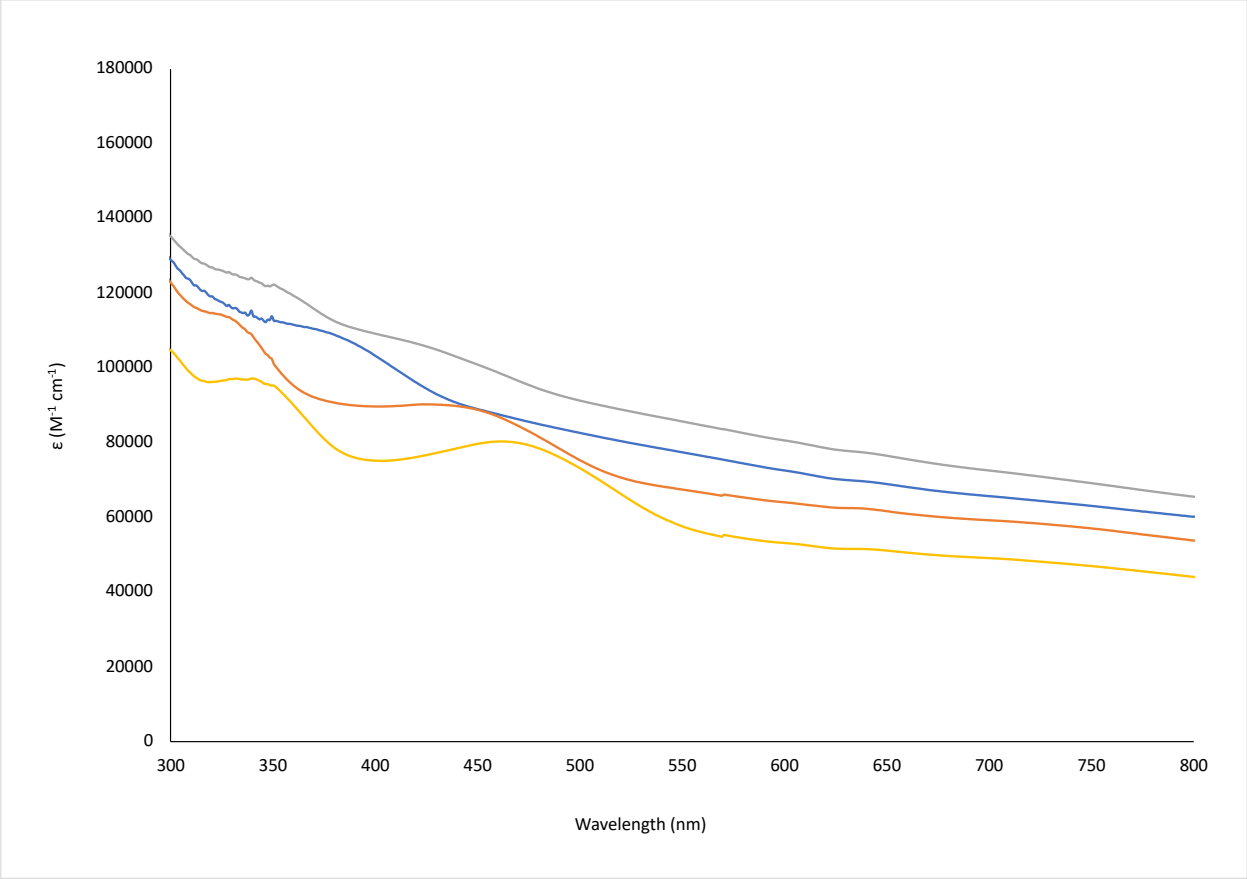

Figure 6-24. Stacked UV-Vis absorption spectra of probe 1 (blue, excess), 2 (orange, excess), 7 (grey, excess), and 8 (yellow, excess) with $In(OTf)_3$ in PhCl; 12.5 μM samples.

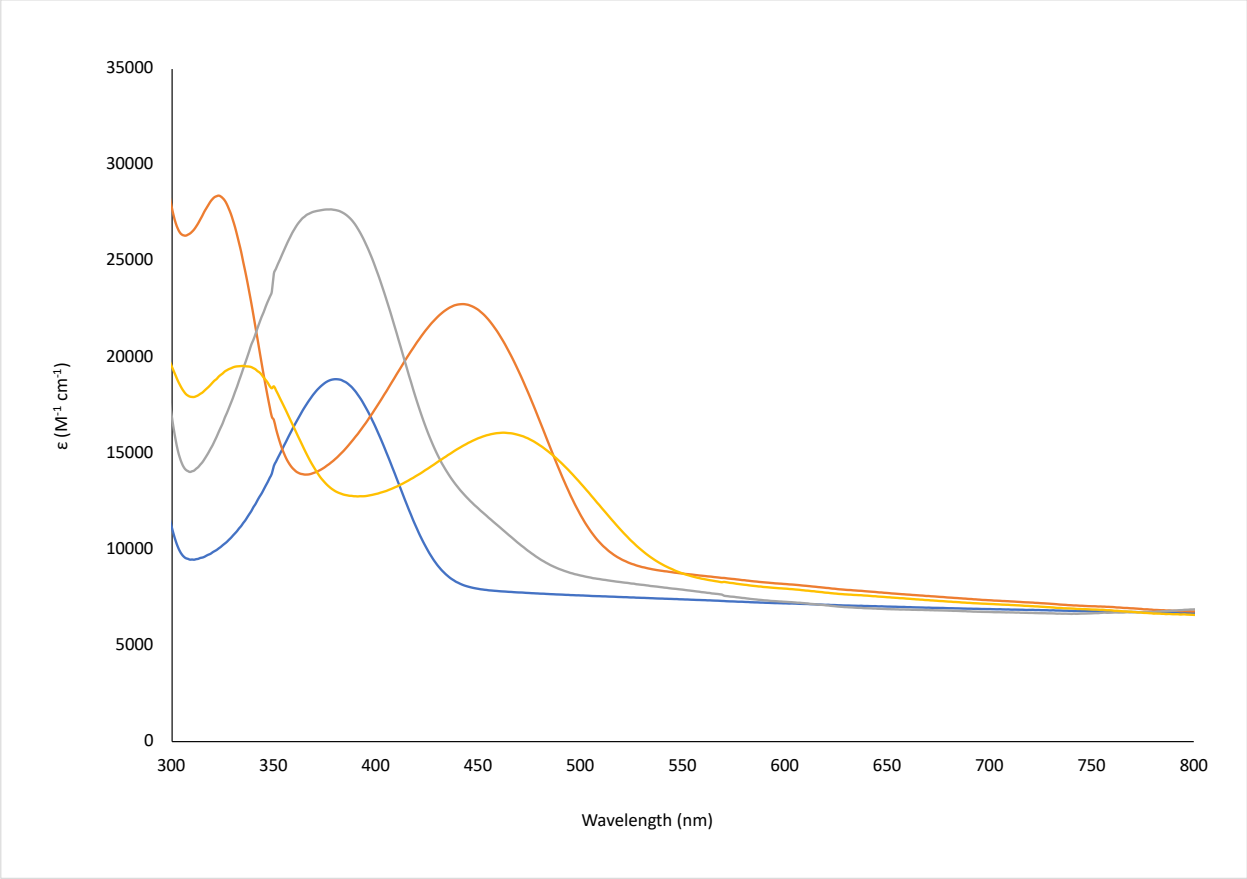

Figure 6-25. Stacked UV-Vis absorption spectra of probe 1 (blue, excess), 2 (orange, excess), 7 (grey, excess), and 8 (yellow, excess) with $In(OTf)_3$ in Et_2O; 12.5 μM samples.

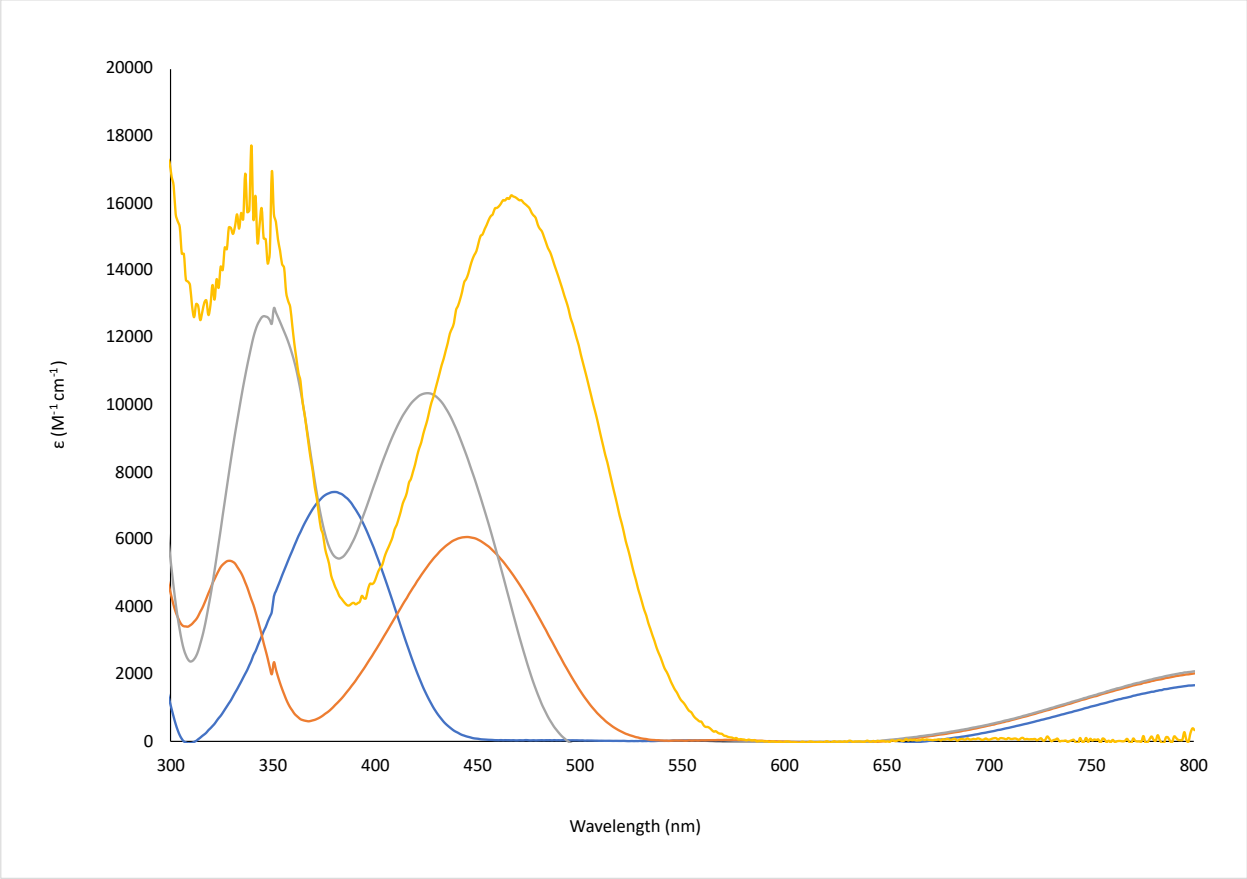

Figure 6-26. Stacked UV-Vis absorption spectra of probe 1 (blue, excess), 2 (orange, excess), 7 (grey, excess), and 8 (yellow, excess) with $In(OTf)_3$ in DCM; 12.5 μM samples.

6.2.2.9. $Sc(OTf)_3$

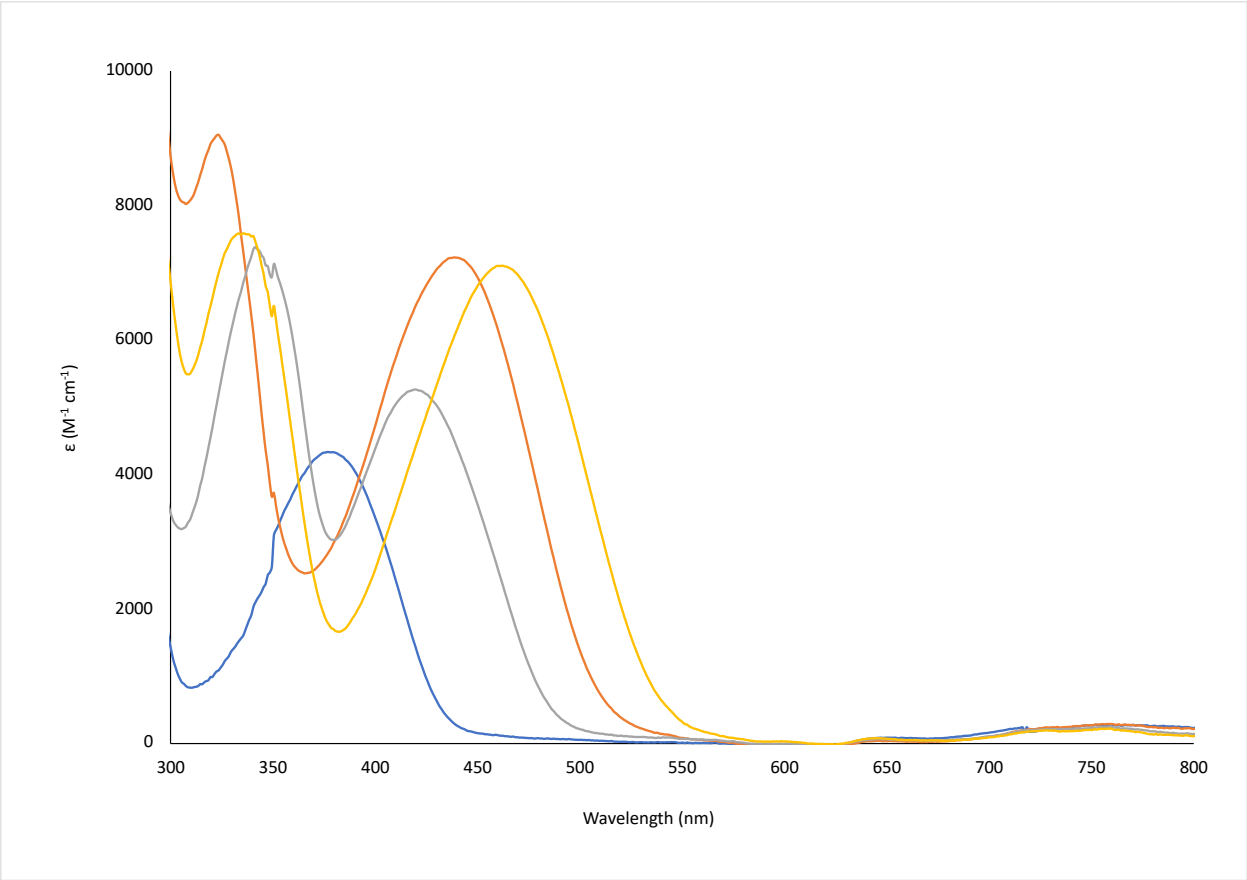

Figure 6-27. Stacked UV-Vis absorption spectra of probe 1 (blue, excess), 2 (orange, excess), 7 (grey, excess), and 8 (yellow, excess) with $Sc(OTf)_3$ in MeCN; 12.5 μM samples.

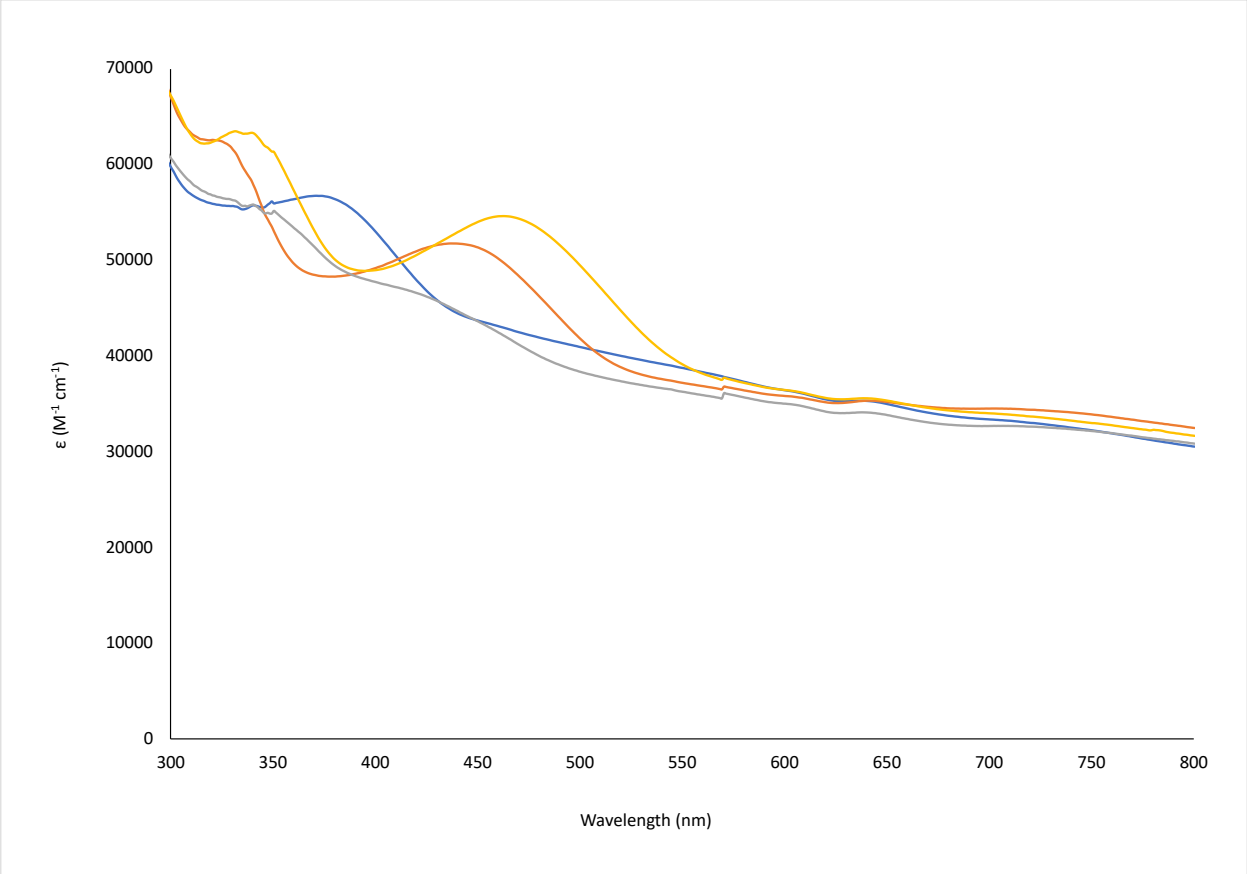

Figure 6-28. Stacked UV-Vis absorption spectra of probe 1 (blue, excess), 2 (orange, excess), 7 (grey, excess), and 8 (yellow, excess) with $Sc(OTf)_3$ in PhCl; 12.5 μM samples.

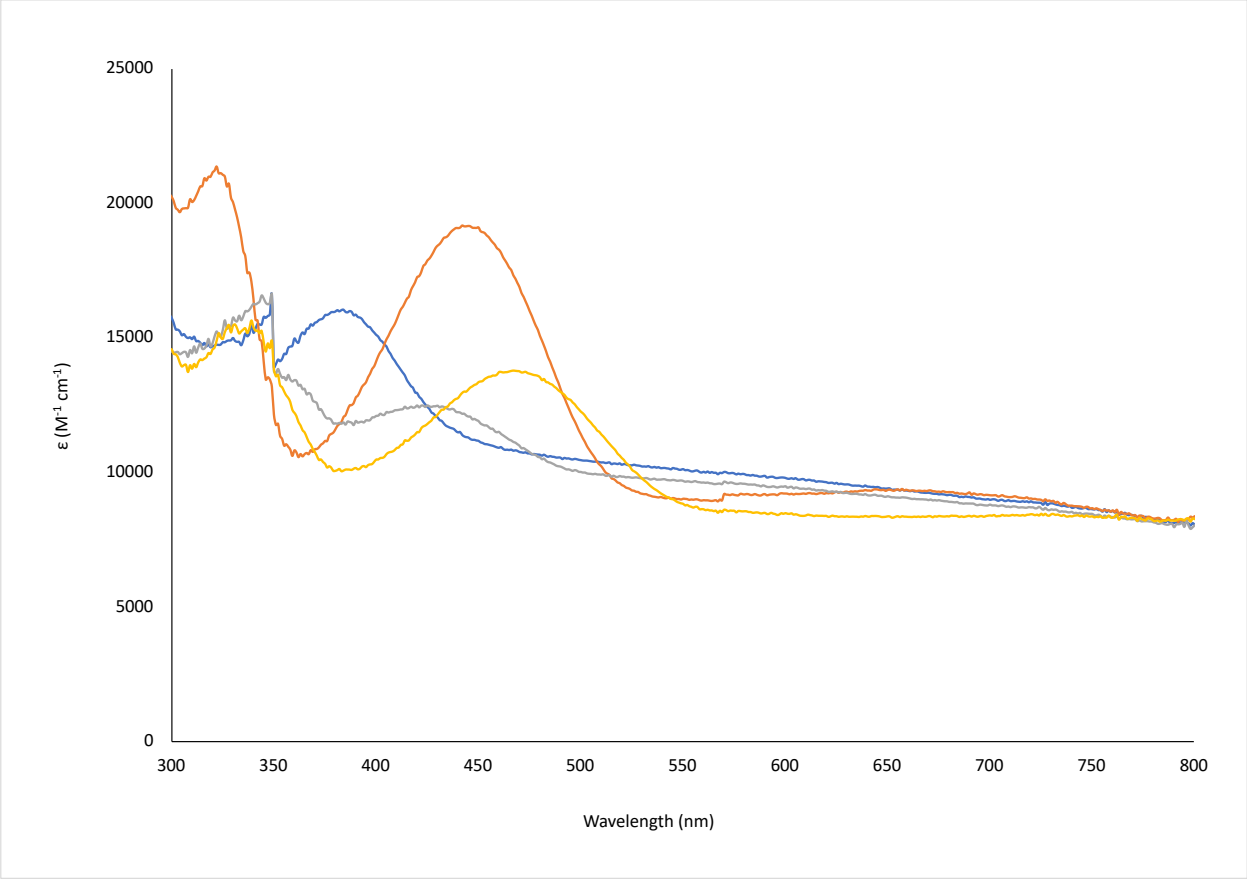

Figure 6-29. Stacked UV-Vis absorption spectra of probe 1 (blue, excess), 2 (orange, excess), 7 (grey, excess), and 8 (yellow, excess) with $Sc(OTf)_3$ in Et_2O; 12.5 μM samples.

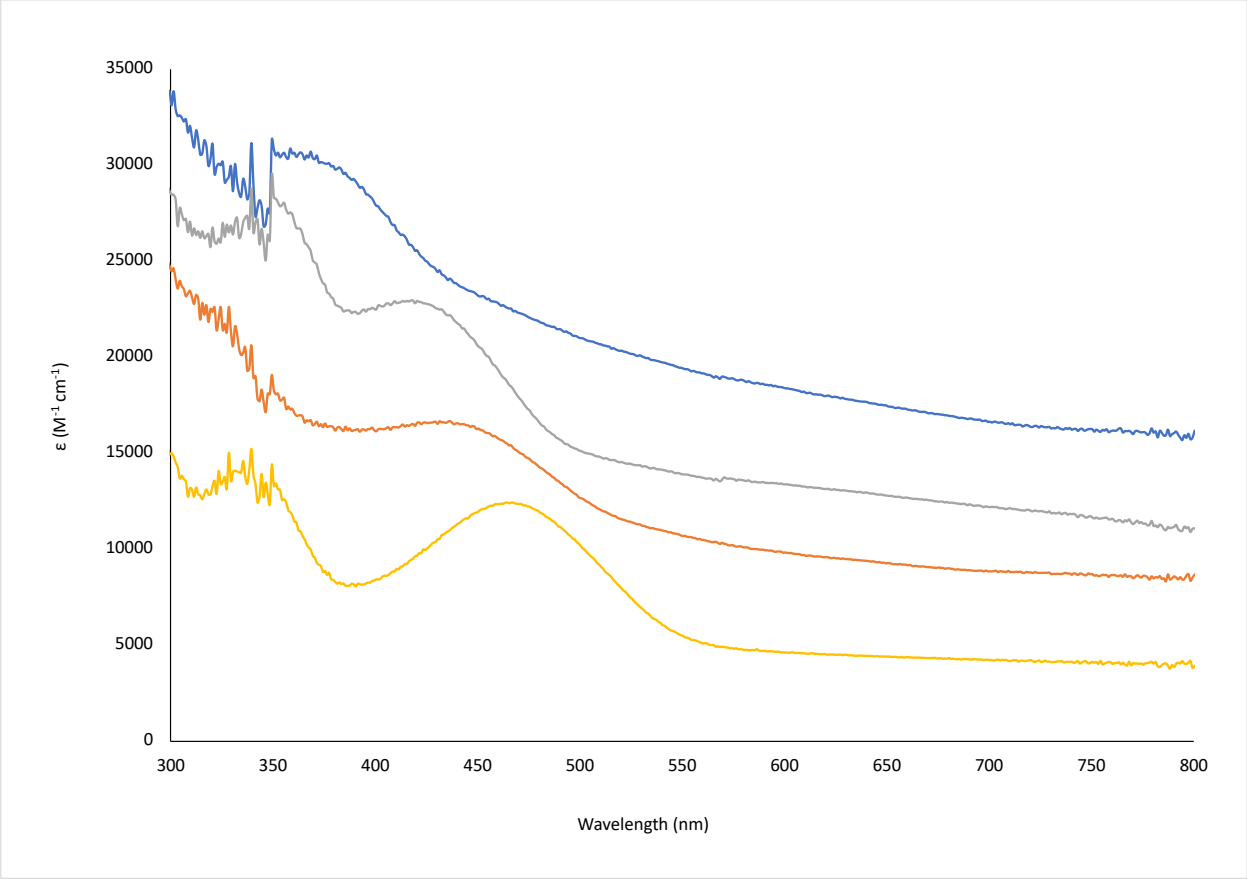

Figure 6-30. Stacked UV-Vis absorption spectra of probe 1 (blue, excess), 2 (orange, excess), 7 (grey, excess), and 8 (yellow, excess) with $Sc(OTf)_3$ in DCM; 12.5 μM samples.

6.2.2.10. $Zn(OTf)_2$

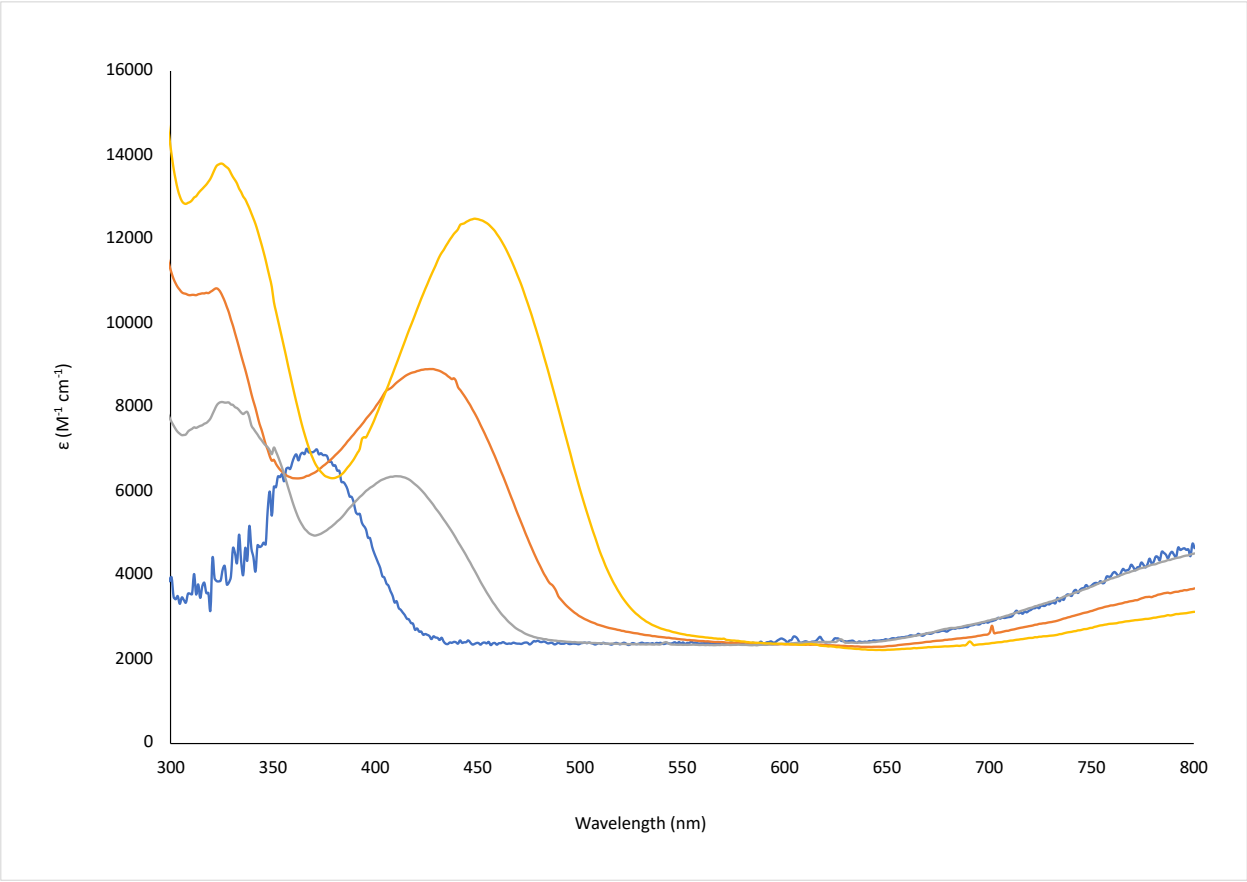

Figure 6-31. Stacked UV-Vis absorption spectra of probe 1 (blue, excess), 2 (orange, excess), 7 (grey, excess), and 8 (yellow, excess) with $Zn(OTf)_2$ in MeCN; 12.5 µM samples.

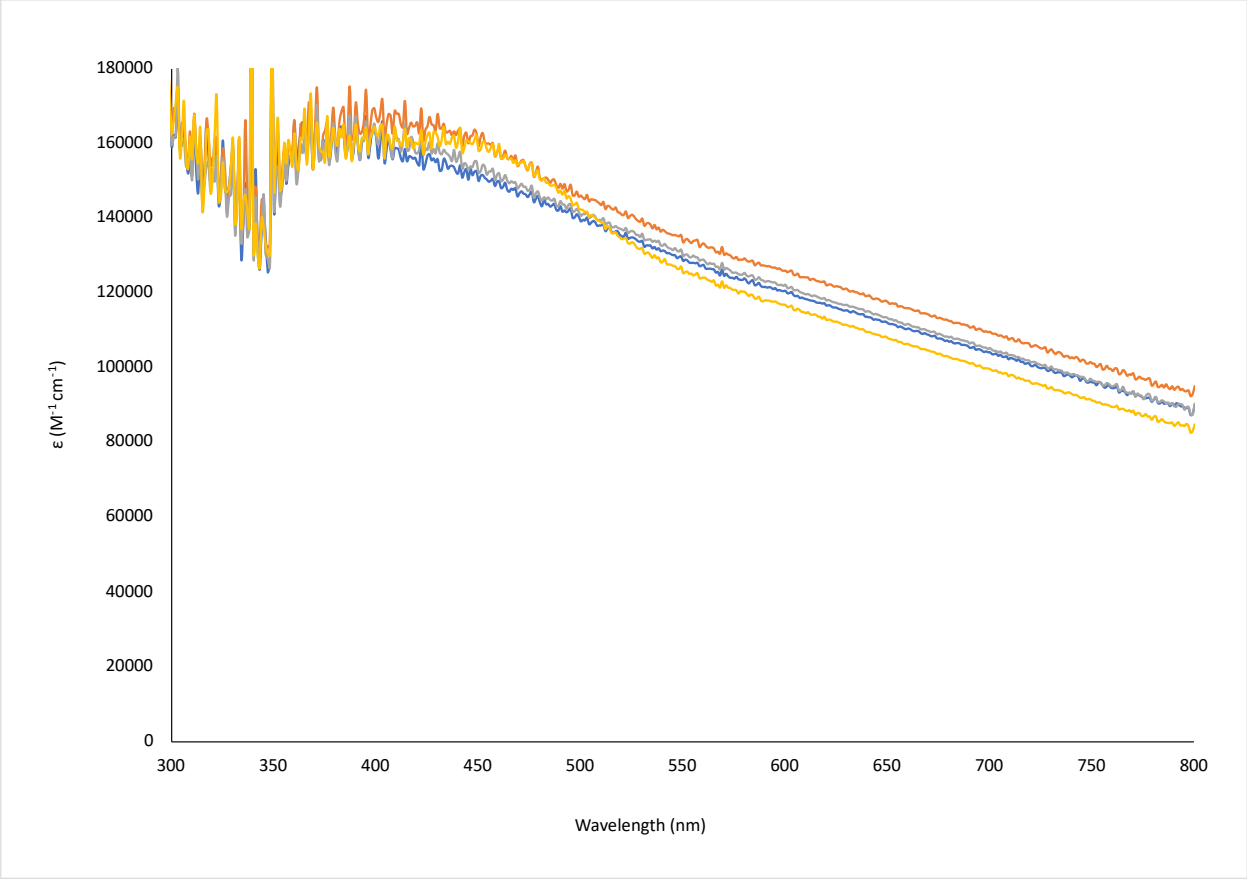

Figure 6-32. Stacked UV-Vis absorption spectra of probe 1 (blue, excess), 2 (orange, excess), 7 (grey, excess), and 8 (yellow, excess) with $Zn(OTf)_2$ in PhCl; 12.5 μM samples.

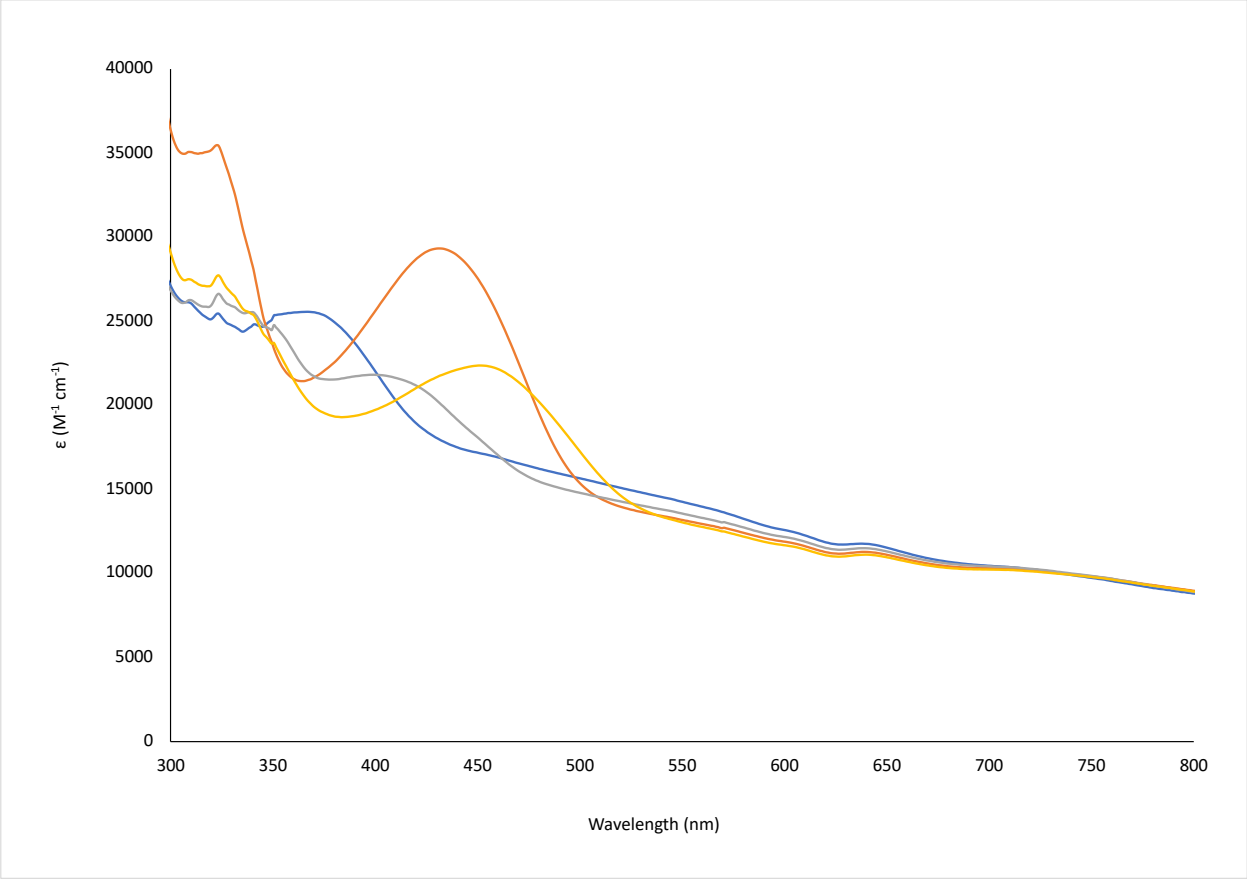

Figure 6- 33. Stacked UV-Vis absorption spectra of probe 1 (blue, excess), 2 (orange, excess), 7 (grey, excess), and 8 (yellow, excess) with $Zn(OTf)_2$ in Et_2O; 12.5 μM samples.

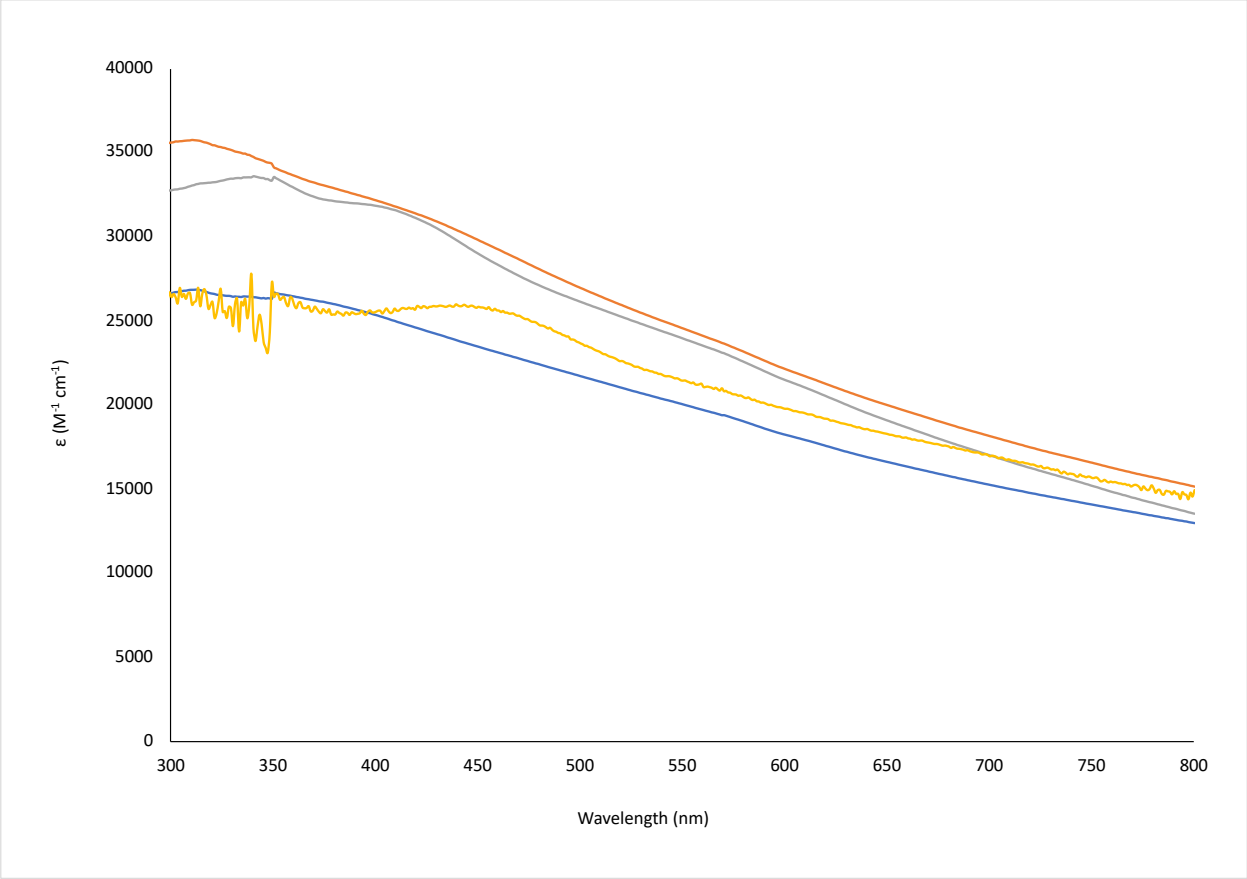

Figure 6-34. Stacked UV-Vis absorption spectra of probe 1 (blue, excess), 2 (orange, excess), 7 (grey, excess), and 8 (yellow, excess) with $Zn(OTf)_2$ in DCM; 12.5 μM samples.

6.2.3. Emission and Excitation Spectra

6.2.3.1. AlCl3

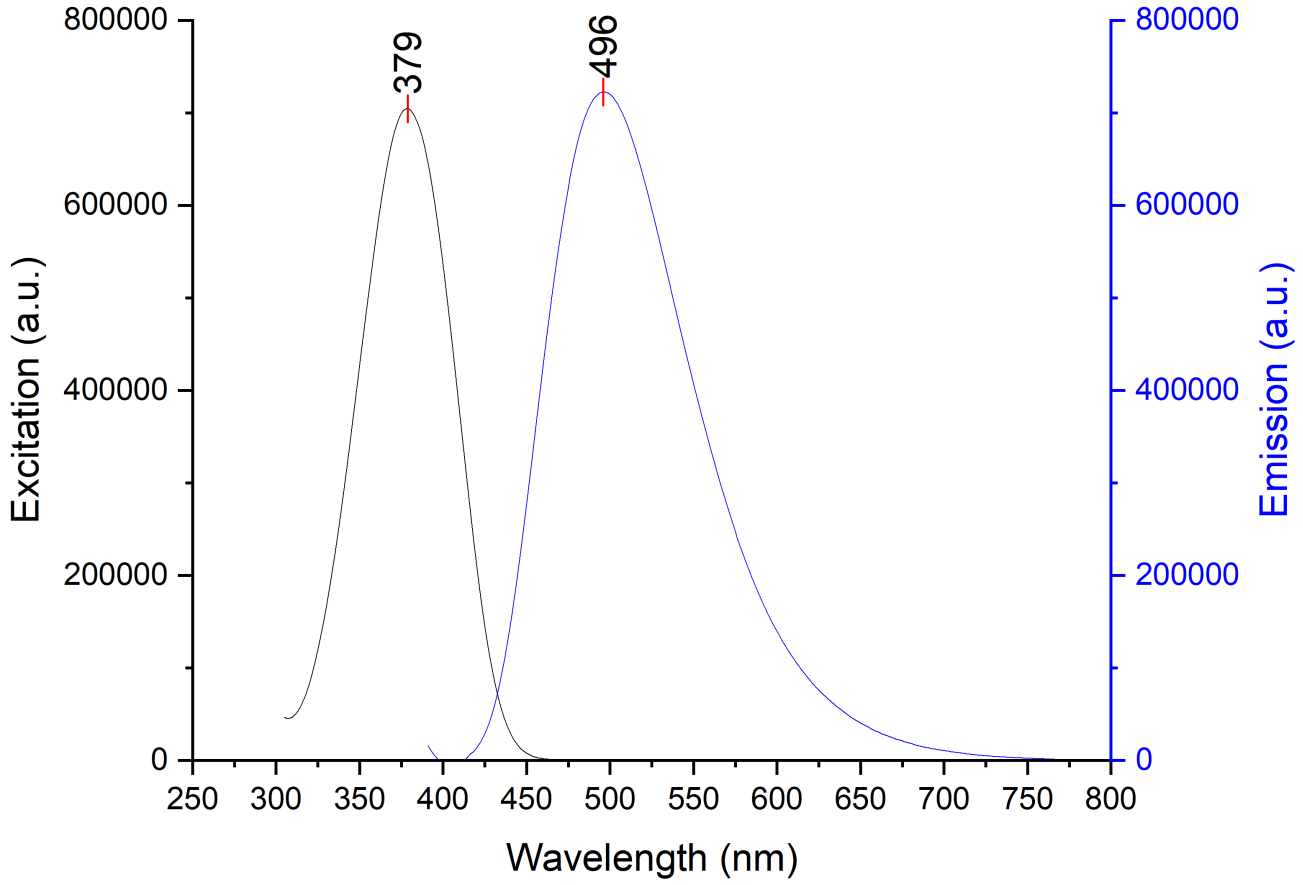

Figure 6-35. Stacked excitation (step: 1.0 nm/s, dwell time: 0.125 s, slit width: 1.0 nm) and emission (step: 1.0 nm/s, dwell time: 0.125 s, slit width: 1.0 nm) spectra of probe 1 and $AlCl_3$ in MeCN; 12.5 μM sample.

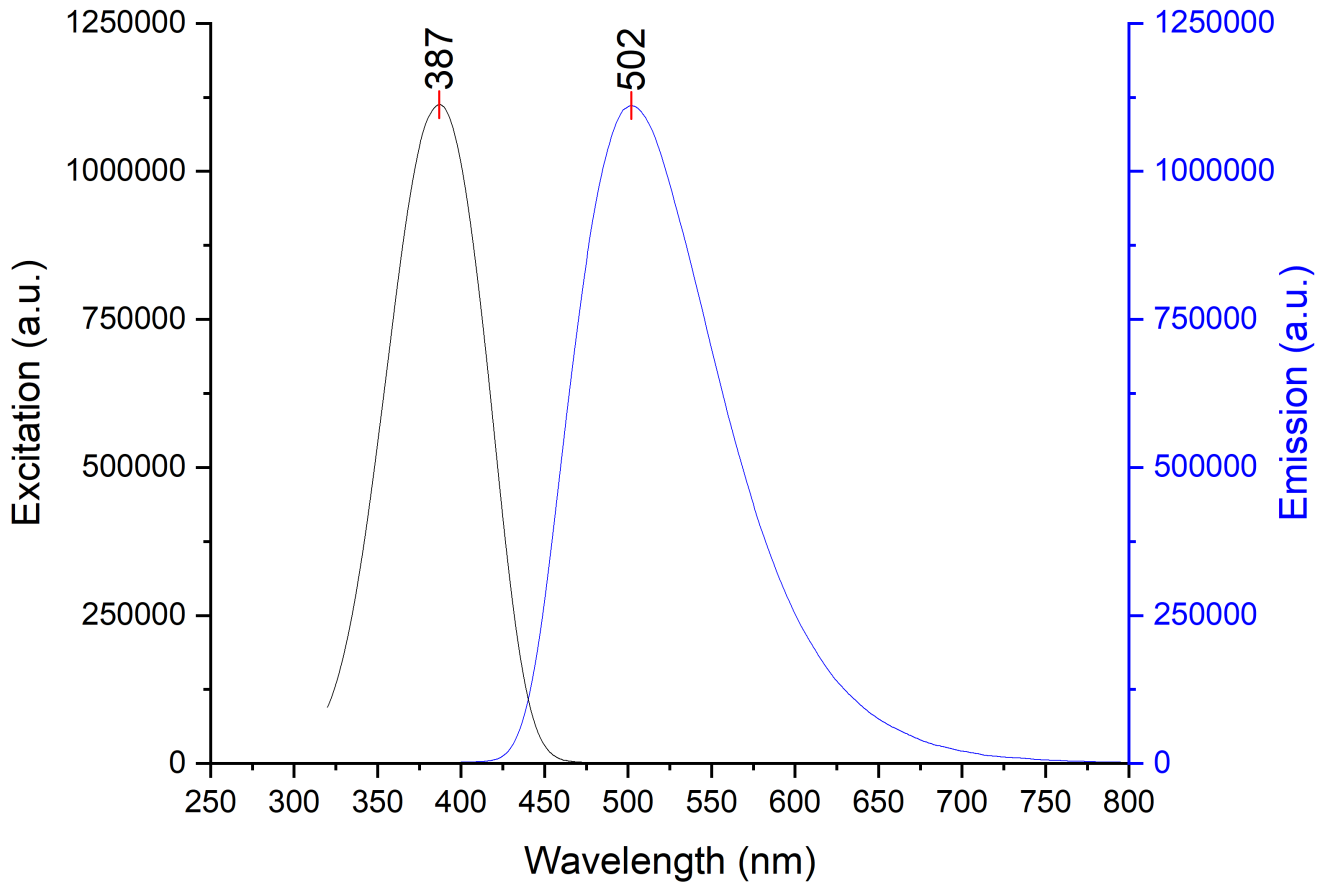

Figure 6-36. Stacked excitation (step: 1.0 nm/s, dwell time: 0.125 s, slit width: 1.0 nm) and emission (step: 1.0 nm/s, dwell time: 0.125 s, slit width: 1.0 nm) spectra of probe 1 and $AlCl_3$ in PhCl; 12.5 μM sample.

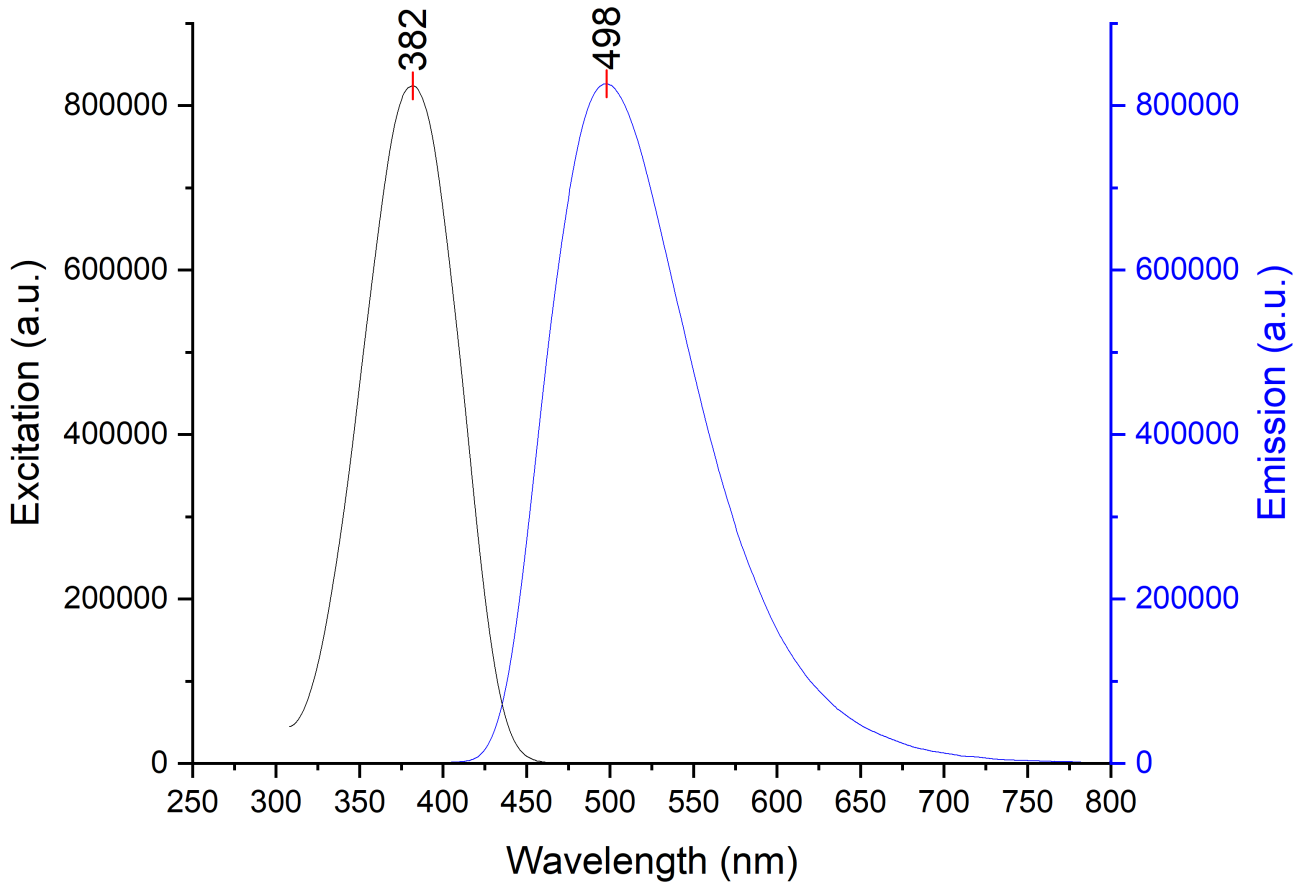

Figure 6-37. Stacked excitation (step: 1.0 nm/s, dwell time: 0.125 s, slit width: 1.0 nm) and emission (step: 1.0 nm/s, dwell time: 0.125 s, slit width: 1.0 nm) spectra of probe 1 and $AlCl_3$ in Et_2O; 12.5 μM sample.

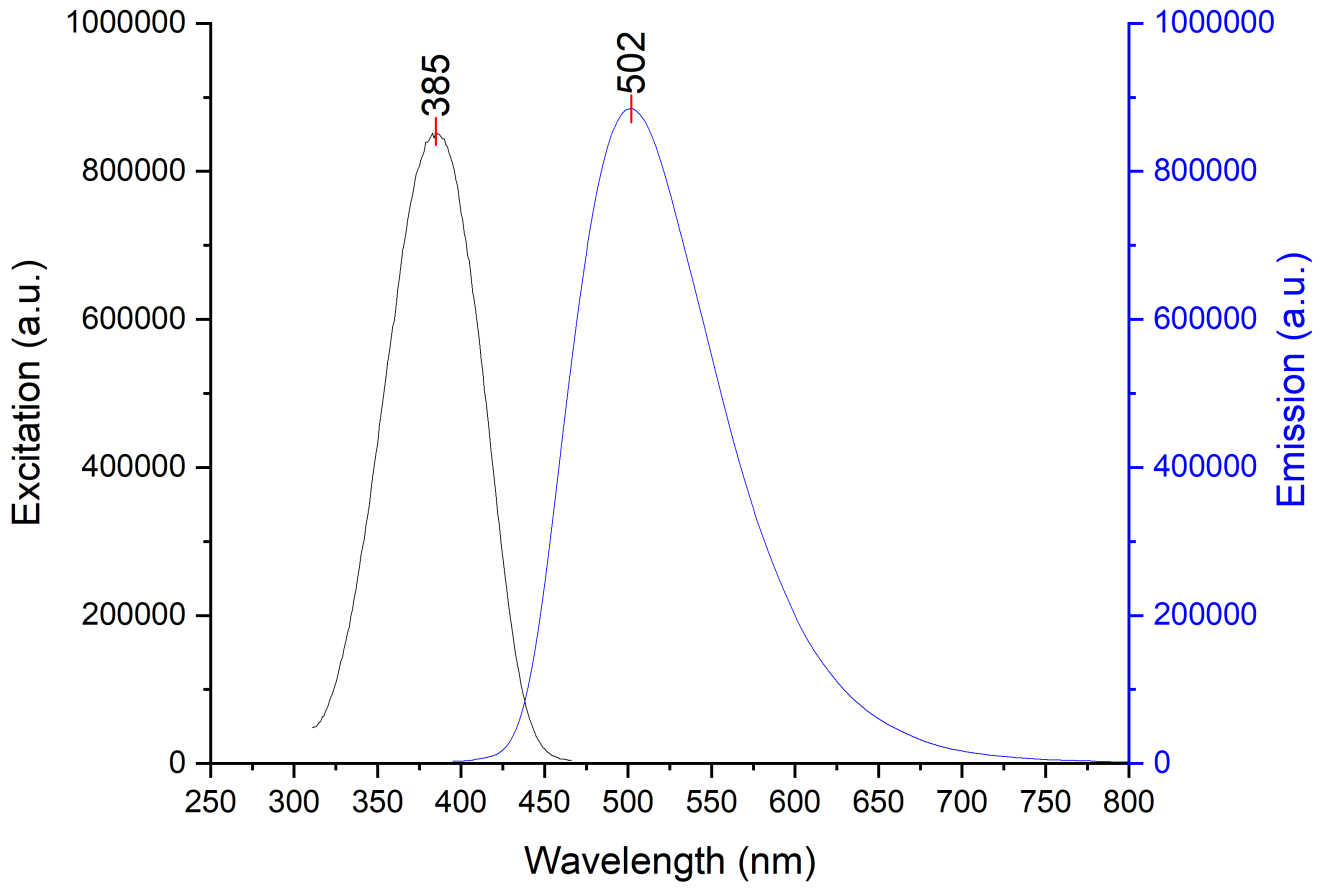

Figure 6-38. Stacked excitation (step: 1.0 nm/s, dwell time: 0.125 s, slit width: 1.0 nm) and emission (step: 1.0 nm/s, dwell time: 0.125 s, slit width: 1.0 nm) spectra of probe 1 and $AlCl_3$ in DCM; 12.5 μM sample.

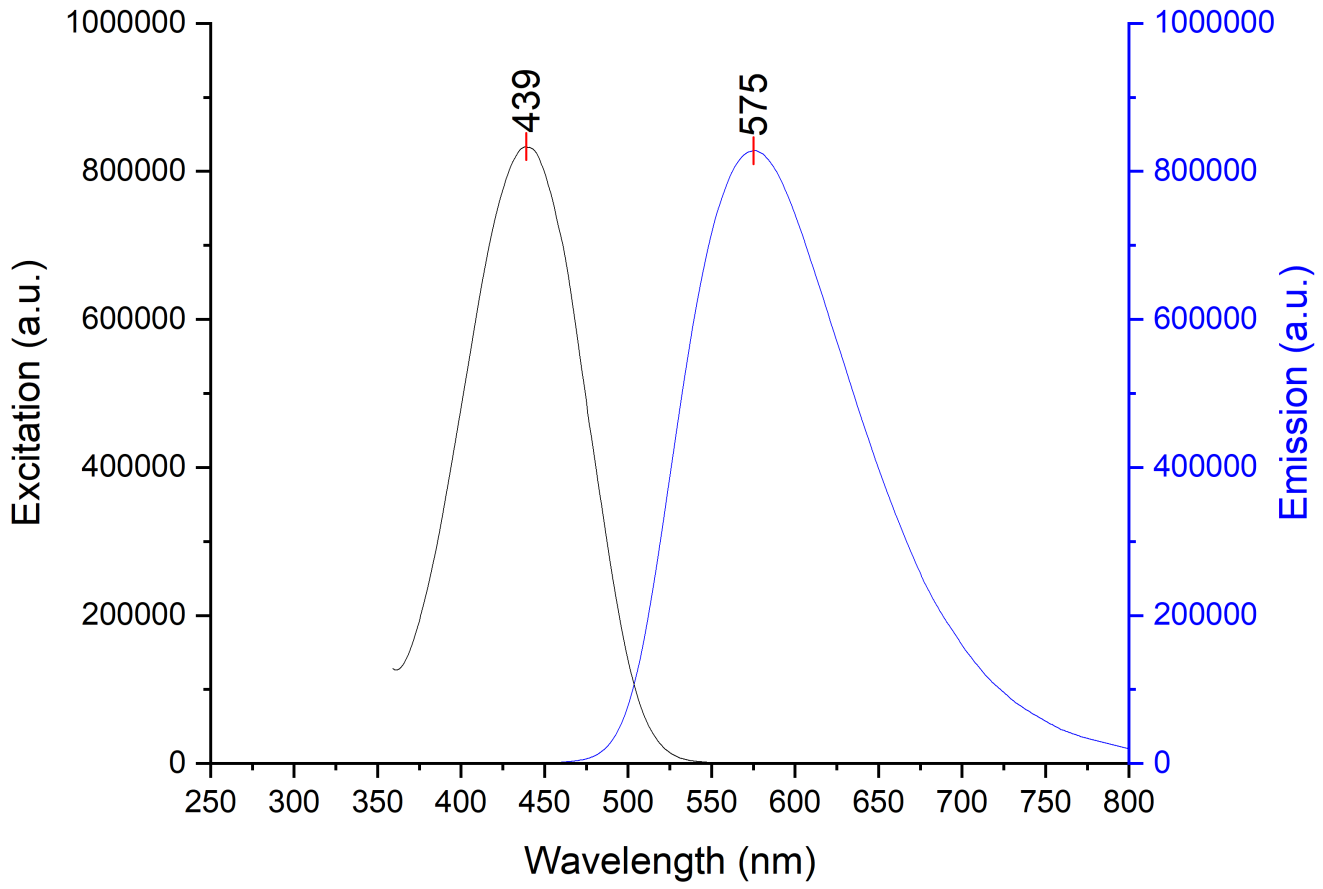

Figure 6-39. Stacked excitation (step: 1.0 nm/s, dwell time: 0.125 s, slit width: 1.0 nm) and emission (step: 1.0 nm/s, dwell time: 0.125 s, slit width: 1.0 nm) spectra of probe 2 and $AlCl_3$ in MeCN; 12.5 μM sample.

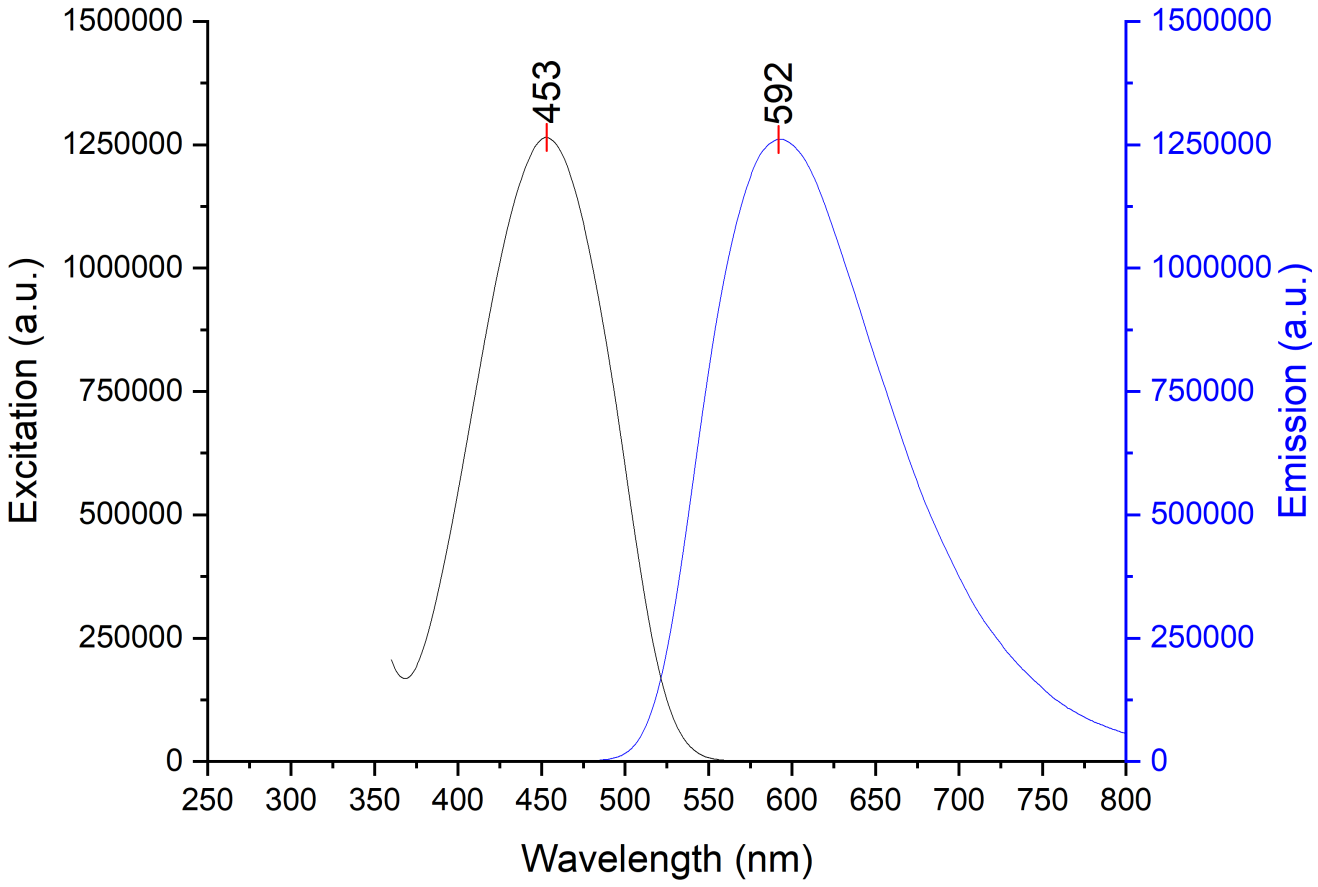

Figure 6-40. Stacked excitation (step: 1.0 nm/s, dwell time: 0.125 s, slit width: 1.0 nm) and emission (step: 1.0 nm/s, dwell time: 0.125 s, slit width: 1.0 nm) spectra of probe 2 and $AlCl_3$ in PhCl; 12.5 μM sample.

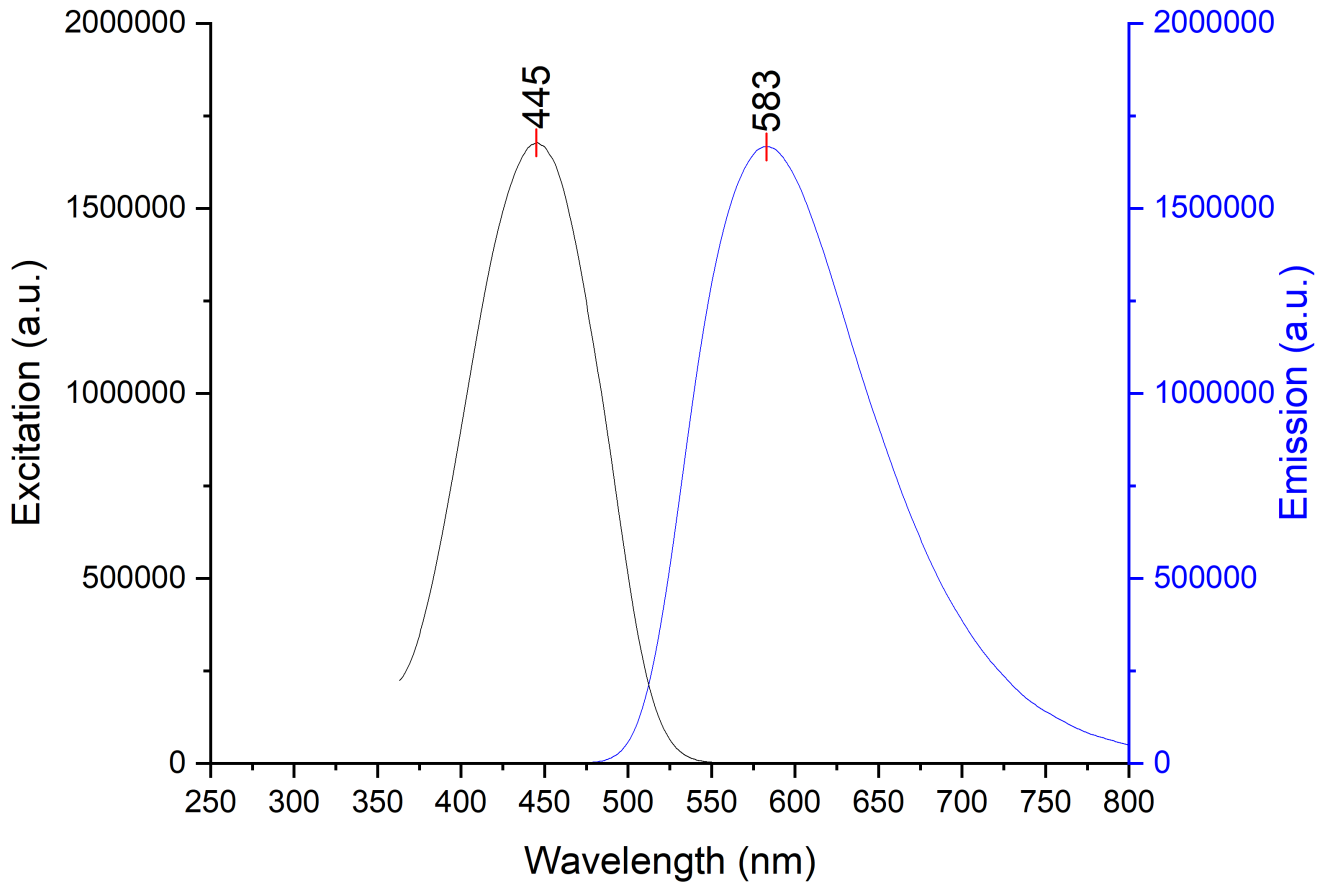

Figure 6-41. Stacked excitation (step: 1.0 nm/s, dwell time: 0.125 s, slit width: 1.0 nm and emission (step: 1.0 nm/s, dwell time: 0.125 s, slit width: 1.0 nm) spectra of probe 2 and $AlCl_3$ in Et_2O; 12.5 μM sample.

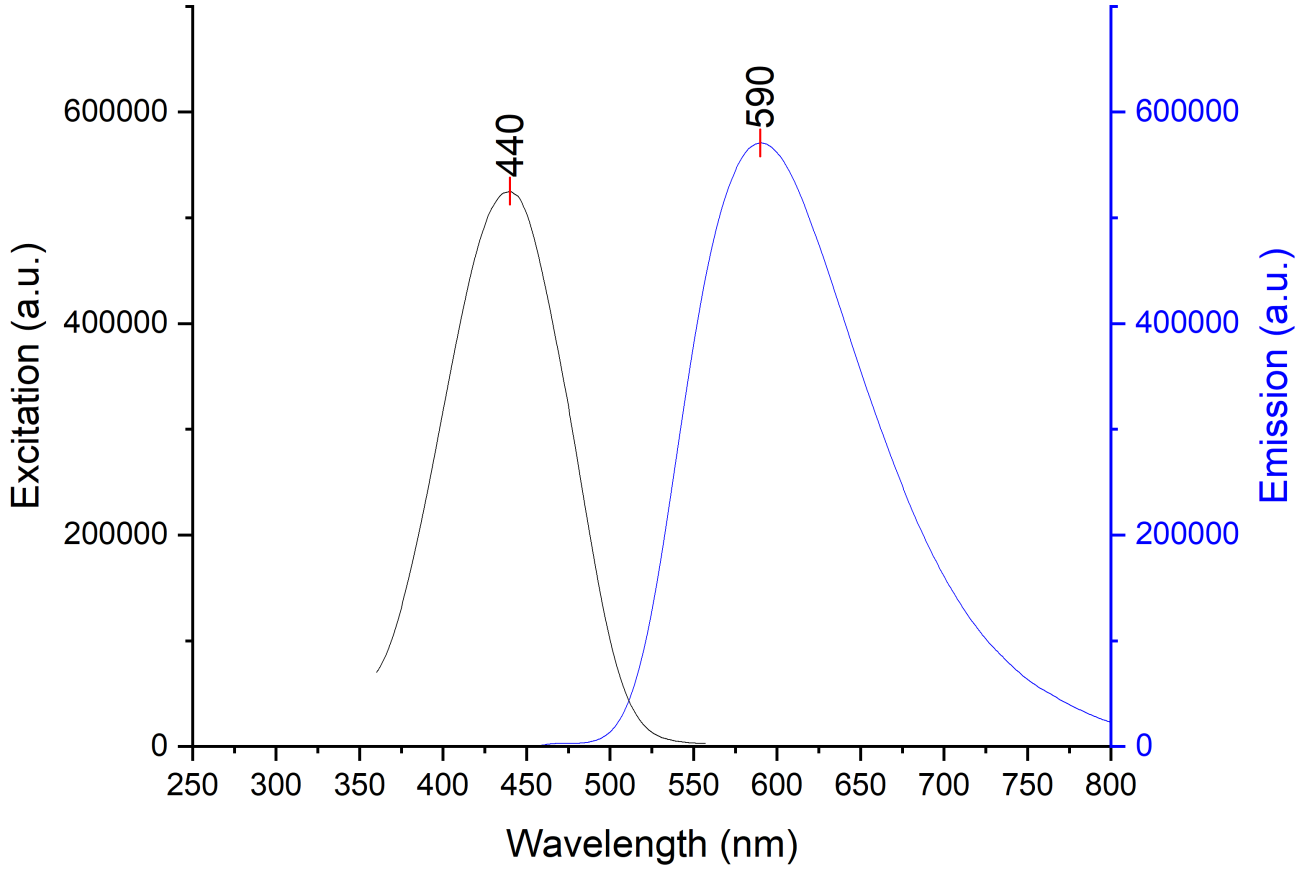

Figure 6-42. Stacked excitation (step: 1.0 nm/s, dwell time: 0.125 s, slit width: 1.0 nm) and emission (step: 1.0 nm/s, dwell time: 0.125 s, slit width: 1.0 nm) spectra of probe 2 and $AlCl_3$ in DCM; 12.5 μM sample.

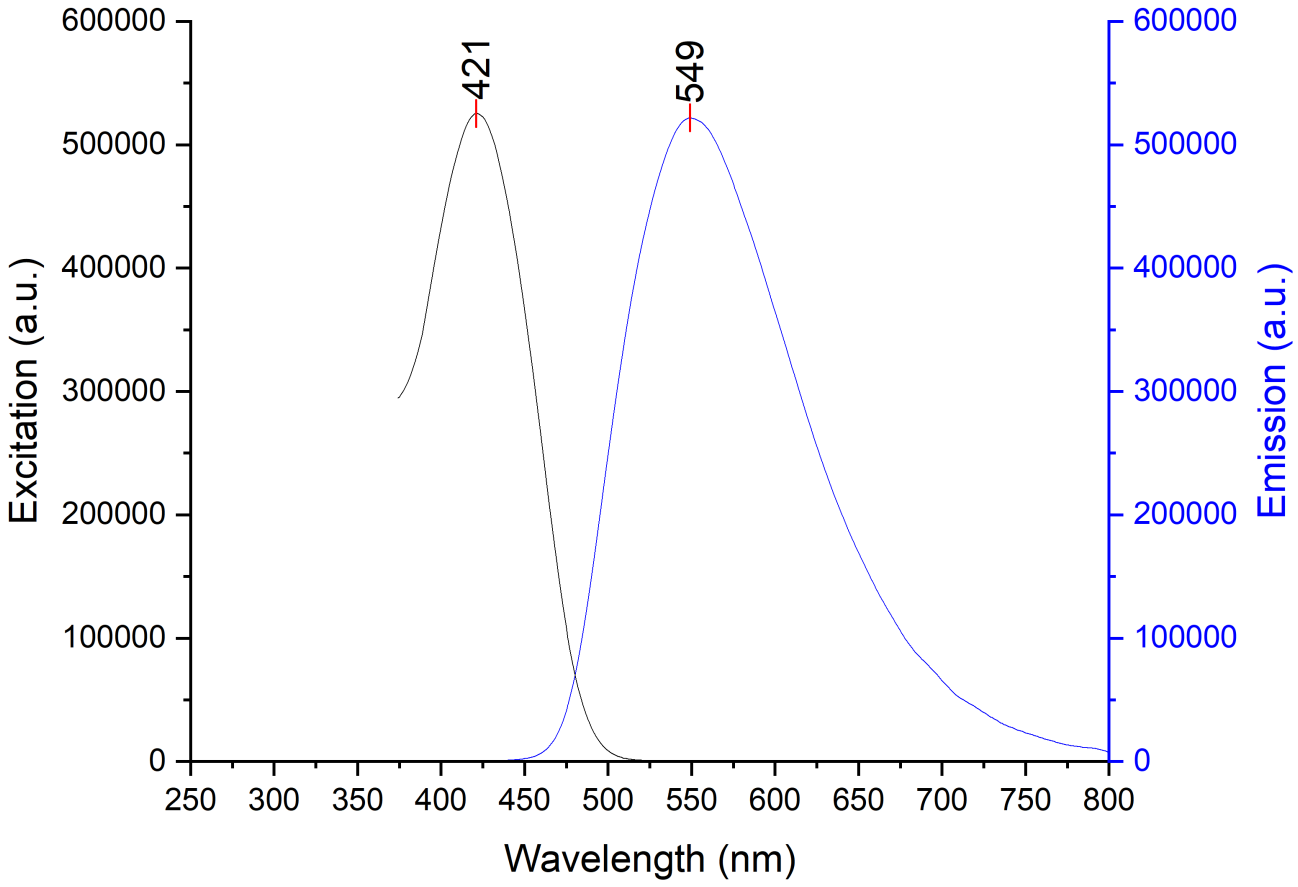

Figure 6-43. Stacked excitation (step: 1.0 nm/s, dwell time: 0.125 s, slit width: 1.0 nm) and emission (step: 1.0 nm/s, dwell time: 0.125 s, slit width: 1.0 nm) spectra of probe 7 and $AlCl_3$ in MeCN; 12.5 μM sample.

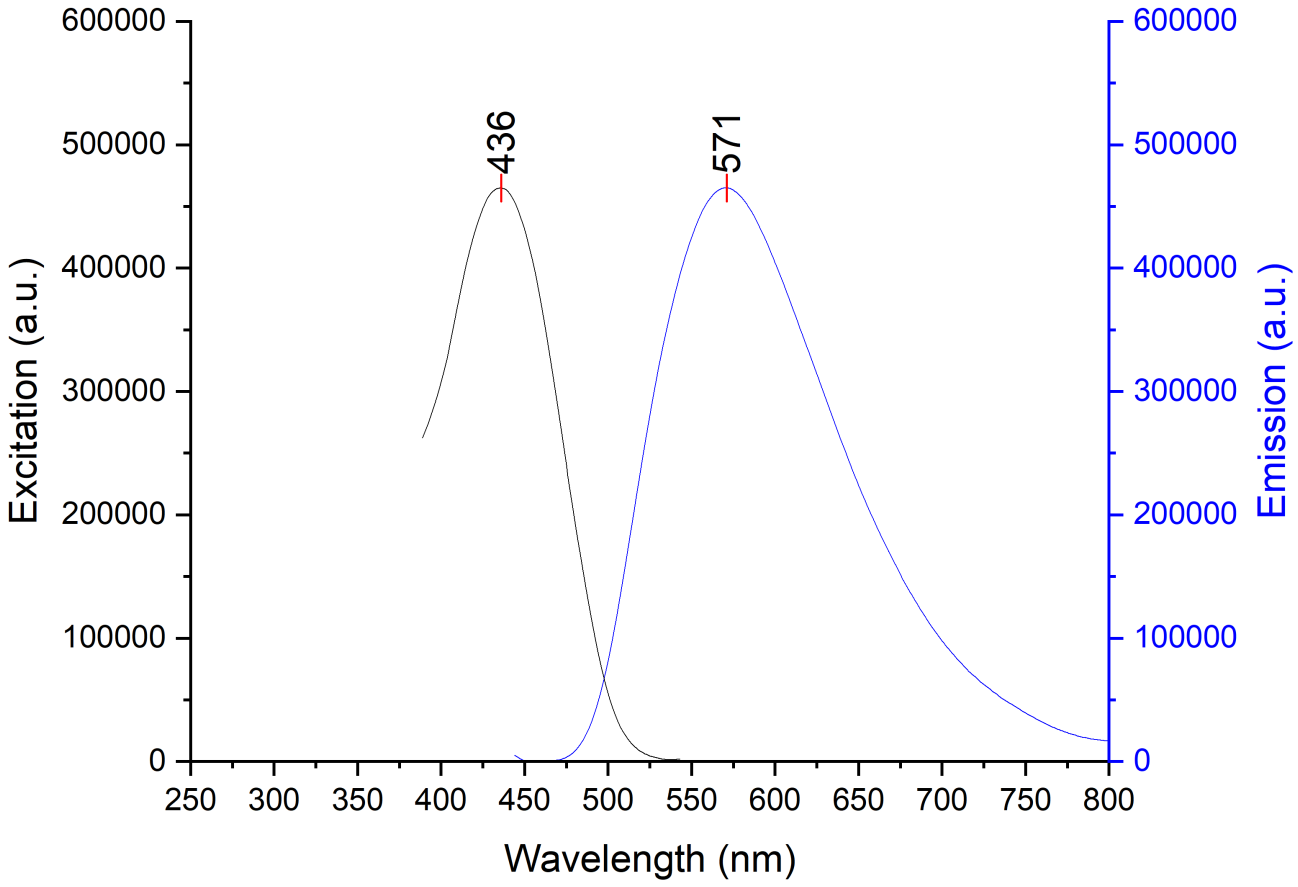

Figure 6-44. Stacked excitation (step: 1.0 nm/s, dwell time: 0.125 s, slit width: 1.0 nm) and emission (step: 1.0 nm/s, dwell time: 0.125 s, slit width: 1.0 nm) spectra of probe 7 and $AlCl_3$ in PhCl; 12.5 μM sample.

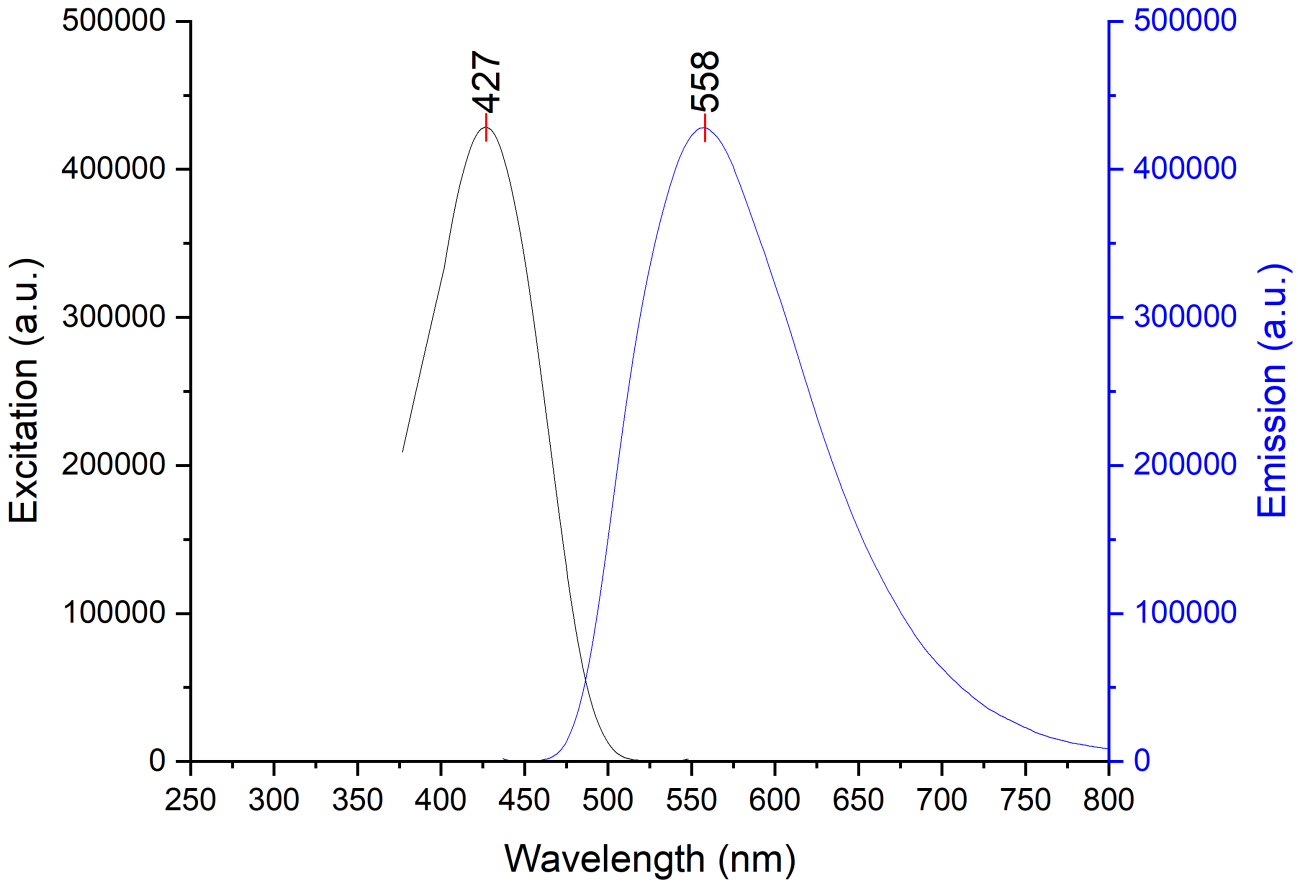

Figure 6-45. Stacked excitation (step: 1.0 nm/s, dwell time: 0.125 s, slit width: 1.0 nm) and emission (step: 1.0 nm/s, dwell time: 0.125 s, slit width: 1.0 nm) spectra of probe 7 and $AlCl_3$ in Et_2O; 12.5 µM sample.

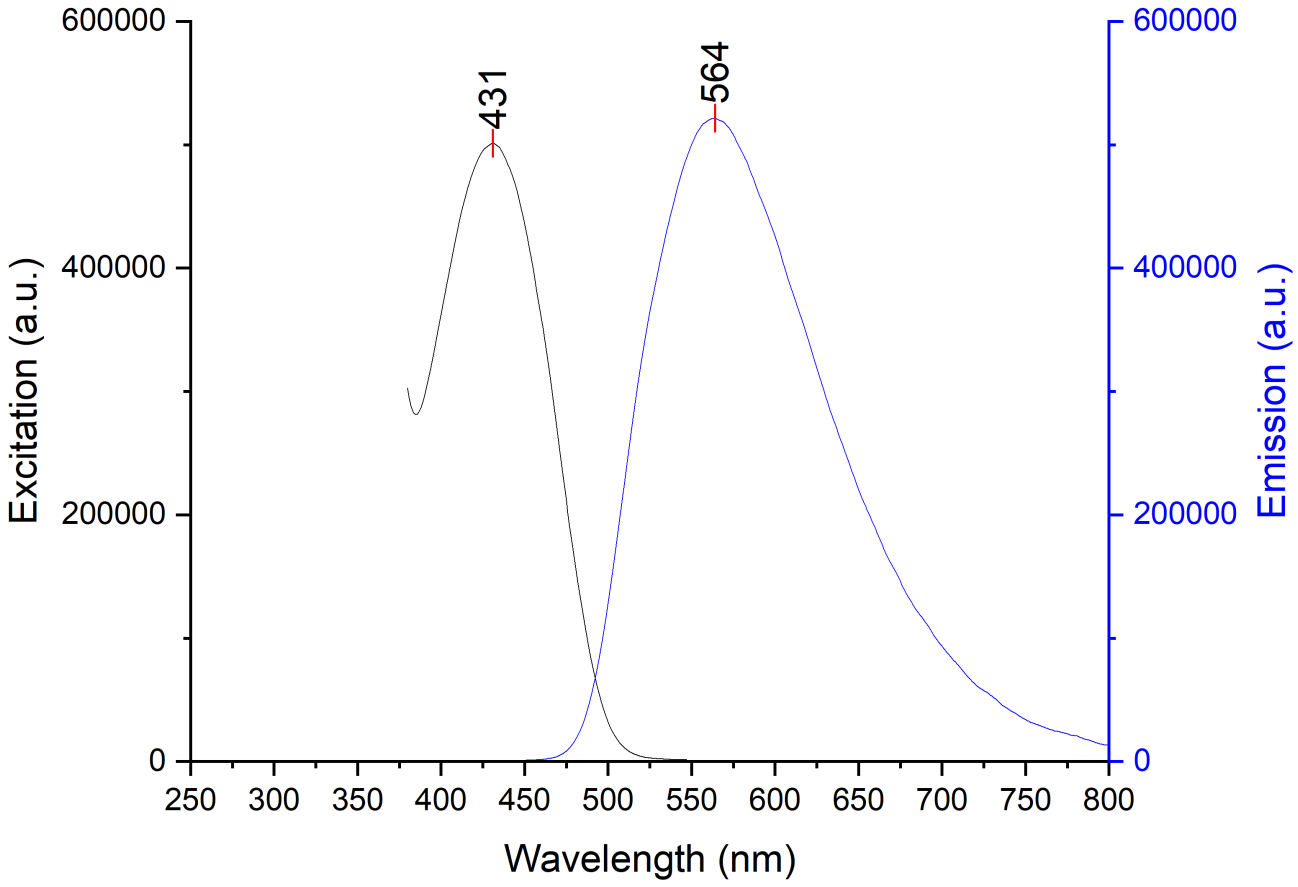

Figure 6-46. Stacked excitation (step: 0.5 nm/s, dwell time: 0.125 s, slit width: 0.80 nm) and emission (step: 0.5 nm/s, dwell time: 0.125 s, slit width: 0.80 nm) spectra of probe 7 and $AlCl_3$ in DCM; 12.5 µM sample.

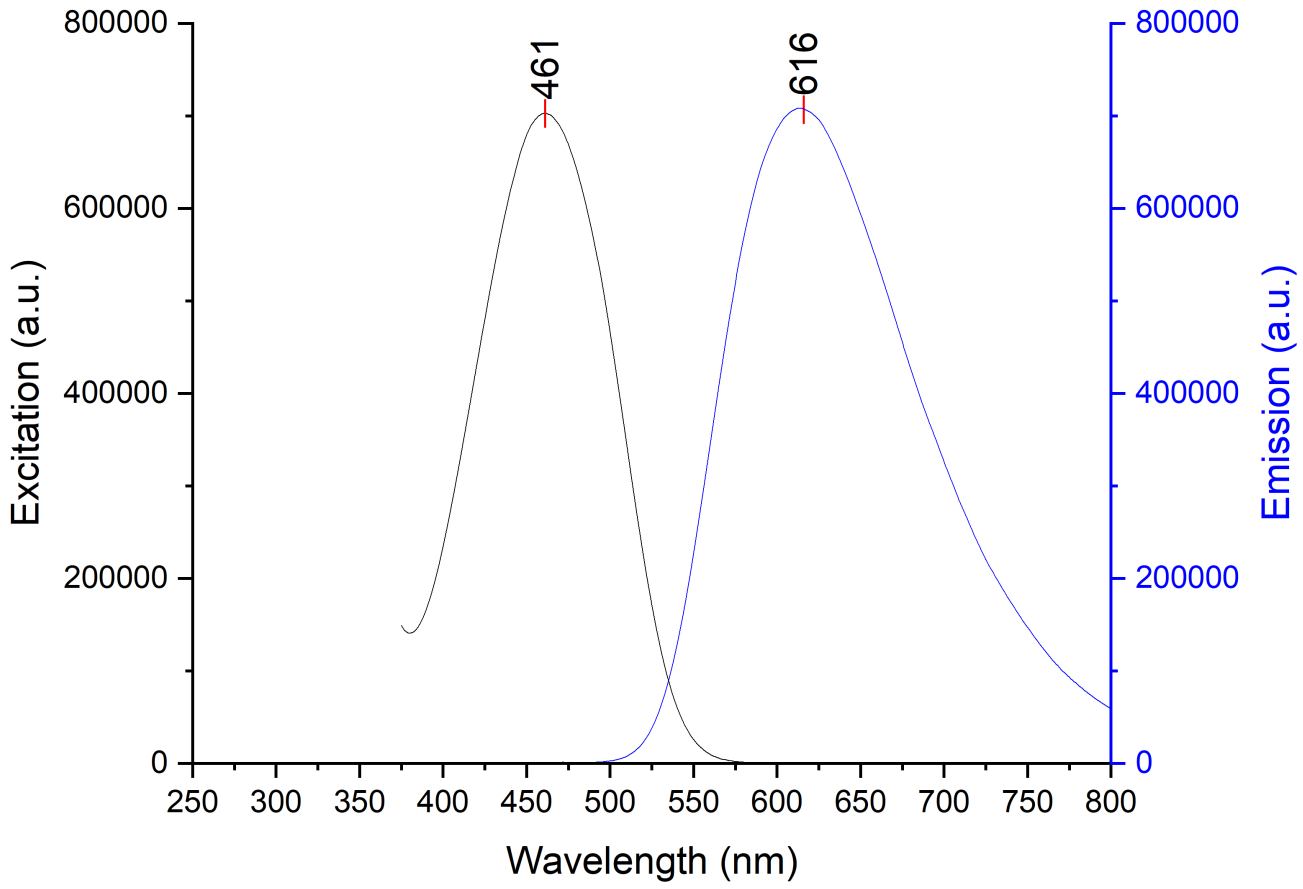

Figure 6-47. Stacked excitation (step: 1.0 nm/s, dwell time: 0.125 s, slit width: 1.0 nm) and emission (step: 1.0 nm/s, dwell time: 0.125 s, slit width: 1.0 nm) spectra of probe 8 and $AlCl_3$ in MeCN; 12.5 µM sample.

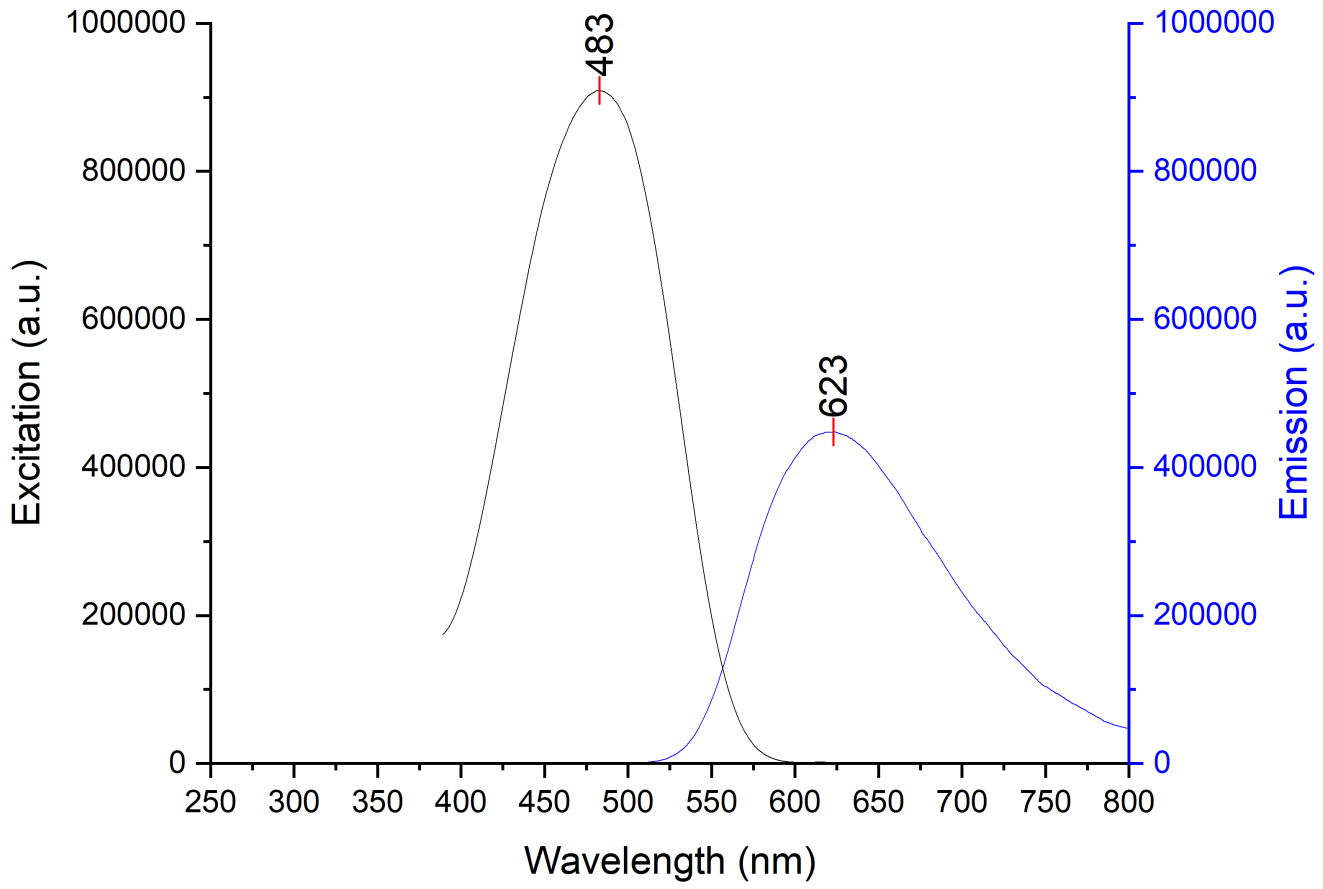

Figure 6-48. Stacked excitation (step: 1.0 nm/s, dwell time: 0.125 s, slit width: 1.0 nm) and emission (step: 1.0 nm/s, dwell time: 0.125 s, slit width: 1.0 nm) spectra of probe 8 and $AlCl_3$ in PhCl; 12.5 µM sample.

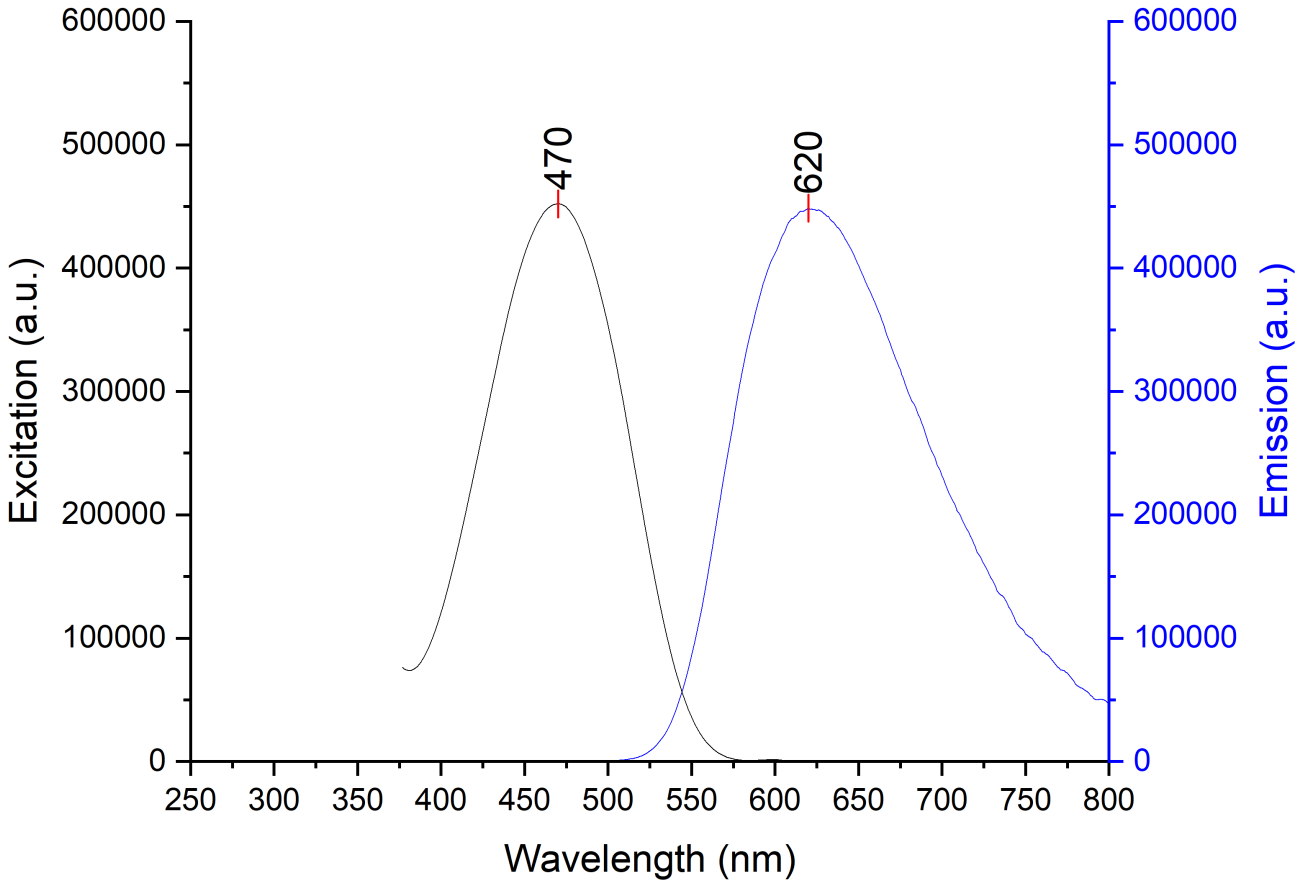

Figure 6-49. Stacked excitation (step: 1.0 nm/s, dwell time: 0.125 s, slit width: 1.0 nm) and emission (step: 1.0 nm/s, dwell time: 0.125 s, slit width: 1.0 nm) spectra of probe 8 and $AlCl_3$ in Et_2O; 12.5 µM sample.

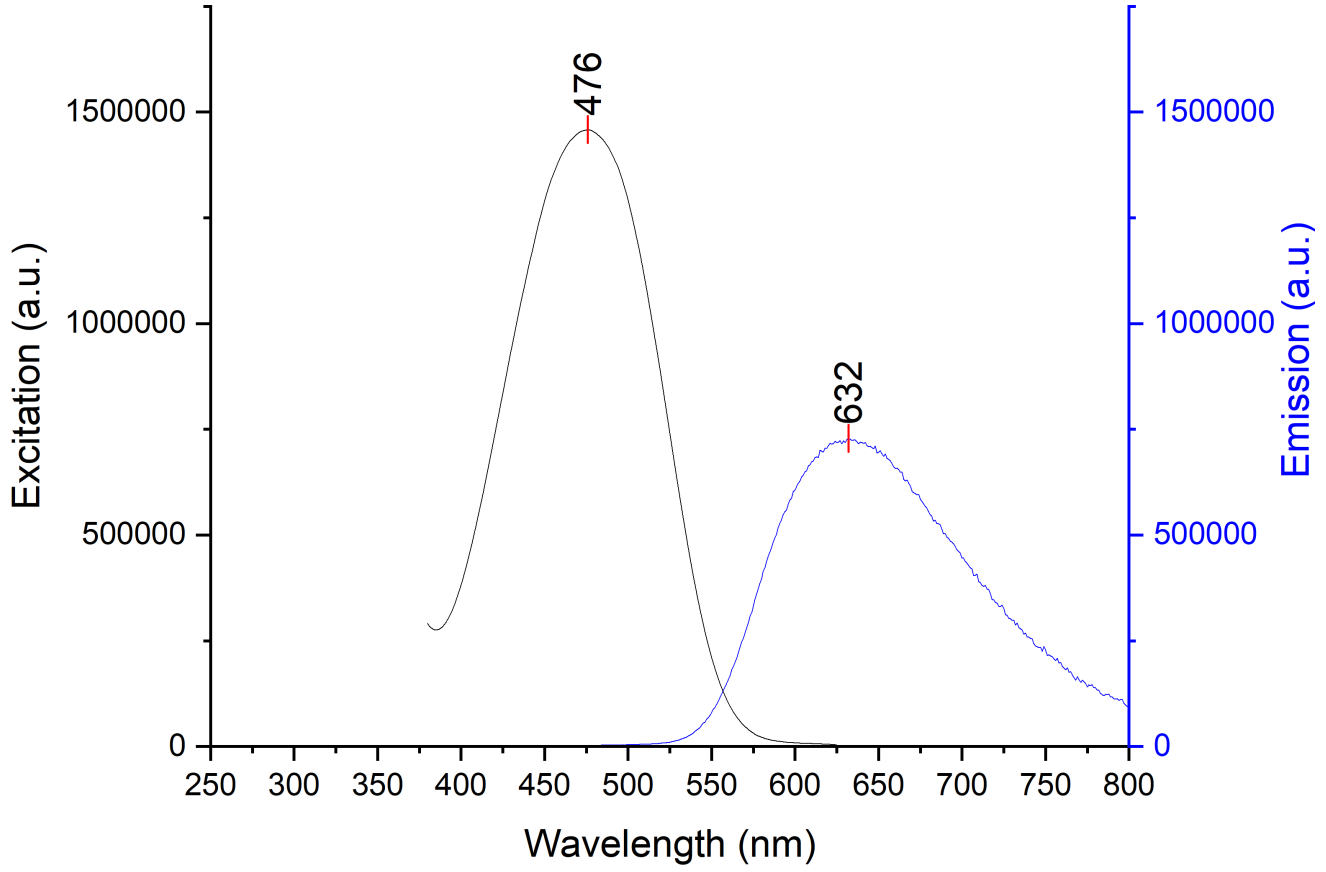

Figure 6-50. Stacked excitation (step: 1.0 nm/s, dwell time: 0.125 s, slit width: 1.0 nm) and emission (step: 1.0 nm/s, dwell time: 0.125 s, slit width: 1.0 nm) spectra of probe 8 and $AlCl_3$ in DCM; 12.5 μM sample.

6.2.3.2. $B(4\text{-}F\text{-}C_6H_4)_3$

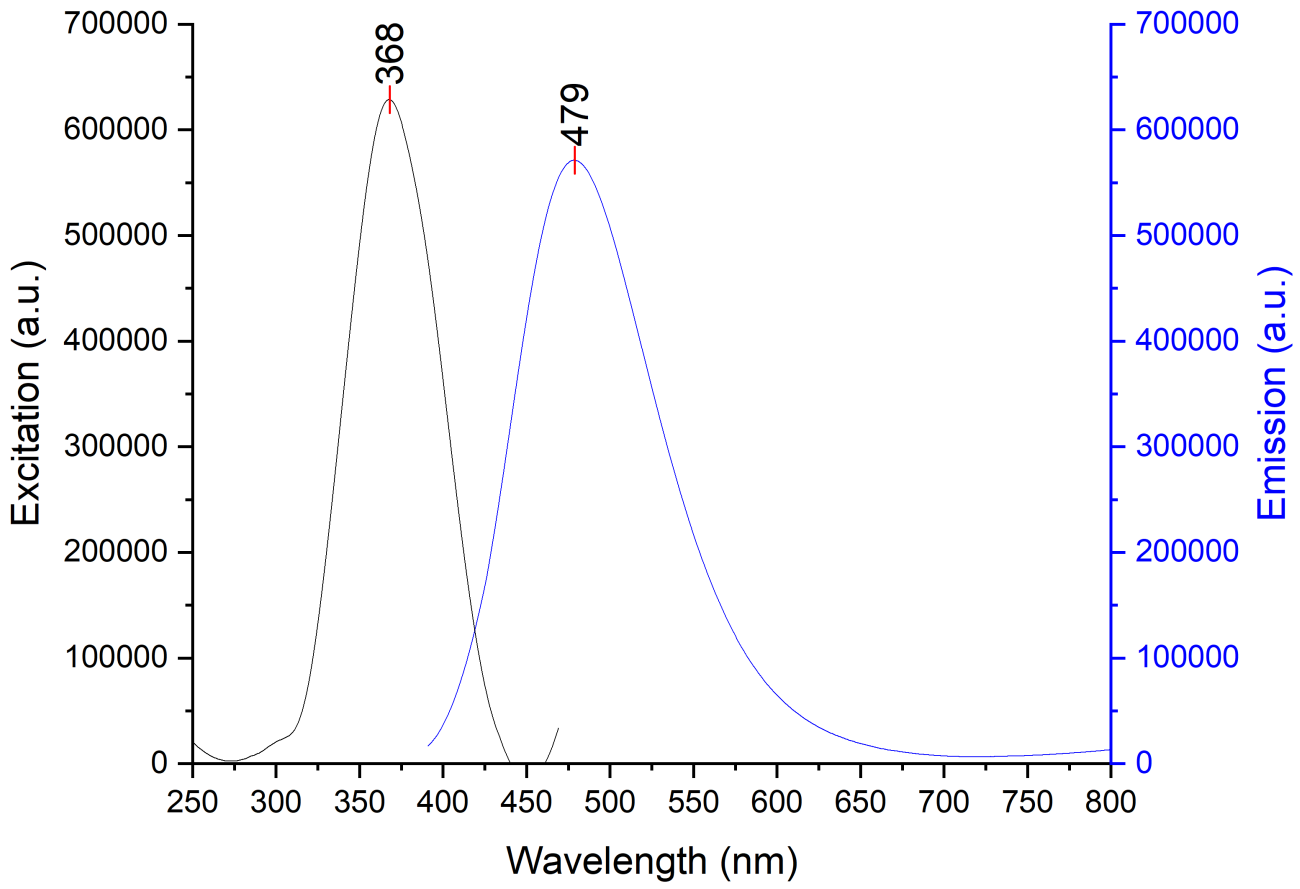

Figure 6-51. Stacked excitation (step: 1.0 nm/s, dwell time: 0.125 s, slit width: 1.0 nm) and emission (step: 1.0 nm/s, dwell time: 0.125 s, slit width: 1.0 nm) spectra of probe 1 and $B(4\text{-}F\text{-}C_6H_4)_3$ in PhCl; 12.5 μM sample.

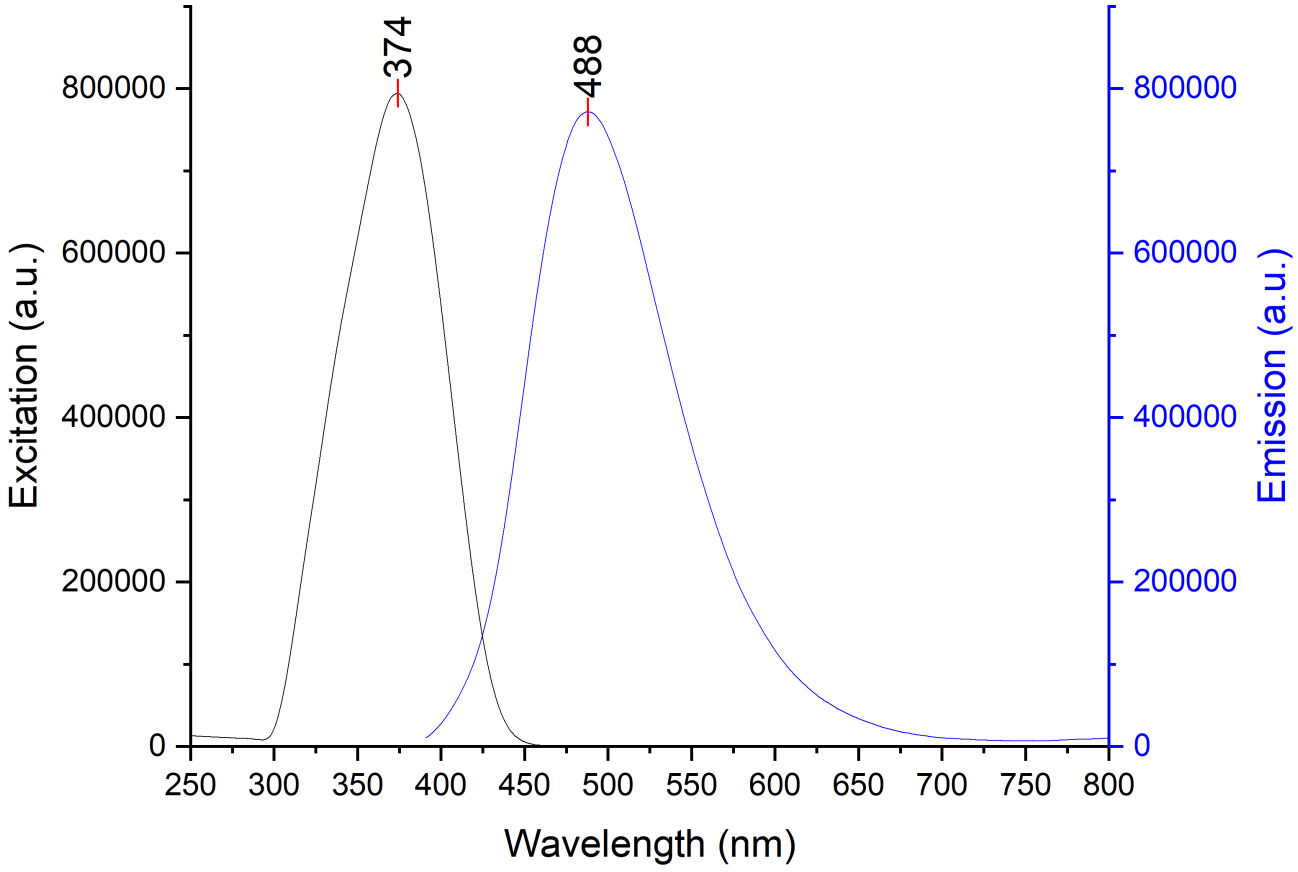

Figure 6-52. Stacked excitation (step: 1.0 nm/s, dwell time: 0.125 s, slit width: 1.0 nm) and emission (step: 1.0 nm/s, dwell time: 0.125 s, slit width: 1.0 nm) spectra of probe 1 and $B(4\text{-}F\text{-}C_6H_4)_3$ in Et_2O; 12.5 μM sample.

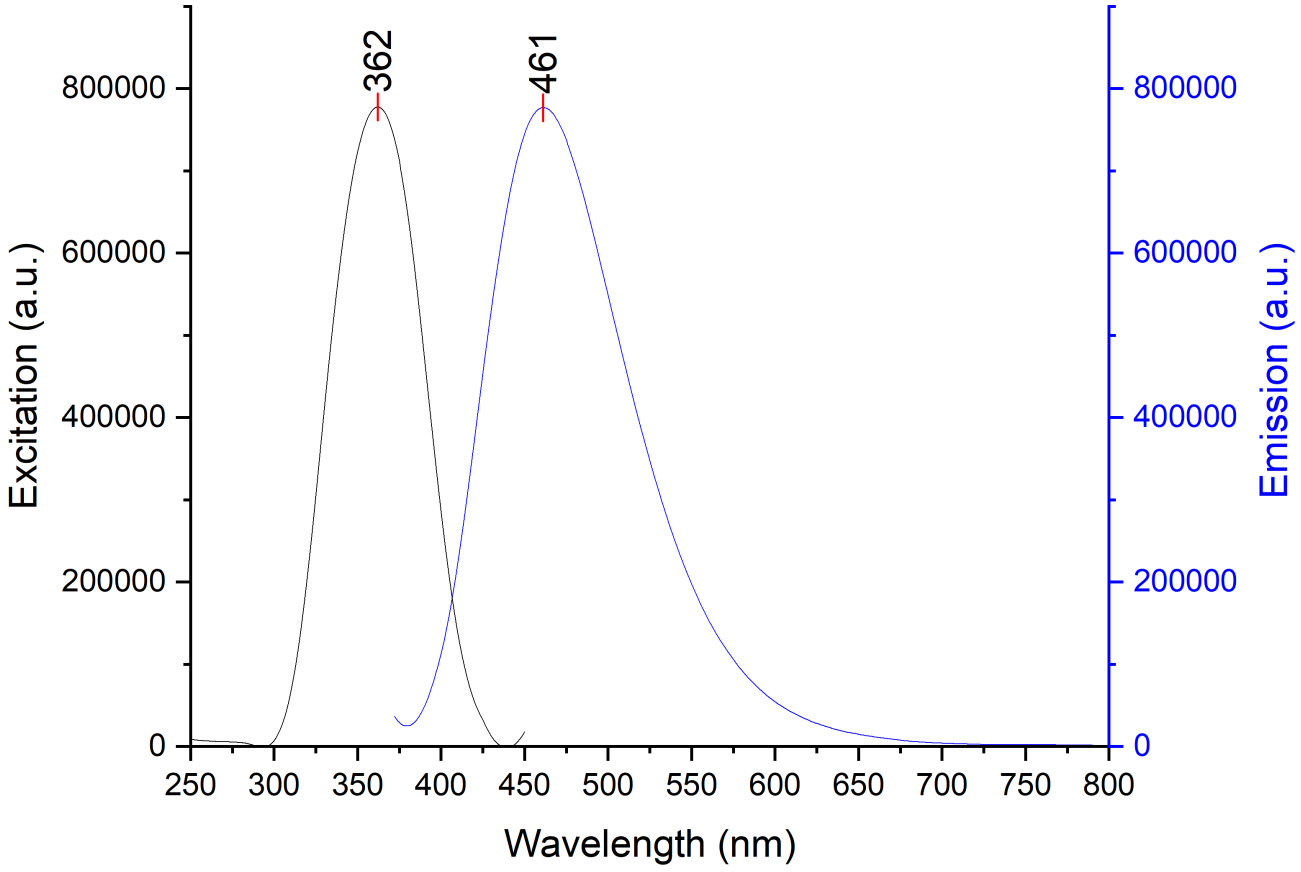

Figure 6-53. Stacked excitation (step: 1.0 nm/s, dwell time: 0.125 s, slit width: 0.70 nm) and emission (step: 1.0 nm/s, dwell time: 0.125 s, slit width: 0.70 nm) spectra of probe 1 and $B(4\text{-}F\text{-}C_6H_4)_3$ in DCM; 12.5 μM sample.

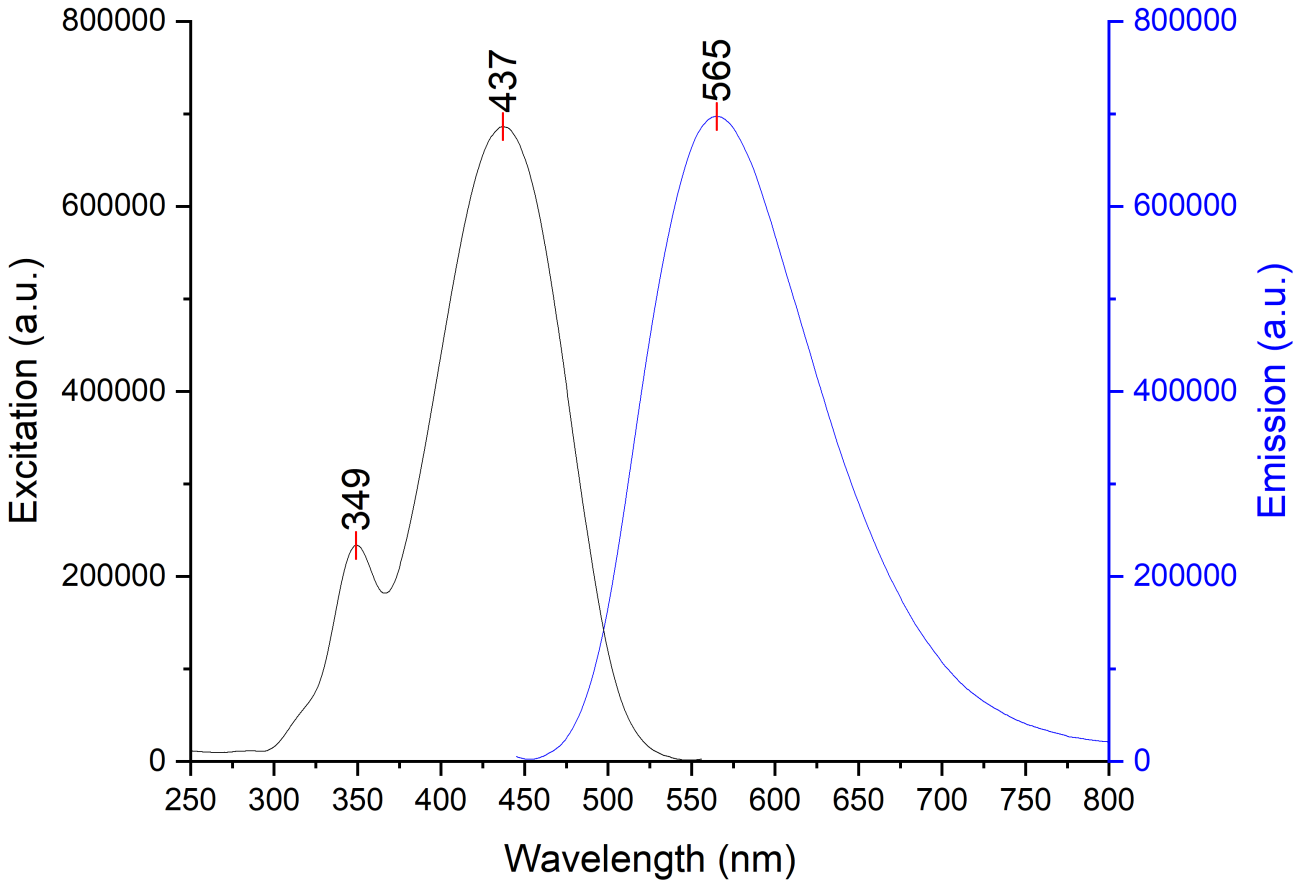

Figure 6-54. Stacked excitation (step: 1.0 nm/s, dwell time: 0.125 s, slit width: 1.0 nm) and emission (step: 1.0 nm/s, dwell time: 0.125 s, slit width: 1.0 nm) spectra of probe 2 and $B(4\text{-}F\text{-}C_6H_4)_3$ in PhCl; 12.5 μM sample.

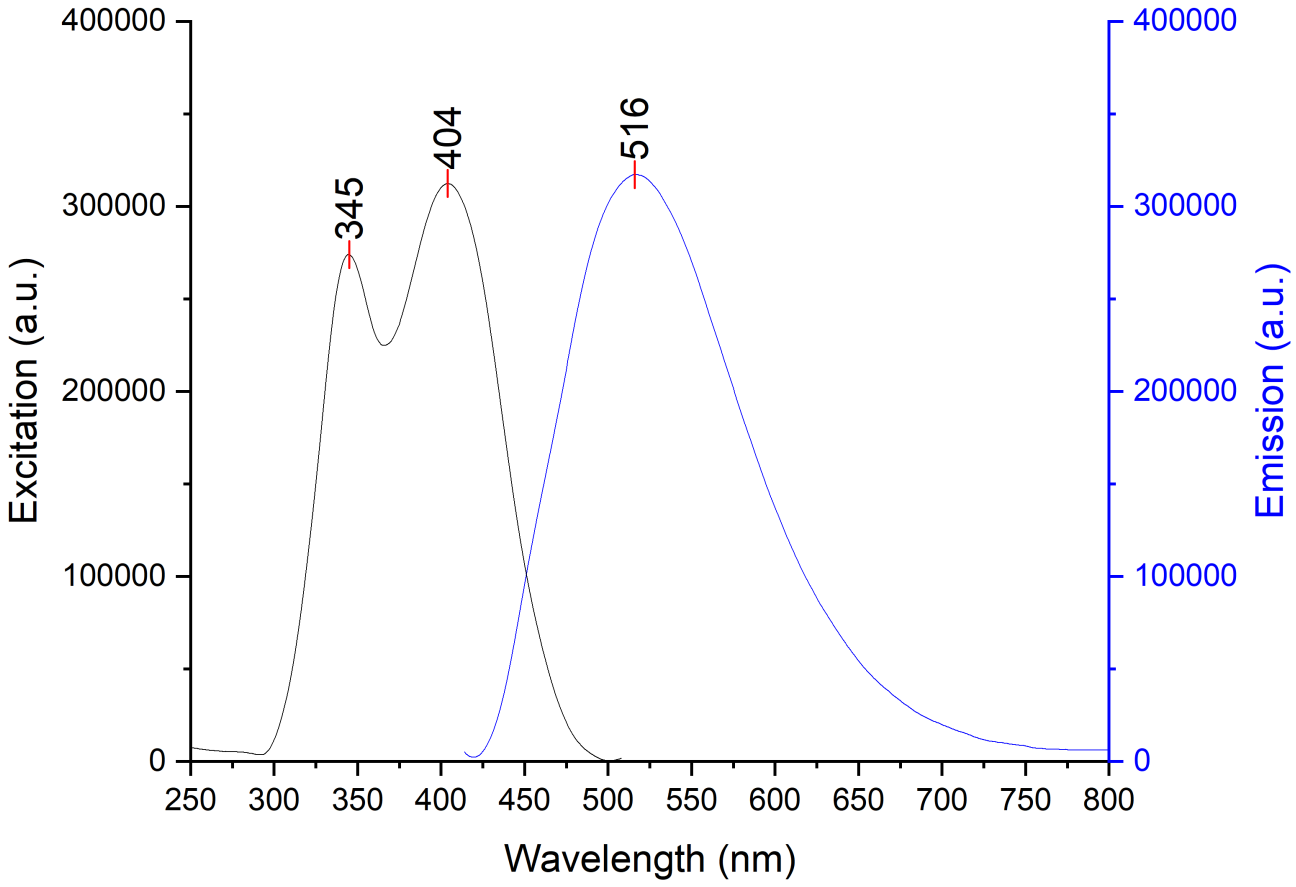

Figure 6-55. Stacked excitation (step: 1.0 nm/s, dwell time: 0.125 s, slit width: 1.0 nm) and emission (step: 1.0 nm/s, dwell time: 0.125 s, slit width: 1.0 nm nm) spectra of probe 2 and $B(4\text{-}F\text{-}C_6H_4)_3$ in Et_2O; 12.5 μM sample.

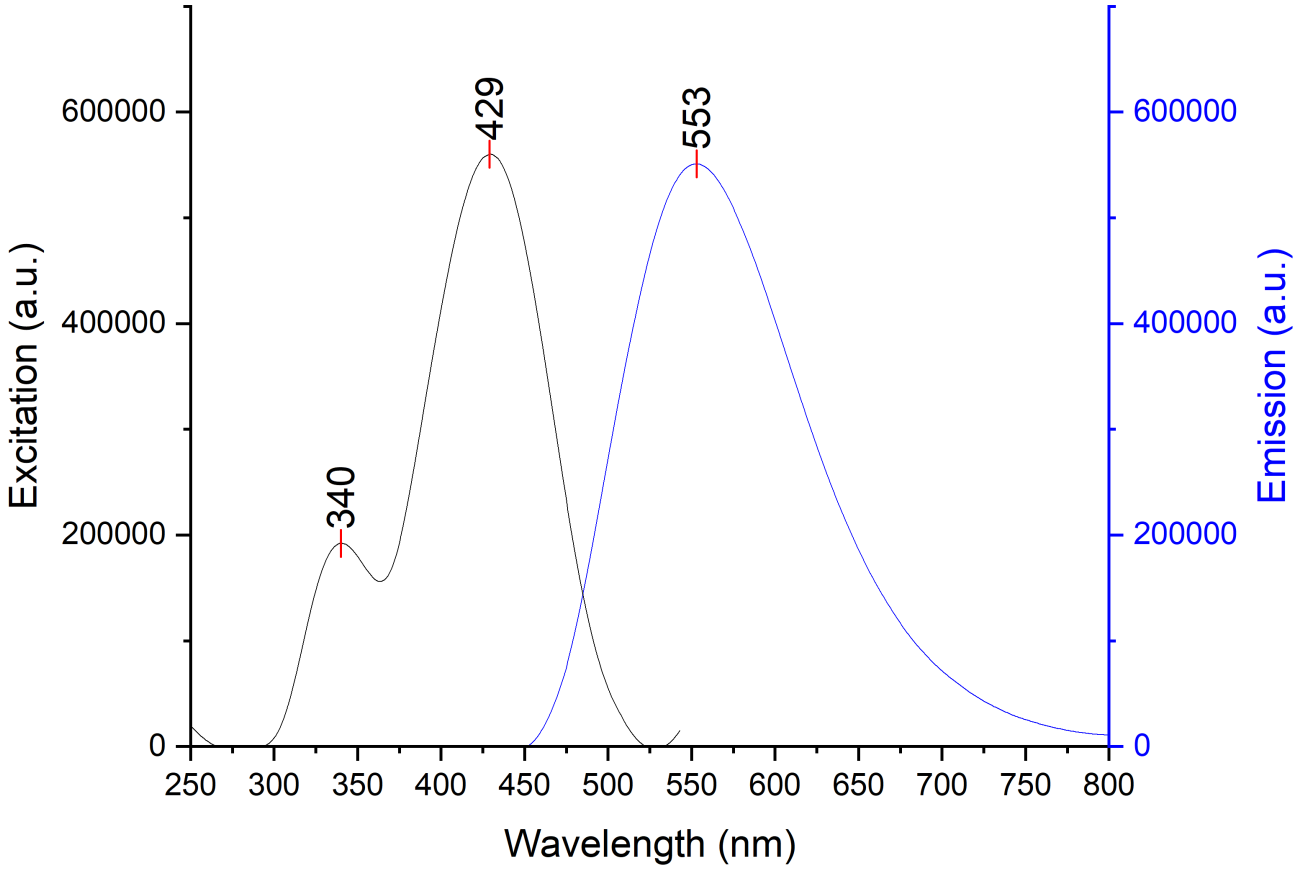

Figure 6-56. Stacked excitation (step: 1.0 nm/s, dwell time: 0.125 s, slit width: 0.70 nm) and emission (step: 1.0 nm/s, dwell time: 0.125 s, slit width: 0.70 nm) spectra of probe 2 and $B(4\text{-}F\text{-}C_6H_4)_3$ in DCM; 12.5 µM sample.

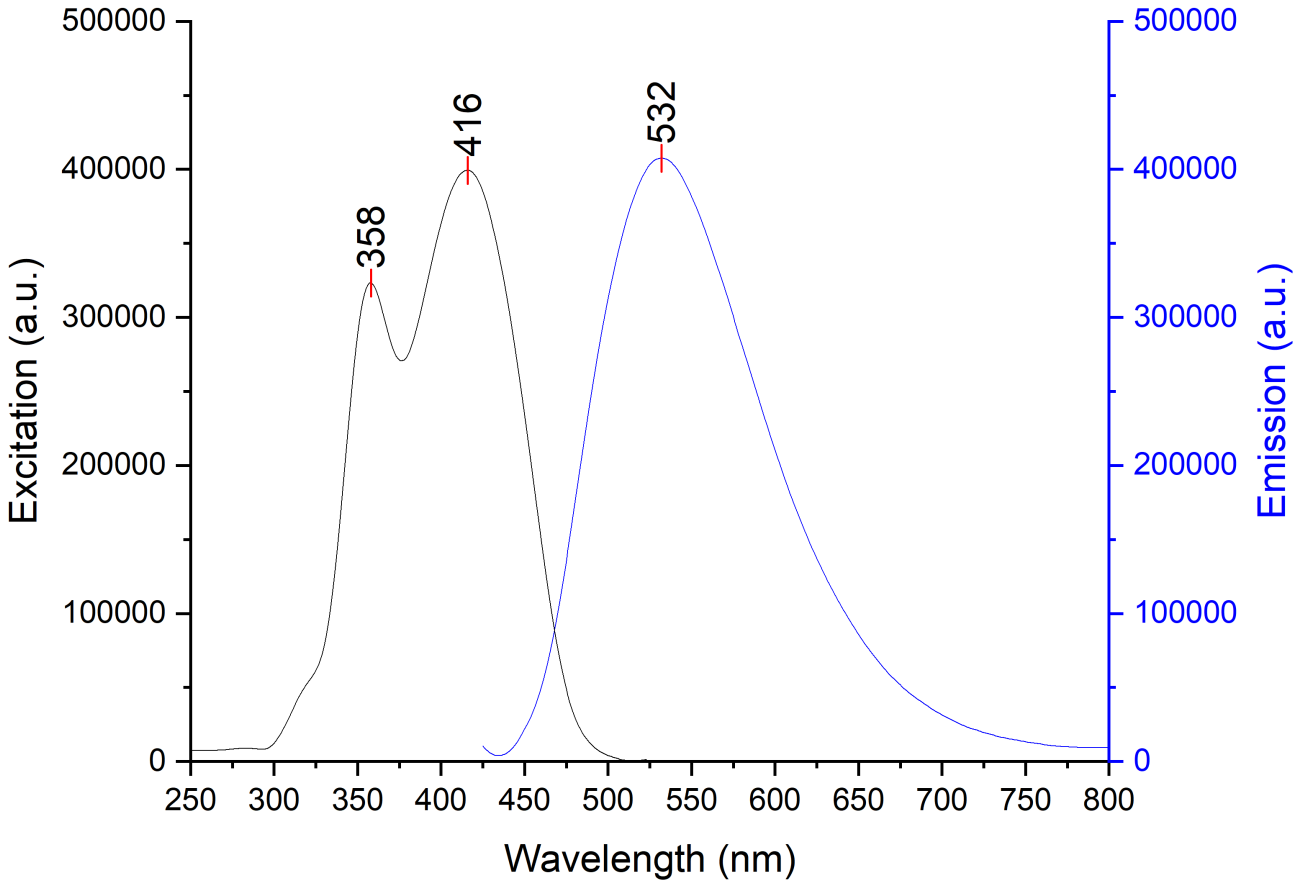

Figure 6-57. Stacked excitation (step: 1.0 nm/s, dwell time: 0.125 s, slit width: 1.0 nm) and emission (step: 1.0 nm/s, dwell time: 0.125 s, slit width: 1.0 nm) spectra of probe 7 and $B(4\text{-}F\text{-}C_6H_4)_3$ in PhCl; 12.5 μM sample.

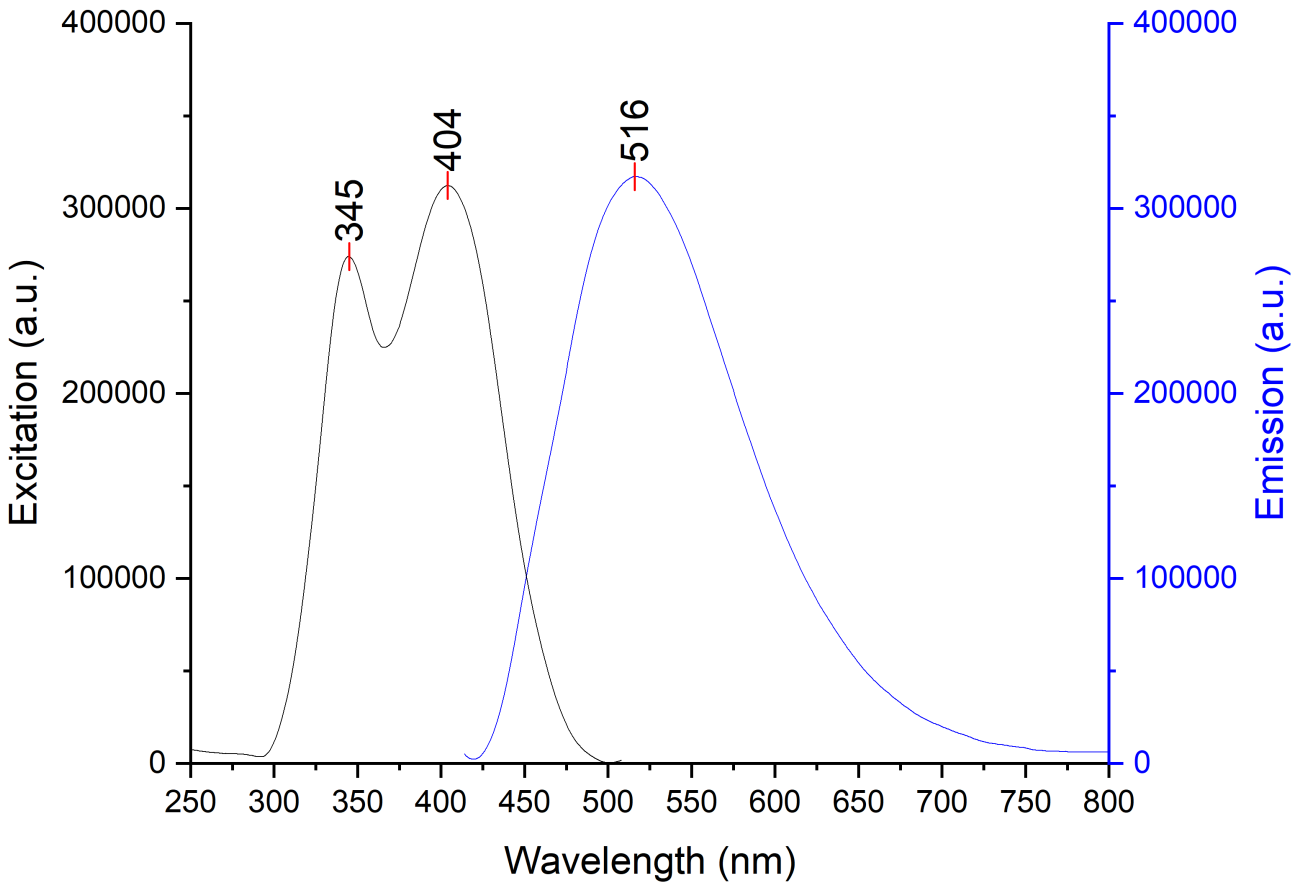

Figure 6-58. Stacked excitation (step: 1.0 nm/s, dwell time: 0.125 s, slit width: 1.0 nm) and emission (step: 1.0 nm/s, dwell time: 0.125 s, slit width: 1.0 nm) spectra of probe 7 and $B(4\text{-}F\text{-}C_6H_4)_3$ in Et_2O; 12.5 μM sample.

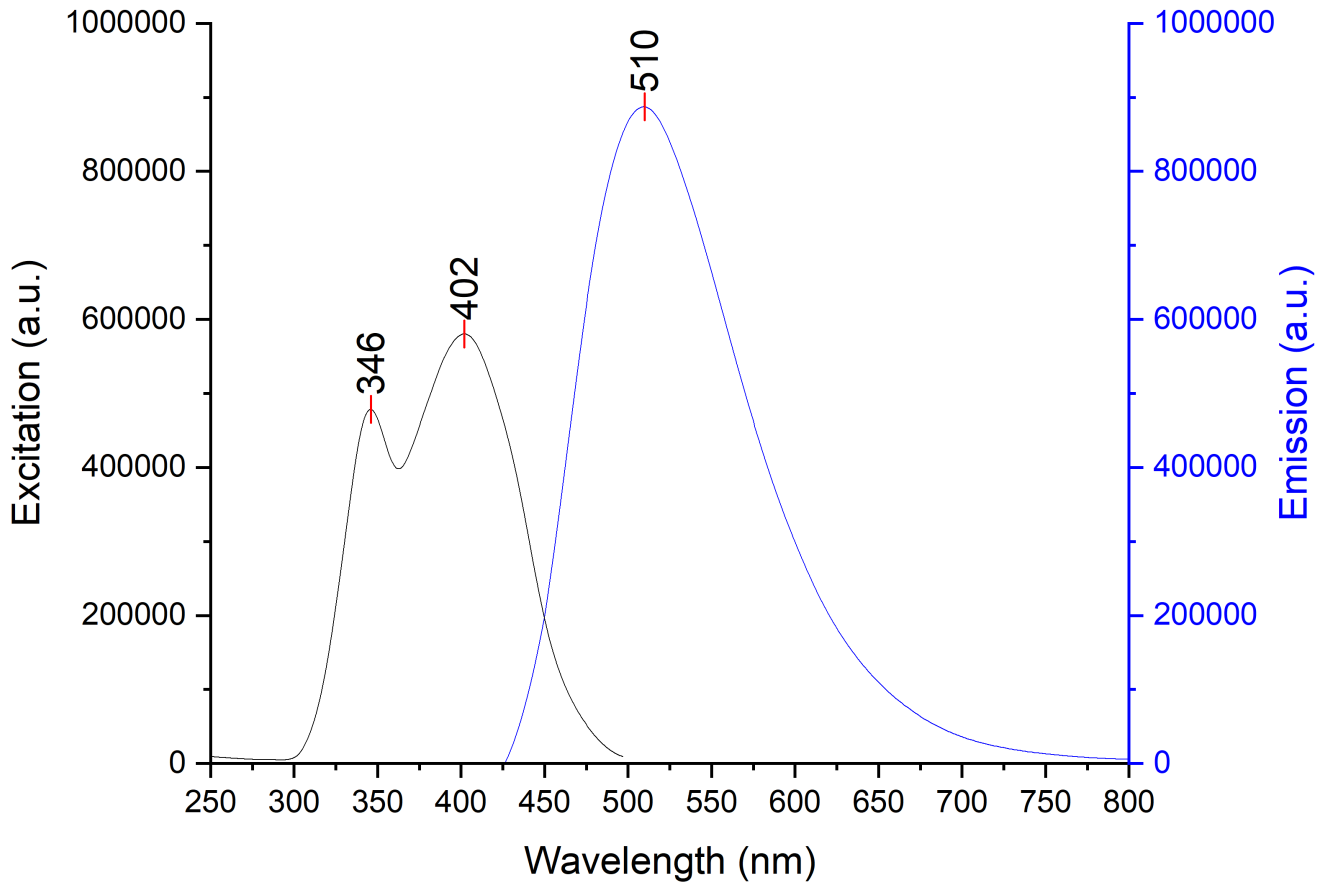

Figure 6-59. Stacked excitation (step: 1.0 nm/s, dwell time: 0.125 s, slit width: 0.70 nm) and emission (step: 1.0 nm/s, dwell time: 0.125 s, slit width: 0.70 nm) spectra of probe 7 and $B(4\text{-}F\text{-}C_6H_4)_3$ in DCM; 12.5 µM sample.

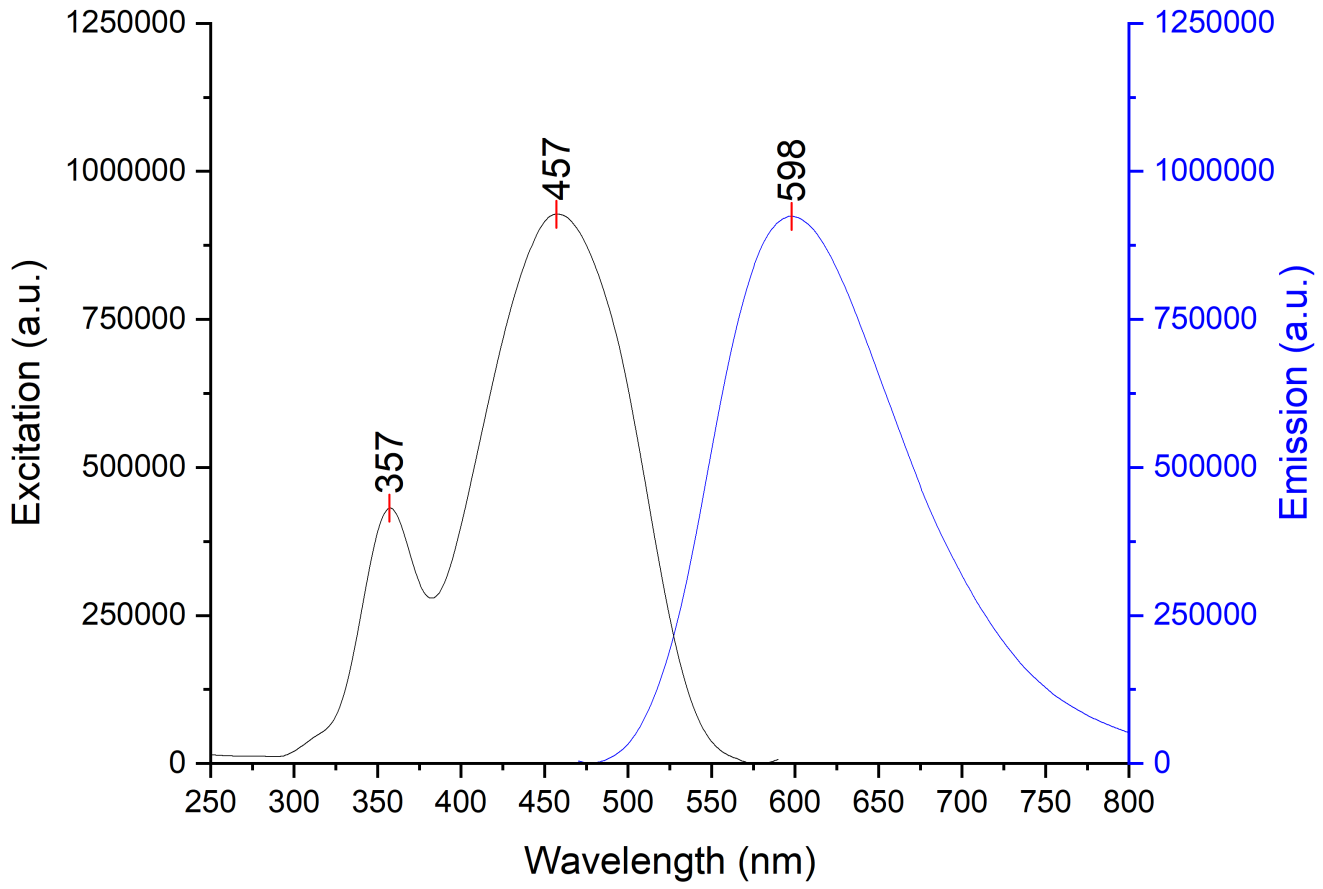

Figure 6-60. Stacked excitation (step: 1.0 nm/s, dwell time: 0.125 s, slit width: 1.0 nm) and emission (step: 1.0 nm/s, dwell time: 0.125 s, slit width: 1.0 nm) spectra of probe 8 and $B(4\text{-}F\text{-}C_6H_4)_3$ in PhCl; 12.5 μM sample.

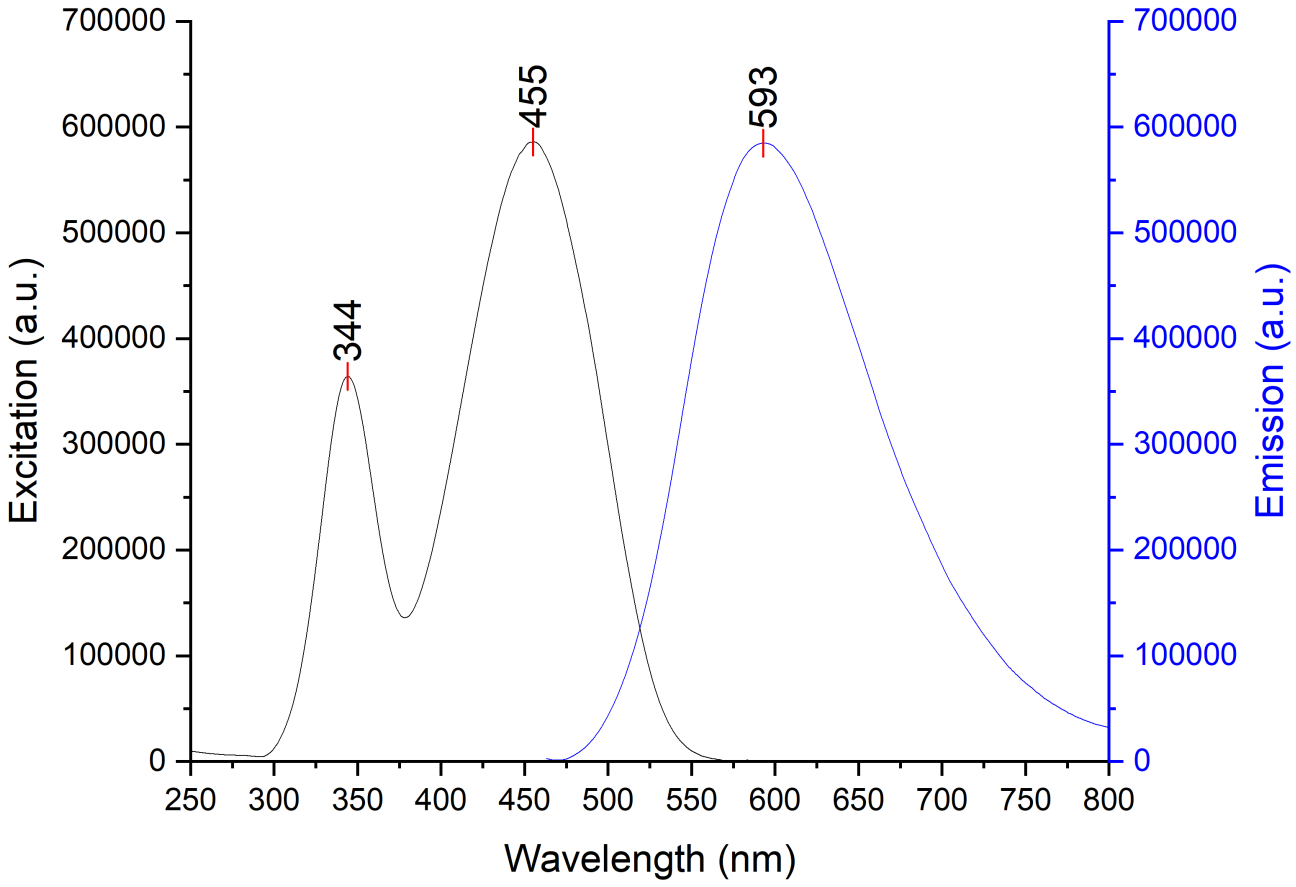

Figure 6-61. Stacked excitation (step: 1.0 nm/s, dwell time: 0.125 s, slit width: 1.0 nm and emission (step: 1.0 nm/s, dwell time: 0.125 s, slit width: 1.0 nm) spectra of probe 8 and $B(4\text{-}F\text{-}C_6H_4)_3$ in Et_2O; 12.5 µM sample.

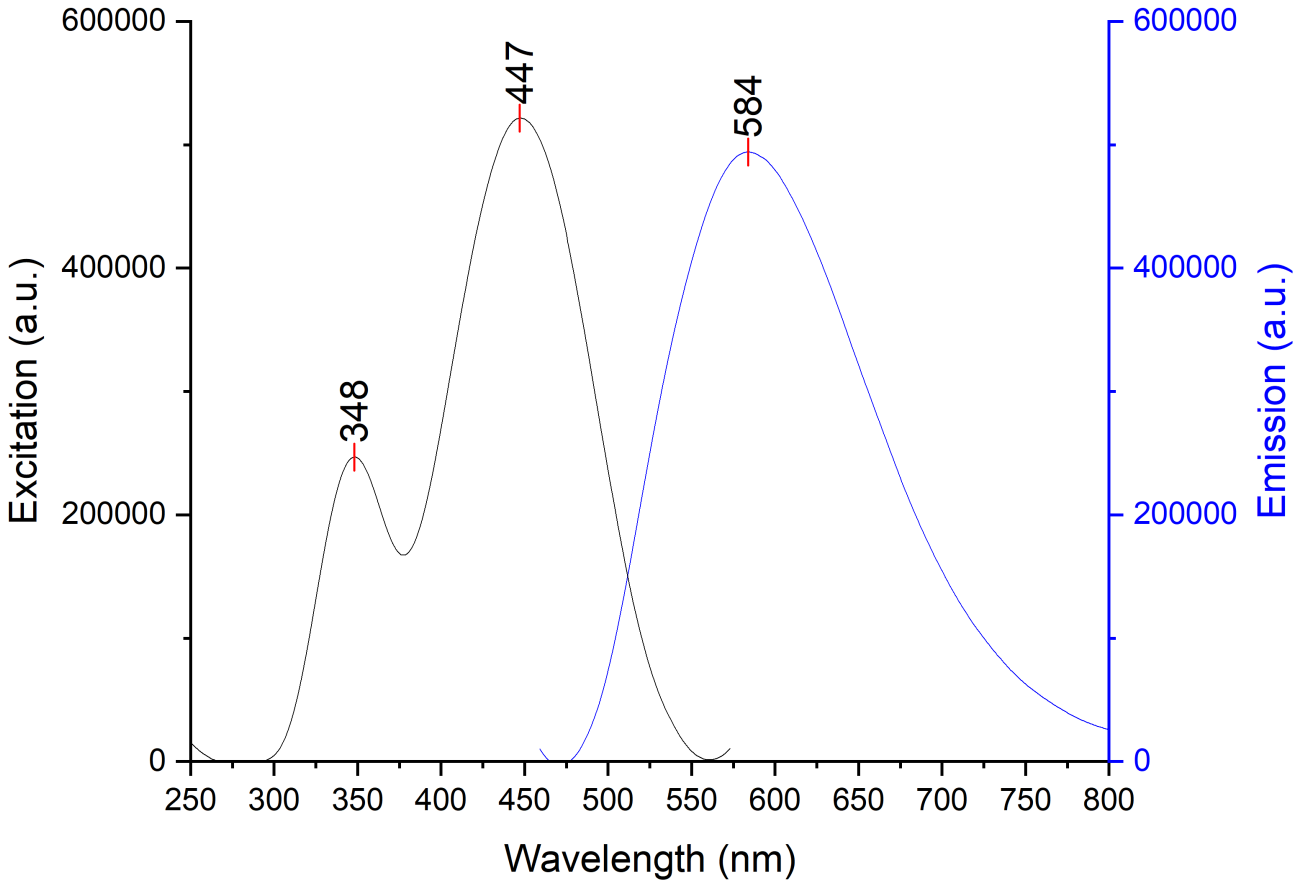

Figure 6-62. Stacked excitation (step: 1.0 nm/s, dwell time: 0.125 s, slit width: 0.70 nm) and emission (step: 1.0 nm/s, dwell time: 0.125 s, slit width: 0.70 nm) spectra of probe 8 and $B(4\text{-}F\text{-}C_6H_4)_3$ in DCM; 12.5 µM sample.

6.2.3.3. $B(3,4\text{-}F_2\text{-}C_6H_3)_3$

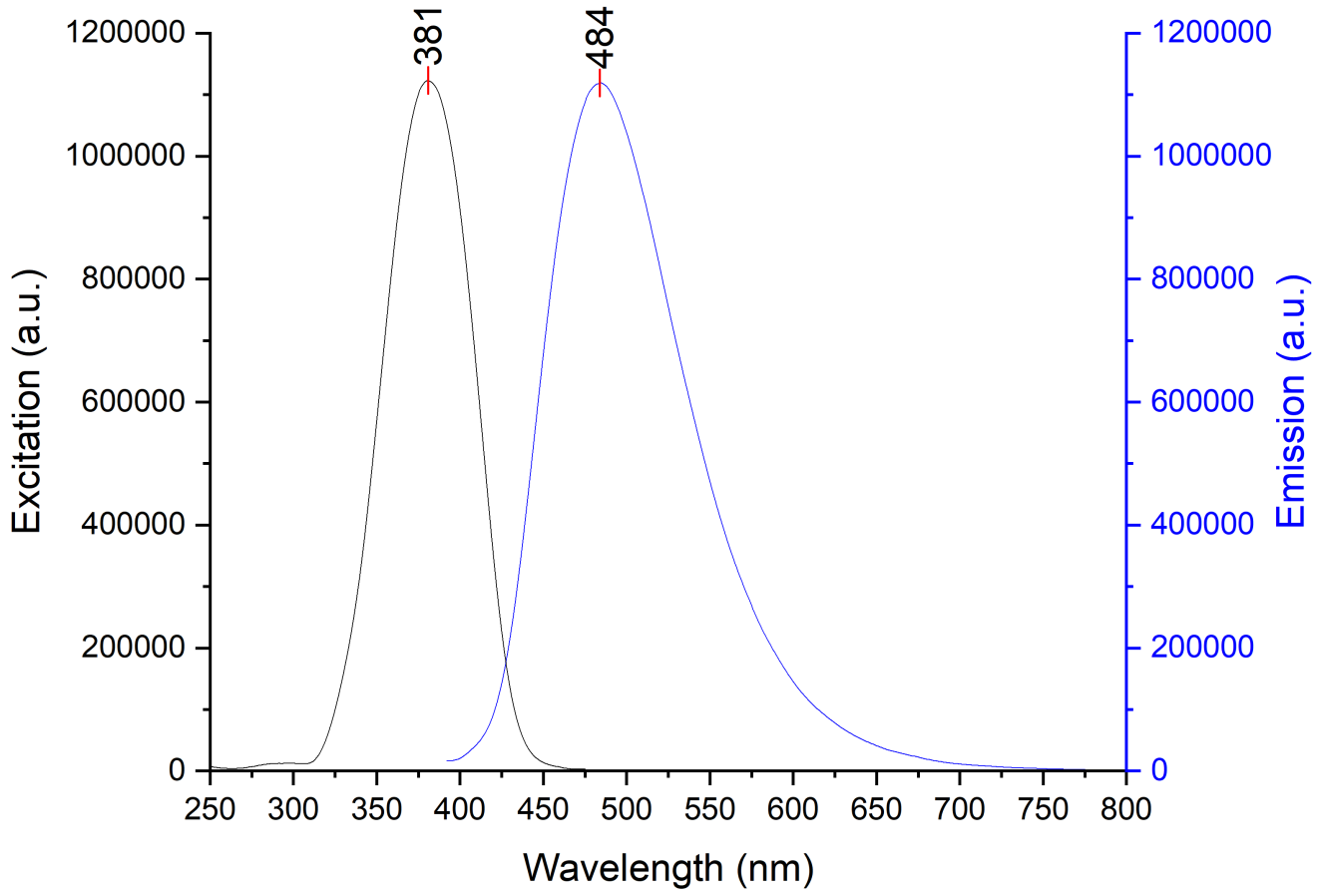

Figure 6-63. Stacked excitation (step: 1.0 nm/s, dwell time: 0.125 s, slit width: 1.0 nm) and emission (step: 1.0 nm/s, dwell time: 0.125 s, slit width: 1.0 nm spectra of probe 1 and $B(3,4\text{-}F_2\text{-}C_6H_3)_3$ in PhCl; 12.5 μM sample.

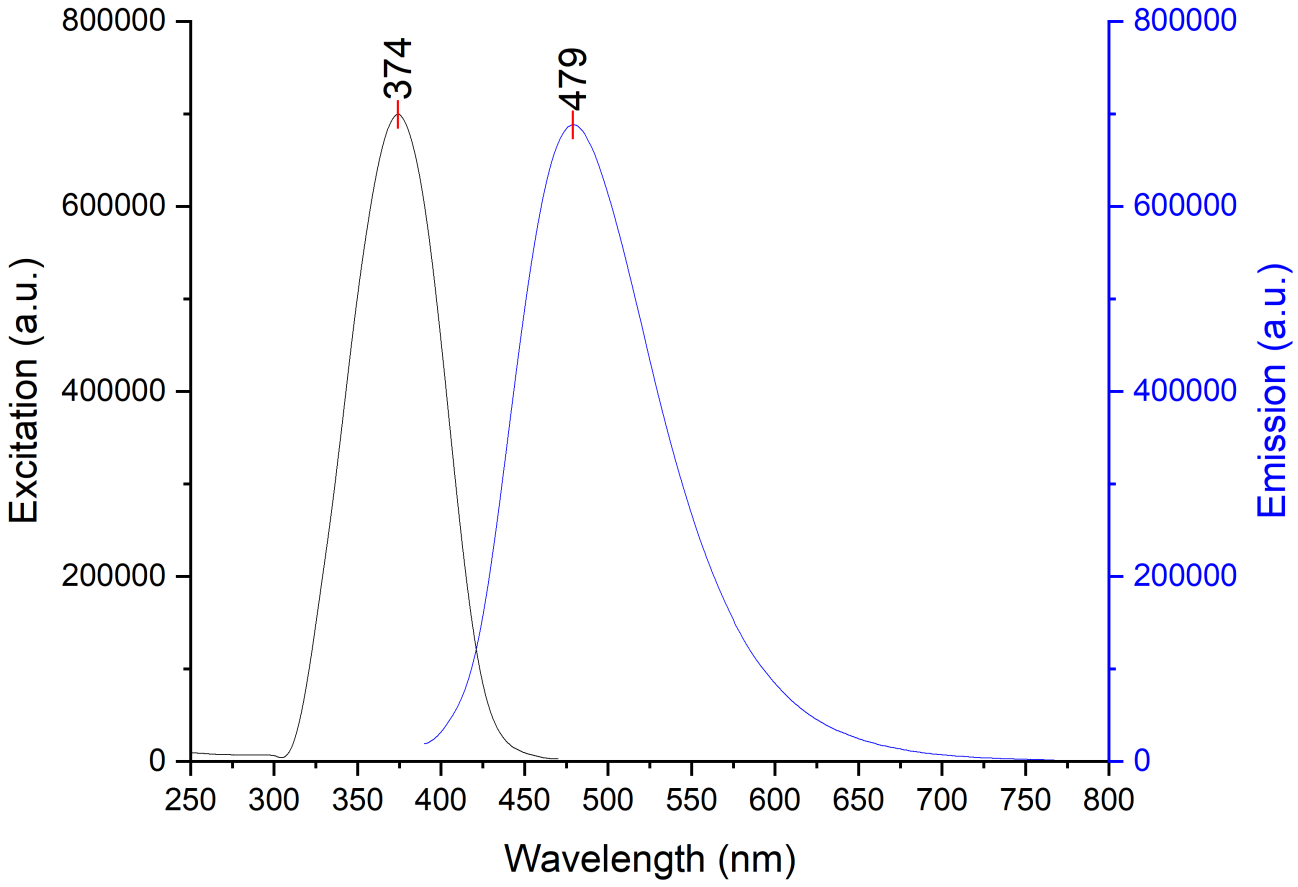

Figure 6-64. Stacked excitation (step: 1.0 nm/s, dwell time: 0.125 s, slit width: 1.0 nm) and emission (step: 1.0 nm/s, dwell time: 0.125 s, slit width: 1.0 nm) spectra of probe 1 and $B(3,4\text{-}F_2\text{-}C_6H_3)_3$ in Et_2O; 12.5 μM sample.

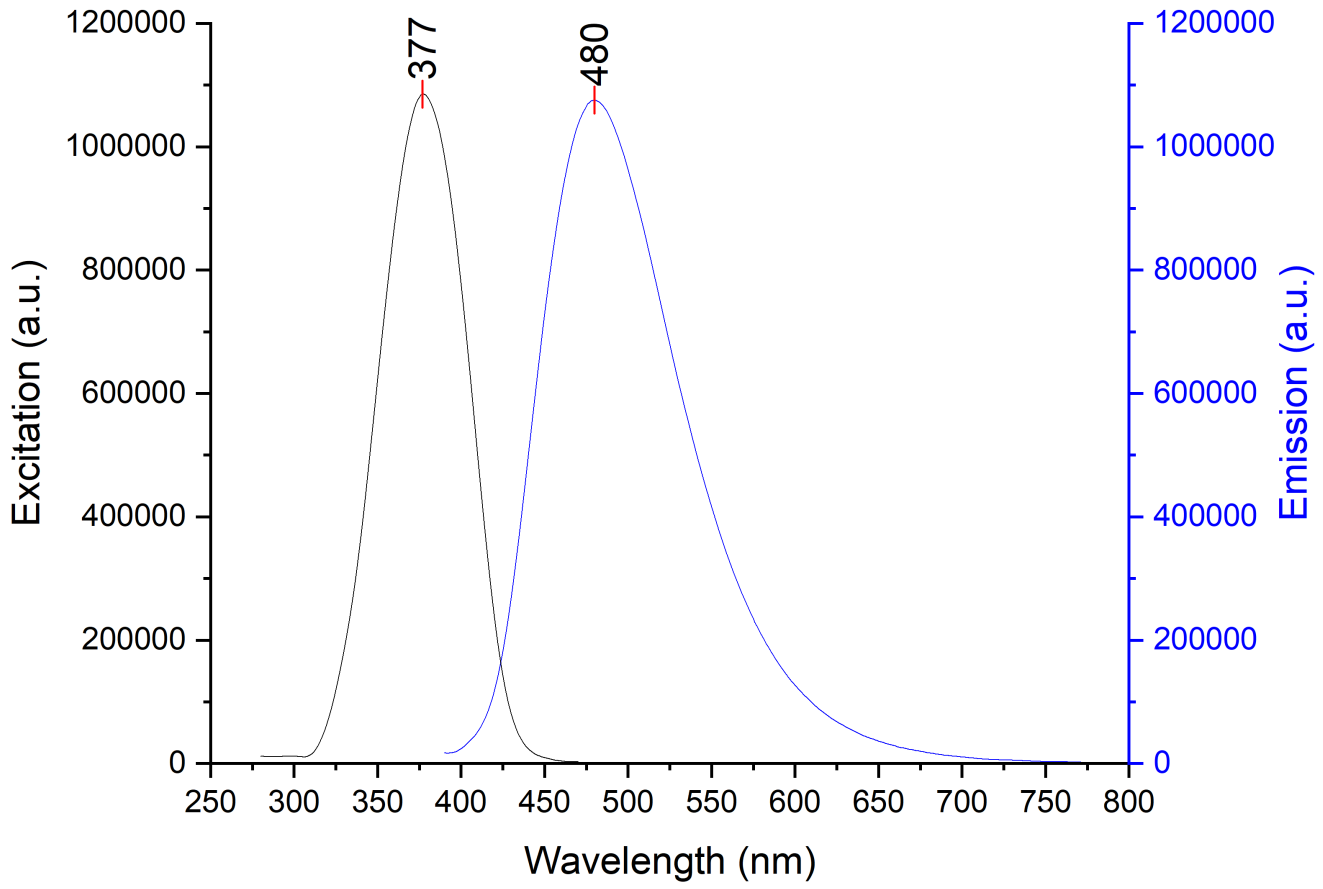

Figure 6-65. Stacked excitation (step: 1.0 nm/s, dwell time: 0.125 s, slit width: 0.80 nm) and emission (step: 1.0 nm/s, dwell time: 0.125 s, slit width: 0.80 nm) spectra of probe 1 and $B(3,4\text{-}F_2\text{-}C_6H_3)_3$ in DCM; 12.5 µM sample.

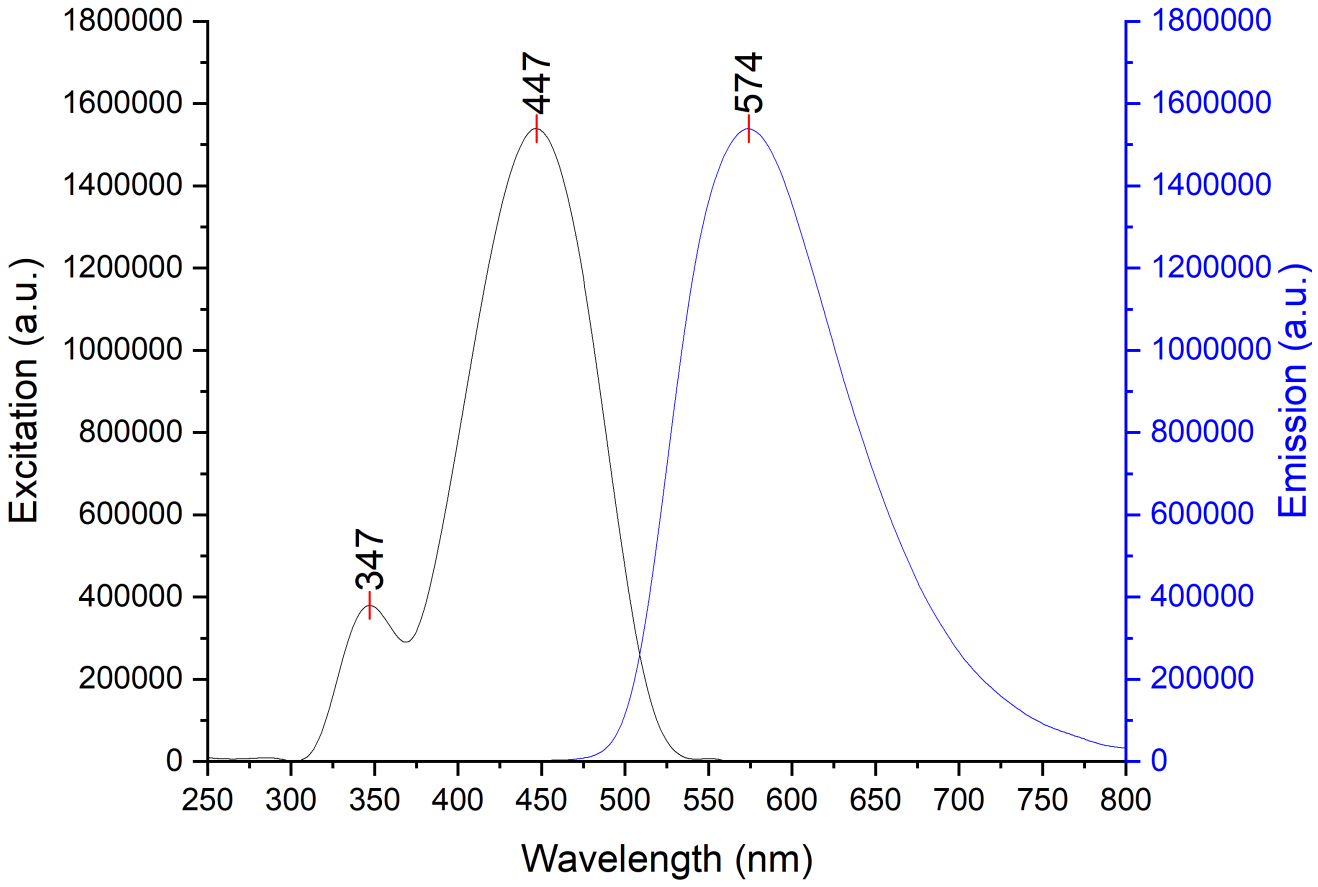

Figure 6-66. Stacked excitation (step: 1.0 nm/s, dwell time: 0.125 s, slit width: 1.0 nm) and emission (step: 1.0 nm/s, dwell time: 0.125 s, slit width: 1.0 nm) spectra of probe 2 and $B(3,4\text{-}F_2\text{-}C_6H_3)_3$ in PhCl; 12.5 μM sample.

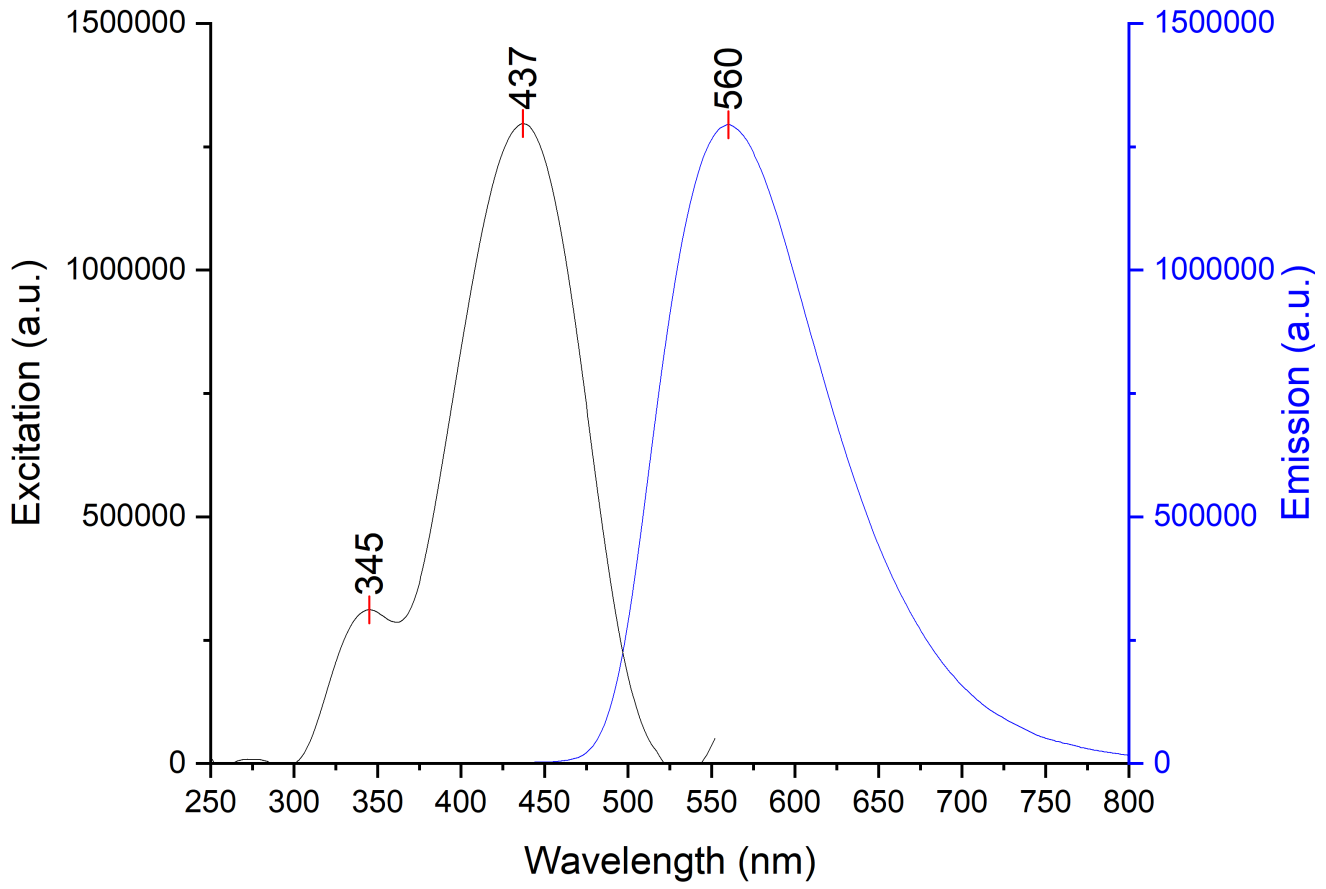

Figure 6-67. Stacked excitation (step: 1.0 nm/s, dwell time: 0.125 s, slit width: 0.80 nm) and emission (step: 1.0 nm/s, dwell time: 0.125 s, slit width: 0.80 nm) spectra of probe 2 and $B(3,4\text{-}F_2\text{-}C_6H_3)_3$ in Et_2O; 12.5 µM sample.

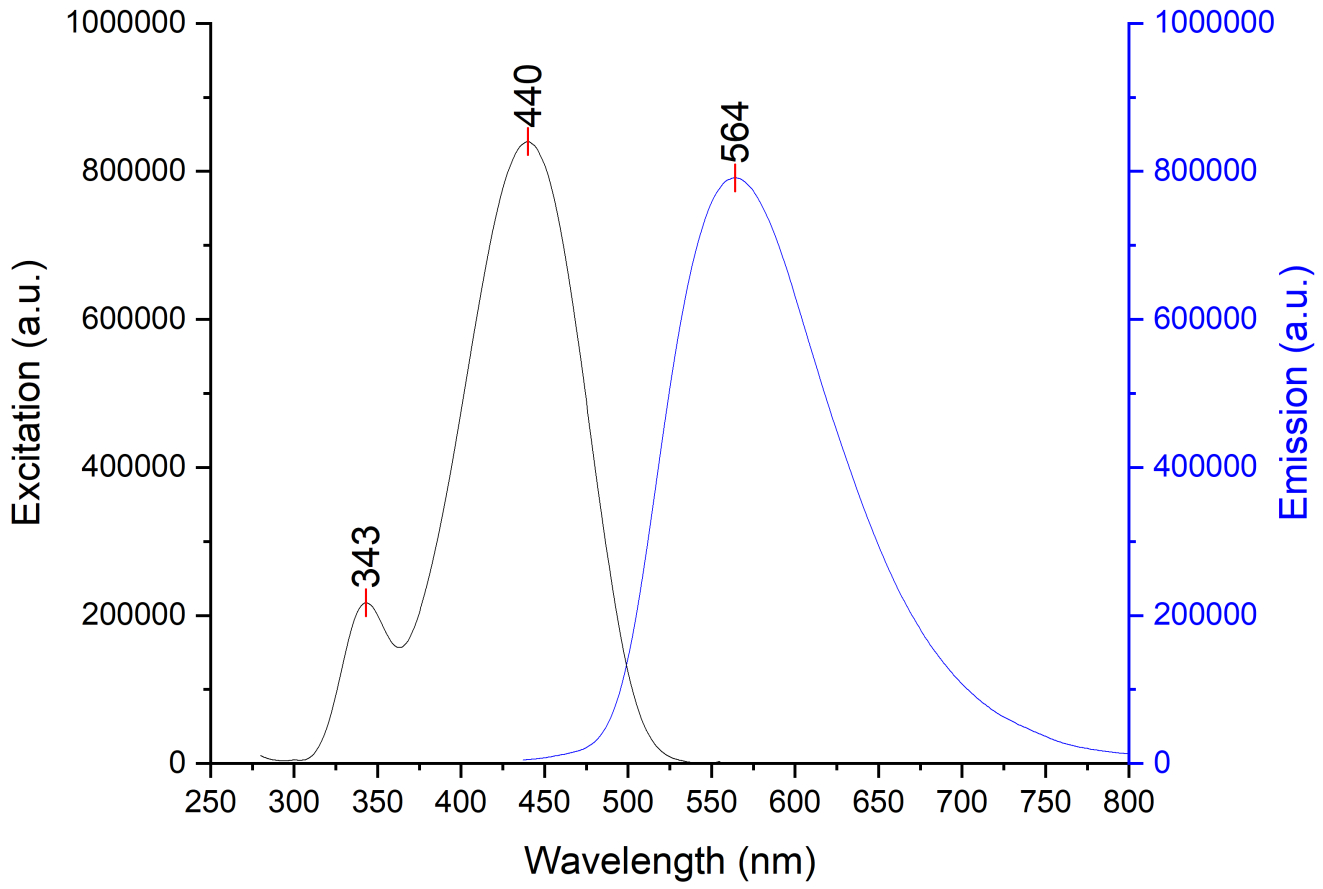

Figure 6-68. Stacked excitation (step: 1.0 nm/s, dwell time: 0.125 s, slit width: 1.0 nm) and emission (step: 1.0 nm/s, dwell time: 0.125 s, slit width: 1.0 nm) spectra of probe 2 and $B(3,4\text{-}F_2\text{-}C_6H_3)_3$ in DCM; 12.5 µM sample.

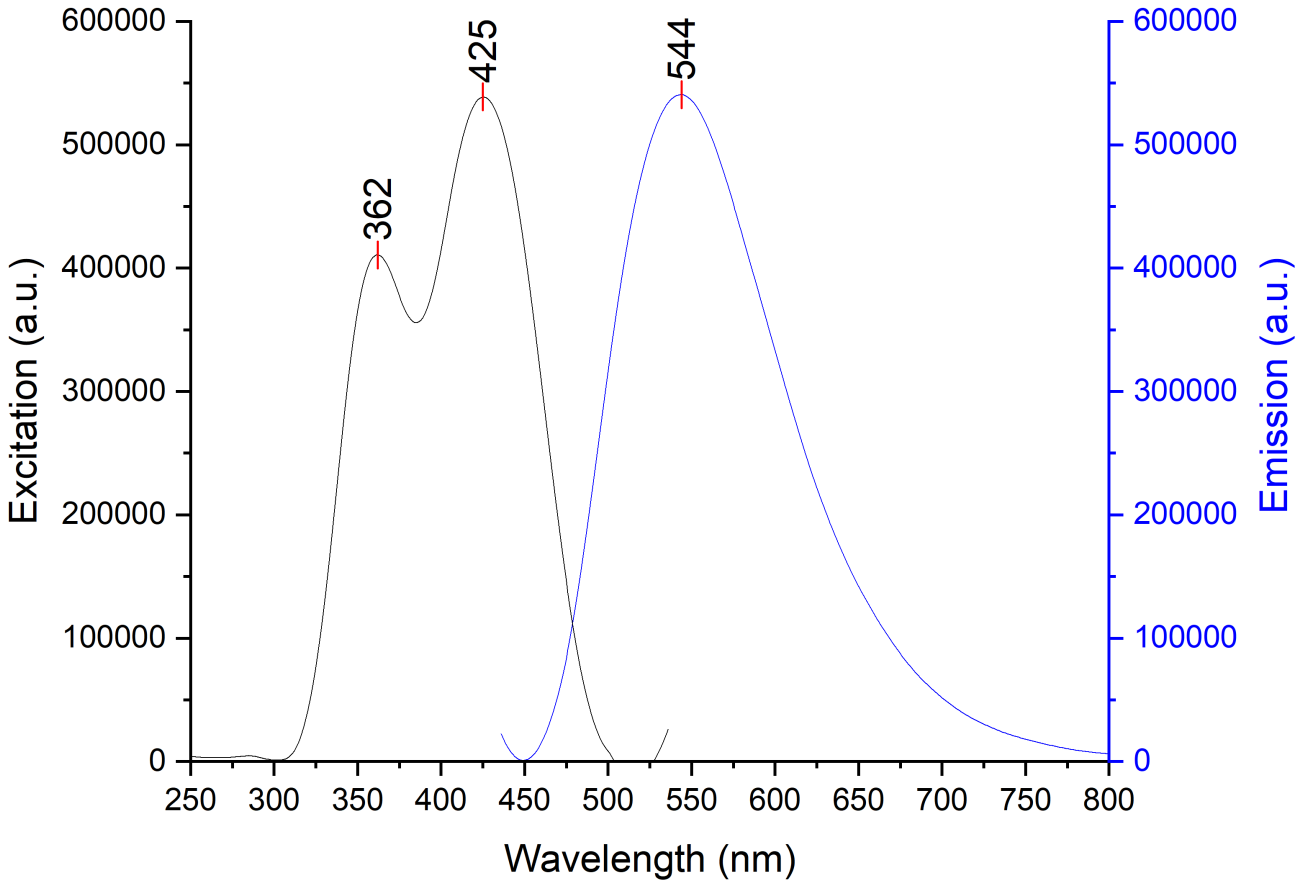

Figure 6-69. Stacked excitation (step: 1.0 nm/s, dwell time: 0.125 s, slit width: 1.0 nm) and emission (step: 1.0 nm/s, dwell time: 0.125 s, slit width: 1.0 nm) spectra of probe 7 and $B(3,4\text{-}F_2\text{-}C_6H_3)_3$ in PhCl; 12.5 μM sample.

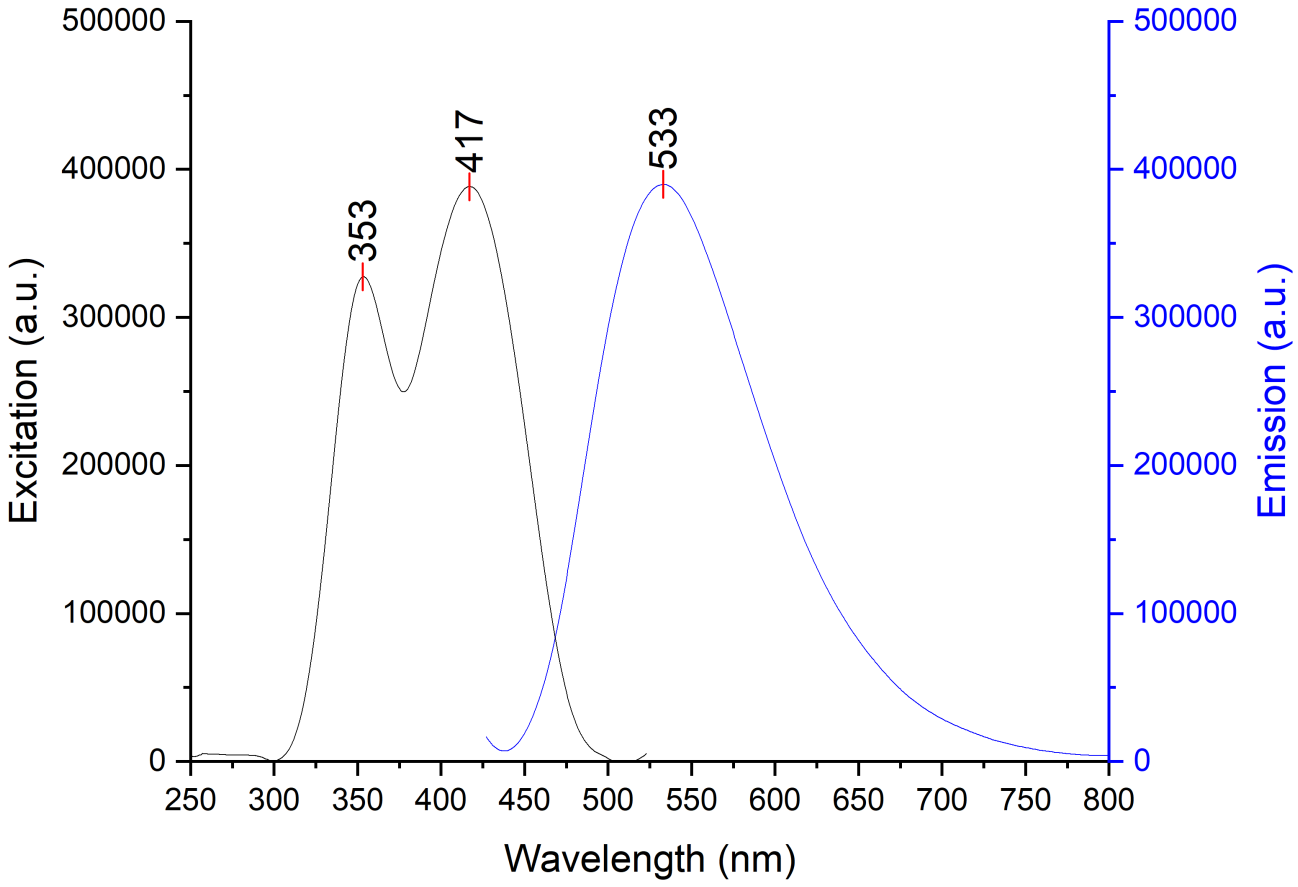

Figure 6-70. Stacked excitation (step: 1.0 nm/s, dwell time: 0.125 s, slit width: 1.0 nm) and emission (step: 1.0 nm/s, dwell time: 0.125 s, slit width: 1.0 nm) spectra of probe 7 and $B(3,4\text{-}F_2\text{-}C_6H_3)_3$ in Et_2O; 12.5 µM sample.

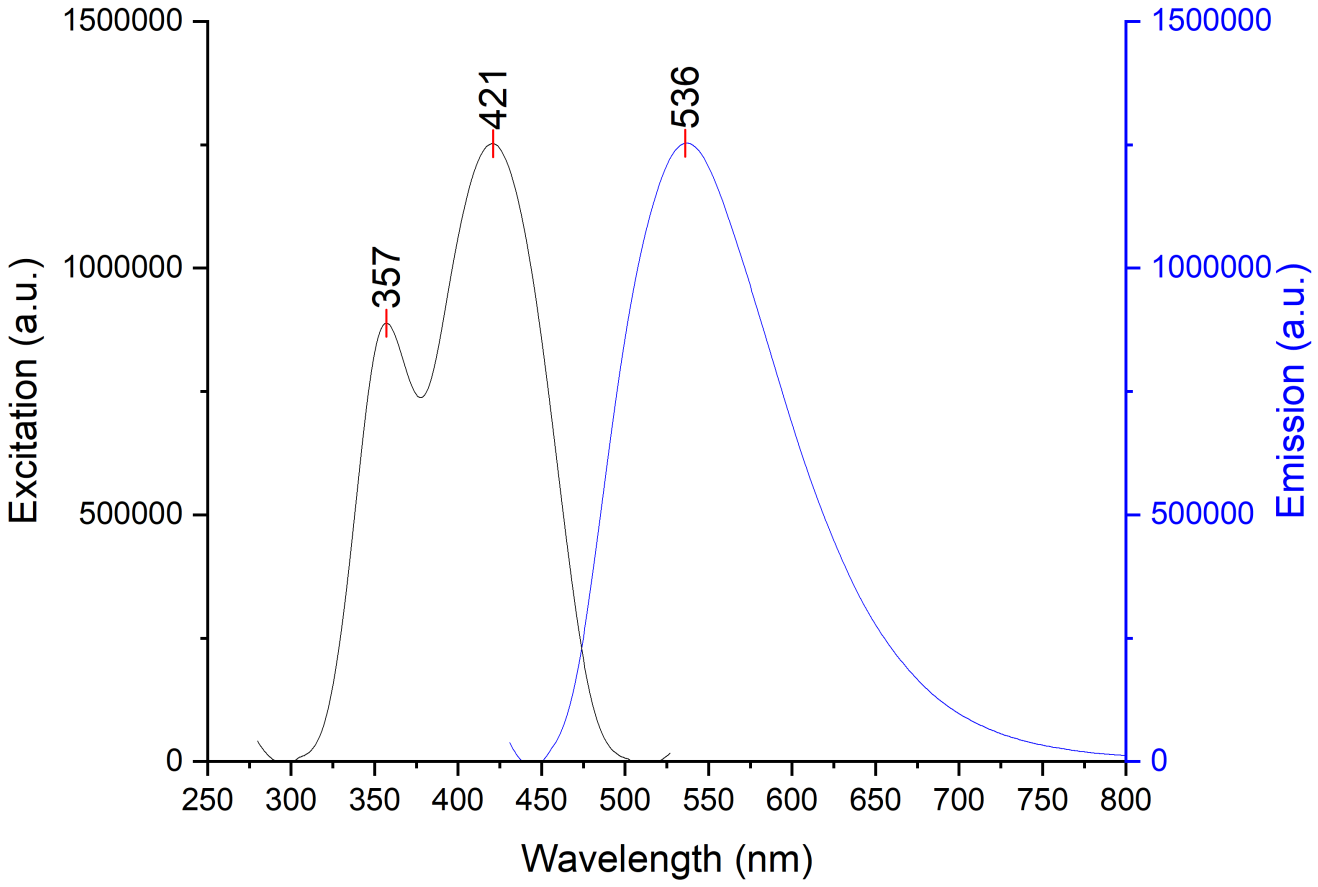

Figure 6-71. Stacked excitation (step: 1.0 nm/s, dwell time: 0.125 s, slit width: 0.80 nm) and emission (step: 1.0 nm/s, dwell time: 0.125 s, slit width: 0.80 nm) spectra of probe 7 and $B(3,4\text{-}F_2\text{-}C_6H_3)_3$ in DCM; 12.5 µM sample.

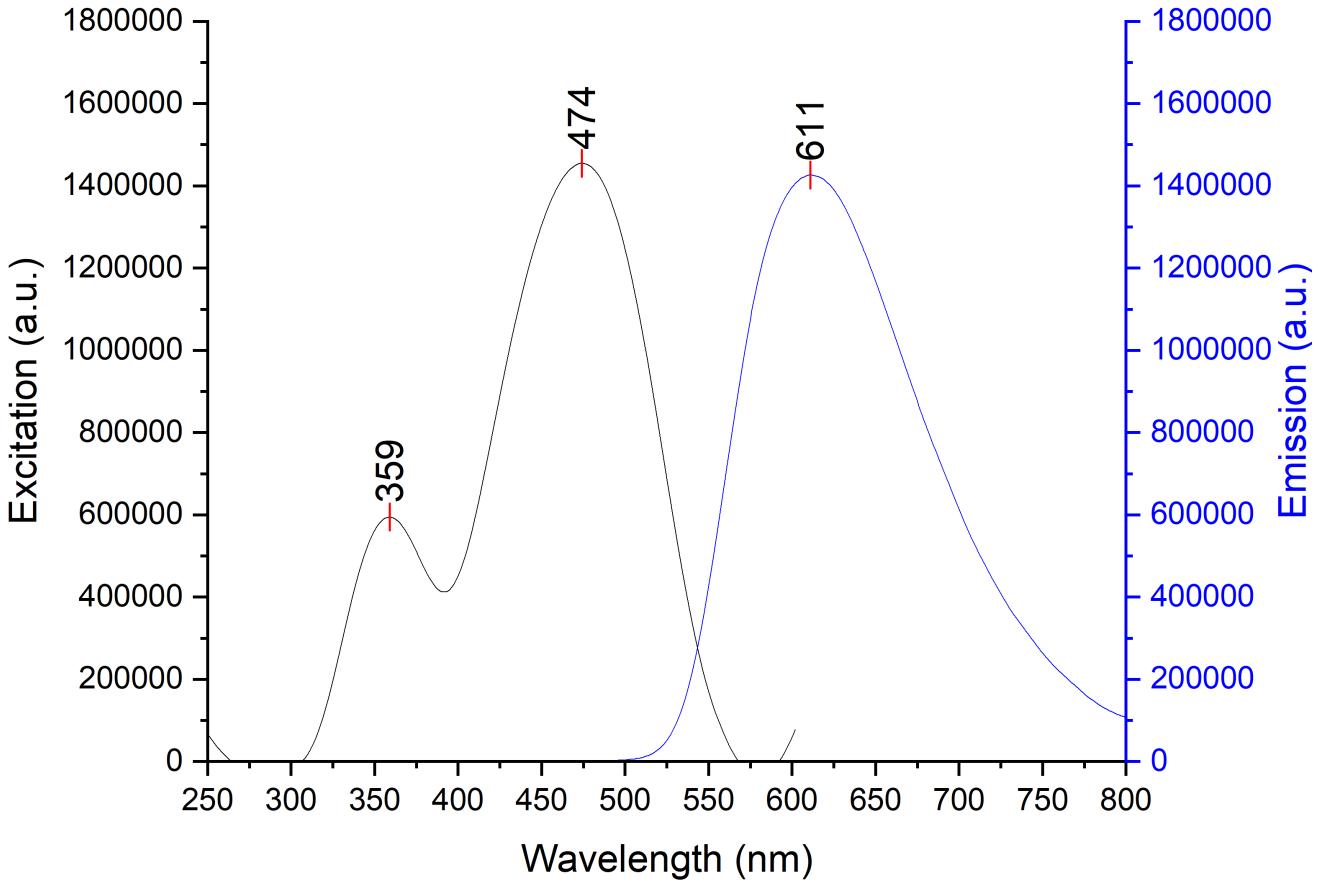

Figure 6-72. Stacked excitation (step: 1.0 nm/s, dwell time: 0.125 s, slit width: 1.0 nm) and emission (step: 1.0 nm/s, dwell time: 0.125 s, slit width: 1.0 nm) spectra of probe 8 and $B(3,4\text{-}F_2\text{-}C_6H_3)_3$ in PhCl; 12.5 μM sample.

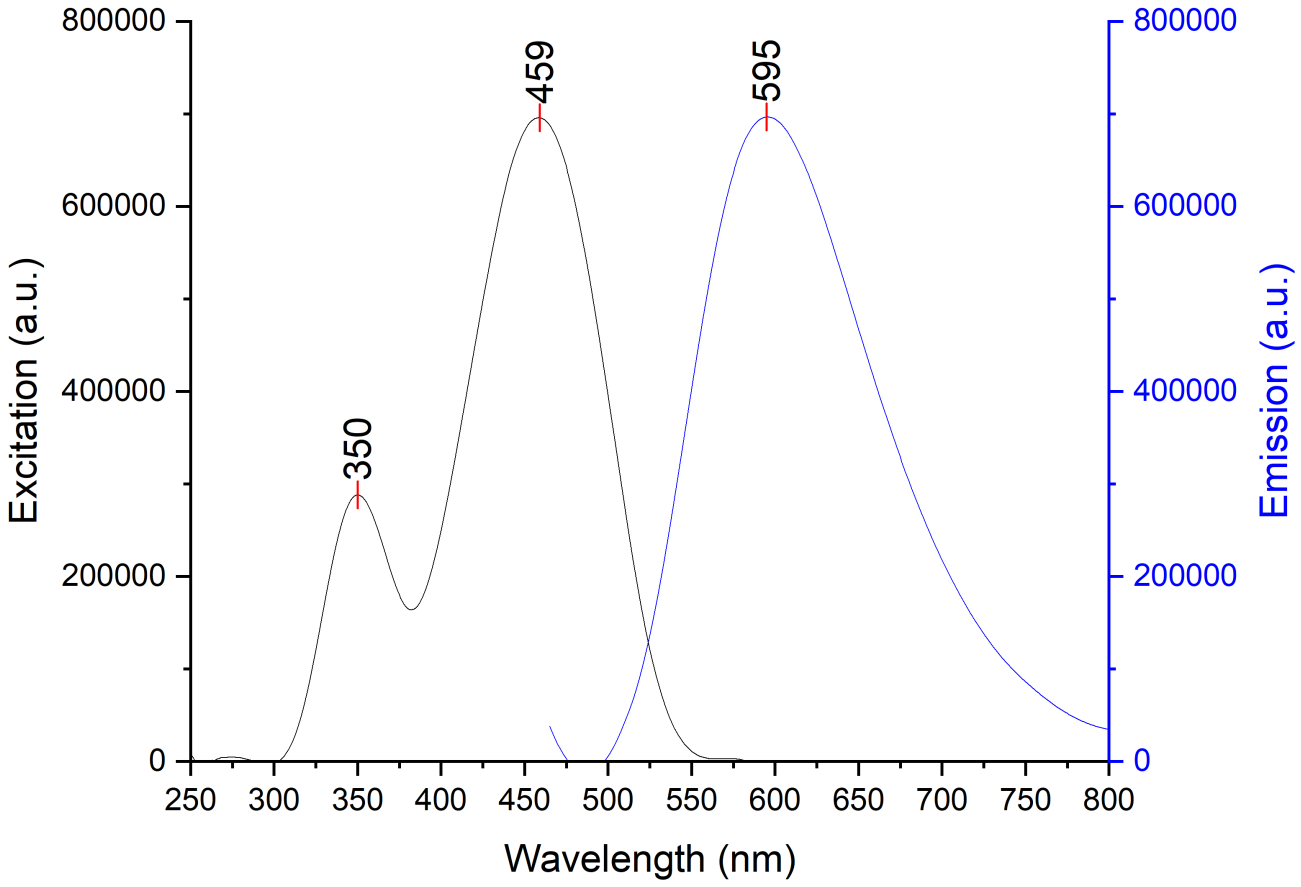

Figure 6-73. Stacked excitation (step: 1.0 nm/s, dwell time: 0.125 s, slit width: 1.0 nm) and emission (step: 1.0 nm/s, dwell time: 0.125 s, slit width: 1.0 nm) spectra of probe 8 and $B(3,4\text{-}F_2\text{-}C_6H_3)_3$ in Et_2O; 12.5 µM sample.

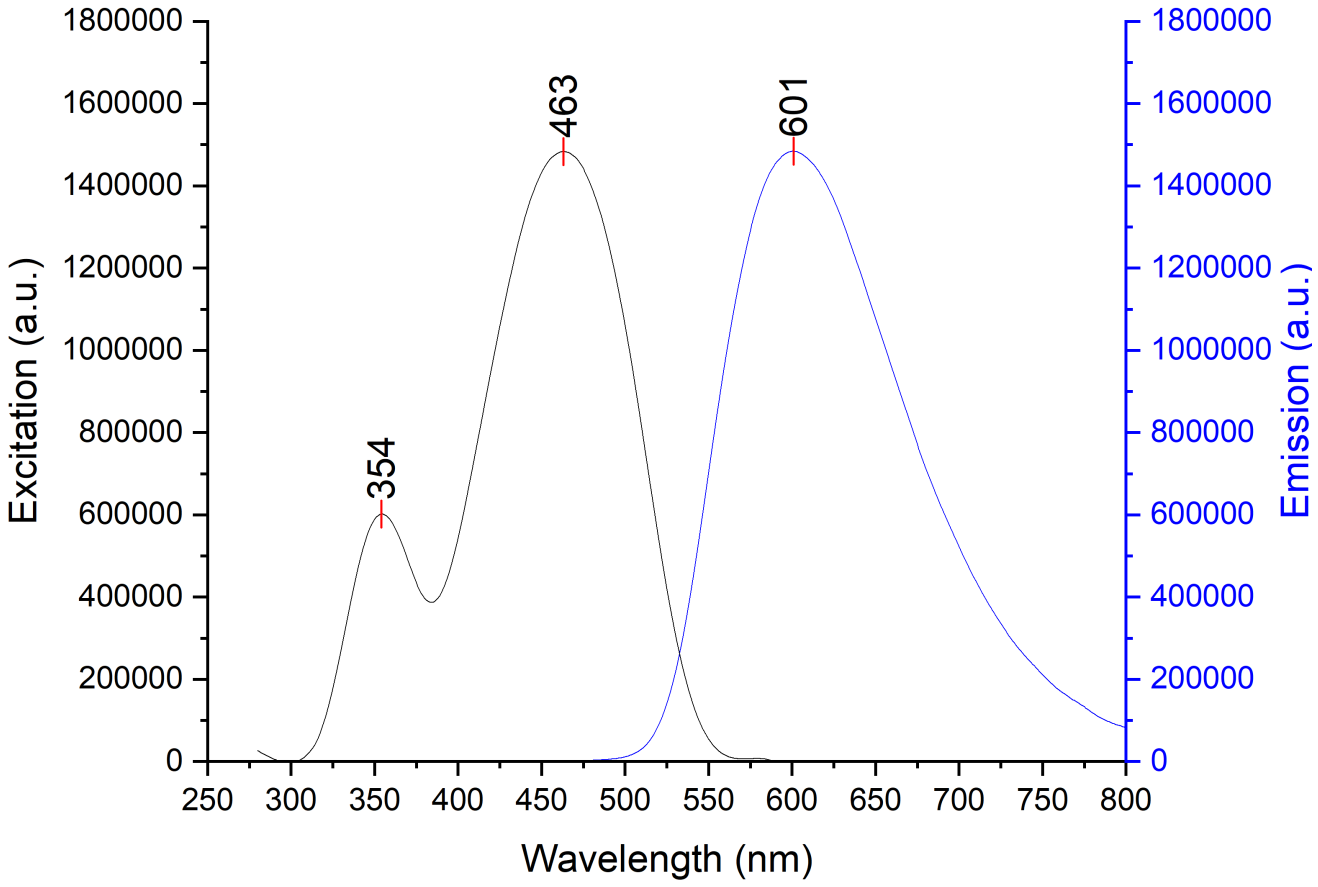

Figure 6-74. Stacked excitation (step: 1.0 nm/s, dwell time: 0.125 s, slit width: 1.0 nm) and emission (step: 1.0 nm/s, dwell time: 0.125 s, slit width: 1.0 nm) spectra of probe 8 and $B(3,4\text{-}F_2\text{-}C_6H_3)_3$ in DCM; 12.5 µM sample.

6.2.3.4. $B(2,4,6\text{-}F_3\text{-}C_6H_2)_3$

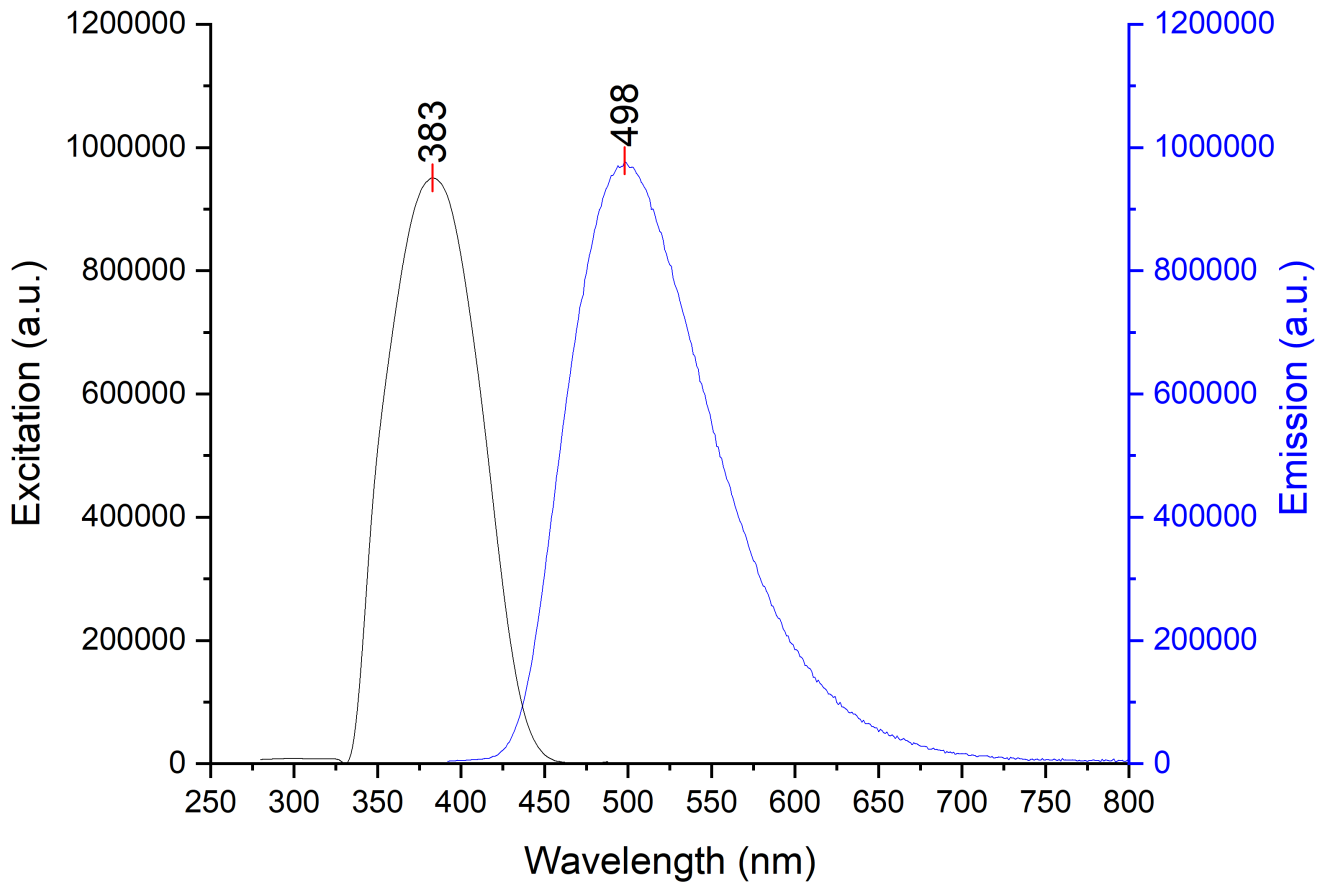

Figure 6-75. Stacked excitation (step: 1.0 nm/s, dwell time: 0.125 s, slit width: 0.80 nm) and emission (step: 1.0 nm/s, dwell time: 0.125 s, slit width: 0.80 nm) spectra of probe 1 and $B(2,4,6\text{-}F_3\text{-}C_6H_2)_3$ in PhCl; 12.5 μM sample.

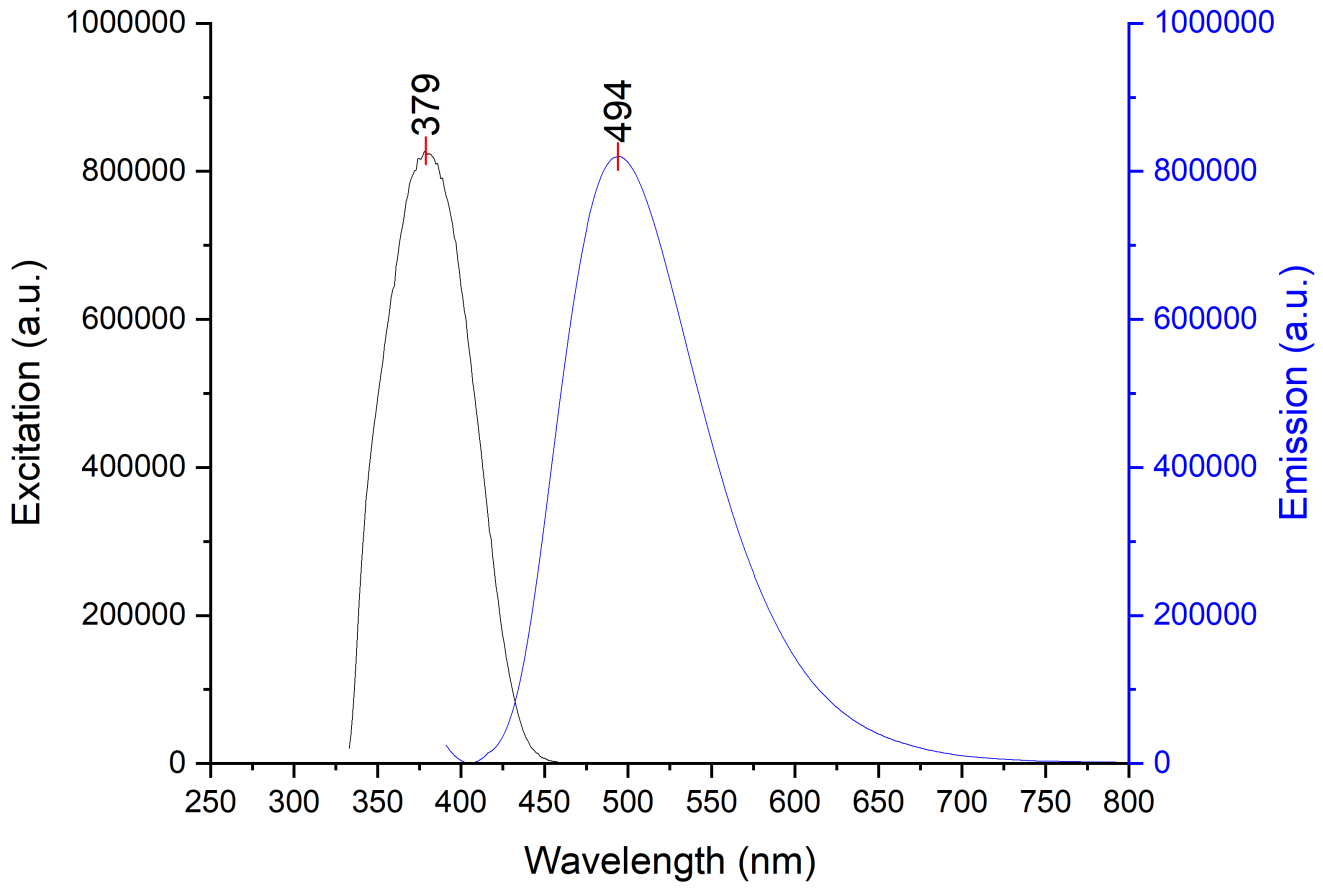

Figure 6-76. Stacked excitation (step: 1.0 nm/s, dwell time: 0.125 s, slit width: 1.0 nm) and emission (step: 1.0 nm/s, dwell time: 0.125 s, slit width: 1.0 nm) spectra of probe 1 and $B(2,4,6\text{-}F_3\text{-}C_6H_2)_3$ in Et_2O; 12.5 μM sample.

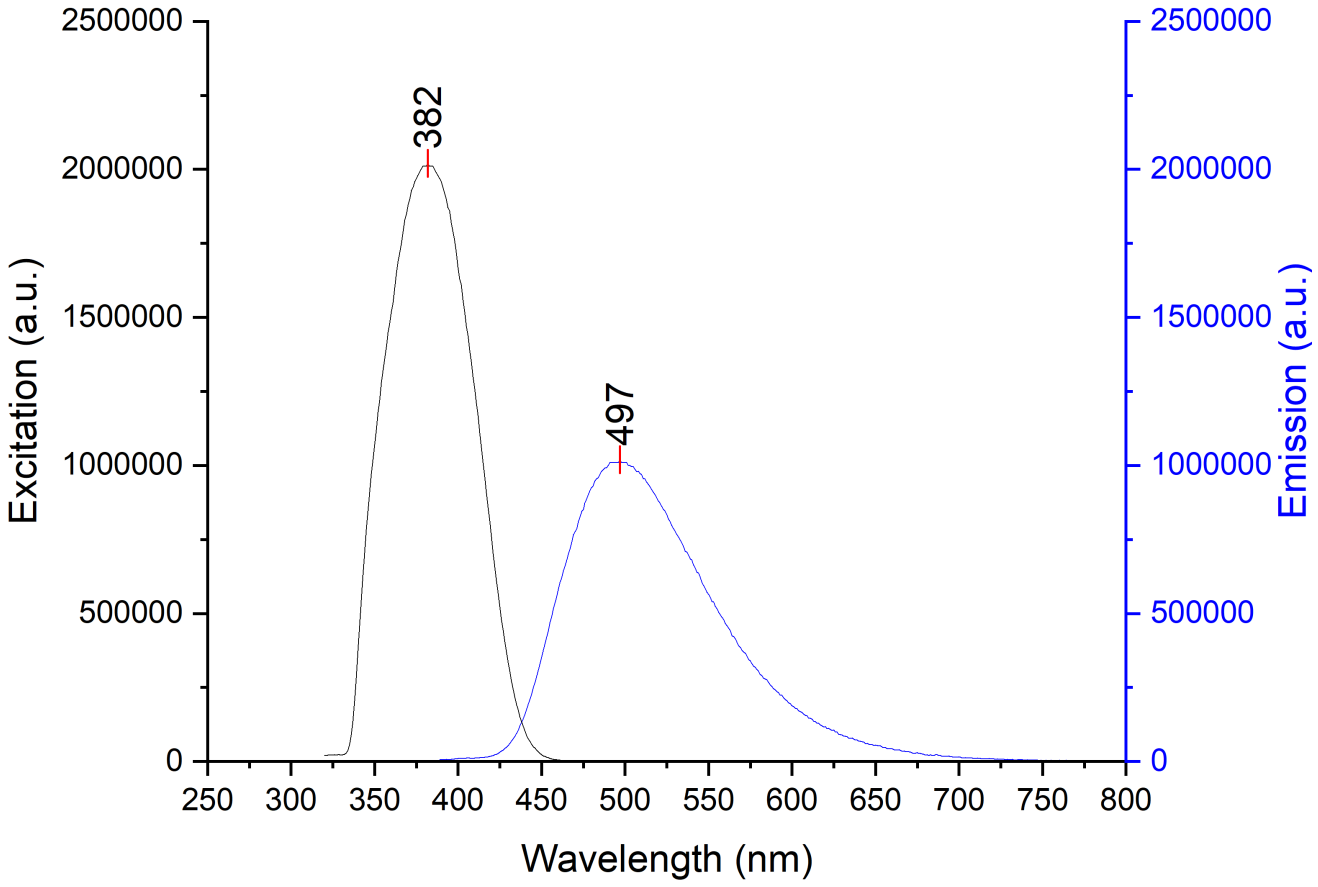

Figure 6-77. Stacked excitation (step: 1.0 nm/s, dwell time: 0.125 s, slit width: 1.0 nm) and emission (step: 1.0 nm/s, dwell time: 0.125 s, slit width: 1.0 nm) spectra of probe 1 and $B(2,4,6\text{-}F_3\text{-}C_6H_2)_3$ in DCM; 12.5 μM sample.

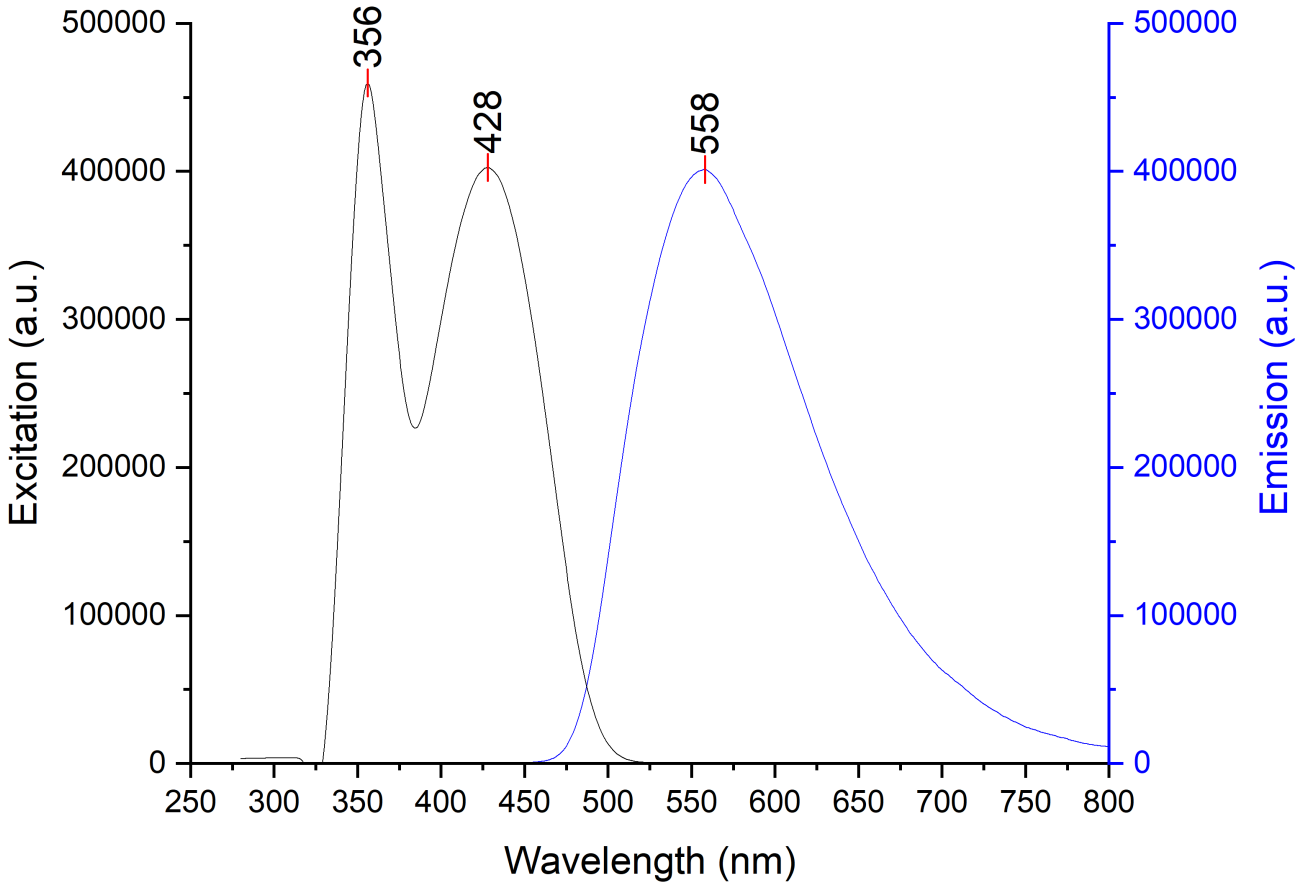

Figure 6-78. Stacked excitation (step: 1.0 nm/s, dwell time: 0.125 s, slit width: 0.80 nm) and emission (step: 1.0 nm/s, dwell time: 0.125 s, slit width: 0.80 nm) spectra of probe 2 and $B(2,4,6\text{-}F_3\text{-}C_6H_2)_3$ in PhCl; 12.5 μM sample.

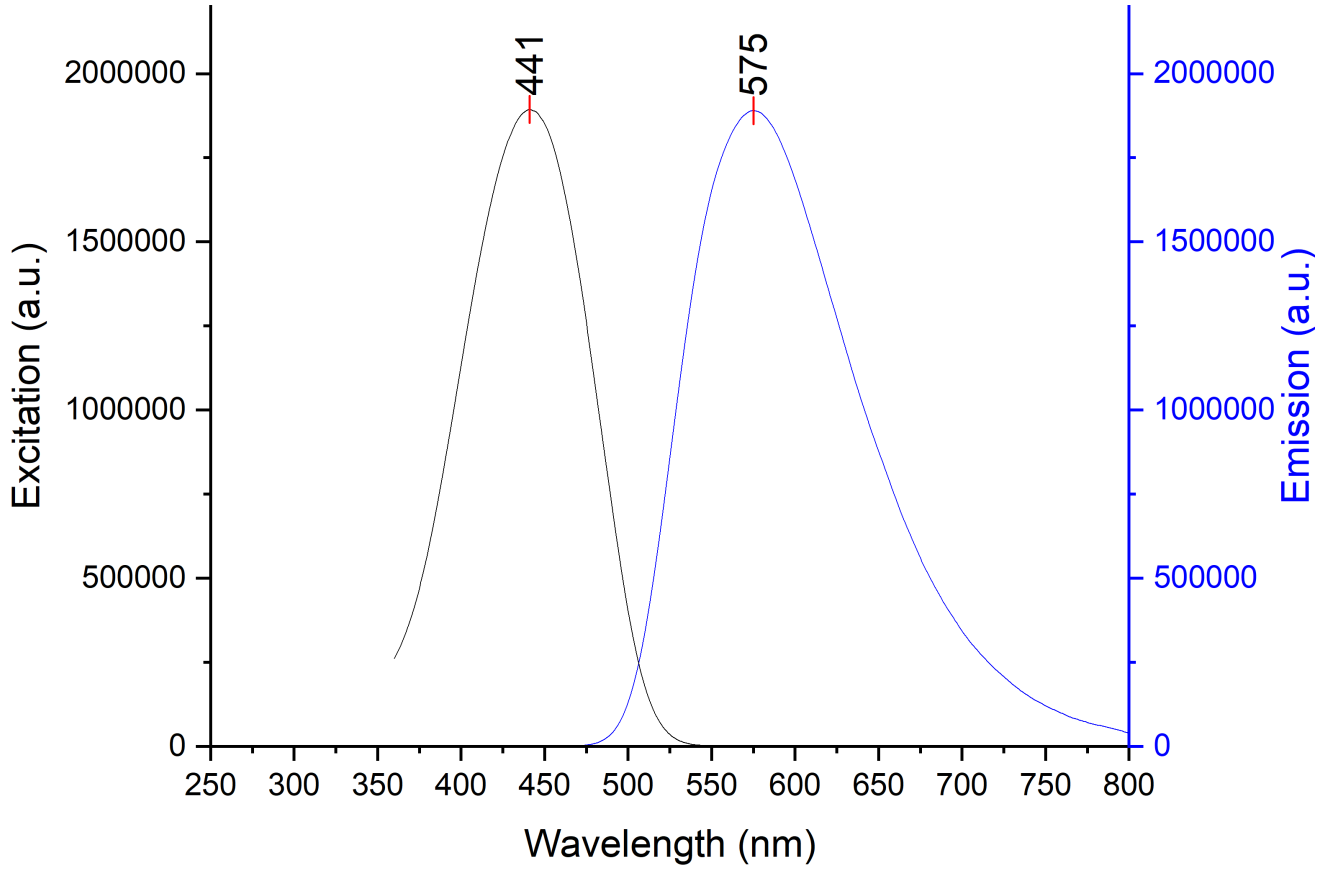

Figure 6-79. Stacked excitation (step: 1.0 nm/s, dwell time: 0.125 s, slit width: 1.0 nm nm) and emission (step: 1.0 nm/s, dwell time: 0.125 s, slit width: 1.0 nm) spectra of probe 2 and $B(2,4,6\text{-}F_3\text{-}C_6H_2)_3$ in Et_2O; 12.5 μM sample.

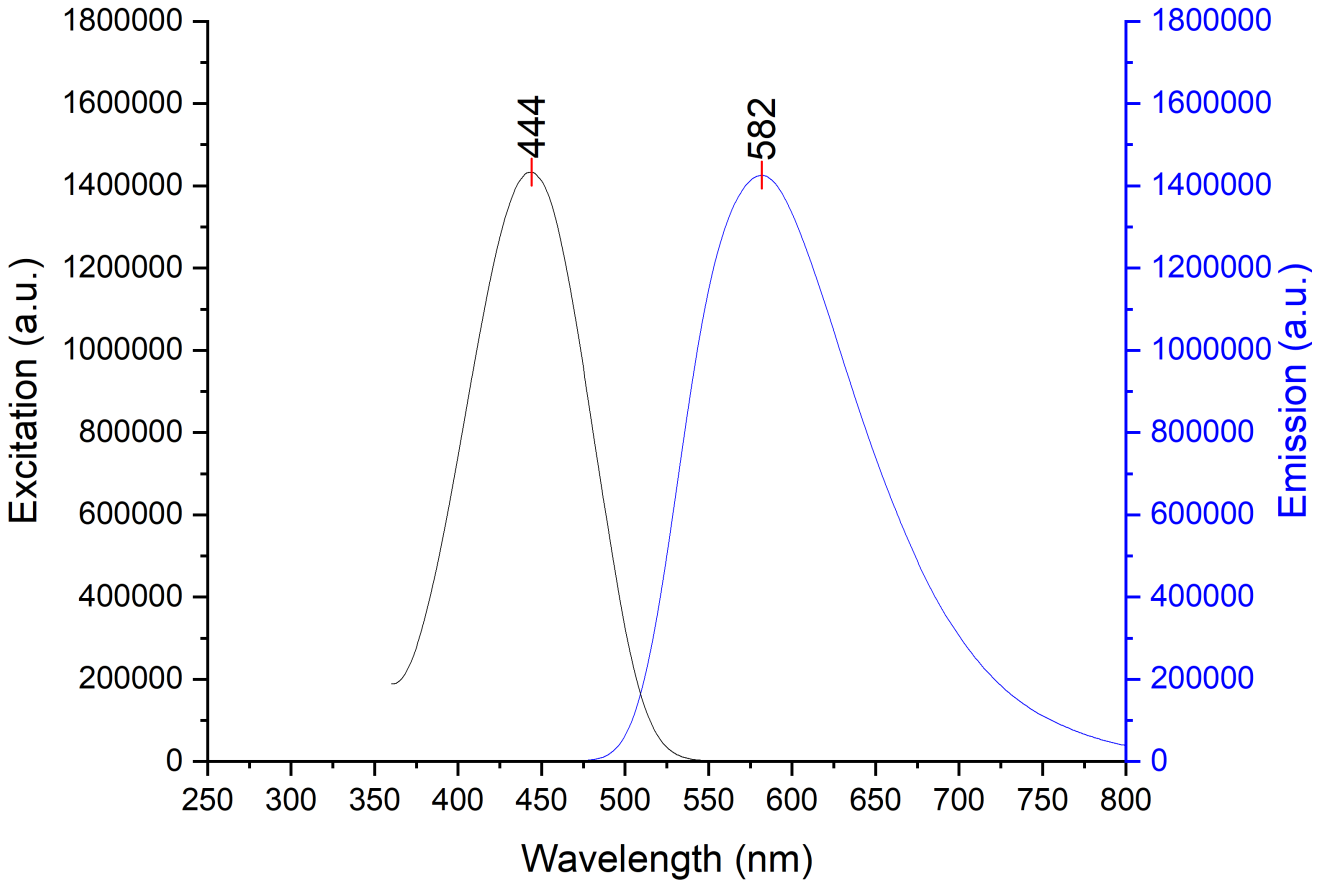

Figure 6-80. Stacked excitation (step: 1.0 nm/s, dwell time: 0.125 s, slit width: 1.0 nm) and emission (step: 1.0 nm/s, dwell time: 0.125 s, slit width: 1.0 nm) spectra of probe 2 and $B(2,4,6\text{-}F_3\text{-}C_6H_2)_3$ in DCM; 12.5 μM sample.

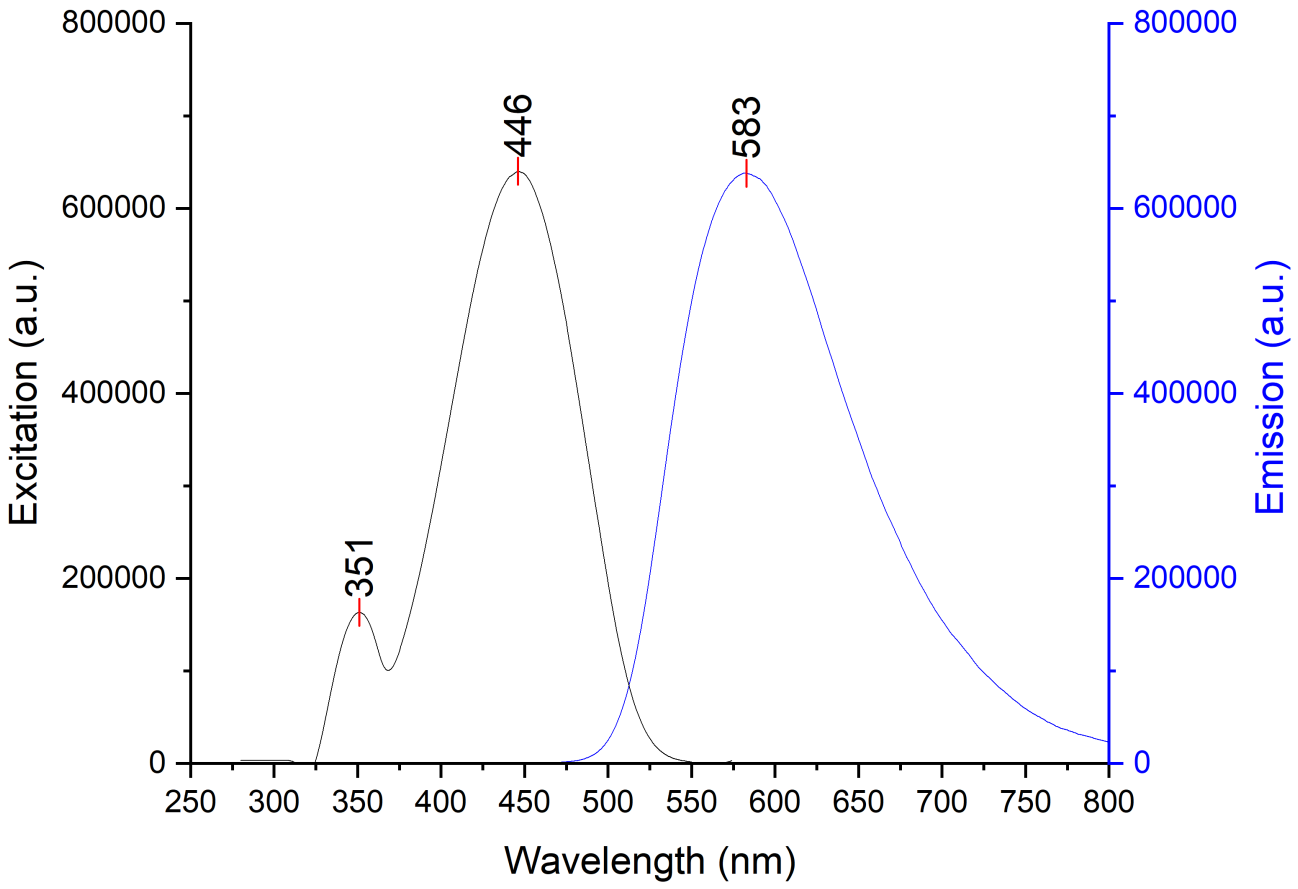

Figure 6-81. Stacked excitation (step: 1.0 nm/s, dwell time: 0.125 s, slit width: 0.80 nm) and emission (step: 1.0 nm/s, dwell time: 0.125 s, slit width: 0.80 nm) spectra of probe 7 and $B(2,4,6\text{-}F_3\text{-}C_6H_2)_3$ in PhCl; 12.5 μM sample.

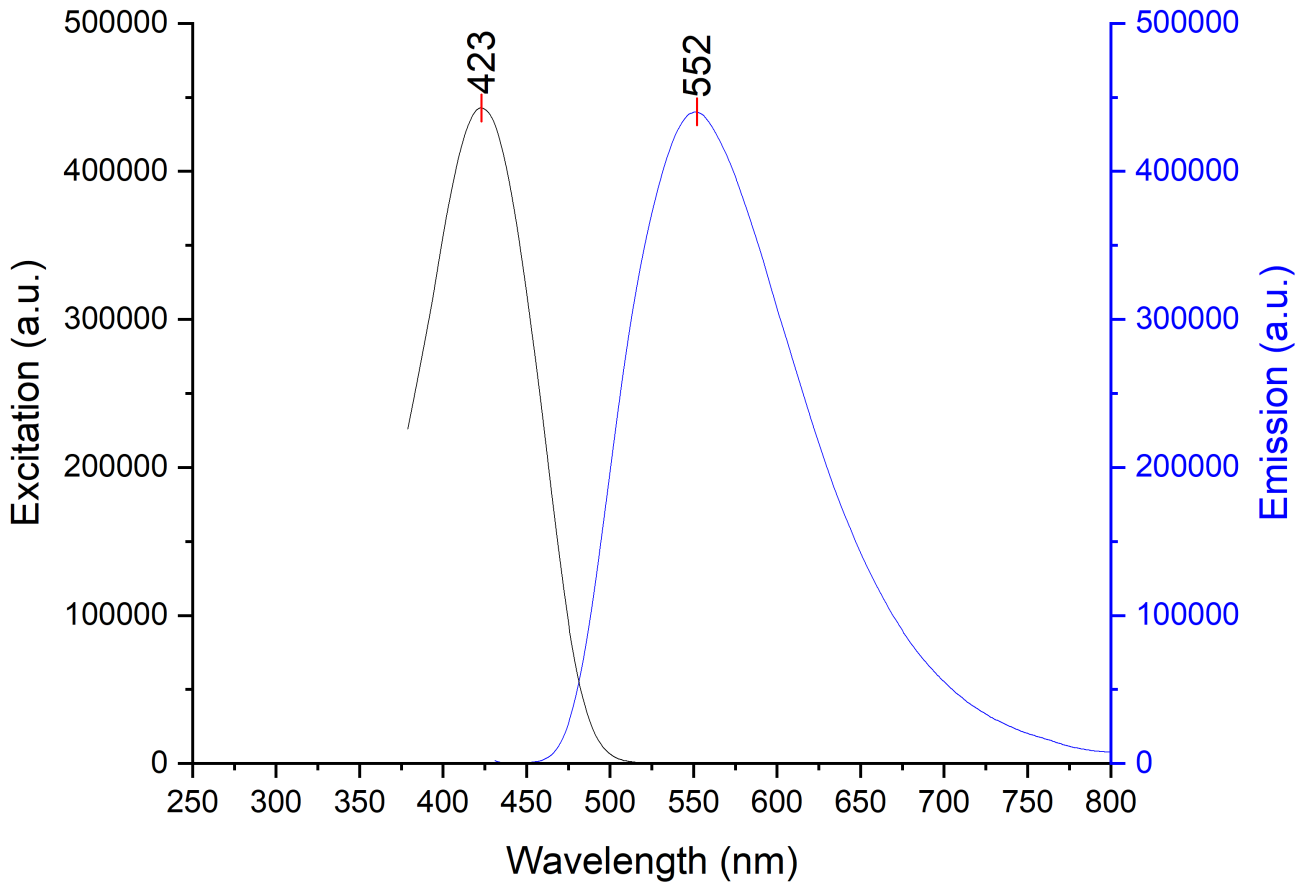

Figure 6-82. Stacked excitation (step: 1.0 nm/s, dwell time: 0.125 s, slit width: 1.0 nm) and emission (step: 1.0 nm/s, dwell time: 0.125 s, slit width: 1.0 nm) spectra of probe 7 and $B(2,4,6\text{-}F_3\text{-}C_6H_2)_3$ in Et_2O; 12.5 µM sample.

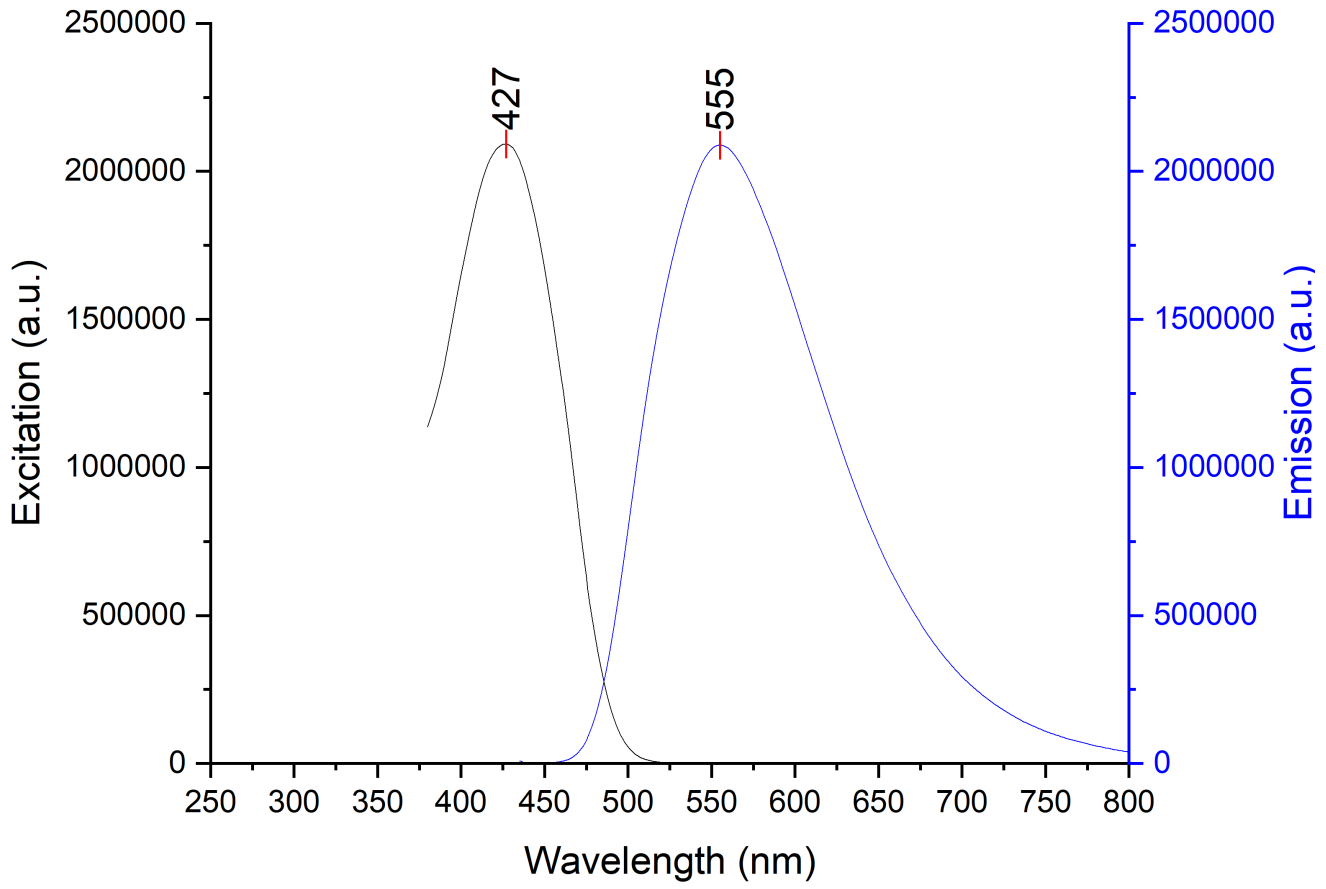

Figure 6-83. Stacked excitation (step: 1.0 nm/s, dwell time: 0.125 s, slit width: 1.0 nm) and emission (step: 1.0 nm/s, dwell time: 0.125 s, slit width: 1.0 nm) spectra of probe 7 and $B(2,4,6\text{-}F_3\text{-}C_6H_2)_3$ in DCM; 12.5 µM sample.

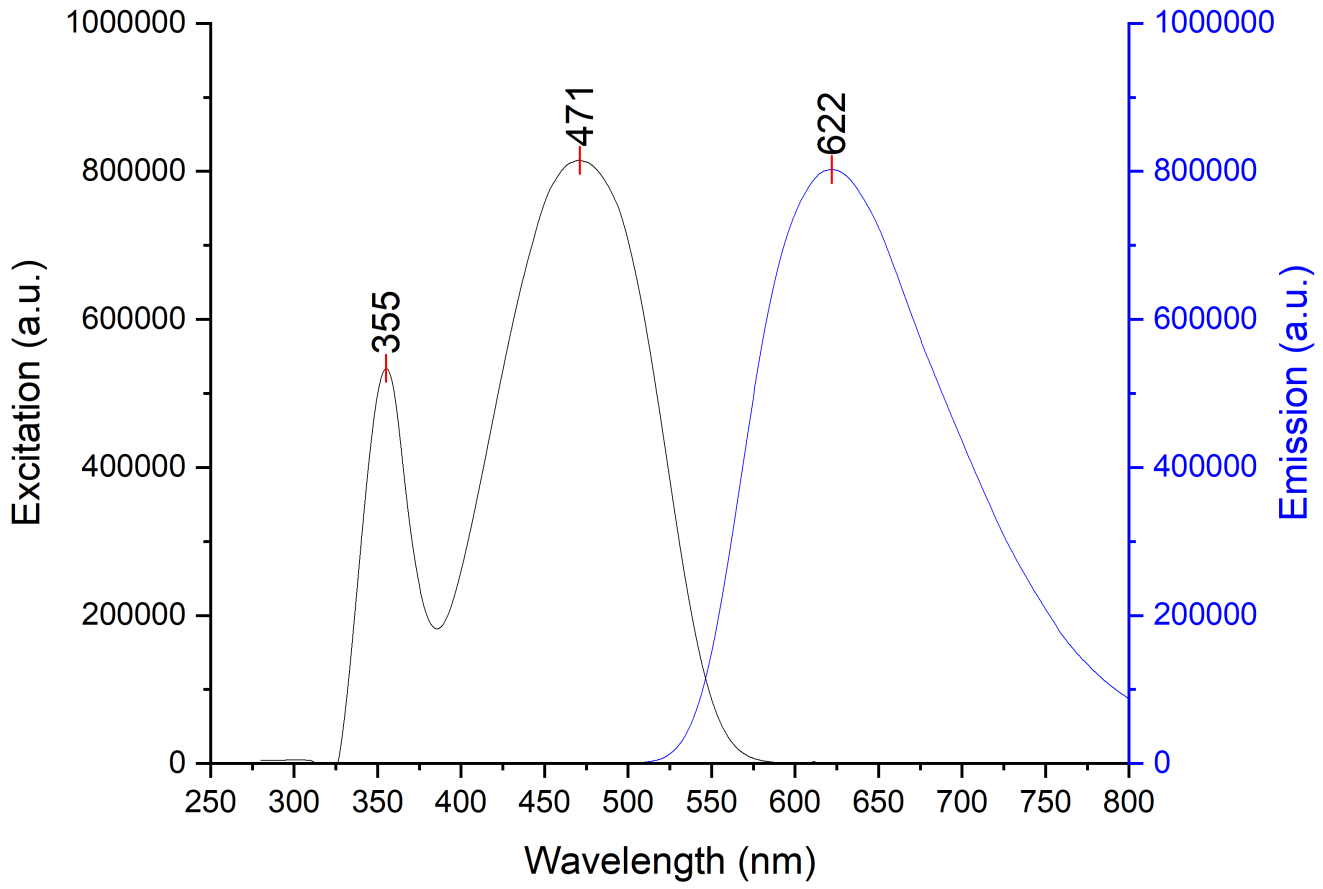

Figure 6-84. Stacked excitation (step: 1.0 nm/s, dwell time: 0.125 s, slit width: 0.80 nm) and emission (step: 1.0 nm/s, dwell time: 0.125 s, slit width: 0.80 nm) spectra of probe 8 and $B(2,4,6\text{-}F_3\text{-}C_6H_2)_3$ in PhCl; 12.5 μM sample.

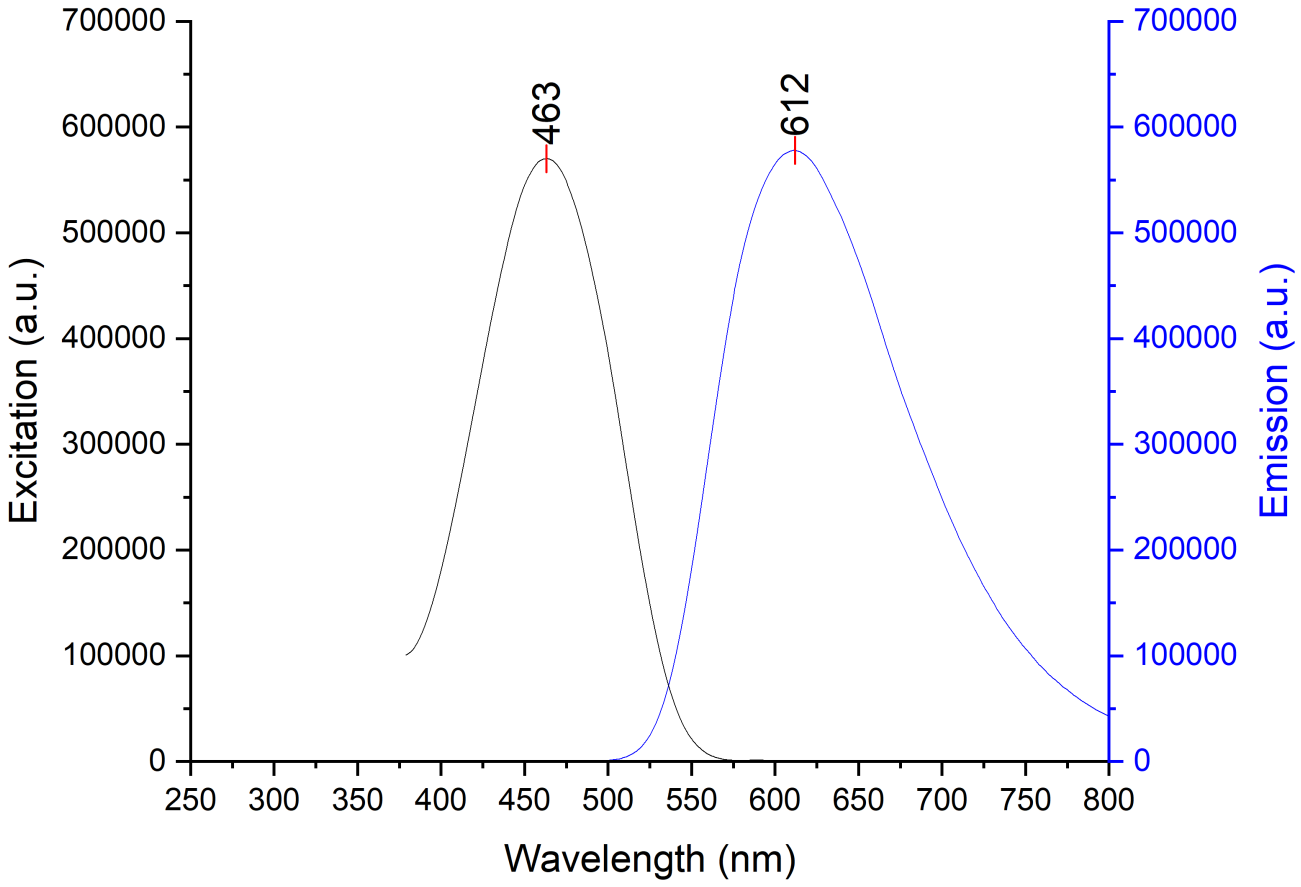

Figure 6-85. Stacked excitation (step: 1.0 nm/s, dwell time: 0.125 s, slit width: 1.0 nm) and emission (step: 1.0 nm/s, dwell time: 0.125 s, slit width: 1.0 nm) spectra of probe 8 and $B(2,4,6\text{-}F_3\text{-}C_6H_2)_3$ in Et_2O; 12.5 μM sample.

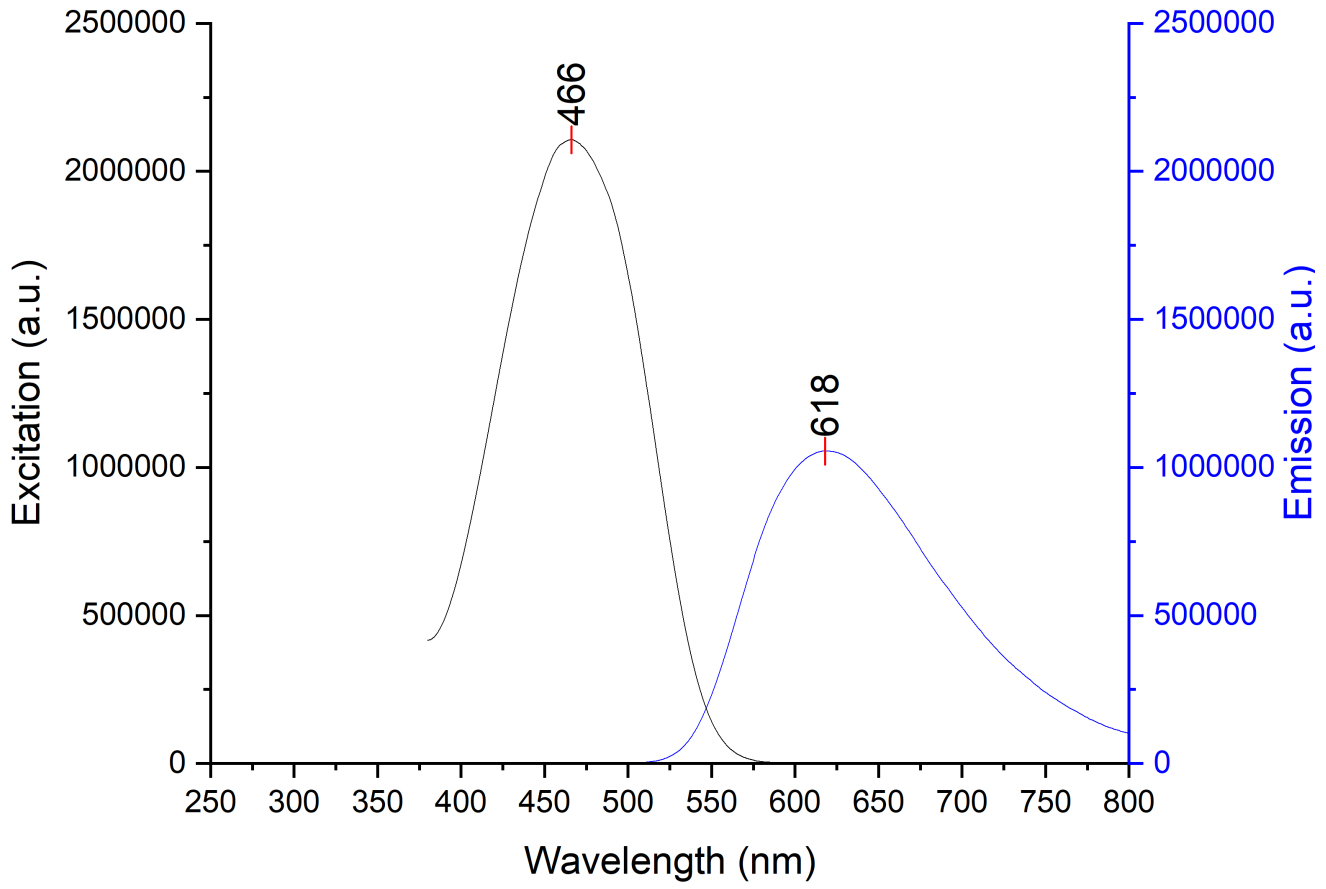

Figure 6-86. Stacked excitation (step: 1.0 nm/s, dwell time: 0.125 s, slit width: 1.0 nm) and emission (step: 1.0 nm/s, dwell time: 0.125 s, slit width: 1.0 nm) spectra of probe 8 and $B(2,4,6\text{-}F_3\text{-}C_6H_2)_3$ in DCM; 12.5 μM sample.

6.2.3.5. $B(OC_6F_5)_3$

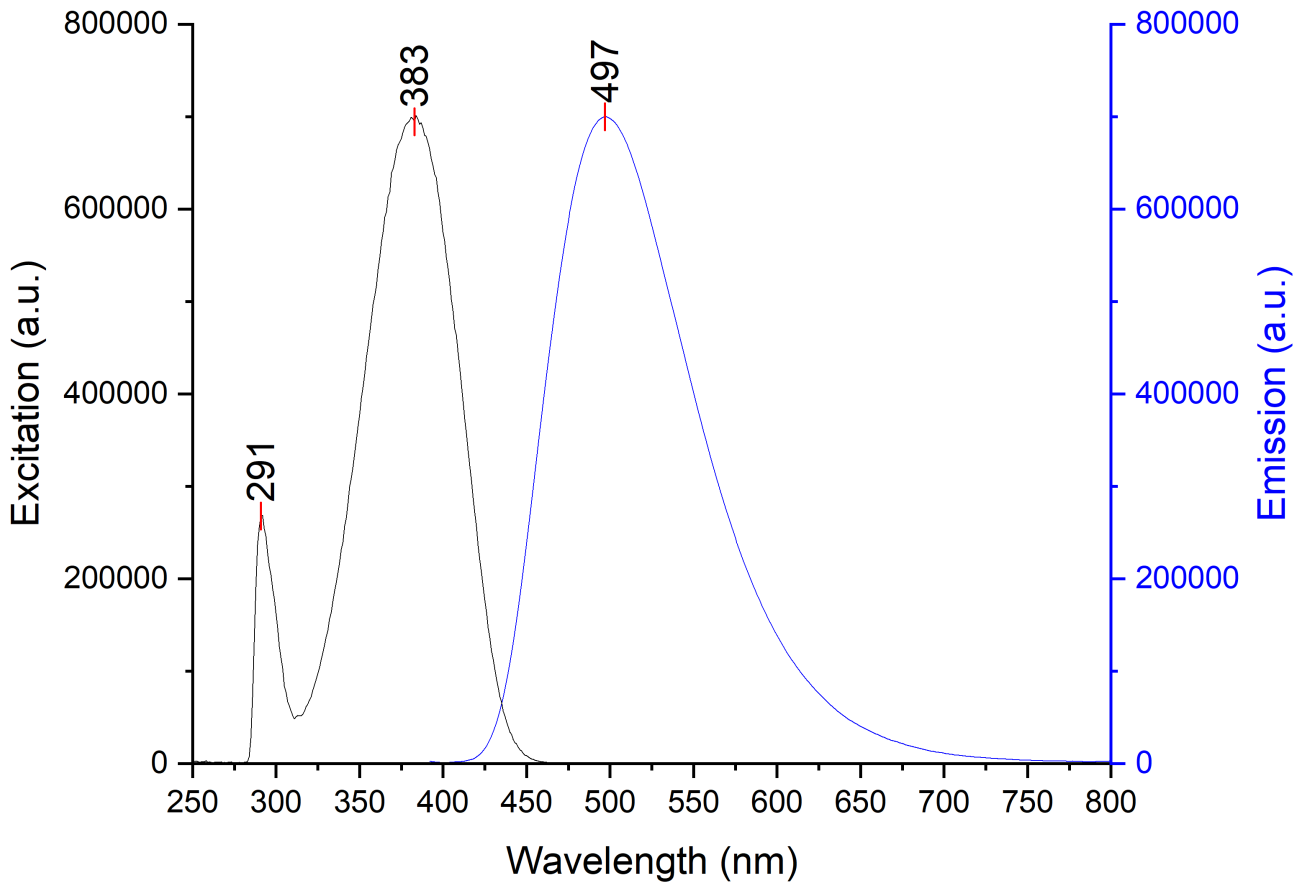

Figure 6-87. Stacked excitation (step: 1.0 nm/s, dwell time: 0.125 s, slit width: 1.0 nm) and emission (step: 1.0 nm/s, dwell time: 0.125 s, slit width: 1.0 nm) spectra of probe 1 and $B(OC_6F_5)_3$ in PhCl; 12.5 μM sample.

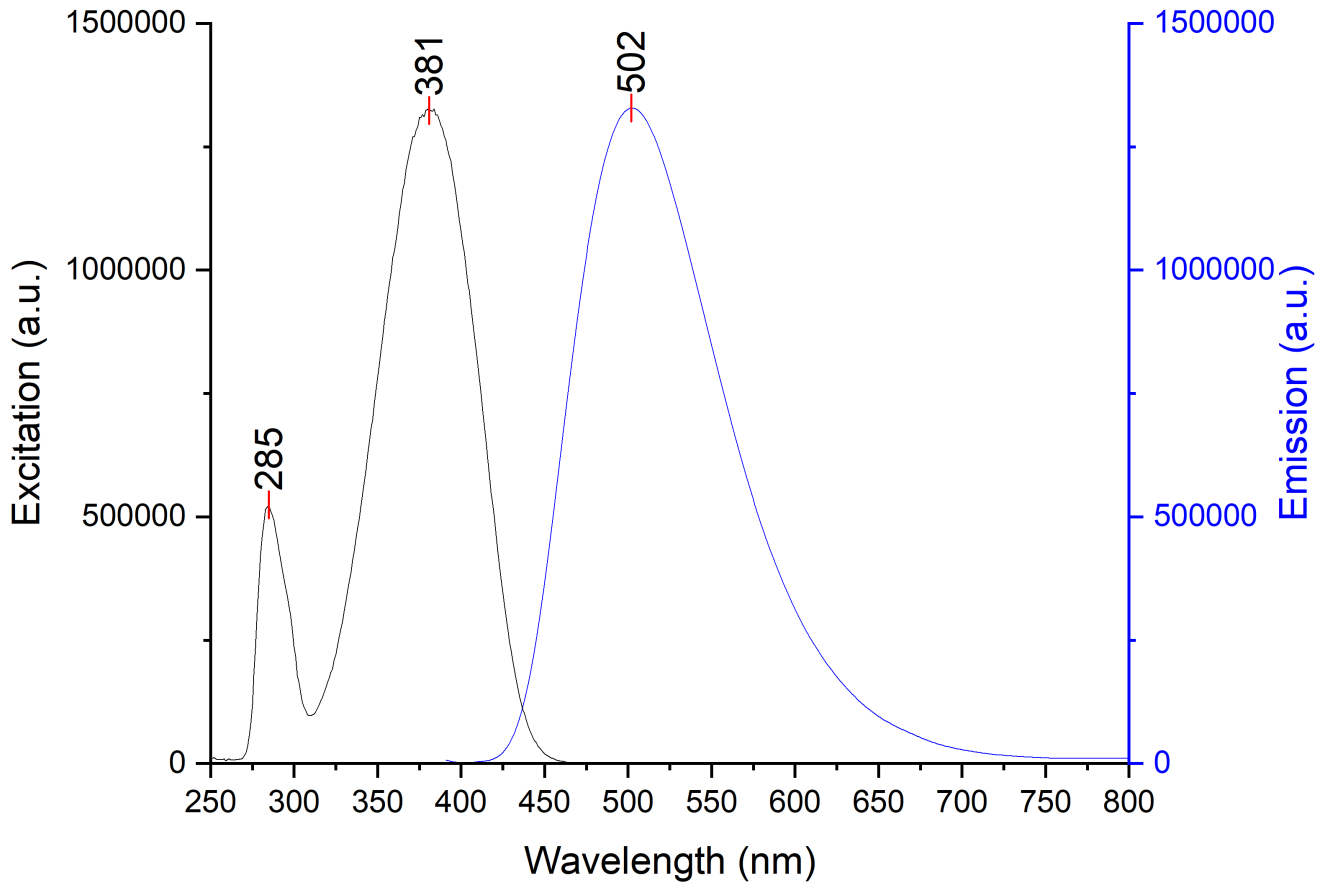

Figure 6-88. Stacked excitation (step: 1.0 nm/s, dwell time: 0.125 s, slit width: 1.0 nm) and emission (step: 1.0 nm/s, dwell time: 0.125 s, slit width: 1.0 nm) spectra of probe 1 and $B(OC_6F_5)_3$ in Et_2O; 12.5 μM sample.

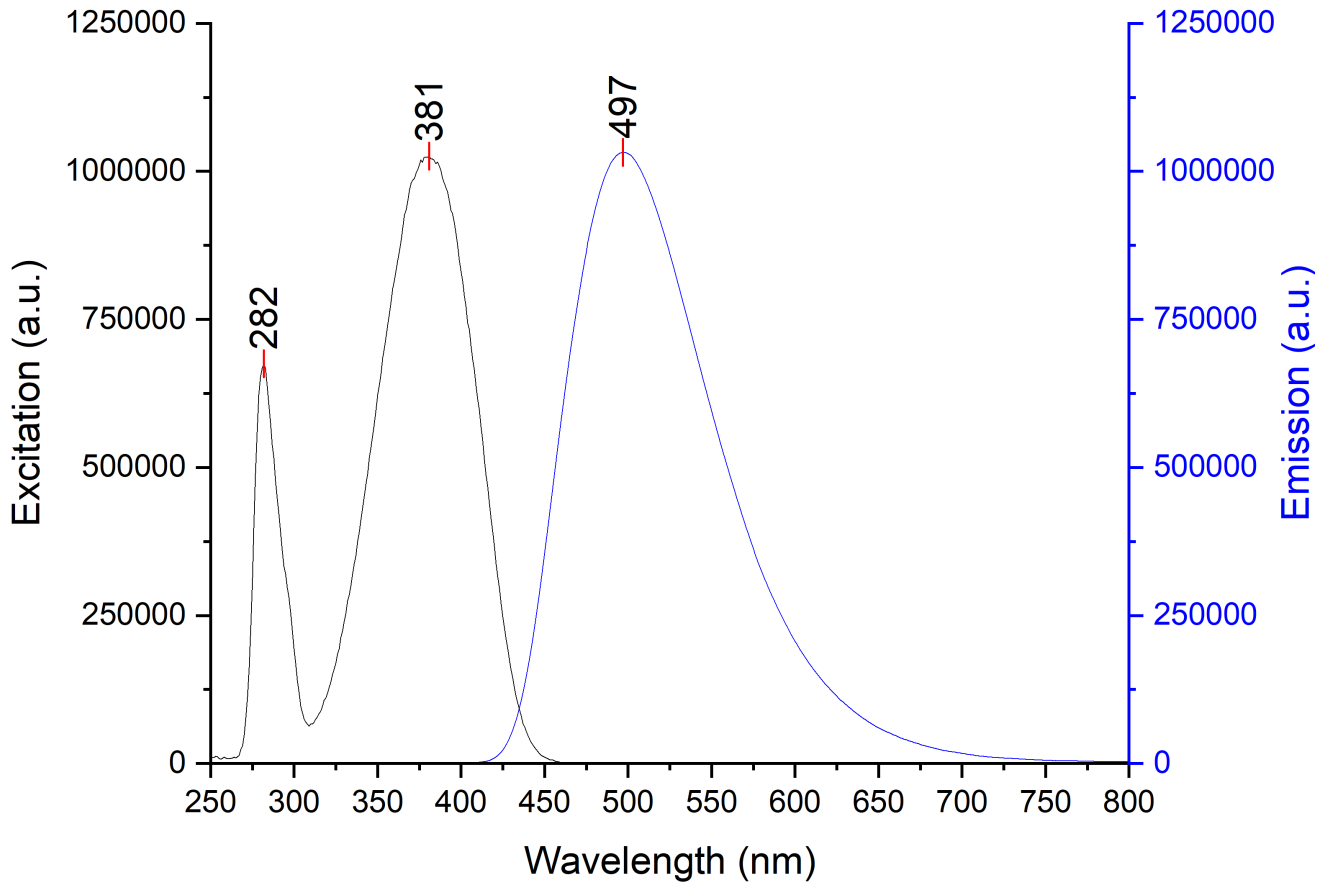

Figure 6-89. Stacked excitation (step: 1.0 nm/s, dwell time: 0.125 s, slit width: 0.80 nm) and emission (step: 1.0 nm/s, dwell time: 0.125 s, slit width: 0.80 nm) spectra of probe 1 and $B(OC_6F_5)_3$ in DCM; 12.5 μM sample.

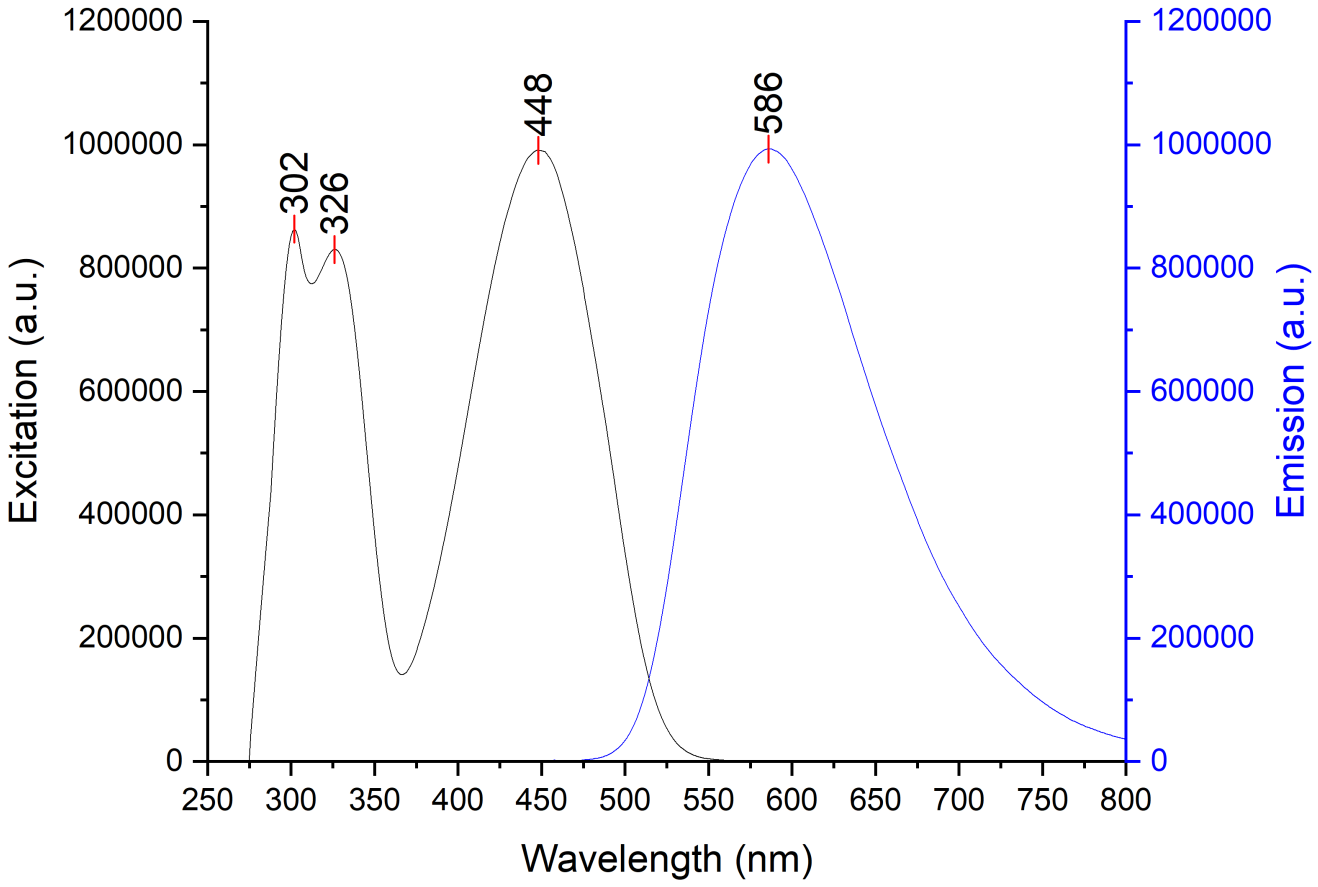

Figure 6-90. Stacked excitation (step: 1.0 nm/s, dwell time: 0.125 s, slit width: 1.0 nm) and emission (step: 1.0 nm/s, dwell time: 0.125 s, slit width: 1.0 nm) spectra of probe 2 and $B(OC_6F_5)_3$ in PhCl; 12.5 μM sample.

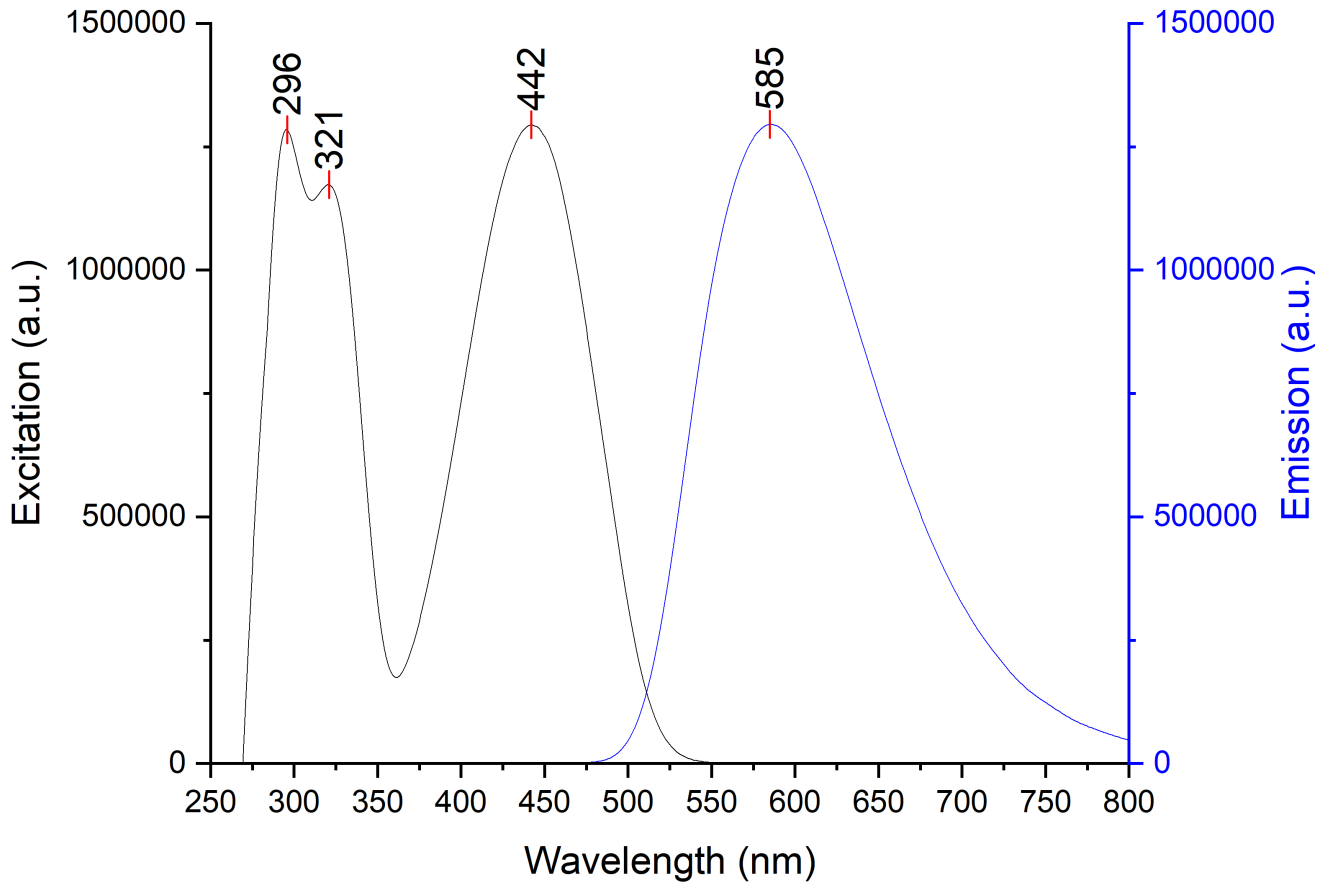

Figure 6-91. Stacked excitation (step: 1.0 nm/s, dwell time: 0.125 s, slit width: 1.0 nm) and emission (step: 1.0 nm/s, dwell time: 0.125 s, slit width: 1.0 nm) spectra of probe 2 and $B(OC_6F_5)_3$ in Et_2O; 12.5 μM sample.

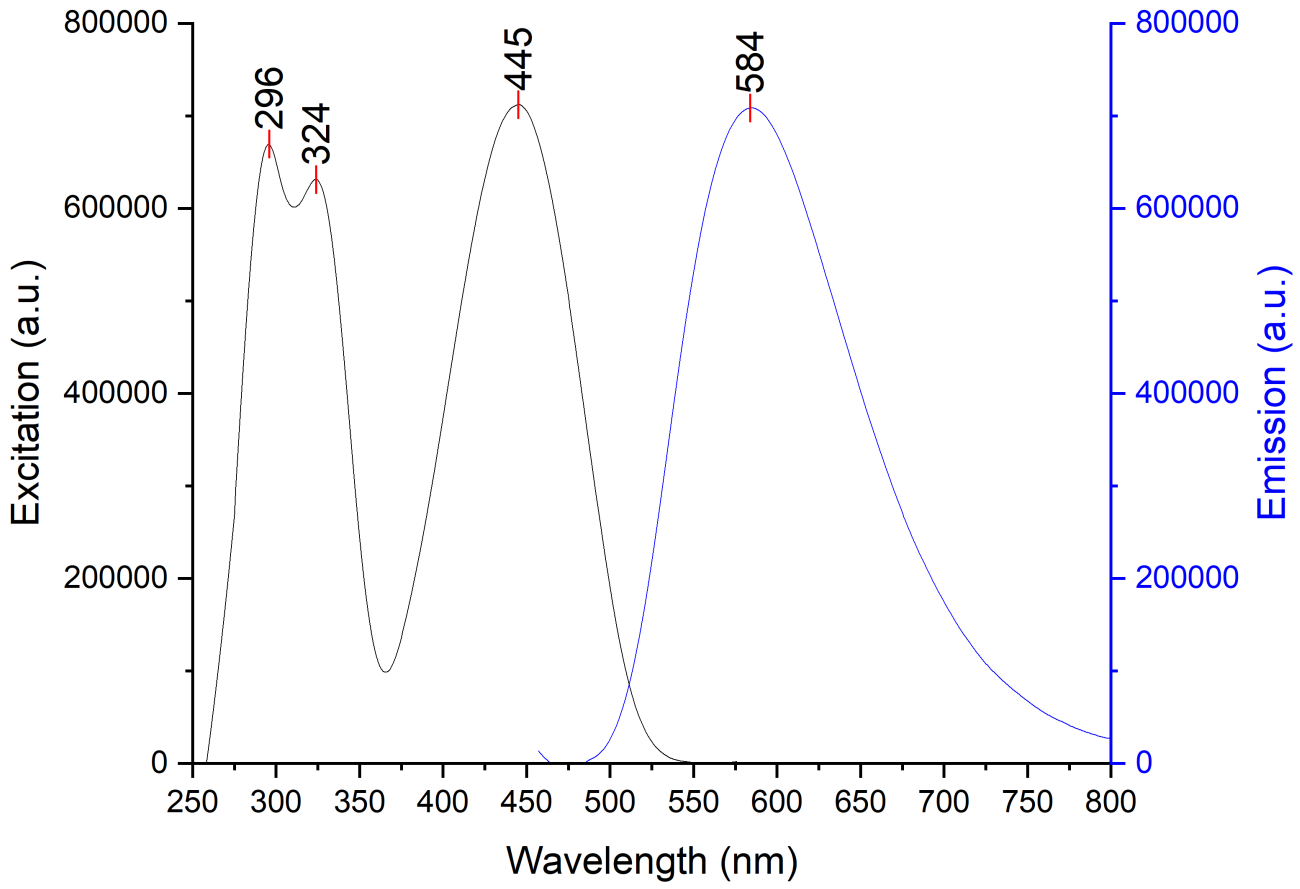

Figure 6-92. Stacked excitation (step: 1.0 nm/s, dwell time: 0.125 s, slit width: 0.80 nm) and emission (step: 1.0 nm/s, dwell time: 0.125 s, slit width: 0.80 nm) spectra of probe 2 and $B(OC_6F_5)_3$ in DCM; 12.5 μM sample.

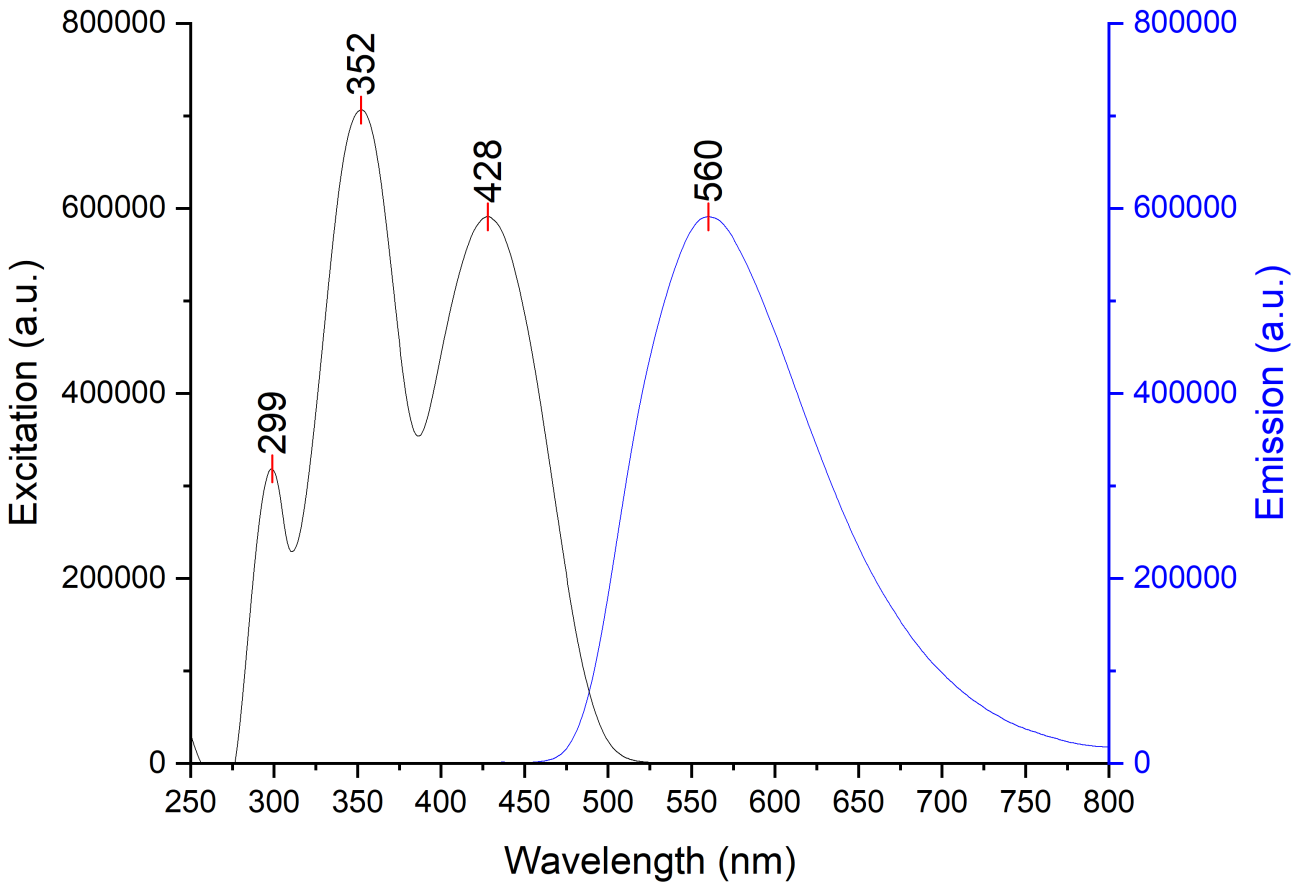

Figure 6-93. Stacked excitation (step: 1.0 nm/s, dwell time: 0.125 s, slit width: 1.0 nm) and emission (step: 1.0 nm/s, dwell time: 0.125 s, slit width: 1.0 nm) spectra of probe 7 and $B(OC_6F_5)_3$ in PhCl; 12.5 μM sample.

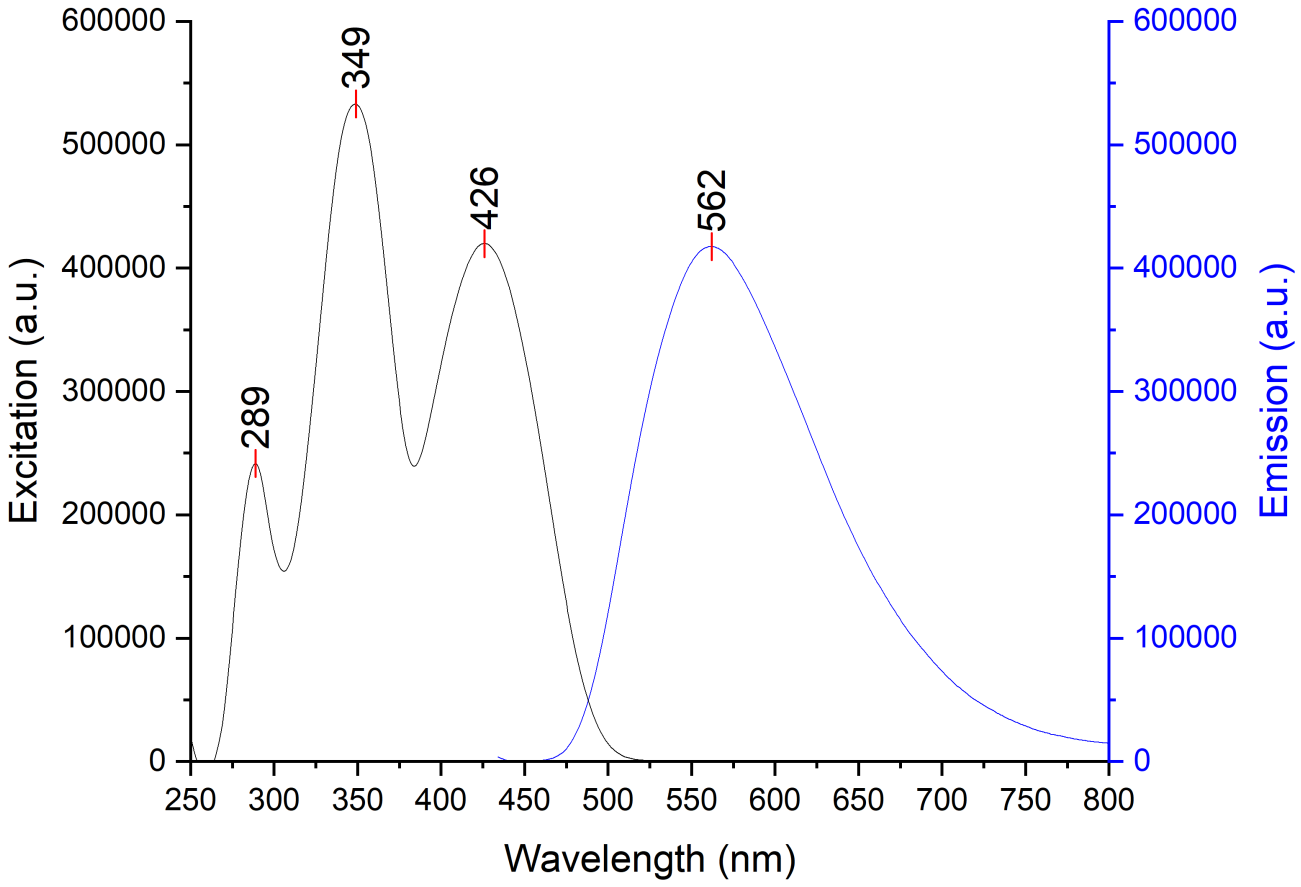

Figure 6-94. Stacked excitation (step: 1.0 nm/s, dwell time: 0.125 s, slit width: 1.0 nm) and emission (step: 1.0 nm/s, dwell time: 0.125 s, slit width: 1.0 nm) spectra of probe 7 and $B(OC_6F_5)_3$ in Et_2O; 12.5 μM sample.

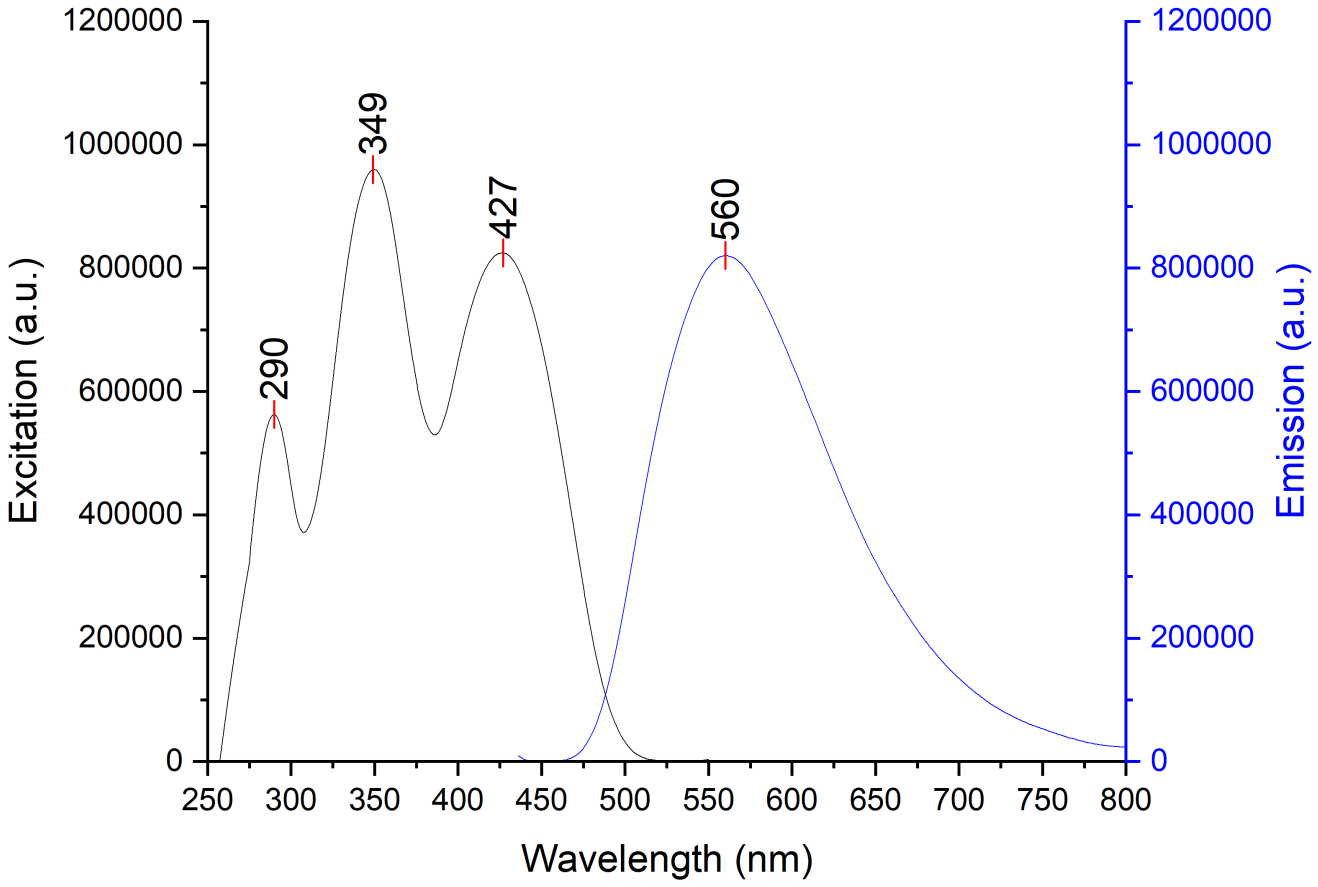

Figure 6-95. Stacked excitation (step: 1.0 nm/s, dwell time: 0.125 s, slit width: 0.80 nm) and emission (step: 1.0 nm/s, dwell time: 0.125 s, slit width: 0.80 nm) spectra of probe 7 and $B(OC_6F_5)_3$ in DCM; 12.5 μM sample.

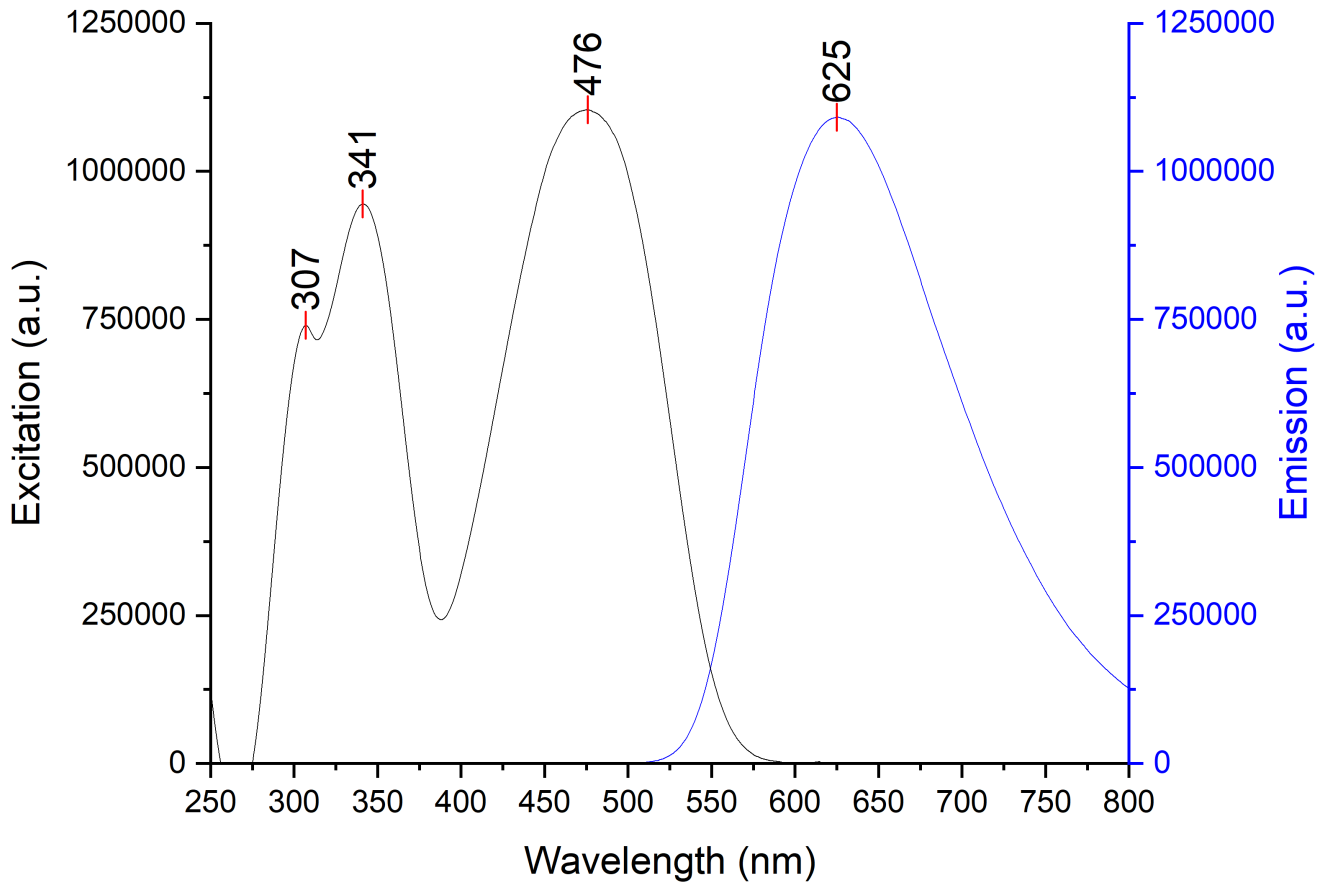

Figure 6-96. Stacked excitation (step: 1.0 nm/s, dwell time: 0.125 s, slit width: 1.0 nm) and emission (step: 1.0 nm/s, dwell time: 0.125 s, slit width: 1.0 nm) spectra of probe 8 and $B(OC_6F_5)_3$ in PhCl; 12.5 μM sample.

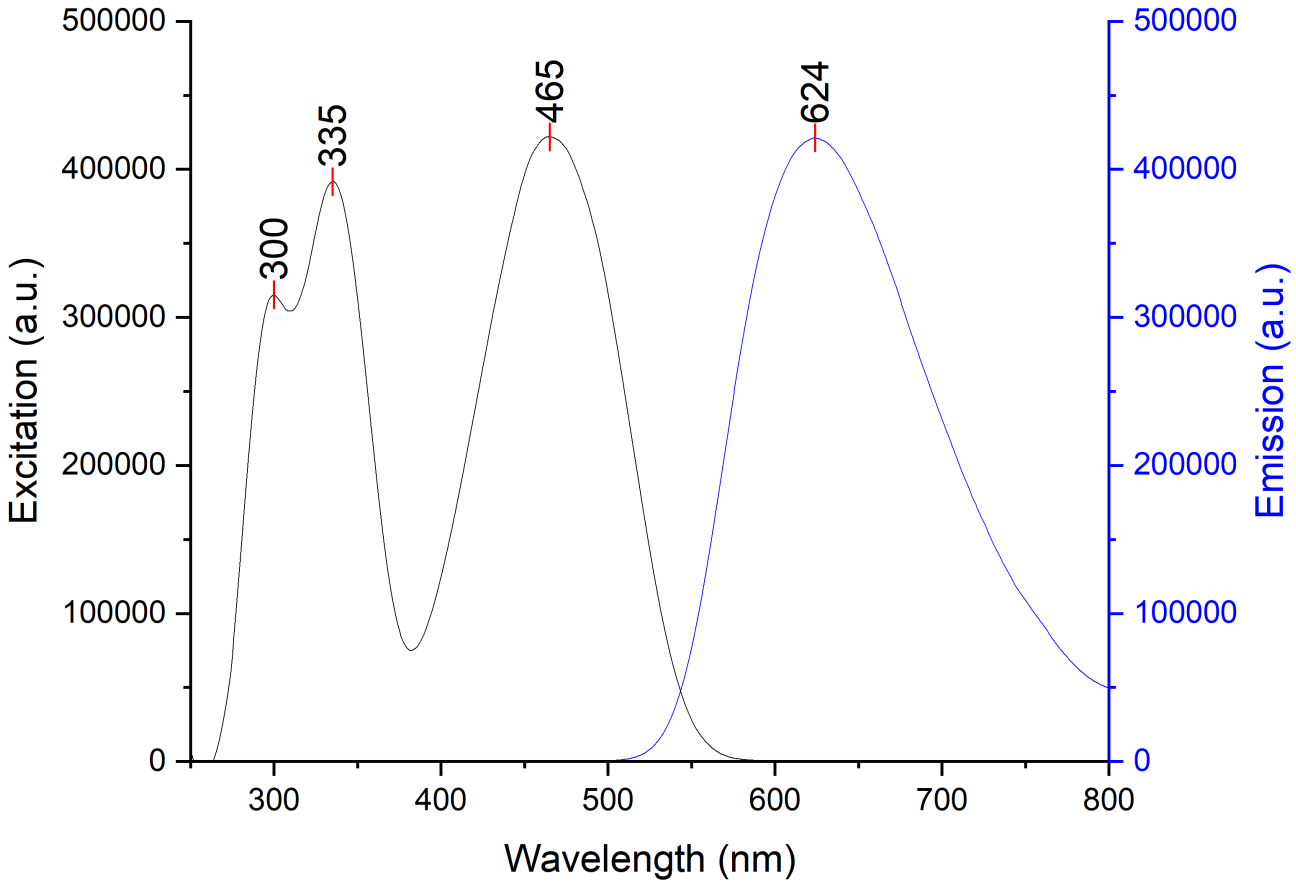

Figure 6-97. Stacked excitation (step: 1.0 nm/s, dwell time: 0.125 s, slit width: 1.0 nm) and emission (step: 1.0 nm/s, dwell time: 0.125 s, slit width: 1.0 nm) spectra of probe 8 and $B(OC_6F_5)_3$ in Et_2O; 12.5 μM sample.

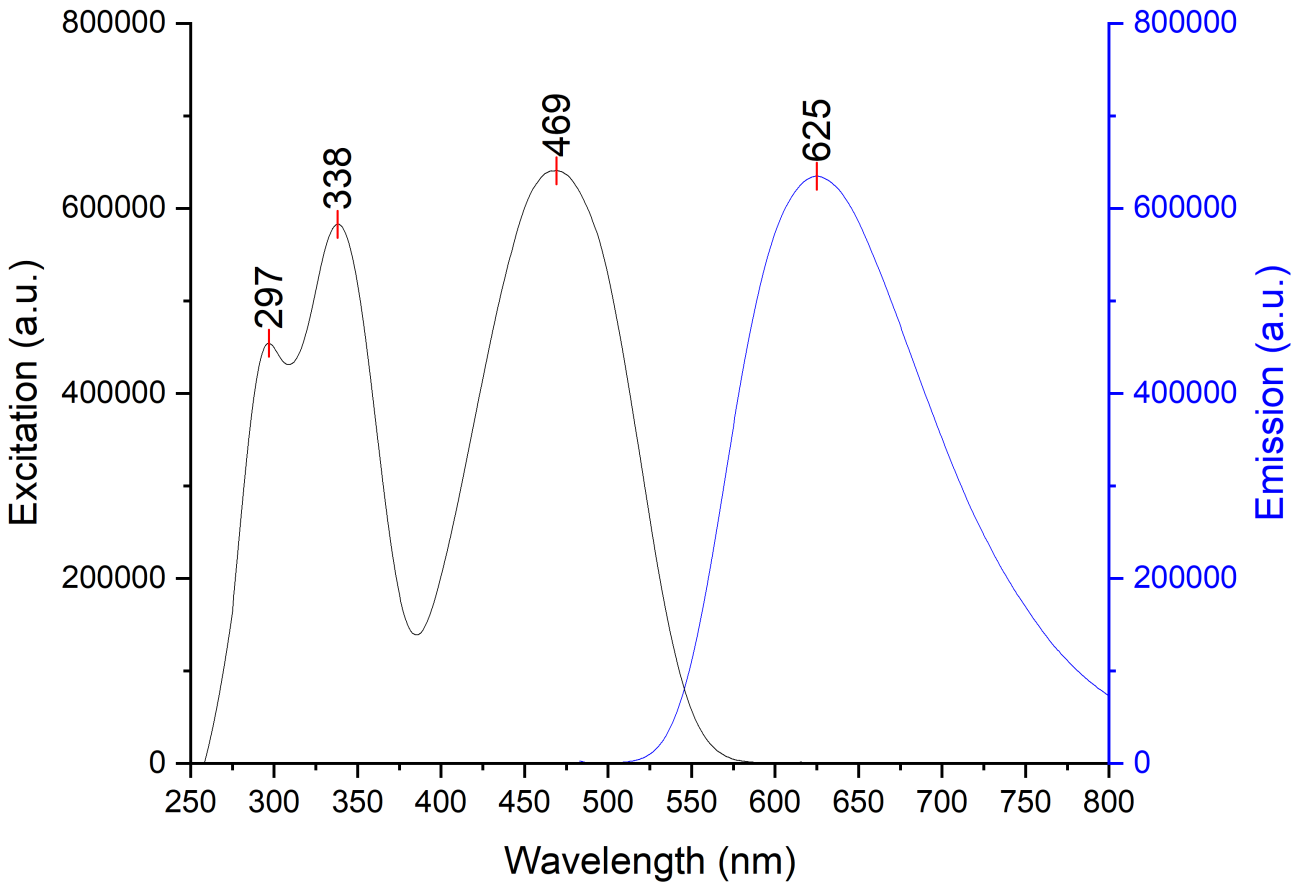

Figure 6-98. Stacked excitation (step: 1.0 nm/s, dwell time: 0.125 s, slit width: 0.80 nm) and emission (step: 1.0 nm/s, dwell time: 0.125 s, slit width: 0.80 nm) spectra of probe 8 and $B(OC_6F_5)_3$ in DCM; 12.5 μM sample.

6.2.3.6. $B(C_6F_5)_3$

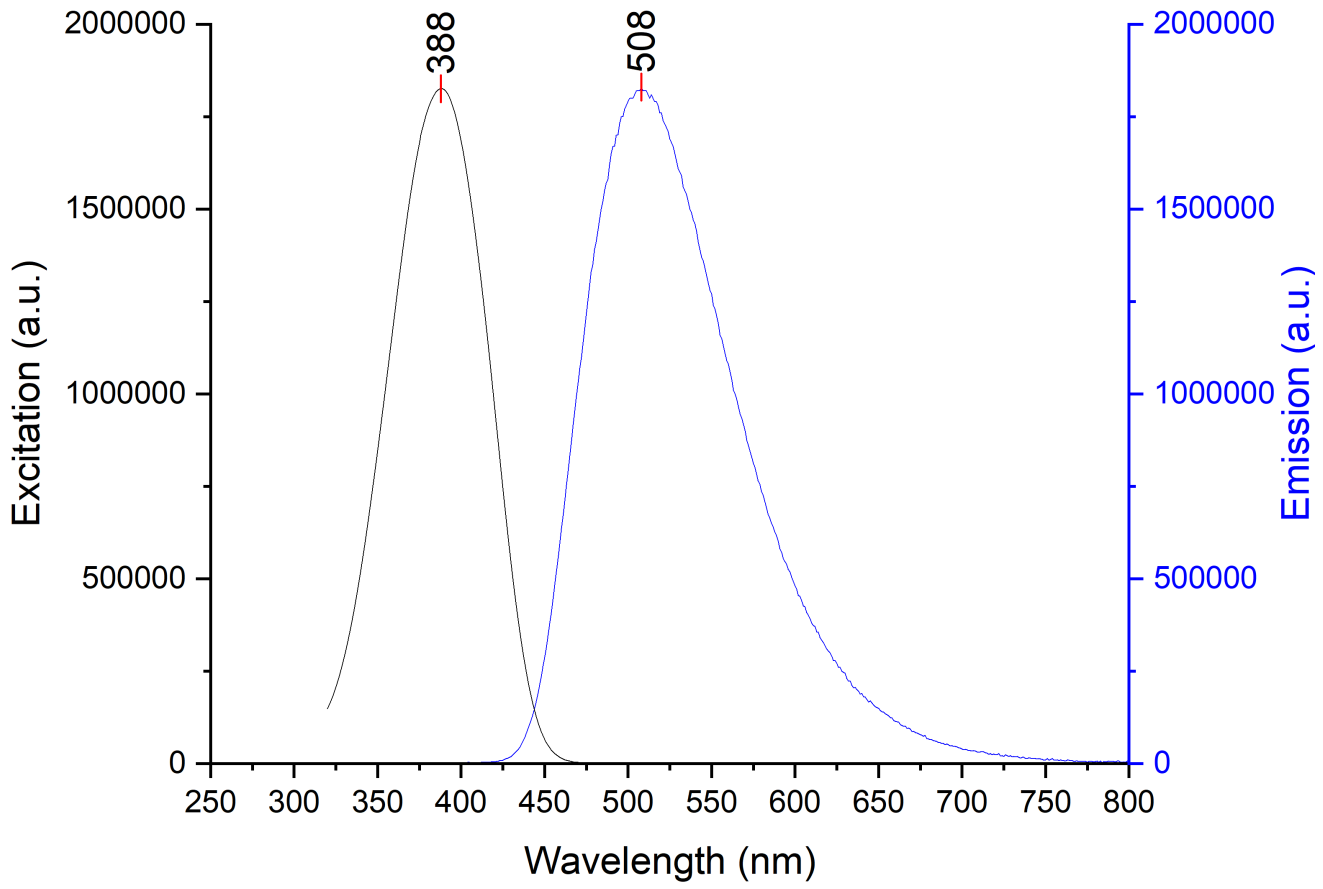

Figure 6-99. Stacked excitation (step: 1.0 nm/s, dwell time: 0.125 s, slit width: 1.0 nm) and emission (step: 1.0 nm/s, dwell time: 0.125 s, slit width: 1.0 nm) spectra of probe 1 and $B(C_6F_5)_3$ in PhCl; 12.5 μM sample.

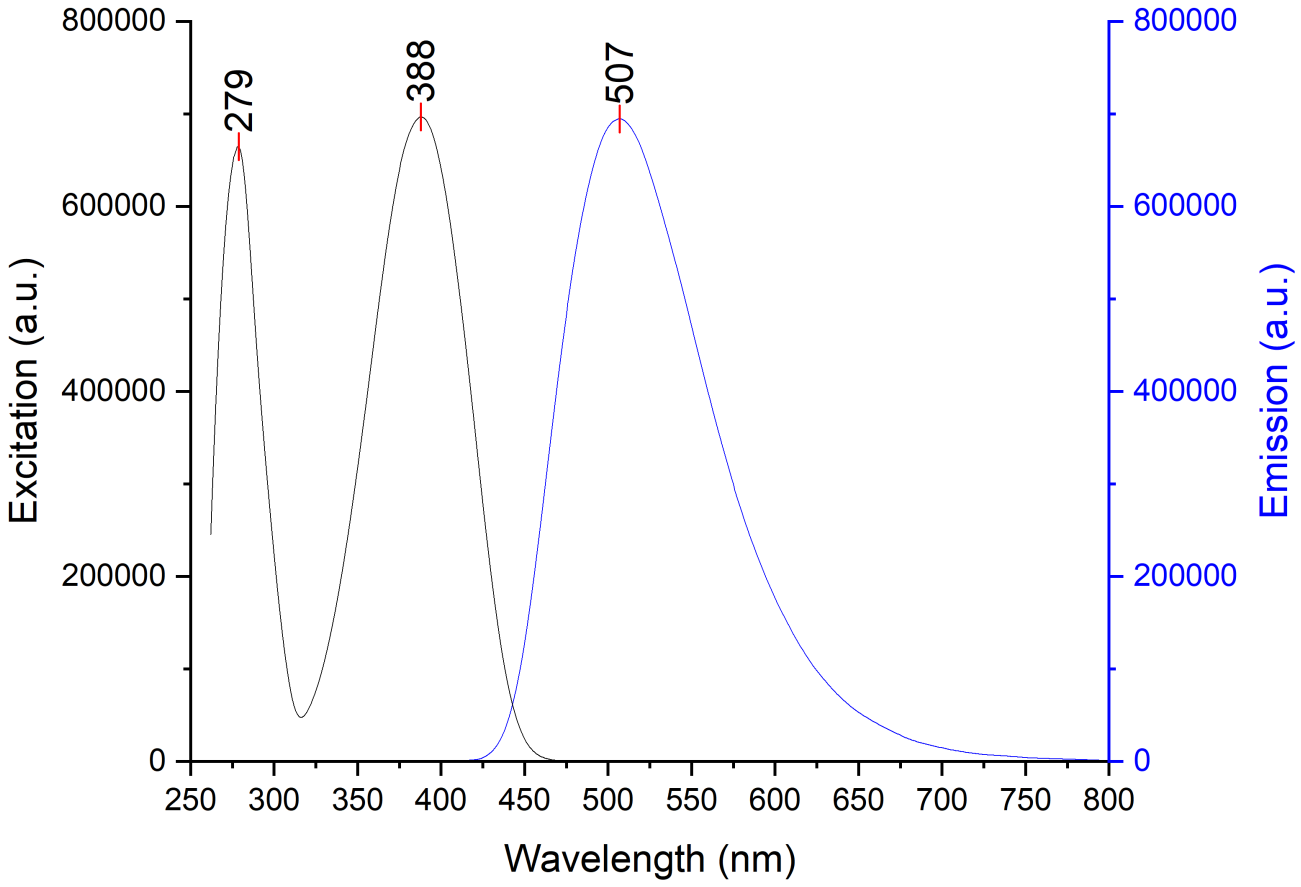

Figure 6-100. Stacked excitation (step: 1.0 nm/s, dwell time: 0.125 s, slit width: 1.0 nm and emission (step: 1.0 nm/s, dwell time: 0.125 s, slit width: 1.0 nm) spectra of probe 1 and $B(C_6F_5)_3$ in Et_2O; 12.5 µM sample.

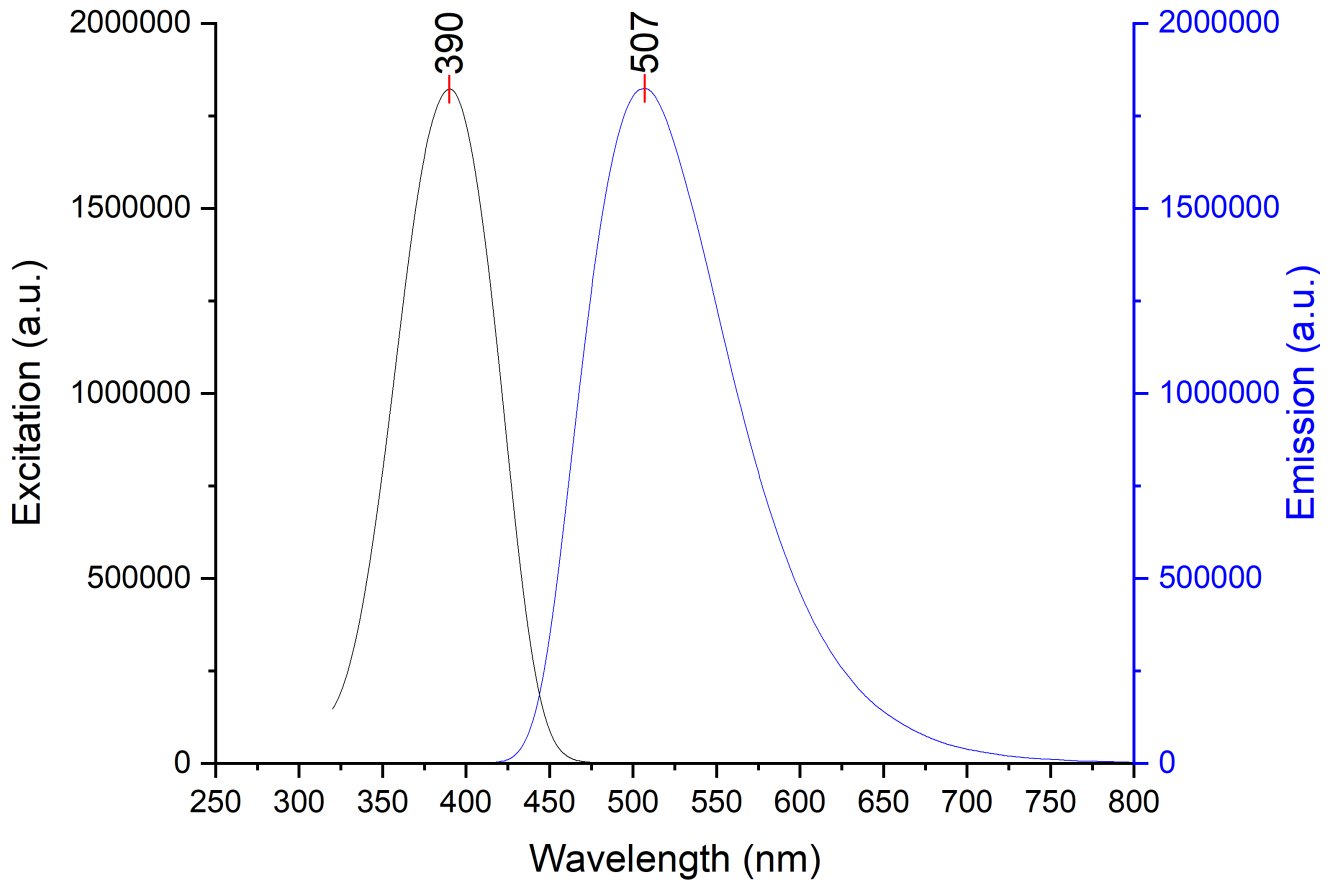

Figure 6-101. Stacked excitation (step: 1.0 nm/s, dwell time: 0.125 s, slit width: 1.0 nm) and emission (step: 1.0 nm/s, dwell time: 0.125 s, slit width: 1.0 nm) spectra of probe 1 and $B(C_6F_5)_3$ in DCM; 12.5 µM sample.

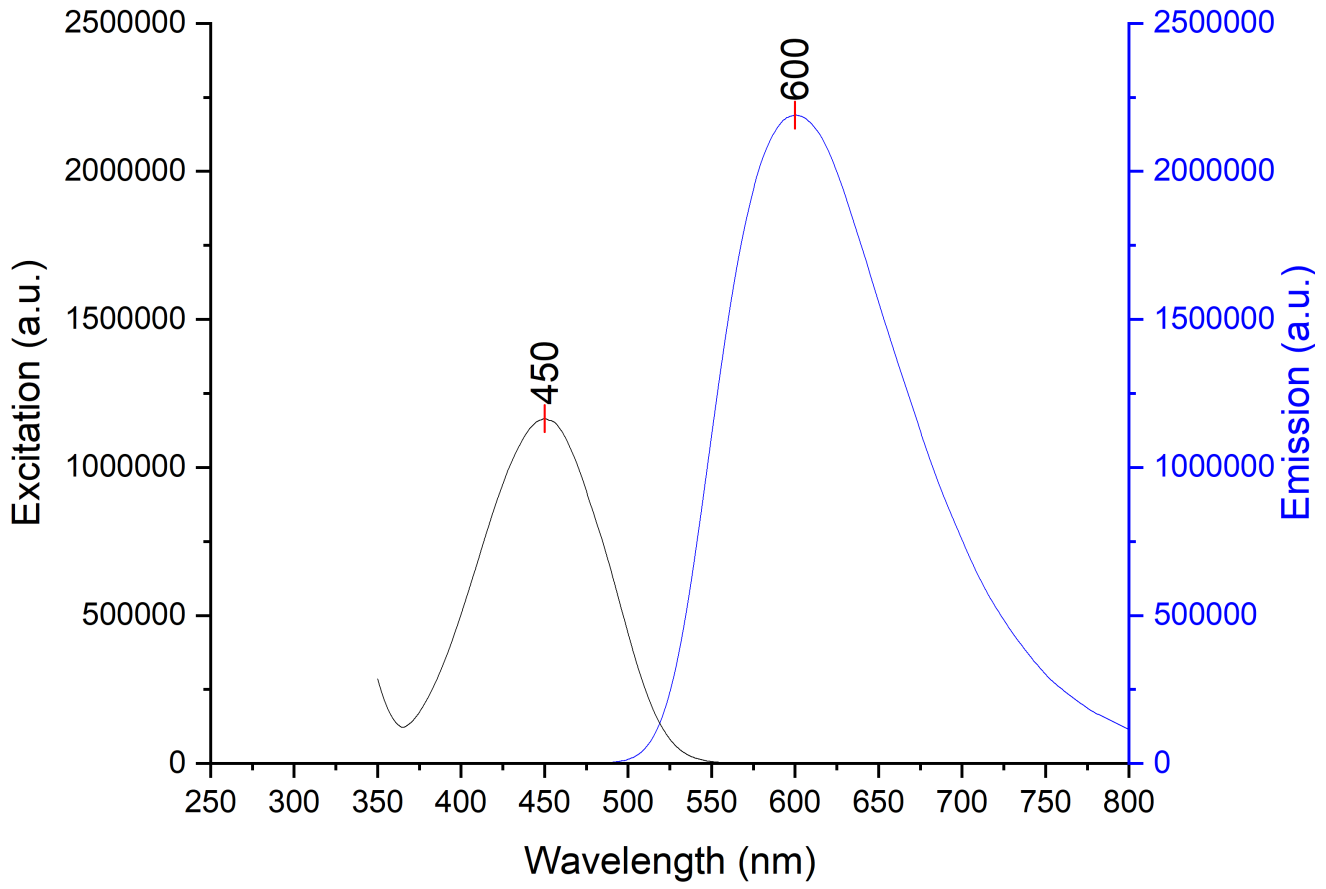

Figure 6-102. Stacked excitation (step: 1.0 nm/s, dwell time: 0.125 s, slit width: 1.0 nm) and emission (step: 1.0 nm/s, dwell time: 0.125 s, slit width: 1.0 nm) spectra of probe 2 and $B(C_6F_5)_3$ in PhCl; 12.5 µM sample.

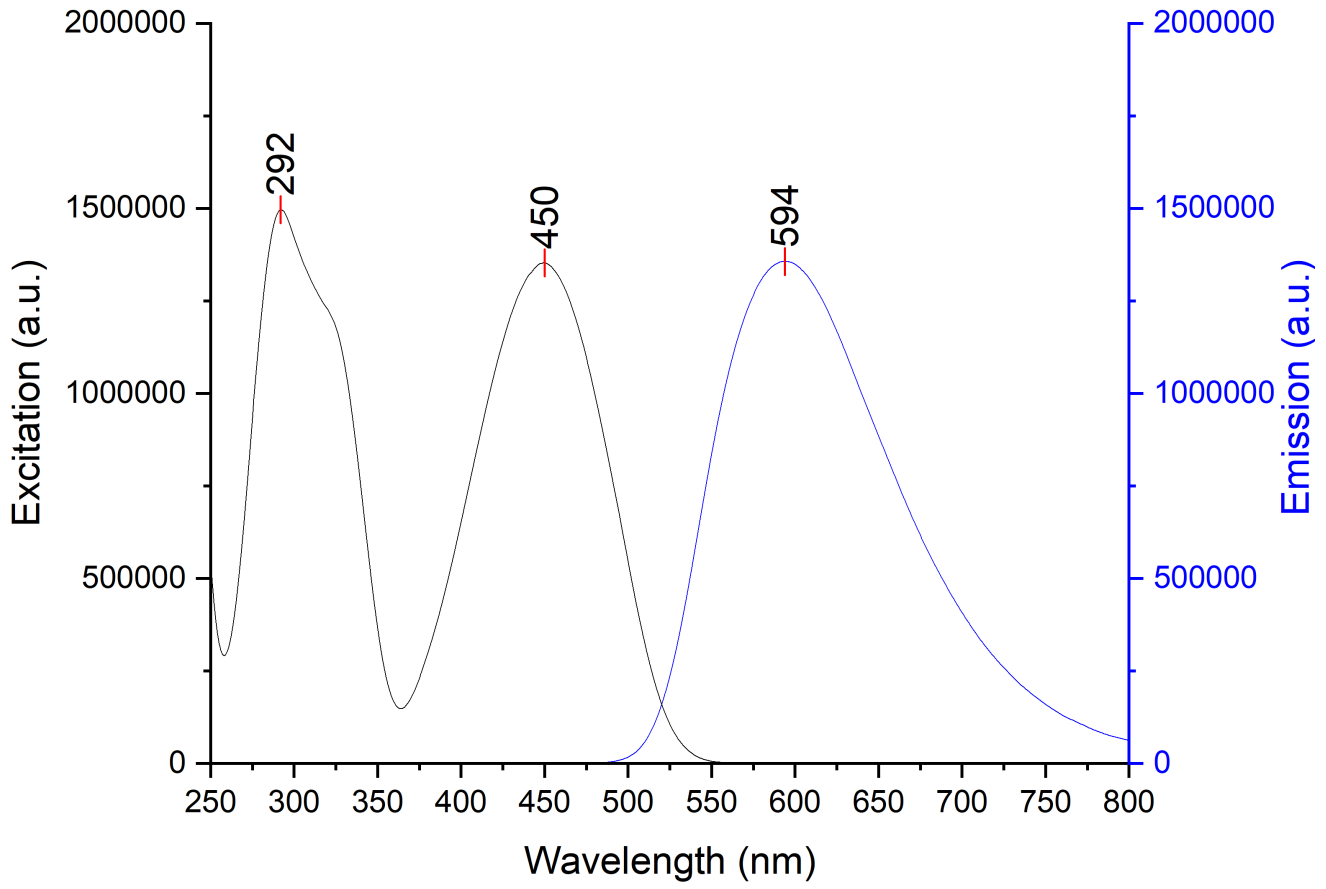

Figure 6-103. Stacked excitation (step: 1.0 nm/s, dwell time: 0.125 s, slit width: 1.0 nm) and emission (step: 1.0 nm/s, dwell time: 0.125 s, slit width: 1.0 nm) spectra of probe 2 and $B(C_6F_5)_3$ in Et_2O; 12.5 µM sample.

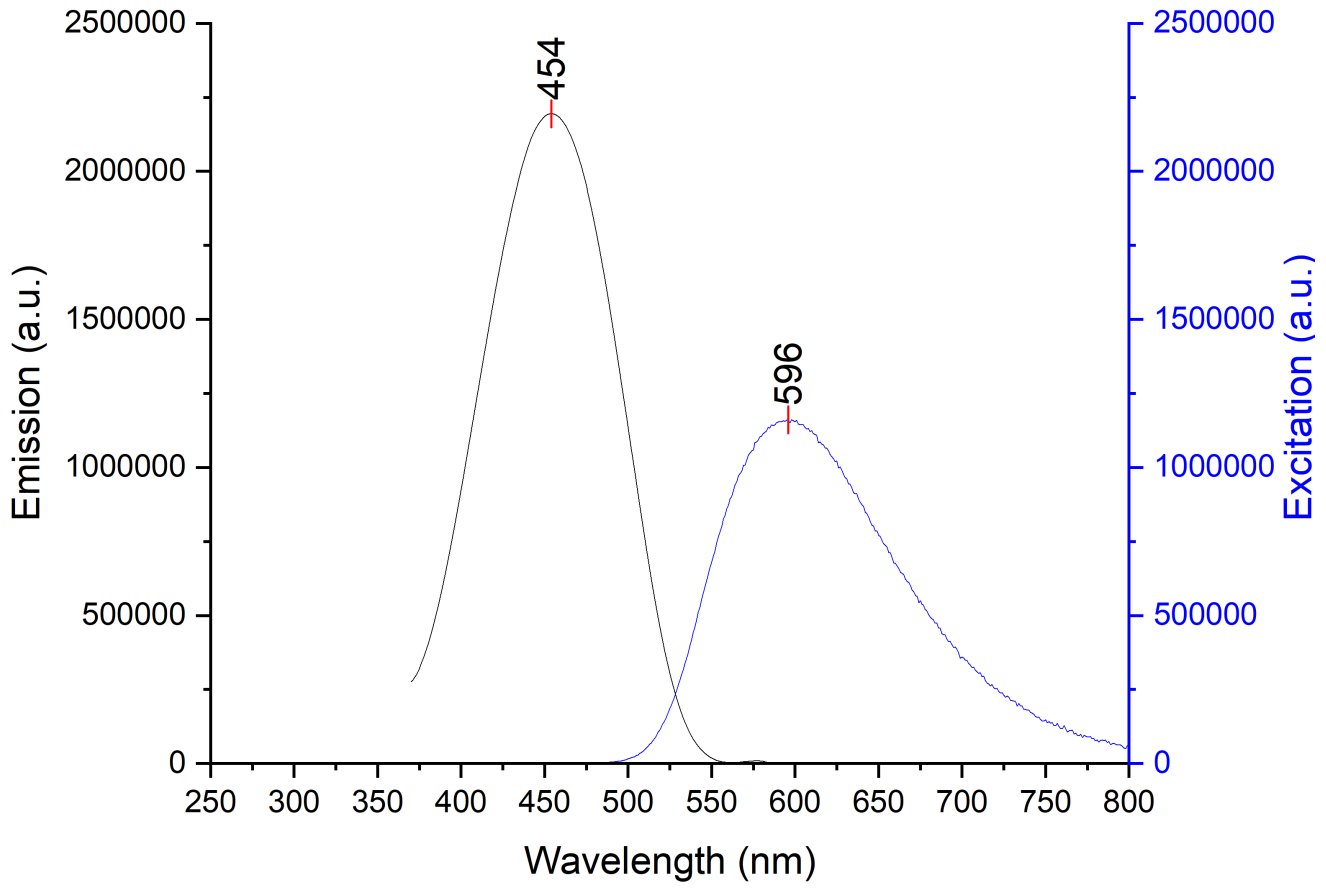

Figure 6-104. Stacked excitation (step: 1.0 nm/s, dwell time: 0.125 s, slit width: 1.0 nm) and emission (step: 1.0 nm/s, dwell time: 0.125 s, slit width: 1.0 nm) spectra of probe 2 and $B(C_6F_5)_3$ in DCM; 12.5 µM sample.

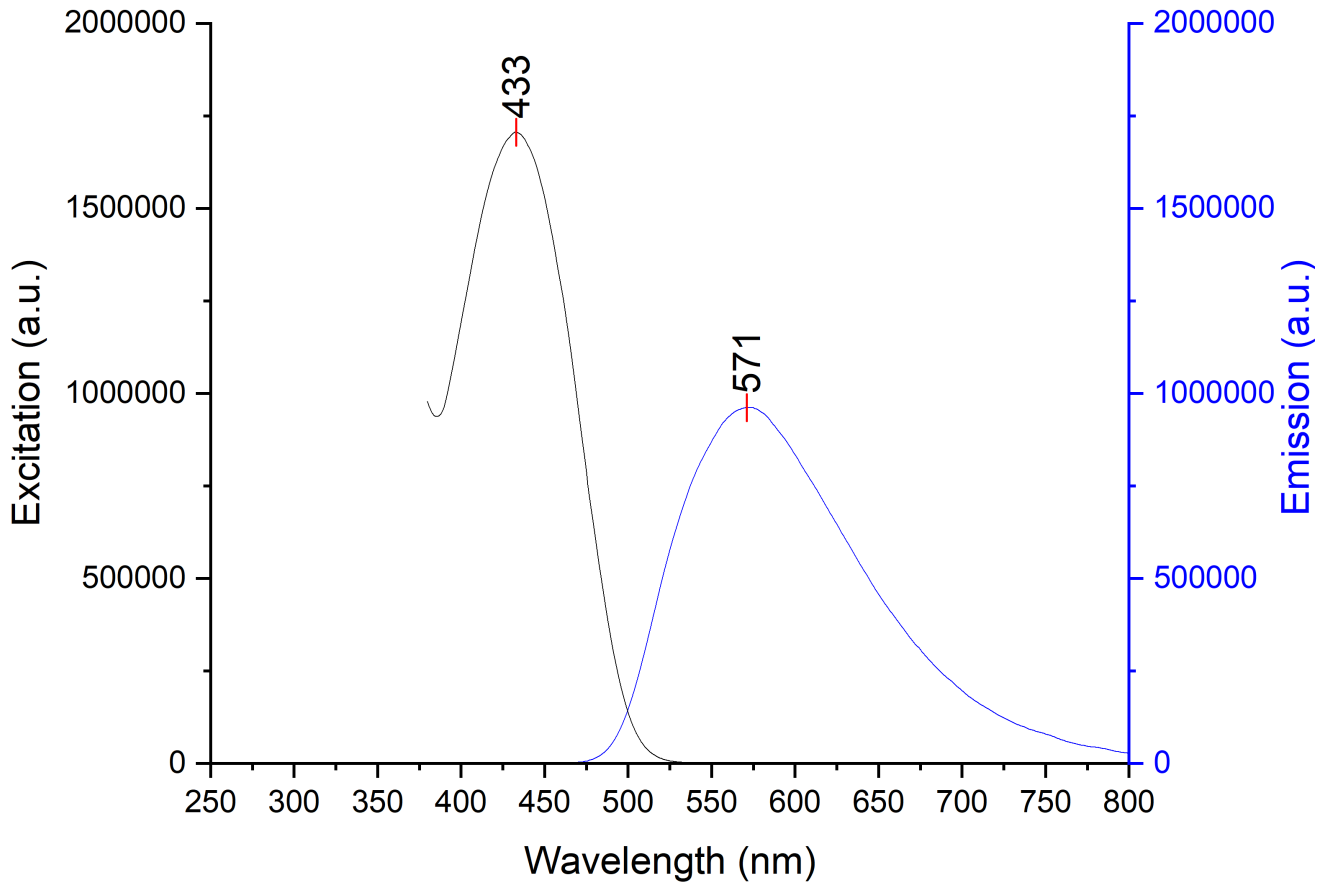

Figure 6-105. Stacked excitation (step: 1.0 nm/s, dwell time: 0.125 s, slit width: 1.0 nm) and emission (step: 1.0 nm/s, dwell time: 0.125 s, slit width: 1.0 nm) spectra of probe 7 and $B(C_6F_5)_3$ in PhCl; 12.5 µM sample.

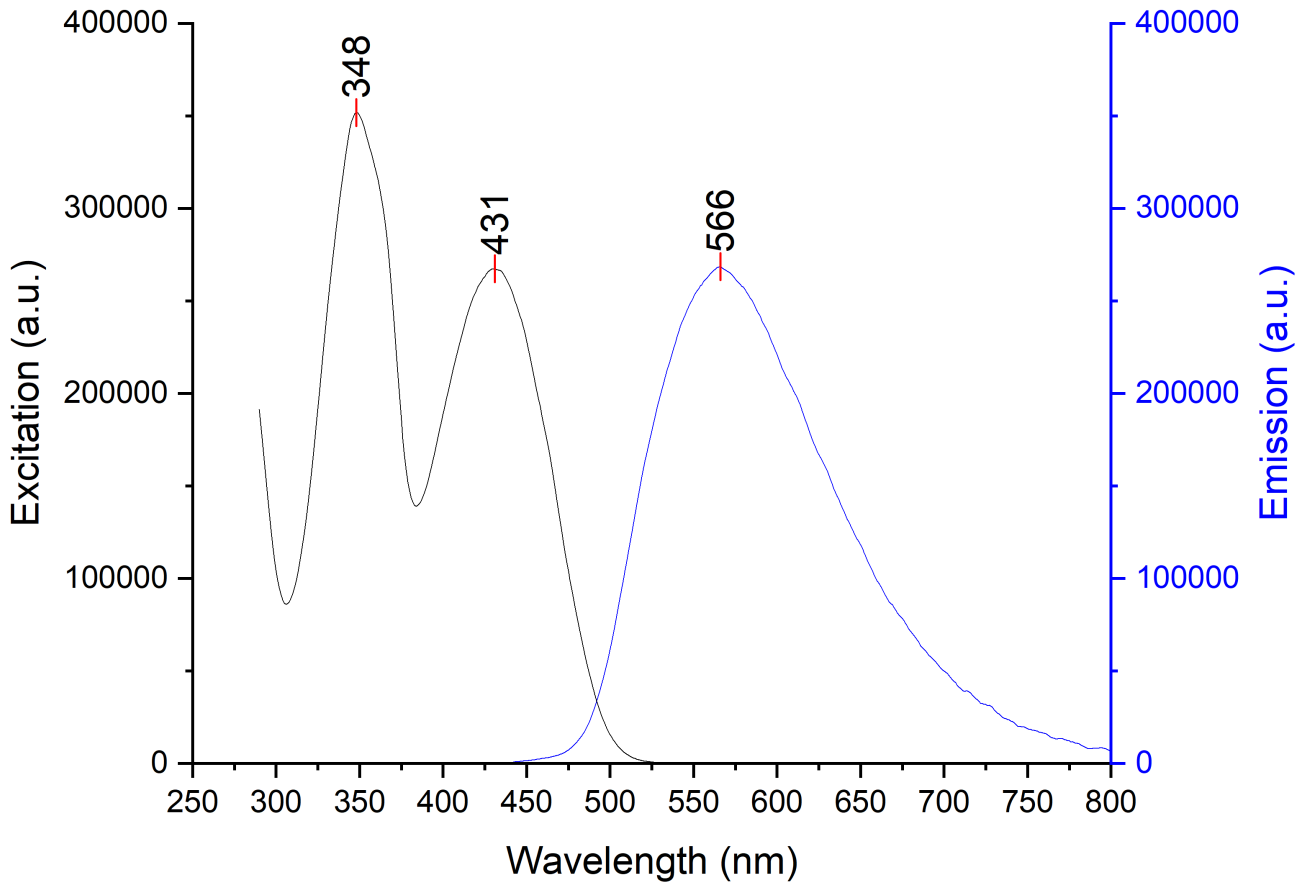

Figure 6-106. Stacked excitation (step: 1.0 nm/s, dwell time: 0.125 s, slit width: 1.0 nm) and emission (step: 1.0 nm/s, dwell time: 0.125 s, slit width: 1.0 nm) spectra of probe 7 and $B(C_6F_5)_3$ in Et_2O; 12.5 µM sample.

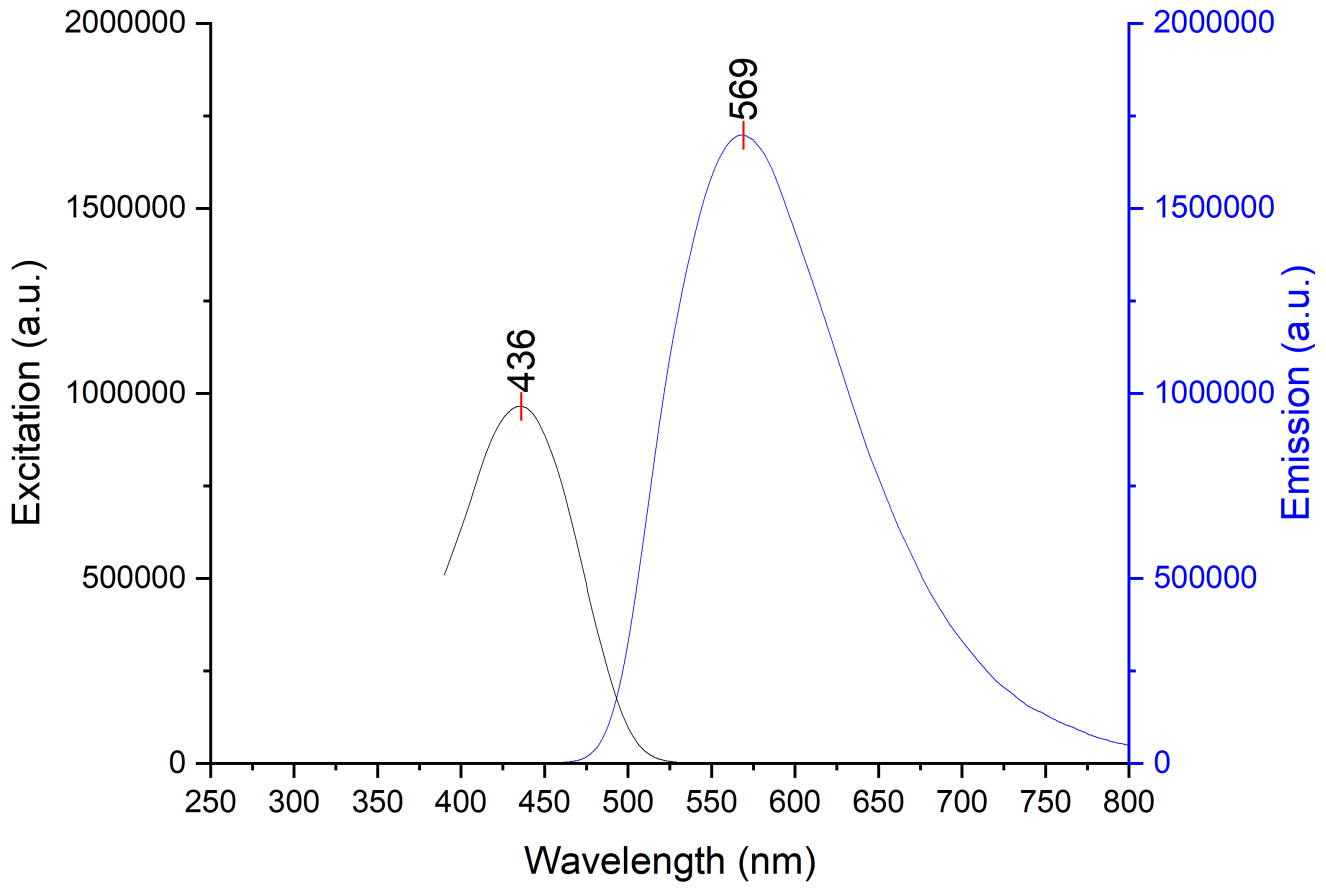

Figure 6-107. Stacked excitation (step: 1.0 nm/s, dwell time: 0.125 s, slit width: 1.0 nm) and emission (step: 1.0 nm/s, dwell time: 0.125 s, slit width: 1.0 nm) spectra of probe 7 and $B(C_6F_5)_3$ in DCM; 12.5 µM sample.

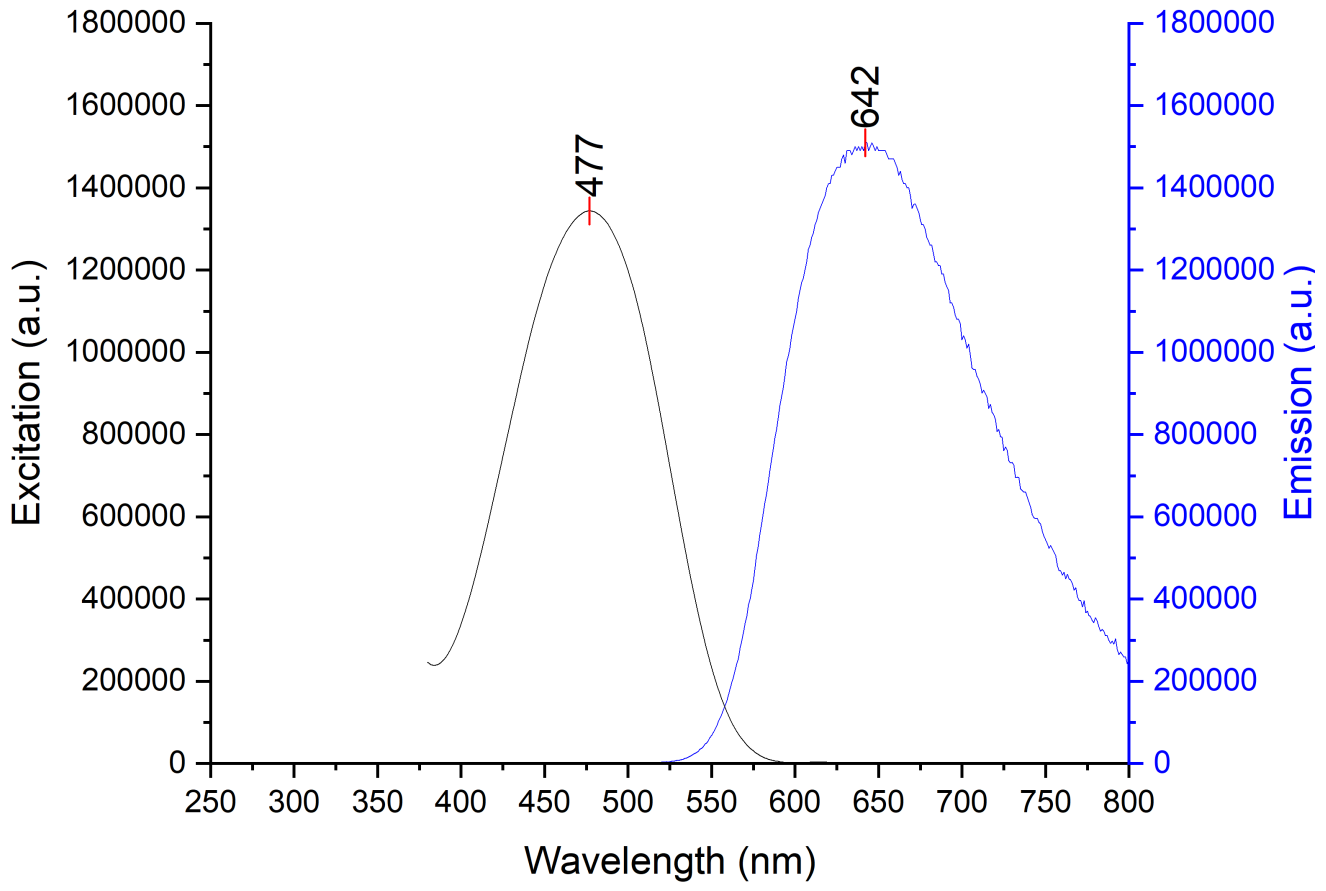

Figure 6-108. Stacked excitation (step: 1.0 nm/s, dwell time: 0.125 s, slit width: 1.0 nm) and emission (step: 1.0 nm/s, dwell time: 0.125 s, slit width: 1.0 nm) spectra of probe 8 and $B(C_6F_5)_3$ in PhCl; 12.5 µM sample.

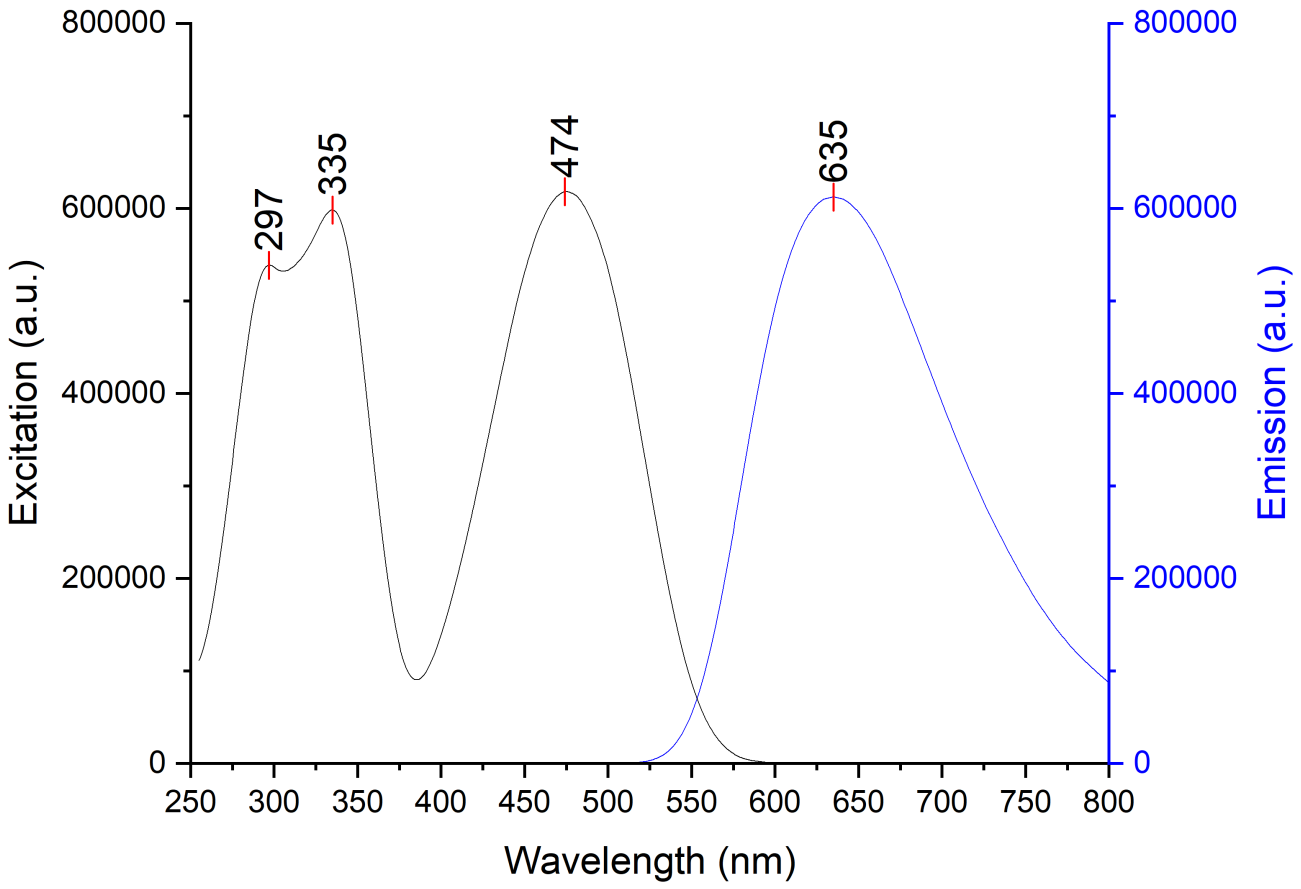

Figure 6-109. Stacked excitation (step: 1.0 nm/s, dwell time: 0.125 s, slit width: 1.0 nm) and emission (step: 1.0 nm/s, dwell time: 0.125 s, slit width: 1.0 nm) spectra of probe 8 and $B(C_6F_5)_3$ in Et_2O; 12.5 µM sample.

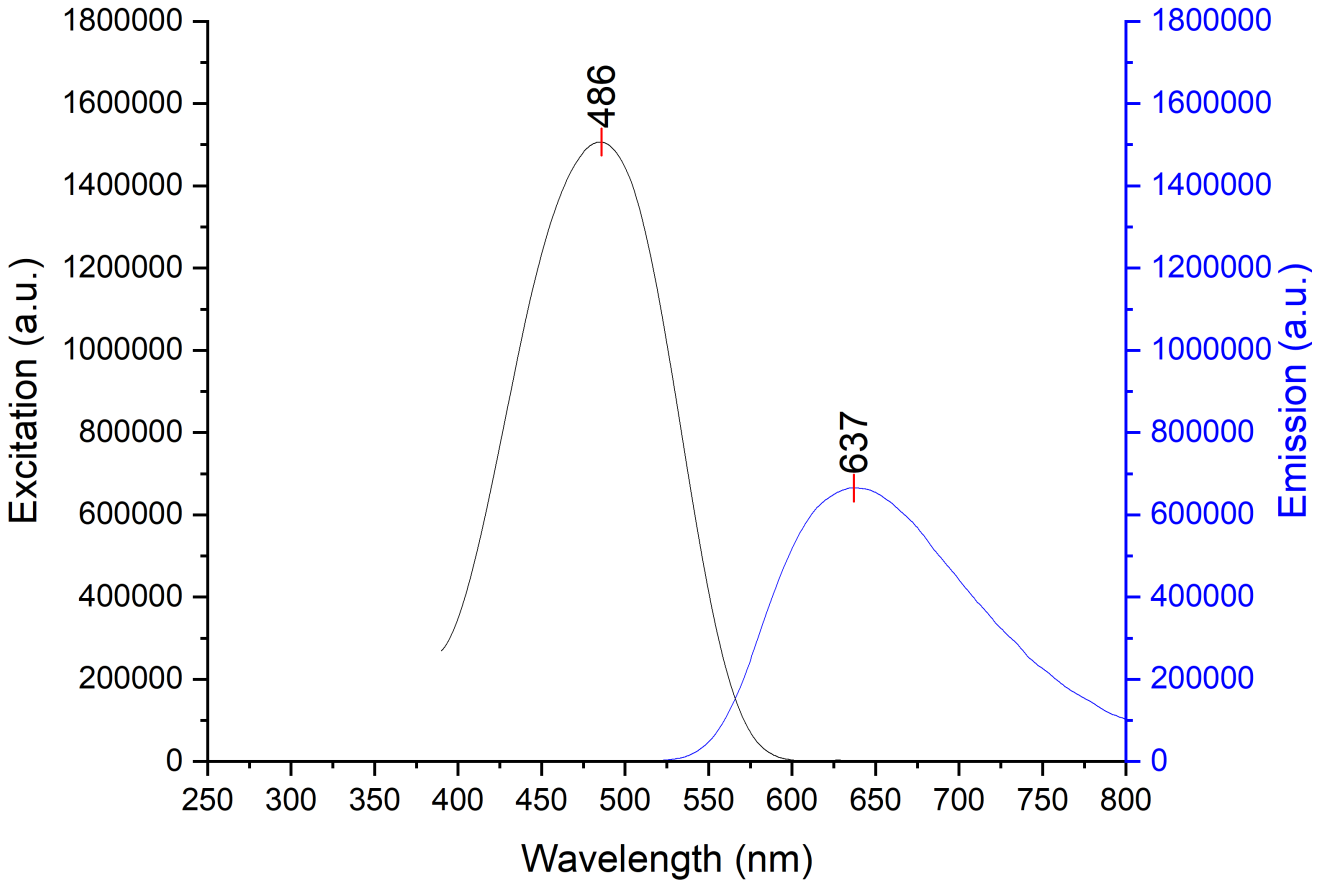

Figure 6-110. Stacked excitation (step: 1.0 nm/s, dwell time: 0.125 s, slit width: 1.0 nm) and emission (step: 1.0 nm/s, dwell time: 0.125 s, slit width: 1.0 nm) spectra of probe 8 and $B(C_6F_5)_3$ in DCM; 12.5 µM sample.

6.2.3.7. $B(p\text{-}C_6F_4H)_3$

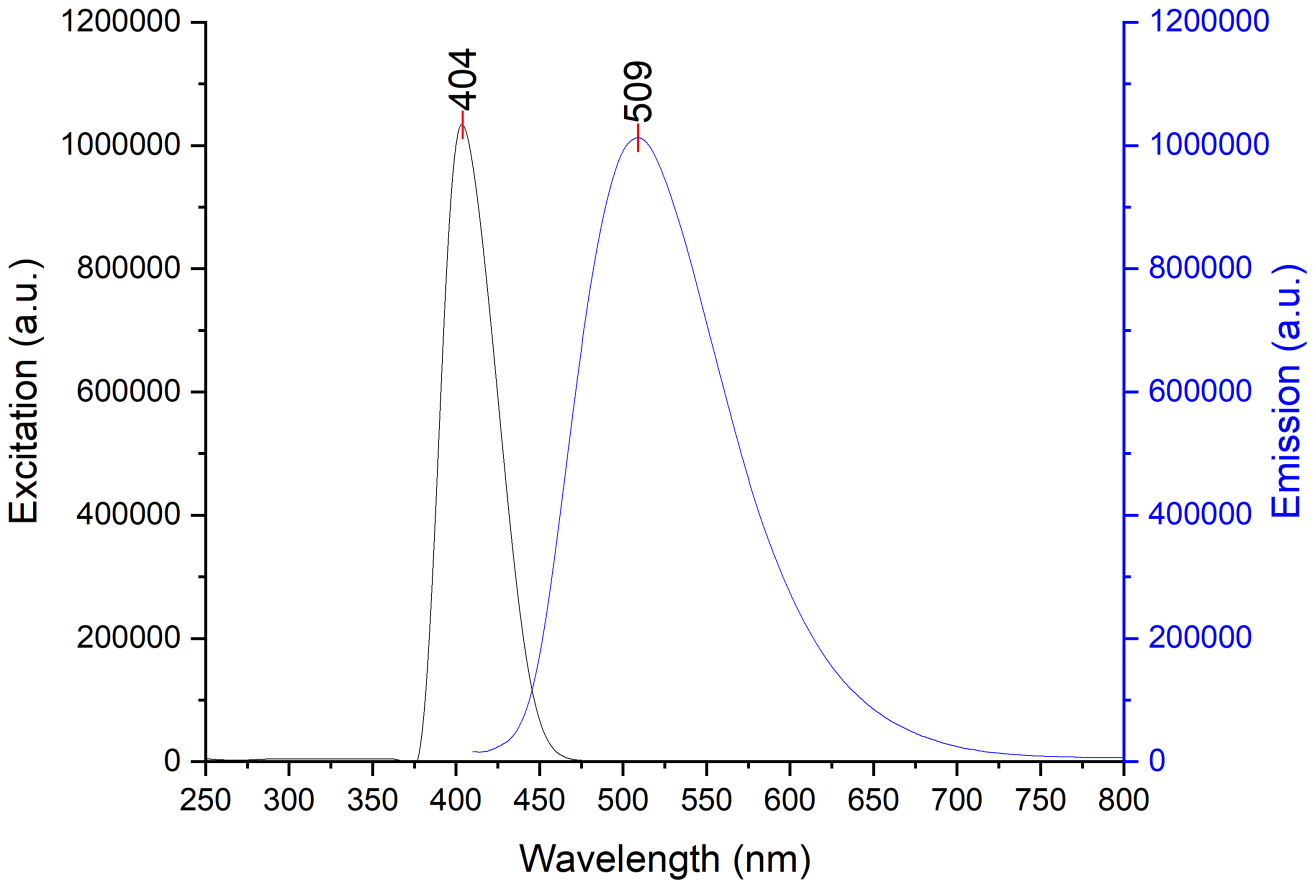

Figure 6-111. Stacked excitation (step: 1.0 nm/s, dwell time: 0.125 s, slit width: 0.80 nm) and emission (step: 1.0 nm/s, dwell time: 0.125 s, slit width: 0.80 nm) spectra of probe 1 and B(*p*-F_4-$C_6H)_3$ in PhCl; 12.5 μM sample.

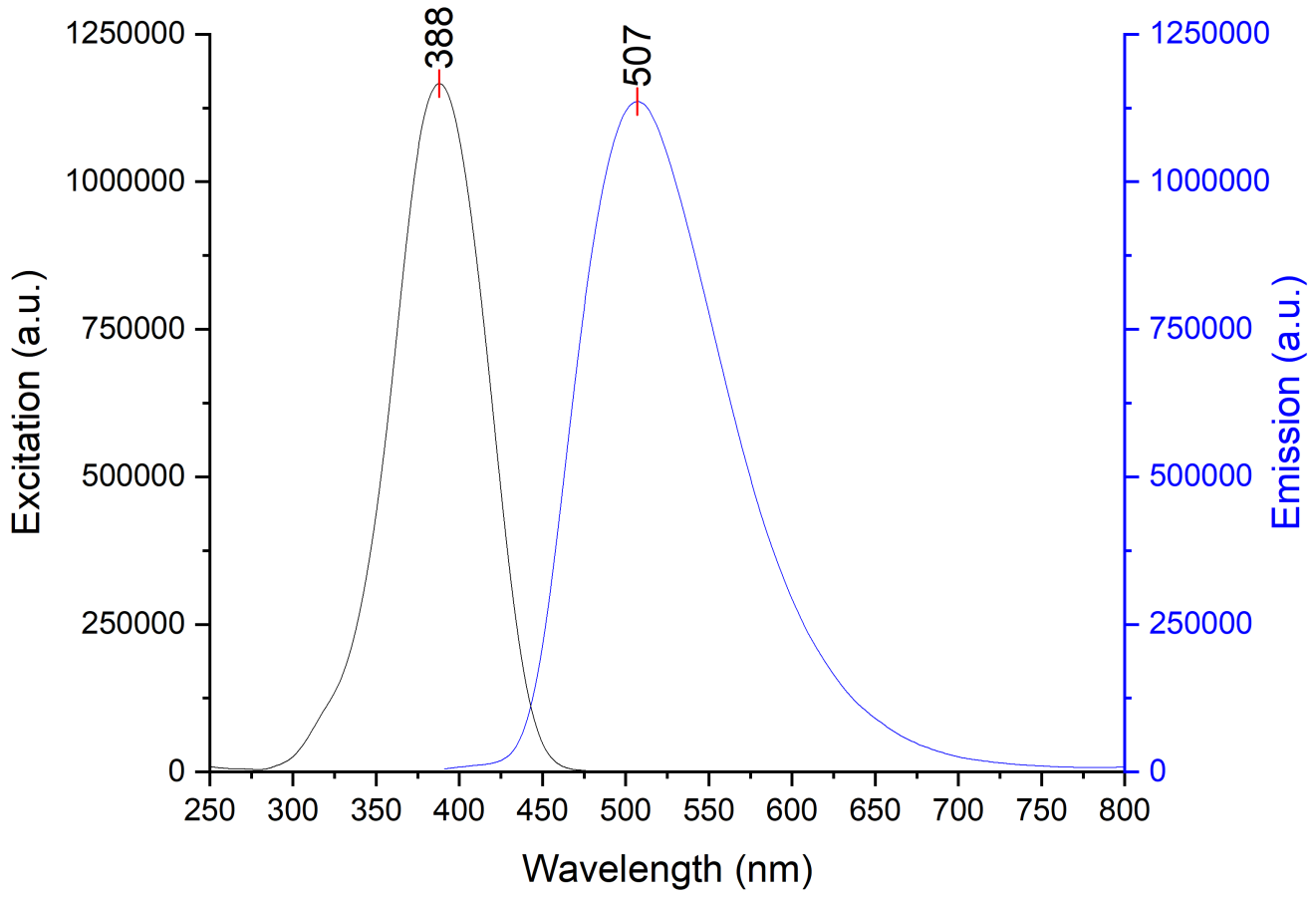

Figure 6-112. Stacked excitation (step: 1.0 nm/s, dwell time: 0.125 s, slit width: 1.0 nm) and emission (step: 1.0 nm/s, dwell time: 0.125 s, slit width: 1.0 nm spectra of probe 1 and B(*p*-F_4-$C_6H)_3$ in Et_2O; 12.5 μM sample.

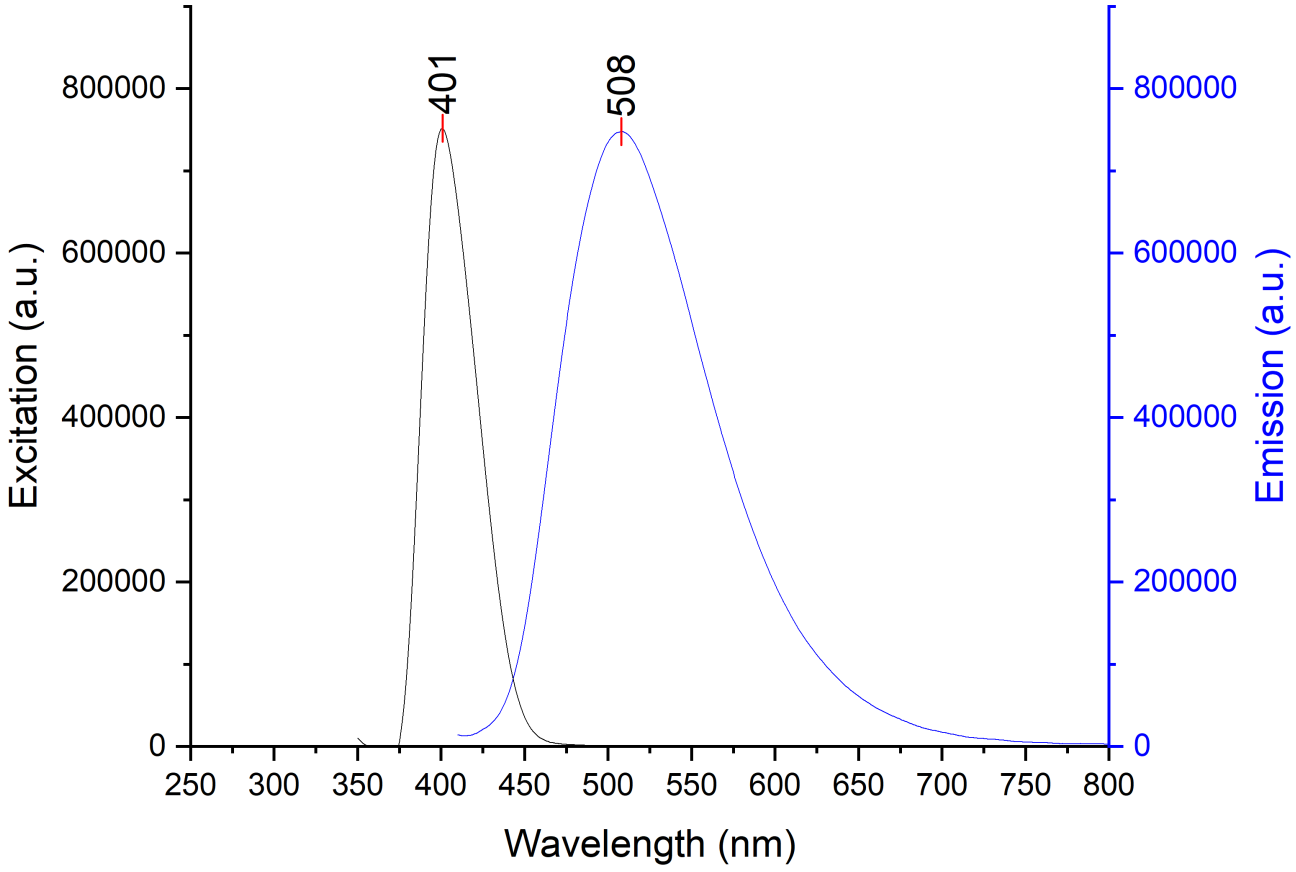

Figure 6-113. Stacked excitation (step: 1.0 nm/s, dwell time: 0.125 s, slit width: 0.80 nm) and emission (step: 1.0 nm/s, dwell time: 0.125 s, slit width: 0.80 nm) spectra of probe 1 and B B(p-F_4-C_6H)$_3$ in DCM; 12.5 µM sample.

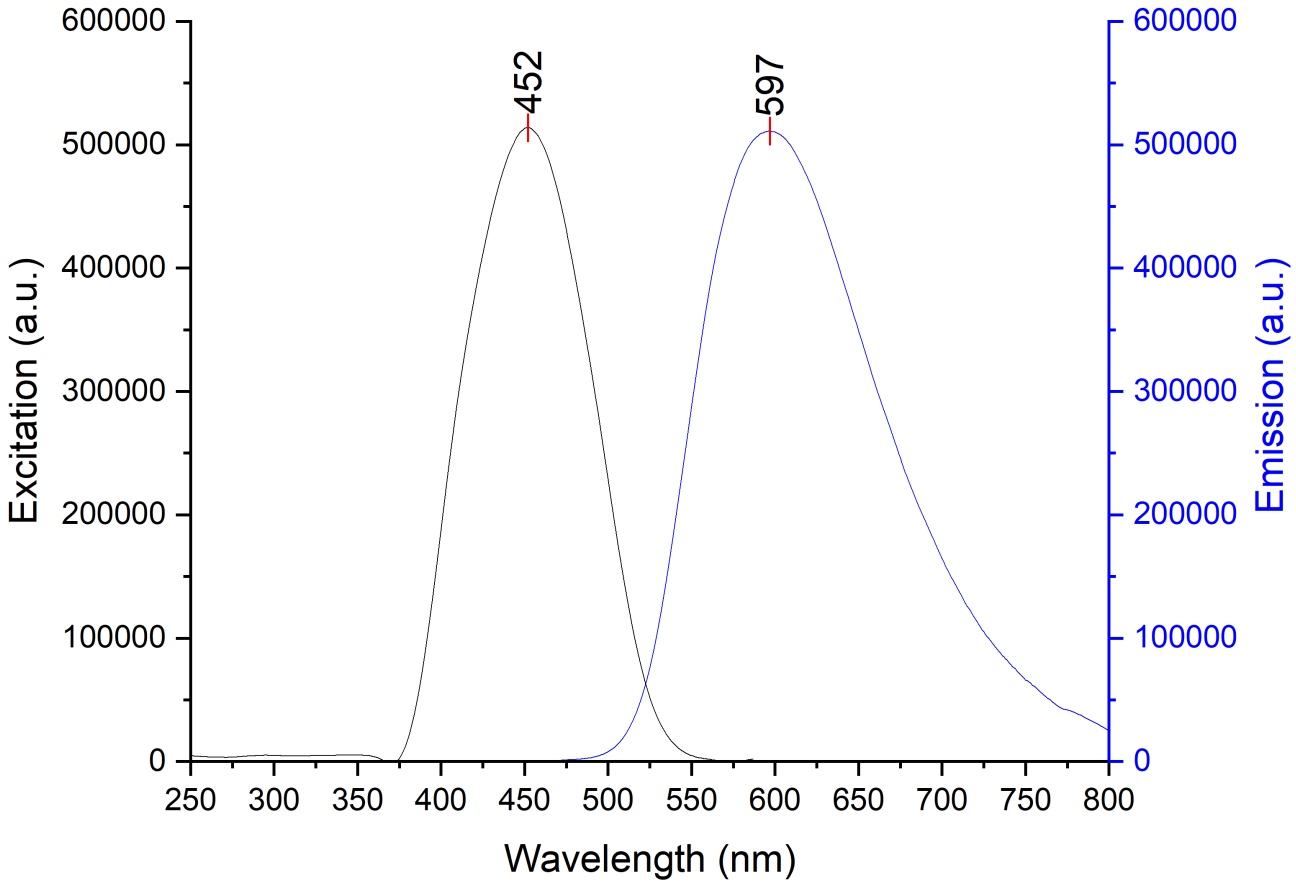

Figure 6-114. Stacked excitation (step: 1.0 nm/s, dwell time: 0.125 s, slit width: 0.80 nm) and emission (step: 1.0 nm/s, dwell time: 0.125 s, slit width: 0.80 nm) spectra of probe 2 and B(p-F_4-C_6H)$_3$ in PhCl; 12.5 μM sample.

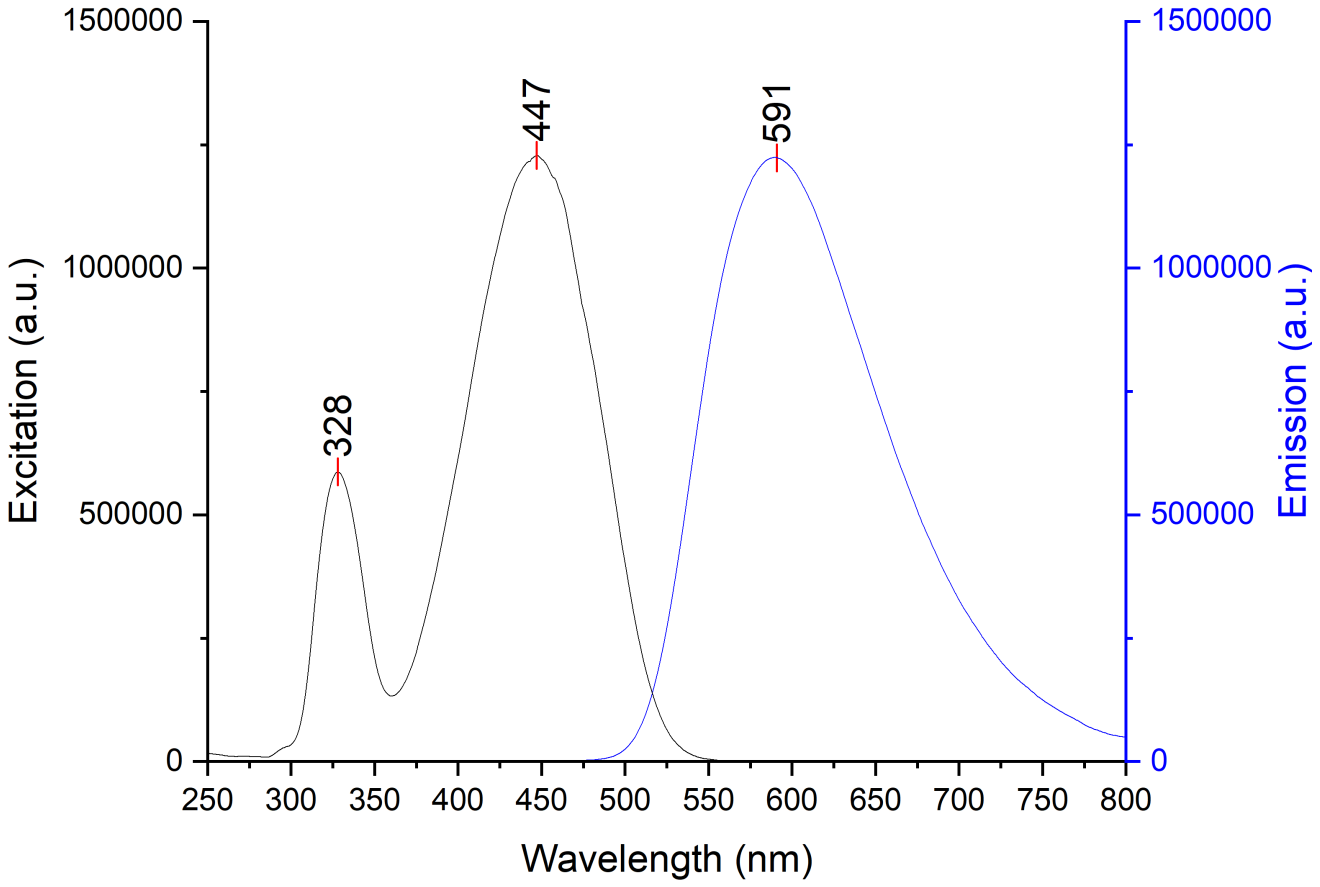

Figure 6-115. Stacked excitation (step: 1.0 nm/s, dwell time: 0.125 s, slit width: 1.0 nm) and emission (step: 1.0 nm/s, dwell time: 0.125 s, slit width: 1.0 nm) spectra of probe 2 and B(*p*-F_4-$C_6H)_3$ in Et_2O; 12.5 μM sample.

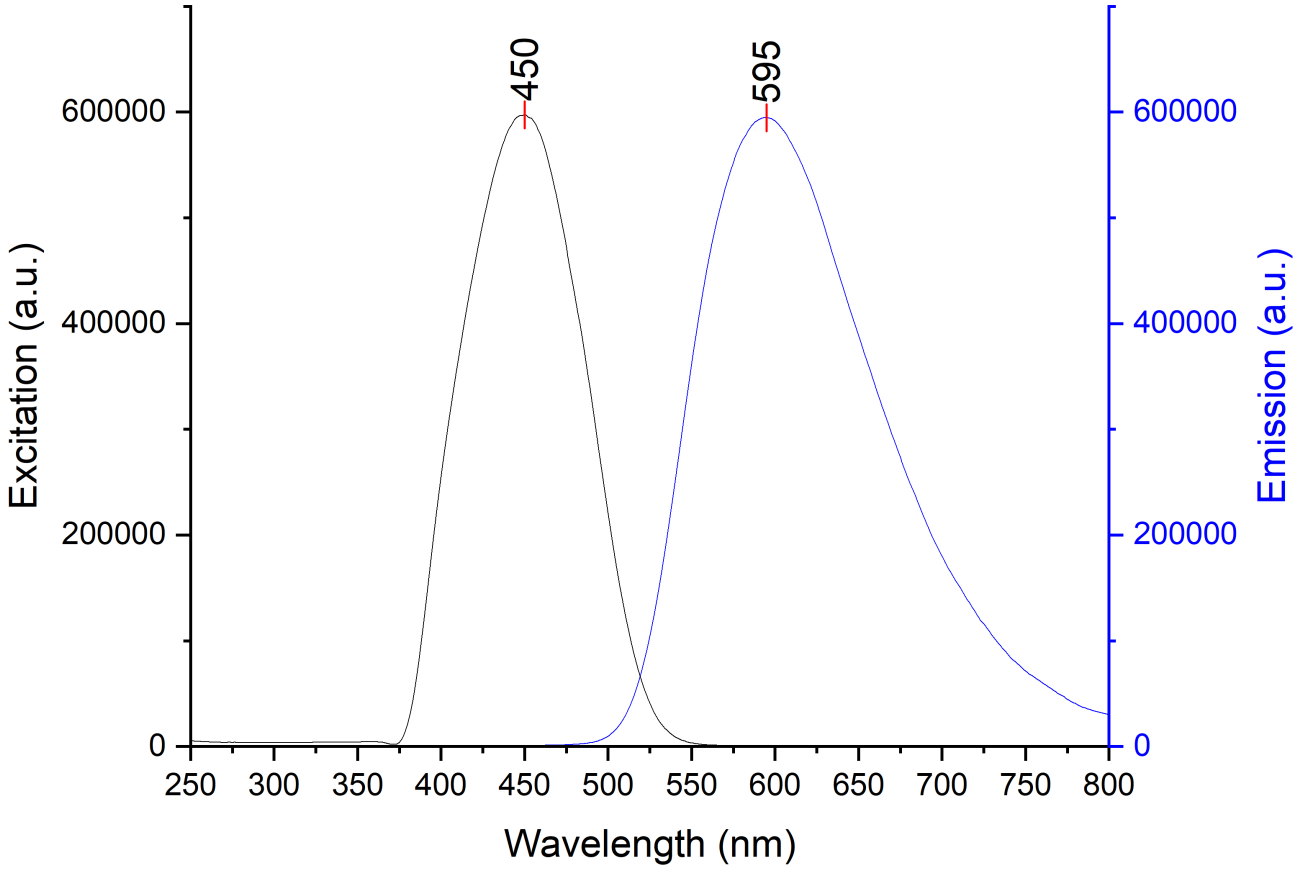

Figure 6-116. Stacked excitation (step: 1.0 nm/s, dwell time: 0.125 s, slit width: 0.80 nm) and emission (step: 1.0 nm/s, dwell time: 0.125 s, slit width: 0.80 nm) spectra of probe 2 and B(*p*-F_4-$C_6H)_3$ in DCM; 12.5 µM sample.

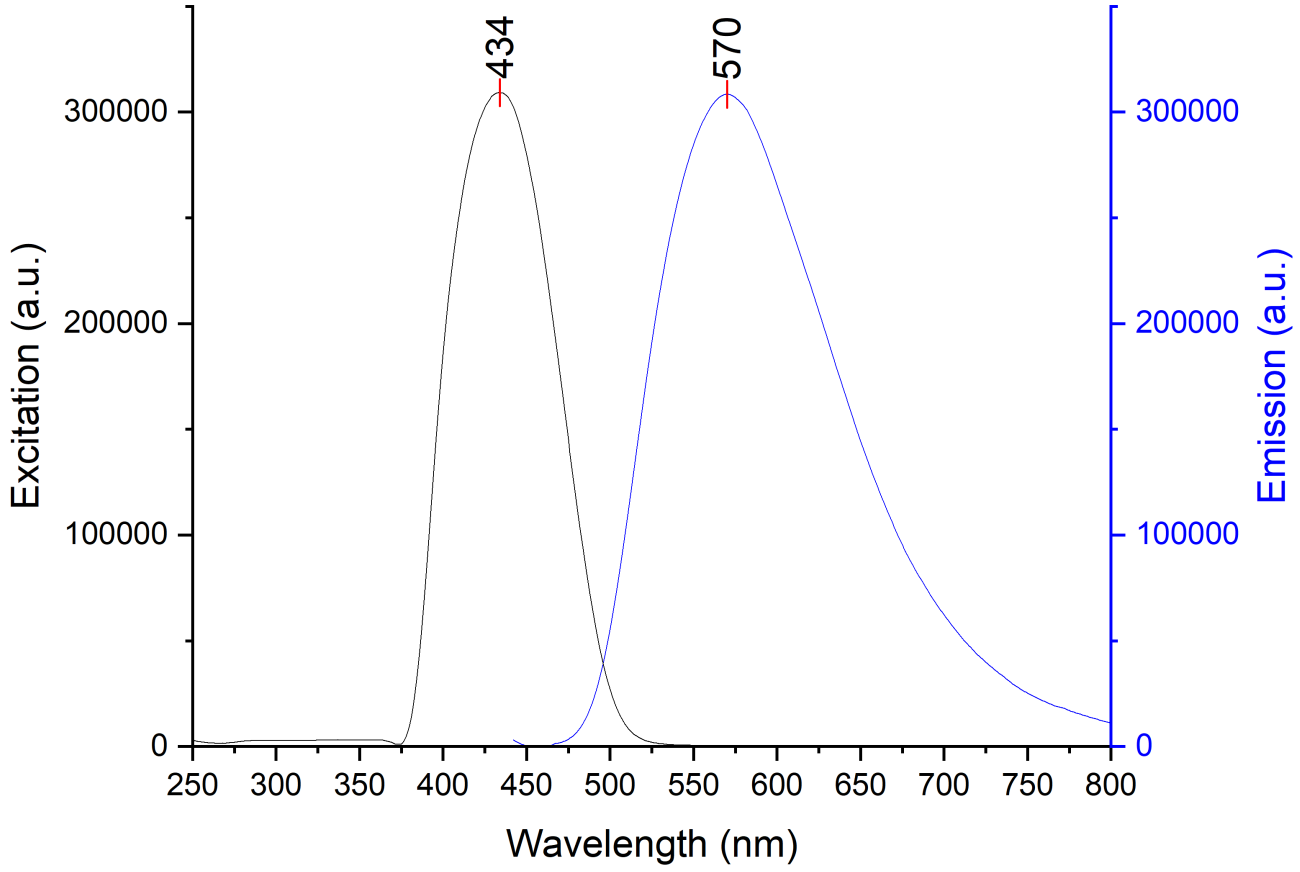

Figure 6-117. Stacked excitation (step: 1.0 nm/s, dwell time: 0.125 s, slit width: 0.80 nm) and emission (step: 1.0 nm/s, dwell time: 0.125 s, slit width: 0.80 nm) spectra of probe 7 and B(*p*-F_4-C_6H)$_3$ in PhCl; 12.5 μM sample.

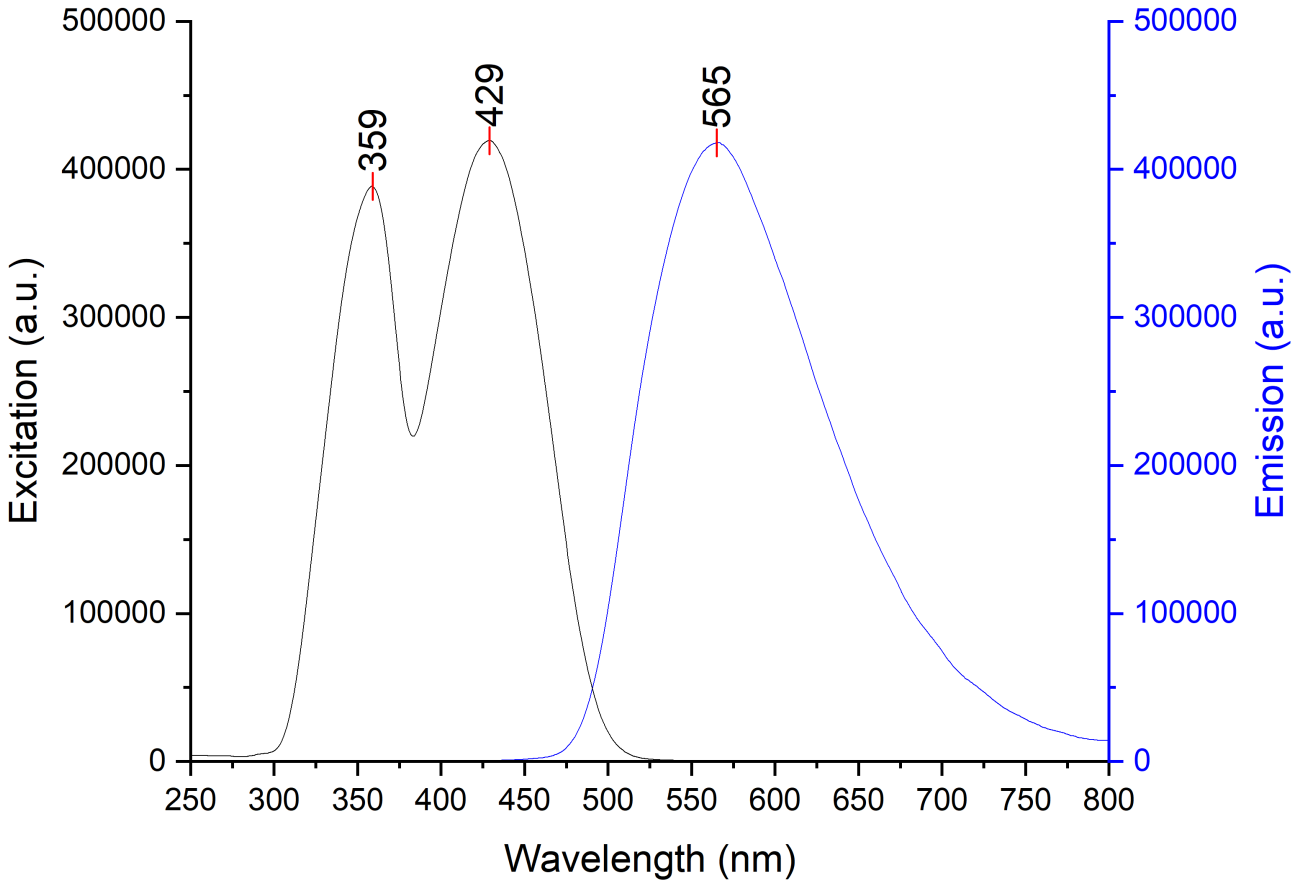

Figure 6-118. Stacked excitation (step: 1.0 nm/s, dwell time: 0.125 s, slit width: 1.0 nm) and emission (step: 1.0 nm/s, dwell time: 0.125 s, slit width: 1.0 nm) spectra of probe 7 and B(*p*-F_4-$C_6H)_3$ in Et_2O; 12.5 μM sample.

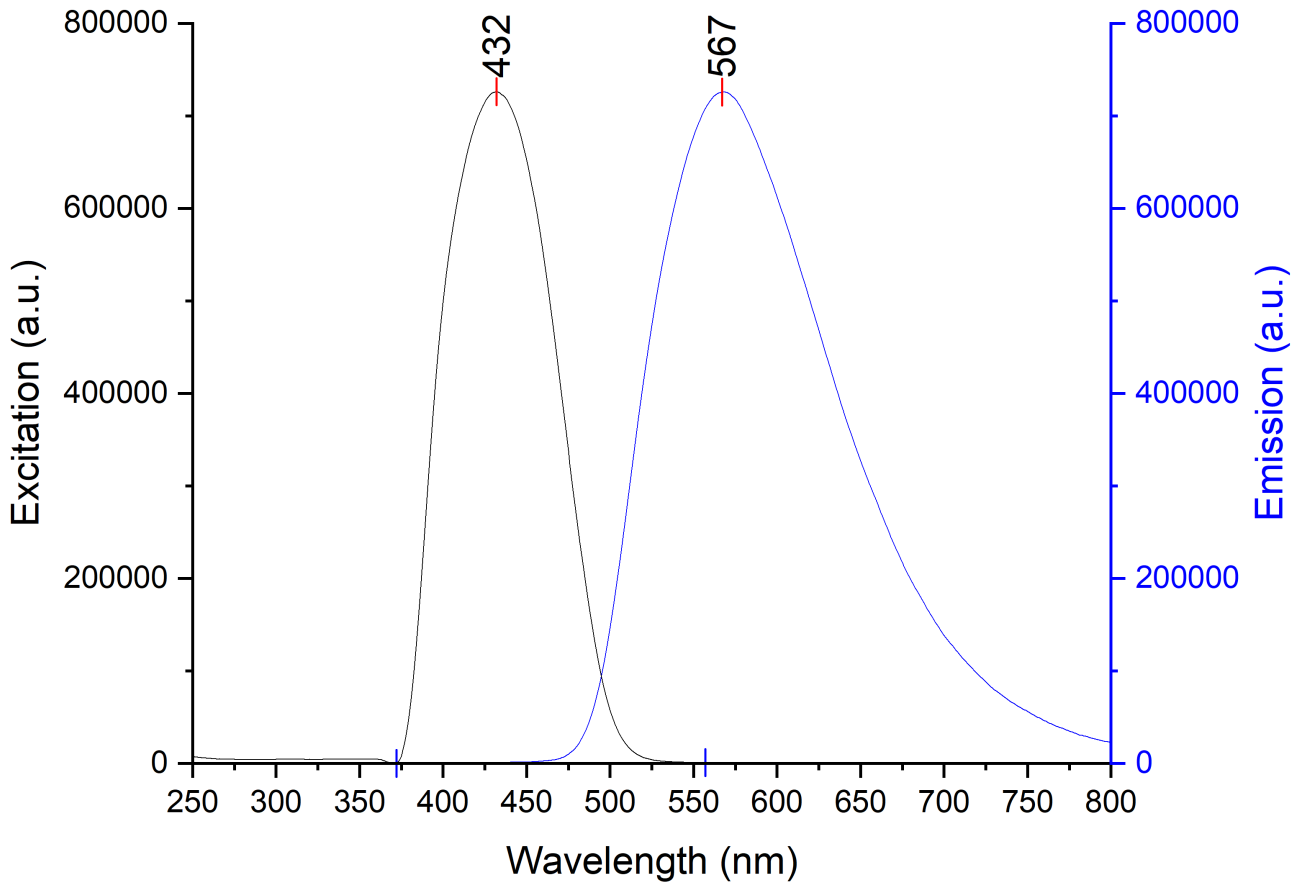

Figure 6-119. Stacked excitation (step: 1.0 nm/s, dwell time: 0.125 s, slit width: 0.80 nm) and emission (step: 1.0 nm/s, dwell time: 0.125 s, slit width: 0.80 nm) spectra of probe 7 and B(*p*-F_4-$C_6H)_3$ in DCM; 12.5 µM sample.

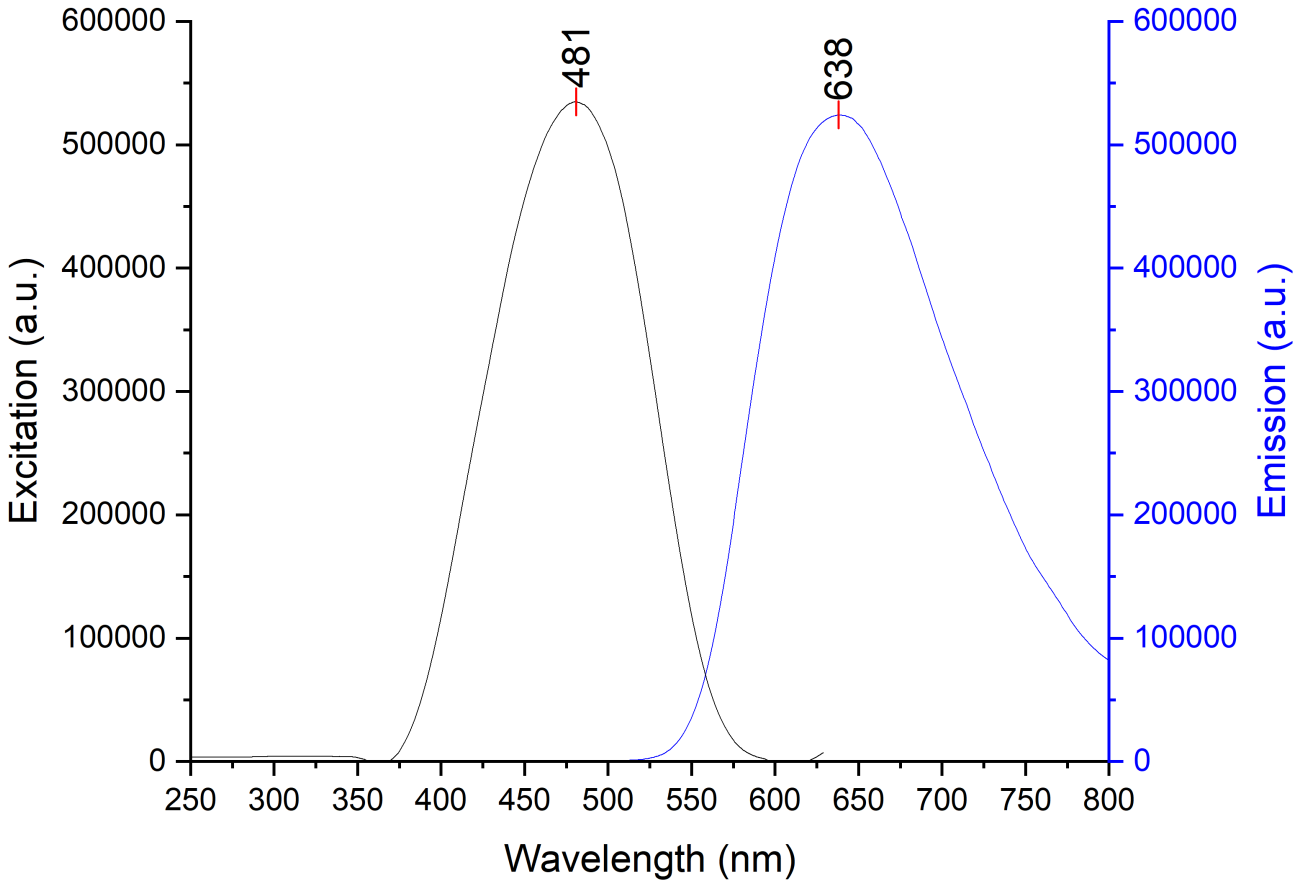

Figure 6-120. Stacked excitation (step: 1.0 nm/s, dwell time: 0.125 s, slit width: 0.80 nm) and emission (step: 1.0 nm/s, dwell time: 0.125 s, slit width: 0.80 nm) spectra of probe 8 and B(*p*-F_4-C_6H)$_3$ in PhCl; 12.5 μM sample.

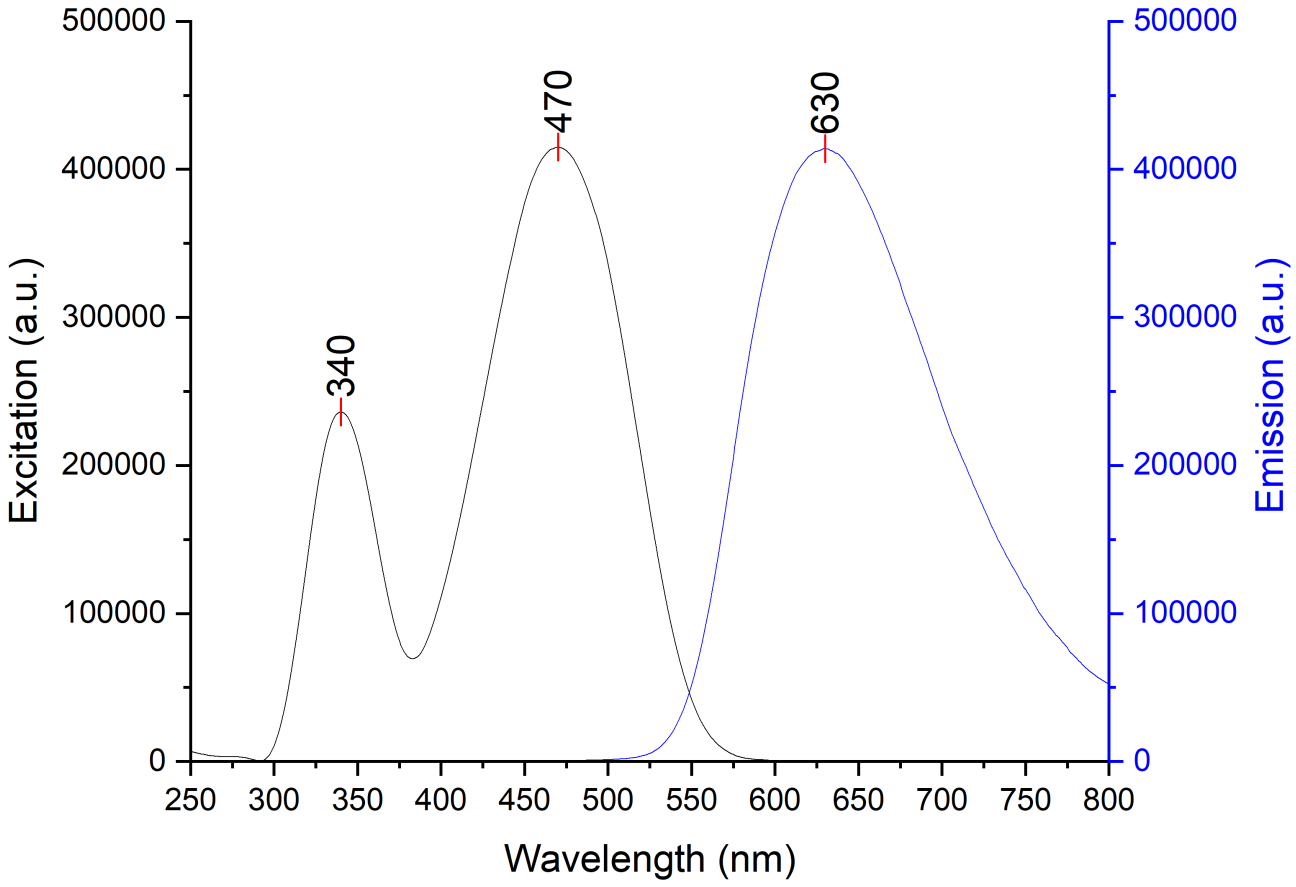

Figure 6-121. Stacked excitation (step: 1.0 nm/s, dwell time: 0.125 s, slit width: 1.0 nm) and emission (step: 1.0 nm/s, dwell time: 0.125 s, slit width: 1.0 nm) spectra of probe 8 and B(*p*-F_4-$C_6H)_3$ in Et_2O; 12.5 μM sample.

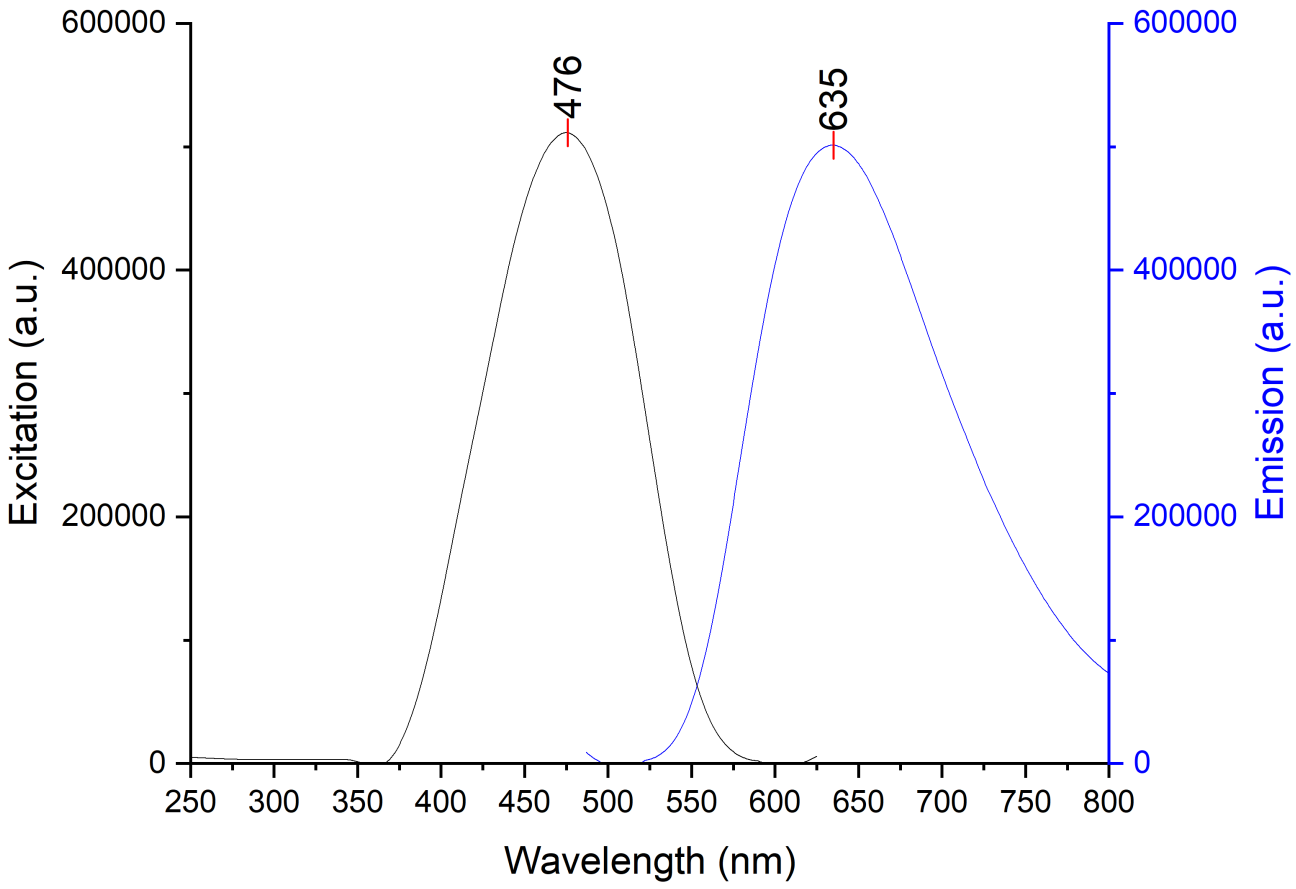

Figure 6-122. Stacked excitation (step: 1.0 nm/s, dwell time: 0.125 s, slit width: 0.80 nm) and emission (step: 1.0 nm/s, dwell time: 0.125 s, slit width: 0.80 nm) spectra of probe 8 and B(*p*-F_4-$C_6H)_3$ in DCM; 12.5 µM sample.

6.2.3.8. $In(OTf)_3$

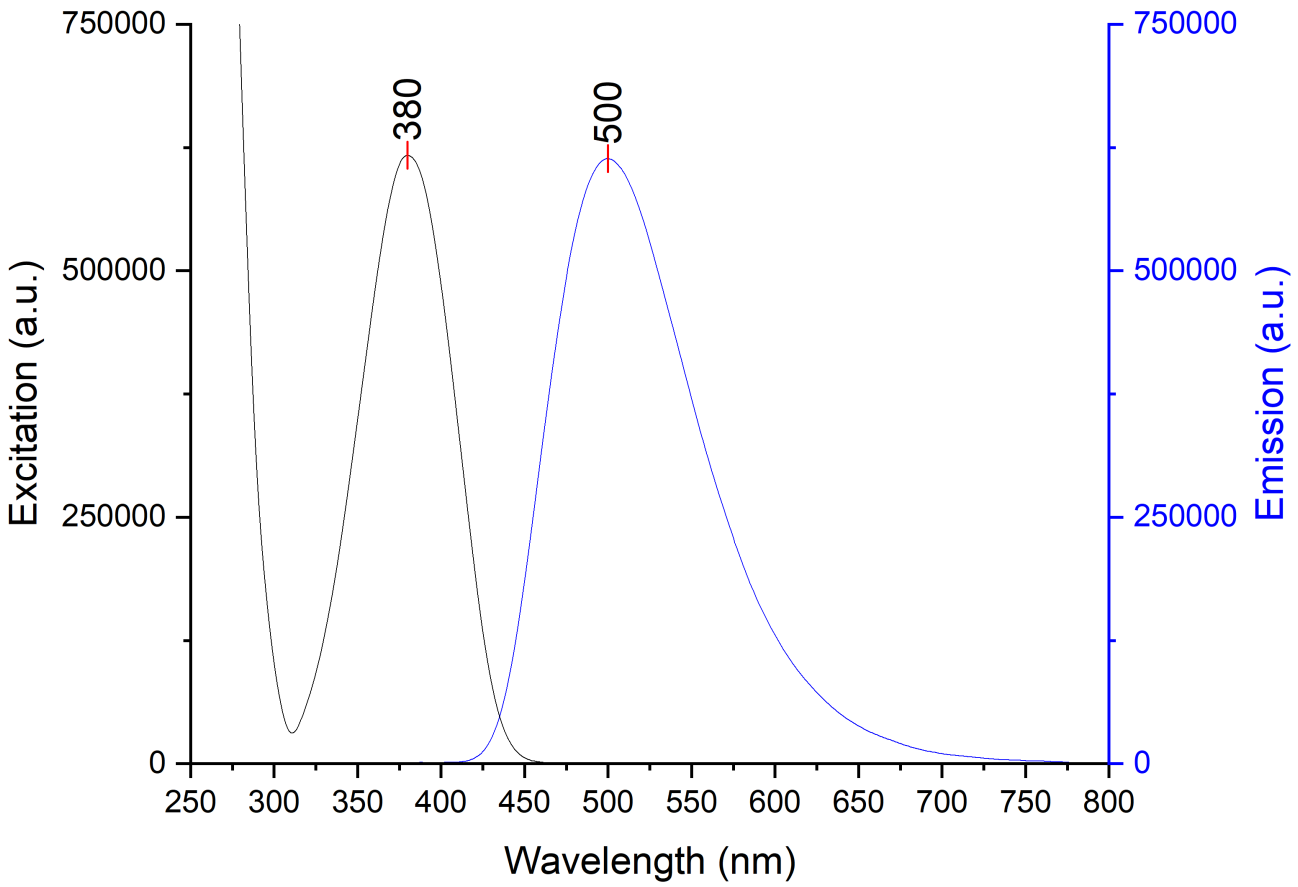

Figure 6-123. Stacked excitation (step: 1.0 nm/s, dwell time: 0.125 s, slit width: 1.0 nm) and emission (step: 1.0 nm/s, dwell time: 0.125 s, slit width: 1.0 nm) spectra of probe 1 and $In(OTf)_3$ in MeCN; 12.5 μM sample.

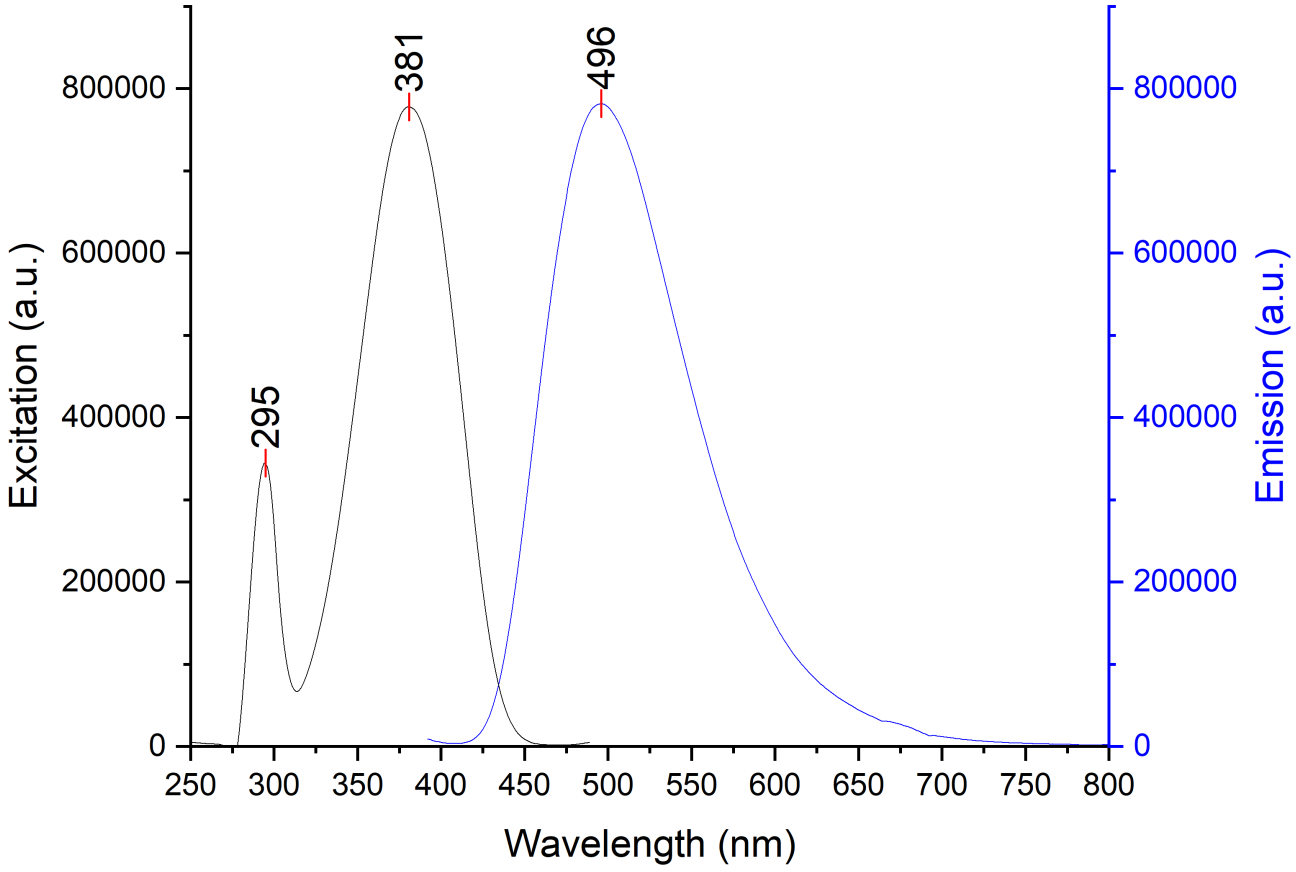

Figure 6-124. Stacked excitation (step: 1.0 nm/s, dwell time: 0.125 s, slit width: 1.0 nm) and emission (step: 1.0 nm/s, dwell time: 0.125 s, slit width: 1.0 nm) spectra of probe 1 and $In(OTf)_3$ in PhCl; 12.5 µM sample.

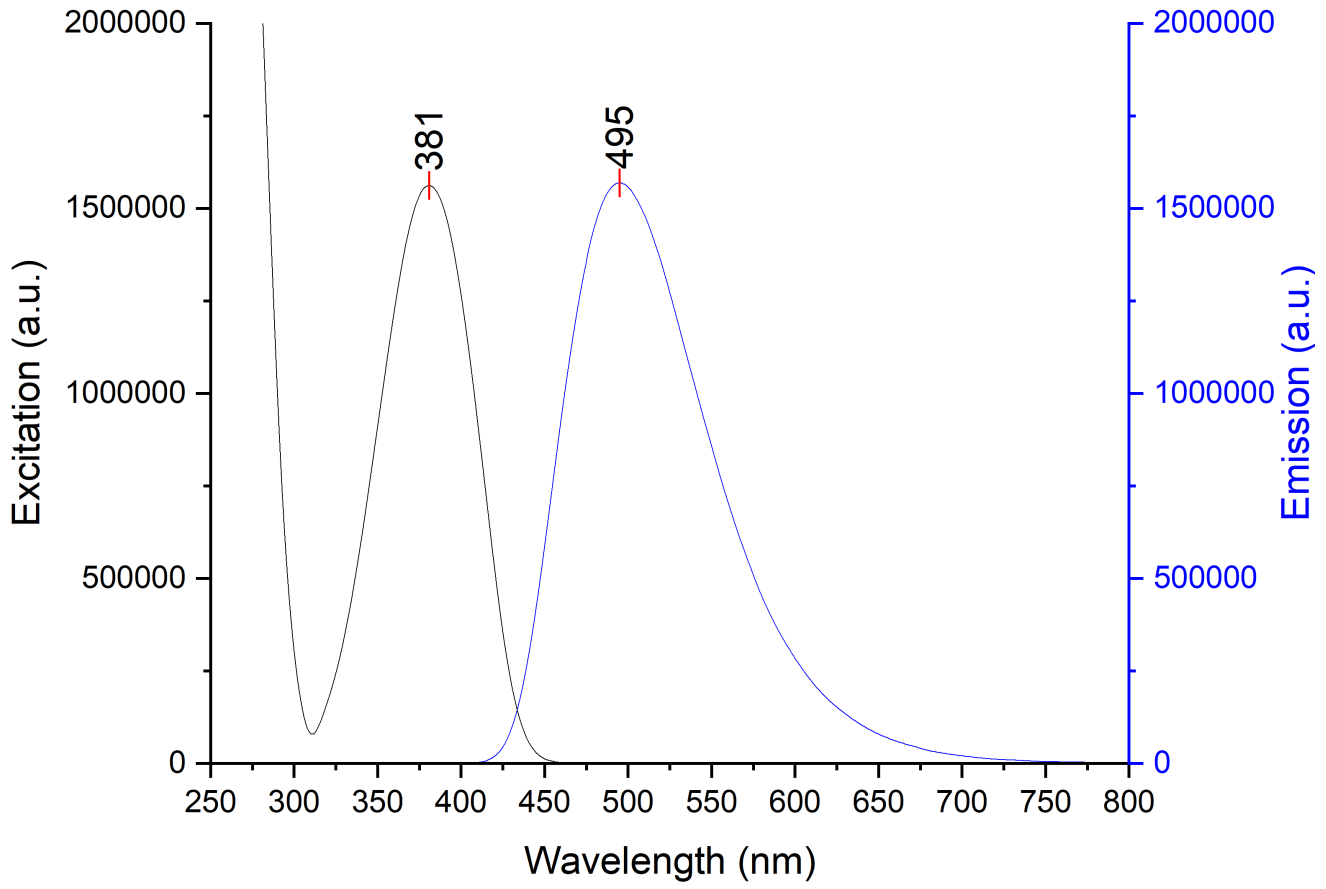

Figure 6-125. Stacked excitation (step: 1.0 nm/s, dwell time: 0.125 s, slit width: 1.0 nm) and emission (step: 1.0 nm/s, dwell time: 0.125 s, slit width: 1.0 nm) spectra of probe 1 and $In(OTf)_3$ in Et_2O; 12.5 μM sample.

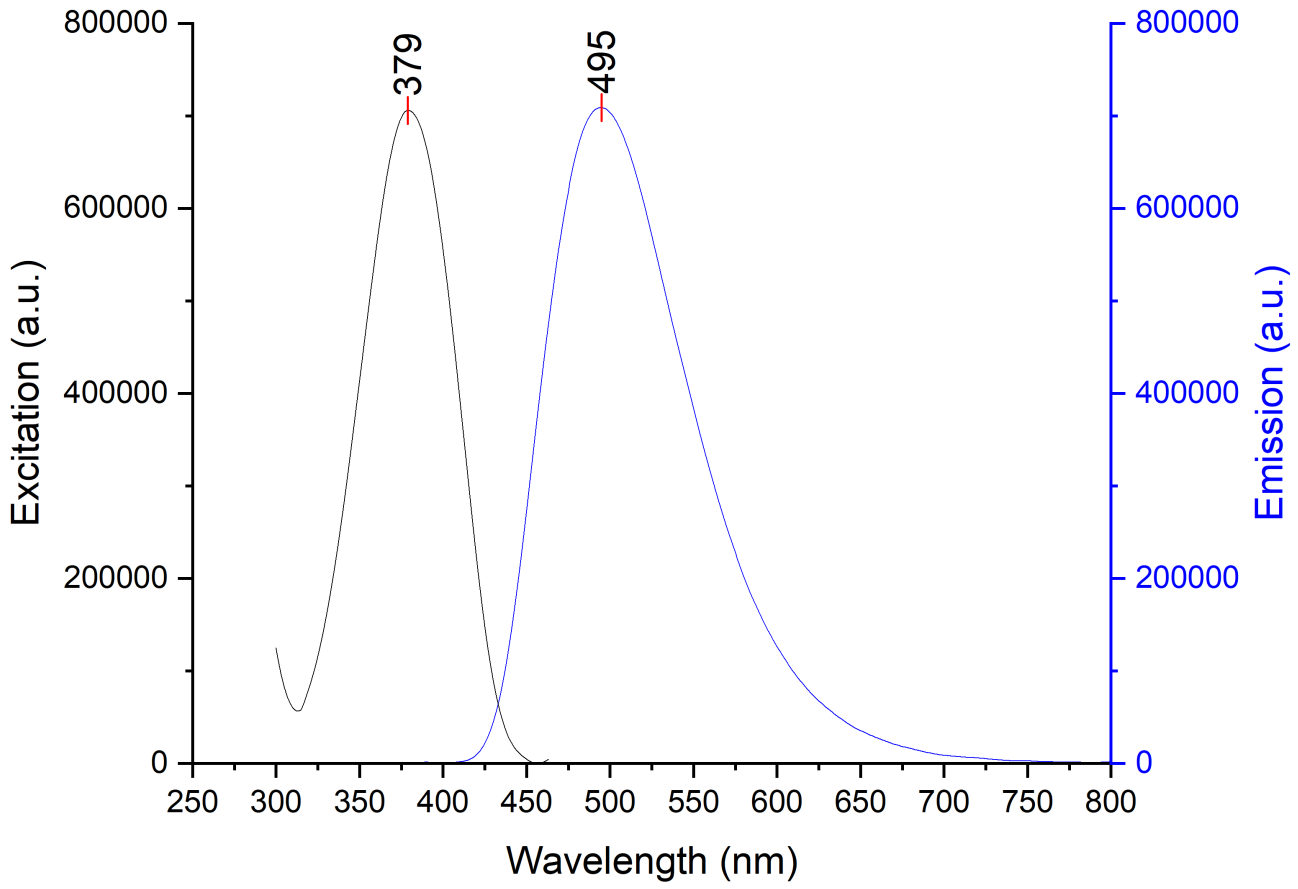

Figure 6-126. Stacked excitation (step: 1.0 nm/s, dwell time: 0.125 s, slit width: 1.0 nm) and emission (step: 1.0 nm/s, dwell time: 0.125 s, slit width: 1.0 nm) spectra of probe 1 and $In(OTf)_3$ in DCM; 12.5 μM sample.

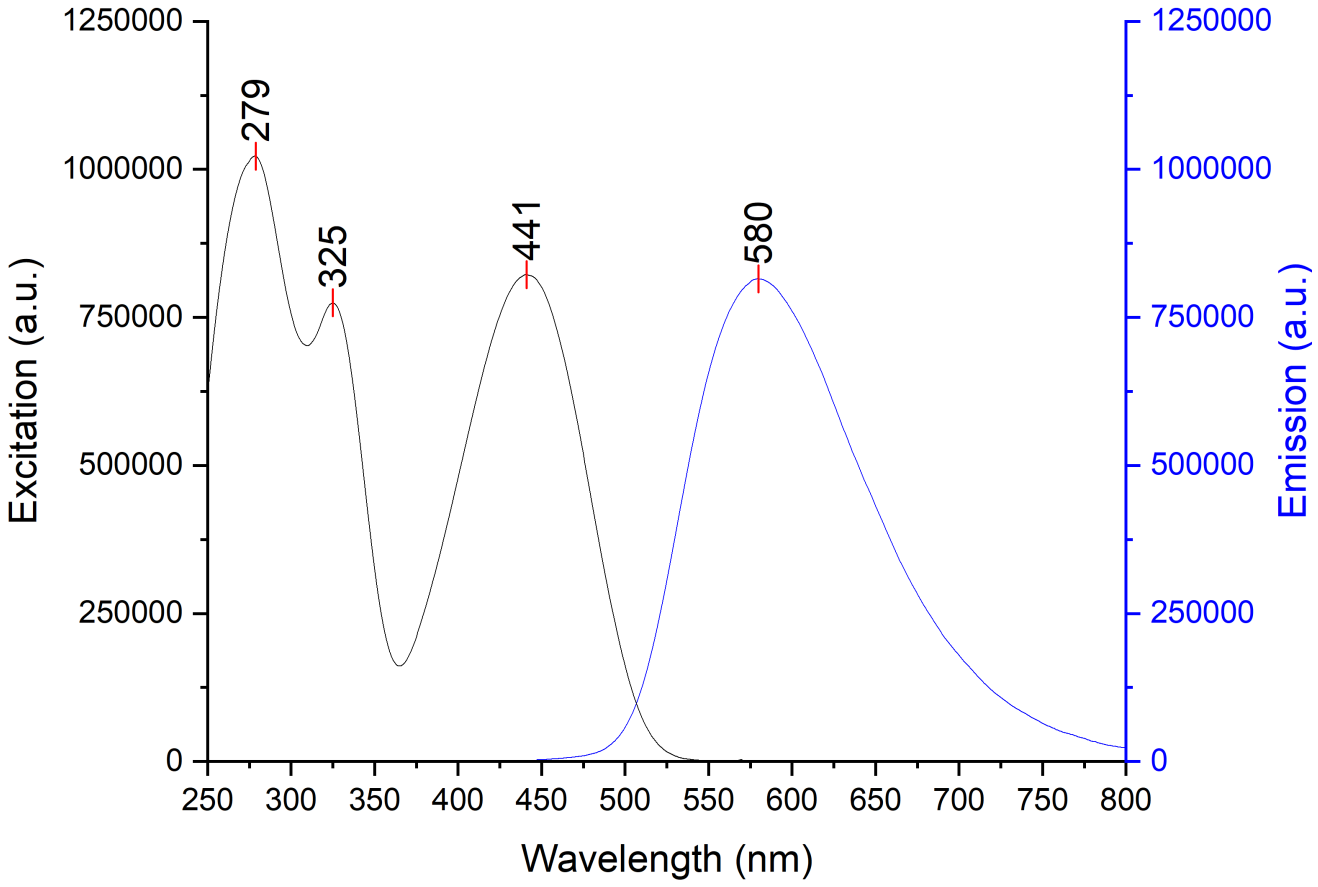

Figure 6-127. Stacked excitation (step: 1.0 nm/s, dwell time: 0.125 s, slit width: 1.0 nm) and emission (step: 1.0 nm/s, dwell time: 0.125 s, slit width: 1.0 nm) spectra of probe 2 and $In(OTf)_3$ in MeCN; 12.5 μM sample.

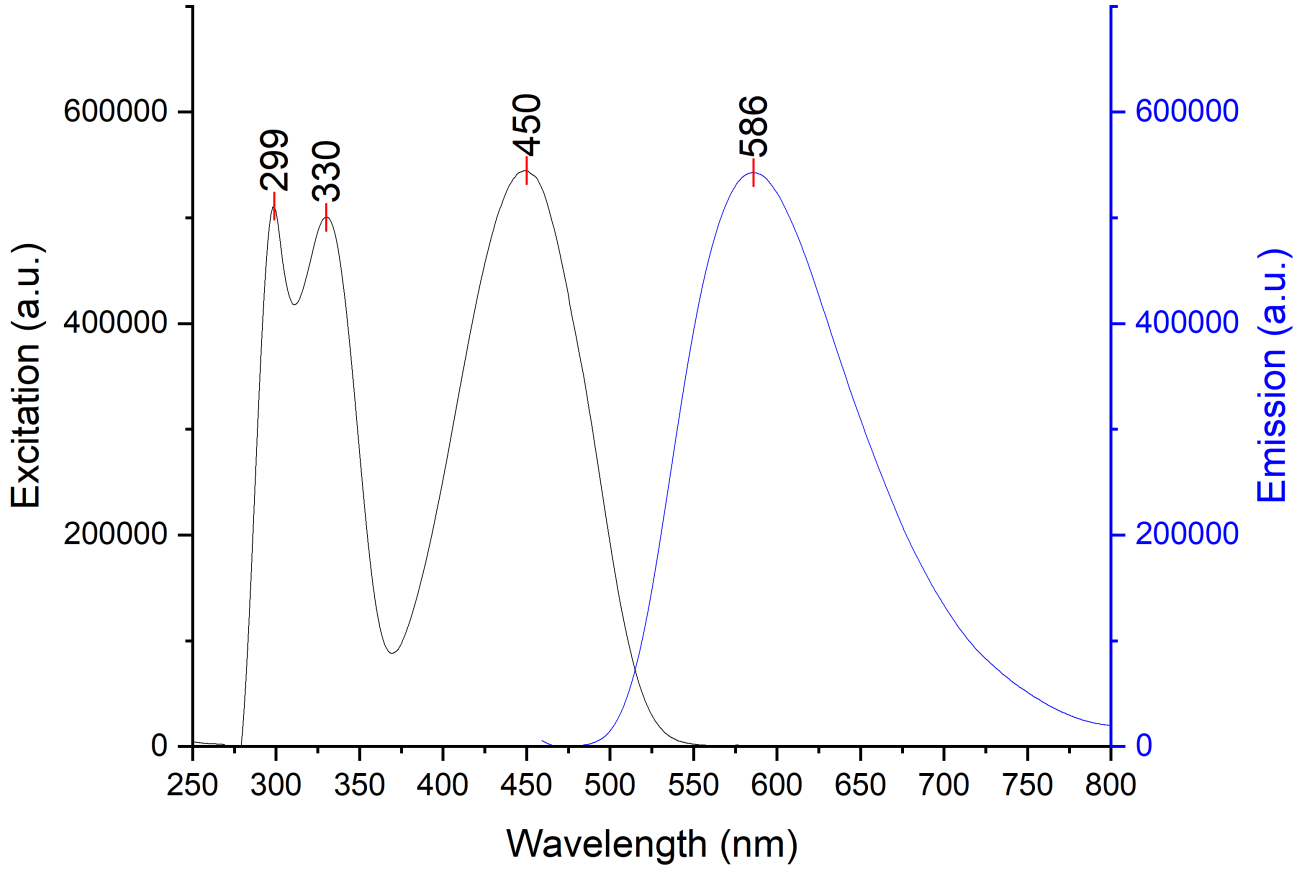

Figure 6-128. Stacked excitation (step: 1.0 nm/s, dwell time: 0.125 s, slit width: 1.0 nm) and emission (step: 1.0 nm/s, dwell time: 0.125 s, slit width: 1.0 nm) spectra of probe 2 and $In(OTf)_3$ in PhCl; 12.5 µM sample.

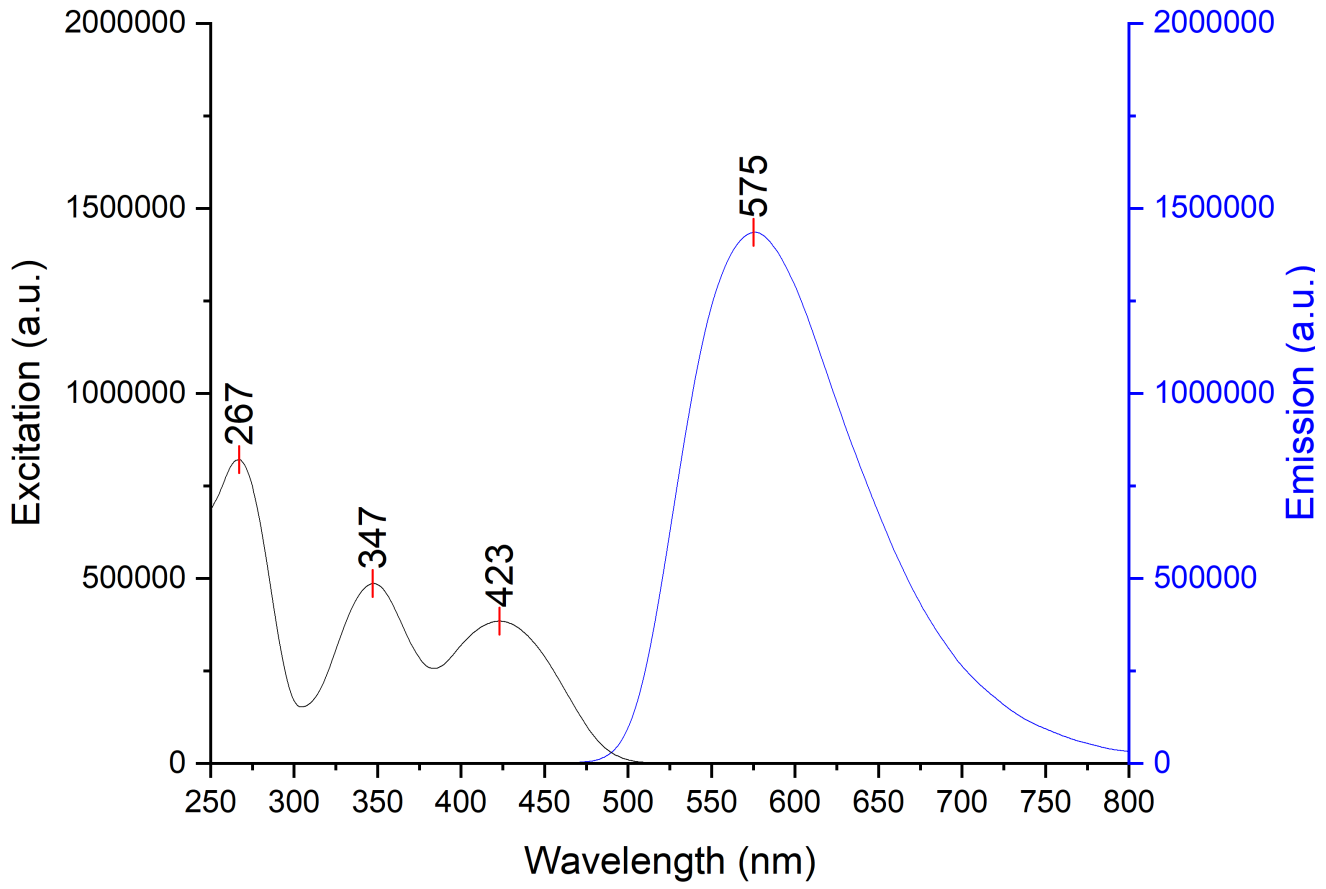

Figure 6-129. Stacked excitation (step: 1.0 nm/s, dwell time: 0.125 s, slit width: 1.0 nm) and emission (step: 1.0 nm/s, dwell time: 0.125 s, slit width: 1.0 nm) spectra of probe 2 and $In(OTf)_3$ in Et_2O; 12.5 µM sample.

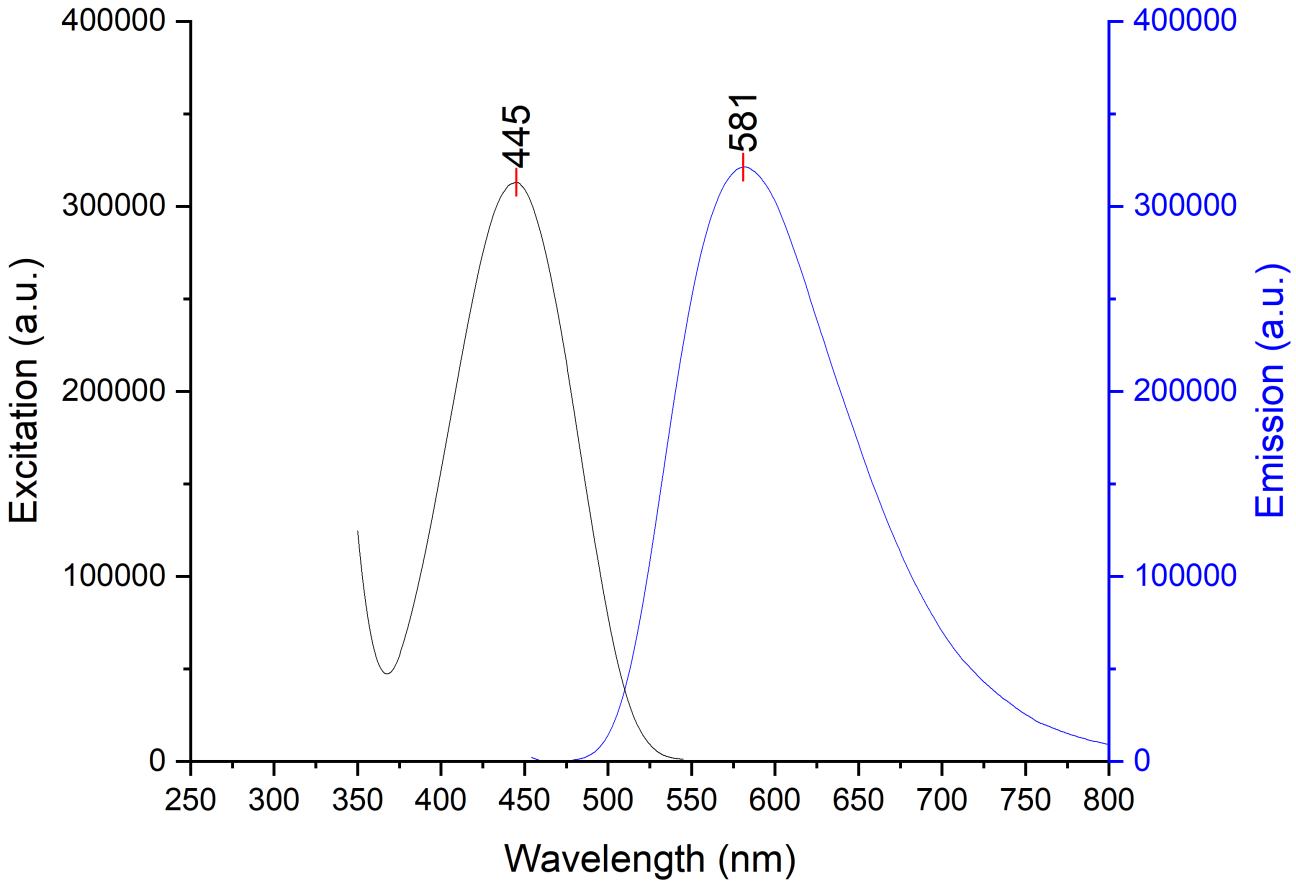

Figure 6-130. Stacked excitation (step: 1.0 nm/s, dwell time: 0.125 s, slit width: 1.0 nm) and emission (step: 1.0 nm/s, dwell time: 0.125 s, slit width: 1.0 nm) spectra of probe 2 and $In(OTf)_3$ in DCM; 12.5 µM sample.

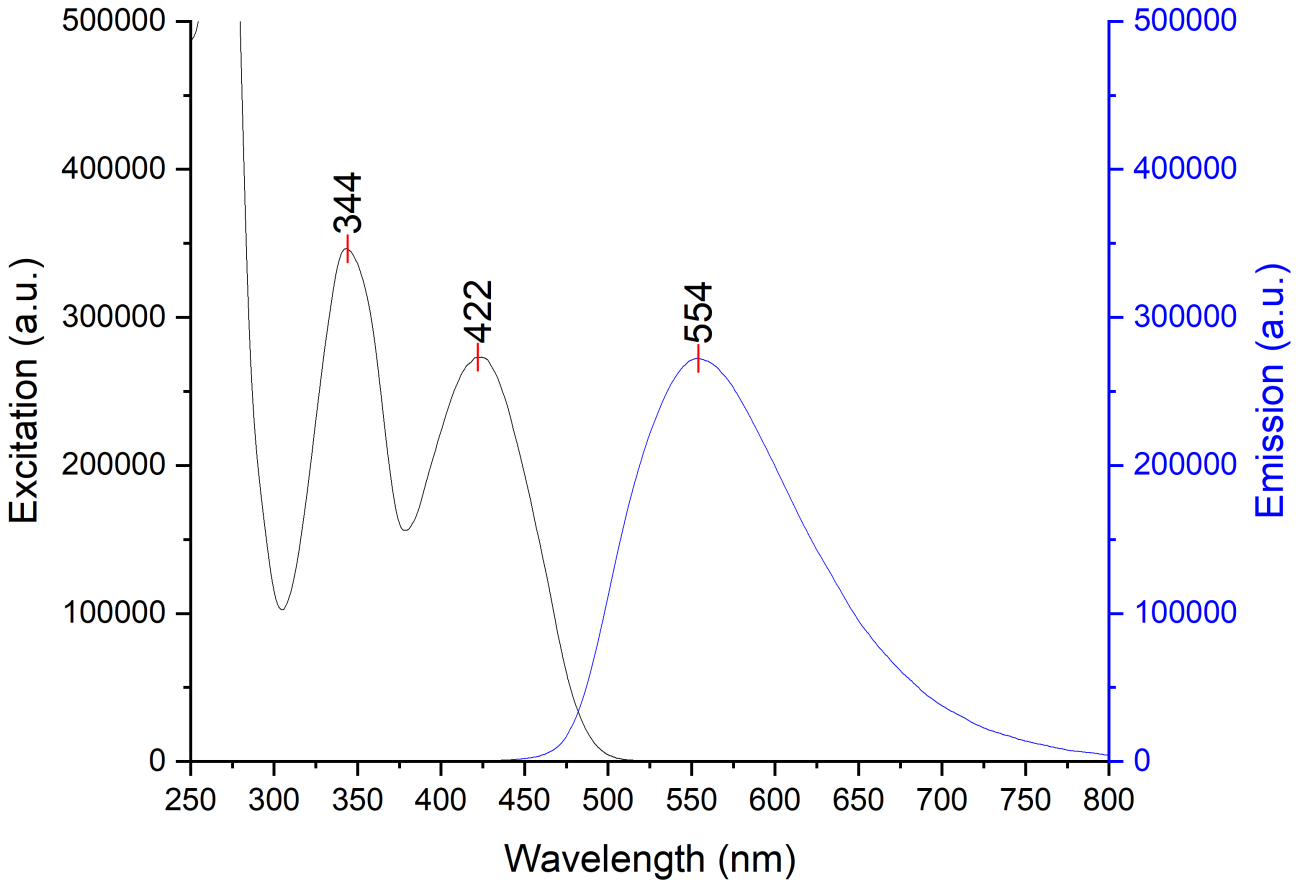

Figure 6-131. Stacked excitation (step: 1.0 nm/s, dwell time: 0.125 s, slit width: 1.0 nm) and emission (step: 1.0 nm/s, dwell time: 0.125 s, slit width: 1.0 nm) spectra of probe 7 and $In(OTf)_3$ in MeCN; 12.5 μM sample.

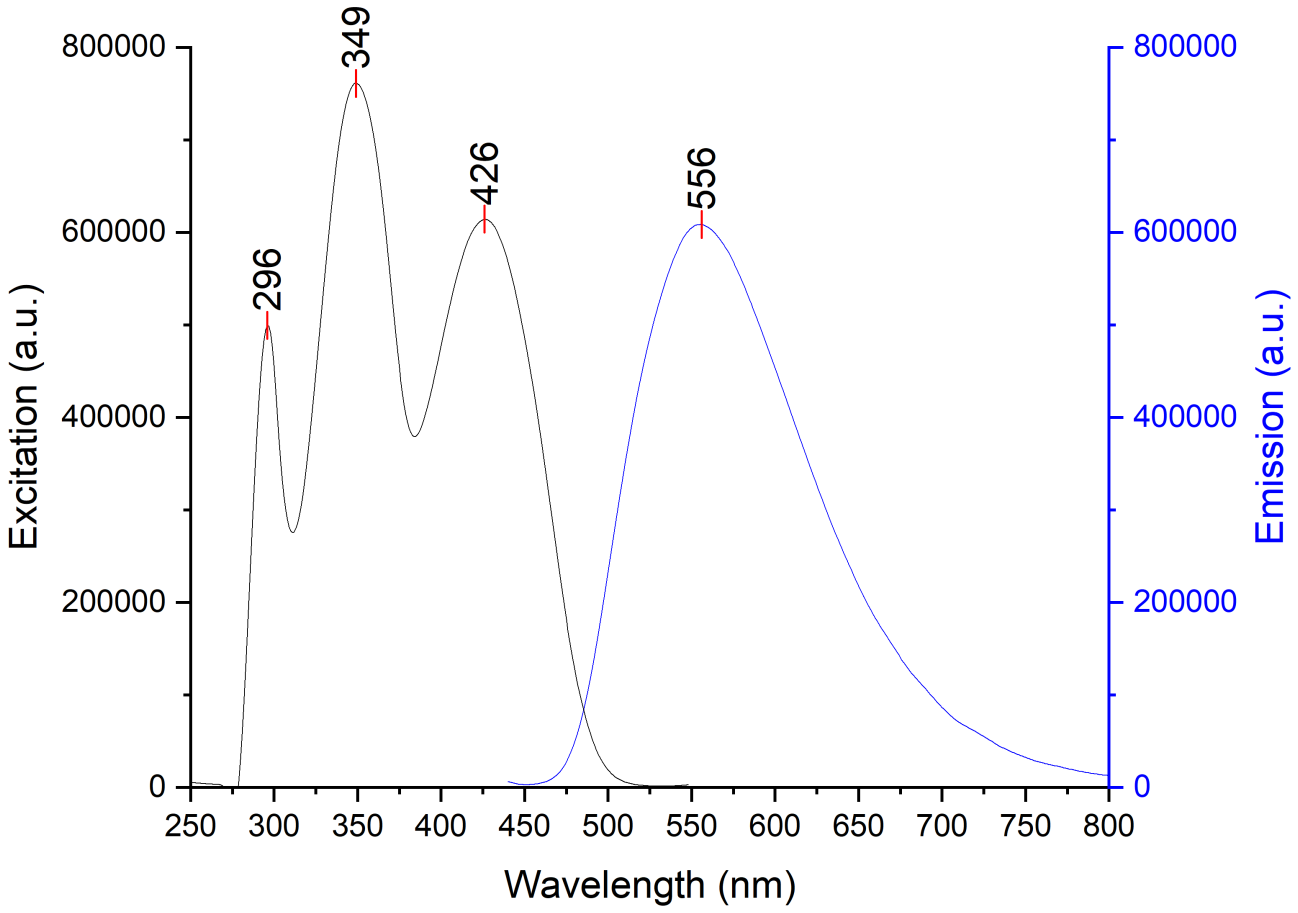

Figure 6-132. Stacked excitation (step: 1.0 nm/s, dwell time: 0.125 s, slit width: 1.0 nm) and emission (step: 1.0 nm/s, dwell time: 0.125 s, slit width: 1.0 nm) spectra of probe 7 and $In(OTf)_3$ in PhCl; 12.5 µM sample.

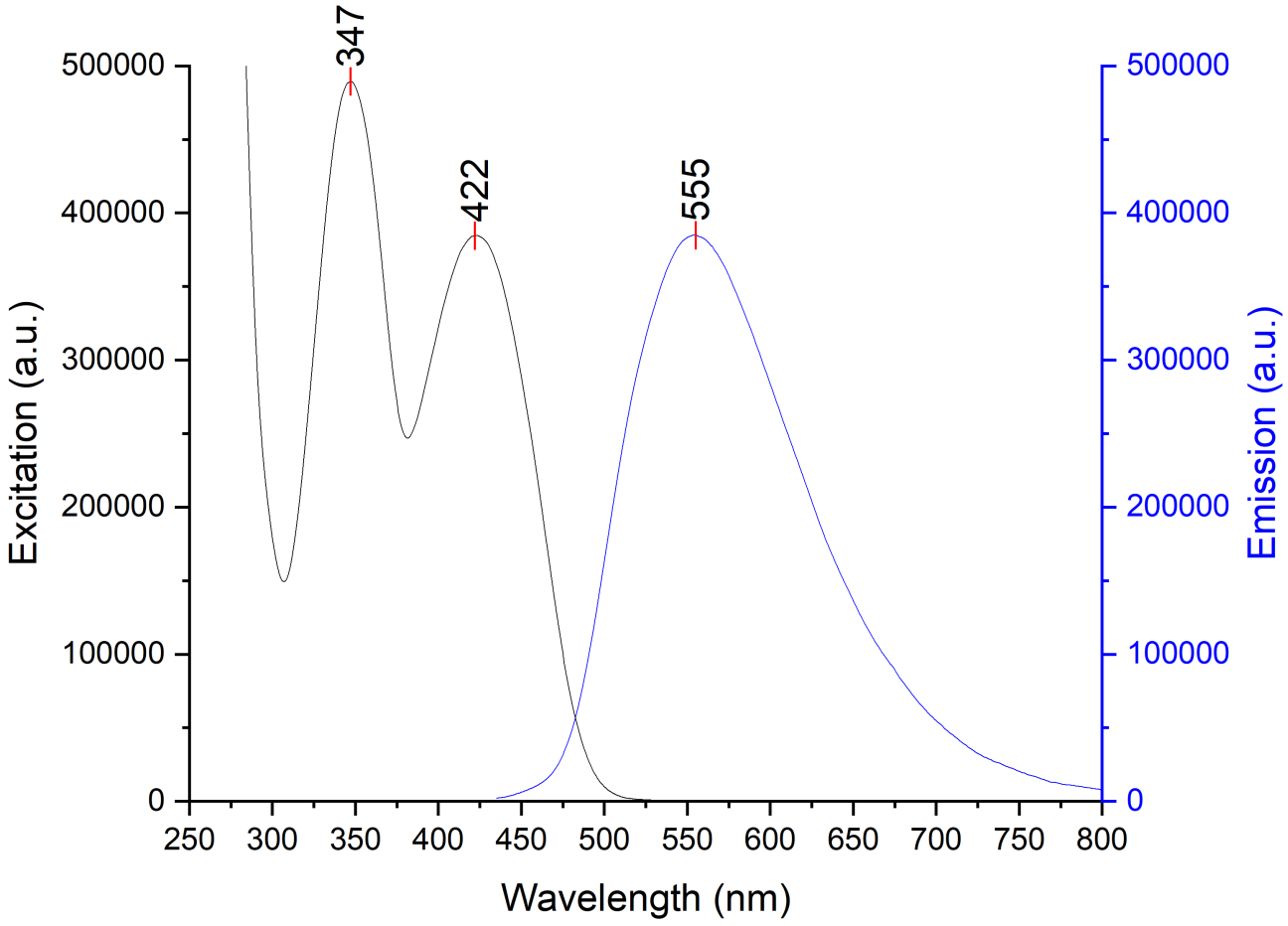

Figure 6-133. Stacked excitation (step: 1.0 nm/s, dwell time: 0.125 s, slit width: 1.0 nm) and emission (step: 1.0 nm/s, dwell time: 0.125 s, slit width: 1.0 nm) spectra of probe 7 and $In(OTf)_3$ in Et_2O; 12.5 µM sample.

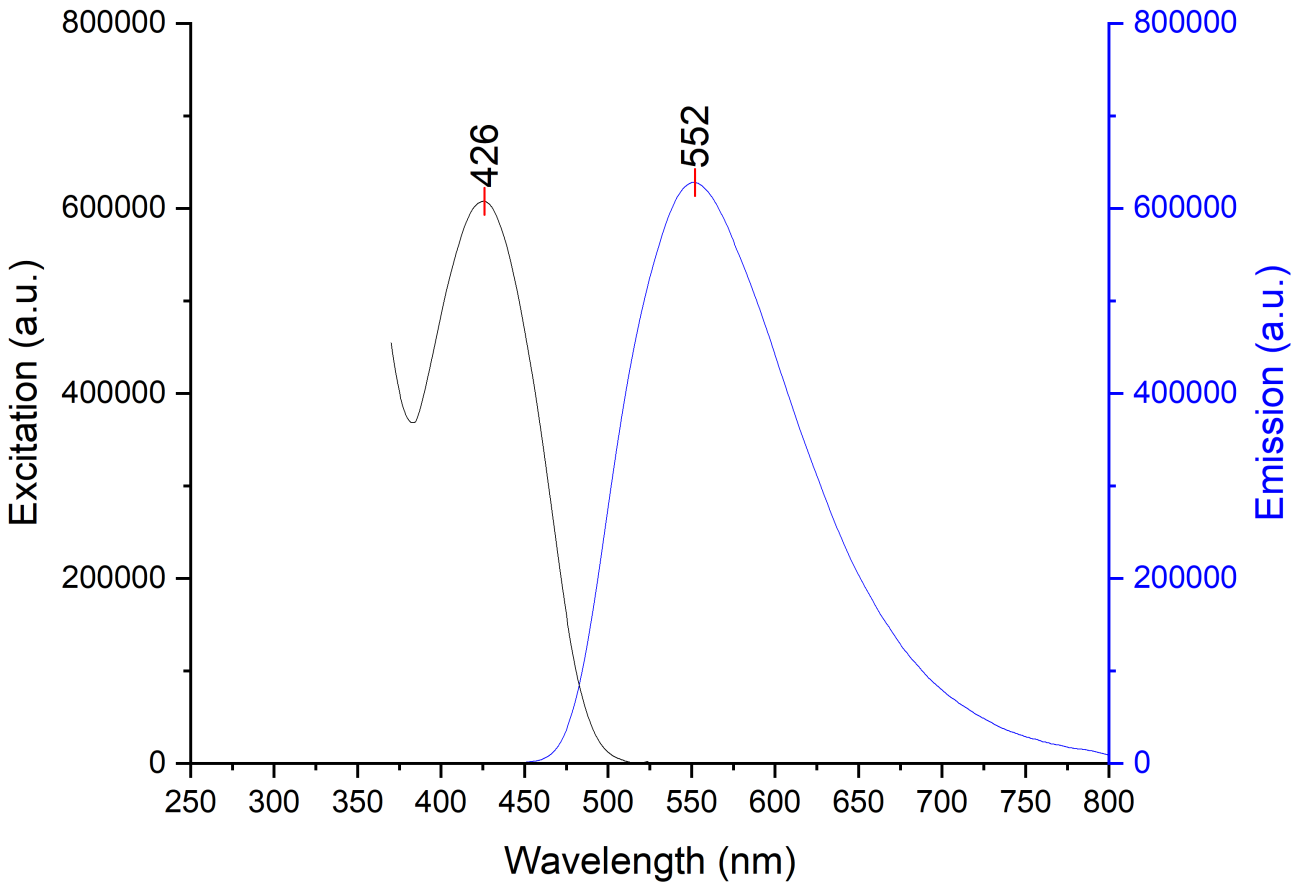

Figure 6-134. Stacked excitation (step: 1.0 nm/s, dwell time: 0.125 s, slit width: 1.0 nm) and emission (step: 1.0 nm/s, dwell time: 0.125 s, slit width: 1.0 nm) spectra of probe 7 and $In(OTf)_3$ in DCM; 12.5 µM sample.

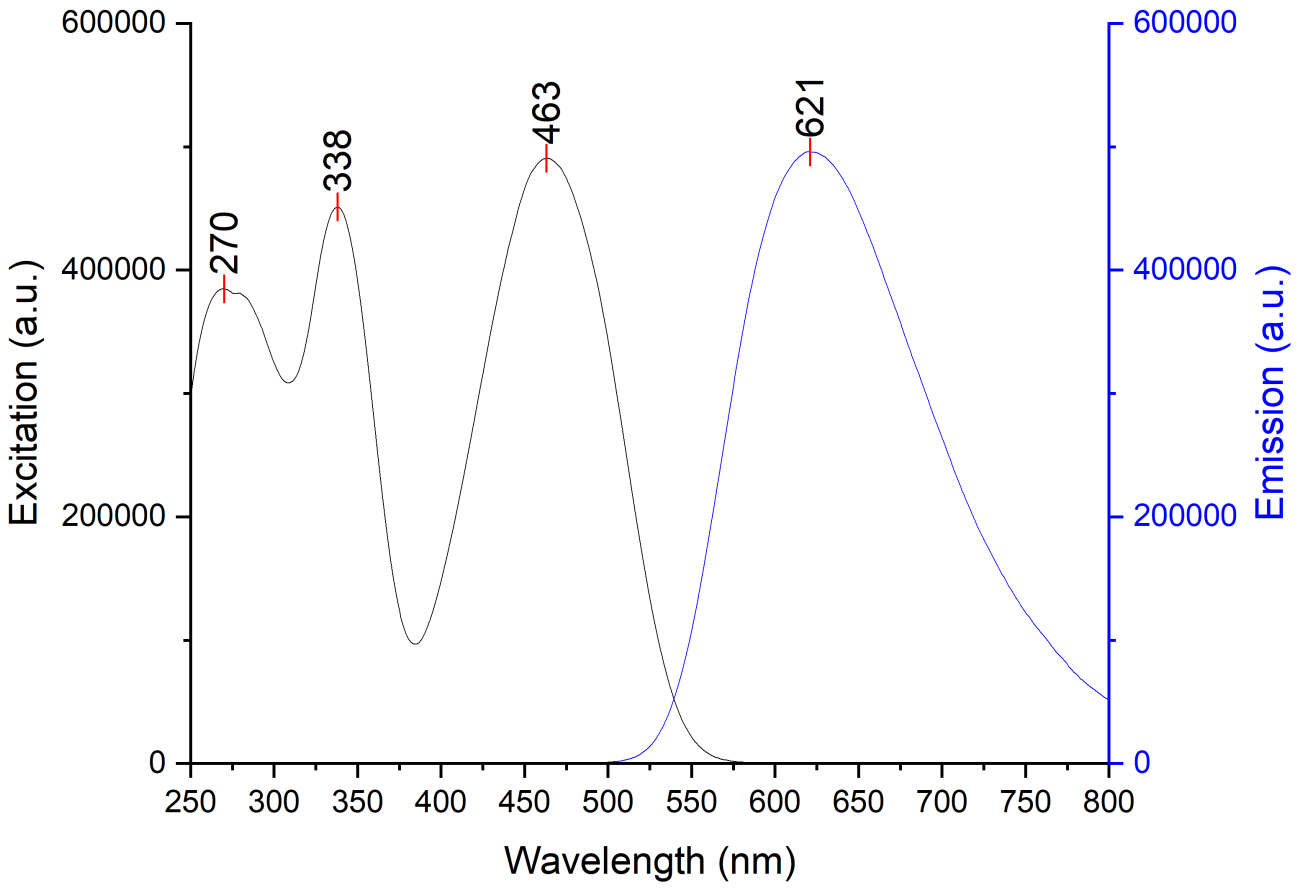

Figure 6-135. Stacked excitation (step: 1.0 nm/s, dwell time: 0.125 s, slit width: 1.0 nm) and emission (step: 1.0 nm/s, dwell time: 0.125 s, slit width: 1.0 nm) spectra of probe 8 and $In(OTf)_3$ in MeCN; 12.5 μM sample.

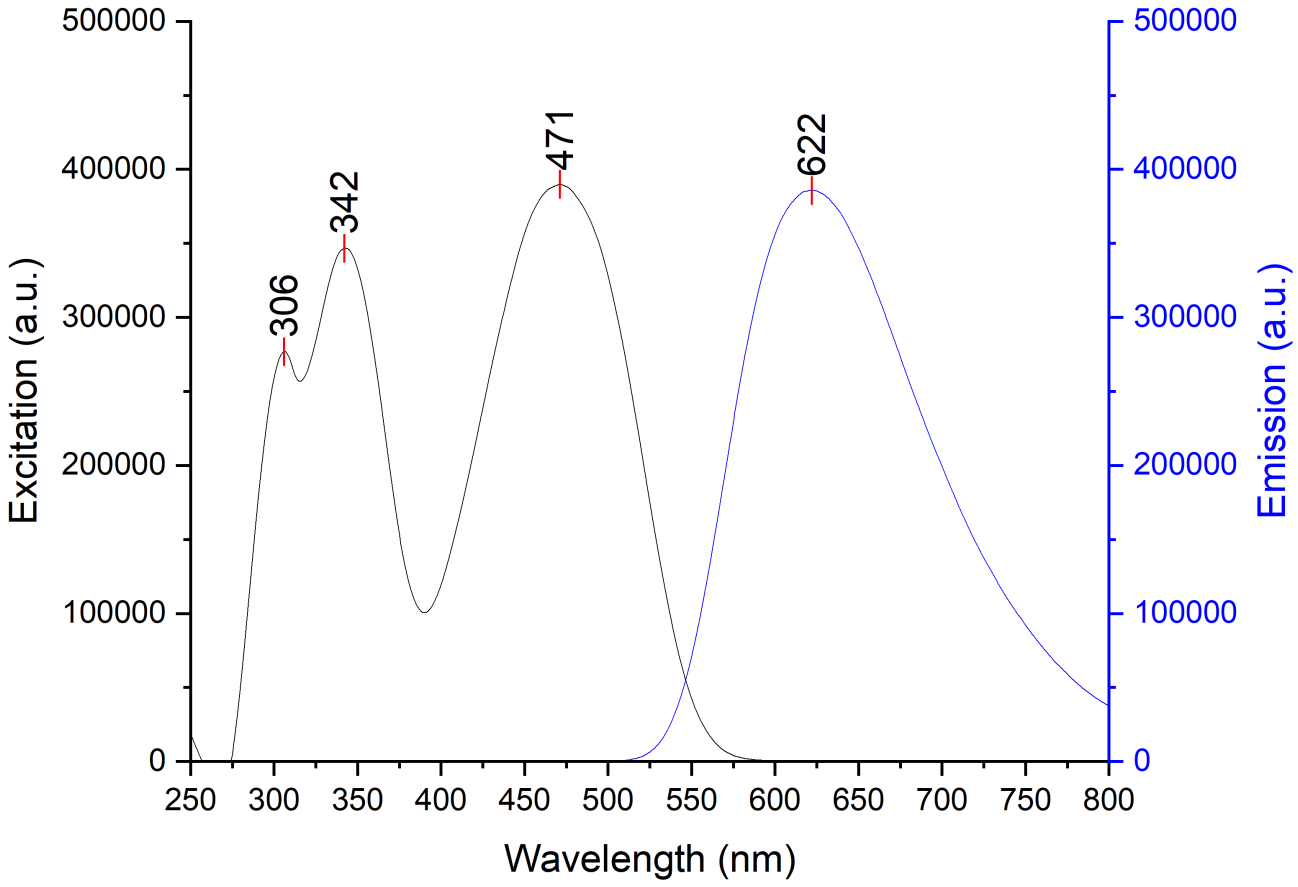

Figure 6-136. Stacked excitation (step: 1.0 nm/s, dwell time: 0.125 s, slit width: 1.0 nm) and emission (step: 1.0 nm/s, dwell time: 0.125 s, slit width: 1.0 nm) spectra of probe 8 and $In(OTf)_3$ in PhCl; 12.5 µM sample.

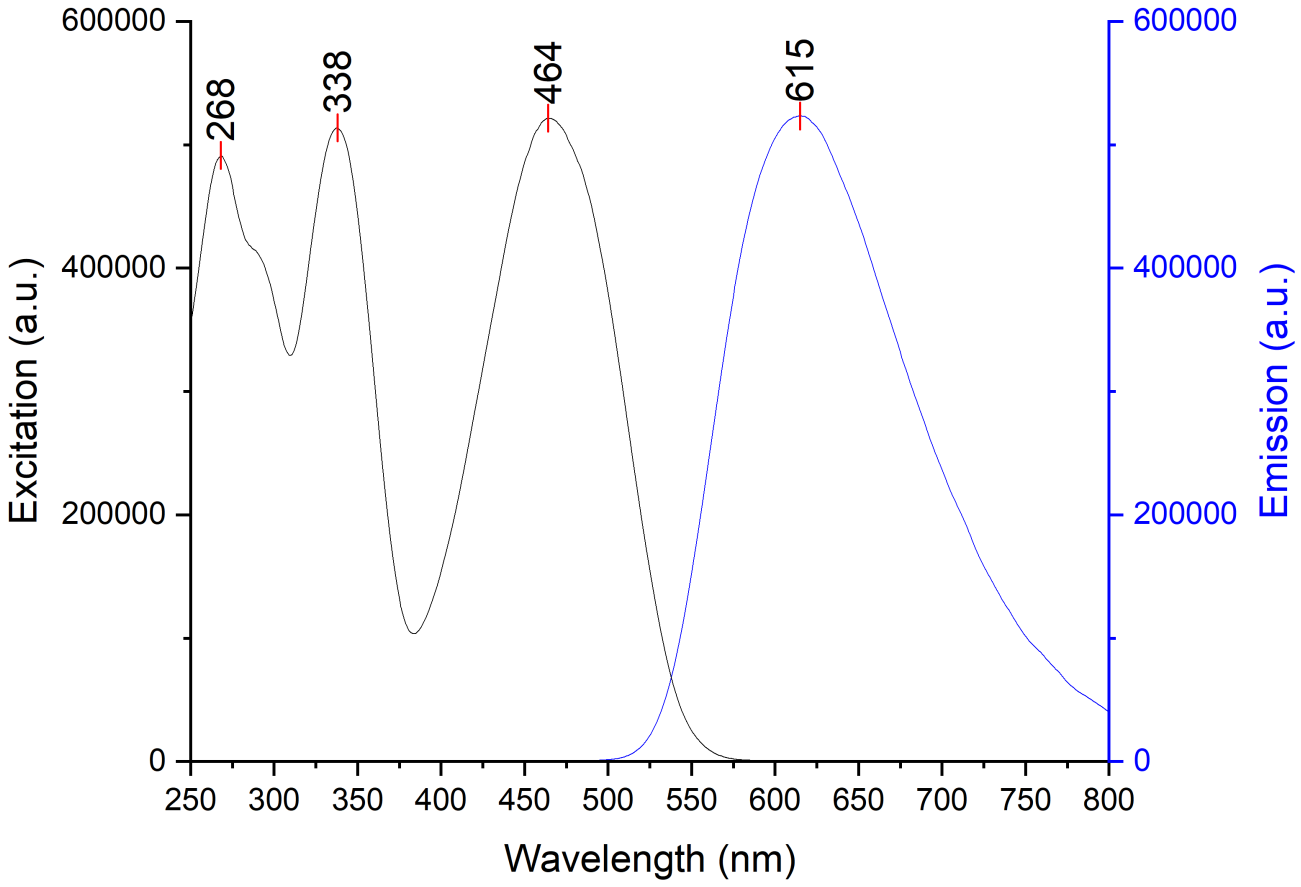

Figure 6-137. Stacked excitation (step: 1.0 nm/s, dwell time: 0.125 s, slit width: 1.0 nm) and emission (step: 1.0 nm/s, dwell time: 0.125 s, slit width: 1.0 nm) spectra of probe 8 and $In(OTf)_3$ in Et_2O; 12.5 µM sample.

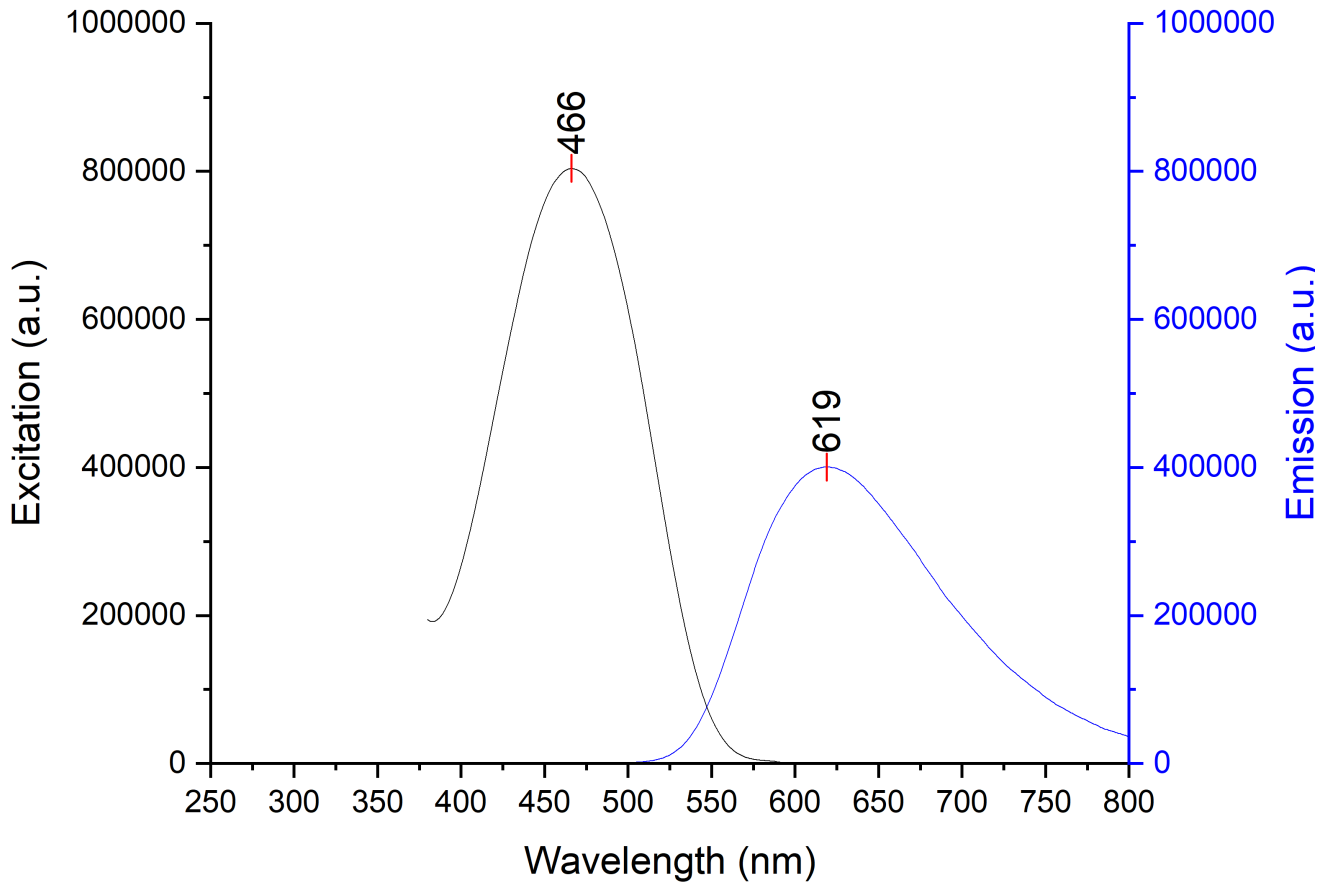

Figure 6-138. Stacked excitation (step: 1.0 nm/s, dwell time: 0.125 s, slit width: 1.0 nm) and emission (step: 1.0 nm/s, dwell time: 0.125 s, slit width: 1.0 nm) spectra of probe 8 and $In(OTf)_3$ in DCM; 12.5 µM sample.

6.2.3.9. $Sc(OTf)_3$

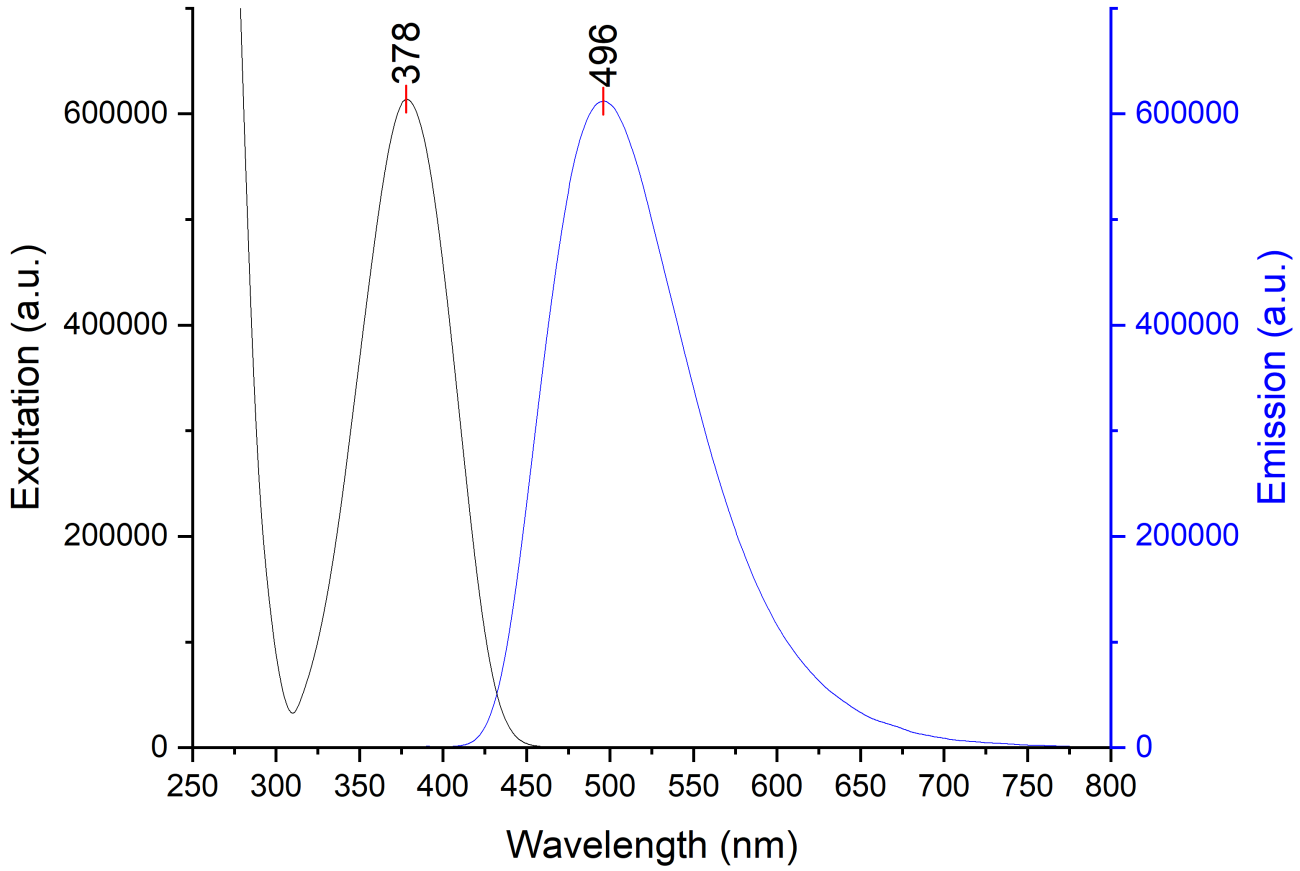

Figure 6-139. Stacked excitation (step: 1.0 nm/s, dwell time: 0.125 s, slit width: 1.0 nm) and emission (step: 1.0 nm/s, dwell time: 0.125 s, slit width: 1.0 nm) spectra of probe 1 and $Sc(OTf)_3$ in MeCN; 12.5 μM sample.

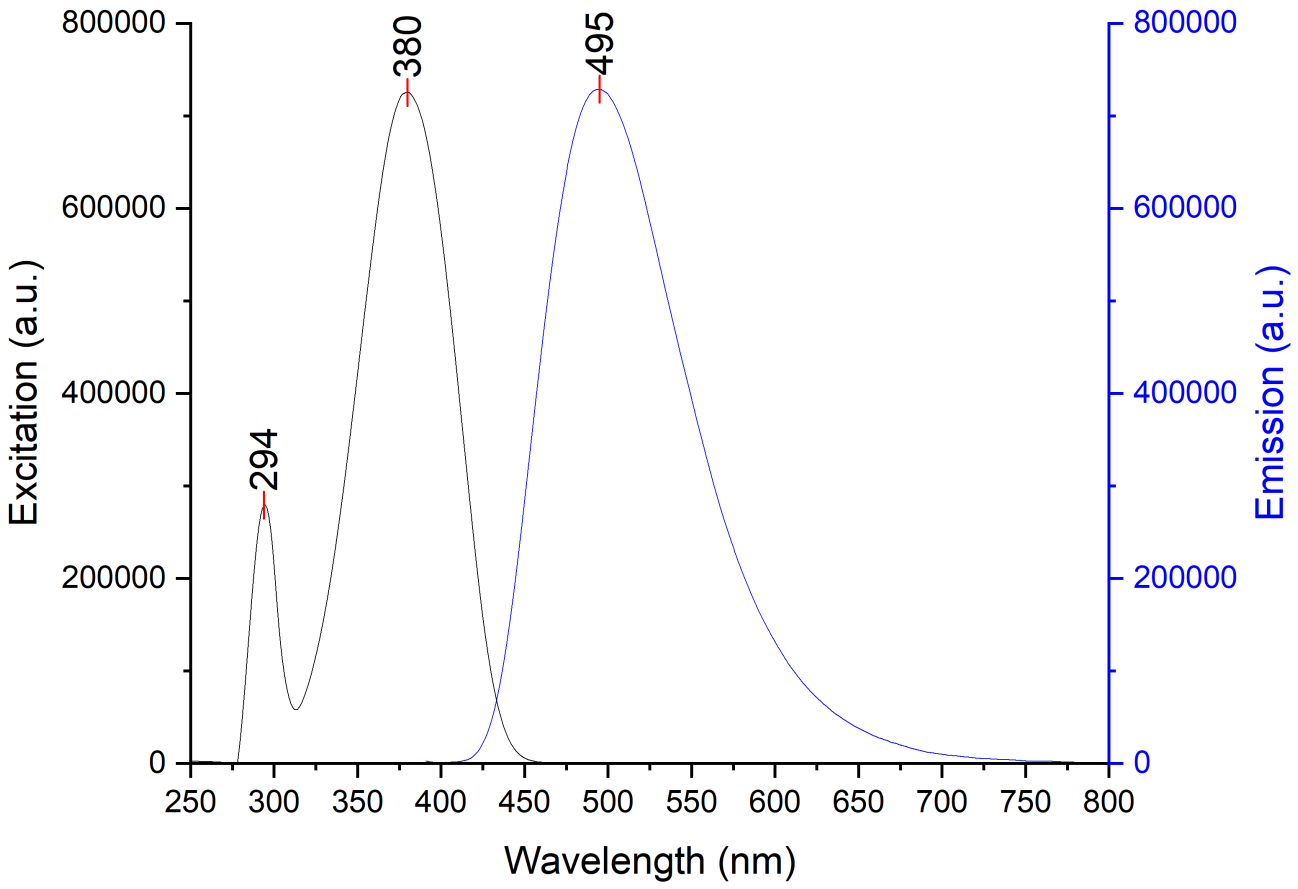

Figure 6-140. Stacked excitation (step: 1.0 nm/s, dwell time: 0.125 s, slit width: 1.0 nm) and emission (step: 1.0 nm/s, dwell time: 0.125 s, slit width: 1.0 nm) spectra of probe 1 and $Sc(OTf)_3$ in PhCl; 12.5 µM sample.

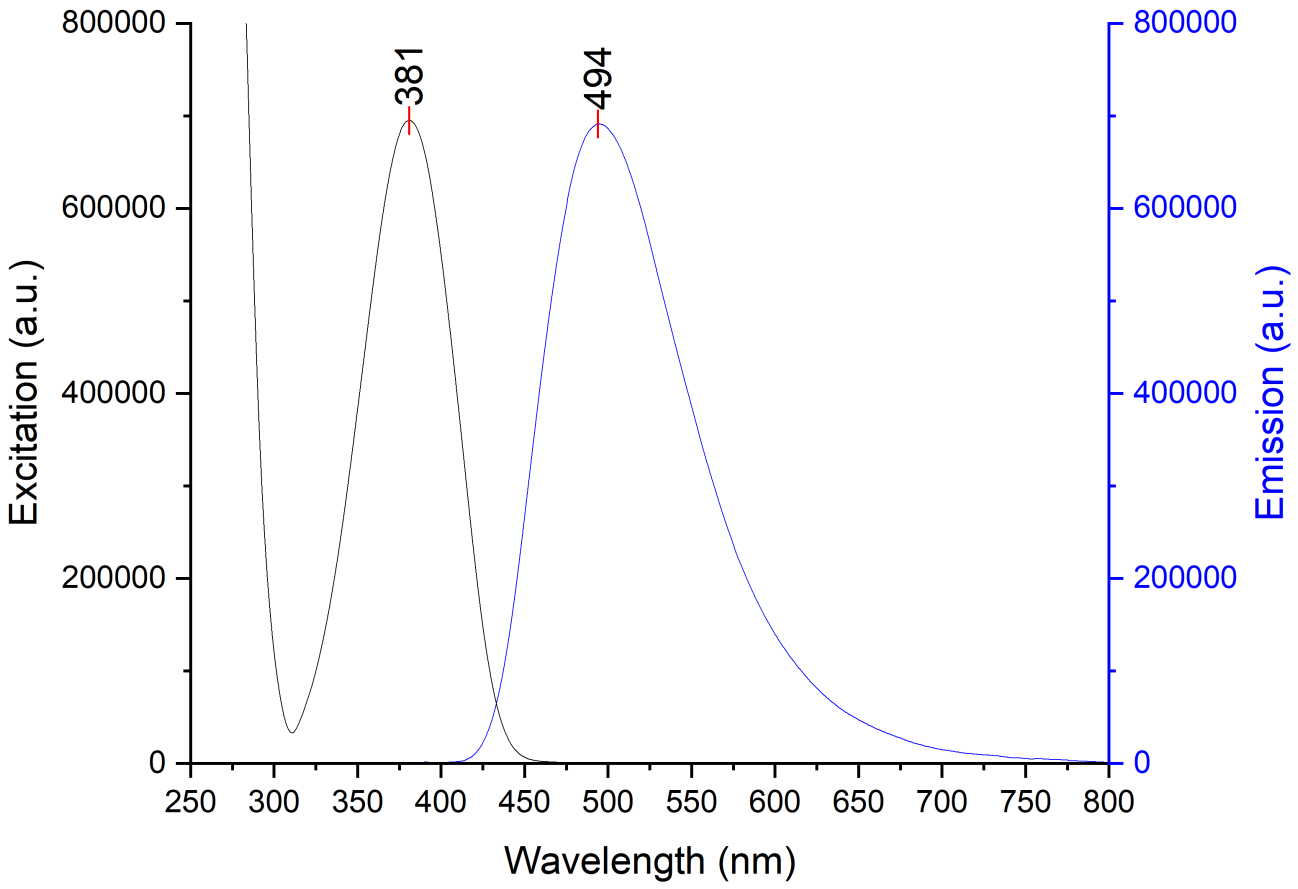

Figure 6-141. Stacked excitation (step: 1.0 nm/s, dwell time: 0.125 s, slit width: 1.0 nm) and emission (step: 1.0 nm/s, dwell time: 0.125 s, slit width: 1.0 nm) spectra of probe 1 and $Sc(OTf)_3$ in Et_2O; 12.5 µM sample.

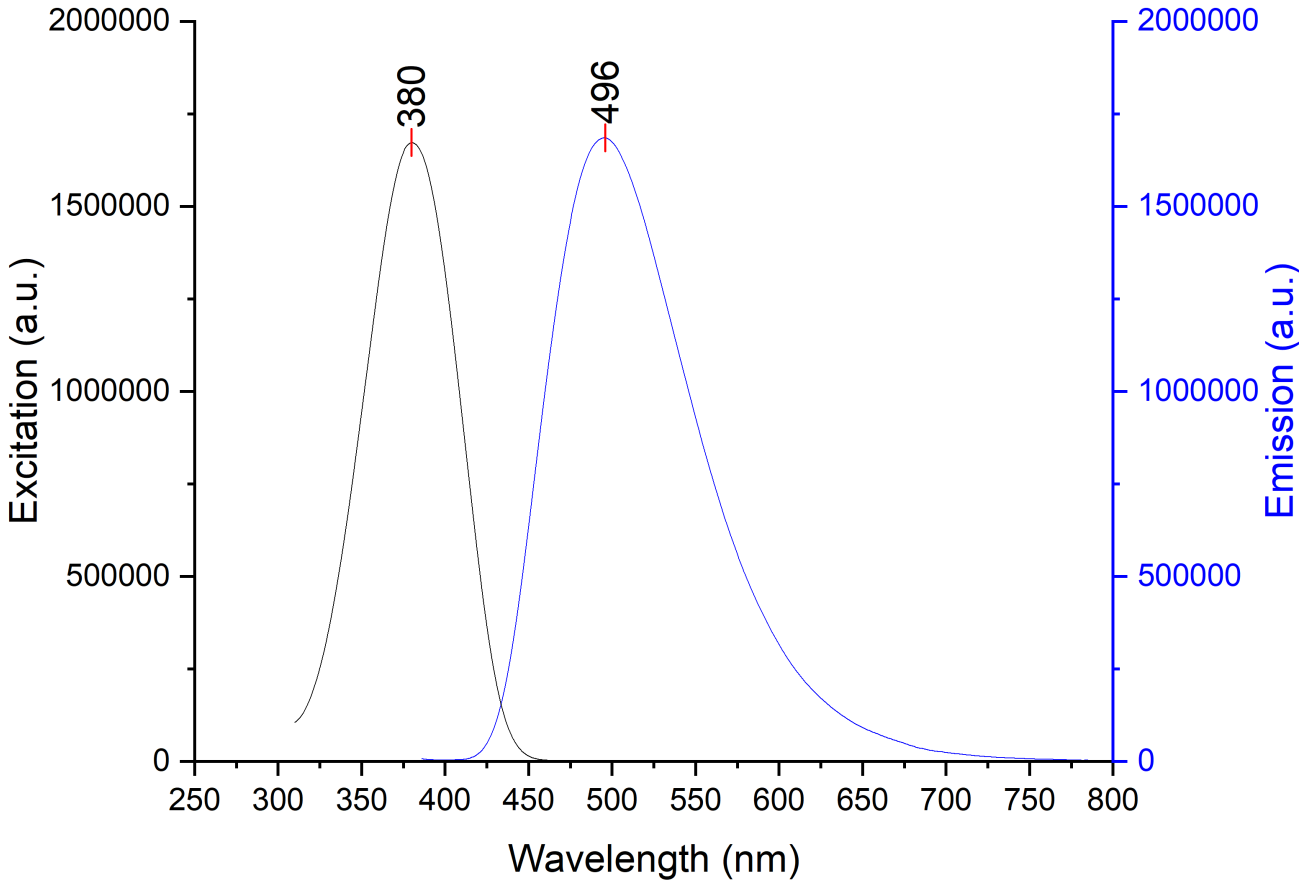

Figure 6-142. Stacked excitation (step: 1.0 nm/s, dwell time: 0.125 s, slit width: 1.50 nm) and emission (step: 1.0 nm/s, dwell time: 0.125 s, slit width: 1.50 nm) spectra of probe 1 and $Sc(OTf)_3$ in DCM; 12.5 μM sample.

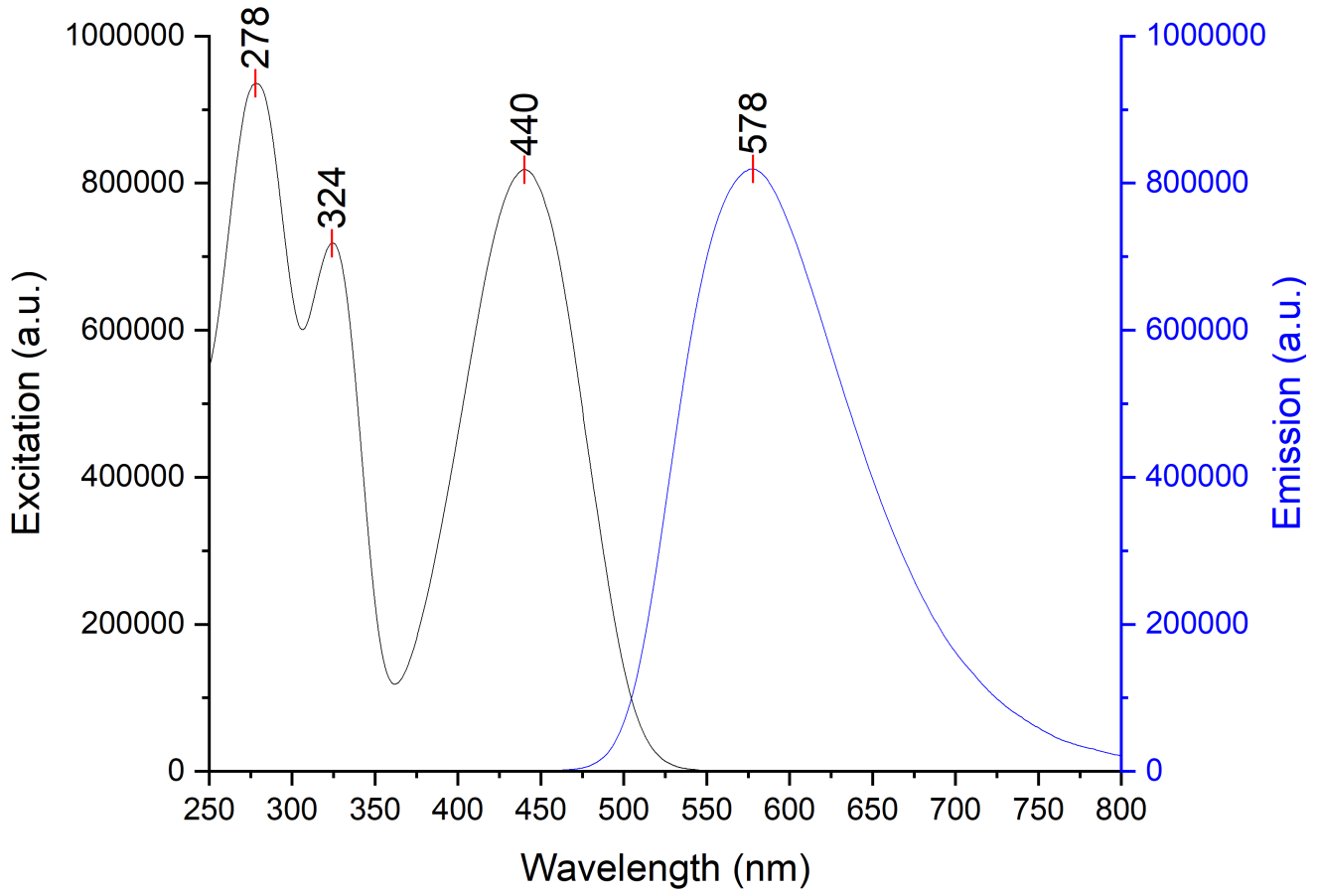

Figure 6-143. Stacked excitation (step: 1.0 nm/s, dwell time: 0.125 s, slit width: 1.0 nm) and emission (step: 1.0 nm/s, dwell time: 0.125 s, slit width: 1.0 nm) spectra of probe 2 and $Sc(OTf)_3$ in MeCN; 12.5 μM sample.

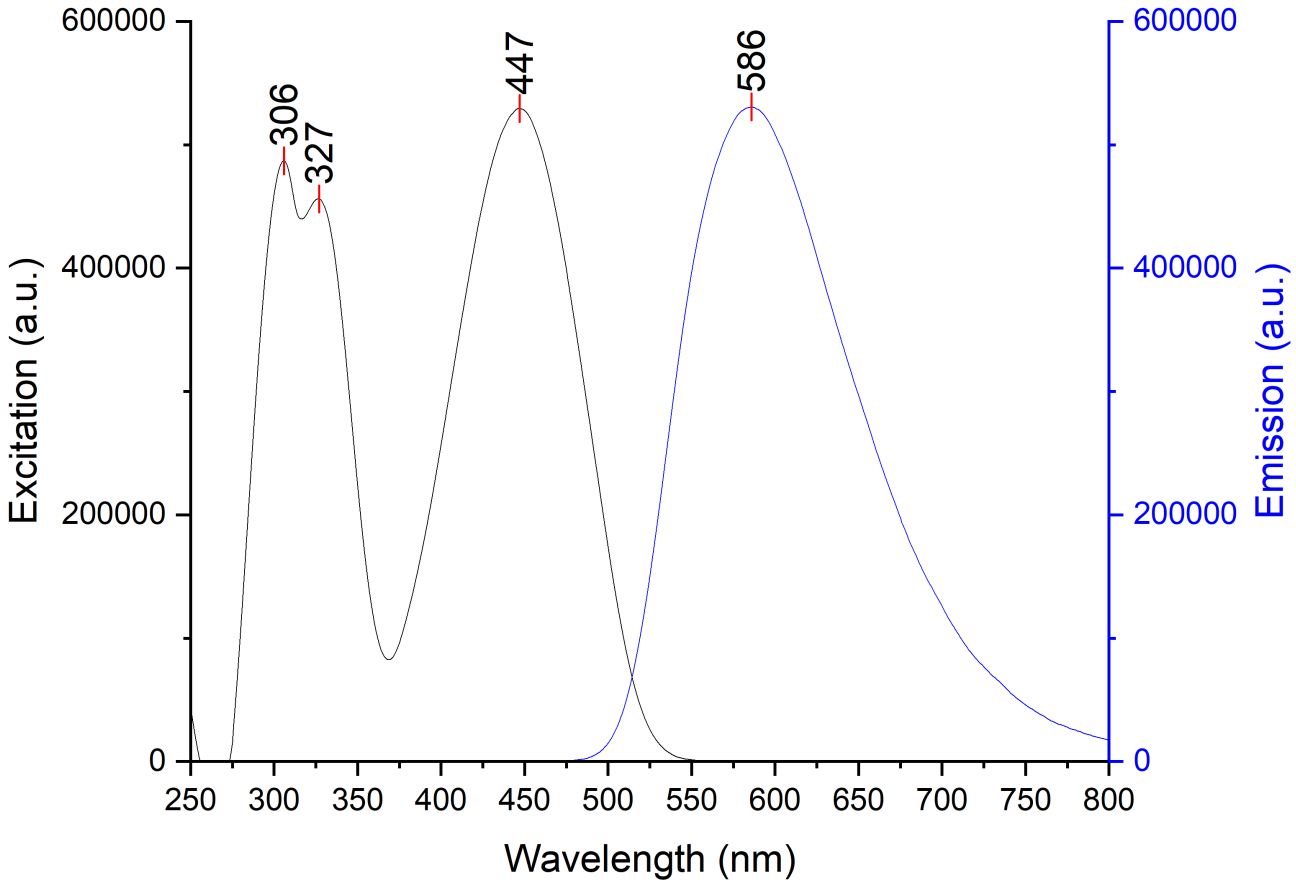

Figure 6-144. Stacked excitation (step: 1.0 nm/s, dwell time: 0.125 s, slit width: 1.0 nm) and emission (step: 1.0 nm/s, dwell time: 0.125 s, slit width: 1.0 nm) spectra of probe 2 and $Sc(OTf)_3$ in PhCl; 12.5 µM sample.

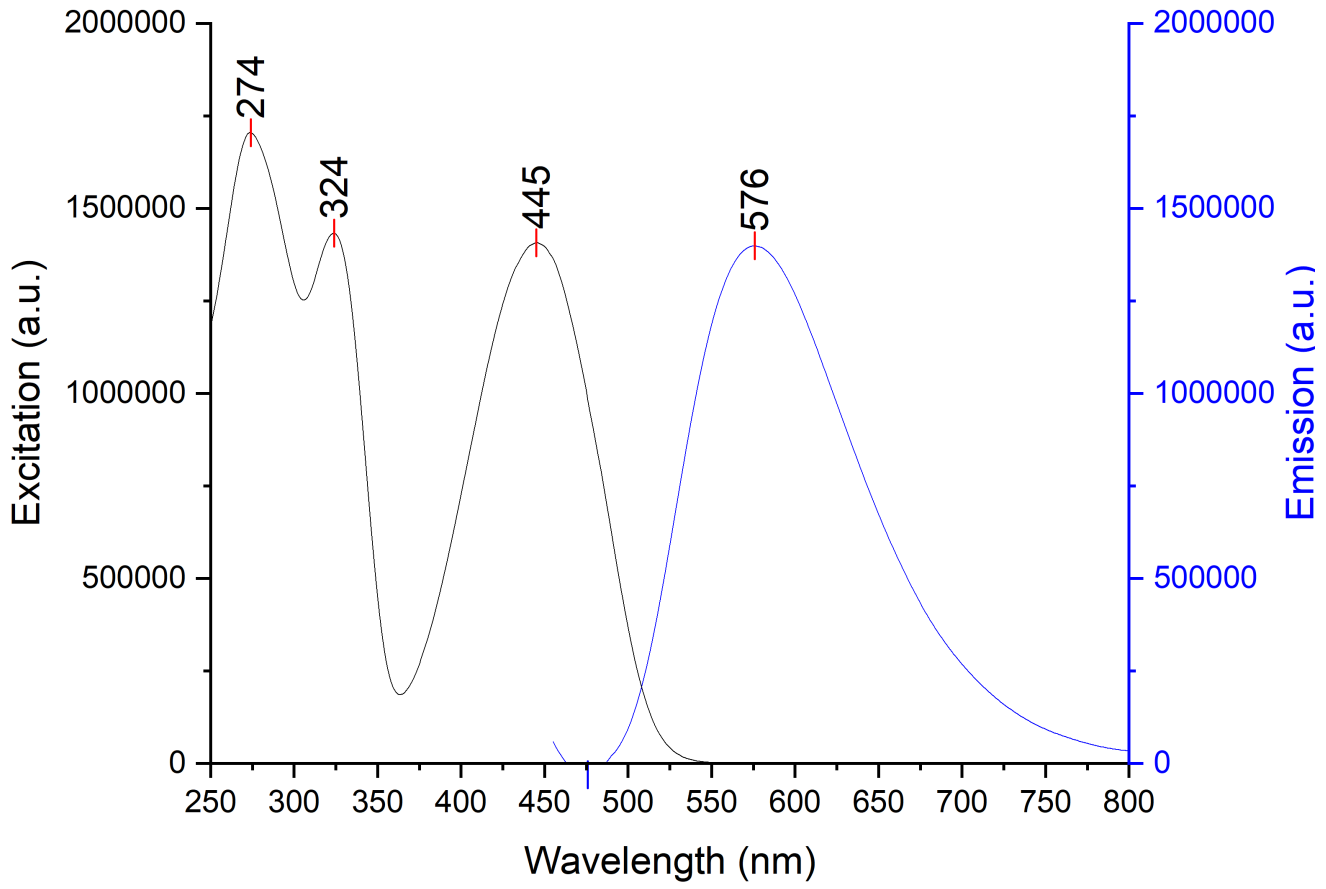

Figure 6-145. Stacked excitation (step: 1.0 nm/s, dwell time: 0.125 s, slit width: 1.0 nm) and emission (step: 1.0 nm/s, dwell time: 0.125 s, slit width: 1.0 nm) spectra of probe 2 and $Sc(OTf)_3$ in Et_2O; 12.5 µM sample.

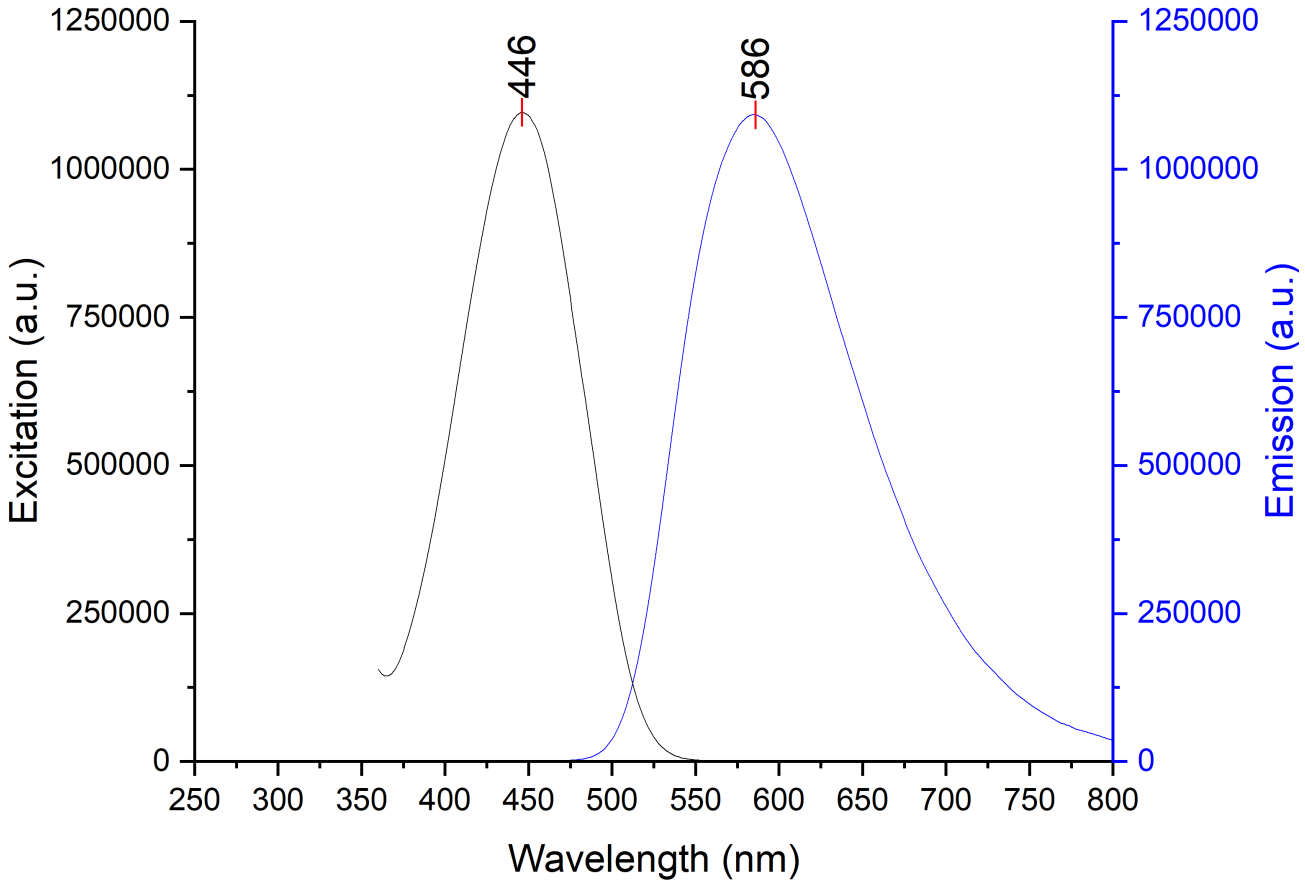

Figure 6-146. Stacked excitation (step: 1.0 nm/s, dwell time: 0.125 s, slit width: 1.50 nm) and emission (step: 1.0 nm/s, dwell time: 0.125 s, slit width: 1.50 nm) spectra of probe 2 and $Sc(OTf)_3$ in DCM; 12.5 μM sample.

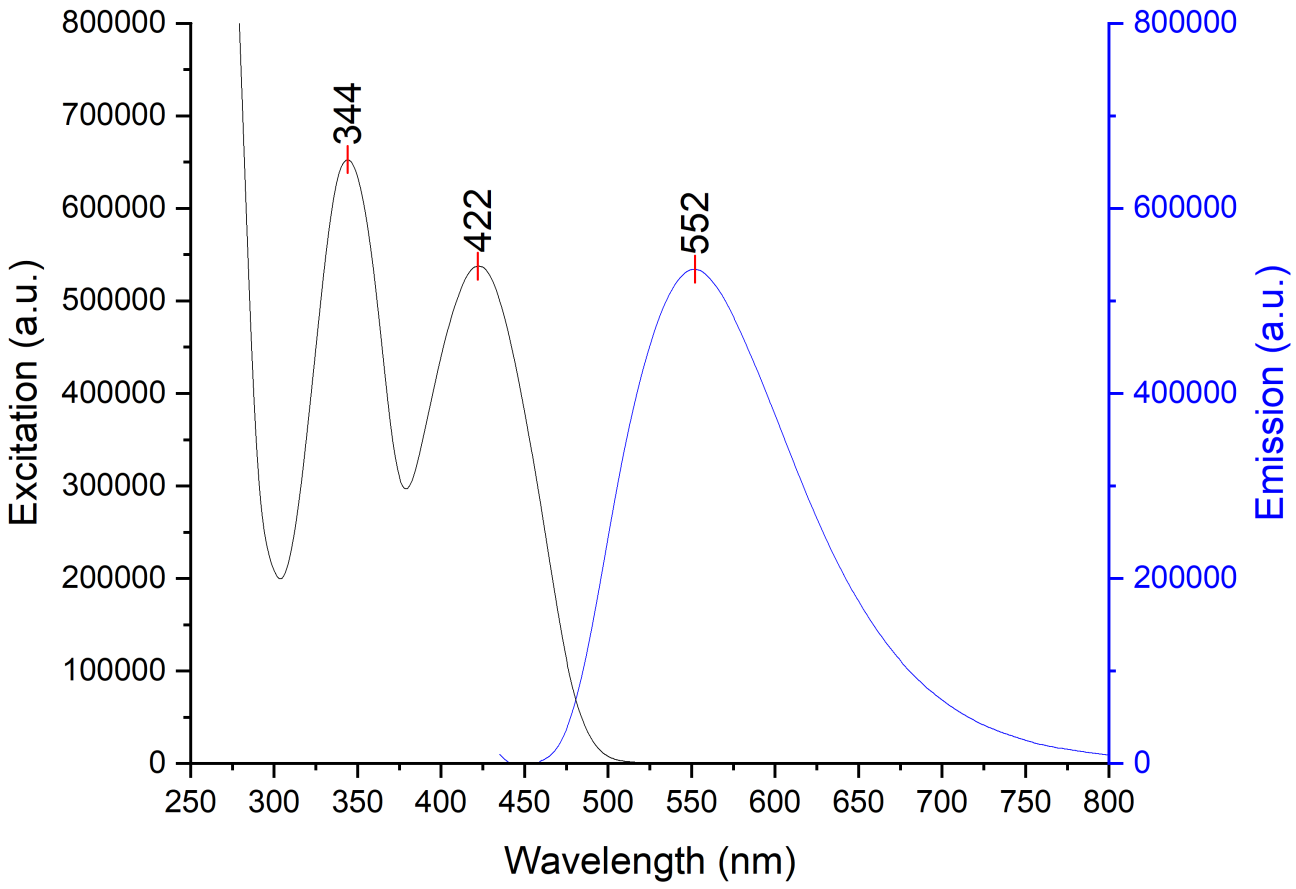

Figure 6-147. Stacked excitation (step: 1.0 nm/s, dwell time: 0.125 s, slit width: 1.0 nm) and emission (step: 1.0 nm/s, dwell time: 0.125 s, slit width: 1.0 nm) spectra of probe 7 and $Sc(OTf)_3$ in MeCN; 12.5 μM sample.

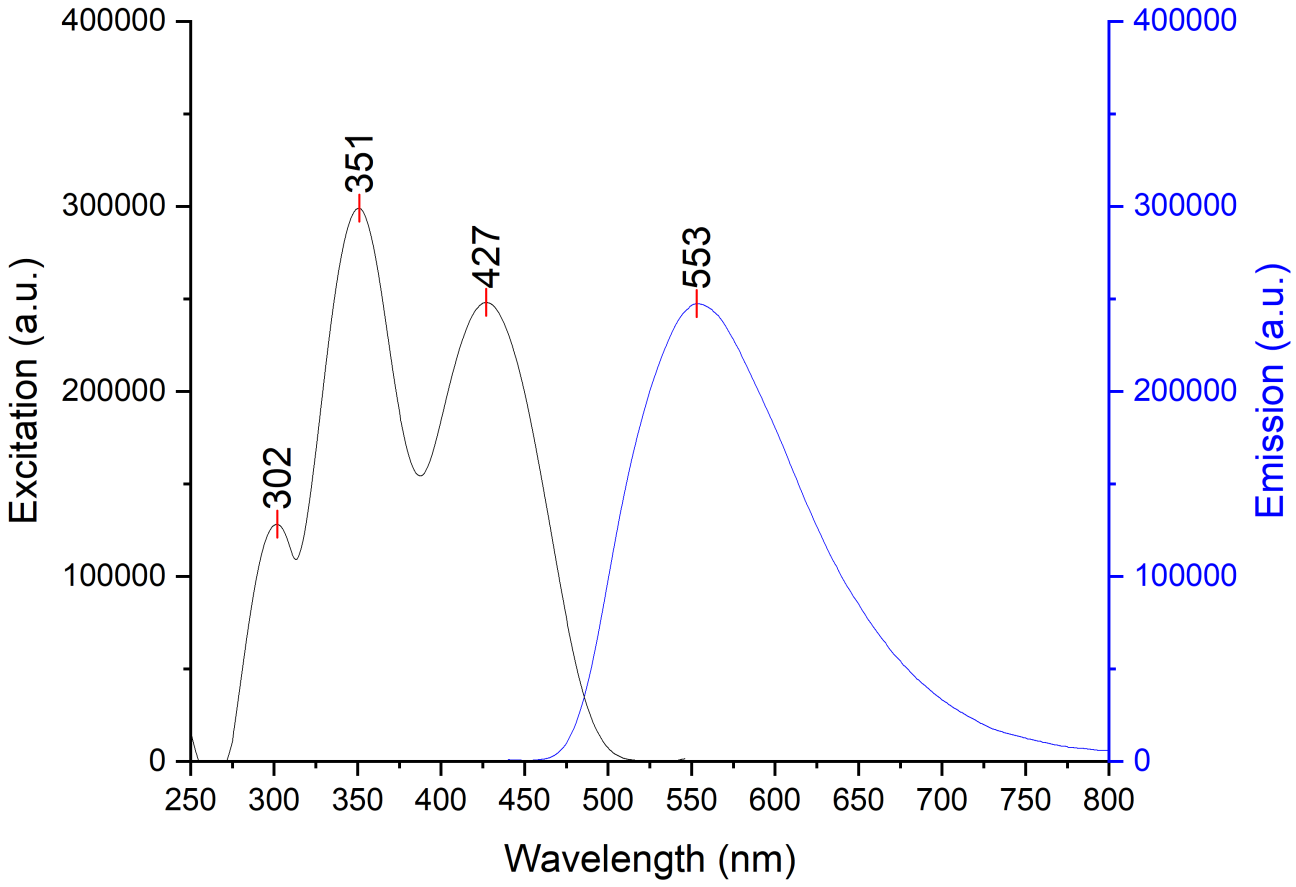

Figure 6-148. Stacked excitation (step: 1.0 nm/s, dwell time: 0.125 s, slit width: 1.0 nm) and emission (step: 1.0 nm/s, dwell time: 0.125 s, slit width: 1.0 nm) spectra of probe 7 and $Sc(OTf)_3$ in PhCl; 12.5 µM sample.

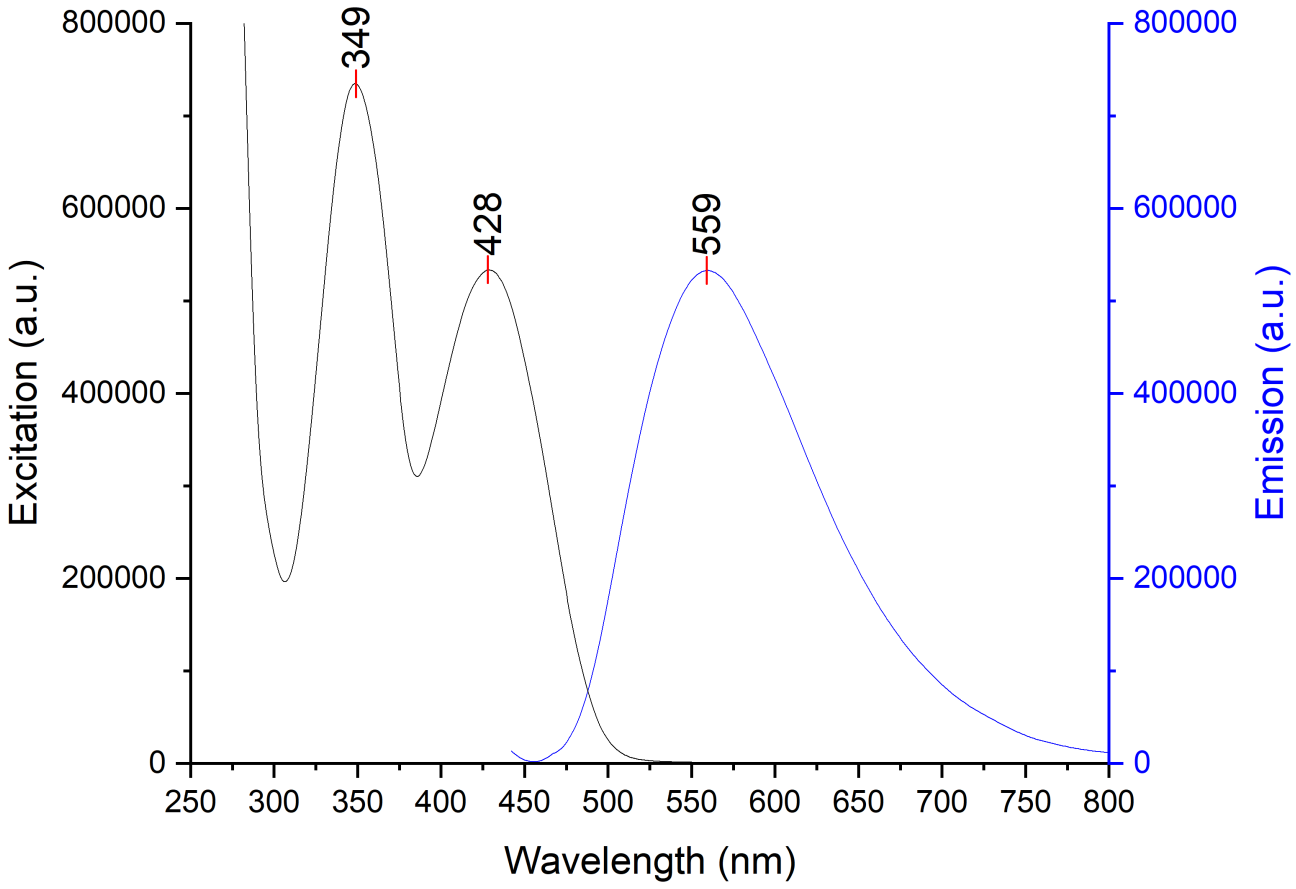

Figure 6-149. Stacked excitation (step: 1.0 nm/s, dwell time: 0.125 s, slit width: 2.50 nm) and emission (step: 1.0 nm/s, dwell time: 0.125 s, slit width: 2.50 nm) spectra of probe 7 and $Sc(OTf)_3$ in Et_2O; 12.5 μM sample.

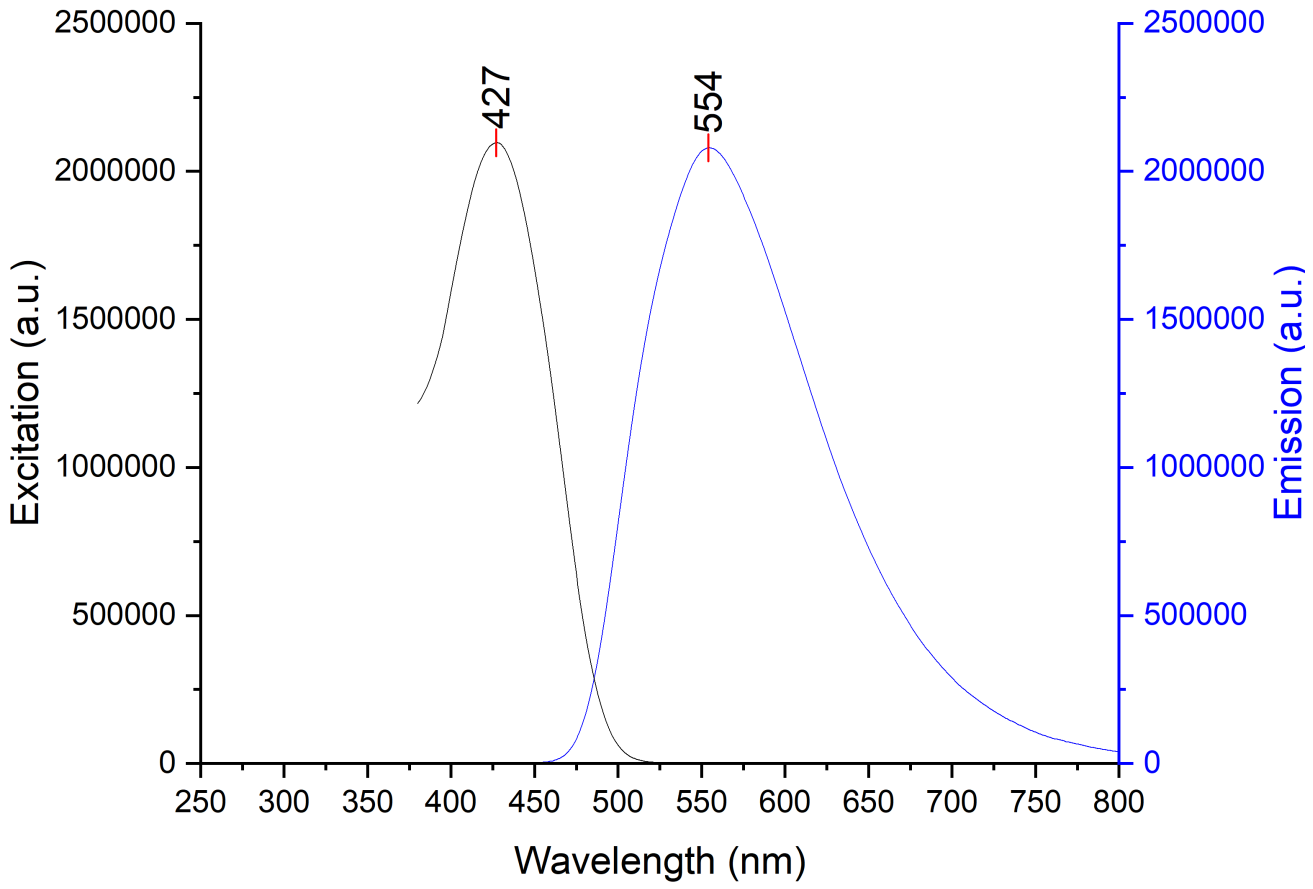

Figure 6-150. Stacked excitation (step: 1.0 nm/s, dwell time: 0.125 s, slit width: 1.5 nm) and emission (step: 1.0 nm/s, dwell time: 0.125 s, slit width: 1.5 nm) spectra of probe 7 and $Sc(OTf)_3$ in DCM; 12.5 μM sample.

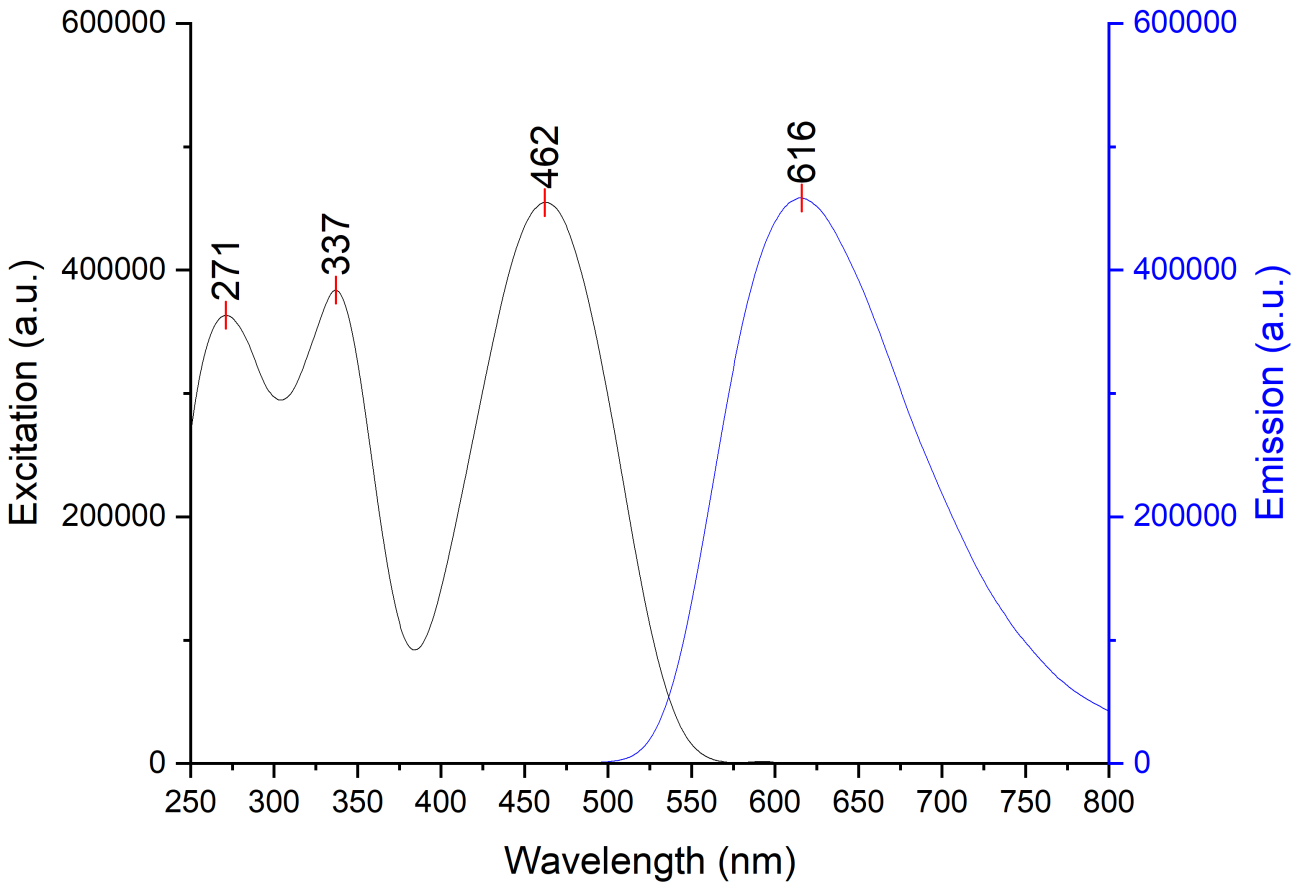

Figure 6-151. Stacked excitation (step: 1.0 nm/s, dwell time: 0.125 s, slit width: 1.0 nm) and emission (step: 1.0 nm/s, dwell time: 0.125 s, slit width: 1.0 nm) spectra of probe 8 and $Sc(OTf)_3$ in MeCN; 12.5 μM sample.

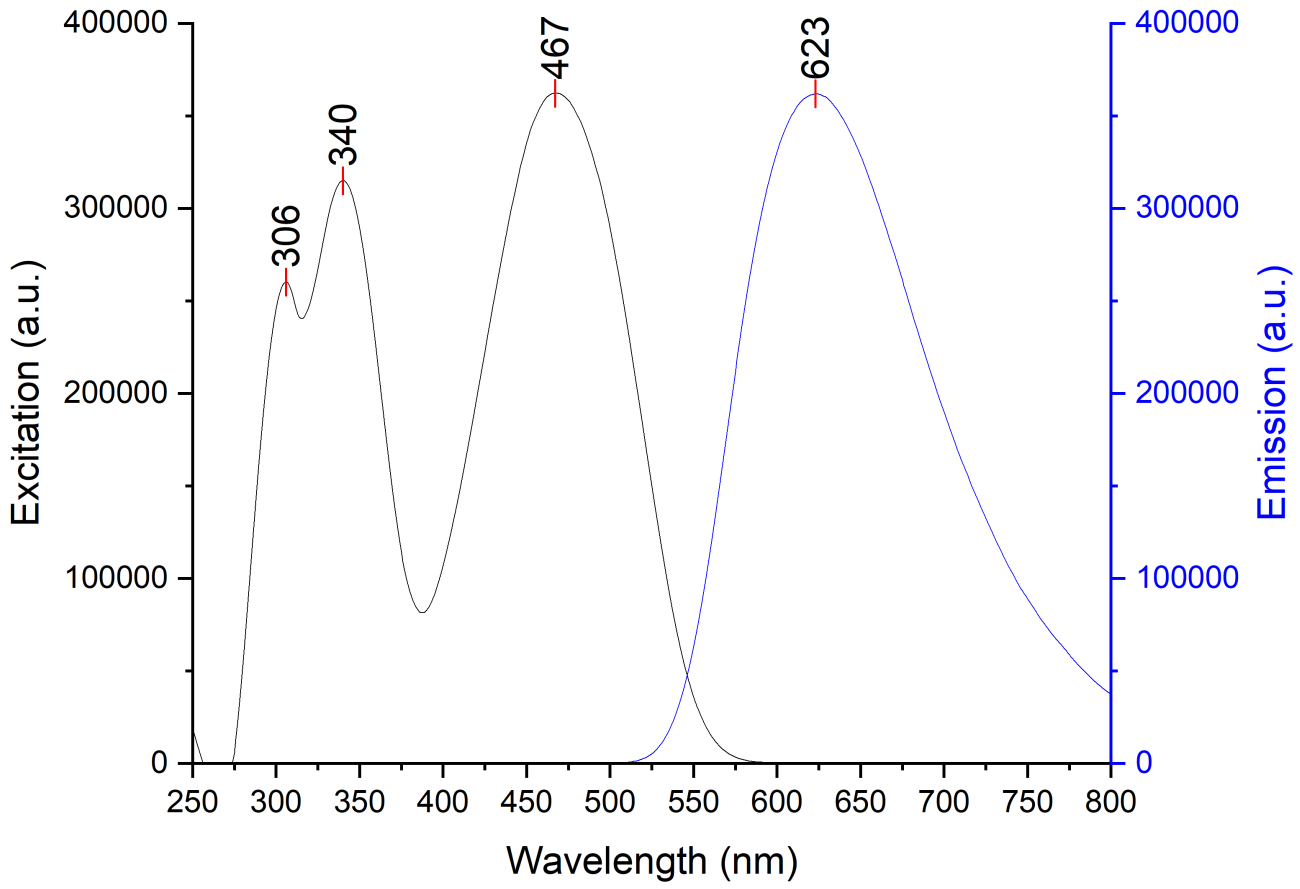

Figure 6-152. Stacked excitation (step: 1.0 nm/s, dwell time: 0.125 s, slit width: 1.0 nm) and emission (step: 1.0 nm/s, dwell time: 0.125 s, slit width: 1.0 nm) spectra of probe 8 and $Sc(OTf)_3$ in PhCl; 12.5 µM sample.

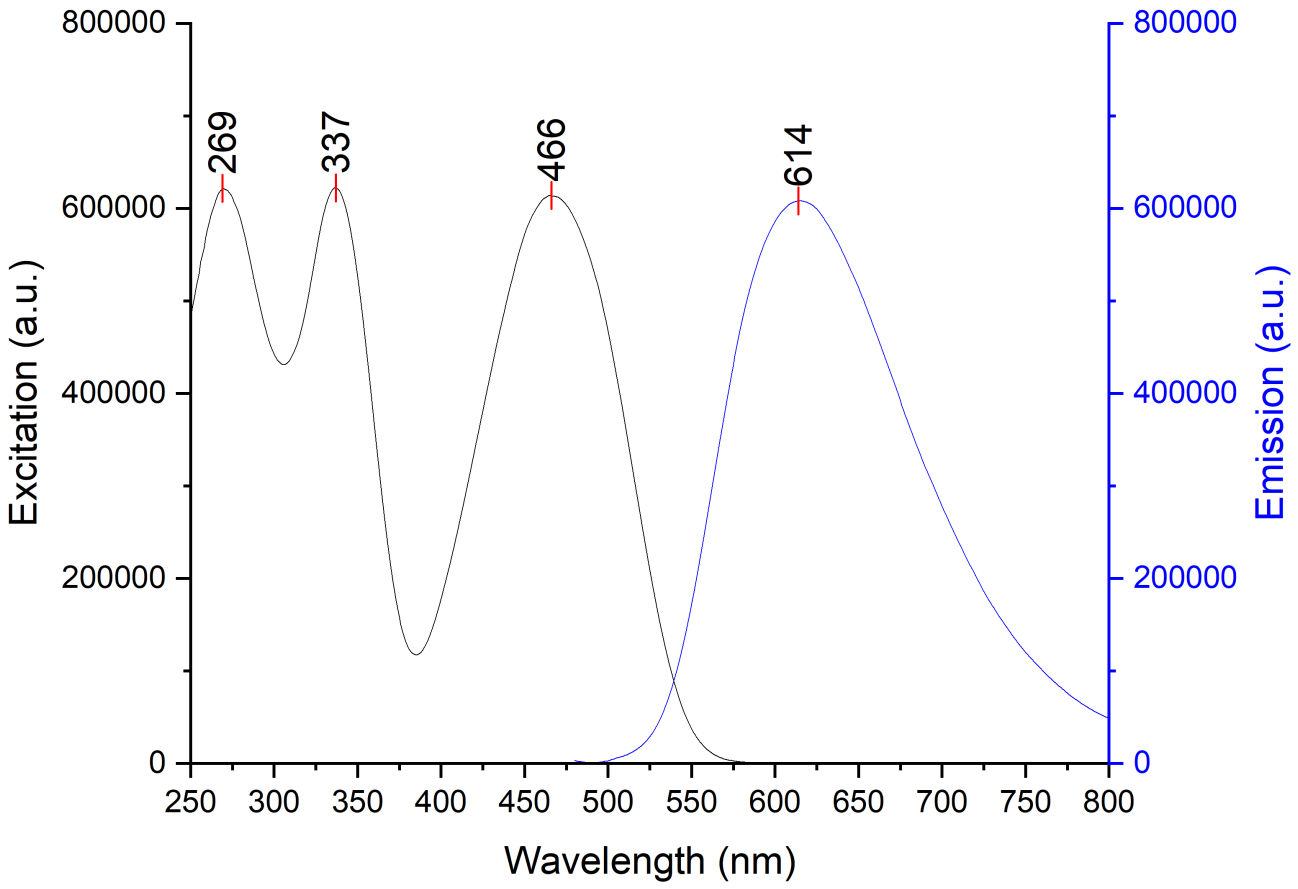

Figure 6-153. Stacked excitation (step: 1.0 nm/s, dwell time: 0.125 s, slit width: 1.0 nm) and emission (step: 1.0 nm/s, dwell time: 0.125 s, slit width: 1.0 nm) spectra of probe 8 and $Sc(OTf)_3$ in Et_2O; 12.5 µM sample.

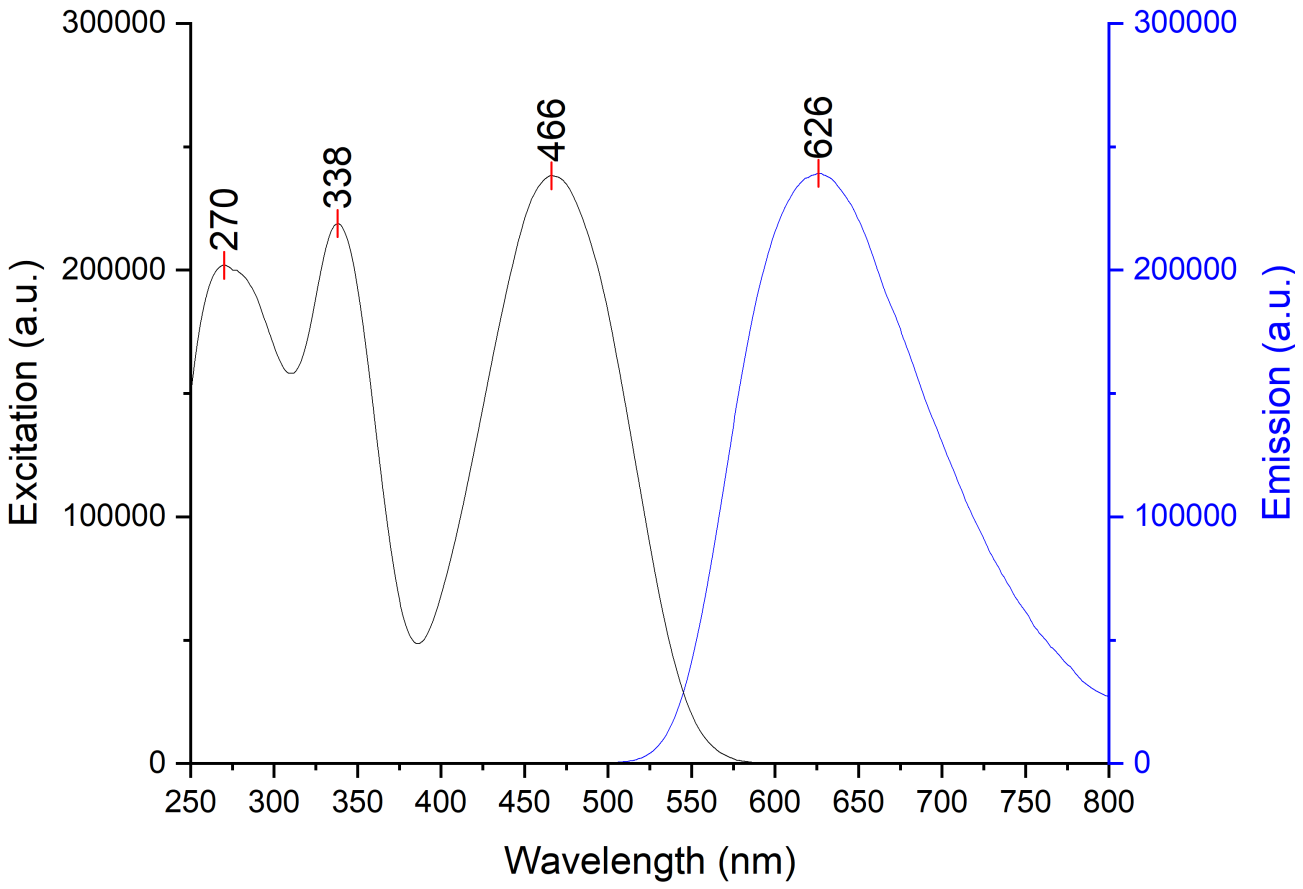

Figure 6-154. Stacked excitation (step: 1.0 nm/s, dwell time: 0.125 s, slit width: 1.0 nm) and emission (step: 1.0 nm/s, dwell time: 0.125 s, slit width: 1.0 nm) spectra of probe 8 and $Sc(OTf)_3$ in DCM; 12.5 µM sample.

6.2.3.10. $Zn(OTf)_2$

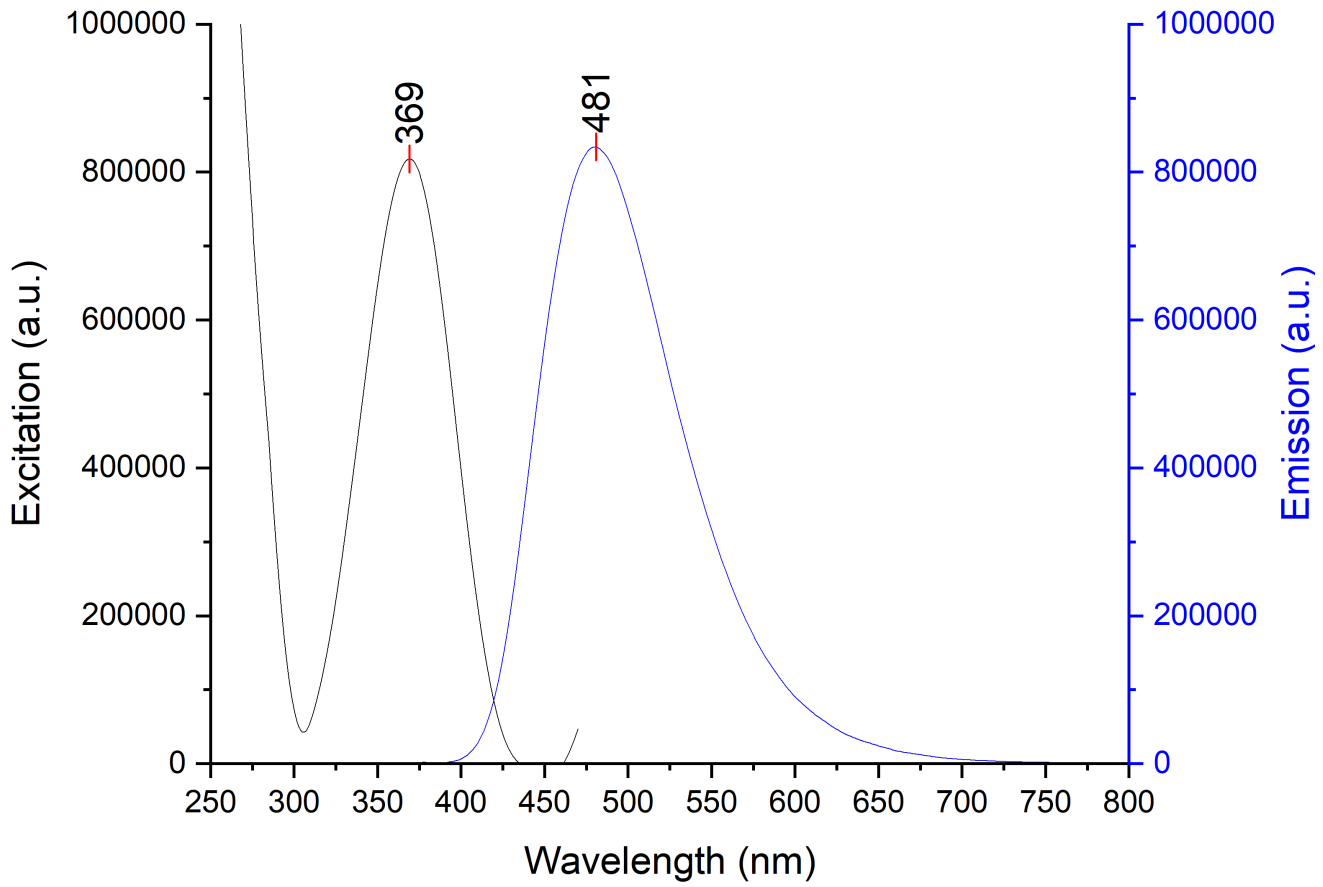

Figure 6-155. Stacked excitation (step: 1.0 nm/s, dwell time: 0.125 s, slit width: 1.0 nm) and emission (step: 1.0 nm/s, dwell time: 0.125 s, slit width: 1.0 nm) spectra of probe 1 and $Zn(OTf)_2$ in MeCN; 12.5 μM sample.

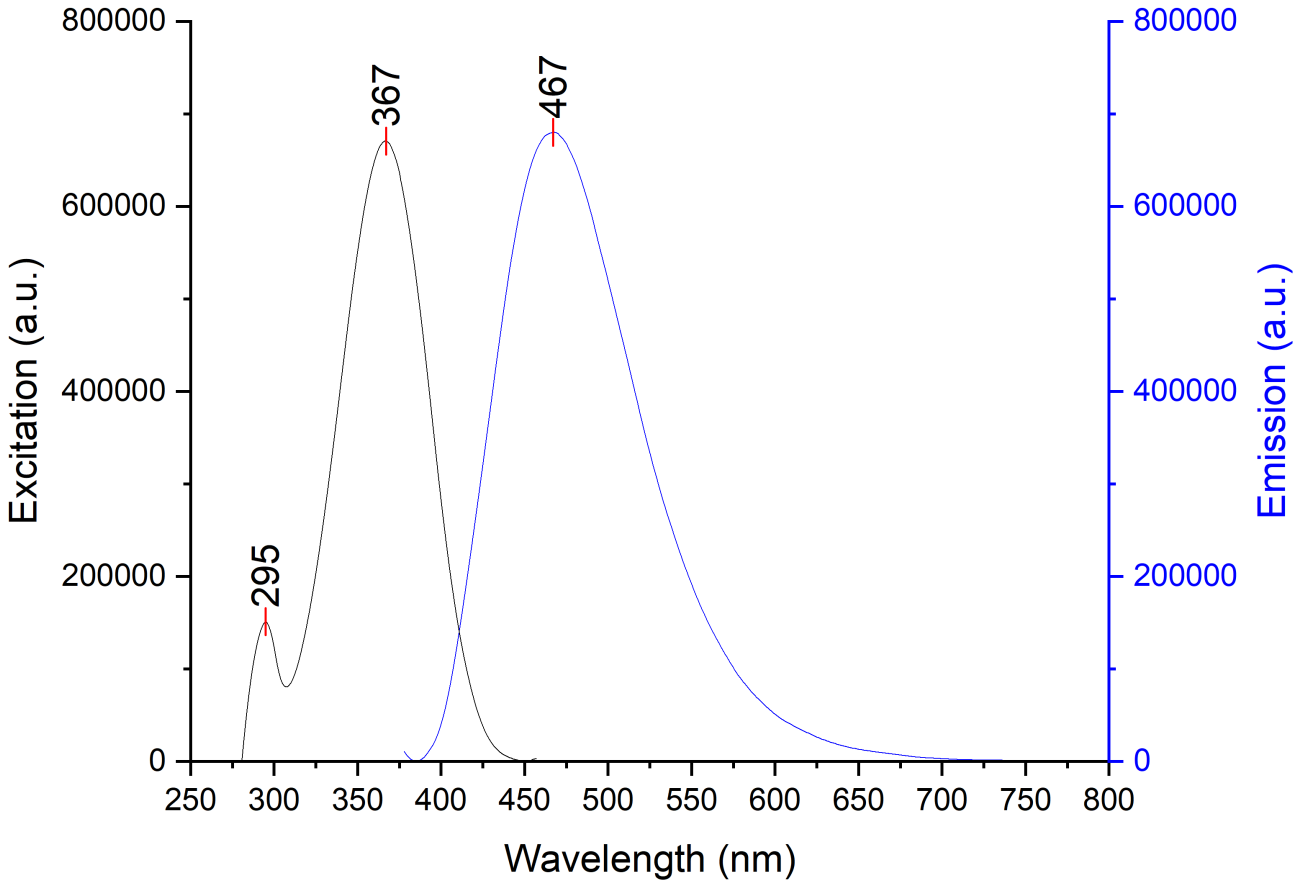

Figure 6-156. Stacked excitation (step: 1.0 nm/s, dwell time: 0.125 s, slit width: 1.0 nm) and emission (step: 1.0 nm/s, dwell time: 0.125 s, slit width: 1.0 nm) spectra of probe 1 and $Zn(OTf)_2$ in PhCl; 12.5 µM sample.

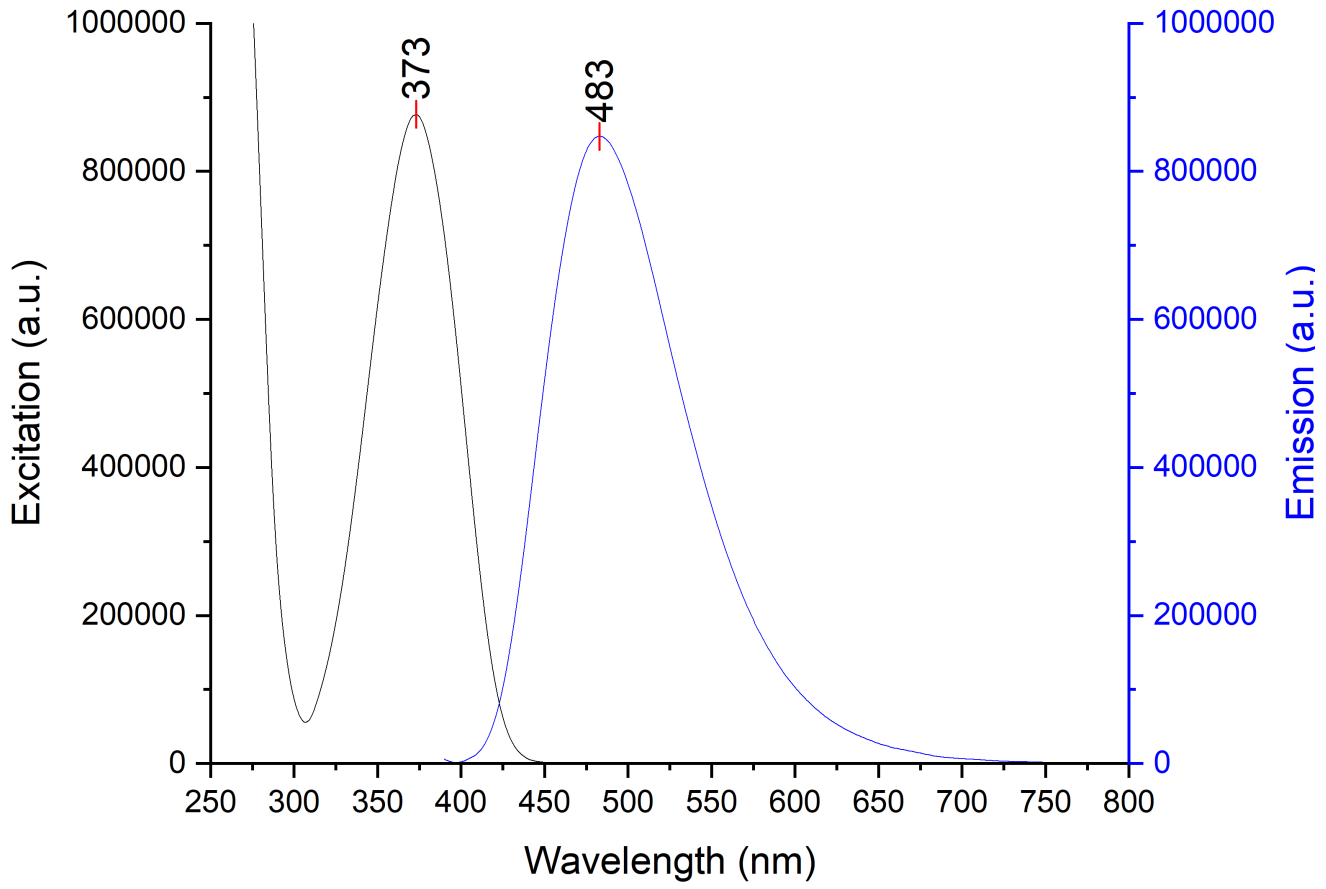

Figure 6-157. Stacked excitation (step: 1.0 nm/s, dwell time: 0.125 s, slit width: 1.0 nm nm) and emission (step: 1.0 nm/s, dwell time: 0.125 s, slit width: 1.0 nm) spectra of probe 1 and $Zn(OTf)_2$ in Et_2O; 12.5 µM sample.

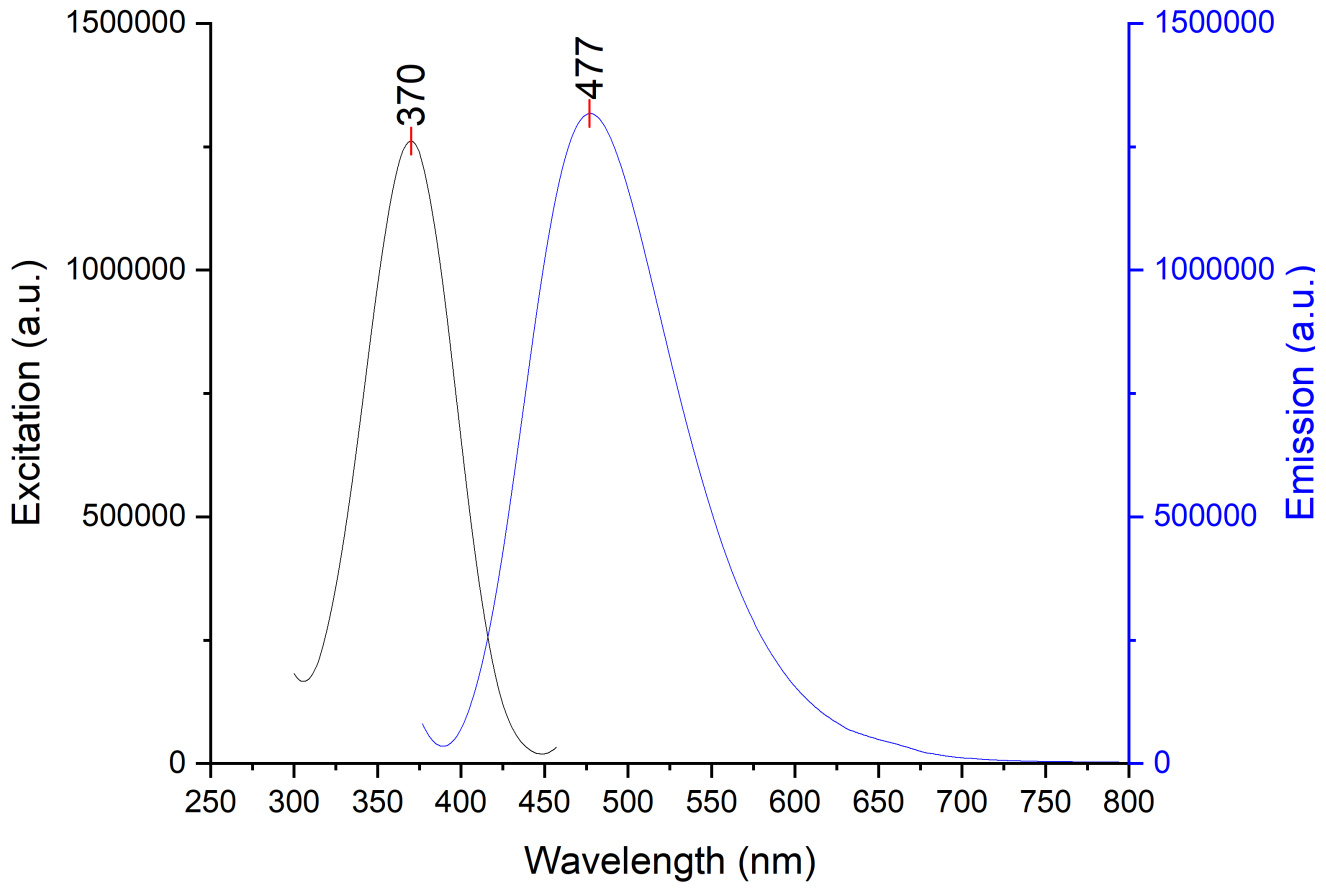

Figure 6-158. Stacked excitation (step: 1.0 nm/s, dwell time: 0.125 s, slit width: 3.0 nm) and emission (step: 1.0 nm/s, dwell time: 0.125 s, slit width: 3.0 nm spectra of probe 1 and $Zn(OTf)_2$ in DCM; 12.5 µM sample.

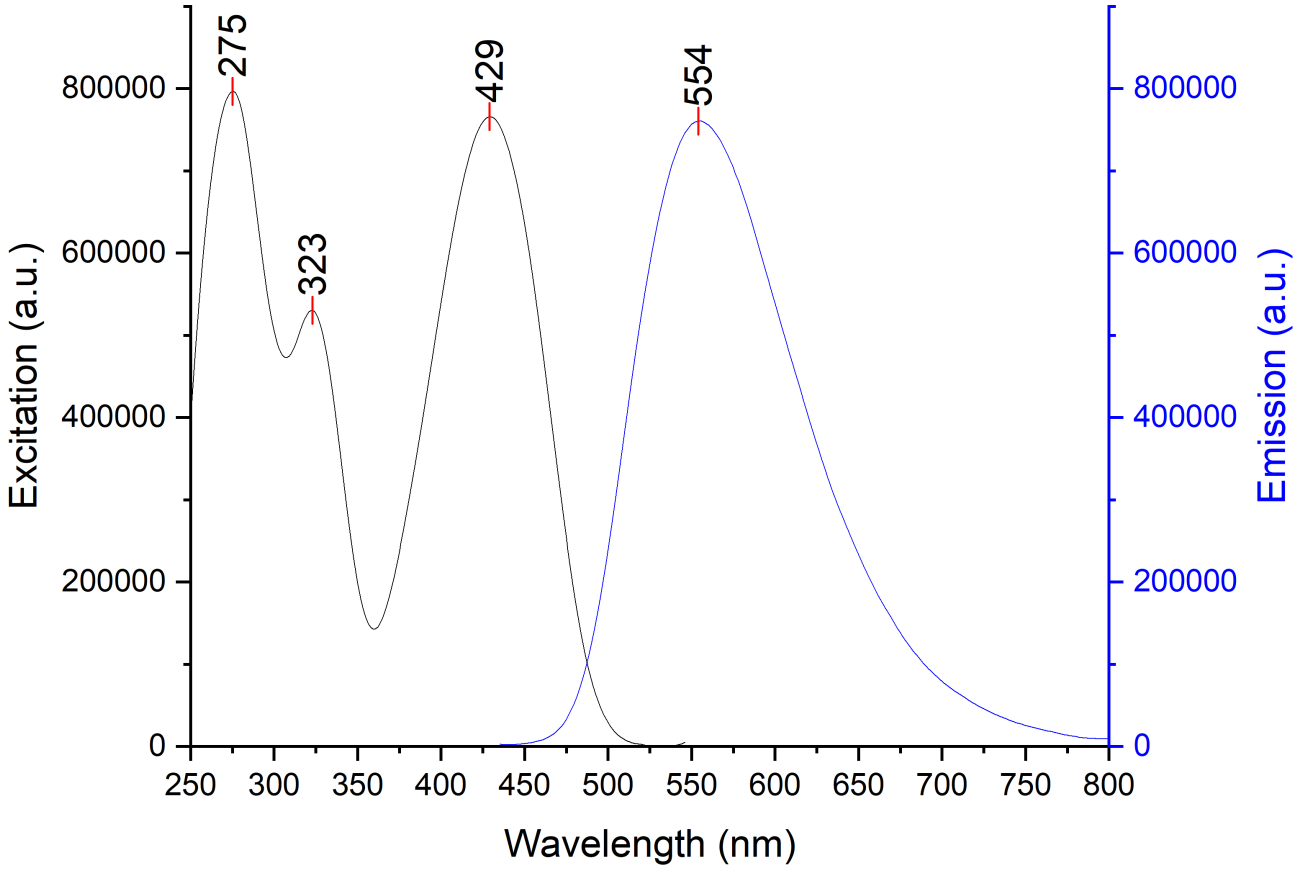

Figure 6-159. Stacked excitation (step: 1.0 nm/s, dwell time: 0.125 s, slit width: 1.0 nm) and emission (step: 1.0 nm/s, dwell time: 0.125 s, slit width: 1.0 nm) spectra of probe 2 and $Zn(OTf)_2$ in MeCN; 12.5 μM sample.

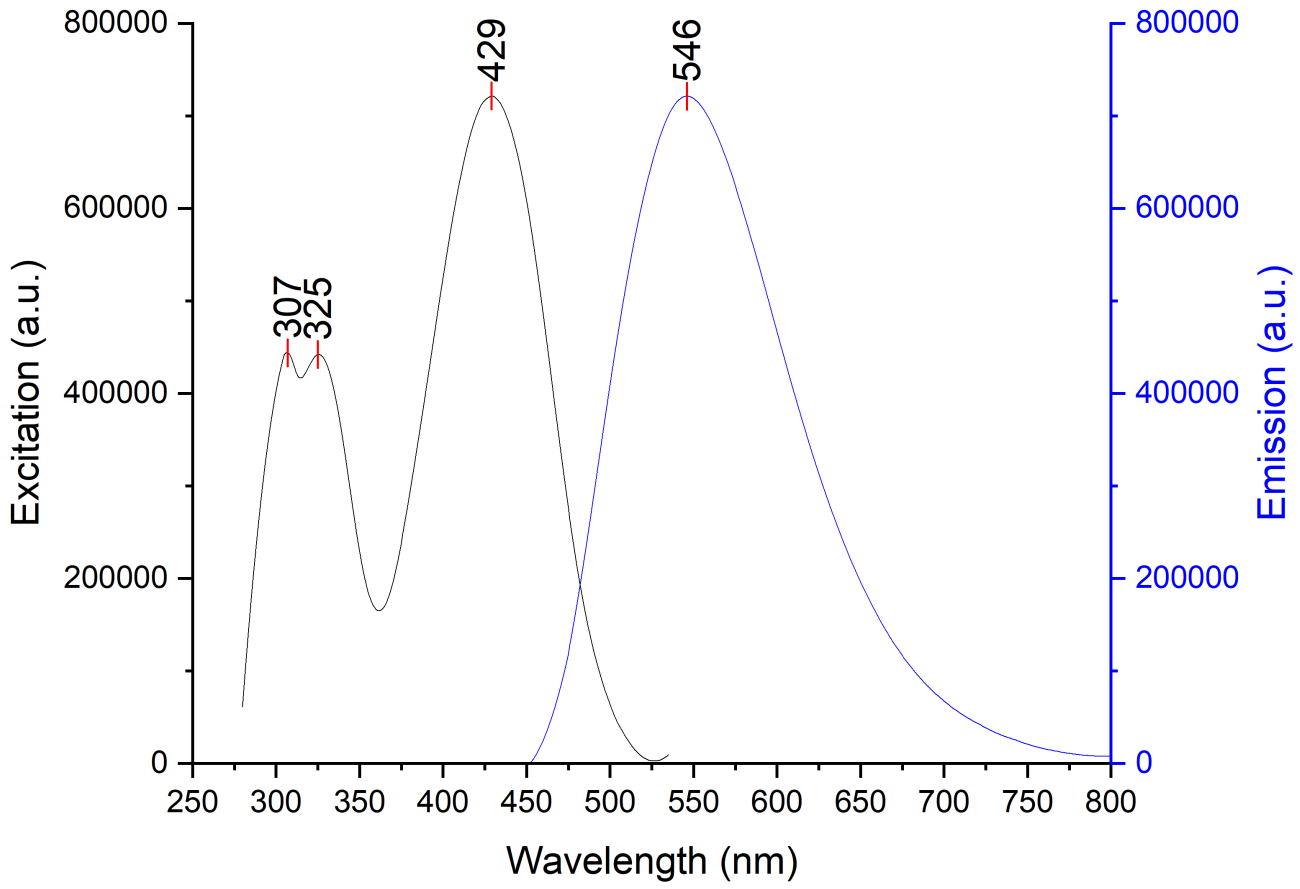

Figure 6-160. Stacked excitation (step: 1.0 nm/s, dwell time: 0.125 s, slit width: 1.0 nm) and emission (step: 1.0 nm/s, dwell time: 0.125 s, slit width: 1.0 nm) spectra of probe 2 and $Zn(OTf)_2$ in PhCl; 12.5 µM sample.

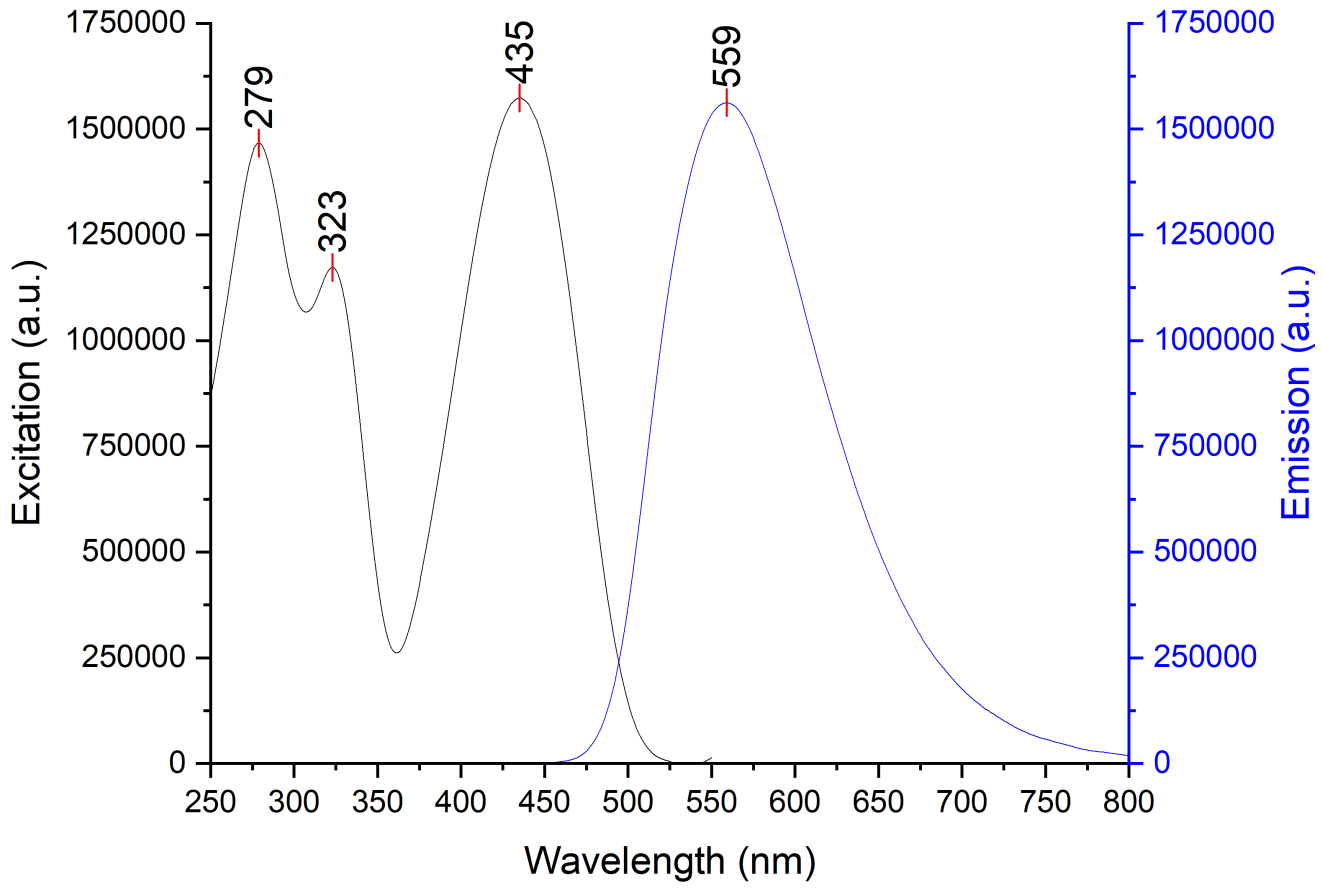

Figure 6-161. Stacked excitation (step: 1.0 nm/s, dwell time: 0.125 s, slit width: 1.0 nm) and emission (step: 1.0 nm/s, dwell time: 0.125 s, slit width: 1.0 nm) spectra of probe 2 and $Zn(OTf)_2$ in Et_2O; 12.5 µM sample.

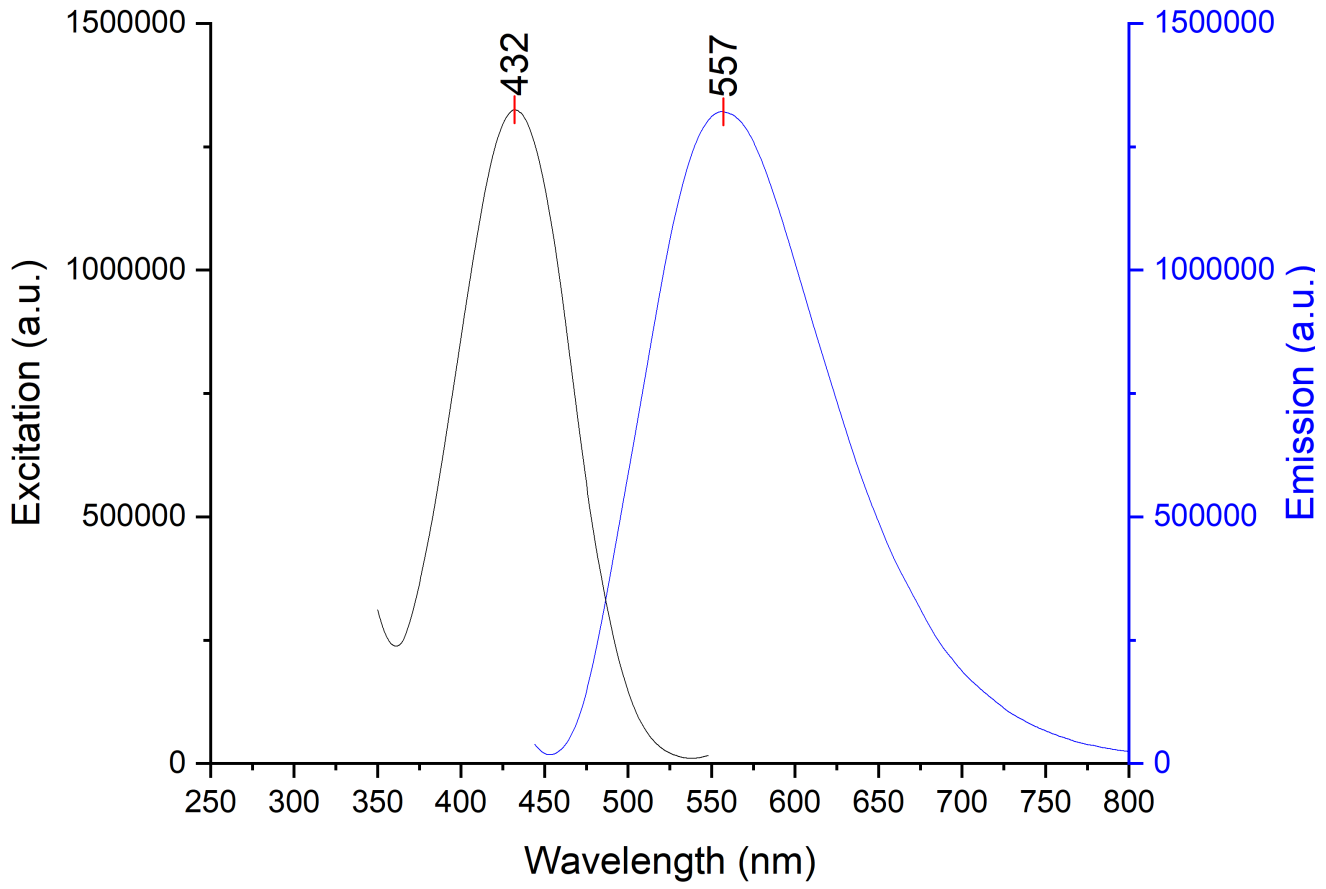

Figure 6-162. Stacked excitation (step: 1.0 nm/s, dwell time: 0.125 s, slit width: 3.0 nm) and emission (step: 1.0 nm/s, dwell time: 0.125 s, slit width: 3.0 nm) spectra of probe 2 and $Zn(OTf)_2$ in DCM; 12.5 μM sample.

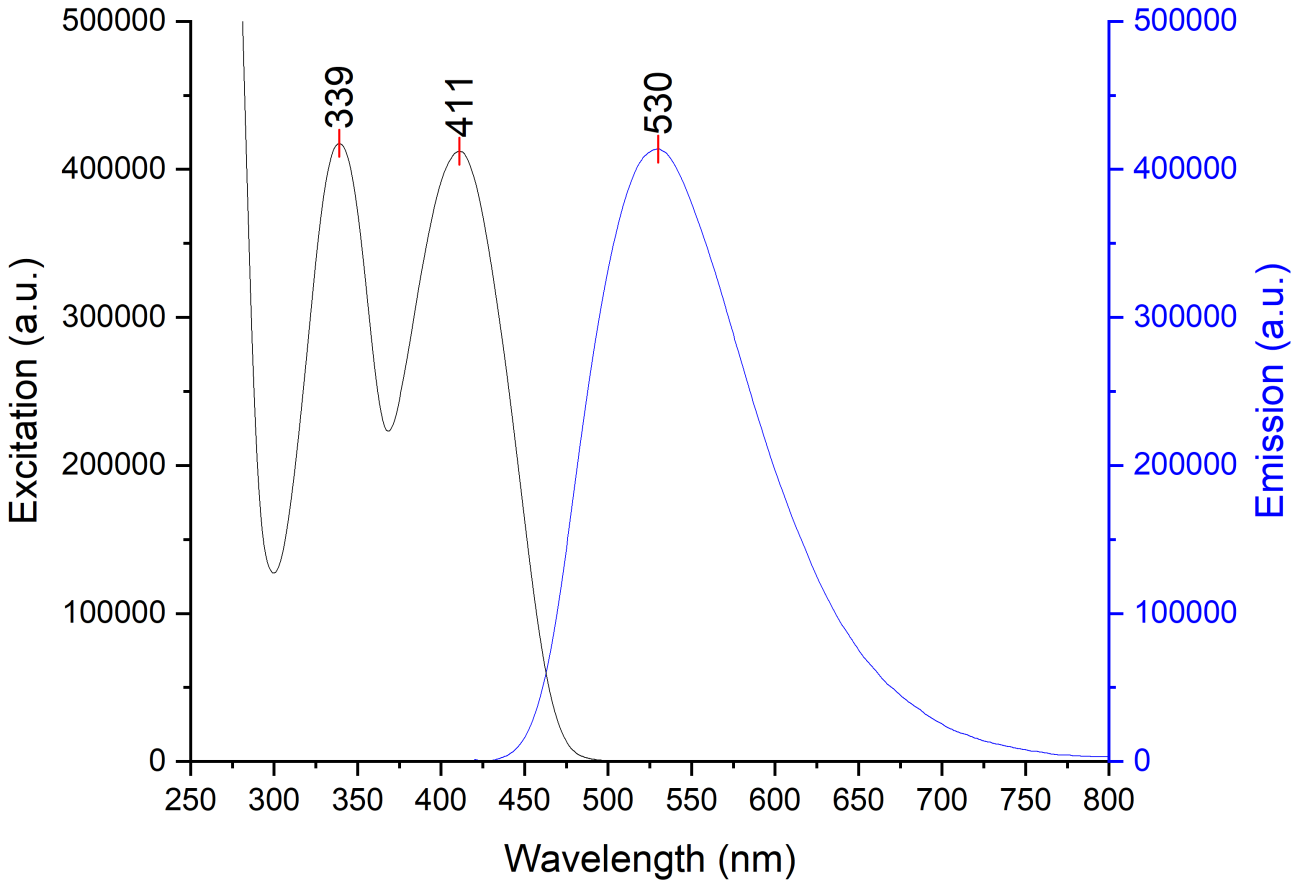

Figure 6-163. Stacked excitation (step: 1.0 nm/s, dwell time: 0.125 s, slit width: 1.0 nm) and emission (step: 1.0 nm/s, dwell time: 0.125 s, slit width: 1.0 nm) spectra of probe 7 and $Zn(OTf)_2$ in MeCN; 12.5 μM sample.

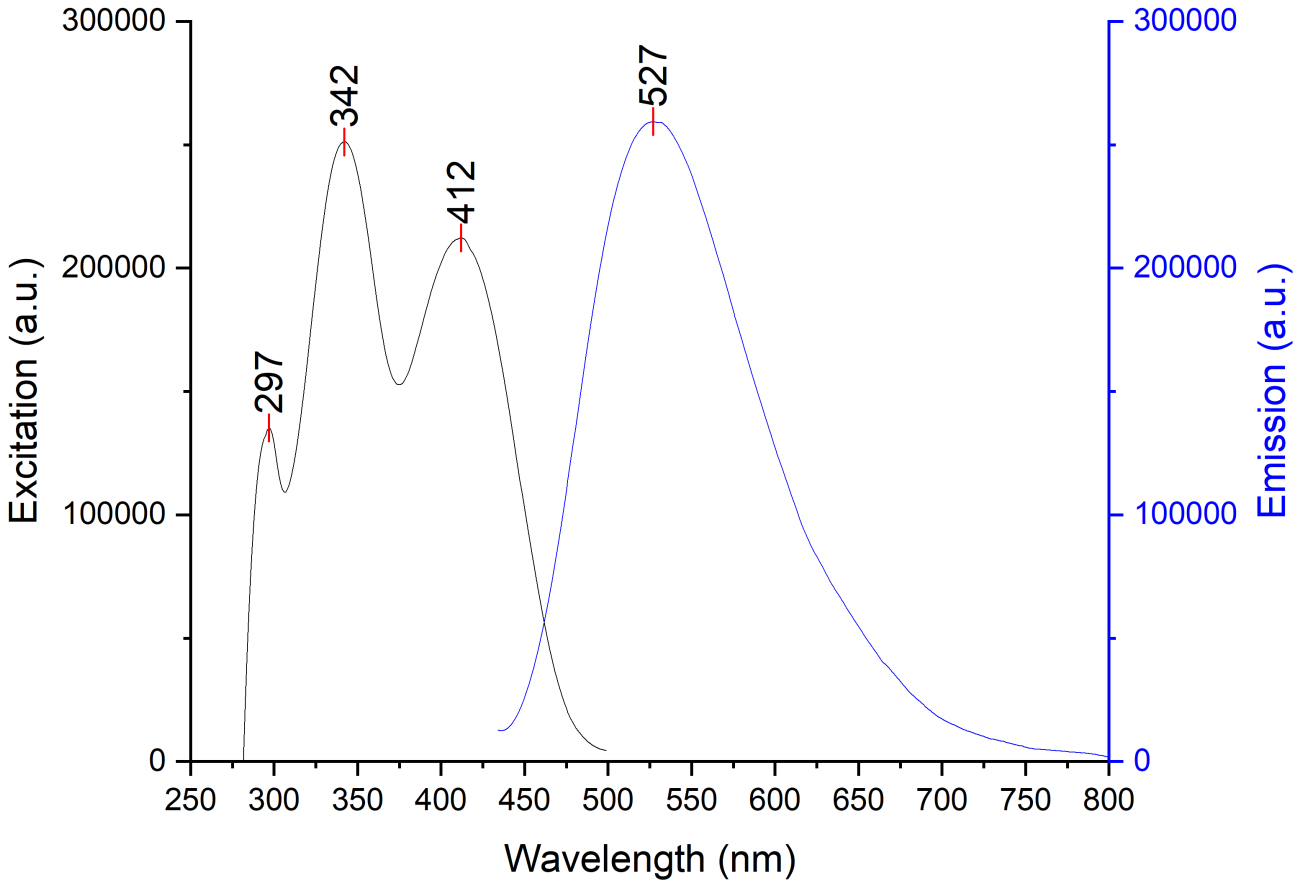

Figure 6-164. Stacked excitation (step: 1.0 nm/s, dwell time: 0.125 s, slit width: 1.0 nm) and emission (step: 1.0 nm/s, dwell time: 0.125 s, slit width: 1.0 nm) spectra of probe 7 and $Zn(OTf)_2$ in PhCl; 12.5 µM sample.

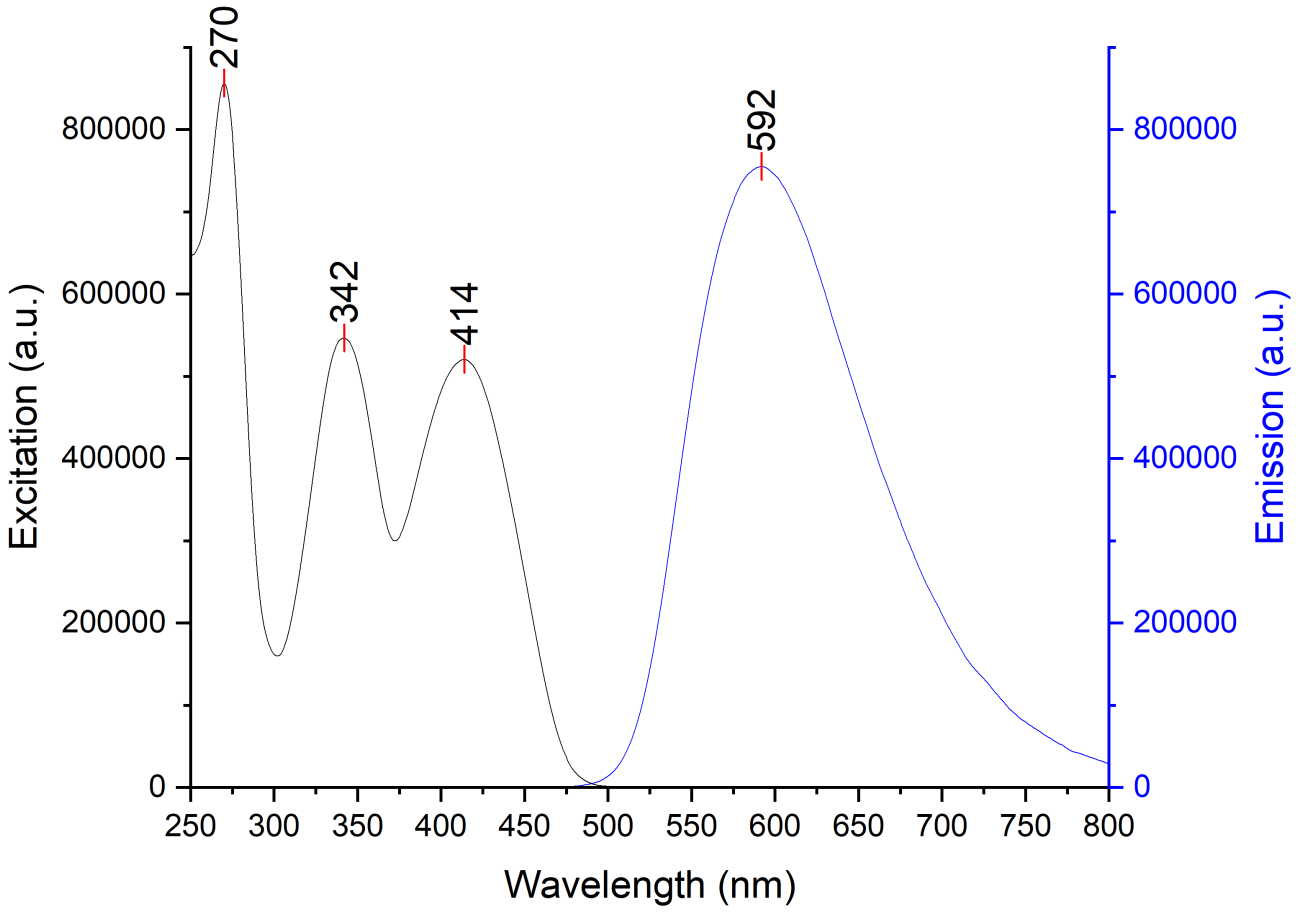

Figure 6-165. Stacked excitation (step: 1.0 nm/s, dwell time: 0.125 s, slit width: 1.0 nm) and emission (step: 1.0 nm/s, dwell time: 0.125 s, slit width: 1.0 nm) spectra of probe 7 and $Zn(OTf)_2$ in Et_2O; 12.5 µM sample.

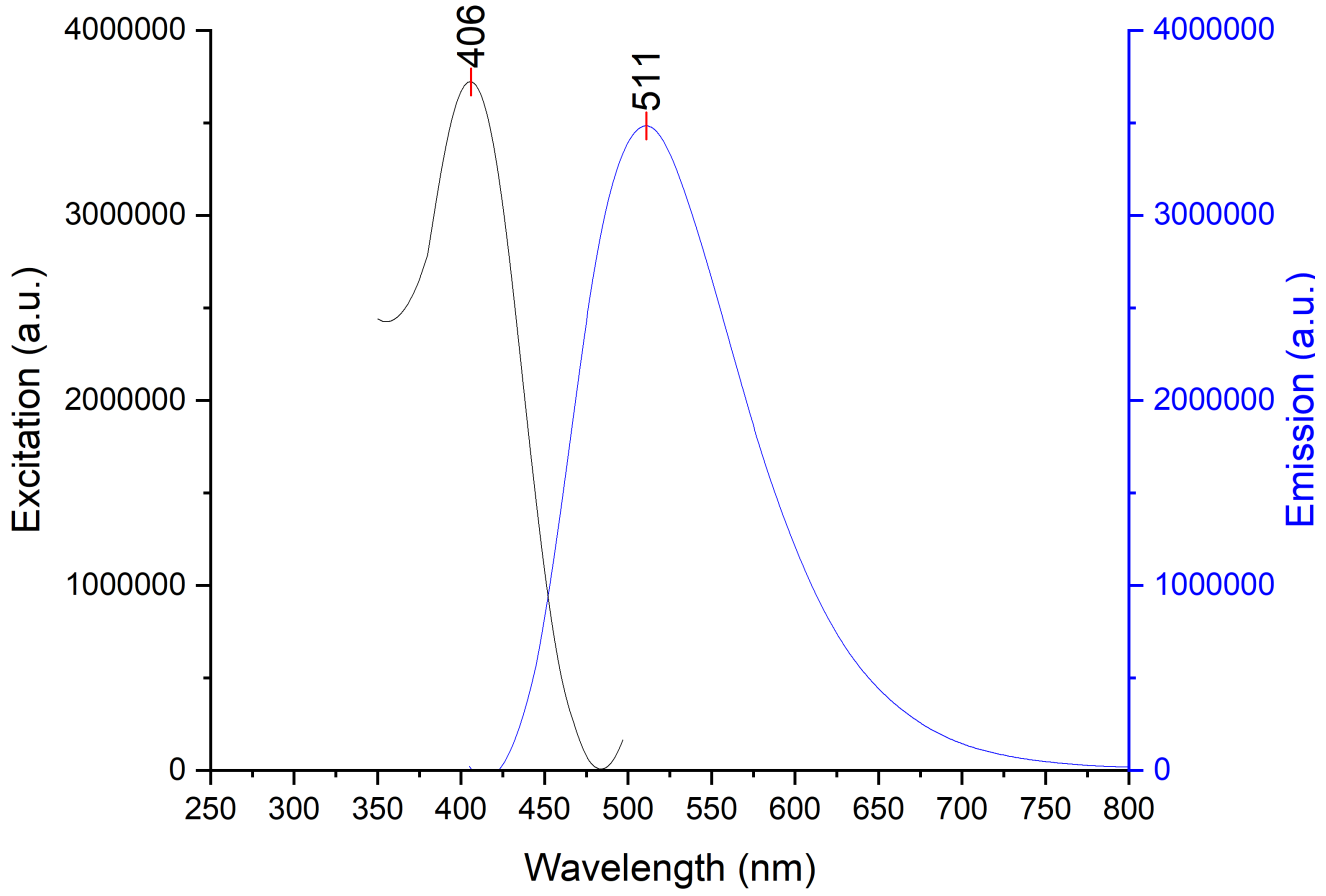

Figure 6-166. Stacked excitation (step: 1.0 nm/s, dwell time: 0.125 s, slit width: 3.0 nm) and emission (step: 1.0 nm/s, dwell time: 0.125 s, slit width: 3.0 nm) spectra of probe 7 and $Zn(OTf)_2$ in DCM; 12.5 μM sample.

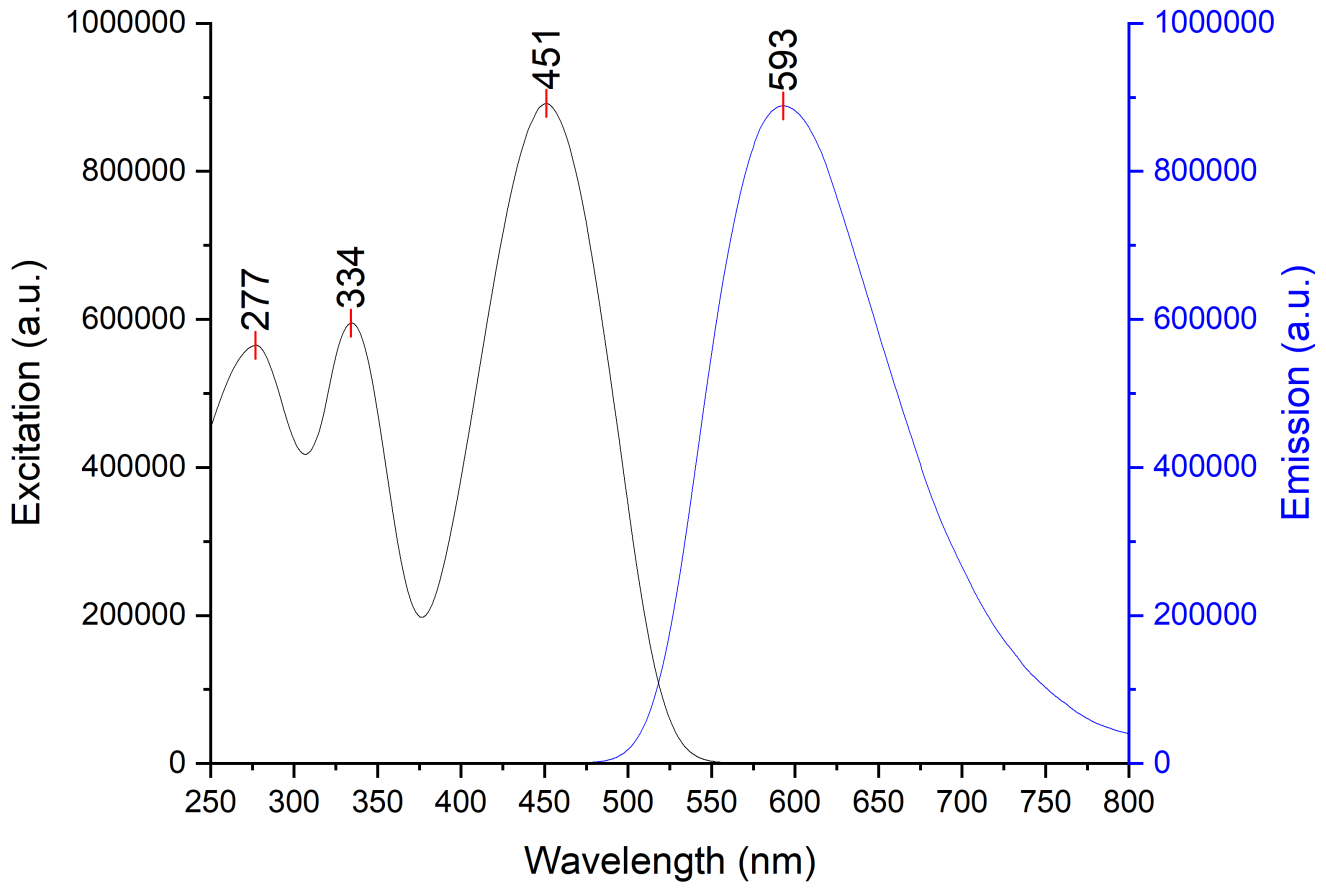

Figure 6-167. Stacked excitation (step: 1.0 nm/s, dwell time: 0.125 s, slit width: 1.0 nm) and emission (step: 1.0 nm/s, dwell time: 0.125 s, slit width: 1.0 nm) spectra of probe 8 and $Zn(OTf)_2$ in MeCN; 12.5 μM sample.

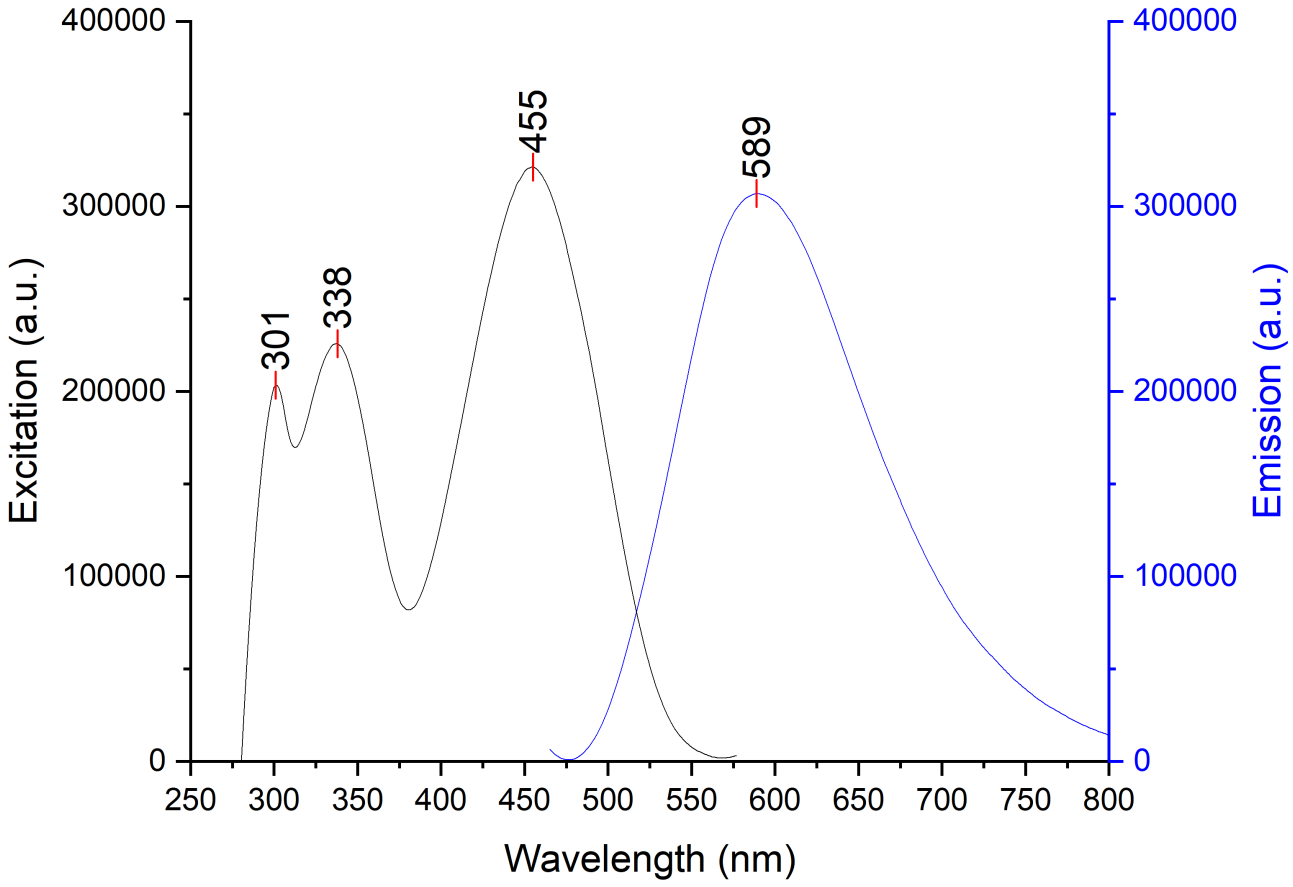

Figure 6-168. Stacked excitation (step: 1.0 nm/s, dwell time: 0.125 s, slit width: 1.0 nm) and emission (step: 1.0 nm/s, dwell time: 0.125 s, slit width: 1.0 nm) spectra of probe 8 and $Zn(OTf)_2$ in PhCl; 12.5 µM sample.

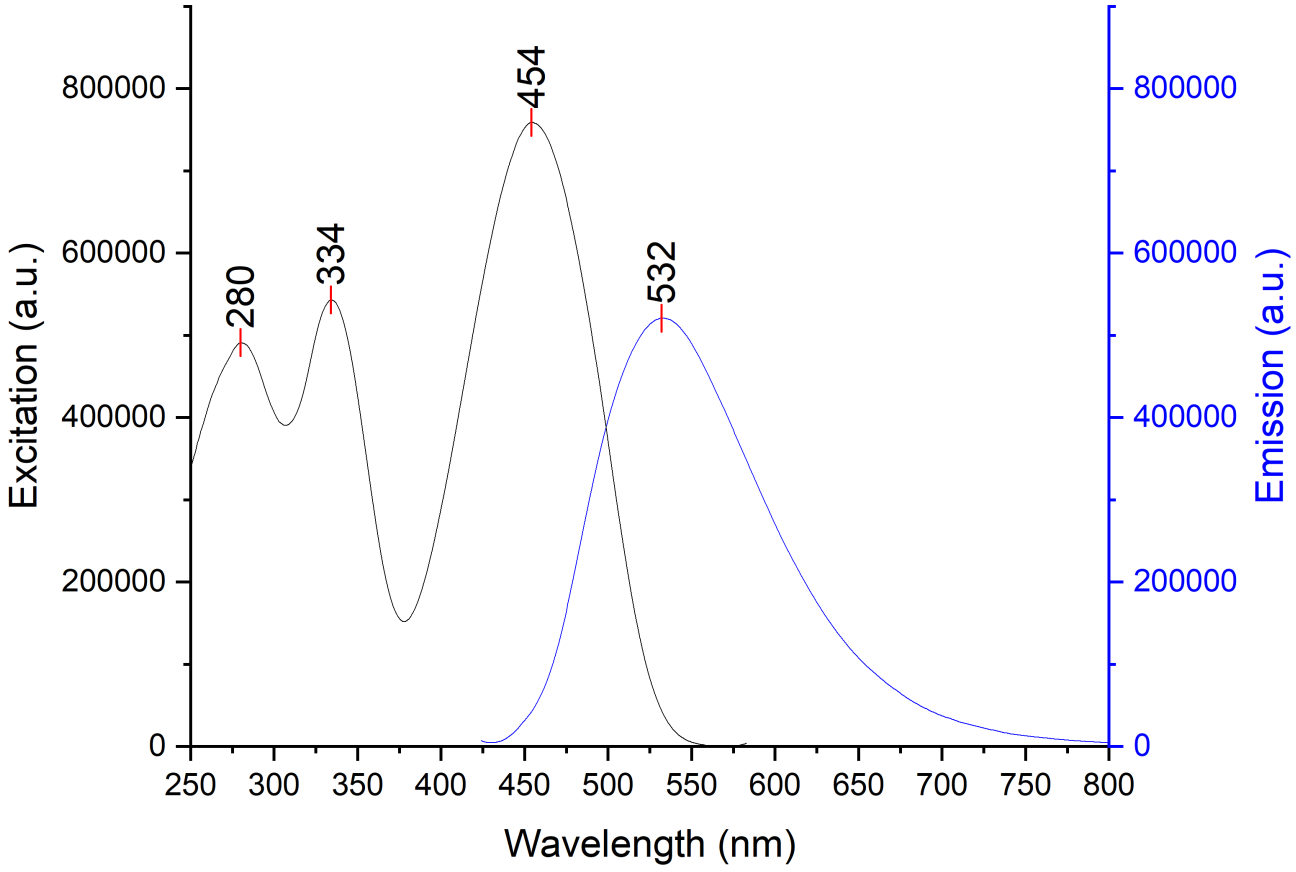

Figure 6-169. Stacked excitation (step: 1.0 nm/s, dwell time: 0.125 s, slit width: 1.0 nm) and emission (step: 1.0 nm/s, dwell time: 0.125 s, slit width: 1.0 nm spectra of probe 8 and $Zn(OTf)_2$ in Et_2O; 12.5 µM sample.

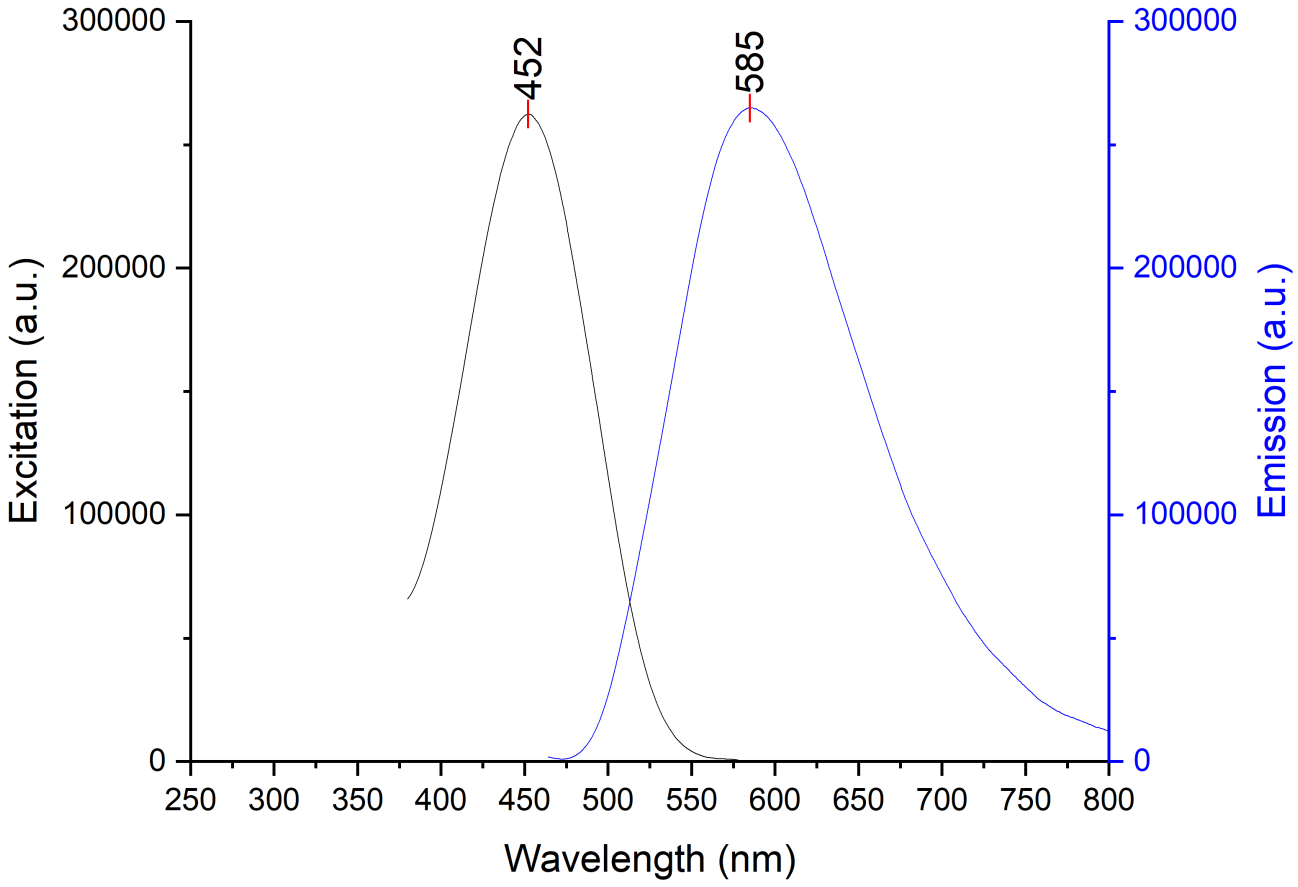

Figure 6-170. Stacked excitation (step: 1.0 nm/s, dwell time: 0.125 s, slit width: 1.0 nm) and emission (step: 1.0 nm/s, dwell time: 0.125 s, slit width: 1.0 nm) spectra of probe 8 and $Zn(OTf)_2$ in DCM; 12.5 μM sample.

6.2.3.11. $[Et_3Si][B(C_6F_5)_4]$

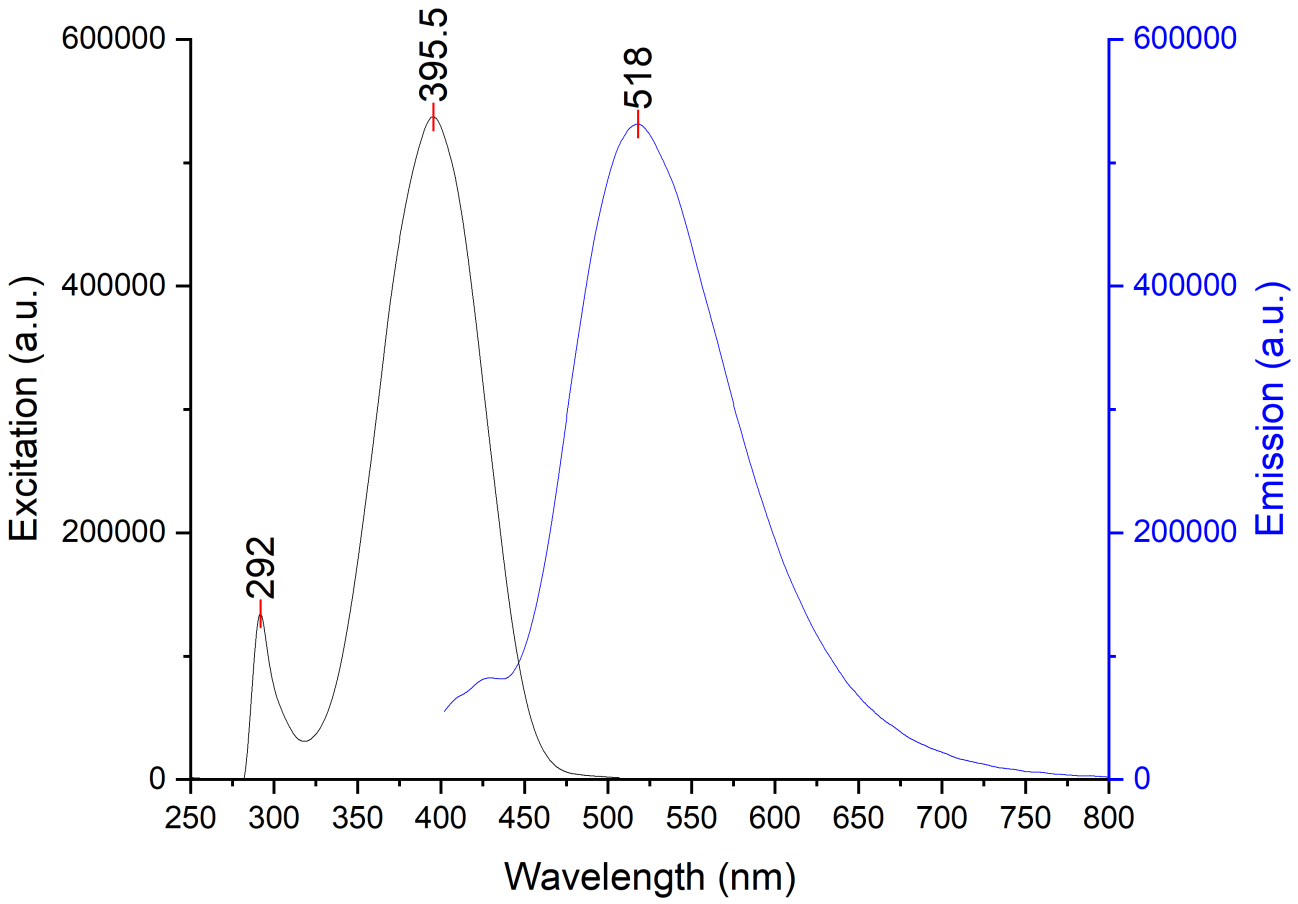

Figure 6-171. Stacked excitation (step: 1.0 nm/s, dwell time: 0.125 s, slit width: 1.0 nm) and emission (step: 1.0 nm/s, dwell time: 0.125 s, slit width: 1.0 nm) spectra of probe 1 and $[Et_3Si][B(C_6F_5)_4]$ in PhCl; 12.5 μM sample.

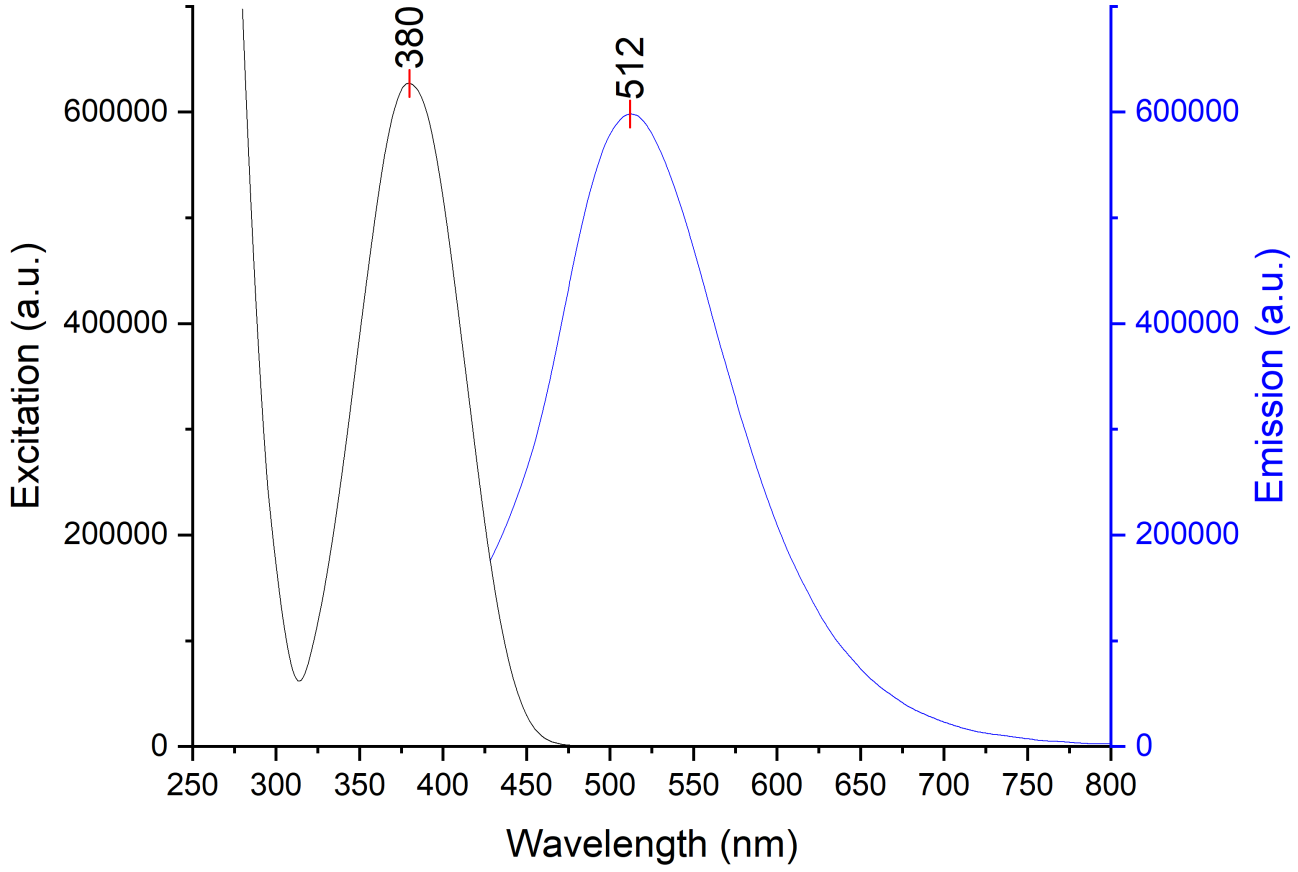

Figure 6-172. Stacked excitation (step: 1.0 nm/s, dwell time: 0.125 s, slit width: 1.0 nm) and emission (step: 1.0 nm/s, dwell time: 0.125 s, slit width: 1.0 nm) spectra of probe 1 and $[Et_3Si][B(C_6F_5)_4]$ in Et_2O; 12.5 μM sample.

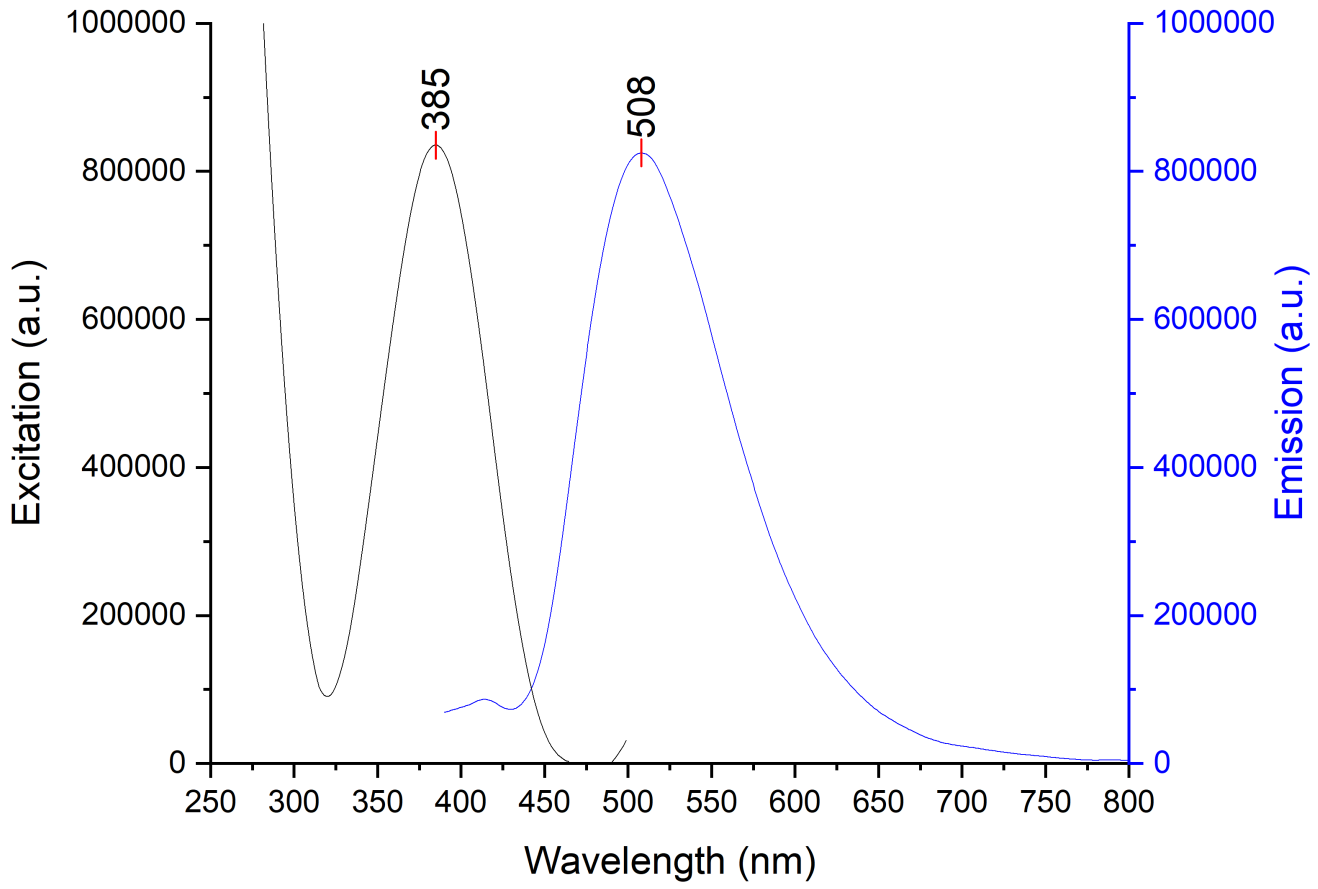

Figure 6-173. Stacked excitation (step: 1.0 nm/s, dwell time: 0.125 s, slit width: 1.0 nm) and emission (step: 1.0 nm/s, dwell time: 0.125 s, slit width: 1.0 nm) spectra of probe 1 and $[Et_3Si][B(C_6F_5)_4]$ in DCM; 12.5 µM sample.

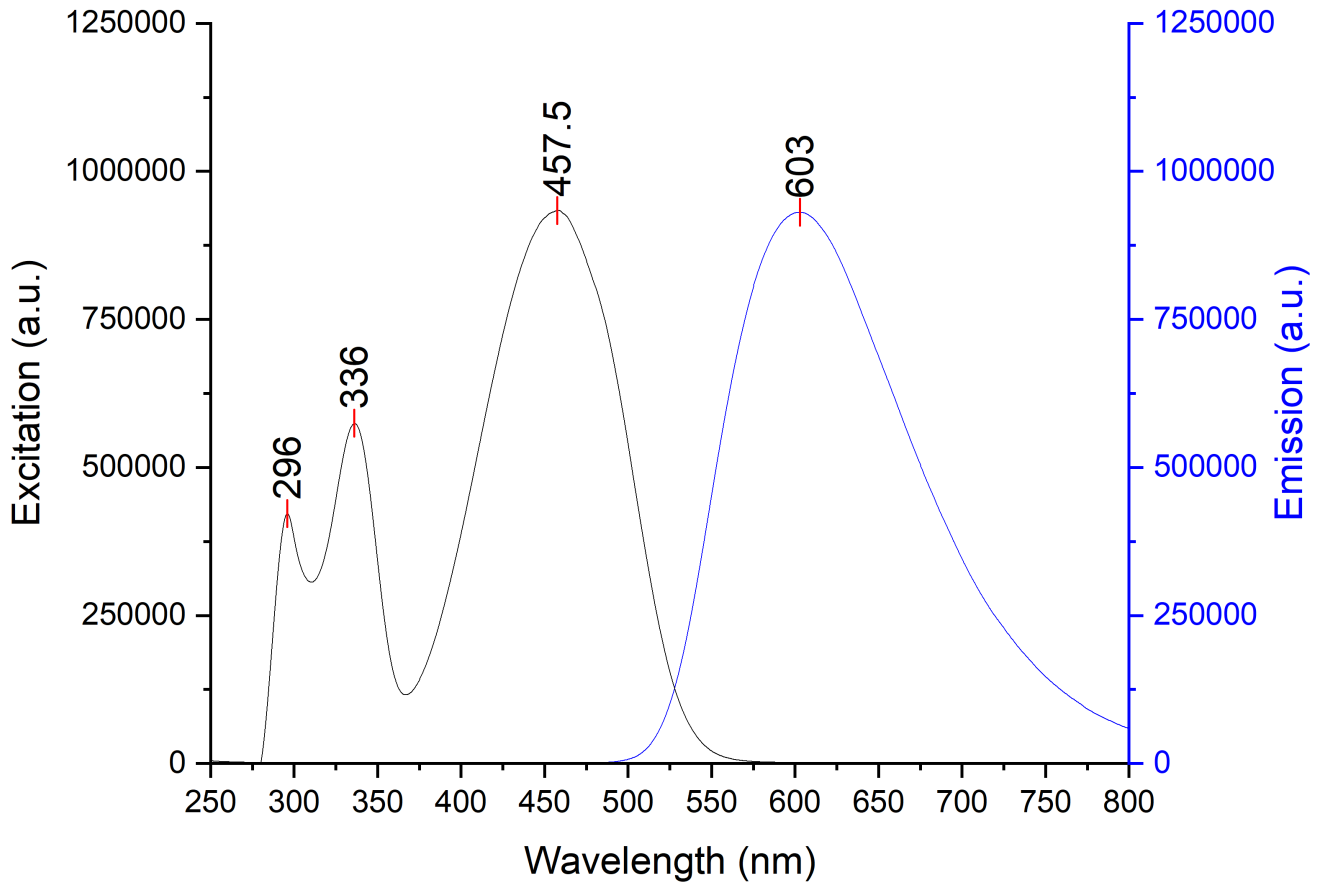

Figure 6-174. Stacked excitation (step: 1.0 nm/s, dwell time: 0.125 s, slit width: 1.0 nm) and emission (step: 1.0 nm/s, dwell time: 0.125 s, slit width: 1.0 nm) spectra of probe 2 and $[Et_3Si][B(C_6F_5)_4]$ in PhCl; 12.5 μM sample.

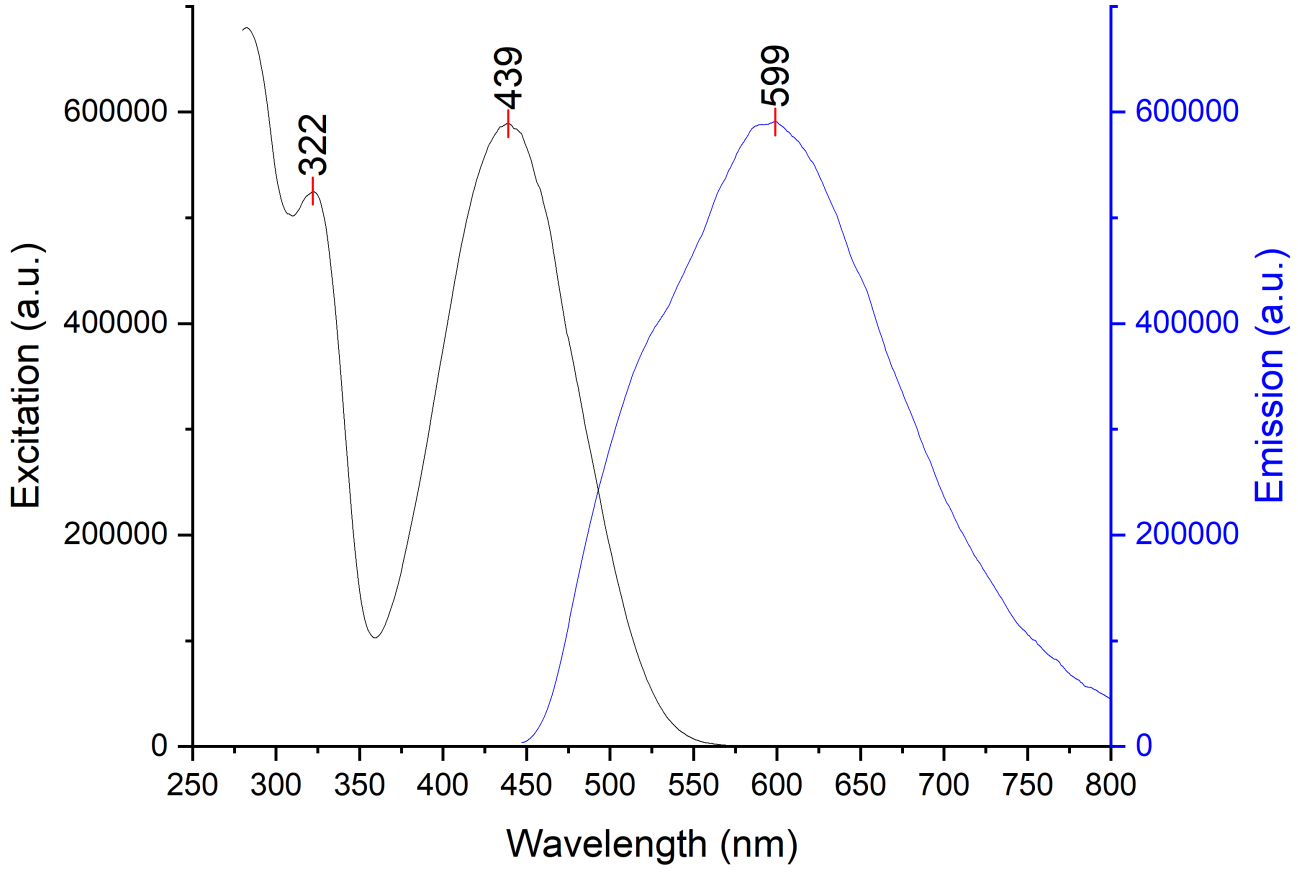

Figure 6-175. Stacked excitation (step: 1.0 nm/s, dwell time: 0.125 s, slit width: 1.0 nm) and emission (step: 1.0 nm/s, dwell time: 0.125 s, slit width: 1.0 nm) spectra of probe 2 and $[Et_3Si][B(C_6F_5)_4]$ in Et_2O; 12.5 μM sample.

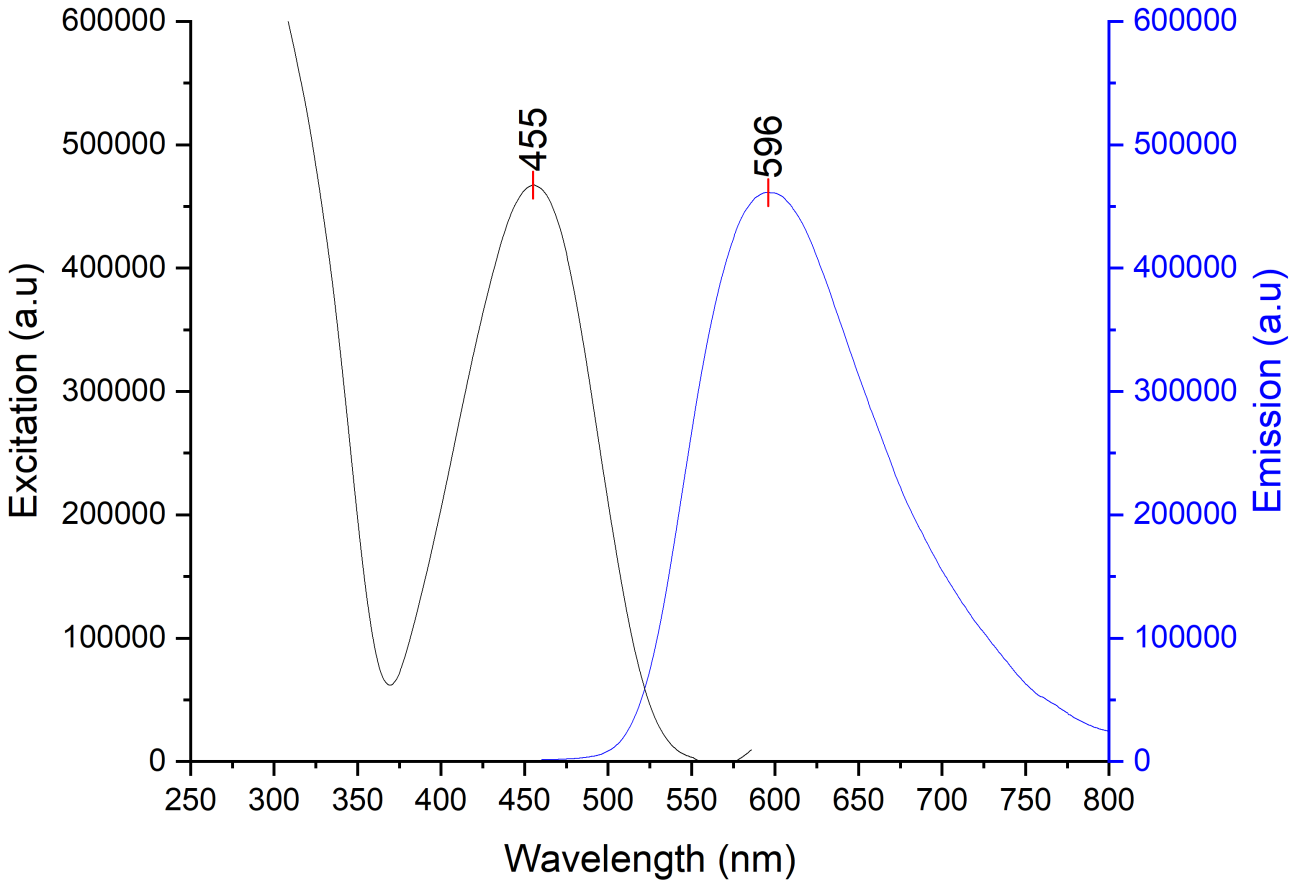

Figure 6-176. Stacked excitation (step: 1.0 nm/s, dwell time: 0.125 s, slit width: 1.0 nm) and emission (step: 1.0 nm/s, dwell time: 0.125 s, slit width: 1.0 nm) spectra of probe 2 and $[Et_3Si][B(C_6F_5)_4]$ in DCM; 12.5 μM sample.

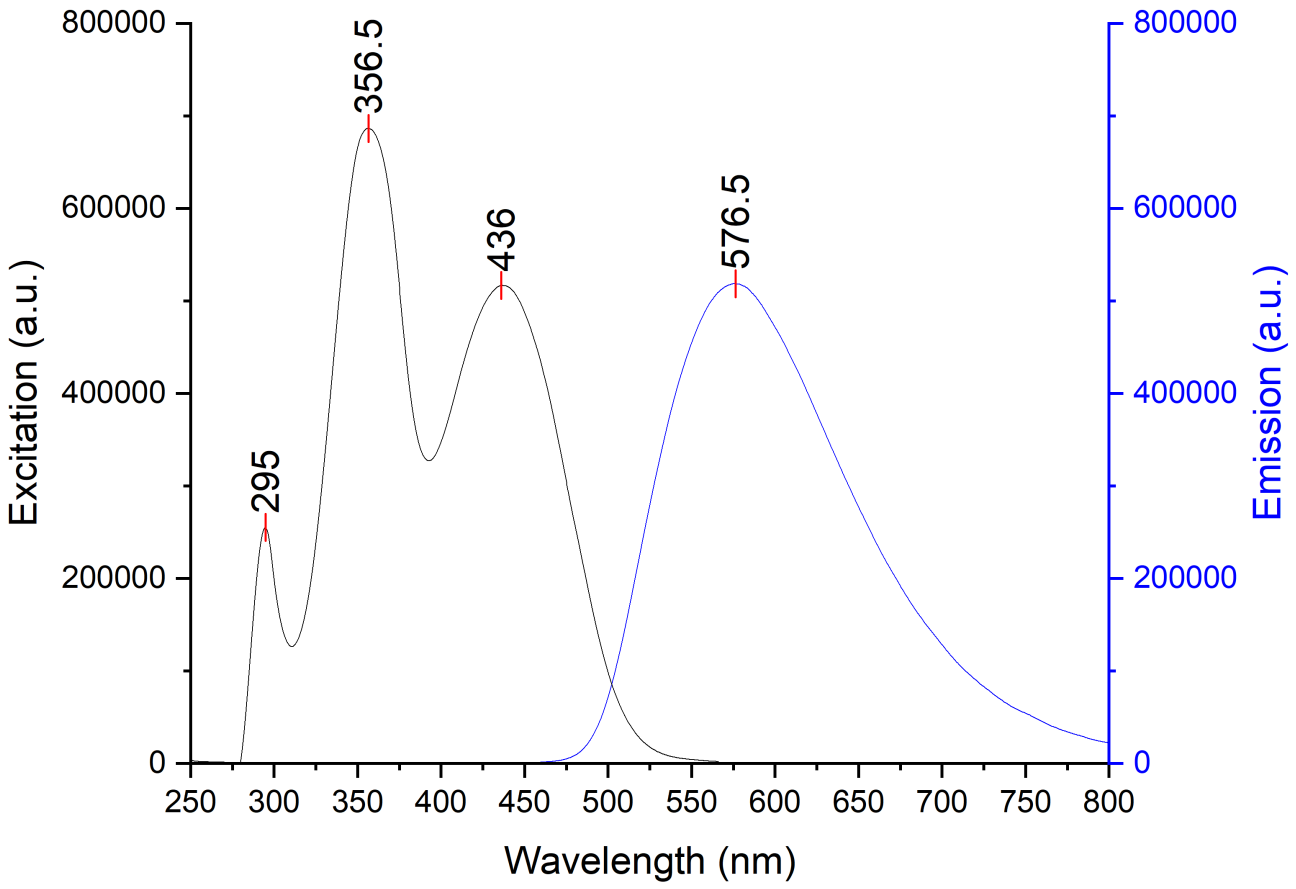

Figure 6-177. Stacked excitation (step: 1.0 nm/s, dwell time: 0.125 s, slit width: 1.0 nm) and emission (step: 1.0 nm/s, dwell time: 0.125 s, slit width: 1.0 nm) spectra of probe 7 and $[Et_3Si][B(C_6F_5)_4]$ in PhCl; 12.5 μM sample.

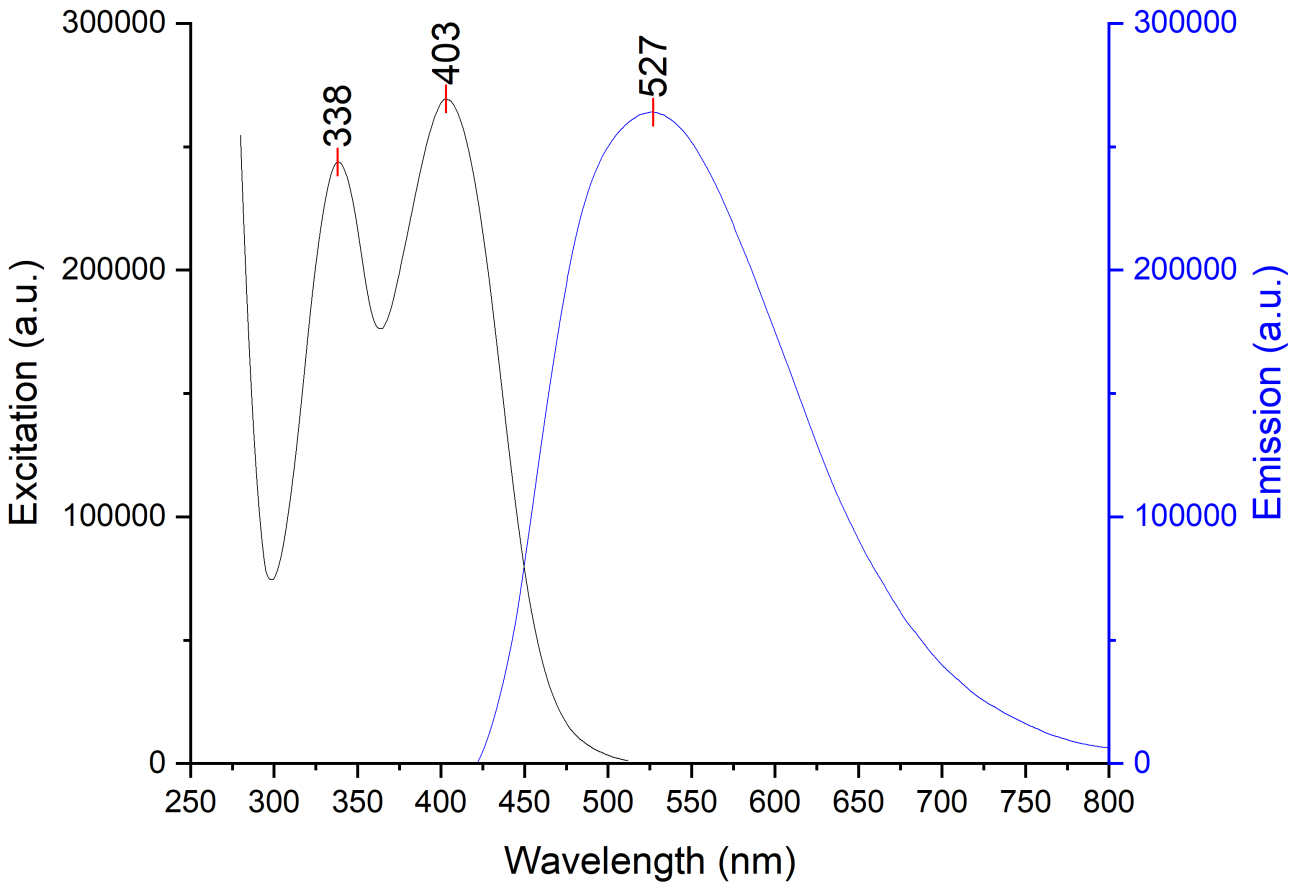

Figure 6-178. Stacked excitation (step: 1.0 nm/s, dwell time: 0.125 s, slit width: 1.0 nm) and emission (step: 1.0 nm/s, dwell time: 0.125 s, slit width: 1.0 nm) spectra of probe 7 and $[Et_3Si][B(C_6F_5)_4]$ in Et_2O; 12.5 μM sample.

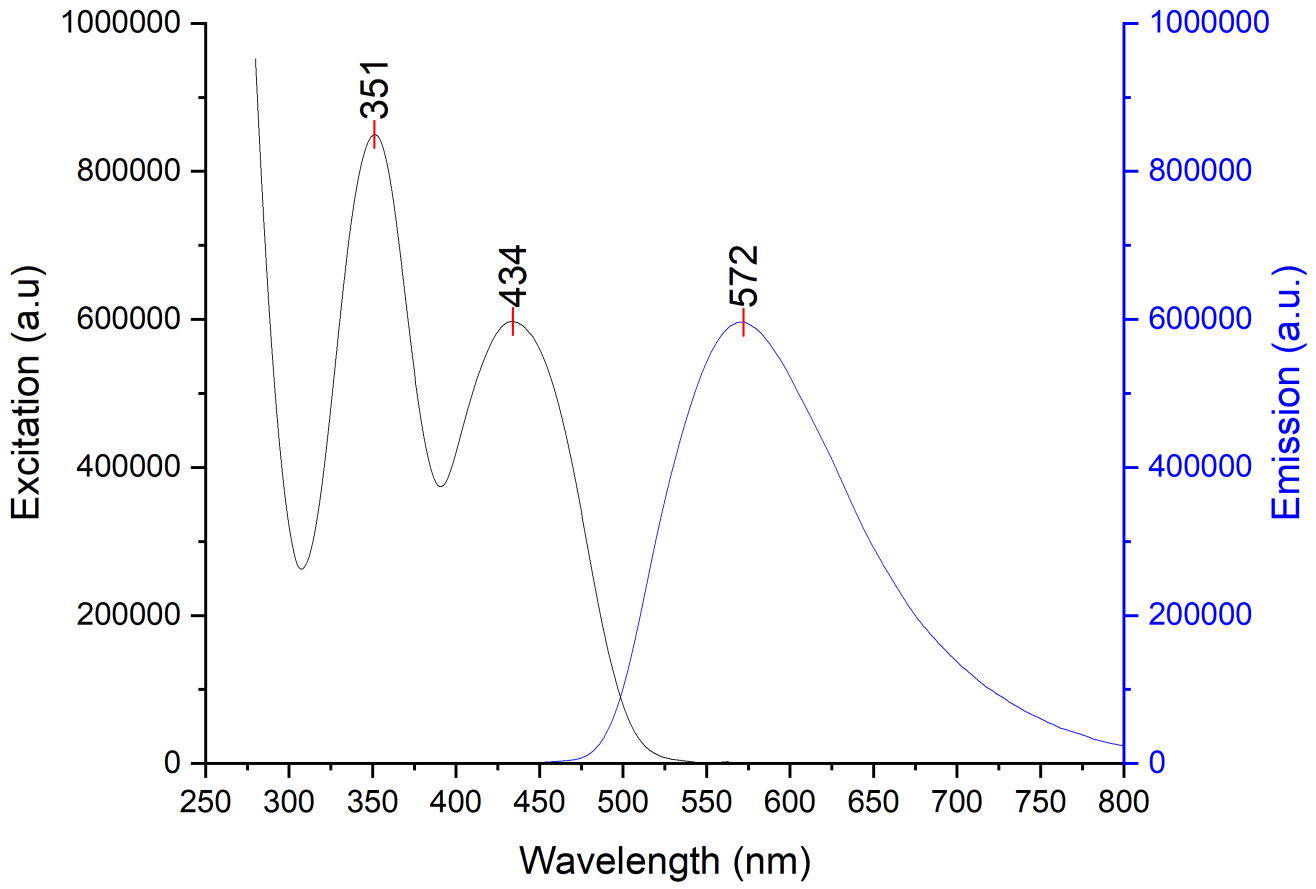

Figure 6-179. Stacked excitation (step: 1.0 nm/s, dwell time: 0.125 s, slit width: 1.0 nm) and emission (step: 1.0 nm/s, dwell time: 0.125 s, slit width: 1.0 nm) spectra of probe 7 and $[Et_3Si][B(C_6F_5)_4]$ in DCM; 12.5 µM sample.

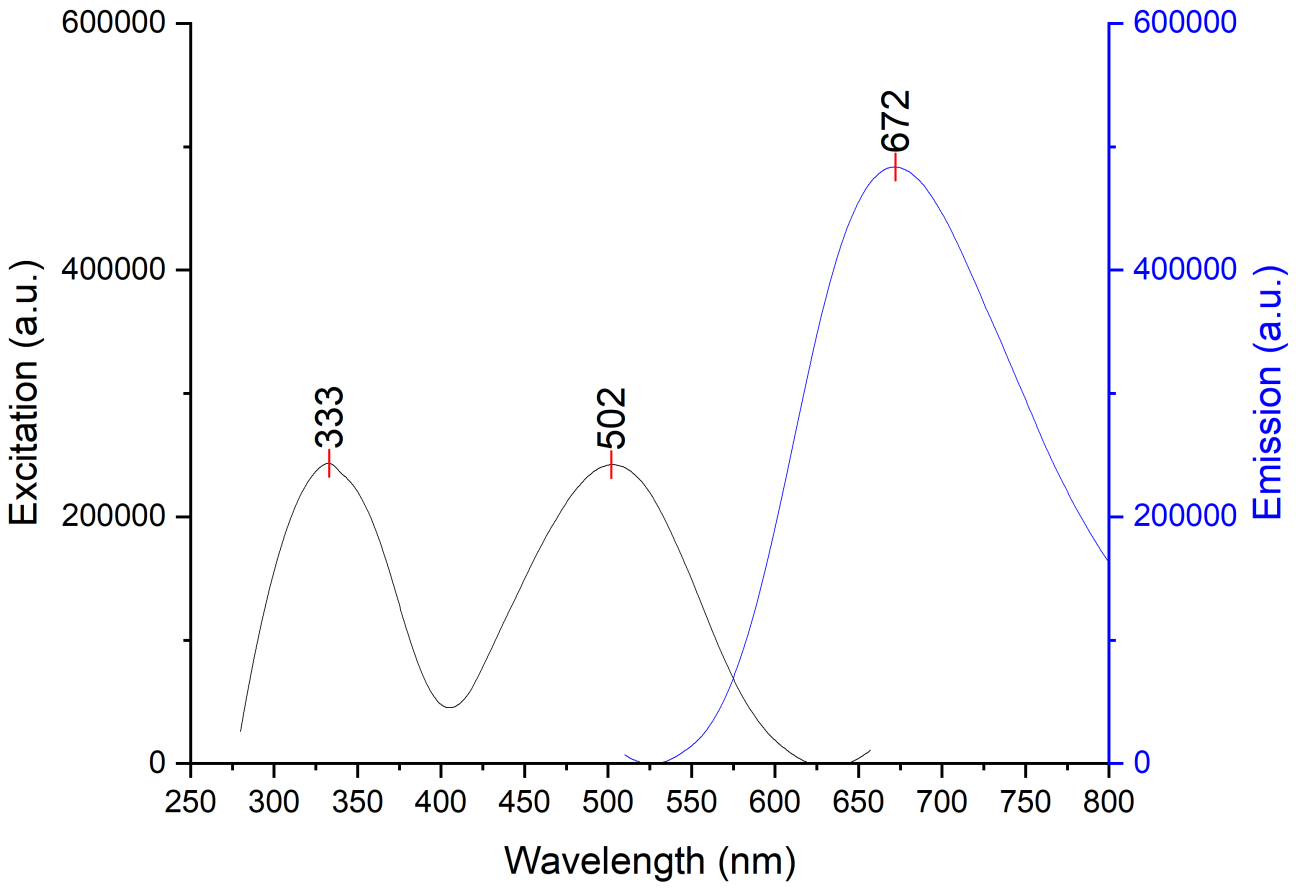

Figure 6-180. Stacked excitation (step: 1.0 nm/s, dwell time: 0.125 s, slit width: 1.0 nm) and emission (step: 1.0 nm/s, dwell time: 0.125 s, slit width: 1.0 nm) spectra of probe 8 and $[Et_3Si][B(C_6F_5)_4]$ in PhCl; 12.5 μM sample.

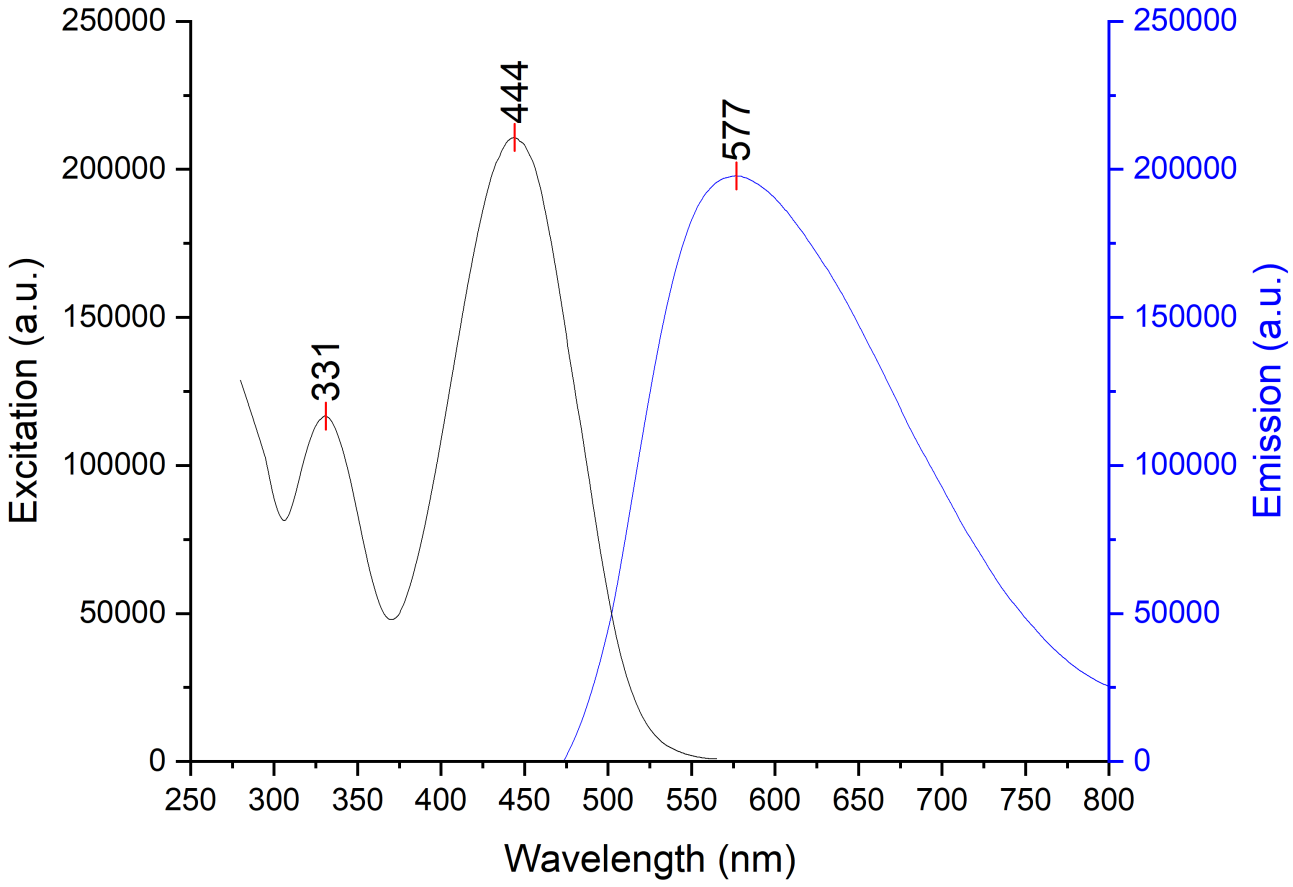

Figure 6-181. Stacked excitation (step: 1.0 nm/s, dwell time: 0.125 s, slit width: 1.0 nm) and emission (step: 1.0 nm/s, dwell time: 0.125 s, slit width: 1.0 nm) spectra of probe 8 and $[Et_3Si][B(C_6F_5)_4]$ in Et_2O; 12.5 µM sample.

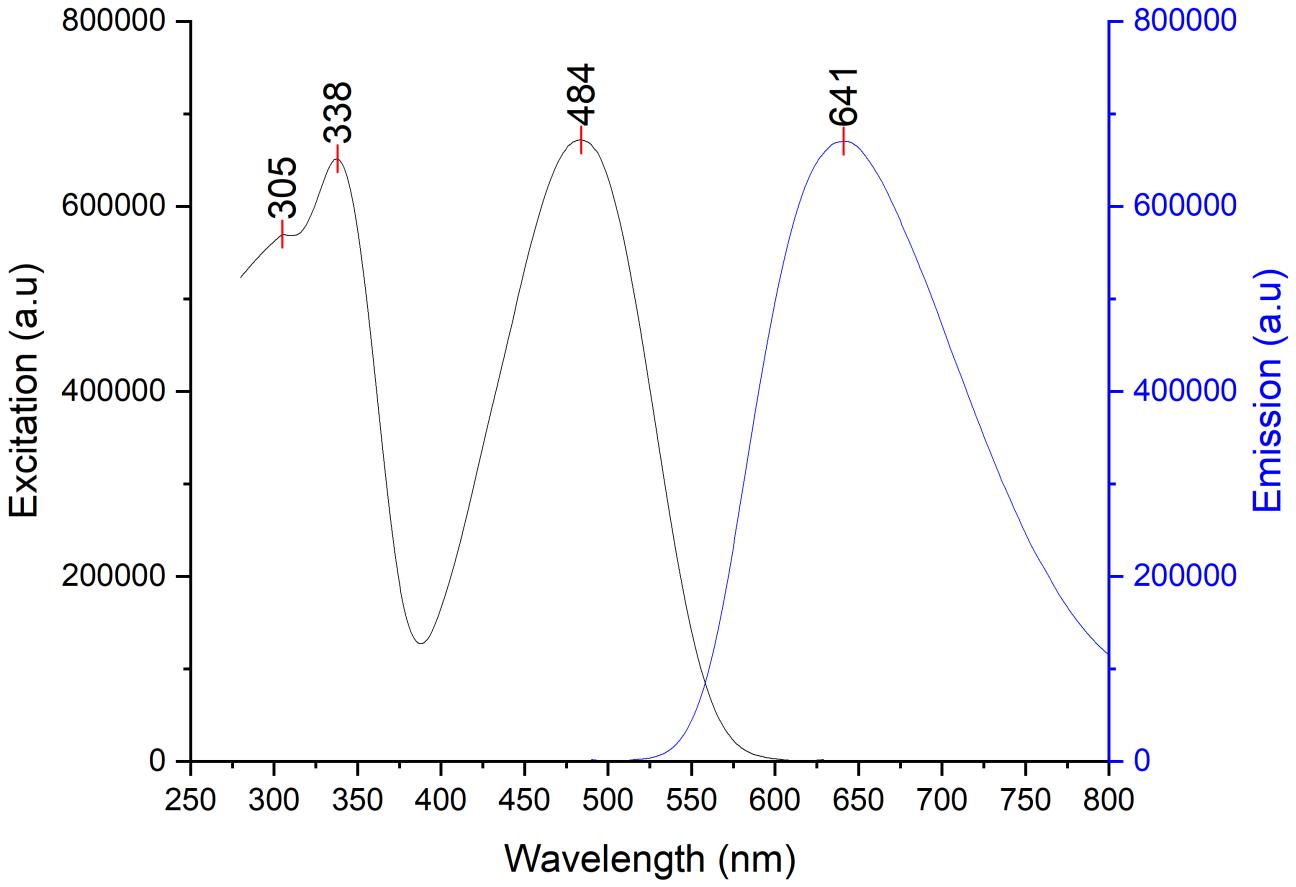

Figure 6-182. Stacked excitation (step: 1.0 nm/s, dwell time: 0.125 s, slit width: 1.0 nm) and emission (step: 1.0 nm/s, dwell time: 0.125 s, slit width: 1.0 nm) spectra of probe 8 and $[Et_3Si][B(C_6F_5)_4]$ in DCM; 12.5 µM sample.

6.3. Titration Data

6.3.1. Binding Constants

Table 6-8. Binding constants and equilibrium concentrations of $B(C_6F_5)_3$ in varying polar solvents with probes **1**, **2**, **7**, **8**.

Solvent	Probe	Equilibrium [$B(C_6F_5)_3$] (M)	Binding Constant, **K** (M^{-1})
Toluene	1	1.04×10^{-5}	106,079
	2	1.14×10^{-5}	97,832
	7	1.00×10^{-5}	66,518
	8	1.46×10^{-5}	54,646
Chlorobenzene	1	2.91×10^{-5}	31,487
	2	2.62×10^{-5}	40,394
	7	2.79×10^{-5}	38,801
	8	4.16×10^{-5}	24,083
Methylene Chloride	1	3.56×10^{-5}	26,508
	2	1.80×10^{-5}	52,525
	7	6.31×10^{-5}	14,230
	8	3.53×10^{-5}	28,923
Diethyl Ether	1	9.67×10^{-5}	3,776
	2	1.01×10^{-5}	2,540
		2.87×10^{-5}	1,438
	7	6.25×10^{-4}	2,521
		1.11×10^{-3}	1,024
	8	7.18×10^{-5}	20,648
		7.99×10^{-4}	1,275
Acetonitrile	1	--	--
	2	--	--
	7	--	--
	8	--	--

6.3.2. Stacked Emission Spectra

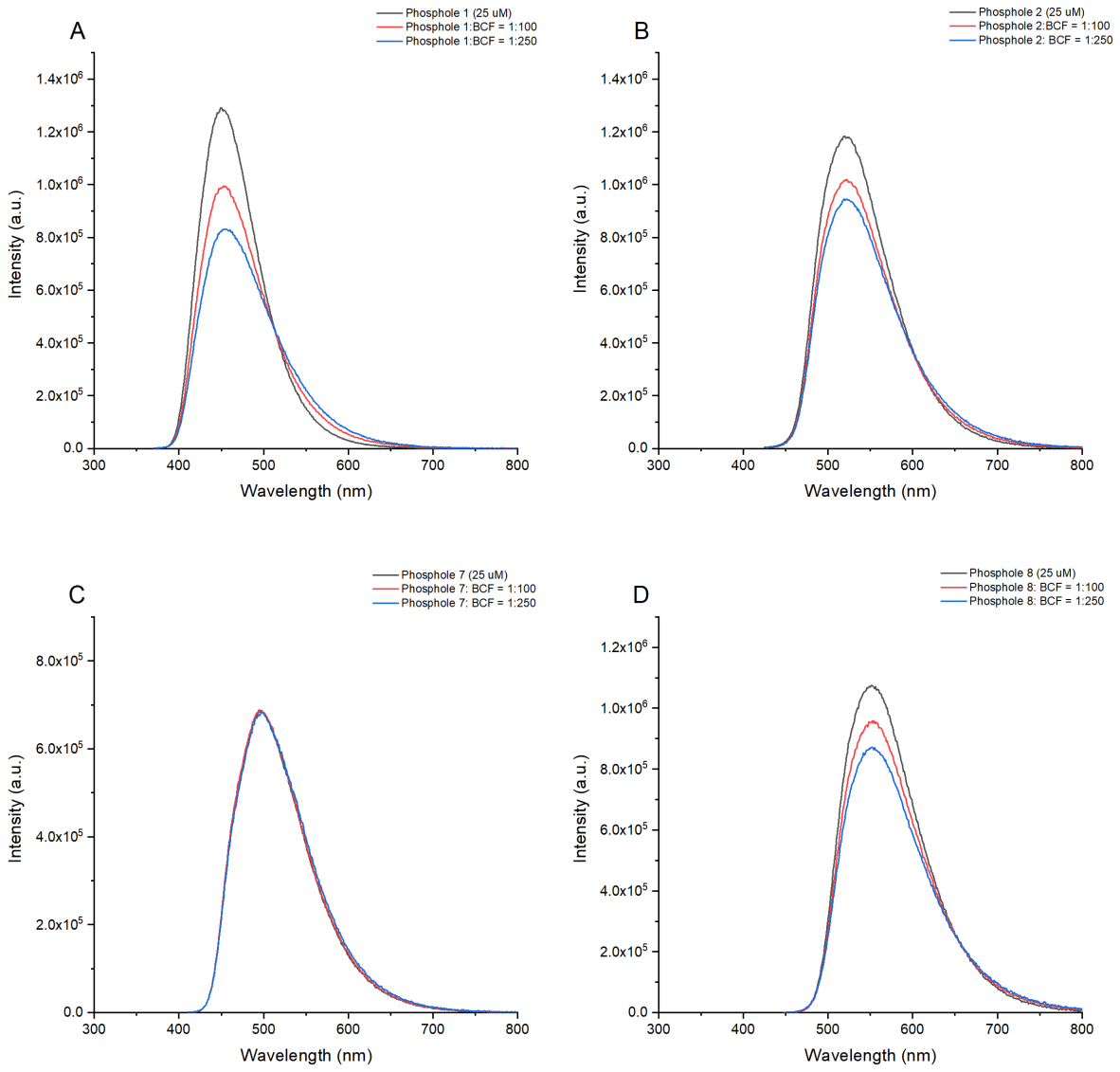

Figure 6-183. Stacked emission spectra of the titration of $B(C_6F_5)_3$ in acetonitrile with probes a) 1, b) 2, c) 7, and d) 8.

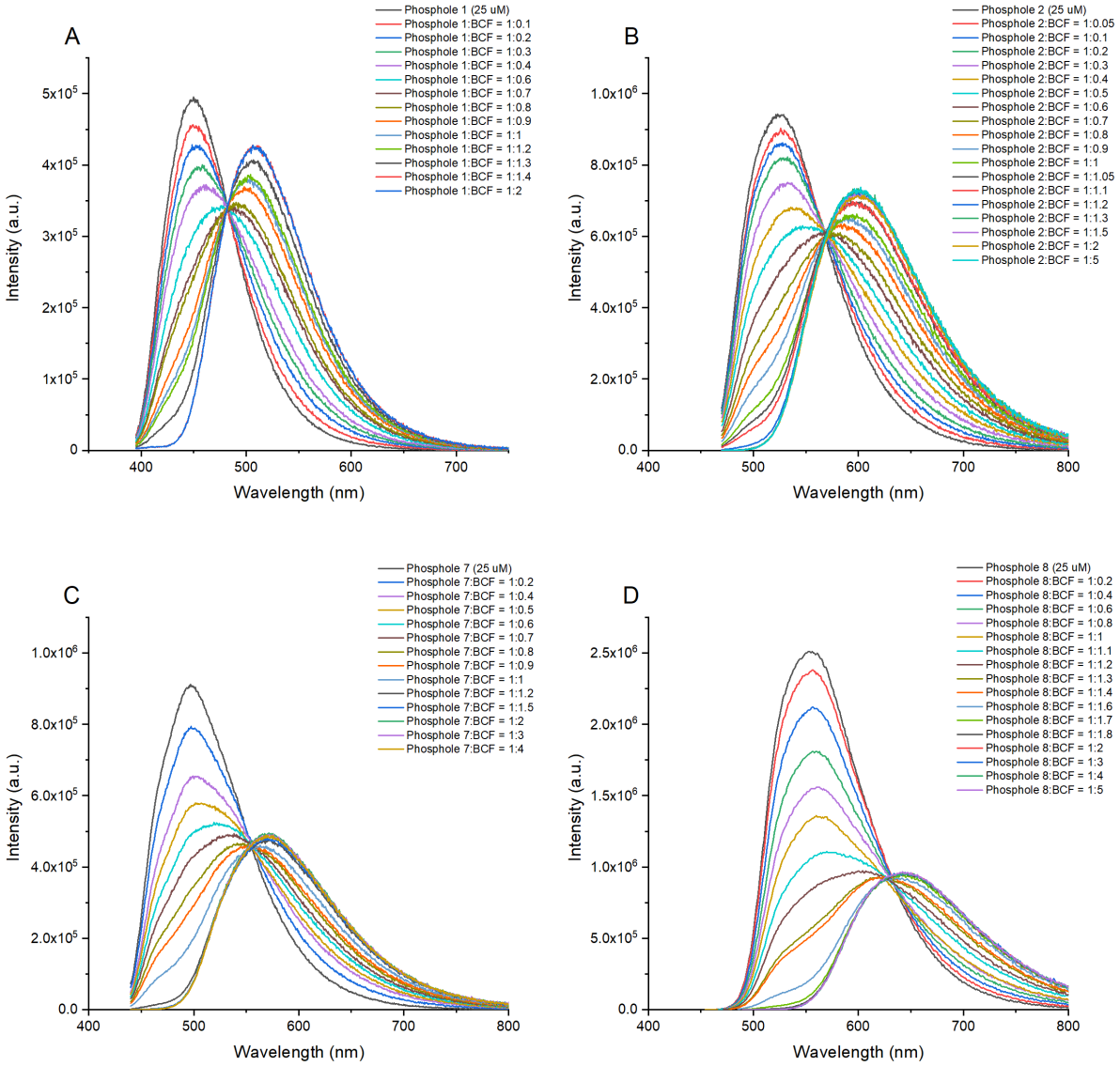

Figure 6-184. Stacked emission spectra of the titration of $B(C_6F_5)_3$ in PhCl with probes a) 1, b) 2, c) 7, and d) 8.

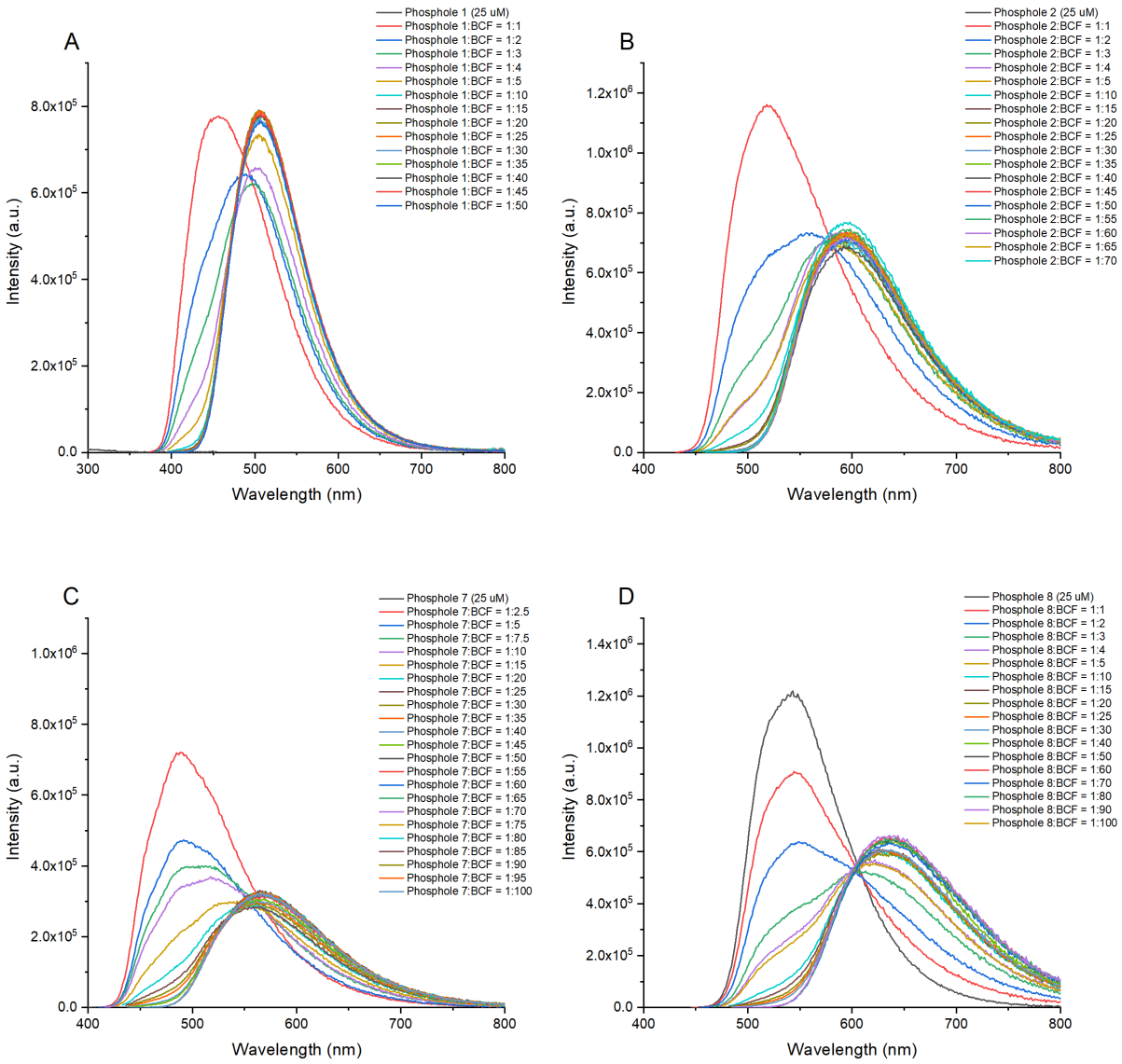

Figure 6-185. Stacked emission spectra of the titration of $B(C_6F_5)_3$ in Et_2O with probes a) 1, b) 2, c) 7, and d) 8.

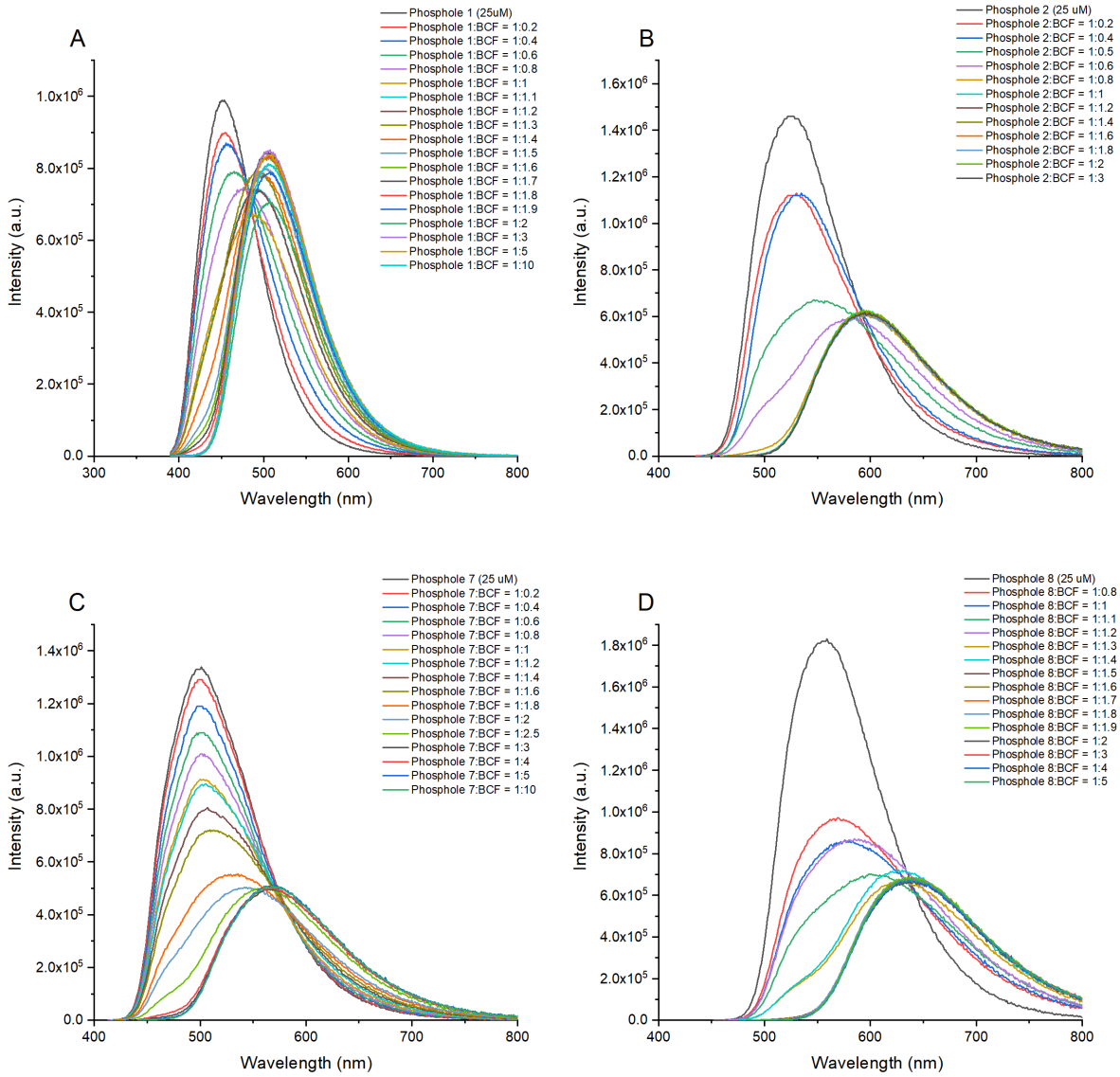

Figure 6-186. Stacked emission spectra of the titration of $B(C_6F_5)_3$ in DCM with probes a) 1, b) 2, c) 7, and d) 8.

6.3.3. Sigmoidal Fits

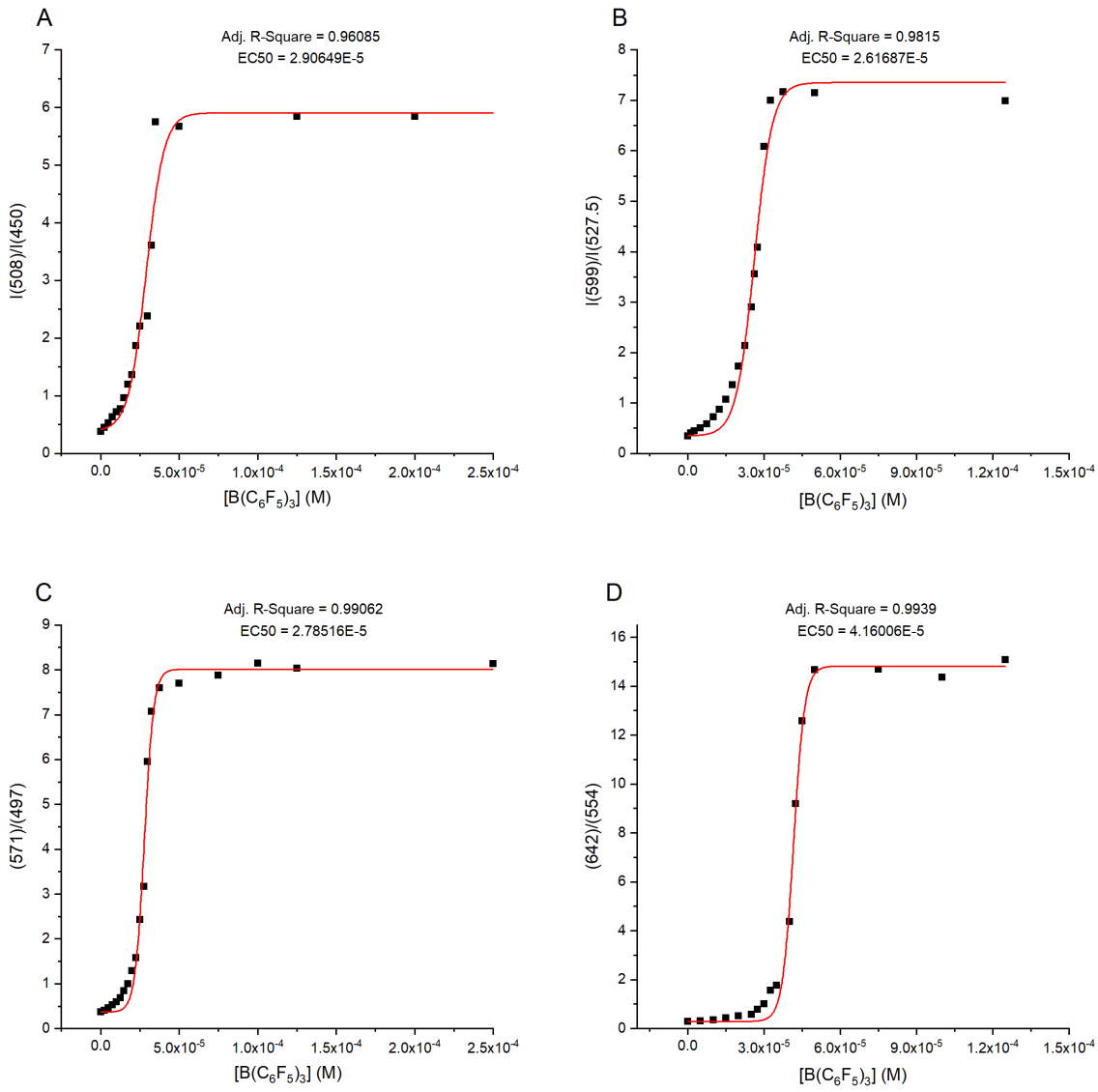

Figure 6-187. Sigmoidal fit of the titration of $B(C_6F_5)_3$ in PhCl with probes a) 1, b) 2, c) 7, and d) 8.

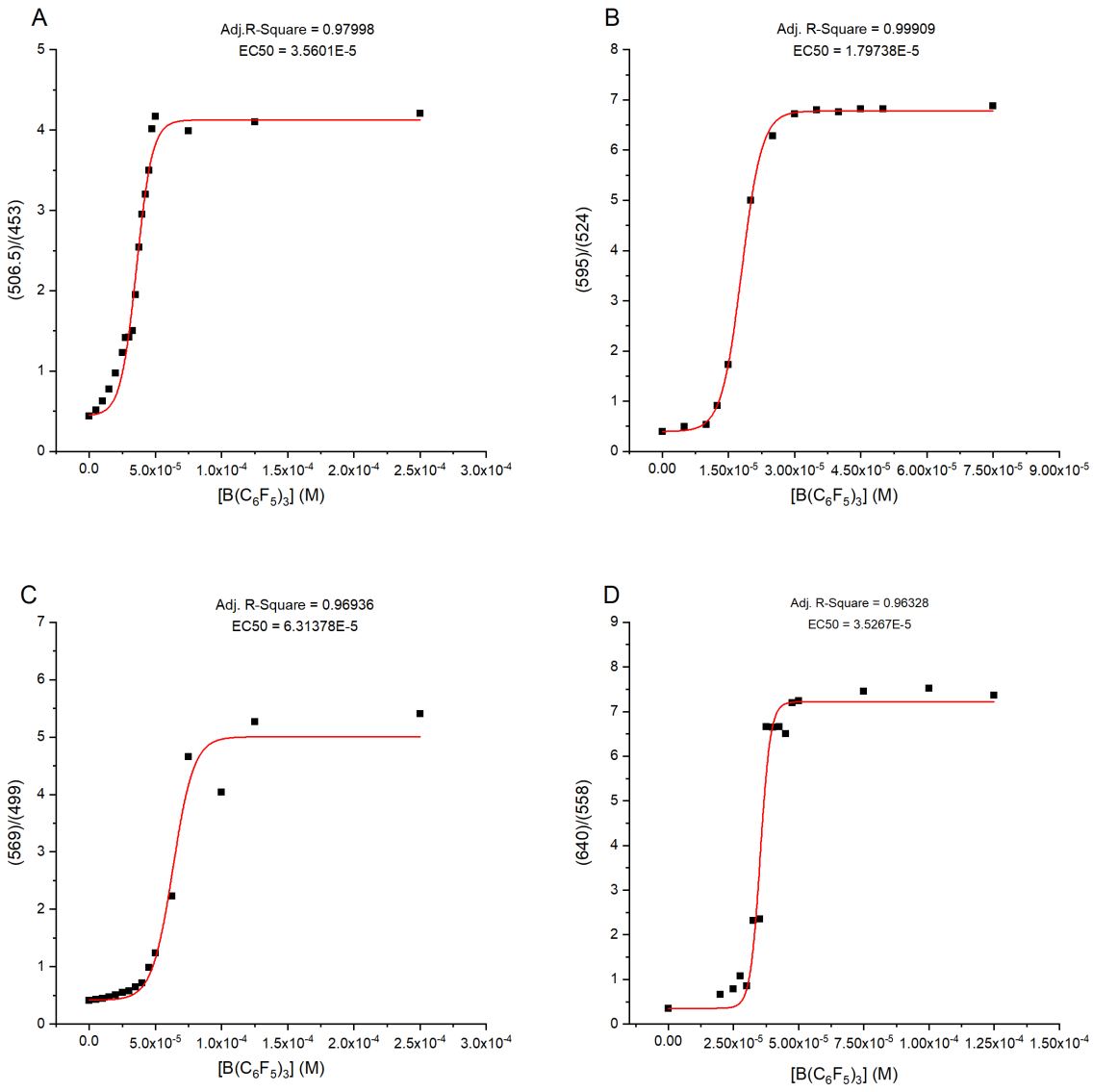

Figure 6-188. Sigmoidal fit of the titration of $B(C_6F_5)_3$ in DCM with probes a) 1, b) 2, c) 7, and d) 8.

6.4. Chemical Reactivity Data

6.4.1. Reaction Monitoring

6.4.1.1. Diels-Alder Cycloaddition

*No product formation observed in the Diels-alder cycloaddition over 6 hours with B(4-F-C_6F_4)$_3$, B(3,4-F_2-C_6F_3)$_3$, and Zn(OTf)$_2$.

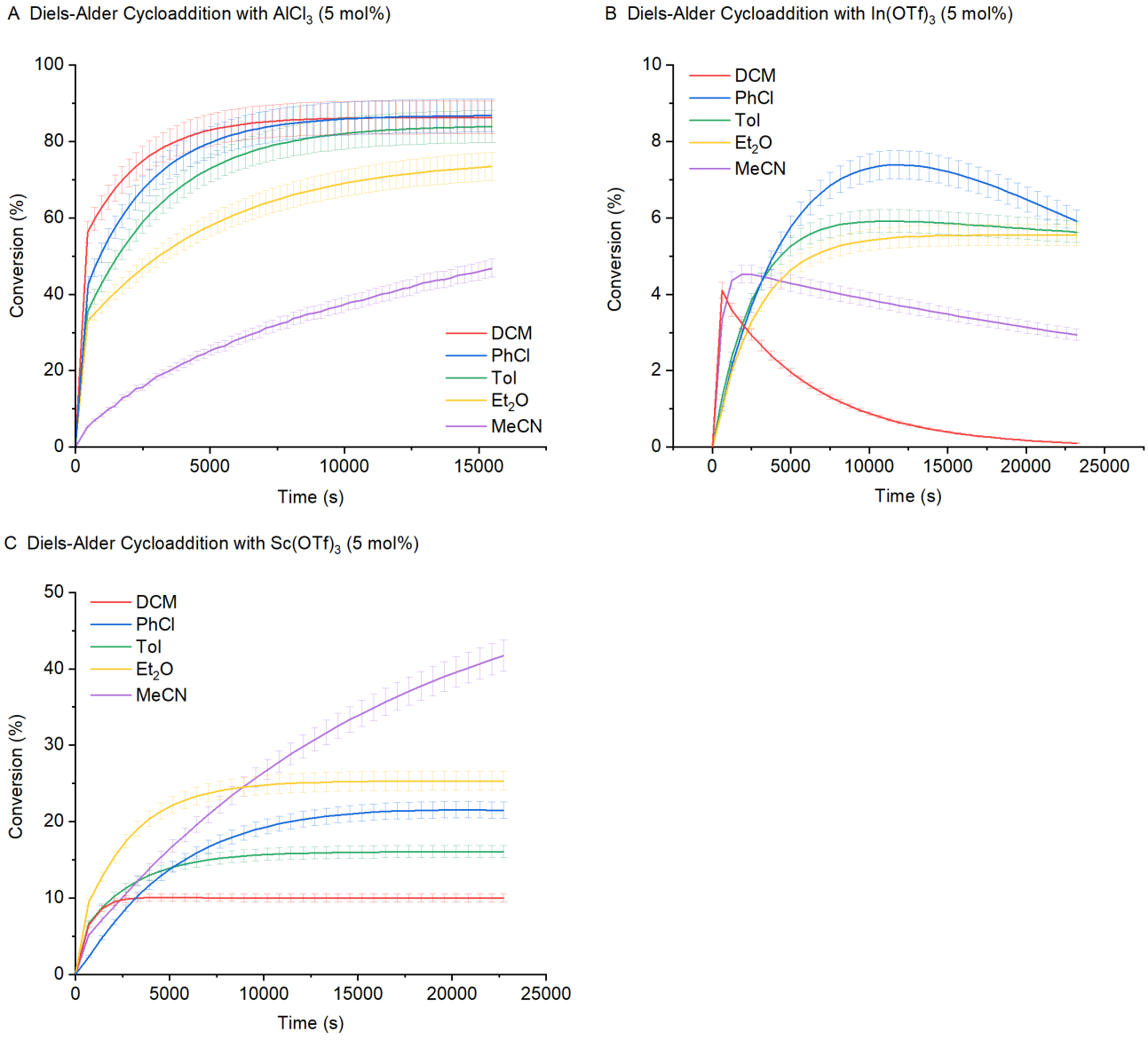

Figure 6-189. Product conversion for the Diels-Alder cycloaddition over 6 hours in varying polar solvents with different Lewis acid catalysts: a) $AlCl_3$, b) In(OTf)$_3$, and c) Sc(OTf)$_3$.

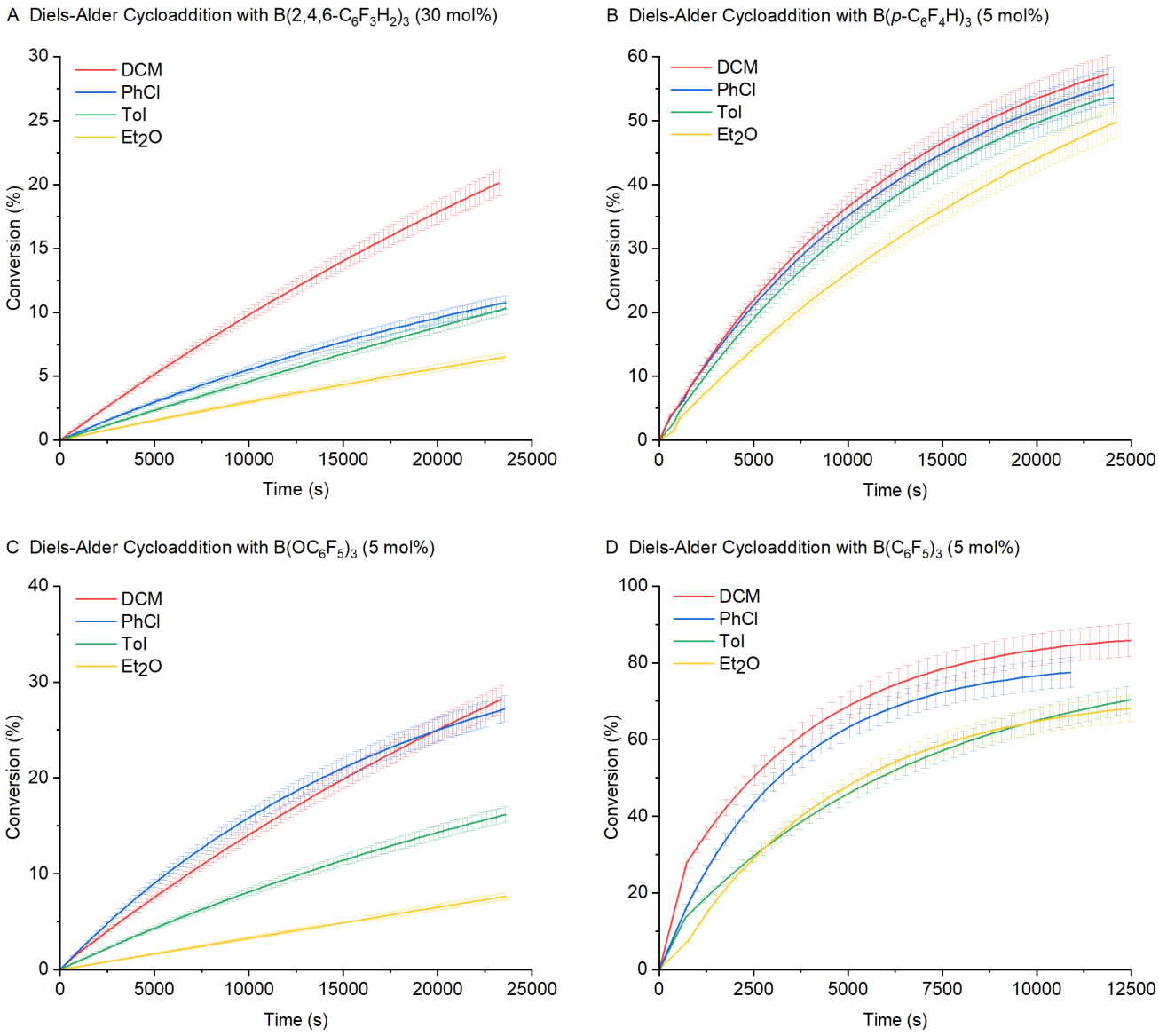

Figure 6-190. Product conversion for the Diels-Alder cycloaddition over 6 hours in varying polar solvents, with different Lewis acid catalysts: a) B(2,4,6-F_3-C_6H_2)$_3$, b) B(*p*-F_4-C_6H)$_3$, c) B(OC_6F_5)$_3$, and d) B(C_6F_5)$_3$.

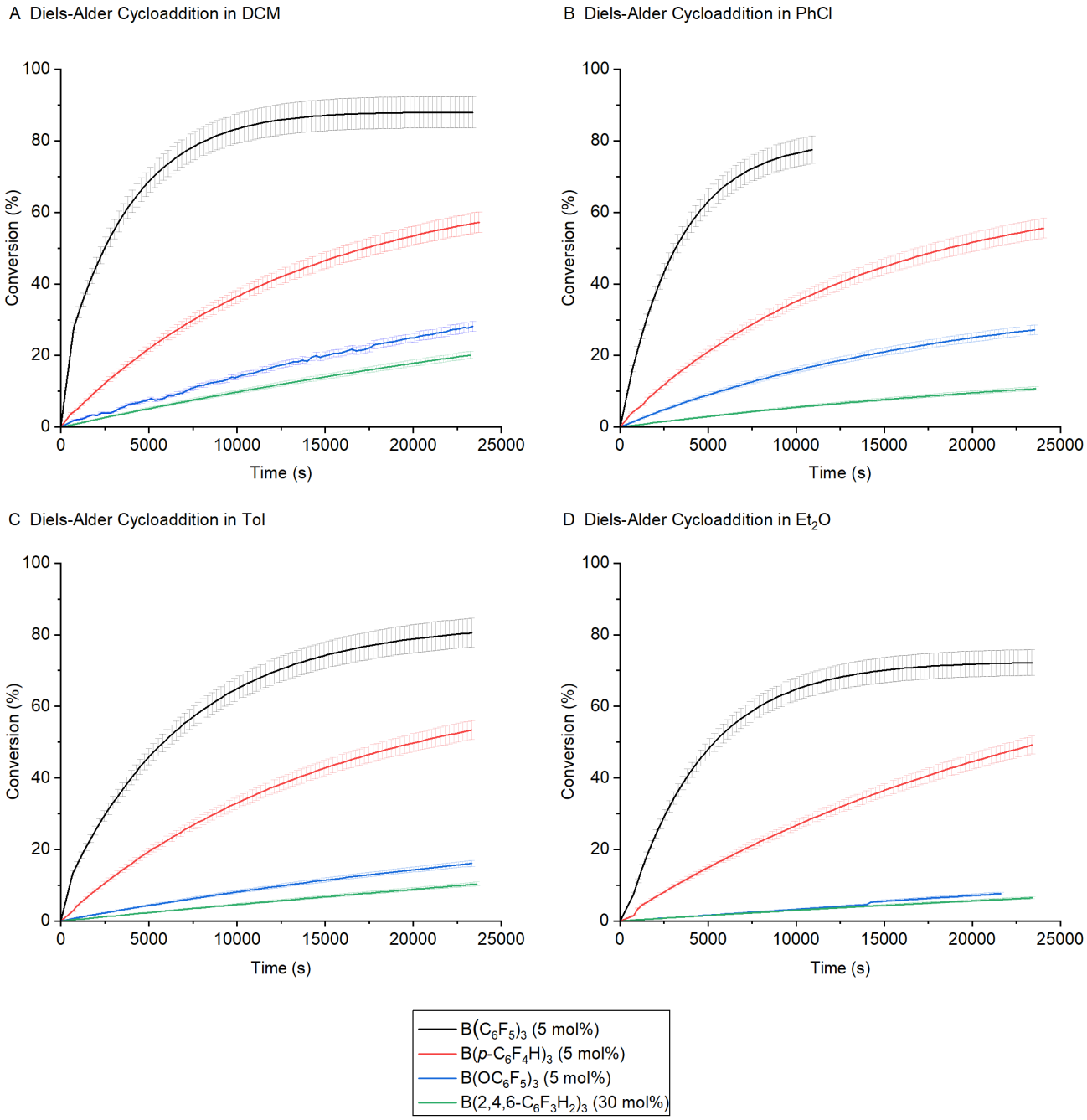

Figure 6-191. Product conversion for the Diels-Alder cycloaddition over 6 hours with $B(C_6F_5)_3$, $B(p\text{-}F_4\text{-}C_6H)_3$, $B(OC_6F_5)_3$, and $B(2,4,6\text{-}F_3\text{-}C_6H_2)_3$ in a) DCM, b) PhCl, c) Tol, and d) Et_2O.

6.4.1.2. Hydrosilylation

*No product formation observed in the hydrosilylation of benzophenone over 1 hour with $AlCl_3$, B(4-F-C_6F_4)$_3$, B(OC_6F_5)$_3$, In(OTf)$_3$, Sc(OTf)$_3$, and Zn(OTf)$_2$.

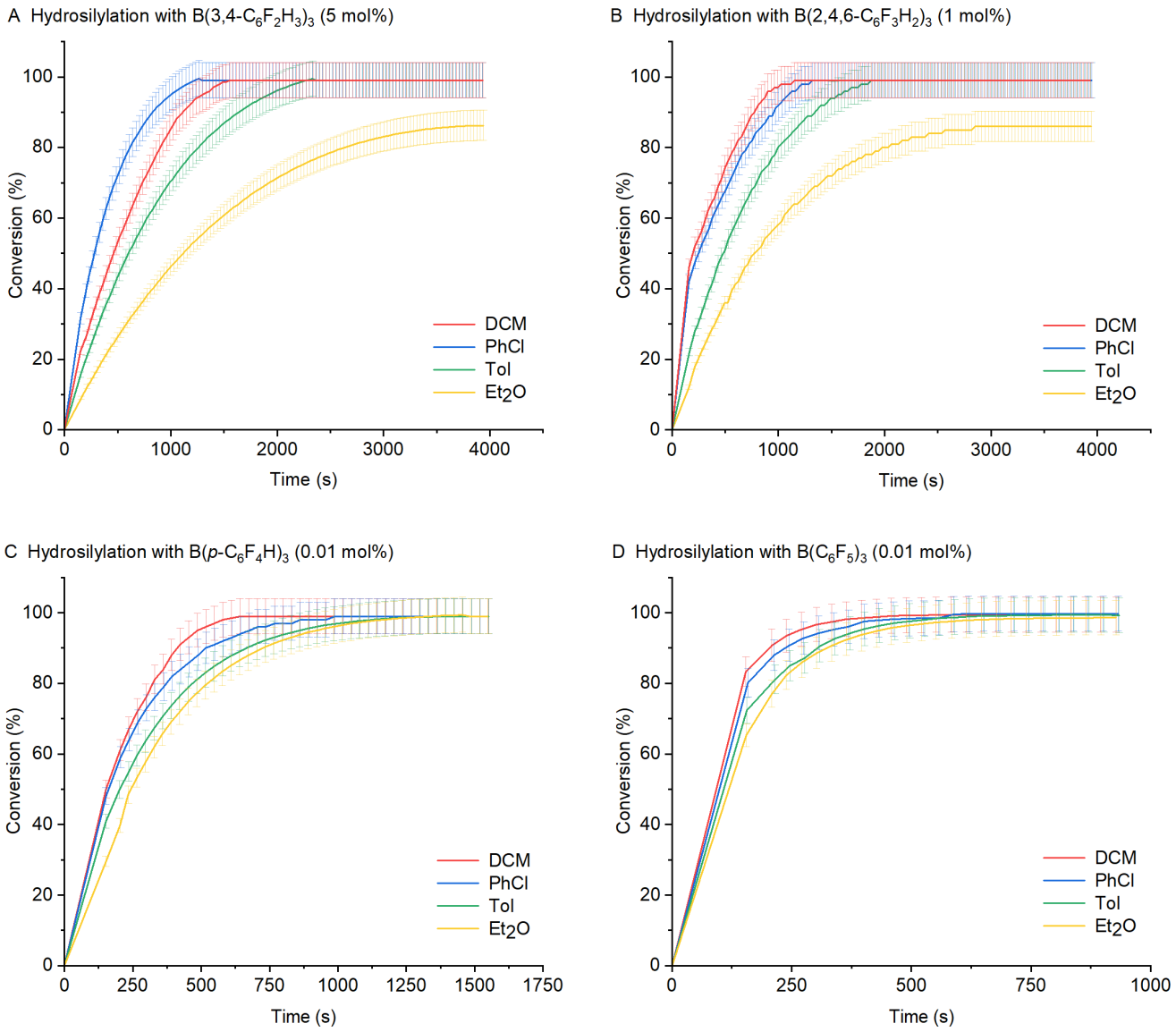

Figure 6-192. Product conversion for the hydrosilylation of benzophenone over 1 hour in varying polar solvents with different Lewis acid catalysts: a) B(3,4-F_2-C_6H_3)$_3$, b) B(2,4,6-F_3-C_6H_2)$_3$, c) B(*p*-F_4-C_6H)$_3$, and d) B(C_6F_5)$_3$.

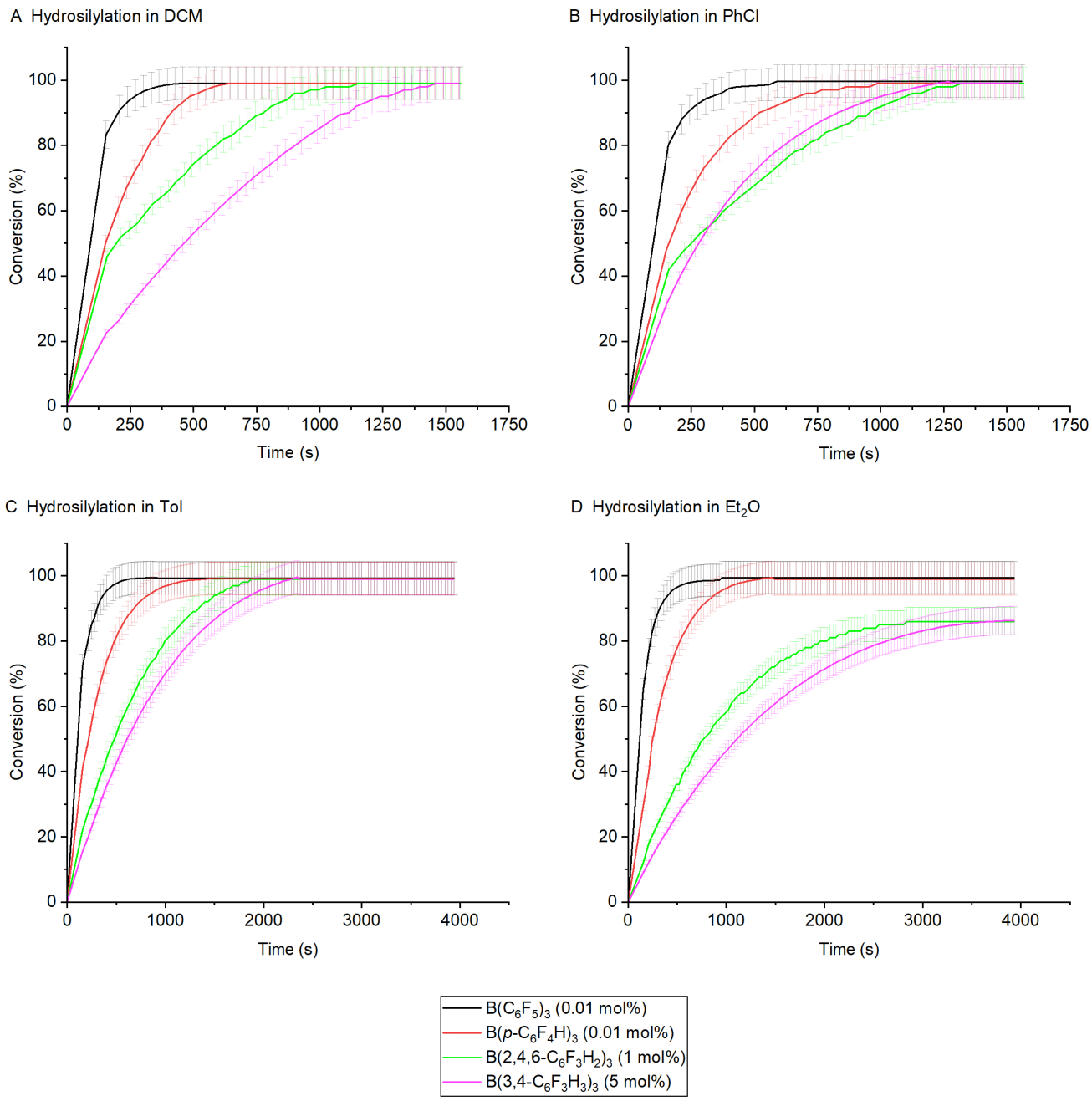

Figure 6-193. Product conversion for the hydrosilylation of benzophenone with $B(C_6F_5)_3$, $B(p\text{-}F_4\text{-}C_6H)_3$, $B(2,4,6\text{-}F_3\text{-}C_6H_2)_3$, and $B(3,4\text{-}F_2\text{-}C_6H_3)_3$ in a) DCM over 25 minutes, b) PhCl over 25 minutes c) Tol over 1 hour, and d) Et_2O over 1 hour.

6.5. Reaction Kinetics

6.5.1. Rate Constants

Table 6-9. Rate constants calculated for the Diels-Alder cycloaddition, utilizing Lewis acid catalysts in various solvents.

Catalyst	Catalyst loading (mol%)	Solvent	Rate Constant, **k** ($M^{-1}s^{-1}$)
$B(OC_6F_5)_3$	5.0	Et_2O	$0.0091 \pm 9.444E^{-4}$
$B(2,4,6\text{-}F_3\text{-}C_6H_2)_3$	30.0	Toluene	0.00122 ± 0.00532
$B(OC_6F_5)_3$	5.0	PhCl	0.00722 ± 0.00422
$B(2,4,6\text{-}F_3\text{-}C_6H_2)_3$	30.0	CH_2Cl_2	$0.00595 \pm 9.981E^{-4}$
$B(p\text{-}C_6F_4H)_3$	5.0	CH_2Cl_2	$0.05004 \pm 5.945E^{-18}$
$B(C_6F_5)_3$	5.0	CH_2Cl_2	1^{st}: 0.16079 ± 0.00425 2^{nd}: 0.1216 ± 0.01895
$B(p\text{-}C_6F_4H)_3$	5.0	Et_2O	0.03234 ± 0.00173
$B(p\text{-}C_6F_4H)_3$	5.0	Toluene	0.04574 ± 0.00166
$B(OC_6F_5)_3$	5.0	Toluene	$0.00401 \pm 5.836E^{-4}$

6.5.2. Determination of Rate Constants

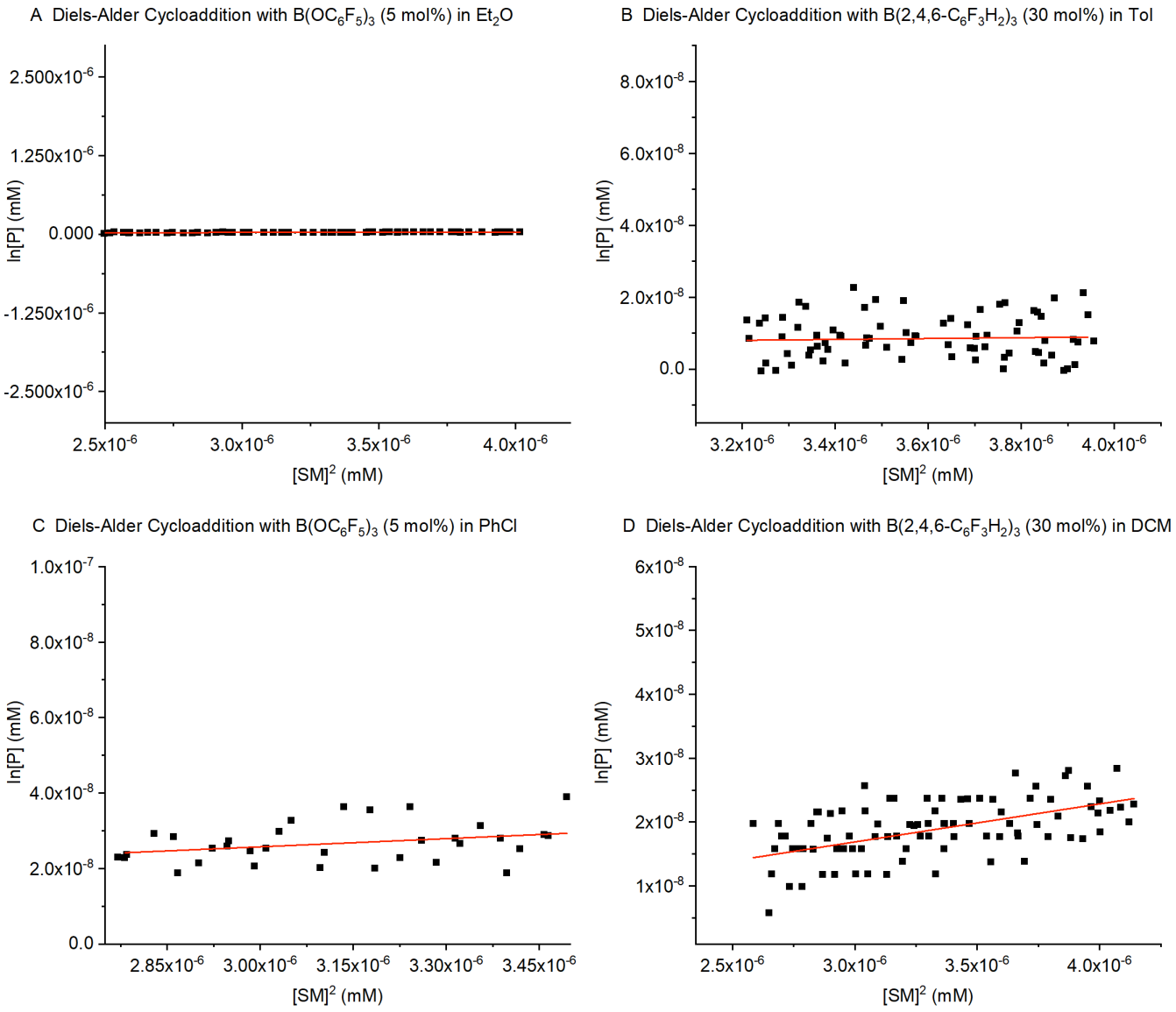

Figure 6-194. Plot of first derivative of the product concentration versus the concentration of starting material squared for the Diels-Alder cycloaddition, rate constant determined by slope: a) $B(OC_6F_5)_3$ in Et_2O, b) $B(2,4,6\text{-}C_6F_3H_2)_3$ in Tol, c) $B(OC_6F_5)_3$ in PhCl, and d) $B(2,4,6\text{-}C_6F_3H_2)_3$ in DCM.

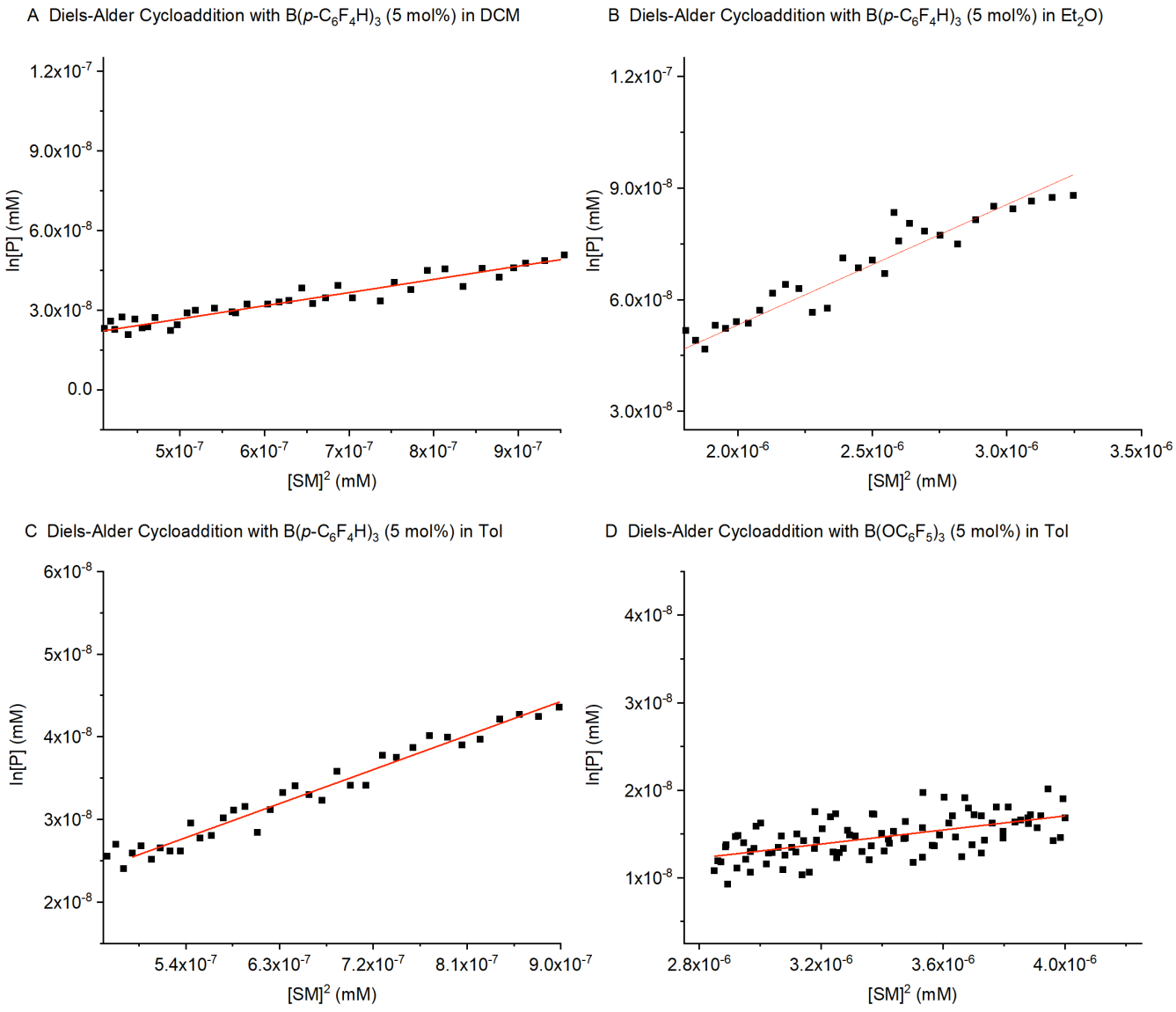

Figure 6-195. Plot of first derivative of the product concentration versus the concentration of starting material squared for the Diels-Alder cycloaddition, rate constant determined by slope: a) B(p-F_4-C_6H)$_3$ in DCM, b) B(p-F_4-C_6H)$_3$ in Et_2O, c) B(p-F_4-C_6H)$_3$ in Tol, and d) B(OC_6F_5)$_3$ in Tol.